

J.F. SEMBLAT, A. PECKER

**Waves and Vibrations in Soils:
Earthquakes, Traffic, Shocks,
Construction works**



SEMLAT
PECKER

Waves and Vibrations in Soils:
Earthquakes, Traffic, Shocks,
Construction works

1x M 644256 O-1-2
Houtschild International Booksellers

Waves and Vibrations in Soils. Earthquakes,



000186015900476070010010544256

mpsmn
551
2009
WAV

120,00
euro

@Seismicisolation



IUSS Press

Istituto Universitario di Studi Superiori di Pavia

JEAN-FRANÇOIS SEMBLAT

Jean-François Semblat is Head of the Dynamics, Waves and Vibrations unit in the Division for Soil and Rock Mechanics at Laboratoire Central des Ponts et Chaussées (Paris, France) and Associate Professor at Ecole Polytechnique (Palaiseau, France). He has published over 100 technical papers in journals and conferences. He is on the editorial board of the International Journal of Geomechanics (ASCE) and European Journal of Environmental and Civil Engineering. He is member of the Scientific Committees of the French Association for Earthquake Eng. and the French Society of Soil Mechanics and Geotechnical Engineering. He is member of the board of the International Association for Computer Methods and Advances in Geomechanics and is associate member of the American Society of Civil Engineers (ASCE). He has received several awards for his work: French Association for Earthquake Eng., European Association of Geoscientists and Eng., International Association for Computer Methods in Geomechanics.

ALAIN PECKER

Alain Pecker is Chairman and Managing Director of Géodynamique Structure, Professor at Ecole Nationale des Ponts et Chaussées and visiting Faculty at the Centre for Post-Graduate Training and Research in Earthquake Engineering and Engineering Seismology (DSE School, IUSS Pavia). He is member of the French National Academy of Technologies, Honorary President of the French Association for Earthquake Engineering, Past President of the French Society of Soil Mechanics and Geotechnical Engineering, President of the French Committee for Seismic Building Codes. He is also a member of several international technical committees dealing with earthquake geotechnical engineering. He has also published over 80 technical papers in journals and conferences and has been invited as a Master or State of the Art speaker in several international events. He is on the editorial boards of three international journals. He has received several awards for his work, among which one from the French National Academy of Sciences.

OBJECTIVE OF THE BOOK

The main scientific and engineering goal of this book is to deal simultaneously with soil dynamics/vibrations and wave propagation in soils (including seismic waves). These various fields are generally considered separately and the important links between them, both from scientific and practical points of view, are unfortunately not investigated. They are usually considered in separate disciplines such as earthquake geotechnical engineering, civil engineering, mechanics, geophysics, seismology, numerical modelling, etc.

The objective of the book is to offer in a single publication an overview of soil dynamics and wave propagation in soils with emphasis on engineering applications. It starts from a wide variety of practical problems (e.g. traffic induced vibrations, dynamic compaction, vibration isolation), then deals with 1D and 2D/3D wave propagation in heterogeneous and attenuating media (with application to laboratory and in situ dynamic characterization of soils), gives an overview of various numerical methods (e.g. FEM, BEM) to simulate wave propagation (including numerical errors, radiation/absorbing conditions, etc) and finally investigates seismic wave propagation and amplification in complex geological structures (e.g. irregular topographies, alluvial deposits).

Contents

Nessuna parte di questa pubblicazione può essere riprodotta o trasmessa in qualsiasi forma o con qualsiasi mezzo elettronico, meccanico o altro senza l'autorizzazione scritta dei proprietari dei diritti e dell'editore.

No parts of this publication may be copied or transmitted in any shape or form, and by any type of electronic, mechanical or different means, without the prior written permission of the copyright holder and the publisher.

©Copyright 2009 - IUSS Press

prodotto e distribuito da:
produced and distributed by:

Fondazione EUCENTRE
Via Ferrata 1 - 27100 Pavia, Italy
Tel.: (+39) 0382.516911 - fax: (+39) 0382.529131
Email: info@iusspress.it - web: www.iusspress.it

ISBN: 978-88-6198-030-3

UNIVERSITY OF W.A.
LIBRARY

Introduction	11
Acknowledgements	13
List of symbols	15
1 Waves and vibrations in soils	19
1.1 Various fields and applications	19
1.2 Vibrations due to construction works	20
1.2.1 Pile driving	20
1.2.2 Dynamic compaction	24
1.2.3 Vibratory compaction	28
1.3 Vibrations induced by wind turbines	31
1.4 Blast induced vibrations	33
1.4.1 Vibrations induced in mines	33
1.4.2 Vibrations induced in quarries	34
1.5 Traffic induced vibrations	36
1.5.1 Vibrations due to road traffic	36
1.5.2 Vibrations due to railways	39
1.5.3 Theoretical analysis of moving loads	40
1.6 Vibration isolation	42
1.6.1 Practical problem	42
1.6.2 Experimental results	44
1.6.3 Numerical models	44
1.6.4 Values of the mechanical parameters	48
1.7 Earthquake engineering and seismology	49
1.7.1 Analysis at various scales	49
1.7.2 Seismic wave propagation in soils	50
1.7.3 Values of the mechanical parameters	51
1.8 Synthesis of the various parameters	52

2 1D-wave propagation	53
2.1 Introduction	53
2.2 Dynamic equilibrium of a beam	53
2.2.1 Kinematics and main assumptions	53
2.2.2 Virtual rate of work by internal forces	54
2.2.3 Virtual rate of work by external forces	56
2.2.4 Virtual rate of work by quantities of acceleration	57
2.2.5 Equilibrium equation	57
2.3 Longitudinal vibrations of beams	59
2.3.1 Dynamic equilibrium	59
2.3.2 Homogeneous equation	60
2.3.3 Solution in terms of stresses	62
2.3.4 Eigenmodes of the bar	62
2.3.5 Example 1: pile driving	64
2.3.6 Example 2: characterization of a heterogeneous bar	68
2.3.7 Absorbing boundaries	70
2.4 Torsional vibrations of beams	71
2.4.1 Dynamic equilibrium	71
2.4.2 Homogeneous equation	72
2.4.3 Stresses in the beam	73
2.4.4 Eigenmodes of the beam	73
2.5 Shear vibrations of beams	75
2.5.1 Bending-shear vibrations	75
2.5.2 From bending-shear to pure shear	75
2.6 Behaviour of dissipative media	76
2.6.1 Dissipative phenomena	76
2.6.2 Viscoelastic behaviour	76
2.6.3 Rheological models	79
2.7 Wave propagation in viscoelastic media	84
2.7.1 Dynamic equilibrium	84
2.7.2 Viscoelastic behaviour	84
2.7.3 Wave equation in viscoelastic media	85
2.7.4 Complex wavenumber	85
2.7.5 Relationship between α and Q^{-1}	86
2.7.6 Dispersion laws	87
2.8 Examples of propagation in viscoelastic media	88
2.8.1 Example 1 : propagation of a triangular signal	88
2.8.2 Example 2 : propagation of a seismic wave.	91
2.9 Other linear and nonlinear models	91
2.9.1 Constant Q (CQ) model	91
2.9.2 Frequency dependent Q model	92
2.9.3 Nearly Constant Q (NCQ) model	92
2.9.4 Equivalent linear viscoelasticity	94
2.9.5 Frequency dependent models	95
2.9.6 Nonlinear viscoelastic models	96

2.10 Application 1: dynamic characterization on resonant column	97
2.10.1 Principles of the test	97
2.10.2 Description of the specimen motion	98
2.10.3 Actual resonant column test	99
2.10.4 Estimation of damping	101
2.10.5 Results from resonant column tests	102
2.11 Application 2: dynamic characterization under fast loadings	103
2.11.1 Split Hopkinson Pressure Bar test	103
2.11.2 Experimental device	104
2.11.3 Stress wave in the specimen	104
2.11.4 Determination of the mechanical parameters	106
2.11.5 3D Split Hopkinson Pressure Bar test	108
2.11.6 3D fast dynamic response of sand	110
2.12 Application 3: response of a heterogeneous soil profile	112
2.12.1 Soil behaviour	112
2.12.2 Wave equation for a heterogeneous profile	113
2.12.3 Boundary conditions	114
2.12.4 Eigenfrequencies and mode participation factors	118
2.13 Application 4: soil-structure interaction	119
2.13.1 Basic principles	119
2.13.2 Equations of motion for the soil	120
2.13.3 Case of a surface excitation	120
2.13.4 Influence of the wave velocity in the soil	122
2.14 Experimental estimation of damping	122
2.14.1 Various experimental methods	122
2.14.2 Methods for the estimation of attenuation	124
2.14.3 Definitions of attenuation: synthesis	125
2.14.4 Variations of attenuation	126
2.14.5 Characterization of the various approaches	127
2.14.6 Comparison of the governing parameters	127
3 2D/3D-wave propagation	131
3.1 Introduction	131
3.2 Dynamic equilibrium of a continuous medium	131
3.2.1 Equilibrium equation - principle of virtual work	132
3.2.2 Constitutive equation	133
3.2.3 Equilibrium equations in terms of displacements	134
3.2.4 Decomposition of the displacement field	134
3.2.5 Uncoupled wave equations	135
3.2.6 Body waves	135
3.2.7 Wave propagation in anisotropic media	137
3.3 Wave propagation in unbounded media	138
3.3.1 Wave equations for plane waves	138
3.3.2 Plane monochromatic waves	140
3.3.3 Reflection-refraction of plane waves at an interface	142

3.3.4	Plane waves in layered media: vibration isolation	152
3.4	Spherical waves	174
3.4.1	Wave equation	174
3.4.2	Solution wavefield	174
3.4.3	Geometrical damping	175
3.5	Waves in a homogeneous or heterogeneous half-space	176
3.5.1	Surface waves: <i>SH</i> case	176
3.5.2	Surface waves: <i>P/SV</i> case	177
3.5.3	Propagation of a plane <i>SH</i> -wave in a surface layer	180
3.5.4	Amplification of seismic waves in layered media	186
3.6	Application 1: waves in centrifuged models	188
3.6.1	Historical summary	188
3.6.2	Equivalence principle	188
3.6.3	Calculation of the scaling factors	189
3.6.4	Dynamic experiments in the centrifuge	190
3.6.5	Examples of dynamic centrifuge experiments	192
3.6.6	Analysis of the threedimensional wavefield	194
3.6.7	Modelling propagation in dissipative soils	196
3.6.8	Simulations for drop-ball experiments	199
3.6.9	Influence of frequency on attenuation factor	203
3.6.10	Numerical modelling of centrifuge experiments	204
3.6.11	Removing reflections by homomorphic filtering	206
3.6.12	Analysis of dispersion	207
3.7	Application 2: Spectral Analysis of Surface Waves and in situ tests	208
3.7.1	Dispersion of Love waves in a single-layered half-space	208
3.7.2	Dispersion of surface waves in a heterogeneous half-space	214
3.7.3	Steady State Rayleigh method	218
3.7.4	Spectral Analysis of Surface Waves: experiments	218
3.7.5	Seismic refraction	224
3.7.6	In-hole tests	226
3.7.7	Microtremor methods	235
3.7.8	Conclusions on field tests	236
4	Modelling wave propagation	239
4.1	Numerical methods for wave propagation	239
4.1.1	Modelling wave propagation	239
4.1.2	Numerical Modelling in Elastodynamics	240
4.1.3	Time domain vs frequency domain	240
4.1.4	Actual or synthetic signals	241
4.2	The Finite Element Method	246
4.2.1	Strong formulation	246
4.2.2	Weak formulation	247
4.2.3	Approximate minimization: Galerkin method	248
4.2.4	Finite elements	248
4.2.5	Time integration algorithms	253

4.2.6	Spectral elements	255
4.3	Numerical dispersion	257
4.3.1	Physical dispersion and attenuation	257
4.3.2	Numerical errors for wave propagation	258
4.3.3	Theoretical numerical dispersion	260
4.3.4	Time-step estimates for some simple cases	264
4.3.5	Numerical dispersion for low order elements	264
4.3.6	Influence of the geometrical arrangement	265
4.3.7	Influence of mass matrix formulation	268
4.3.8	Efficiency of higher order elements	269
4.4	Physical and numerical damping	275
4.4.1	Rayleigh and Caughey damping	275
4.4.2	Rheological interpretation of Rayleigh damping	276
4.4.3	Attenuation models for geomaterials	277
4.4.4	Numerical damping	281
4.5	Modelling wave propagation in unbounded media	283
4.5.1	Absorbing boundaries in 1D	283
4.5.2	Absorbing boundaries in 2D	284
4.5.3	Infinite elements	286
4.5.4	Absorbing layers (PML)	289
4.5.5	Coupled approaches	296
4.6	The Boundary Element Method	298
4.6.1	Interest of the method in dynamics	298
4.6.2	Maxwell-Betti theorem	298
4.6.3	Integral equations in elastodynamics	298
4.6.4	Discretization and regularization principle	301
4.6.5	Wave propagation in unbounded media	302
4.6.6	Numerical Implementation	303
4.6.7	Validation and influence of the regularization	304
4.6.8	Advanced formulation: the Fast Multipole Method	306
4.6.9	Elastodynamics in time domain	308
4.7	Applications to wave propagation in soil	308
4.7.1	Diffraction of a plane wave in unbounded media	308
4.7.2	Vibrations of a foundation	312
4.7.3	Vibration isolation using piles or trenches	313
4.7.4	Traffic induced vibrations in railway tunnels	321
5	Seismic wave propagation and amplification	323
5.1	Introduction	323
5.2	Seismic wave amplification	324
5.2.1	Main governing phenomena	324
5.2.2	Experimental characterization	327
5.3	Seismic wave amplification in layered media	328
5.3.1	From transfer function to time-domain response	328
5.3.2	Amplification in single-layered media	330

5.3.3	Amplification in multi-layered media	333
5.4	Amplification due to the topography	333
5.4.1	Main phenomena and simplified analysis	333
5.4.2	Amplification by crests and hills	336
5.4.3	Amplification by canyons	340
5.4.4	Amplification on actual topographies	345
5.5	Amplification of seismic waves in 2D alluvial basins	351
5.5.1	Amplification by wedges	351
5.5.2	Theoretical basins	356
5.5.3	Cylindrical basins	361
5.5.4	Cylindrical basin vs horizontally layered soil	362
5.5.5	Elliptical basins with variable shape ratio	365
5.5.6	2D/1D aggravation factor	366
5.6	Amplification of seismic waves in 3D alluvial basins	367
5.6.1	Semi-spherical basin	367
5.6.2	Sine-shaped basin	369
5.6.3	Semi-spherical basin and oblique incidences	370
5.6.4	Semi-ellipsoidal basin	372
5.6.5	Moon-valley model	372
5.7	Modal approaches to analyze site effects	374
5.7.1	Amplification of the seismic motion and resonance	374
5.7.2	Various types of modal approaches	374
5.7.3	Simplified modal method	375
5.7.4	Features of the various modal methods	376
5.7.5	Fundamental frequency of a geological structure	376
5.7.6	Modal estimation of the fundamental frequency	378
5.7.7	Simplified modal method vs experimental spectral ratios	379
5.8	Amplification in shallow basins (e.g. Nice)	380
5.8.1	Analysis of site effects in Nice (France)	380
5.8.2	Amplification from 1D transfer functions	382
5.8.3	2D model of the geological profile	383
5.8.4	Amplification of a plane <i>SH</i> -wave	384
5.8.5	Influence of attenuation	386
5.8.6	1D and 2D amplification vs experimental results	387
5.8.7	2D/1D aggravation factor	388
5.8.8	Comparison with the simplified modal method	389
5.8.9	Time-domain simulations	390
5.8.10	Comparisons with a deep alluvial basin	390
5.9	Amplification in a deep basin (Volvi)	393
5.9.1	The Volvi EuroSeisTest	393
5.9.2	Simplified and complete models of the Volvi basin	396
5.9.3	SH wave amplification in the Volvi basin	397
5.9.4	Comparisons between simplified and complete models	400
5.9.5	SV-wave amplification in the Volvi basin	406
5.9.6	2D/1D aggravation factor	406

5.9.7	Conclusions on site effects in Volvi	408
5.10	Wave-structure interaction	410
5.10.1	From soil-structure to wave-structure interaction	410
5.10.2	Seismic analysis for buildings	410
5.10.3	Seismic interaction with underground structures	412
5.10.4	Seismic interactions at the local and global scales	413

Appendices

419

A	Several operators in mechanics	419
A.1	Vectors and product of vectors	419
A.2	Tensors and product	419
A.3	Gradient and Laplacian	419
A.3.1	Definitions	419
A.3.2	Examples	420
B	Synthetic wavelets	421
B.1	Ricker wavelet	421
B.2	Gabor wavelet	424
B.3	Mavroeidis & Papageorgiou wavelet	425
B.4	Generalized Rayleigh wavelet	426
B.5	Küpper wavelet	427
B.6	Ormsby wavelet	428
B.7	Morlet wavelet	429
B.8	Meyer wavelet	430
B.9	Double- <i>M</i> wavelet	432
C	Spectral analysis and filtering	433
C.1	Fourier transform	433
C.1.1	Definitions	433
C.1.2	Main properties	434
C.1.3	Usual transforms	434
C.1.4	Fourier transforms of synthetic wavelets	435
C.1.5	Wave propagation in viscoelastic media	435
C.1.6	Fourier transforms of actual signals	438
C.2	Filtering	439
C.2.1	Classical filters	439
C.2.2	Filtered signals: examples	439
C.3	Hilbert transform and envelope curve	440
C.3.1	Definition	440
C.3.2	Envelope curves	441

D Propagating waves: duration, velocity, echoes	443
D.1 From acceleration to displacement	443
D.1.1 Integration of accelerograms	443
D.1.2 Baseline correction	443
D.1.3 Spectral methods	443
D.2 PGA, PGV, PGD	444
D.3 Signal duration	445
D.4 Estimation of wave velocity	447
D.4.1 Peak to peak estimation	447
D.4.2 Cross-correlation function	448
D.5 Detection of reflected waves and echoes	449
D.5.1 Autocorrelation function	449
D.5.2 Real cepstrum	449
D.5.3 Time phase	449
E Echo removal by homomorphic filtering	451
E.1 Basic principles	451
E.2 Computation of the complex cepstrum	451
E.3 Removing echoes thanks to cepstral filtering	453
E.3.1 Principle of the method	453
E.3.2 Homomorphic filtering: summary	453
E.3.3 Application to actual measurements	454
References	459
Index	493

Introduction

Various types of mechanical waves may propagate through soils: traffic induced vibrations, seismic waves, blast or impact induced loadings, etc. The frequency ranges, the wavelengths, the amplitudes are different from one application to another. However, the fundamental theory of mechanical waves in heterogeneous elastic or attenuating media may be considered to investigate such various fields of interest. The related experimental and numerical techniques may also apply to a wide range of dynamic problems in soils.

The main scientific and engineering goal of this book is thus to deal simultaneously with soil dynamics/vibrations and wave propagation in soils (including seismic waves). These various fields are generally considered separately and the important links between them, from both scientific as well as practical points of views, are unfortunately not investigated. They are usually considered in separate disciplines such as earthquake geotechnical engineering, civil engineering, mechanics, geophysics, seismology, computational engineering, etc.

The objective of the book is to offer in a single publication an overview of soil dynamics and wave propagation in soils with emphasis on engineering applications. The structure of the book is the following:

- It starts (*Chapter 1*) with the presentation of a wide variety of practical problems: traffic induced vibrations, wind turbines, dynamic compaction, earthquake engineering, etc. Pictures from practical applications are shown together with signal recordings from the field and numerical simulations from various methods.
- The 1D-wave theory is detailed in *Chapter 2* for various types of waves (axial, torsion, shear). It is then applied to the dynamic characterization of soil from 1D laboratory tests (resonant column, Hopkinson pressure bars), the dynamic response of a heterogeneous soil profile as well as dynamic soil-structure interaction.
- *Chapter 3* deals with the analysis of 2D/3D wave propagation in layered media (body waves as well as surface waves). Some simple equations are derived for applications in the field of vibration isolation as well as surface wave propagation. Using the 2D/3D theory, the dynamic characterization of soils is considered. Wave propagation in reduced-scale models is first discussed. The dispersion of surface

waves in layered soils is then investigated and field SASW tests¹ are presented. Other types of in situ tests (e.g. in-hole tests) are also investigated.

- Modelling wave propagation in soils may be performed using various types of numerical methods. *Chapter 4* gives an overview of various numerical approaches and investigates two of them: the Finite Element Method and the Boundary Element Method. Such important issues as numerical errors and radiation conditions are discussed. Several numerical examples are then proposed (e.g. vibration isolation).
- Finally, *Chapter 5* investigates seismic wave propagation and amplification in complex geological structures such as irregular topographies or alluvial deposits. Some classical theoretical results are recalled first. Several examples are also presented: Mexico, Los Angeles, Caracas, Nice, Volvi, etc. Such parameters as the topographic aggravation factor (for irregular topographies) or the 2D/1D aggravation factor (for alluvial basins) are discussed.

In addition to these five chapters, five appendices deal with various types of synthetic wavelets, spectral analysis, signal integration, signal duration or echo removal.

Acknowledgements

The authors would like to thank first Pr Michael Pender, from the University of Auckland, New-Zealand, for his careful and detailed review of this book. His valuable suggestions improved significantly our original manuscript.

We would like to acknowledge the help of several colleagues with whom we shared common researches or teaching activities throughout the years in various fields of dynamics. Many foreign colleagues from various places in the world were also supporting our project providing fruitful ideas, discussions, figures, papers.

Our deepest thanks, also, to our families and relatives for their continuous patience. We were often thinking and talking about waves in soils during the last months and they were always supporting us towards our goal.

¹Spectral Analysis of Surface Waves

List of symbols

Notation conventions

a	scalar variable
\dot{a}	time derivative of scalar variable a
a^*	Fourier transform of variable a
a_R	real part of complex variable a
a_I	imaginary part of complex variable a
$ a $	modulus of complex variable a
\bar{a}	normalized scalar variable
\underline{a}	vector (analytical expressions)
$\hat{\underline{a}}$	virtual (vectorial) field
a_j	j^{th} component of vector \underline{a}
$a_{j,k}$	spatial derivative of the j^{th} component of vector \underline{a} with respect to the k^{th} spatial coordinate
$\{a\}$	vector (discretized expressions)
$\underline{\underline{A}}$	2^{nd} order tensor
$[A]$	matrix (discretized expressions)

Symbols

Latin symbols

\underline{a}	acceleration vector
A_j	amplitude of incident j -wave ($j = P, SV, SH$)
c	wave velocity
$\underline{\underline{C}}$	elasticity tensor
\underline{c}	complex cepstrum (homomorphic filtering)
$\underline{\underline{d}}$	strain rate tensor
\underline{d}	polarization vector

List of symbols

E	Young's modulus
f	frequency
\underline{f}	body force vector
\mathcal{F}	Fourier transform
\mathcal{H}	Hilbert transform
i	square root of -1
\underline{k}	wave vector
\underline{l}	normalized wave vector
m_0	unrelaxed modulus
m_∞	relaxed modulus
M	complex modulus
\underline{M}	moment
M_t	torsional moment
M_b	bending moment
\underline{n}	normal vector
N	normal force
$\mathcal{P}_i, \mathcal{P}_e$	rate of work by internal (resp. external) forces
Q	quality factor
Q^{-1}	attenuation
R_j	amplitude of reflected j -wave ($j = P, SV, SH$)
S	cross-section area
t	time
t_b	Ricker wavelet breadth
t_p	Ricker wavelet fundamental period
t_s	Ricker wavelet delay
T	transfer function as the ratio between the surface motion and the interface motion
\bar{T}	transfer function as the ratio between the surface motion and the outcrop motion
$T_{i,j}$	transfer function between layers i and j
T_j	amplitude of transmitted/refracted j -wave ($j = P, SV, SH$)
T_j	transmission coefficient for the j -wave ($j = P, SV, SH$)
T_i^k	fundamental solution (traction)
\underline{V}	shear force
\underline{u}	displacement vector
U_i^k	fundamental solution (displacement)
v	(particle) velocity

List of symbols

\underline{v}	velocity vector
V_P	wave velocity of P -waves
V_R	wave velocity of Rayleigh waves
V_S	wave velocity of S -waves
\underline{x}	position vector
x, y, z	spatial coordinates
Greek symbols	
α	attenuation factor
γ	shear strain (in Chapters 2 and 5)
	2^{nd} parameter of the Newmark scheme (in Chapter 4)
δ	logarithmic decrement
Δh	finite element size
Δt	time step
$\underline{\epsilon}$	strain tensor
η	viscosity
θ	angle
κ	aspect ratio
λ	1st Lamé elasticity constant
Λ	wavelength
μ	shear modulus or 2nd Lamé elasticity constant
ν	Poisson's ratio
ξ	damping ratio
ρ	mass density
$\underline{\sigma}$	(Cauchy) stress tensor
Σ_{ij}^k	fundamental solution (stress tensor)
τ_e	strain relaxation time
τ_σ	stress relaxation time
ϕ	creep function (in Chapter 2) scalar potential for P -waves (in Chapter 3)
χ	velocity ratio
ψ	relaxation function (in Chapter 2)
$\underline{\psi}$	vectorial potential for S -waves (in Chapter 3)
ω	circular frequency
Ω	domain
$\partial\Omega$	boundary of domain Ω

Chapter 1

Waves and vibrations in soils *Actual problems*

1.1 Various fields and applications

The analysis of soil response under dynamic loadings is of great interest for various applications in the field of Civil and Environmental engineering. In many practical situations, dynamic or vibratory excitations are very important since:

- they allow some improvement of the mechanical properties of the soil (e.g. vibratory or dynamic compaction): the aim is to *optimize the improvement process* of the soil mechanical features,
- they may originate some annoyances to the public (e.g. traffic induced vibrations): the goal is to *reduce the vibration level* through isolation techniques,
- they can lead to some instabilities in the considered soil mass or to the damaging of a structure resting on it (for instance in case of seismic loading): the objective is then to *limit their consequences*.

This chapter presents and discusses several important domains of application related to *soil dynamics*, an expression designating a wide range of practical situations since the main mechanical parameters are very different from one case to another (stress and strain level, frequency, strain rate...). As depicted in Fig.1.1, the different practical problems are related to various shear strain ranges:

- in the case of *machine vibrations* or *traffic induced vibrations*, the shear strain ranges between 10^{-6} and 10^{-5} and the soil behaviour remains in the linear range,
- for *strong earthquake motions*, the shear strain may be larger than 10^{-4} thus leading to nonlinear effects in the soil response,
- for very strong loadings such as *explosions or impacts*, the shear strain may be as large as 10^{-3} or 10^{-2} which is beyond the scope of this book.

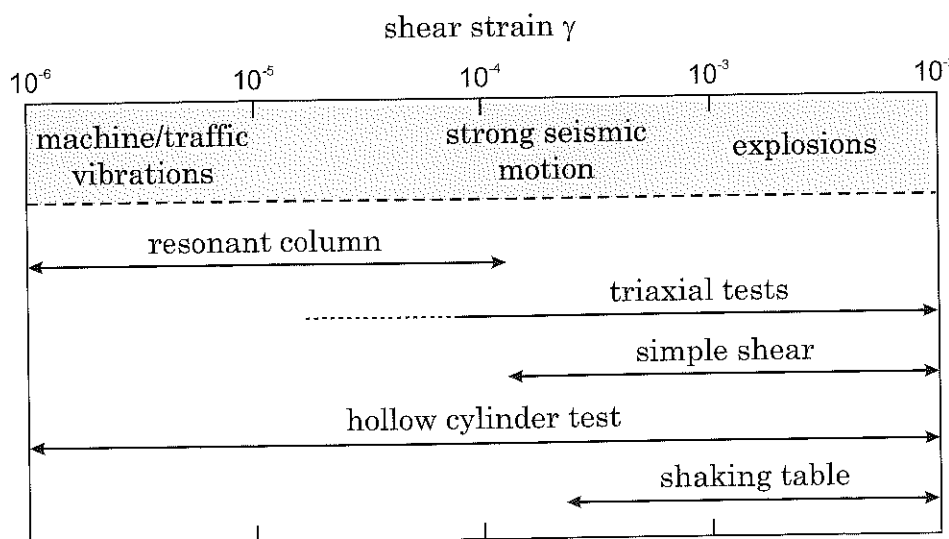


Fig. 1.1: Ranges of various problems in terms of shear strain (top) and related experimental methods (bottom).

The experimental methods available in the laboratory for the dynamic characterization of soils in such strain ranges are also detailed in Fig.1.1. They allow the identification of the soil dynamic/cyclic behaviour. Nevertheless, they generally involve homogeneous strain states in a soil specimen whereas actual waves propagating in real soils lead to complex 3D stress-strain paths varying with time. Field experiments allow the detailed analysis of such propagation process but do not lead to the full identification of the soil behaviour. Laboratory experiments will be discussed in Chapter 2 and several field experiments will also be presented in Chapter 3.

1.2 Vibrations due to construction works

1.2.1 Pile driving

Interest and related problems

Piles are involved in many foundation systems for large structures. Two different types of problems then arise: on the one hand it is necessary to estimate the *bearing capacity* of the pile(s), on the other hand, one has to determine both the *stresses induced in the pile* and the *dynamic excitation of the neighbouring soil* during the driving process. The first problem corresponds to the design of geotechnical structures whereas the second deals with the question of vibratory nuisances.

These two types of problems generally raise the need for two different approaches: a

static approach to determine, for instance, the bearing capacity of the pile or pile group and a *dynamic approach* to analyze the transient and resulting stress field in the pile and the soil around it. After construction, pile foundations may also undergo dynamic excitation in the case of: structures in seismic areas, tall structures subjected to wind loads, offshore structures, etc.

Basic principles of the driving process

Dynamic pile driving. As depicted in Fig.1.2 (left), dynamic pile driving consist in "driving" a pile with a falling mass of known kinetic energy. The soil resistance during the driving process can be estimated through various parameters characterizing the test: number of blows, penetration per blow, kinetic energy per blow (mass and falling height), penetration resistance, etc. The penetration resistance of a sand increases for larger relative densities or lateral pressure, but decreases for larger water contents. Two types of resistance are generally considered: the *tip resistance* and the *total resistance*.

The bearing capacity of piles changes in various ways for cohesive and cohesionless soils. For sands, two main phenomena have to be considered: on the one hand the density modifications around the pile because of compaction phenomena, on the other hand larger in depth tip resistance and lateral friction. From a dynamic point of view, the impact of the hammer on the pile head generates transient phenomena in the pile and at the soil-pile interface. A simple example of such phenomenon is proposed in the following sections.

The detailed analysis of the soil-pile interaction (axial or radial loading) was proposed by many authors (Bourdin *et al.*, 1989; Huang *et al.*, 1992; el Naggar and Novak, 1994; Masoumi *et al.*, 2007). They analyzed the driving process and determined the static (bearing capacity) as well as the dynamic (stiffness and damping) parameters. During the driving process, the dynamic loadings correspond to fast shear and pressure forces. The pressure dynamic forces are mainly significant around the pile tip. The lateral friction induces shear stresses in the soil. El Naggar and Novak (1994) proposed to define an annular area around the pile with weaker soil mechanical properties than in the neighbouring soil (lower shear modulus). Furthermore, they take into account a dependency on the strain rate. Dynamic soil response for large strain rates was also studied in details by Semblat *et al.* (1999) using Split Hopkinson Pressure Bar systems. This experimental approach will be presented in Chapter 2.

1D wave propagation in a pile. To estimate the stresses induced in the pile, it is necessary to investigate wave propagation phenomena in the pile. As depicted in Fig.1.3, the dynamic loading may be decomposed into several transient parts: the falling mass first generates in the pile a step load involving both a *loading wave* and an *unloading wave*. As this example neglects the lateral friction (beginning of the pile driving), this step load propagates several times along the pile: each time the wave reaches the pile tip the strain energy is partly transmitted to the soil and partly reflected into the pile. For each blow at the pile head, a complex wavefield is thus generated leading to a pile

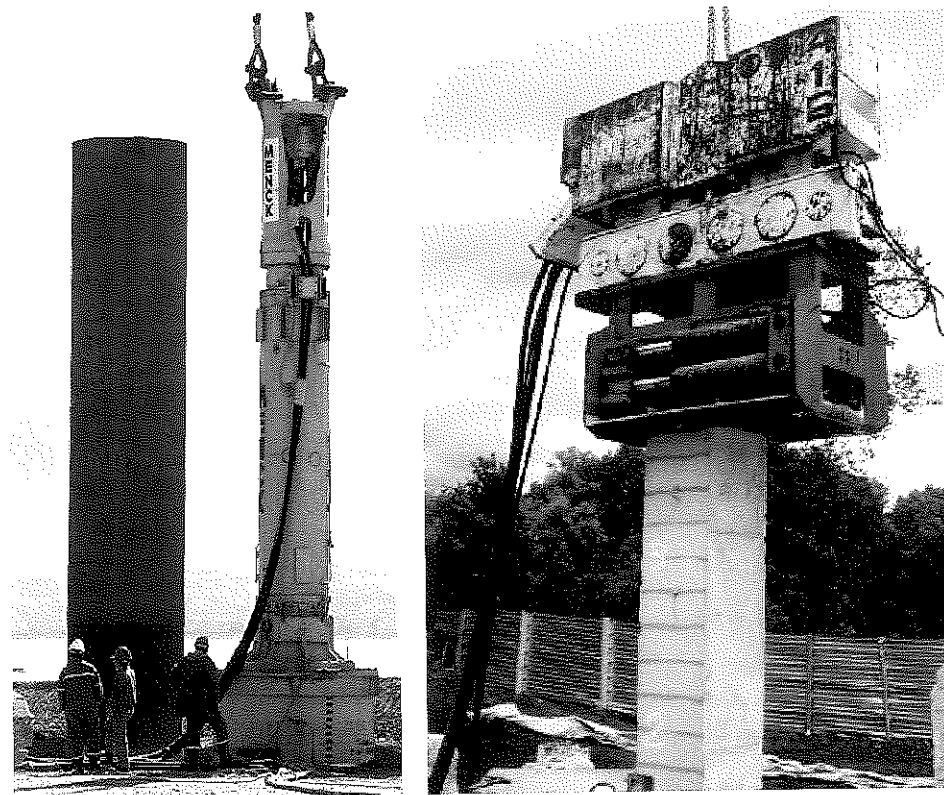


Fig. 1.2: Dynamic pile driving (left) and vibratory pile driving (right).

penetration in several (dynamic) steps (see Fig.1.3). The penetration process is thus not governed by an instantaneous phenomenon. In actual cases, the lateral friction rapidly plays an important role since a significant part of the energy is dissipated or radiated along the soil-pile interface (Masoumi *et al.*, 2007). However, the fast dynamic processes discussed previously are still significant in all cases.

The pile driving process is then controlled by propagation phenomena in the pile itself as well as multiple soil-pile interactions. Indeed each penetration step depends on the mechanical characteristics of the soil, of the pile and of the soil-pile interface. Many theoretical results will be given in the next chapter to analyse 1D wave propagation in piles.

Vibratory pile driving. In the case of vibratory pile driving, the excitation at the pile head is given through a vibratory load (Fig.1.2, right). The main difference with the dynamic pile driving technique is that the energy of the vibratory pile driving equipment

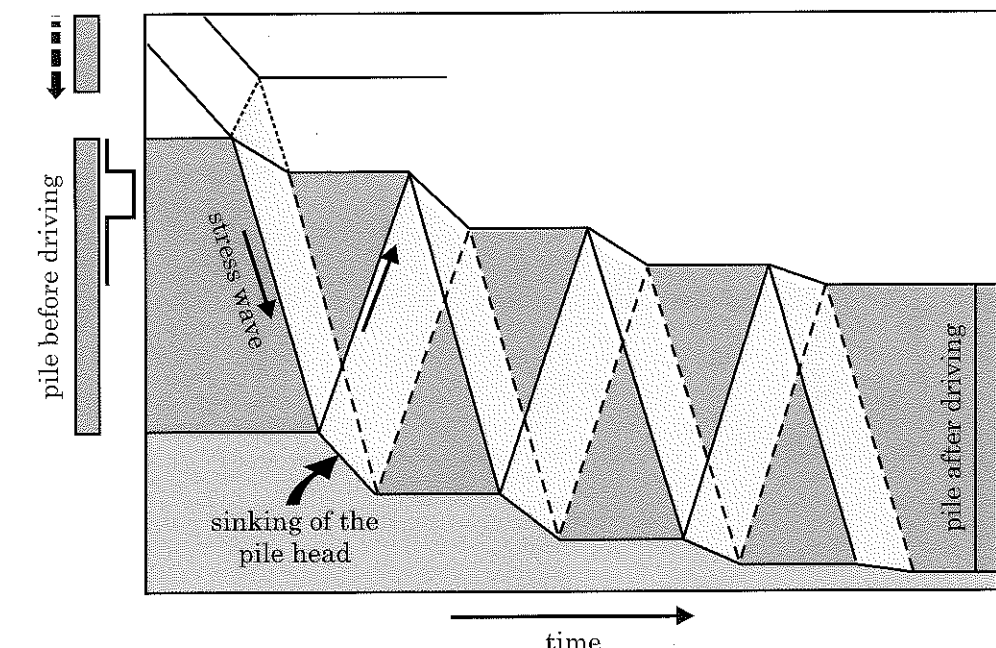


Fig. 1.3: Propagation of loading and unloading waves in a pile during the driving phase, from (Meunier, 1979).

is transmitted progressively to the pile as well as to the neighbouring soil. There are no more alternate dynamic and static steps in the process but a vibratory/cyclic continuous excitation at the pile head. The problem of pile bearing capacity and vibratory nuisances are combined: the balance between the dissipated energy and the radiated energy is the key issue for such a problem.

As shown in Fig.1.4, for vibratory pile driving experiments performed by Rocher-Lacoste *et al.* (2007), the analysis of the experimental results along the pile and in the neighbouring soil is very complicated. The amplitude measured at the free-surface depends on the penetration depth. Dynamic phenomena take place in the pile, along the soil-pile interface and the soil layers around the pile (waves propagating in the soil up to the free surface). Various types of theoretical and experimental approaches are proposed in (Transvib, 2006).

Values of the mechanical parameters

For the theoretical and numerical analysis of pile driving, the following range may be considered for the mechanical parameters:

- particle velocity (soil): several mm/s,

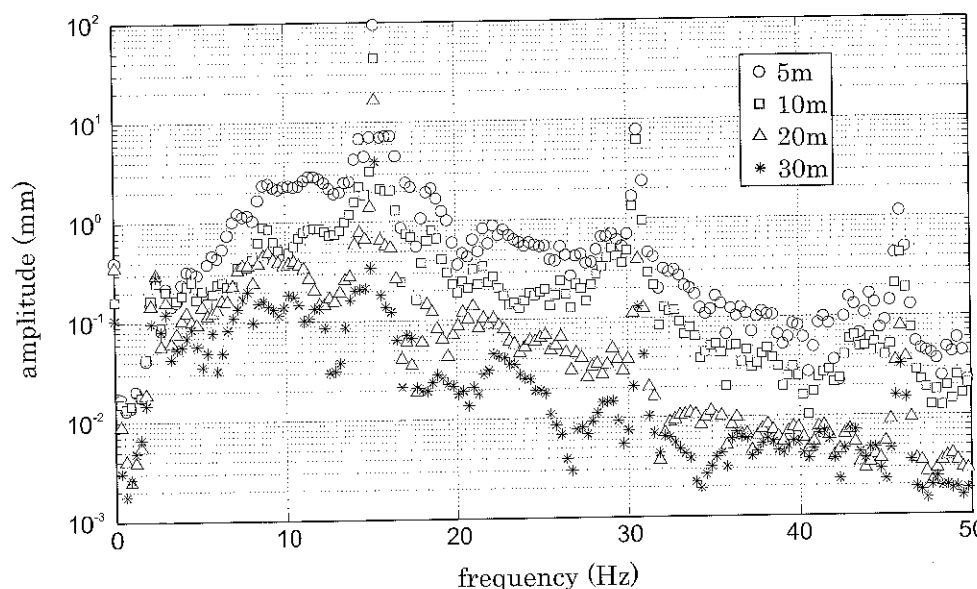


Fig. 1.4: Vibratory pile driving: amplitude at the free-surface for various penetration depths (Rocher-Lacoste *et al.*, 2007).

- force at the pile head: from 10 to 10,000 kN,
- driving energy: 10 to 3000 J (per blow),
- displacement: from several mm to several dm (per blow).

1.2.2 Dynamic compaction

Principle of the process

The main goal of this technique, mainly developed by L. Ménard (Ménard, 1974), is to improve, down to a 4 to 6 m depth, the density of the soil. To do so, as depicted in Fig.1.5, a mass of several tens of tons is dropped on the soil to compact it. The falling height is generally very large (10 to 40 m). To improve the soil properties in a given area, it is necessary to define different lines along which the dynamic compaction will be performed at regular spacings. The improvement of the mechanical properties of the compacted soil may be very important since the soil modulus can, for instance, be multiplied by a factor 2 or 3 (Ménard, 1974).

The characteristic parameters of dynamic compaction are the following:

- depth of soil to densify,

1.2 Vibrations due to construction works

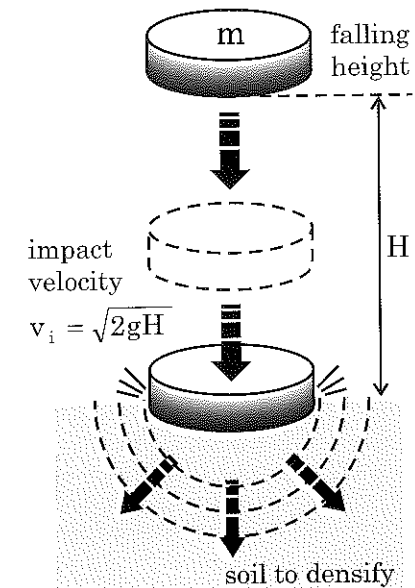
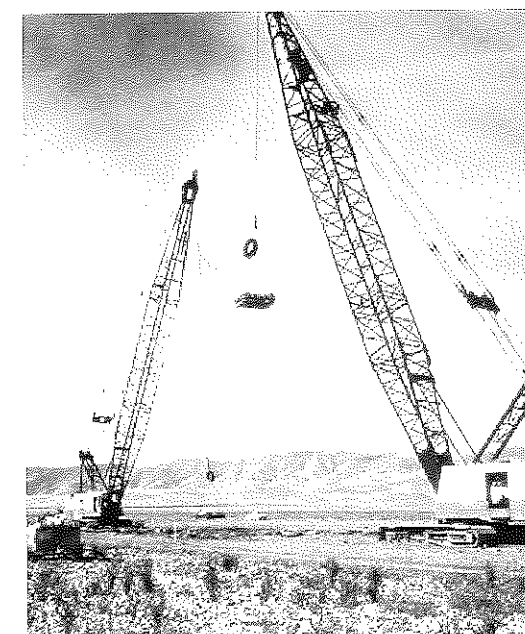


Fig. 1.5: Dynamic compaction of soils: picture of the experimental arrangement (left) and principle of the process (right).

- nature of the soil, permeability,
- mass of the impactor m ,
- impact velocity v_i ,
- number of shock steps (delay between each step).

Experimental results

Some experimental results in terms of particle velocities are displayed in Fig.1.6 (Ménard-Soltraitement, 2002). These signals correspond to a falling height $H=23$ m, a falling mass $m=16$ t, that is an energy $E=3,610,080$ J. Two sensors were located at the soil surface at the following distances: $d_1=97$ m for sensor 1 and $d_2=197$ m for sensor 2 (Ménard-Soltraitement, 2002). The duration of the signal is larger at sensor 2 than at sensor 1 and the maximum amplitudes are not reached for the same component (Ménard-Soltraitement, 2002). The wavefield generated by the impact is very complex and it is difficult to assess the efficiency of the process only considering the radiated waves.

In dry soils, the impact generates transient elastic waves as well as plastic loading and unloading waves. The former are mainly responsible for the dynamic compaction.

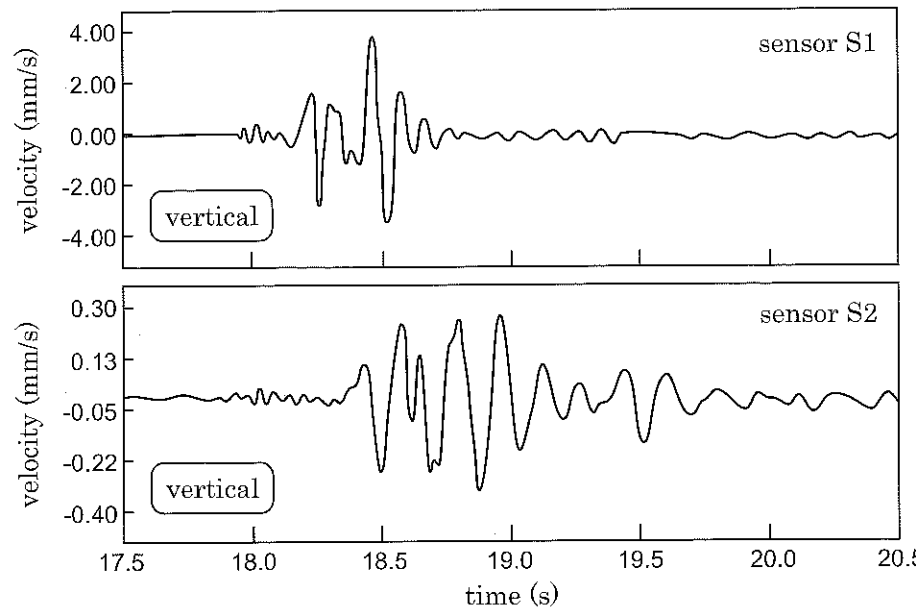


Fig. 1.6: Velocities measured in the soil during a dynamic compaction experiment (Ménard-Soltraitement, 2002).

In *saturated soils*, pressure waves propagate in the fluid phase. The pore pressure may increase until the soil skeleton collapses. A grain rearrangement in a denser configuration is then possible.

Several empirical formulae have been proposed to make the link between the soil thickness for densification and the impact energy. Some authors also tried to estimate the optimal distance between two impact points (Mayne and Jones, 1983; Ménard, 1974; Gabin, 1985).

Theoretical analysis of the impact

L. Ménard was one of the first to develop dynamic compaction (Ménard, 1974). He proposed a comparison between static and dynamic compaction. The fundamental assumptions of these two types of compaction are different on many aspects: friction, stiffness and drainage. All these phenomena are strongly influenced by the compaction velocity. The dynamic soil response may be different depending on the strain rate. Such results were demonstrated on fast dynamic tests performed in the lab by Semblat *et al.* (1999).

Many authors performed theoretical analyses of the soil-mass interaction during the dynamic compaction process (Chou *et al.*, 1991; Chow *et al.*, 1990, 1992; Poran *et al.*,

1.2 Vibrations due to construction works

1992; Scott and Pearce, 1975; Sieffert *et al.*, 1990). Nowacki and Ranicki (1987) proposed a theoretical study on dynamic compaction by spherical explosive sources. Hata and Tateyama (1991) investigated plastic wave propagation due to the impact. Several researches on metals have some similarities with dynamic compaction in soils (Brothers *et al.*, 1977; Edlinger *et al.*, 1993; Hardy *et al.*, 1971; Sinclair *et al.*, 1985; Studman *et al.*, 1977).

Experimental point of view: dynamic stiffness

During dynamic compaction tests, Poran *et al.* (1992) measured several mechanical parameters and characterized the dynamic response of the soil under impact. The acceleration (or deceleration) of the falling mass, the pressure at the impact location, the settlement of the mass allow the calculation of the *Dynamic Settlement Modulus* M_d . This settlement modulus involves the global dynamic interaction between the soil and the falling mass.

The displacement of the mass d_t as a function of time is estimated from acceleration measures (initial conditions). The stress at the impact location, denoted p_t , is derived from the following expression:

$$p_t = \frac{m \cdot a_t}{A} \quad (1.1)$$

where m and A are the mass and the surface area of the falling weight and a_t its acceleration.

Poran *et al.* (1992) determined the *dynamic settlement modulus* of the soil M_d from the experimental curves using the following expression:

$$M_d = \frac{\Delta p_t}{\Delta \left(\frac{d_t}{D} \right)} \quad (1.2)$$

where D represents the diameter of the falling weight.

Poran *et al.* (1992) proposed a comparison between the dynamic settlement modulus and the elastic properties of the soil. Furthermore, they related the measurements of the density of the compacted soil to the impact energy for several tests.

Values of the mechanical parameters

The main parameters of dynamic compaction tests are the following (also see the complete Table 1.1):

- particle velocity: from 10 to 30 ms⁻¹,
- acceleration of the mass: from 50 to 500 ms⁻²,
- impact energy: several MJ,
- stresses: from 10 to 500 kPa.

1.2.3 Vibratory compaction

Principle and example

The vibratory compaction technique is widely used in civil engineering. As depicted in Fig.1.7, it leads to soil densification thanks to a heavy rolling and vibrating cylinder. The main parameters of the soil-cylinder interaction are the frequency, the force at the surface, the speed of the cylinder axis and the number of passes (Pietzsch and Poppy, 1992; Yoo and Selig, 1979). The vibrations of the cylinder on the soil surface induce a cyclic loading which is supposed to increase the density of the medium. The main goal of the works dedicated to this topic is the optimization of the compaction parameters to get the larger densification of the soil.

For such experiments, as shown in Fig.1.8, the number of loading cycles is very large since steady-state cyclic loadings are applied to the soil. However, since the cylinder moves along the soil surface at various speeds, the source of vibrations changes with time. The particle velocities displayed in Fig.1.8 are thus very complex signals also depending on the propagation process through the soil.

Some experimental examples are given in Fig.1.9 for three different types of vibratory rollers and two distances from the road. In Fig.1.9, only the maximum particle velocity is thus considered. It is very large close to the track (up to 40 mm/s) and it decreases with the distance (around 6 mm/s at a larger distance). The maximum particle velocity generally increases with the number of loadings: it is due to the fact that the soil being progressively densified, the radiated wavefield is more easily propagated through the soil. However, the influence of the type of vibratory roller is very strong since there is a large discrepancy in the measured particle velocities.

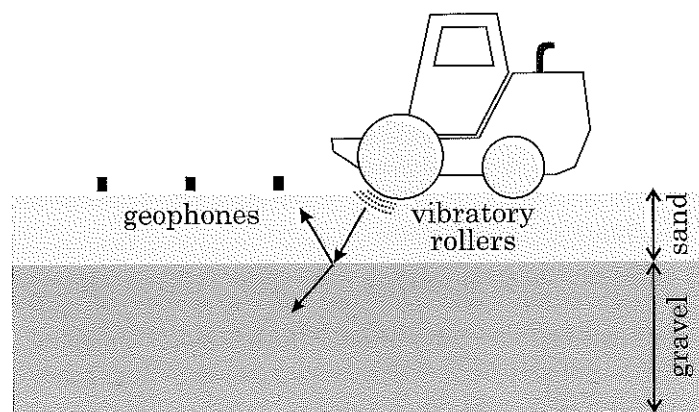


Fig. 1.7: Principle of vibratory compaction and type of measurements performed (from CER-Rouen, France).

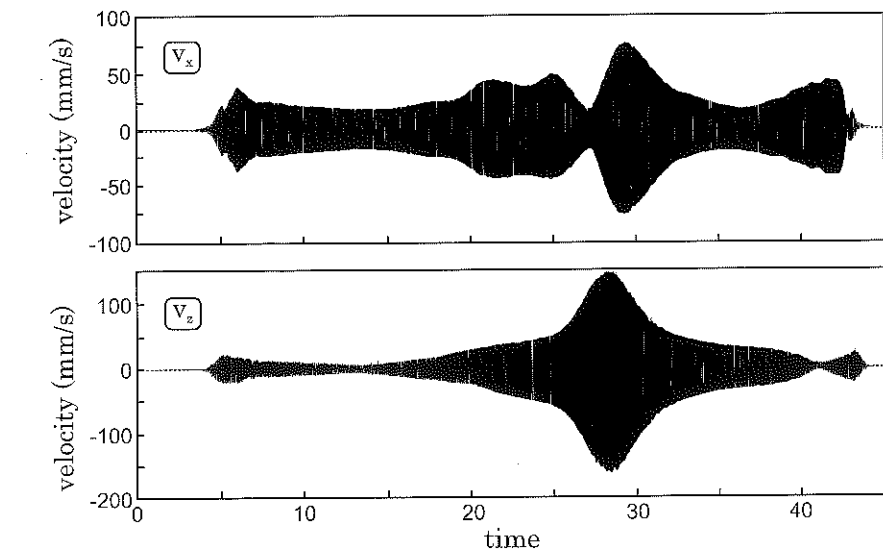


Fig. 1.8: Horizontal (top) and vertical (bottom) particle velocities measured during vibratory compaction (from CER-Rouen, France).

Main phenomena

The way the soil is compacted thus depends on the applied vibratory loading. For instance, Pietzsch and Poppy (1992) consider that the vibrating mass may be uplifted above the soil whereas Yoo and Selig (1979) assume a permanent contact between the soil and the vibrating cylinder.

Furthermore, one has to consider two different loading cases:

- *stationary case*: the same soil volume undergoes the vertical harmonic force,
- *non stationary case*: the cylindric mass moves and the vibratory excitation is applied at various points.

In the latter case, the behaviour parameters of the soil cannot be determined with classical tests because the loading is non stationary.

The displacement of the whole compacting system changes with frequency. The vibratory features of the system strongly influence the stress level at the soil surface. The displacement-frequency curve has two peaks: the first one is mainly influenced by the vibratory features of the whole system whereas the former actually depends on the vibratory response of the cylinder. All these remarks allow the previous authors to relate the motion of the vibrating mass and the compaction level in the soil.

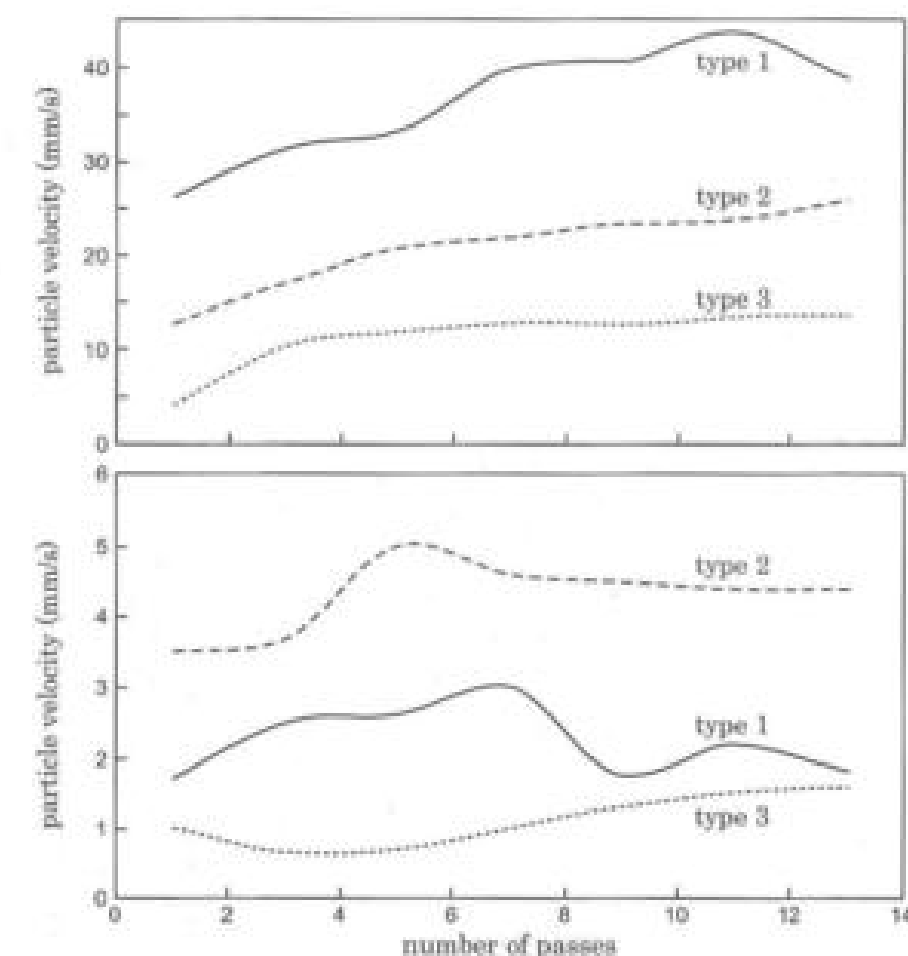


Fig. 1.9: Maximum vertical particle velocity measured at two distances, $d_1=1.35$ m (top) and $d_2=8$ m (bottom), for different types of vibratory rollers (from CER-Rouen, France).

Values of the mechanical parameters

The main parameters for problems in the field of vibratory compaction are the following:

- frequency: 10 to 80 Hz,
- force: 50 to 200 kN,
- speed of the cylinder axis: several m s^{-1} ,
- vertical displacement: several mm.

1.3 Vibrations induced by wind turbines

Wind turbines are very large structures undergoing strong wind loadings. When the turbine is turning, it may induce acoustic waves (noise) as well as vibrations in the soil. The latter depend on the type of foundation and the properties of the soil.

As depicted in Fig. 1.10, experiments to assess the seismic wavefield radiated by wind farms were for instance performed by Schofield (2004). He measured the ground motion at different distances from a wind farm located nearby the Laser Interferometric Gravitational wave Observatory (*LIGO*) located in Hanford, Washington, USA. Since the observatory is very sensitive to ground vibrations, a detailed study was performed.



Fig. 1.10: Picture of a wind turbine and a seismometer used for the assessment of turbine induced vibrations in the soil nearby the Laser Interferometric Gravitational wave Observatory (*LIGO*) in Hanford, USA (Schofield, 2004).

Andersen and Clausen (2008) proposed a numerical model to analyze the impedance of a wind turbine foundation. They showed the strong influence of soil layering on the impedance of a rigid hexagonal foundation footing for a wind turbine. As discussed by Andersen and Clausen (2008), for low frequencies around 0.25 Hz, corresponding to the first resonance frequency of a 3 MW wind turbine, changes in the impedance are stronger for deep soft layers overlying a stiff half-space.

The amplitude of the ground motion measured by Schofield (2004) is displayed versus frequency in Fig.1.11 for distances ranging from 24 m to 18 km from the wind farm. Schofield (2004) also proposed some simple attenuation relationships to estimate the ground motion for future wind farms projects. As shown in Fig.1.11, the motion amplitude reaches its maximum at 4.3 Hz which is not close to the fundamental frequency of the seismic isolation system of the observatory. The motion amplitudes range between $4 \cdot 10^{-10}$ to $2 \cdot 10^{-7}$ at the various sites. Depending on the wind speed, the ground motion induced by the wind turbines may influence the background noise level at the observatory (Schofield, 2004). He also pointed out the potential influence of the local geological structure (e.g. basalt ridge). For sites located close to a wind farm, the vibrations originated by the wind turbines into the soil may imply some annoyances to the buildings or the public.

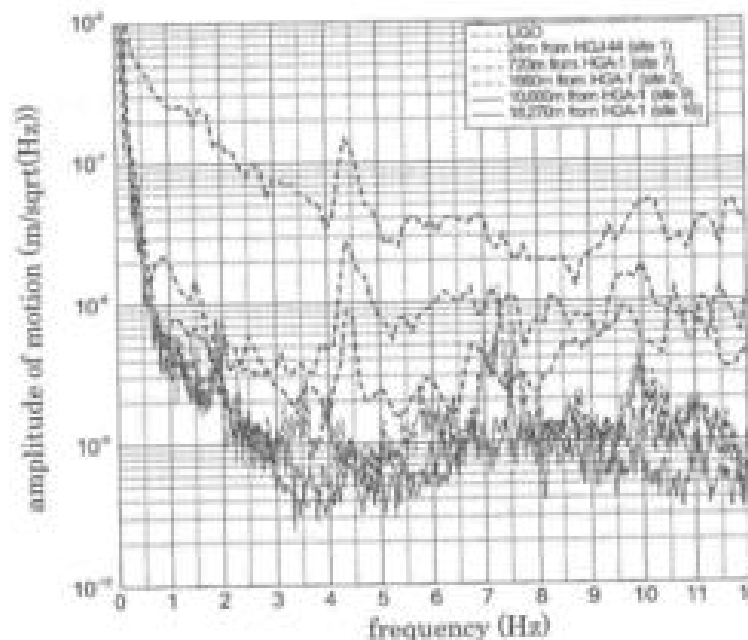


Fig. 1.11: Vibrations induced in the soil by a wind farm: ground motion spectra at different distances (Schofield, 2004).

1.4 Blast induced vibrations

1.4.1 Vibrations induced in mines

Mines and quarries are important sources of waves and vibrations during the exploitation process (use of explosive sources) or even after it has been exploited (failure of mines roof generating a seismic wave in the soil). As depicted in Fig.1.12, waves may be generated into the geological layers due to the exploitation process (Dowding, 1985).

For explosive sources located at the free-surface (quarries, construction works, etc), pressure waves are also generated into the air. Furthermore, the various wavefields propagating into the soil as well as into the air may interact leading to so-called ground-borne noise. Ground vibrations and ground-borne noise may thus be a source of annoyances in the environment at the surface.

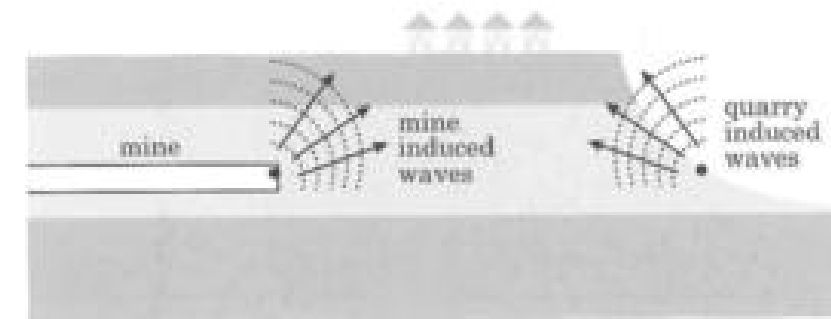


Fig. 1.12: Mine and quarry induced waves propagating into the soil: description of the problem.

Several experimental results are displayed in Fig.1.13. They correspond to the spectral ratios between the horizontal and vertical components of motion measured by Drind-Lebeau et al. (2009) above the Gardanne coal mine located in Provence, France. This mine is nearly 1 km deep and the motion is measured at several locations at the free-surface. From Fig.1.13, it can be noticed that some locations lead to larger spectral ratios: amplitudes range between 3 and 13 in the frequency band 3-8 Hz. As shown by Drind-Lebeau et al. (2009), such locations correspond to shallow alluvial sites overlying marls of lower Rognacien. The impedance contrast between these two formations leads to a significant motion amplification (also see Chapter 5). The annoyances caused in the environment may be large in the frequency range characterized by the spectral ratios. Numerical simulations were also performed by Lokmane et al. (2003) for the Gardanne mine taking into account the soil layering as well as the layers geometry.

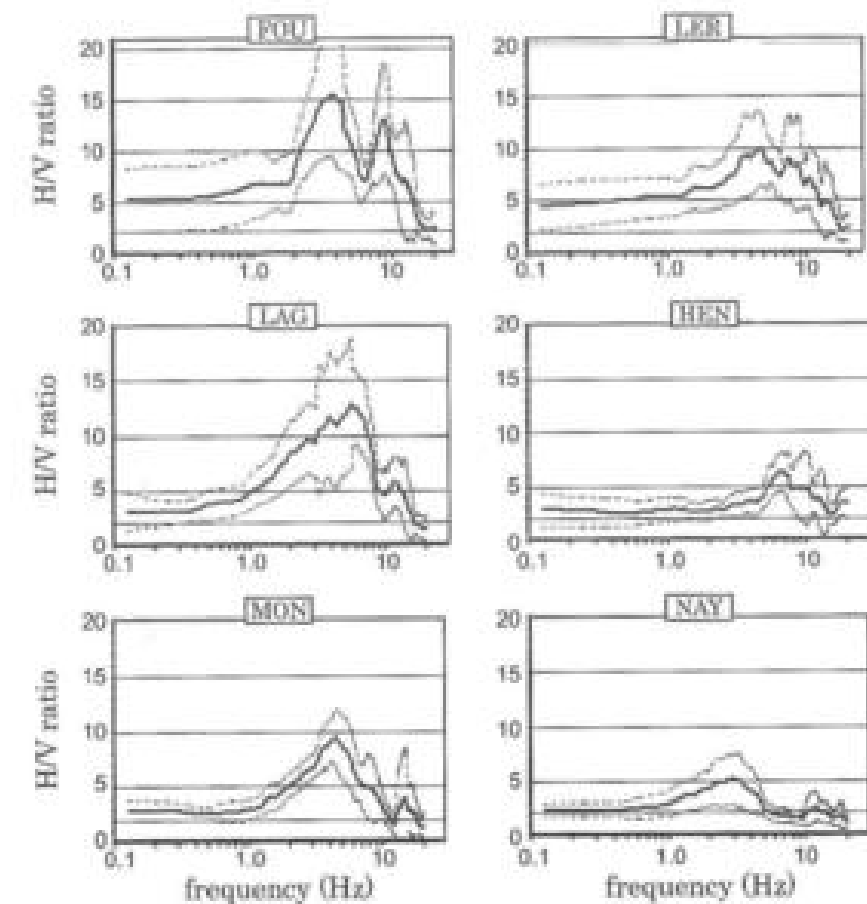


Fig. 1.13: Mine induced vibrations measured at the soil surface for the Gardanne coal mine, France, by Driad-Lebeau *et al.* (2009).

1.4.2 Vibrations induced in quarries

The energy of explosions in quarries or construction works is generally very large and may generate seismic waves propagating along long distances. As depicted in Fig.1.14 in the case of construction works, the blast generates two wave types: mechanical waves through the soil (vibrations) and pressure waves through the air (e.g. noise).

In the case of a quarry, several experimental results are displayed in Fig.1.15 showing the ground motion measured close to a bridge foundation (from CETE-Lyon, France). The mechanical waves are generated by explosive sources located in 60 holes having a 6 m length and using a 25 ms delay.

As shown in Fig.1.15 (CETE-Lyon, France), the signal duration is less than 1 s. The maximum particle velocity $v_p = 10 \text{ mm/s}$ is obtained for the vertical component (left). The mechanical waves propagating into the soil may have a significant influence on the neighbouring structures.



Fig. 1.14: Picture of the blasting phase in construction works (from CETE-Lyon, France).

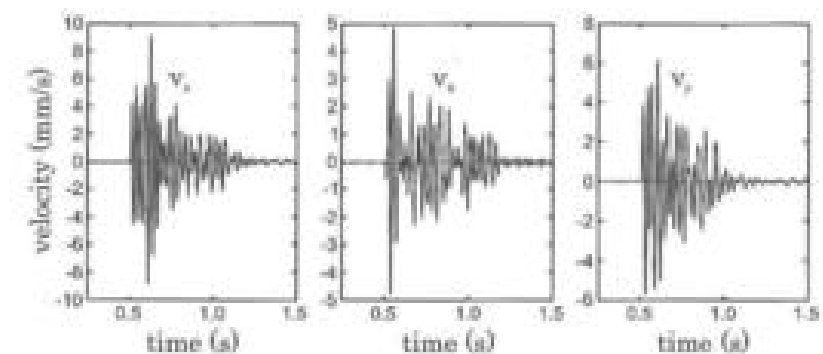


Fig. 1.15: Ground motion (velocities) due to an explosive source close to a bridge foundation (from CETE-Lyon, France).

1.5 Traffic induced vibrations

The main problem for traffic induced vibrations is the fact that they are originated by a moving source. Furthermore, the interaction between the vehicle and the road/track generally implies contact/sliding processes and may be very complex to describe. It is thus more difficult to characterize the dynamic loading or to model the wave propagation process than in the previous cases.

1.5.1 Vibrations due to road traffic

Experimental assessment

Vibrations induced by road traffic are due to the regular passage of vehicles as well as the interaction with some elements of the road structure. As shown in Fig.1.16, if there are some variations in the pavement structure, it may induce significant interactions with the vehicle and its suspension system. Such interactions will generate dynamic loadings on the pavement that may be propagated to the soil and the neighbouring structures.

As illustrated in Fig.1.16, the vibrations induced by road traffic may be measured using geophones. This picture was taken from an experimental study performed in an urban environment by the CETE-Lyon (France). Several types of loadings related to different vehicle features were analyzed.



Fig. 1.16: Measurement of traffic induced vibrations around a variation of the pavement structure (from CETE-Lyon, France).

1.5 Traffic induced vibrations

The particle velocities measured at different points for a truck driving at 50 km/h are displayed in Fig.1.17: the first signal (top) was measured at the soil surface 10 m from the road; the second signal (middle) was measured at the center of the first floor of a neighbouring building; the third signal (bottom) was measured at the center of the second floor of the same building (from CETE-Lyon, France).

As shown in Fig.1.17, the maximum velocity is approximately 0.1 mm/s at the soil surface whereas it reaches 0.3 mm/s at the second floor in the building. The annoyance due to traffic induced vibrations thus depends on the source, the propagation through the soil, soil-structure interaction as well as the dynamic features of the structure itself. Finally, Fig.1.17 also allows the estimation of the delay between the passage of each truck axle (from the signals measured at the soil surface as well as those recorded in the building). The parameters governing the signal features are thus also the vehicle mass, dimensions and speed. As it will be shown hereafter, this issue may be critical for train induced vibrations.

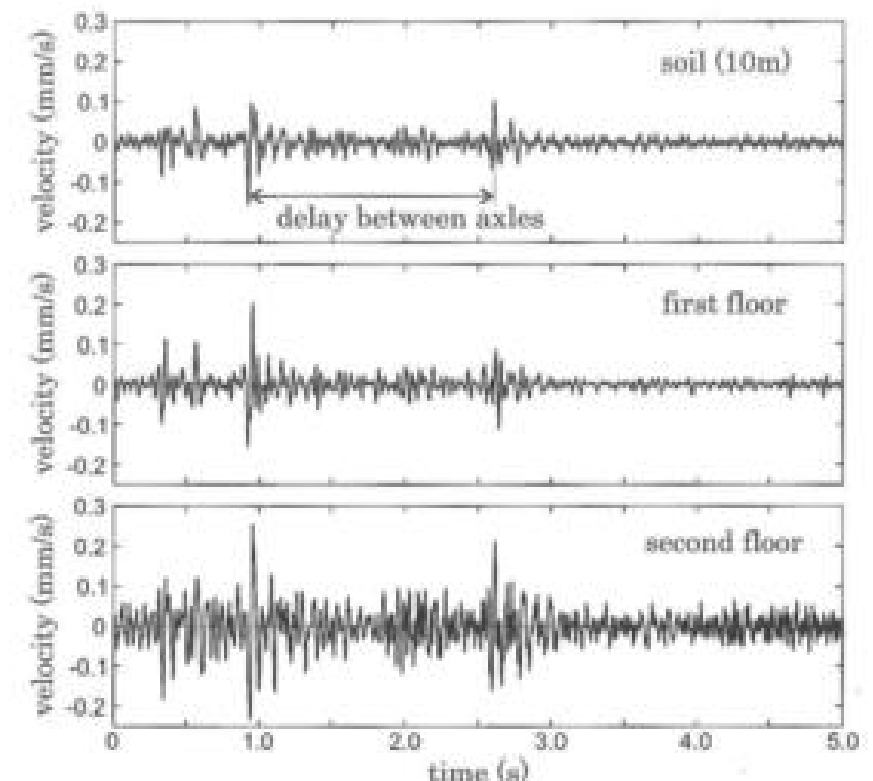


Fig. 1.17: Traffic induced vibrations: particle velocities measured along the road for different types of vehicles (from CETE-Lyon, France).

Numerical simulation

It is also possible to investigate traffic induced vibrations in soils considering numerical methods (Ekevid and Wilberg, 2002; Lombaert and Degrande, 2003; Sheng et al., 2006). Since such problems involve moving loadings, special numerical formulations have been proposed (Clouet et al., 2001).

As shown in Fig.1.18 (François et al., 2007), the passage of a two-axle truck on a traffic plateau generates vibrations into the soil.

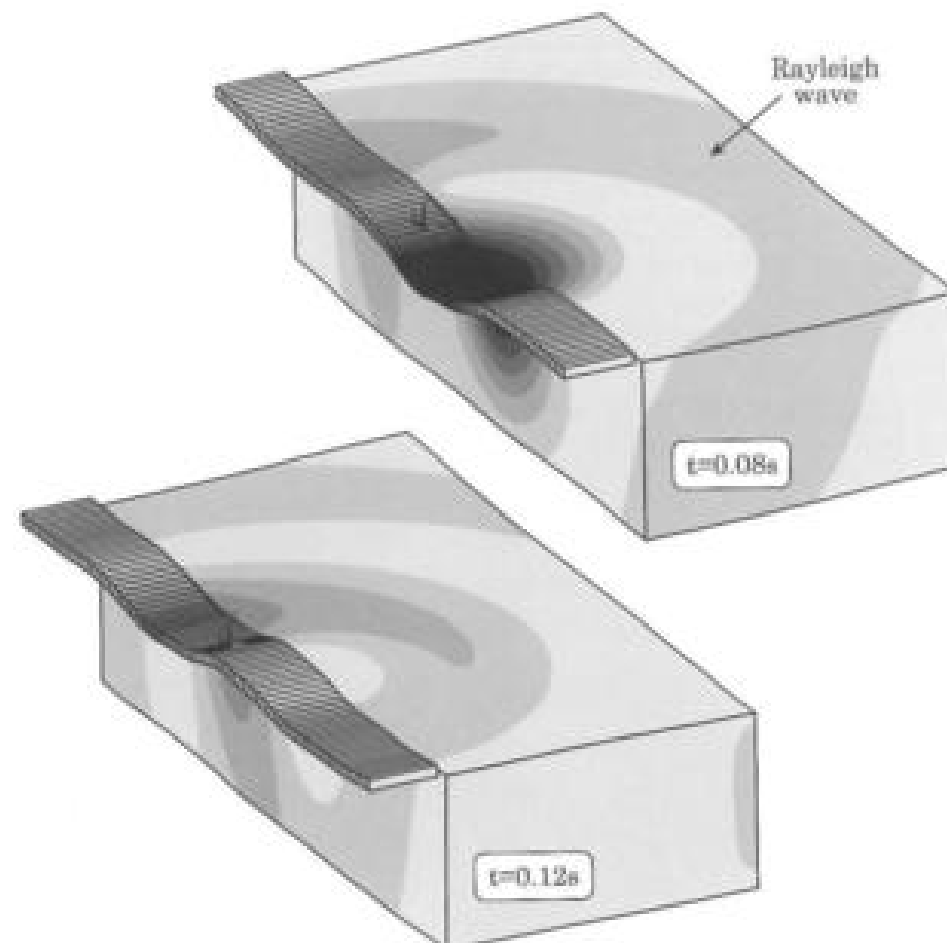


Fig. 1.18: Waves propagating into the soil due the passage of a two-axle truck (speed 14 m/s): computed displacements at different times (François et al., 2007).

The bending stiffness of the road being negligible with respect to the stiffness of the soil, cylindrical Rayleigh waves can clearly be observed (Fig.1.18). François et al. (2007) considered the influence of dynamic soil-structure interaction since such waves may excite neighbouring structures. They analyzed the response of a two-storey single family dwelling for different foundation types. François et al. (2007) evidenced that the potential damages in such structures, due to excessive deformations, depend on the ratio between the soil stiffness and the structure stiffness. As it will be shown in Chapter 3, the influence of the soil layering on wave propagation in soils may also be very large.

1.5.2 Vibrations due to railways

In the case of trains, as described in Fig.1.19, vibrations are generated at the wheel-track contact and radiate waves into the soil (as well as noise in the air). Annoyances in the environment have thus to be dealt with and depend on the train/track features, the soil properties and the soil-building interaction (Piala et al., 2007; Sheng et al., 2006; Paolucci et al., 2003).

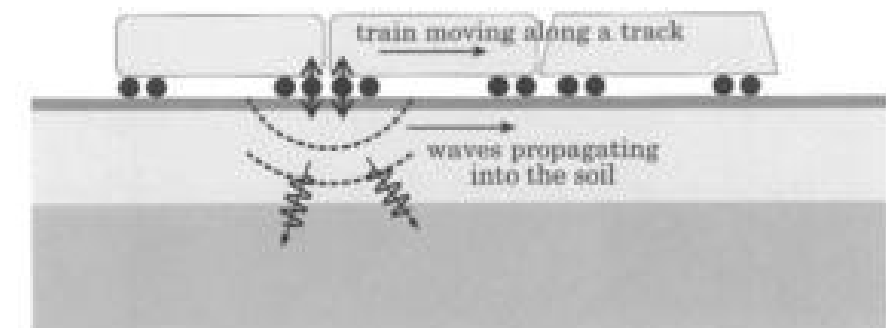


Fig. 1.19: Train induced vibrations: schematic of the problem.

In the case of high speed trains on soft soils, the train speed v_t may be close to the surface wave velocity V_R (Rayleigh waves). The energy may not be completely radiated in the environment thus leading to a large energy storage under the train. The specific problem of *supersismic ranges* is thus important since the infrastructure itself may be damaged (see next paragraph).

Ground motion measurements from a site on the Swedish West Coast Line were studied by Paolucci et al. (2003). As shown in Fig.1.20, the train speed has a strong influence on the ground motion. At 70 km/h, the Peak Ground Velocity is decreased by almost two orders of magnitude at only 7.5 m from the track. The same reduction occurs at distances larger than 50 m for a train speed of 186 km/h (Paolucci et al., 2003). As it will be shown later, Paolucci and Spinelli (2006) also performed numerical simulations to assess the influence of the strain speed on the induced ground vibrations.

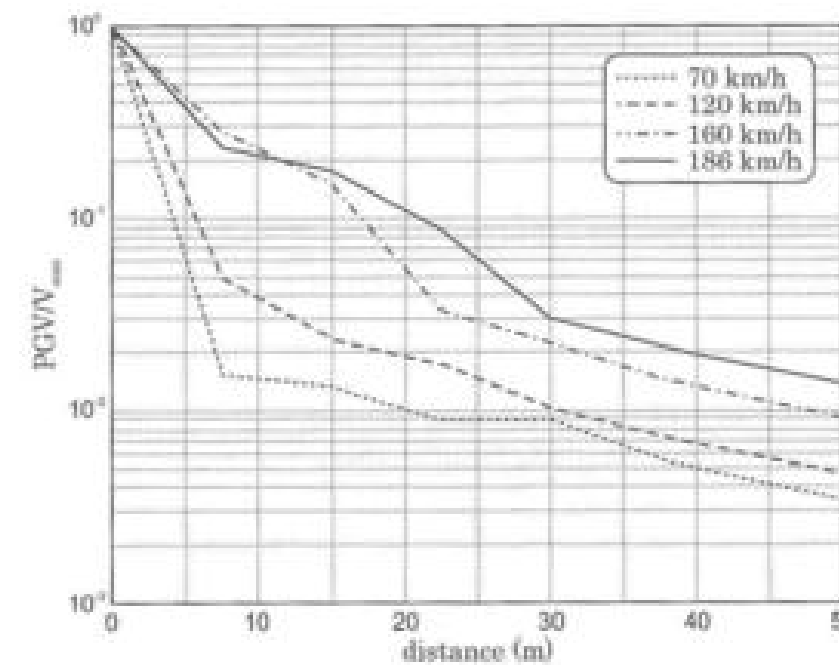


Fig. 1.20: Ground motion decay for various train speeds: Peak Ground Velocity normalized by the peak velocity at the track V_{\max} (Paolucci et al., 2003).

1.5.3 Theoretical analysis of moving loads

Various authors studied the influence of the train speed/wave velocity ratio on the generated wavefield (Ju and Lin, 2004; Lefevre-Mesgouez et al., 1998, 2002; Paolucci and Spinelli, 2006). When the train speed v_t is not far from the Rayleigh wave velocity V_R , the energy radiation process may be strongly modified.

As discussed by Lefevre-Mesgouez et al. (2002) or Paolucci and Spinelli (2006), two different cases are possible:

- 'sub-Rayleigh' case: for $v_t < V_R$, the velocity of Rayleigh waves propagating into the soil is larger than the train speed and the energy is radiated beyond the train as usual,
- 'super-Rayleigh' case: for $v_t \geq V_R$, the train speed is larger than the Rayleigh wave velocity and some energy is stored under the train, possibly leading to some damages in the track.

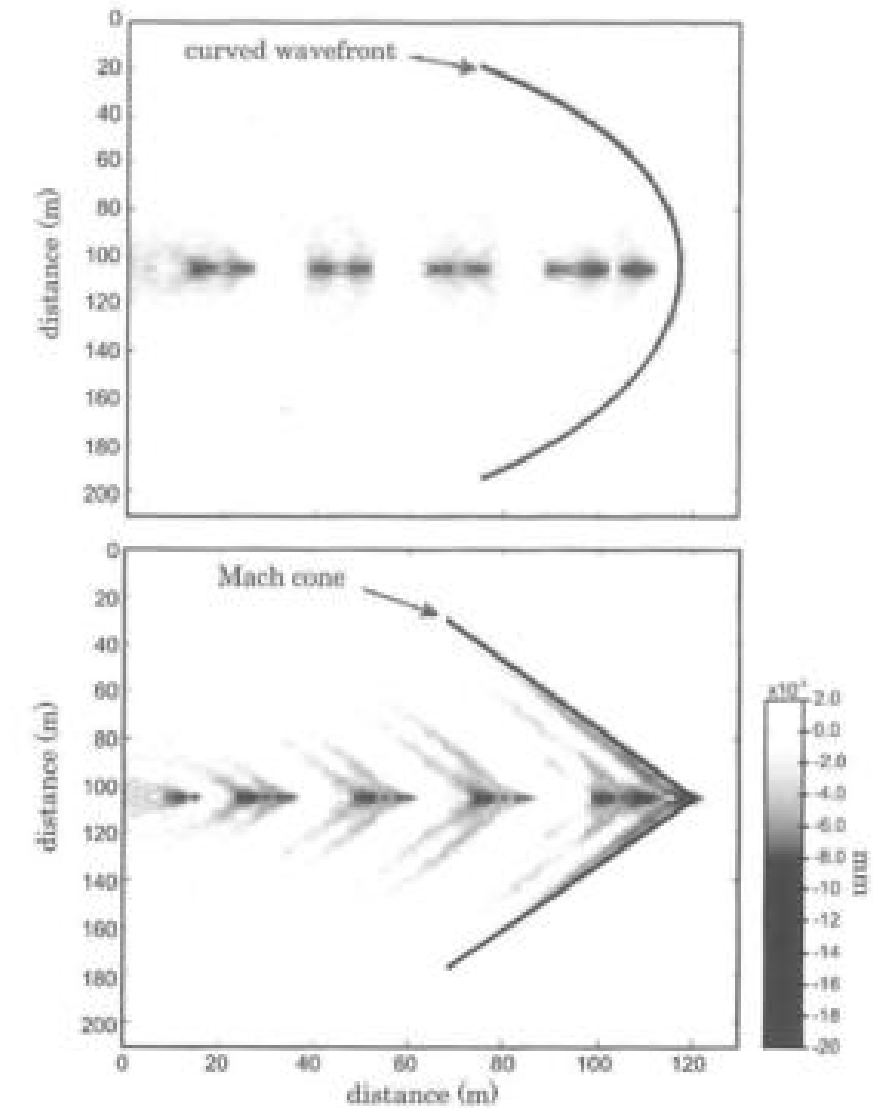


Fig. 1.21: Wavefield originated by standard (top, $v_t = 0.78V_R$) and fast trains (bottom, $v_t = V_R$), from Paolucci and Spinelli (2006).

As shown in Fig.1.21 (Paolucci and Spinelli, 2006), the first case (top, $v_t = 0.78V_R$) leads to a curved wave front whereas the second case (bottom, $v_t = V_R$) produces Mach type cones similar to that obtained for supersonic flights. They are called 'super-seismic' Mach cones.

1.6 Vibration isolation

1.6.1 Practical problem

The vibrations generated by various sources (rotating machines, road traffic...) may induce nuisances in neighbouring buildings or for specific types of activities (electronic industries, particle accelerators...). Wave propagation due to sources on/in the soil may actually induce particle velocities (or accelerations) disturbing for the people or the industries in the vicinity.

To solve this problem, it is necessary to either limit the vibrations transmitted to the environment (*active isolation*), or to modify the propagation in the soil or the transmission to the structures (*passive isolation*). To limit the wave propagation, several isolation methods have been proposed. They generally try to change the soil characteristics to modify the propagation process. It is thus necessary to insert a different material in the soil which can consist in:

- a soil volume with a different density from the neighbouring soil (e.g. trench mix technique, jet grouting),
- a linear or cylindrical trench which can be empty or filled with another material (e.g. damping material),
- an embedded screen constituted of a stiff material (e.g. concrete),
- one or several pile groups (or cylindrical cavities) in the soil.

The parameters mainly influencing the wave propagation process in the modified soil are the following:

- the velocity contrast between the soil and the material,
- the isolation system geometry (depth, width),
- in the case of pile groups or cylindrical cavities, the ratio between the pile diameter and their spacing.

1.6.2 Experimental results

Several books (Richart *et al.*, 1970; Skipp, 1966) deal with vibration isolation in Civil and Environmental Engineering. A review of codes and standards was proposed by Skipp (1997).

Isolation by trenches

Experiments performed by Woods (1968) and Richart *et al.* (1970). As depicted in Fig.1.22, Woods (1968) and Richart *et al.* (1970) analyzed the efficiency of various trench geometries (circular, rectangular, etc) as an isolation system. A rotating machine is installed at the center of a circular trench and the amplitude is measured

1.6 Vibration isolation

43

along various radii originating from the trench (Fig.1.22). The amplitude reduction is estimated by comparing the motion amplitude with the trench and the motion amplitude without the trench.

Their analysis deals with surface (Rayleigh) wave propagation generated by harmonic vibration sources at the soil surface for frequencies ranging from 200 to 350 Hz. Woods (1968) considered various trench types characterized by their dimensions: depth H , width w and distance from the source of vibrations R . These geometrical parameters are given as fractions of the Rayleigh (surface waves) wavelength Λ_R :

- *circular trench*: $H = 1.45\Lambda_R$ and $R = 0.73\Lambda_R$,
- *semi-circular trench* : $H = 0.60\Lambda_R$ and $R = 0.60\Lambda_R$,
- *rectangular trench* : $H = 1.19\Lambda_R$; $R = 2.97\Lambda_R$ and length $L = 1.79\Lambda_R$.

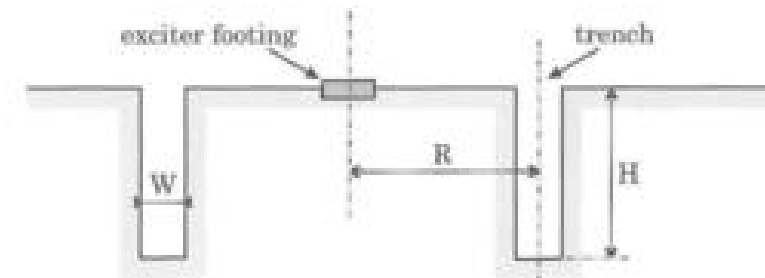


Fig. 1.22: Vibratory isolation using circular trench: description of the experimental set-up (Woods, 1968).

Efficiency of trenches as isolation system. The efficiency of the isolation system is assessed by estimating the amplitude reduction factor. In Fig.1.23, the amplitude reduction factor is plotted against the distance from the source for various trench depth to wavelength ratios: $H/\Lambda_R=0.363$, 0.726 and 1.452 (resp.). The efficiency of the trench is found to be larger for deeper trenches since the maximum reduction is found to be larger than 90%.

The amplitude reduction all around the trench is displayed in Fig.1.24 for a semi-circular trench and a rectangular trench. These results show that low amplitude areas (< 0.125) appear beyond the trench, whereas some areas may experience a significant motion amplification (> 1.25) before the trench. The efficiency of the isolation system studied by Woods (1968) and Richart *et al.* (1970) is thus very good.

The optimal trench dimensions depend on the main wavelength of the problem. The minimum values of the ratios between the system dimensions and the wavelength (that

is H/Λ_R and w/Λ_R) only allow applications at frequencies down to several hundreds of Hz (keeping wavelengths not too large). Another remark on the isovalue plots displayed in Fig.1.24 concerns the non-symmetric features of the results. In actual soil deposits, the soil layering is not perfectly flat and some heterogeneities may occur: the isolation efficiency is thus not fully symmetric.

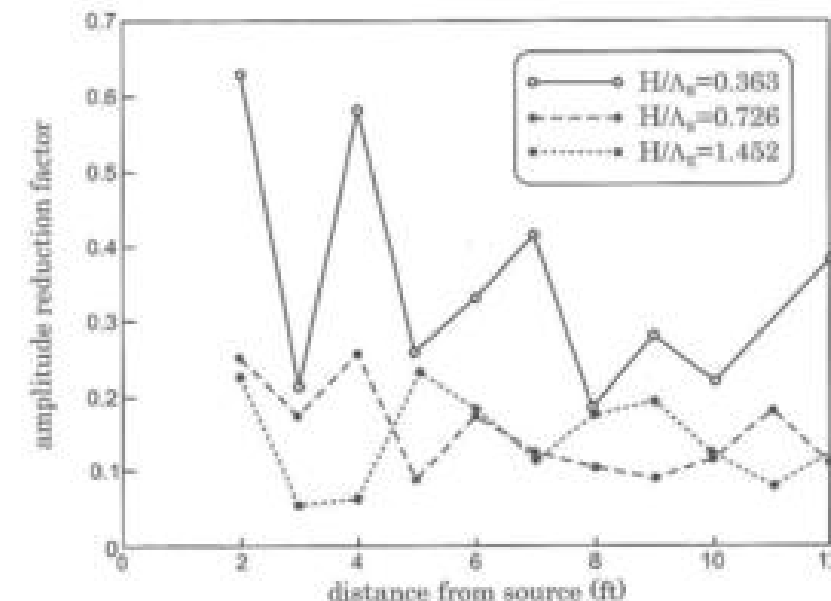


Fig. 1.23: Amplitude reduction factor for different normalized trench depths, from Woods (1968).

1.6.3 Numerical models

Various approaches in different fields

Many different authors have studied wave isolation methods and systems (Aviles and Sánchez-Sesma, 1983; Banerjee et al., 1988; Beskos et al., 1986; Haupt, 1977; Liao and Sangrey, 1978; May and Bolt, 1982; Segol et al., 1978; Woods et al., 1974).

Haupt (1977) mainly investigated isolation using stiff embedded screens. Banerjee et al. (1988) considered a Boundary Element Method to simulate the field experiments performed by Richart et al. (1970) (see Fig.1.24 and Chapter 4). Comparing different results indicate that an isolation system involving an empty trench is generally more efficient.

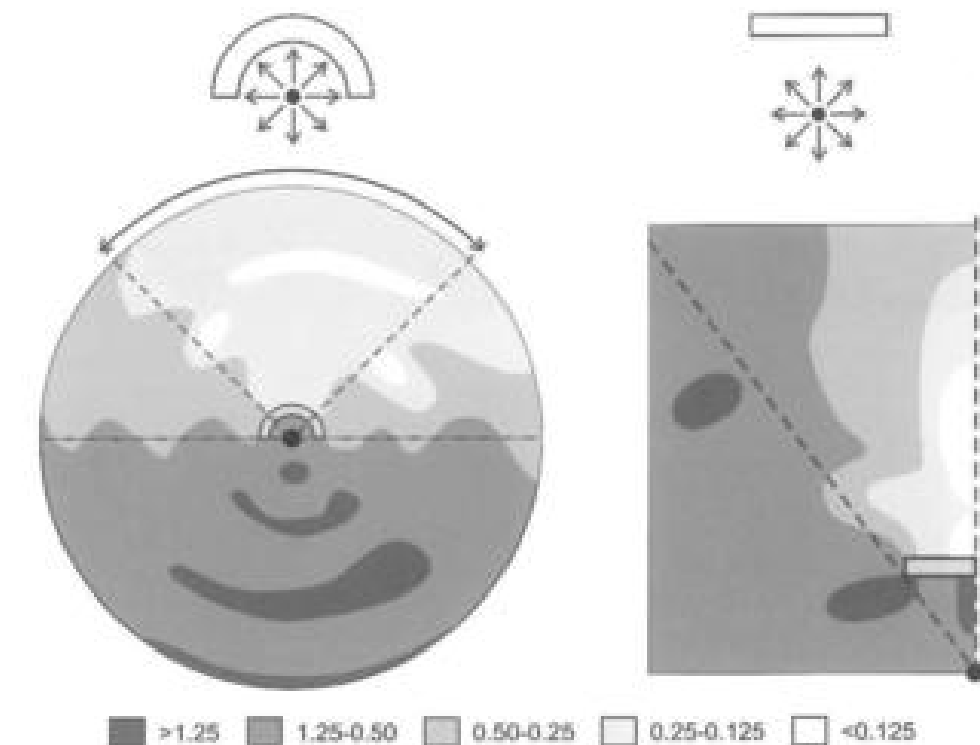


Fig. 1.24: Vibratory isolation using different trench types: semi-circular (left) and rectangular (right), from Woods (1968).

Other experimental works were performed by Woods et al. (1974) to analyze vibratory isolation by rows of (empty or filled) cylindrical wells. To estimate the influence of the isolation system on the wave propagation process, Woods considered an holographic technique. Woods gives the global efficiency of the system as a function of the wells diameter and their relative distance. Numerical simulations of such a problem are proposed in Chapter 4.

In recent years, the extensive use of numerical techniques in 2D and 3D has motivated new researches in this field:

- Karlström and Bostrom (2007), Sheng et al. (2006); Andersen and Nielsen (2005) or Ju and Lin (2004) for train induced vibrations,
- François et al. (2007), Lombaert and Degrande (2003) or Clouet et al. (2001) for road traffic induced vibrations,
- Chehab and el Naggar (2003) for hammers and presses induced vibrations.

Modelling the efficiency of trenches for trains

Karlström and Boström (2007) studied the efficiency of trenches on the isolation of wave induced vibrations propagating into the soil. Three cases are compared in Fig.1.25: the case without any isolation technique (right), the case involving two trenches (middle) and the case using one trench only (left). As shown in Fig.1.25 by the numerical results of Karlström and Boström (2007), the efficiency of the trench is very good. However, the vibration level being reduced in the environment, the mechanical waves seem to be trapped in the track structure (Fig.1.25, middle). It may lead to some damages to the track structure.

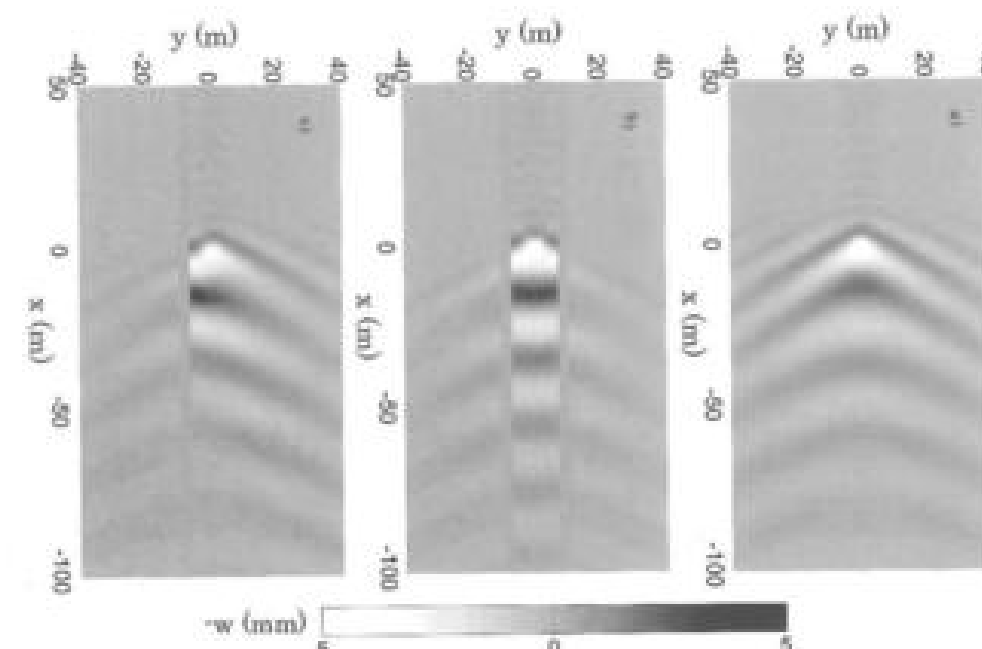


Fig. 1.25: Numerical analysis of various isolation techniques for train induced vibrations by Karlström and Boström (2007): no isolation (right), two trenches (middle) and one trench (left).

Modelling various isolation techniques

Andersen and Nielsen (2005) studied numerically various isolation techniques. As shown in Fig.1.26, the wavefield radiated in the vicinity of the track is significantly different from one case to the other. The efficiency of the open trench (bottom left) and the concrete screen (bottom right) appears to be larger than that of the improved soil (top right).

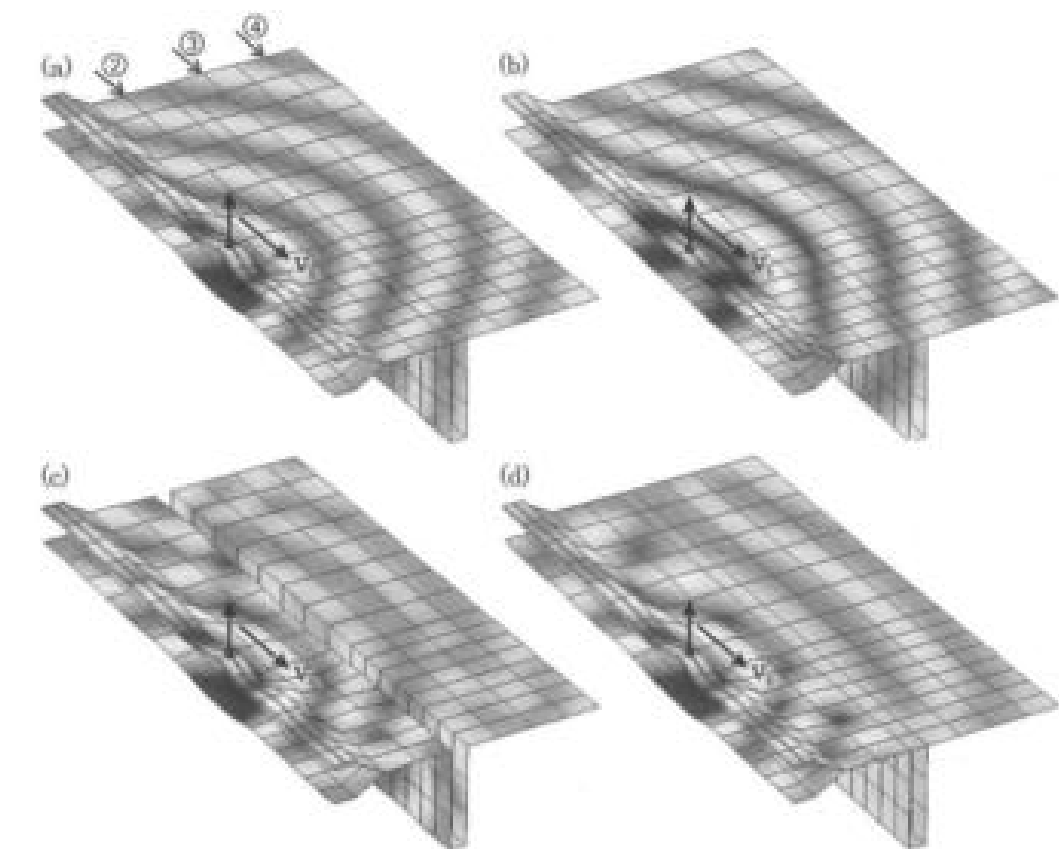


Fig. 1.26: Numerical analysis of various isolation techniques for train induced vibrations by Andersen and Nielsen (2005): (a) original track and subsoil; (b) soil improvement; (c) open trench and (d) trench backfilled with concrete.

Considering different lines parallel to the track (denoted 2, 3 and 4 in Fig.1.26), Andersen and Nielsen (2005) assessed the efficiency of each isolation system along these lines. For a pair of vertical forces, the results are displayed in Fig.1.27 in terms of pseudo-resultant displacement ($PRD = \sqrt{|u_x|^2 + |u_y|^2 + |u_z|^2}$) at two frequencies: 10 Hz (left) and 20 Hz (right). Along lines 3 and 4 (i.e. beyond the isolation system), the efficiency of the deepest open trench (c_2) is the largest and that of the concrete screen (d) is close to the deep trench far from the track. The efficiency is larger at 20 Hz (Fig.1.27, right) since the related wavelength is shorter (the isolation system geometry thus 'appears' larger).

The soil improvement technique (b) does not appear as a very efficient technique in terms of isolation away from the track. However, before the isolation system (Fig.1.27, top), the soil improvement technique (b) leads to smaller displacements close to the track

Modelling the efficiency of trenches for trains

Karlström and Boström (2007) studied the efficiency of trenches on the isolation of wave induced vibrations propagating into the soil. Three cases are compared in Fig.1.25: the case without any isolation technique (right), the case involving two trenches (middle) and the case using one trench only (left). As shown in Fig.1.25 by the numerical results of Karlström and Boström (2007), the efficiency of the trench is very good. However, the vibration level being reduced in the environment, the mechanical waves seem to be trapped in the track structure (Fig.1.25, middle). It may lead to some damages to the track structure.

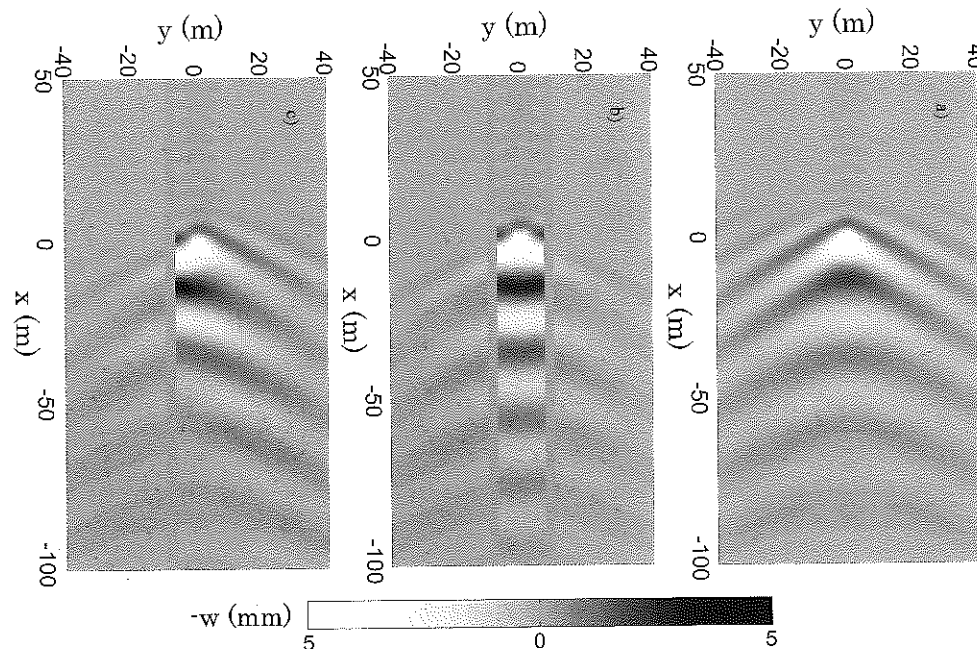


Fig. 1.25: Numerical analysis of various isolation techniques for train induced vibrations by Karlström and Boström (2007): no isolation (right), two trenches (middle) and one trench (left).

Modelling various isolation techniques

Andersen and Nielsen (2005) studied numerically various isolation techniques. As shown in Fig.1.26, the wavefield radiated in the vicinity of the track is significantly different from one case to the other. The efficiency of the open trench (bottom left) and the concrete screen (bottom right) appears to be larger than that of the improved soil (top right).

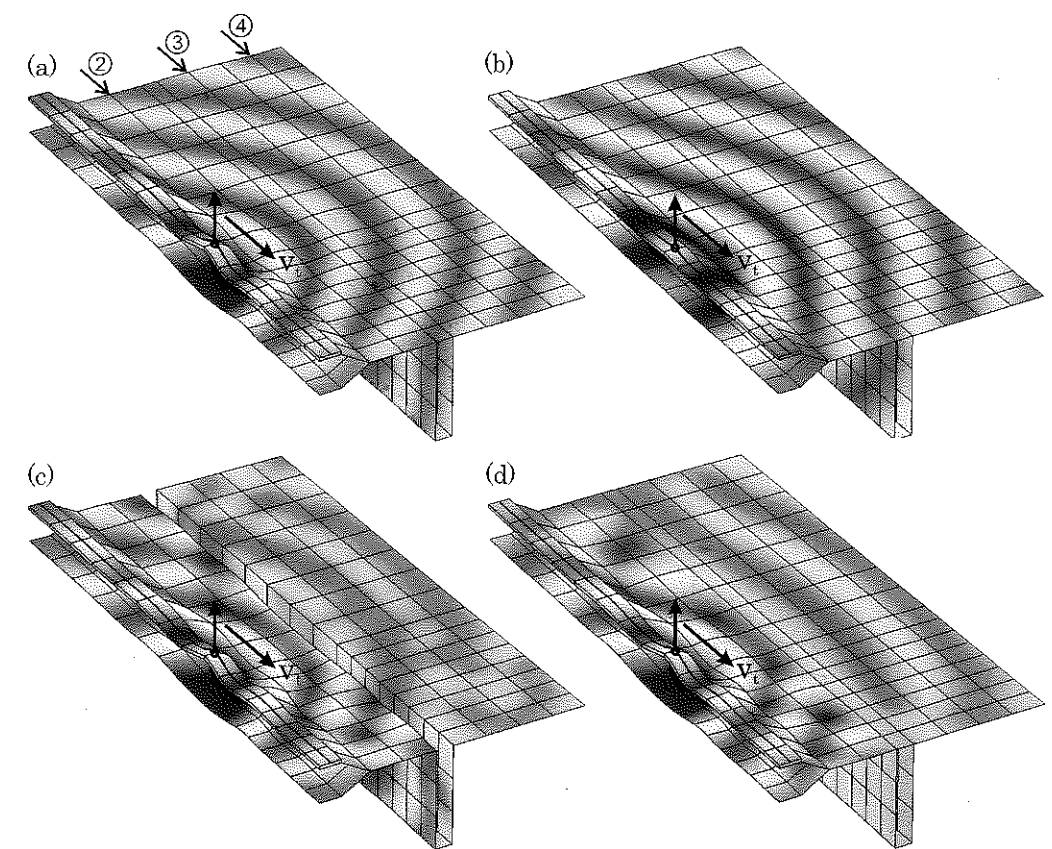


Fig. 1.26: Numerical analysis of various isolation techniques for train induced vibrations by Andersen and Nielsen (2005): (a) original track and subsoil; (b) soil improvement; (c) open trench and (d) trench backfilled with concrete.

Considering different lines parallel to the track (denoted 2, 3 and 4 in Fig.1.26), Andersen and Nielsen (2005) assessed the efficiency of each isolation system along these lines. For a pair of vertical forces, the results are displayed in Fig.1.27 in terms of pseudo-resultant displacement ($PRD = \sqrt{|u_x|^2 + |u_y|^2 + |u_z|^2}$) at two frequencies: 10 Hz (left) and 20 Hz (right). Along lines 3 and 4 (i.e. beyond the isolation system), the efficiency of the deepest open trench (c_2) is the largest and that of the concrete screen (d) is close to the deep trench far from the track. The efficiency is larger at 20 Hz (Fig.1.27, right) since the related wavelength is shorter (the isolation system geometry thus "appears" larger).

The soil improvement technique (b) does not appear as a very efficient technique in terms of isolation away from the track. However, before the isolation system (Fig.1.27, top), the soil improvement technique (b) leads to smaller displacements close to the track

and may reduce the potential damages when compared to other isolation techniques.

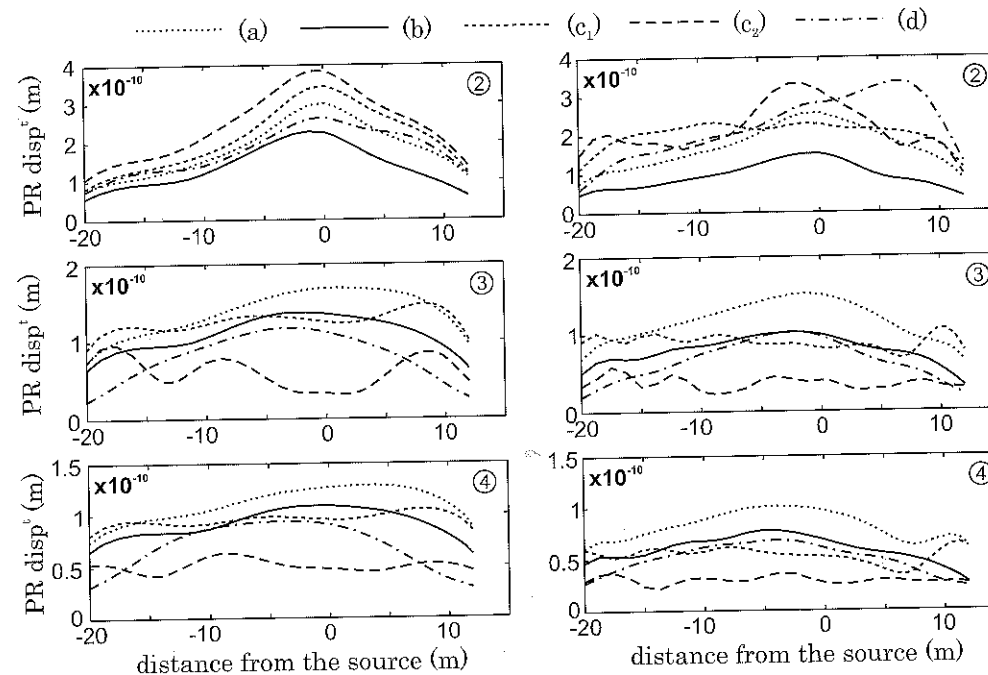


Fig. 1.27: Efficiency of various isolation techniques for train induced vibrations: pseudo-resultant displacement in the vicinity of the track (lines 2, 3 and 4); (a) original track and subsoil; (b) soil improvement; (c₁) 2 m deep open trench; (c₂) 6 m deep open trench and (d) trench backfilled with concrete (Andersen and Nielsen, 2005).

1.6.4 Values of the mechanical parameters

The main mechanical parameters for vibration isolation problems are the following :

- frequency: 10 to 5000 Hz,
- amplitude reduction: divided by a factor 4 or 8 (see figure (1.24)),
- trench or inclusion depth: up to one wavelength,
- corresponding width: from 0.1 to 0.5 wavelength.

1.7 Earthquake engineering and seismology

1.7.1 Analysis at various scales

Wave propagation in surface soil layers is a key issue in the field of engineering seismology and earthquake geotechnical engineering. Investigating seismic wave propagation in soils is necessary to estimate the seismic ground motion at the surface, to study the response of large constructions (bridge, dam, power plant...) or the behaviour of geotechnical structures such as embankments or retaining walls. The assessment of the propagation process in the surficial soil layers is thus mandatory to characterize the seismic wavefield in such cases. As will be discussed in details in Chapter 5, seismic wave amplification (or *site effects*) and slope stability are important topics (Bard and Bouchon, 1985; Seed, 1974; Semblat *et al.*, 2005).

As depicted in Fig.1.28, seismic hazard and risk may be considered at various scales. From a phenomenological point of view, seismic wave propagation can generally be analyzed considering one of the following points of view:

- regional propagation from the seismic source,
- local propagation in surficial geological structures,
- propagation and interactions at the scale of one or several constructions.

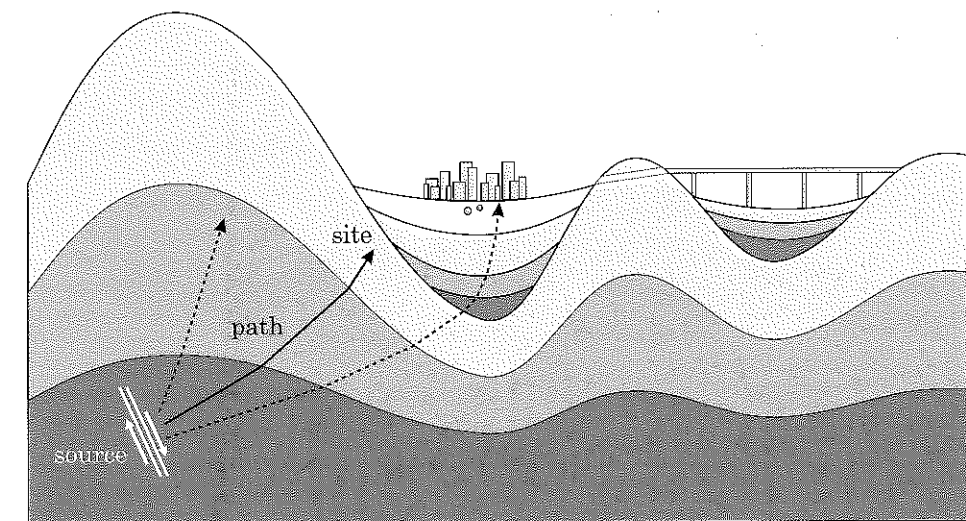


Fig. 1.28: Various scales to analyze seismic wave propagation in geological structures.

1.7.2 Seismic wave propagation in soils

The second topic of the previous list mainly considers the local geological (and geometrical) conditions near the free-surface since they may influence the propagation process. Due to complex refraction and scattering phenomena detailed in Chapter 5, seismic waves may be amplified in alluvial deposits or on topographic irregularities (Bard and Bouchon, 1985; Dobrin *et al.*, 1954; Moeen-Vaziri and Trifunac, 1988; Sánchez-Sesma *et al.*, 2000).

As shown in Fig.1.29 for the Kobe basin, the geological structure (top) is strongly heterogeneous and leads to complex propagation phenomena (Kawase *et al.*, 2000). In such cases, as computed by Matsushima and Kawase (2006), the seismic wavefield is thus amplified in the surficial layers as shown in the Peak Ground Velocity plot (bottom).

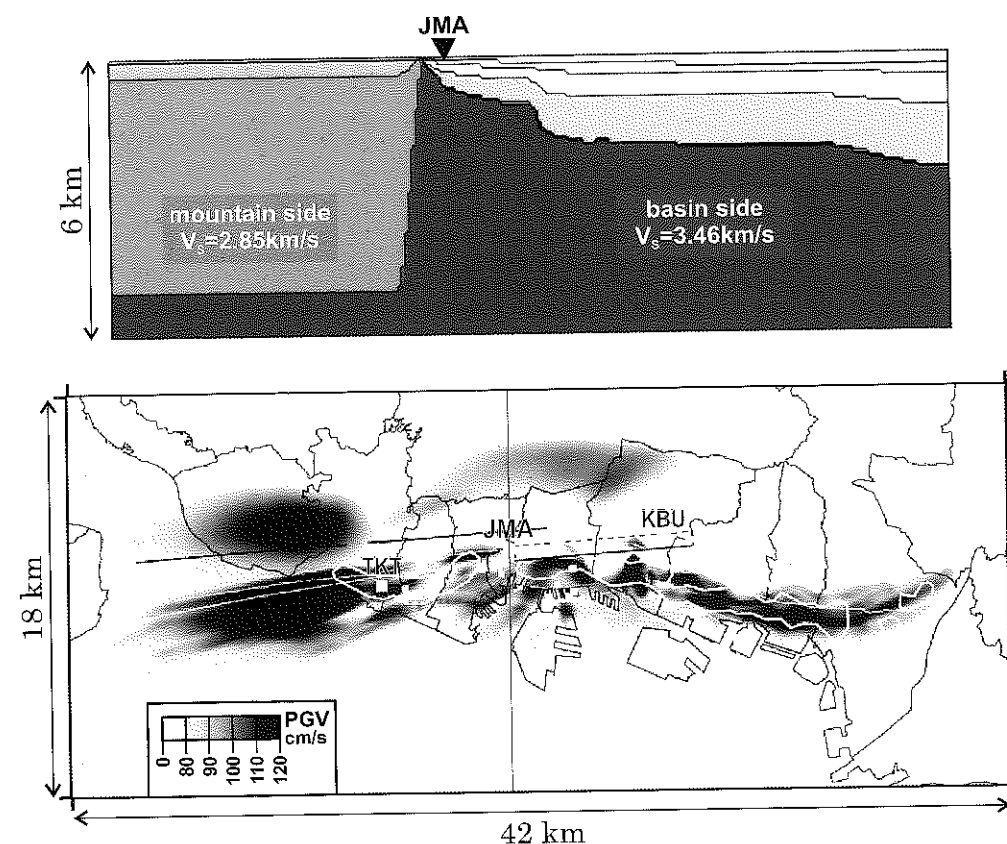


Fig. 1.29: Seismic wave propagation in the Kobe area (Japan): geological structure (top) and computed Peak Ground Velocity for the Kobe 1995 earthquake (Matsushima and Kawase, 2006).

The seismic ground motion to consider for the design of buildings or bridges is thus influenced by such complex propagation phenomena. Seismic code provisions are generally based on simplified 1D analyses (horizontally layered soils). However, actual amplification levels due to the local geology may raise the need for improvements to current code provisions (e.g. aggravation factors) or for more complex experimental/numerical analyses (Gélis *et al.*, 2008; Makra *et al.*, 2005). Such issues will be extensively discussed in Chapter 5.

The analysis of soil-structure interaction generally considers seismic wave propagation under a simplified form. The main issues to be emphasized are the boundary conditions at the base of the structure (fixed base assumption not valid for soft soils) and the energy radiation into the soil (influence on the overall damping in the structural response). The detailed analysis of the wave propagation process is generally not mandatory except for large structures such as dams, bridges or power plants. In such cases, the influence of the variability of the seismic wavefield may be significant and may lead to different assumptions for their design. For instance, Sextos *et al.* (2003) showed the influence of the seismic wave passage on the design of long span bridges.

For strong seismic motions, the analysis of the dynamic soil response strongly depends on the soil constitutive behaviour as well as on the loading history. Such complex phenomena as the liquefaction process may lead to very large strains as well as very poor bearing capacities. Many various complex constitutive models have been proposed in the literature (Bonilla, 2000; Delépine *et al.*, 2007; Hashash and Park, 2001; Kausel and Assimaki, 2002; Iai *et al.*, 1995; Prevost, 1985) but this issue is beyond the scope of this book mainly dedicated to the propagation process in soils.

1.7.3 Values of the mechanical parameters

Earthquake engineering problems are characterized by the following mechanical parameters:

- frequency: from 0.1 to 20 Hz,
- acceleration: from 0.1 to 20 ms^{-2} ,
- wavelength: from several tens to several hundreds of m,
- strain: from 10^{-4} to 2.10^{-3} m/m .

1.8 Synthesis of the various parameters

For the various domains of application detailed previously, the main parameters correspond to very different ranges of the mechanical parameters (frequency, strain rate, etc). Usual values of these various parameters are synthetized in Table 1.1.

Table 1.1: Characteristic values of the main mechanical parameters.

Type of problem	Main mechanical parameters characterizing the problem	
pile driving	<i>energy</i> 10 to 3000 J	<i>force at pile-head</i> 10 to 10000 kN
	<i>particle velocity</i> several mm/s	<i>displacement</i> several mm to several dm
dynamic compaction	<i>energy</i> several MJ	<i>mass acceleration</i> 50 to 500 m.s ⁻²
	<i>particle velocity</i> 10 to 30 m.s ⁻¹	<i>stress</i> 10 to 500 kPa
vibratory compaction	<i>frequency</i> 10 to 80 Hz	<i>force</i> 50 to 200 kN
	<i>cylinder axis speed</i> around 1 m.s ⁻¹	<i>vertical displacement</i> several mm
vibratory isolation	<i>frequency</i> 10 to 5000 Hz	<i>amplitude reduction</i> divided by 4 or 8
	<i>inclusion depth</i> up to one wavelength	<i>inclusion width</i> from 0.1 to 0.5 wavelength
earthquake engineering	<i>frequency</i> 0.1 to 20 Hz	<i>acceleration</i> 1 to 20 m.s ⁻²
	<i>wavelength</i> several tens to several hundreds of m	<i>strain</i> 10 ⁻⁴ to 2.10 ⁻³ m/m

Chapter 2

1D-wave propagation *Application to the dynamic characterization of soils*

2.1 Introduction

In this chapter, 1D wave propagation is studied considering the equilibrium of curvilinear media. Such media can be described as beams and bars, for which the system of coordinates is reduced to the location of the cross-section in terms of curvilinear abscissa s . The dynamic equilibrium equation of such systems leads to 2nd order partial differential equations with the following independent variables: the point location x , in a specific coordinate system, and the time t . The problem unknowns are represented by the displacement field $\underline{u} = \underline{u}(s, t)$ for the cross-section of abscissa s .

The 1D problem is firstly solved for various types of motion (longitudinal, transverse, etc). The corresponding results then allow the dynamic characterization of soils and rocks (resonant column, Split Hopkinson Pressure Bar, etc). Wave propagation in dissipative media as well as layered media are also discussed in details.

The main interest of the 1D analysis is to lead to scalar wave equations. In the next chapter, 2D/3D theory may be derived under a simplified 1D form to be compared to the present 1D analysis.

2.2 Dynamic equilibrium of a beam

2.2.1 Kinematics and main assumptions

One firstly considers the dynamic equilibrium of a beam. To write the equations of the dynamic equilibrium of the system, the following assumptions are considered:

- the system corresponds to a linear beam,

- the transformations remain small,
- the cross-sections of the beam remain plane during the deformation (Navier-Bernoulli assumption).

The mechanical formulation is written thanks to the Principle of Virtual Work (Salençon, 2001) involving, for any virtual velocity field \hat{U} , the rate of work by internal forces $\mathcal{P}_i(\hat{U})$, the rate of work by external forces $\mathcal{P}_e(\hat{U})$ and the rate of work by quantities of acceleration $\mathcal{A}(\hat{U})$. It leads to:

$$\mathcal{P}_i(\hat{U}) + \mathcal{P}_e(\hat{U}) = \mathcal{A}(\hat{U}) \quad (2.1)$$

The beam kinematic is fully described by a translation $\underline{v}_T(s)$ of a point of the neutral axis and a rotation $\underline{\omega}(s)$ of the cross-section (Fig. 2.1). In such conditions, the virtual velocity fields at point M can be written:

$$\hat{U} = \hat{v}_T(s) + \hat{\omega}(s) \wedge (\underline{x} - \underline{r}(s)) \quad (2.2)$$

where \underline{x} is the location of point M , $\underline{r}(s)$ the curvilinear abscissa of the cross-section and \wedge the vectorial product of two vectors.

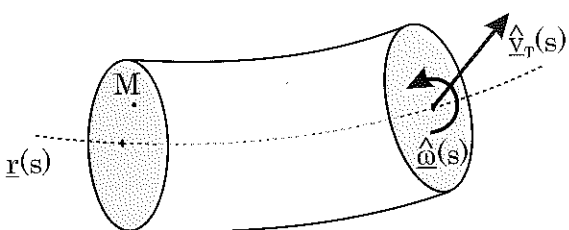


Fig. 2.1: Virtual velocity fields in a beam.

2.2.2 Virtual rate of work by internal forces

The virtual rate of work by internal forces $\mathcal{P}_i(\hat{U})$ for a beam volume $\Omega(s)$ of thickness ds is obtained by integrating a volume density $p_i(\hat{U})$ over $\Omega(s)$ (Salençon, 2001):

$$\mathcal{P}_i(\hat{U}) = \int_{\Omega(s)} p_i(\hat{U}) d\Omega \quad (2.3)$$

This volume density of the virtual work by internal forces, $p_i(\hat{U})$, corresponds to the virtual work by the contact forces in the gradient of the virtual velocity field. The gradient of the virtual velocity fields is derived from Eq. (2.2):

$$\frac{d\hat{U}}{ds} = \frac{d\hat{v}_T(s)}{ds} + \frac{d\hat{\omega}(s)}{ds} \wedge (\underline{x} - \underline{r}(s)) - \hat{\omega}(s) \wedge \frac{\partial \underline{r}(s)}{\partial s} \quad (2.4)$$

2.2 Dynamic equilibrium of a beam

and the contact forces are written using the stress tensor $\underline{\sigma}$ and the outward normal \underline{n} to the section:

$$\begin{aligned} \mathcal{P}_i(\hat{U}) &= \int_{\Omega(s)} p_i(\hat{U}) d\Omega = - \int_{\Omega(s)} (\underline{\sigma} \cdot \underline{n}) \cdot \frac{d\hat{U}}{ds} d\Omega \\ &= - \int_{\Omega(s)} (\underline{\sigma} \cdot \underline{n}) \cdot \frac{d\hat{v}_T}{ds} d\Omega - \int_{\Omega(s)} (\underline{\sigma} \cdot \underline{n}) \cdot \left[\frac{d\hat{\omega}}{ds} \wedge (\underline{x} - \underline{r}(s)) \right] d\Omega \\ &\quad + \int_{\Omega(s)} (\underline{\sigma} \cdot \underline{n}) \cdot \left[\hat{\omega} \wedge \frac{\partial \underline{r}(s)}{\partial s} \right] d\Omega \end{aligned} \quad (2.5)$$

Taking into account the following identity:

$$\underline{v}_1 \cdot \underline{v}_2 \wedge \underline{v}_3 = [\underline{v}_3 \wedge \underline{v}_1] \cdot \underline{v}_2 \quad (2.6)$$

and the relation :

$$\frac{\partial \underline{r}(s)}{\partial s} = \underline{n} \quad (2.7)$$

equation (2.5) can be modified in the following form:

$$\begin{aligned} \mathcal{P}_i(\hat{U}) &= - \int_{\Omega(s)} (\underline{\sigma} \cdot \underline{n}) \cdot \frac{d\hat{v}_T}{ds} d\Omega - \int_{\Omega(s)} [(\underline{x} - \underline{r}(s)) \wedge (\underline{\sigma} \cdot \underline{n})] \cdot \frac{d\hat{\omega}}{ds} d\Omega \\ &\quad + \int_{\Omega(s)} (\underline{\sigma} \cdot \underline{n}) \cdot [\hat{\omega} \wedge \underline{n}] d\Omega \end{aligned} \quad (2.8)$$

At this stage, it is possible to introduce the generalized resulting force acting on the cross-section. It is represented by both the force \underline{V} and the moment \underline{M} :

$$\begin{aligned} \underline{V} &= \int_{S(s)} (\underline{\sigma} \cdot \underline{n}) dS \\ \underline{M} &= \int_{S(s)} [(\underline{x} - \underline{r}(s)) \wedge (\underline{\sigma} \cdot \underline{n})] dS \end{aligned} \quad (2.9)$$

where $S(s)$ is the cross-sectional area at abscissa s .

Introducing these quantities into Eq. (2.8), the virtual rate of work by internal forces between two sections A and B is written:

$$\mathcal{P}_i(\hat{U}) = - \int_A^B \left[\underline{V} \cdot \left(\frac{d\hat{v}_T}{ds} - \hat{\omega} \wedge \underline{n} \right) + \underline{M} \cdot \frac{d\hat{\omega}}{ds} \right] ds \quad (2.10)$$

The force \underline{V} and the moment \underline{M} can be split into two components: one oriented along the section normal \underline{n} and one belonging to the cross-section:

$$\underline{V} = N\underline{n} + \underline{V}_{\perp}, \quad \underline{M} = M_t \underline{n} + \underline{M}_{\perp} \quad (2.11)$$

Under this form, the classical parameters of the beam theory can be identified: the normal force N , the shear force \underline{V}_{\perp} , the torsional moment M_t and the bending moment \underline{M}_{\perp} .

The same decomposition can be performed on the components of the virtual velocity fields $\hat{v}_T(s)$ and $\hat{\omega}(s)$ by introducing Eq. (2.11) into Eq. (2.10) and noticing that the scalar product $\underline{n} \cdot \underline{t}$ is zero. For every vector \underline{t} located in the cross-section, the virtual rate of work by internal forces becomes:

$$\mathcal{P}_i(\hat{U}) = \int_A^B \left[-N \frac{d\hat{v}_n}{ds} - \underline{V}_{\perp} \cdot \left(\frac{d\hat{v}_{\perp}}{ds} - \hat{\omega} \wedge \underline{n} \right) - M_t \frac{d\hat{\omega}_n}{ds} - \underline{M}_{\perp} \cdot \frac{d\hat{\omega}_{\perp}}{ds} \right] ds \quad (2.12)$$

Under this form, the various terms in the right hand term of Eq. (2.12) correspond to the classical parameters of the beam theory:

- first term: elongation of the neutral fiber,
- second term: shearing in the section,
- third term: torsion around the axis normal to the section,
- fourth term: bending around the axis located in the cross-section.

2.2.3 Virtual rate of work by external forces

Assuming the beam being subjected to a volumic density of external forces \underline{f} , the virtual rate of work by external forces may be written:

$$\mathcal{P}_e(\hat{U}) = \int_{\Omega(s)} \underline{f} \cdot \hat{U} d\Omega \quad (2.13)$$

Taking into account the expression of the virtual velocity field given by Eq. (2.2), it yields:

$$\underline{f} \cdot \hat{U} = \underline{f} \cdot \hat{v}_T(s) + \underline{f} \cdot [\hat{\omega}(s) \wedge (\underline{x} - \underline{r}(s))] \quad (2.14)$$

that is, considering Eq. (2.6):

$$\underline{f} \cdot \hat{U} = \underline{f} \cdot \hat{v}_T(s) + [(\underline{x} - \underline{r}(s)) \wedge \underline{f}] \cdot \hat{\omega}(s) \quad (2.15)$$

Introducing the linear density of external forces:

$$\underline{f}_l = \int_{S(s)} \underline{f} dS \quad (2.16)$$

and the linear density of moment from external forces:

$$\underline{m} = \int_{S(s)} [\underline{x} - \underline{r}(s)] \wedge \underline{f} dS \quad (2.17)$$

The virtual rate of work by external forces between two cross-sections A and B is written:

$$\mathcal{P}_e(\hat{U}) = \int_A^B \underline{f}_l \cdot \hat{v} ds + \int_A^B \underline{m} \cdot \hat{\omega} ds \quad (2.18)$$

2.2.4 Virtual rate of work by quantities of acceleration

To simplify the presentation, we neglect the inertial terms in rotation. Denoting ρ the mass density of the beam and S its cross-sectional area, the virtual rate of work by quantities of acceleration is written:

$$\mathcal{A}(\hat{U}) = \int_A^B \rho S [\underline{r}(s) \cdot \hat{v}(s)] ds \quad (2.19)$$

2.2.5 Equilibrium equation

Introducing Eqs (2.12), (2.18) and (2.19) into Eq. (2.1) leads to the dynamic equilibrium equations of the beam. The various terms involved in these equations can be grouped into three categories: the terms involving components normal to the cross-section, components around an axis normal to the cross-section and components belonging to the cross-section. The virtual velocity fields being arbitrary, it is possible to choose fields successively with components normal to the section, around an axis normal to the section and in the cross-section (Salençon, 2001). We thus write the principle of virtual work for each of these fields. The equilibrium equations are detailed in the following.

Component normal to the cross-section: elongation

For the component normal to the cross-section, the following equation is obtained:

$$\int_A^B \left(-N \frac{d\hat{v}_n}{ds} + f_n \hat{v}_n - \rho S \ddot{v}_n \hat{v}_n \right) ds = 0 \quad (2.20)$$

considering free ends and integrating by parts the first term:

$$\int_A^B \left(\frac{\partial N}{\partial s} + f_n - \rho S \ddot{v}_n \right) \hat{v}_n ds = 0 \quad (2.21)$$

which should be valid for every virtual velocity \hat{v}_n . As a result, the equilibrium equation becomes:

$$\frac{\partial N}{\partial s} + f_n - \rho S \ddot{v}_n = 0 \quad (2.22)$$

Component around an axis normal to the section: torsion

For this component, the equilibrium equation is written as follows:

$$\int_A^B \left(-M_t \frac{d\hat{\omega}_t}{ds} + m_t \hat{\omega}_t \right) ds = 0 \quad (2.23)$$

integrating by parts the first term (free ends assumption) and writing that this relation should be valid for every virtual velocity $\hat{\omega}_t$, the equilibrium equation is derived as:

$$\frac{\partial M_t}{\partial s} + m_t = 0 \quad (2.24)$$

or, taking into account the rotational inertia neglected when writing the virtual rate of work by quantities of acceleration, the following form is obtained:

$$\frac{\partial M_t}{\partial s} + m_t - \rho J \ddot{\theta}_t = 0 \quad (2.25)$$

where J is the geometrical torsional inertia of the beam and $\ddot{\theta}_t$ is the torsional angular acceleration.

Component in the cross-section: bending-shear

The following equation is obtained:

$$\begin{aligned} & \int_A^B \left(-V_{\perp} \cdot \frac{d\hat{v}_{\perp}}{ds} + f_{\perp} \cdot \hat{v}_{\perp} - \rho \ddot{u}_{\perp} \cdot \hat{u}_{\perp} \right) ds \\ & + \int_A^B \left(V_{\perp} \cdot (\hat{\omega}_{\perp} \wedge n) - M_{\perp} \cdot \frac{d\hat{\omega}_{\perp}}{ds} + m_{\perp} \cdot \hat{\omega}_{\perp} \right) ds = 0 \end{aligned} \quad (2.26)$$

The previous relation should be valid for every virtual velocity fields \hat{v}_{\perp} and $\hat{\omega}_{\perp}$. Integrating by parts (free ends assumption) and using Eq. (2.6) lead to the two following equilibrium equations:

$$\frac{\partial V_{\perp}}{\partial s} + f_{\perp} - \rho S \ddot{u}_{\perp} = 0 \quad (2.27)$$

$$\frac{\partial M_{\perp}}{\partial s} + m_{\perp} - V_{\perp} \wedge n = 0 \quad (2.28)$$

The previous vectorial equations can be expressed under a scalar form by choosing, in the cross-section, a system of normal axes for which the components of the various parameters are written:

$$\underline{M}_{\perp} = \begin{Bmatrix} M_1 \\ M_2 \\ 0 \end{Bmatrix}, \quad \underline{V}_{\perp} = \begin{Bmatrix} V_1 \\ V_2 \\ 0 \end{Bmatrix}, \quad \underline{m}_{\perp} = \begin{Bmatrix} m_1 \\ m_2 \\ 0 \end{Bmatrix}, \quad \underline{n} = \begin{Bmatrix} 0 \\ 0 \\ 1 \end{Bmatrix} \quad (2.29)$$

Equation (2.28) thus yields the following equations:

$$\begin{cases} V_1 = -\frac{\partial M_2}{\partial s} - m_2 \\ V_2 = +\frac{\partial M_1}{\partial s} + m_1 \end{cases} \quad (2.30)$$

then, introducing into Eq. (2.27), the two equations governing the equilibrium of

2.3 Longitudinal vibrations of beams

moments are obtained, hence leading to the global equilibrium:

$$\begin{cases} V_1 = -\frac{\partial M_2}{\partial s} - m_2 \\ V_2 = +\frac{\partial M_1}{\partial s} + m_1 \\ -\frac{\partial^2 M_2}{\partial s^2} - \frac{\partial m_2}{\partial s} + f_1 - \rho S \ddot{u}_1 = 0 \\ +\frac{\partial^2 M_1}{\partial s^2} + \frac{\partial m_1}{\partial s} + f_2 - \rho S \ddot{u}_2 = 0 \end{cases} \quad (2.31)$$

2.3 Longitudinal vibrations of beams

2.3.1 Dynamic equilibrium

In this section, we consider the longitudinal vibration of beams, that is phenomena controlled by Eq. (2.22). Equation (2.22) was obtained as a specific case of the general equations governing the vibration of beams. It should be noticed that it may also be derived by identifying the axial forces acting on a beam slice and writing that their sum is zero (Fig. 2.2).

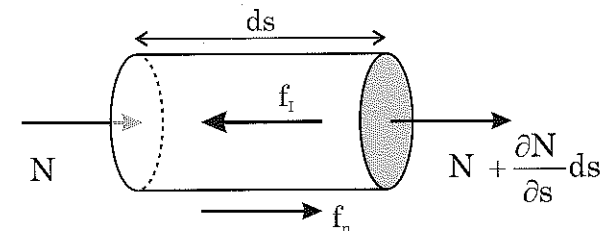


Fig. 2.2: Axial equilibrium of a beam.

This equilibrium equation is written:

$$N + \frac{\partial N}{\partial s} ds + (f_n - f_I) ds - N = 0 \quad (2.32)$$

in which, denoting S the section area and ρ the density, the inertial forces f_I are expressed as:

$$f_I = \rho S \ddot{u}_n \quad (2.33)$$

To derive the problem solution, in addition to Eq. (2.22) describing the equilibrium, it is necessary to write the constitutive law of the beam for purely axial loads. This constitutive law relates the axial force to the elongation of the neutral fiber. Considering linear elasticity and small strains, it is written as follows:

$$N = E S \frac{\partial u}{\partial s} \quad (2.34)$$

where E is the Young's modulus of the medium. In Eq. (2.34) and all equations in the present section, index n is omitted to make the presentation clearer; u corresponds to the displacement oriented along the section normal n .

Introducing Eq. (2.34) into (2.22), the equation describing the axial vibrations of the beam is:

$$\frac{\partial^2 u}{\partial t^2} - \frac{E}{\rho S(s)} \frac{\partial}{\partial s} \left(S(s) \frac{\partial u}{\partial s} \right) = \frac{f}{\rho S(s)} \quad (2.35)$$

For a non-constant cross-sectional area $S(s)$, it is thus necessary to determine the spatial derivative of the $S(s) \frac{\partial u}{\partial s}$ product. For a cylindrical beam ($S(s)$ constant), the equation describing the axial vibrations is as follows:

$$\frac{\partial^2 u}{\partial t^2} - \frac{E}{\rho} \frac{\partial^2 u}{\partial s^2} = \frac{f}{\rho S} \quad (2.36)$$

2.3.2 Homogeneous equation

Assuming the linear density of forces f to be zero, the homogeneous equation of vibrations is the following:

$$\ddot{u}(s, t) - c^2 u''(s, t) = 0 \quad (2.37)$$

in which we introduced the 1D longitudinal wave velocity c , defined as¹:

$$c = \sqrt{\frac{E}{\rho}} \quad (2.38)$$

\ddot{u} and u'' denote the second order partial derivatives with respect to time and space (respectively).

Classical wave velocity values for usual materials are:

- steel: $c=5200$ m/s,
- concrete: $c=3600$ m/s,
- dry sand: $c=300$ -500 m/s.

Equation (2.37) corresponds to a first order hyperbolic differential system. Its solution is classically obtained by introducing the two unknowns U_1 et U_2 defined as:

$$U_1 = u \quad ; \quad U_2 = -\frac{\partial}{\partial s} \int_0^t u(s, \tau) d\tau \quad (2.39)$$

¹As we will see in Chapter 3, the 1D longitudinal wave velocity c differs from the 2D/3D pressure wave velocity V_P because the lateral boundary conditions (free-surface) in a beam are not the same as in 2D/3D

Equation (2.37) is then equivalent to the differential system:

$$\begin{cases} \frac{\partial U_1}{\partial t} + c^2 \frac{\partial U_2}{\partial s} = 0 \\ \frac{\partial U_2}{\partial t} + \frac{\partial U_1}{\partial s} = 0 \end{cases} \quad (2.40)$$

or, under matrix form, denoting $\underline{U}^T = \{U_1, U_2\}$:

$$\frac{\partial \underline{U}}{\partial t} + [A] \frac{\partial \underline{U}}{\partial s} = 0 \quad (2.41)$$

The operator $[A]$ has the following expression:

$$[A] = \begin{bmatrix} 0 & c^2 \\ 1 & 0 \end{bmatrix} \quad (2.42)$$

and its eigenvalues are $+c$ and $-c$. The general solution of the differential system (2.40) is:

$$u(s, t) = u_1(s - ct) + u_2(s + ct) \quad (2.43)$$

Solution (2.43) represents the superposition of two waves, with amplitudes u_1 and u_2 , propagating at velocity c , towards direction $s > 0$ and direction $s < 0$ respectively. During their propagation, both waves keep the same shape (Fig.2.3); these waves are called *non dispersive* waves.

Another form of the solution of differential system (2.40) may be:

$$u(s, t) = u_3 \left(t - \frac{s}{c} \right) + u_4 \left(t + \frac{s}{c} \right) \quad (2.44)$$

which is equivalent to solution (2.43).

Quantities u_1 and u_2 are determined by the initial conditions. The differential equation governing the axial vibration of beams being of second order, two initial conditions are needed:

$$\text{at } t = 0 : \quad u(s, 0) \text{ and } \dot{u}(s, 0) \quad (2.45)$$

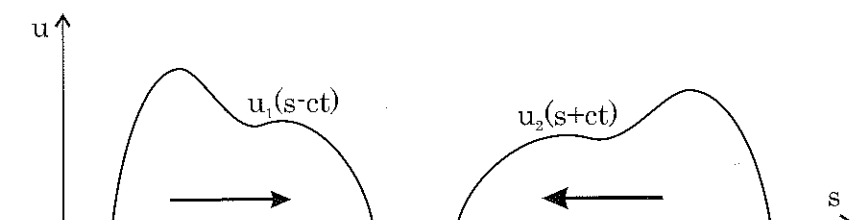


Fig. 2.3: Longitudinal waves propagating in a bar.

Deriving the displacement and the velocity at time $t = 0$ from solution (2.43), for every section of abscissa s , it gives:

$$\begin{cases} u(s, 0) = u_1(s) + u_2(s) \\ \dot{u}(s, 0) = -cu'_1(s) + cu'_2(s) \end{cases} \quad (2.46)$$

It is then possible to write u_1 and u_2 as functions of the initial conditions:

$$\begin{cases} u_1(s) = \frac{1}{2}u(s, 0) - \frac{1}{2c} \int_0^s \dot{u}(\beta, 0) d\beta + a \\ u_2(s) = \frac{1}{2}u(s, 0) + \frac{1}{2c} \int_0^s \dot{u}(\beta, 0) d\beta - a \end{cases} \quad (2.47)$$

where a is an integration constant.

2.3.3 Solution in terms of stresses

The solution being known in terms of displacement, the stress in the beam can be derived from the constitutive law (2.34):

$$\sigma = E \frac{\partial u}{\partial s} = -E [u'_1(s - ct) + u'_2(s + ct)] = g_1(s - ct) + g_2(s + ct) \quad (2.48)$$

The axial stress in the beam is due to the superposition of two non dispersive waves, propagating towards directions $s > 0$ and $s < 0$ respectively. This stress can also be written as a function of velocities \dot{u}_1 and \dot{u}_2 called *particle velocities*. Considering the following relations:

$$\begin{cases} \dot{u}_1(s, t) = \frac{\partial u_1(s, t)}{\partial t} = -cu'_1(s - ct) \\ \dot{u}_2(s, t) = \frac{\partial u_2(s, t)}{\partial t} = +cu'_2(s + ct) \end{cases} \quad (2.49)$$

and noting that $E = \rho c^2$, the axial stress can be written as:

$$\sigma = -\rho c(\dot{u}_1 - \dot{u}_2) \quad (2.50)$$

2.3.4 Eigenmodes of the bar

An example dealing with pile driving (§2.3.5) will now illustrate the difficulty to determine the solution if multiple reflections take place during the propagation process. The calculation of all these reflections, to express the general solution, becomes rapidly impossible. It is often more suitable to try to solve the problem using the decomposition of the solution on the eigenmodes base. The eigenmodes represent the periodic solution of the homogeneous equation (2.37). These solutions take the following form:

$$u(s, t) = X(s)e^{i\omega t} \quad (2.51)$$

2.3 Longitudinal vibrations of beams

Introducing this relation into Eq. (2.37), function $X(s)$ should satisfy:

$$c^2 X''(s) + \omega^2 X(s) = 0 \quad (2.52)$$

The solution of Eq. (2.52) is of the form:

$$X(s) = A \cos\left(\frac{\omega}{c}s\right) + B \sin\left(\frac{\omega}{c}s\right) \quad (2.53)$$

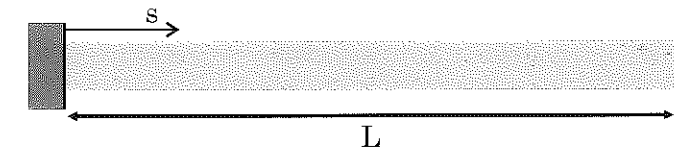


Fig. 2.4: Cantilever beam to estimate the axial eigenmodes.

The integration constants A and B are determined by the boundary conditions. In the case of the cantilever beam depicted in Fig. 2.4, these boundary conditions are given by:

$$\begin{cases} X(0) = 0 \\ N(L) = ES \frac{dX(L)}{ds} = 0 \end{cases} \quad (2.54)$$

Conditions (2.54) imply:

$$\begin{cases} X(0) = 0 \Rightarrow A = 0 \\ X'(L) = 0 \Rightarrow \cos\left(\frac{\omega L}{c}\right) = 0 \end{cases} \quad (2.55)$$

The eigenfrequencies are solutions of Eq. (2.55b), that is:

$$\omega_n = (2n - 1) \frac{\pi c}{2L} \quad (2.56)$$

The related eigenmodes are then given by:

$$X_n(s) = \sin\left[(2n - 1)\frac{\pi s}{2L}\right] \quad (2.57)$$

The eigenmodes defined by Eq. (2.57) fulfil the following condition and thus correspond to an orthogonal base:

$$\int_0^L X_m(s)X_n(s)ds = 0 \quad \text{if } m \neq n \quad (2.58)$$

The solution in terms of eigenmodes can also be written as the superposition of a wave propagating in the positive direction and a wave propagating in the negative direction. Considering the trigonometric identity, for the n^{th} mode, we get:

$$\begin{aligned} u_n(s, t) &= B \sin \left[(2n - 1) \frac{\pi s}{2L} \right] \cos(\omega_n t) \\ &= \frac{B}{2} \sin \left[(2n - 1) \frac{\pi}{2L} (s - ct) \right] + \frac{B}{2} \sin \left[(2n - 1) \frac{\pi}{2L} (s + ct) \right] \end{aligned} \quad (2.59)$$

The general solution of the equation of vibrations (2.36) can then be obtained by superposition of all the eigenmodes:

$$u(s, t) = \sum_{n=1}^{\infty} X_n(s) q_n(t) \quad (2.60)$$

$$\text{and } f(s, t) = \sum_{n=1}^{\infty} X_n(s) f_n(t) \quad (2.61)$$

Introducing expressions (2.60) and (2.61) into Eq. (2.36) and taking into account the orthogonality property (2.58), $q_n(t)$ fulfills the following differential equation:

$$\ddot{q}_n(t) + \omega_n^2 q_n(t) = f_n(t) \quad \text{with } n = 1, +\infty \quad (2.62)$$

$$\text{with: } f_n = \frac{2}{\rho S L} \int_0^L X_n(s) f(s, t) ds$$

The similarity with the analysis of systems with a finite number of degrees of freedom is obvious: the decomposition to eigenmodes leads to the determination of the solution of ordinary 2nd order differential equations (Eq. (2.62)). The only difference is the infinite number of equations corresponding to the infinite number of degrees of freedom of such a continuous system.

2.3.5 Example 1: pile driving

The various results established in the previous sections will be detailed in the simplified case of pile driving. As already shown in Chapter 1, various waves propagate in the pile at each blow. These waves will be analyzed in details hereafter.

Wave propagation in the pile

Consider a pile of length L undergoing, at time $t = 0$, an impact force at the top (falling mass), generally called an *impactor* (Fig. 2.5). This impact is supposed to induce the following axial stress:

$$\sigma_0(t) = -A \sin(\omega t) \quad (2.63)$$

and the pile is not subjected to any other force. This assumption implies that frictional forces generated at the soil-pile interface are negligible (a rough description of reality). In the previous relation, the sign '-' stands for the fact that the axial stress is compressive.

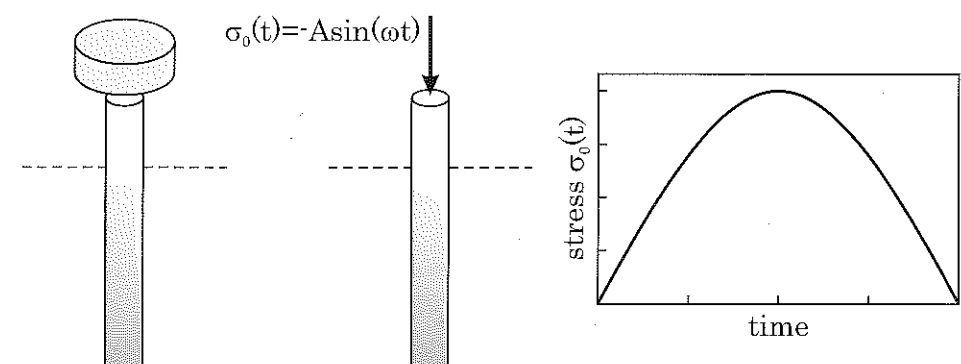


Fig. 2.5: Example of dynamic pile driving and variations of the axial stress.

The steel pile has a longitudinal wave velocity $c = 5200\text{m/s}$ and the shock duration is $T = 0.01\text{s}$ (that is $\omega = 2\pi/T = 628.3\text{rad/s}$).

The impact generates an incident wave, propagating towards the pile end ($s > 0$). No wave can of course propagate toward direction $s < 0$ since there is no pile in this direction. Considering Eq. (2.48), the stress due to the incident wave is as follows:

$$\sigma(s, t) = g_1(s - ct) \quad (2.64)$$

At section $s = 0$, the expression of the axial stress is:

$$\sigma(0, t) = \sigma_0(t) = g_1(-ct) \Rightarrow g_1(-ct) = -A \sin\left(\frac{\omega}{c}ct\right) \quad (2.65)$$

from which the stress formulation in the pile is:

$$\sigma(s, t) = -A \sin\left[\frac{\omega}{c}(ct - s)\right] \quad (2.66)$$

At time $t = \pi/\omega$, the impact has ended (Fig. 2.6) and the stress wave propagates for larger times without any changes along the pile. It reaches the pile end at time $t = L/c$.

Wave reflection at the pile end

Reaching the pile end ($t = L/c$), the incident wave generates a reflected wave ($u_2(s, t)$, $\sigma_2(s, t)$). Its nature depends on the boundary condition at section $s = L$. Let us consider two extreme cases:

- *Fixed end*: it corresponds to the case where the pile reaches a very stiff layer, such as bedrock. The boundary condition is expressed through $u(L, t) = 0$ for all t .
- *Pile end located in a very soft medium*: the force acting in section $s = L$ can be considered to be nearly zero ; the boundary condition is expressed by $N(L, t) = 0$ for all t .

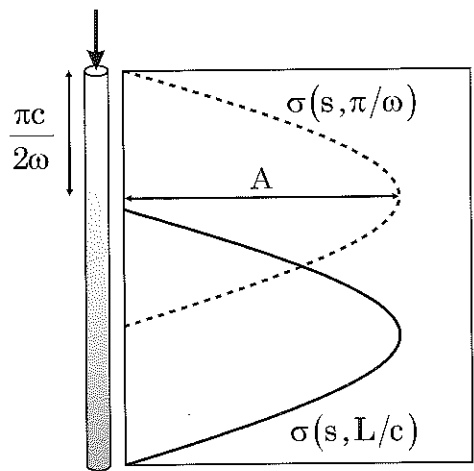


Fig. 2.6: Axial stress distribution in the pile ($t \leq L/c$).

Fixed end: In the case of a fixed end, the solution is straightforward:

$$u(L, t) = 0 \Rightarrow u_1(L - ct) = -u_2(L + ct) \quad (2.67)$$

$$\sigma(L, t) = -\rho c(\dot{u}_1 - \dot{u}_2) = -2\rho c \dot{u}_1(L, t) \quad (2.68)$$

The pressure wave $\sigma_1(s, t)$ is reflected as a pressure wave $\sigma_2(s, t)$ with the same amplitude. During the reflection phase, that is $L/c \leq t \leq L/c + \pi/\omega$, the contributions of the two waves are combined. For larger times, only the reflected wave exists; it propagates towards the pile cap where it will undergo another reflection.

The following equations give the value of the axial stress in the pile until the reflected wave reaches the pile cap:

$$\begin{cases} \sigma_1(s, t) = -A \sin \left[\frac{\omega}{c}(ct - s) \right] \\ \sigma_2(s, t) = -A \sin \left[\frac{\omega}{c}(ct + s) - 2\frac{\omega L}{c} \right] \end{cases} \quad (2.69)$$

That is, superposing the contributions of both waves:

$$\begin{cases} 0 \leq t \leq L/c : & \sigma(s, t) = \sigma_1(s, t) \\ L/c < t \leq L/c + \pi/\omega : & \sigma(s, t) = \sigma_1(s, t) + \sigma_2(s, t) \\ L/c + \pi/\omega < t \leq 2L/c : & \sigma(s, t) = \sigma_2(s, t) \end{cases} \quad (2.70)$$

Figure 2.7 displays the stress diagram corresponding to the reflection phase.

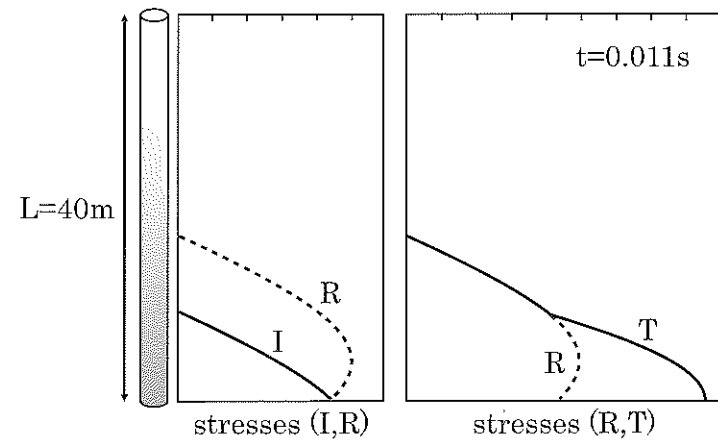


Fig. 2.7: Stresses during the reflection phase - fixed end case (I : incident ; R : reflected ; T : total).

Free end: The free end condition can be written:

$$\sigma(L, t) = 0 \Rightarrow \dot{u}_1(L - ct) = \dot{u}_2(L + ct) \Leftrightarrow u'_1(L - ct) = -u'_2(L + ct) \quad (2.71)$$

that is, after integration:

$$u_1(L - ct) = u_2(L + ct) \quad (2.72)$$

The pressure incident wave $\sigma_1(s, t)$ is reflected as a tensile wave with the same amplitude.

Similarly to the case of a fixed end, the following equations give the axial stress value in the pile until the second reflection takes place at the pile cap:

$$\begin{cases} \sigma_1(s, t) = -A \sin \left[\frac{\omega}{c}(ct - s) \right] \\ \sigma_2(s, t) = +A \sin \left[\frac{\omega}{c}(ct + s) - 2\frac{\omega L}{c} \right] \end{cases} \quad (2.73)$$

The '+' sign in the expression of the reflected wave stands for a tensile stress. Superposing the contributions of both waves:

$$\begin{cases} 0 \leq t \leq L/c : & \sigma(s, t) = \sigma_1(s, t) \\ L/c < t \leq L/c + \pi/\omega : & \sigma(s, t) = \sigma_1(s, t) + \sigma_2(s, t) \\ L/c + \pi/\omega < t \leq 2L/c : & \sigma(s, t) = \sigma_2(s, t) \end{cases} \quad (2.74)$$

Figure 2.8 displays the stress diagram obtained during the reflection phase.

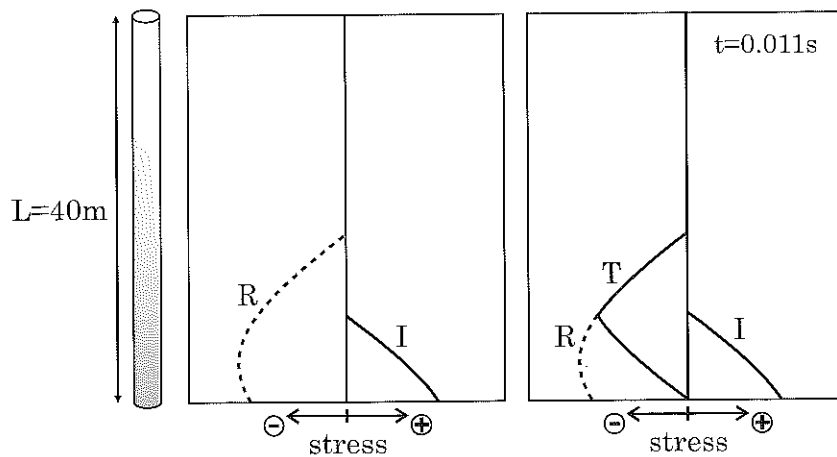


Fig. 2.8: Stresses during the reflection phase - free end case (I : incident ; R : reflected ; T : total).

2.3.6 Example 2: characterization of a heterogeneous bar

Propagation in a heterogeneous bar

The previous section presented simple examples of various boundary conditions. A more complex example corresponds to the case where an incident wave propagates through an interface between two media with different properties (Fig. 2.9). One should now enforce the continuity of both displacements and forces at the interface. Denoting the variables of medium 1 with index 1 and those of medium 2 with index 2, these conditions can be written under the following form:

- continuity of displacement : $u_1 = u_2$
- continuity of forces : $N_1 = N_2$

When the incident wave reaches the interface, a part of its energy is reflected and carried by the reflected wave propagating backward in medium 1. The complementary energy crosses the interface and is carried by another wave, called refracted or transmitted wave, propagating in medium 2. The variables related to medium 1 may be decomposed into incident variables, denoted with index I , and reflected variables, denoted with index R . The variables related to the transmitted wave are written, with index T . The continuity conditions thus write:

$$\begin{cases} u_T = u_I + u_R \\ N_T = N_I + N_R \end{cases} \quad (2.75)$$

2.3 Longitudinal vibrations of beams

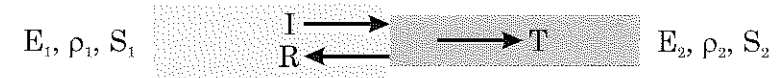


Fig. 2.9: Interface conditions between two media.

Application to Hopkinson bar tests

A practical example is proposed in Fig. 2.10 where the experimental device called Split Hopkinson Pressure Bar (SHPB) is described (Klepaczko *et al.*, 1991; Zhao *et al.*, 1997). A cylindrical specimen of known dimensions, but with unknown mechanical properties, is installed between two cylindrical steel bars². The impact is imposed at the end of a bar; the measurement of the displacement due to the incident and reflected waves allows the estimation of the wave velocity in the specimen. The Split Hopkinson Pressure Bar is presented in details at the end of this chapter and fast dynamic experiments on soils using SHPB are also discussed (§2.11).

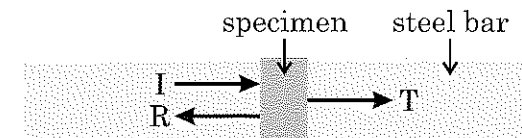


Fig. 2.10: Schematic of the Split Hopkinson Pressure Bar test.

Denoting $\chi = \rho_1 c_1 / \rho_2 c_2$ the ratio of the properties between medium 1 (steel bar) and medium 2 (specimen), we successively apply conditions (2.75). We thus obtain the amplitude ratio between the wave transmitted in the steel bar beyond the specimen and the incident wave in the steel bar before the specimen:

$$\frac{u_T}{u_I} = \frac{4\chi}{(1+\chi)^2} \quad (2.76)$$

This relation allows the estimation of parameter χ as well as the wave velocity c_2 in the specimen. It may depend on the ratio between the cross-sectional areas of the bar and the specimen if they are different. It is due to the expression of the normal forces (Eq. (2.34)), involving the cross-sectional area S , and their continuity at the interfaces (Eq. (2.75)b).

The previous example is a simplified version of the Split Hopkinson Bar experiment considering linear elasticity. This test is indeed very general and actually permits the identification of dynamic constitutive laws well beyond linear elasticity (see §2.11).

²Steel bars are mainly dedicated to experiments on stiff materials such as metals or rocks whereas softer bars (e.g. PMMA/Plexiglas) can be used for soft materials such as soils (see §2.11)

2.3.7 Absorbing boundaries

Numerical computations for wave propagation problems, for instance in the framework of the Finite Element Method (see Chapter 4), raise the need for an accurate description of wave radiation at infinity. Free or fixed boundaries originate wave reflections in their vicinity. These reflections do not generally correspond to realistic phenomena and influence the solution accuracy. In the one-dimensional case, it is possible to control such reflections by introducing, at the model boundaries, specific elements known as *absorbing boundaries*. Their role is to approximate the exact stress conditions at the medium boundaries (Fig. 2.11a).

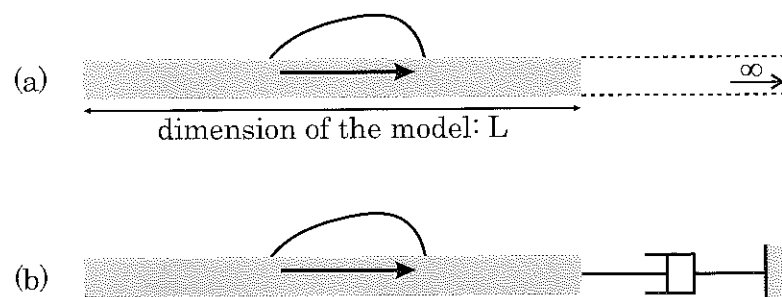


Fig. 2.11: Absorbing boundaries in a 1D medium.

In the example of Fig. 2.11(a), the aim is to represent at section $s = L$ the conditions that would exist if the bar was of infinite dimension. In this cross-section, due to the finite dimension of the model, the displacement (or stress) results from the superposition of two waves, an incident one denoted with index 1 and a reflected one denoted with index 2. The goal is to remove the contribution of the reflected wave, that is to satisfy the following relations:

$$\begin{cases} u(L, t) = u_1(L, t) + u_2(L, t) = u_1(L, t) \\ \sigma(L, t) = \sigma_1(L, t) + \sigma_2(L, t) = \sigma_1(L, t) \end{cases} \quad (2.77)$$

The stresses at the medium free boundary can be written as a function of the particle velocity:

- incident wave : $\sigma_1(L, t) = -\rho c \dot{u}_1(L, t)$ (2.78)

- reflected wave : $\sigma_2(L, t) = +\rho c \dot{u}_1(L, t)$ (2.79)

To remove the contribution of the reflected wave, it is then necessary to impose in this cross-section a stress equal to $-\rho c \dot{u}_1(L, t)$. This stress is precisely that developed in a viscous damper having a viscosity $\eta = \rho c$. Adding such a damper at the beam end removes the contribution of the reflected wave; this system is then equivalent to a beam

2.4 Torsional vibrations of beams

of infinite length.

Proof : Denoting $u(L, t)$ the displacement at section $x = L$ of the model depicted in Fig. 2.11(b), we consider a beam of finite length connected to a damper.

From Eq. (2.50), the stress in this section can be written:

$$\sigma(L, t) = -\rho c [\dot{u}_1(L, t) - \dot{u}_2(L, t)] \quad (2.80)$$

and, due to the effect of the damper, it is equal to:

$$\sigma(L, t) = -\rho c \ddot{u}(L, t) \quad (2.81)$$

Furthermore, the displacement $u(L, t)$ may also be derived as the sum of the contributions of both the incident wave and the reflected wave:

$$u(L, t) = u_1(L, t) + u_2(L, t) \quad (2.82)$$

The combination of Eqs (2.80) and (2.82) yields:

$$\dot{u}_1(L, t) - \dot{u}_2(L, t) = \dot{u}_1(L, t) + \dot{u}_2(L, t) \quad (2.83)$$

which leads to $\dot{u}_2(L, t) = 0$ and then $\sigma_2(L, t) = 0$ and $u_2(L, t) = 0$.

2.4 Torsional vibrations of beams

2.4.1 Dynamic equilibrium

In this section, we focus on the torsional vibration of beams, that is phenomena governed by Eq. (2.25). Equation (2.25) was obtained as a particular case of the general equations governing the vibration of beams. It can also be derived through the identification of the torsional forces acting on a beam slice and considering its equilibrium (Fig. 2.12).

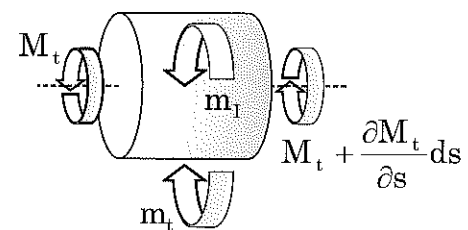


Fig. 2.12: Torsional equilibrium of a beam.

This equilibrium equation is written:

$$M_t + \frac{\partial M_t}{\partial s} ds + (m_t - m_{t+ds}) ds - M_{t+ds} = 0 \quad (2.84)$$

in which the inertial forces m_I are as follows:

$$m_I = \rho J \ddot{\theta} \quad (2.85)$$

In addition to Eq. (2.84), it is necessary to consider the constitutive equation of the beam for torsional excitations. This constitutive equation relates the torsional moment to the cross-section rotation. In the framework of small strains in linear elasticity, it is written:

$$M_t = \mu J \frac{\partial \theta}{\partial s} \quad (2.86)$$

in which μ is the shear modulus of the material, also known as Lamé's modulus. In Eq. (2.86) and other subsequent equations of this section, index t is omitted to make the presentation clearer; θ is the rotation around the normal to the cross-section, denoted \underline{n} . Introducing relation (2.86) into Eq. (2.25), the equation governing the torsional vibrations of beams is the following:

$$\frac{\partial^2 \theta}{\partial t^2} - \frac{\mu}{\rho} \frac{\partial^2 \theta}{\partial s^2} = \frac{m_t}{\rho J} \quad (2.87)$$

The presentation made in this section is similar to that related to longitudinal vibrations since the structure of Eqs (2.36) and (2.87) are identical, only the governing parameters are different.

2.4.2 Homogeneous equation

Assuming the linear density of moment m_t to be zero, the homogeneous equation of vibration can be written:

$$\ddot{\theta}(s, t) - V_S^2 \theta''(s, t) = 0 \quad (2.88)$$

in which the *shear wave velocity* V_S is introduced³. It is defined as follows:

$$V_S = \sqrt{\frac{\mu}{\rho}} \quad (2.89)$$

$\ddot{\theta}$ and θ'' denote the second order partial derivatives with respect to time and space (resp.).

Typical values of the shear wave velocity are proposed hereafter for various civil engineering materials:

- steel: $V_S = 3100$ m/s,
- concrete: $V_S = 2200$ m/s,
- sand: $V_S = 200$ -400 m/s.

³The shear wave velocity V_S will be the same in 2D/3D (Chapter 3) since the lateral boundary conditions in a beam do not influence the solution for pure torsion or pure shear (see §2.5)

Equation (2.88) may be written as a first order hyperbolic differential system for which the general solution is:

$$\theta(s, t) = \theta_1(s - V_S t) + \theta_2(s + V_S t) \quad (2.90)$$

Solution (2.90) corresponds to the superposition of two wavefields, of amplitudes θ_1 and θ_2 , propagating with velocity V_S towards directions $s > 0$ and $s < 0$ respectively. During propagation, the shapes of both wavefields remain unchanged ; these waves are said to be non-dispersive.

2.4.3 Stresses in the beam

The solution being known in terms of displacement, the shear stresses in the beam are obtained from the constitutive relation (2.86):

$$\tau = \mu r \frac{\partial \theta}{\partial s} = \mu r [\theta'_1(s - V_S t) + \theta'_2(s + V_S t)] = g_1(s - V_S t) + g_2(s + V_S t) \quad (2.91)$$

In the previous equation, r denotes the radial distance to the torsion axis of the beam.

The shear stress in the beam is derived from the superposition of two non dispersive waves propagating towards directions $s > 0$ and $s < 0$ respectively. This stress can also be expressed as a function of velocities $\dot{\theta}_1$ and $\dot{\theta}_2$ known as the *angular particle velocities*. Taking into account the following relations:

$$\begin{cases} \dot{\theta}_1(s, t) = \frac{\partial \theta_1(s, t)}{\partial t} = -V_S \theta'_1(s - V_S t) \\ \dot{\theta}_2(s, t) = \frac{\partial \theta_2(s, t)}{\partial t} = +V_S \theta'_2(s + V_S t) \end{cases} \quad (2.92)$$

and recalling that $G = \rho V_S^2$, the shear stress can be written:

$$\tau = -\rho V_S r (\dot{\theta}_1 - \dot{\theta}_2) \quad (2.93)$$

2.4.4 Eigenmodes of the beam

The eigenmodes correspond to the periodic solutions of Eq. (2.88). These solutions are expressed under the form:

$$\theta(s, t) = \Theta(s) e^{i \omega t} \quad (2.94)$$

Introducing this relation into Eq. (2.88), function $\Theta(s)$ must satisfy:

$$V_S^2 \Theta''(s) + \omega^2 \Theta(s) = 0 \quad (2.95)$$

yielding the following solutions:

$$\Theta(s) = A \cos\left(\frac{\omega}{V_s} s\right) + B \sin\left(\frac{\omega}{V_s} s\right) \quad (2.96)$$

The integration of constants A and B is performed using the boundary conditions. In the case of the cantilever beam depicted in Fig.2.4, these boundary conditions are given by:

$$\begin{cases} \Theta(0) = 0 \\ M_t(L) = \mu J \frac{d\Theta(L)}{ds} = 0 \end{cases} \quad (2.97)$$

Conditions (2.97) lead to:

$$\begin{cases} \Theta(0) = 0 \Rightarrow A = 0 \\ \Theta'(L) = 0 \Rightarrow \cos\left(\frac{\omega L}{V_s}\right) = 0 \end{cases} \quad (2.98)$$

The eigenfrequencies are solutions of Eq. (2.98b), that is:

$$\omega_n = (2n - 1) \frac{\pi V_s}{2L} \quad (2.99)$$

The associated eigenmodes are given by:

$$\Theta_n(s) = \sin\left[\left(2n - 1\right) \frac{\pi s}{2L}\right] \quad (2.100)$$

The eigenmodes defined by Eq. (2.100) fulfil the following relation and thus form an orthogonal base:

$$\int_0^L \Theta_m(s) \Theta_n(s) ds = 0 \quad \text{if } m \neq n \quad (2.101)$$

The general solution of the equation of vibrations (2.87) can thus be obtained through the superposition of the eigenmodes:

$$\theta(s, t) = \sum_{n=1}^{\infty} \Theta_n(s) q_n(t) \quad (2.102)$$

$$\text{and } m_t(s, t) = \sum_{n=1}^{\infty} \Theta_n(s) m_{tn}(t) \quad (2.103)$$

Introducing expressions (2.102) and (2.103) into Eq. (2.87) and taking into account the orthogonality property (2.101), $q_n(t)$ satisfies the differential equation:

$$\ddot{q}_n(t) + \omega_n^2 q_n(t) = m_{tn}(t) \quad \text{with } n = 1, +\infty \quad (2.104)$$

$$\text{with: } m_{tn} = \frac{2}{\rho J L} \int_0^t \Theta_n(s) m_t(s, t) dt$$

These results will be used in section 2.10 for the analysis of the resonant column test.

2.5 Shear vibrations of beams

2.5.1 Bending-shear vibrations

In this section, the bending-shear vibrations of beams are firstly considered. These phenomena are governed by Eqs (2.27) and (2.28). Such vibrations are due to motions of the neutral fiber of the plane cross-section as well as rotations of the section around axes located in its plane. Equations (2.27) and (2.28) are vectorial equations which can, by an adequate choice of the system of orthogonal axes located in the plane of the cross-section, be replaced by four scalar equations. In the following, the analysis will be made on two equations only (corresponding to one of the two axes (e.g. axis 1)). Indices will be disregarded to simplify the notation. The two equations governing the dynamic equilibrium are thus written as follows:

$$\frac{\partial V}{\partial s} + f - \rho S \ddot{u} = 0 \quad (2.105)$$

$$V = -\frac{\partial M_b}{\partial s} - m \quad (2.106)$$

where the shear force V , the linear density of transverse external forces f , and the transverse displacement u correspond to the components along direction 1 ; the bending moment M_b and the linear density of external moments m correspond to the components along direction 2.

To fully determine the solution of the problem, it is necessary, in addition to equilibrium equations (2.27) and (2.28), to consider the constitutive laws of the beam for bending and shear loadings. These constitutive laws relate the shear force and the bending moment to the shear strain and rotation ω . Considering linear elasticity and small strains, they are written as follows:

$$V = \mu S' \left(\frac{\partial u}{\partial s} - \omega \right) \quad (2.107)$$

$$M_b = EI \frac{\partial \omega}{\partial s} \quad (2.108)$$

where μ is the shear modulus of the medium, S' and I the shear area of the cross section and the bending inertia of the beam. To derive the differential equation governing the transverse displacement of the neutral fiber, denoted u , it is necessary to eliminate quantities V , M_b and ω from Eqs (2.27), (2.28), (2.107) and (2.108).

2.5.2 From bending-shear to pure shear

To analyze shear waves in soils and rocks, it is generally possible to consider the local rotation (as well as the bending moment) negligible. Equation (2.107) may thus be written under the following form:

$$V = \mu S \frac{\partial u}{\partial s} \quad (2.109)$$

The transverse vibrations of a cylindrical beam are finally expressed as ⁴:

$$\frac{\partial^2 u}{\partial t^2} - \frac{\mu}{\rho} \frac{\partial^2 u}{\partial s^2} = \frac{f}{\rho S} \quad (2.110)$$

It leads to a homogeneous equation similar to Eq (2.36) considering the shear wave velocity V_S , defined as:

$$V_S = \sqrt{\frac{\mu}{\rho}} \quad (2.111)$$

Axial and transverse waves are different since axial waves generates motions along the beam axis whereas transverse waves generates motions perpendicular to the axis. We will discuss the significance of the differences between these two wave types in the next chapter (2D/3D propagation).

2.6 Behaviour of dissipative media

2.6.1 Dissipative phenomena

Cyclic, vibratory and dynamic problems have a common feature since they generally involve energy dissipation phenomena. In soils and rocks, the energy dissipation for a dynamic or vibratory loading may sometimes be very large (Hardin, 1965; Kokusho, 1980; Seed *et al.*, 1986; Stoll, 1979). For wave propagation problems, the attenuation phenomena generally appear under both following forms:

- **geometrical damping** due to the wavefront expansion (effect of radiation),
- **material or intrinsic attenuation** due to energy dissipation mechanisms in the material itself.

Only material attenuation is discussed in this section (geometrical damping will be presented in the next chapter). A convenient way to model attenuation is to consider linear viscoelastic constitutive laws.

2.6.2 Viscoelastic behaviour

Principles of viscoelasticity

For a linear isotropic viscoelastic material, the stress-strain relation is derived from the Boltzmann principle (Bourbié *et al.*, 1987; Fung and Tong, 2001). In the one-dimensional case, it is written under one of the following forms:

$$\sigma(t) = \int_{-\infty}^t \psi(t-\tau) \dot{\varepsilon}(\tau) d\tau \quad (2.112)$$

⁴For a non-constant cross-sectional area $S(s)$, the equation of motion has a different form:

$$\frac{\partial^2 u}{\partial t^2} - \frac{\mu}{\rho S(s)} \frac{\partial}{\partial s} \left(S(s) \frac{\partial u}{\partial s} \right) = \frac{f}{\rho S(s)}$$

$$\varepsilon(t) = \int_{-\infty}^t \phi(t-\tau) \dot{\sigma}(\tau) d\tau \quad (2.113)$$

where $\sigma(t)$ and $\varepsilon(t)$ are specific components of the stress and strain tensors⁵, $\dot{\sigma}(t)$ and $\dot{\varepsilon}(t)$ their time derivatives.

Functions $\psi(t)$ and $\phi(t)$ can be estimated experimentally:

- $\psi(t)$ is called the *relaxation function* and is defined as the stress response for a Heaviside type strain variation,
- $\phi(t)$ is called the *creep function* and is defined as the strain response for a Heaviside type stress variation.

Equations (2.112) and (2.113) indicate that, for viscoelastic materials, the response depends on the loading history whereas in linear elasticity, there is not such a dependency. This phenomenon is often called the *memory effect*.

Causality principle

Equation (2.112) (as well as Eq. (2.113)) assumes that the stress at time t , denoted $\sigma(t)$, linearly depends on the strain history $\varepsilon(\tau)$ until time t (Bourbié *et al.*, 1987). It consequently involves simultaneously the superposition principle and the causality principle. Causality implies that, in Eq. (2.112), the stress $\sigma(t)$ is not influenced by the future values of strain $\varepsilon(\tau)$ for $\tau > t$. Equation (2.112) can then be rewritten under the following form:

$$\sigma(t) = \int_{-\infty}^{+\infty} \psi(t-\tau) \dot{\varepsilon}(\tau) d\tau \quad (2.114)$$

where, due to the causality principle, we assume that:

$$\psi(x) = 0 \quad \text{for } x < 0 \quad (2.115)$$

Using integration by parts, Eq. (2.114) can be rewritten under the following form:

$$\sigma(t) = \int_{-\infty}^{+\infty} m(t-\tau) \varepsilon(\tau) d\tau \quad (2.116)$$

where $m(t)$ stands for the stress response to a strain variation following a Dirac function (Fig. 2.13), leading to the expression:

$$m(t) = \frac{d\psi(t)}{dt} \quad (2.117)$$

⁵One may consider traction/compression components for longitudinal vibrations or shear components for transverse vibrations.

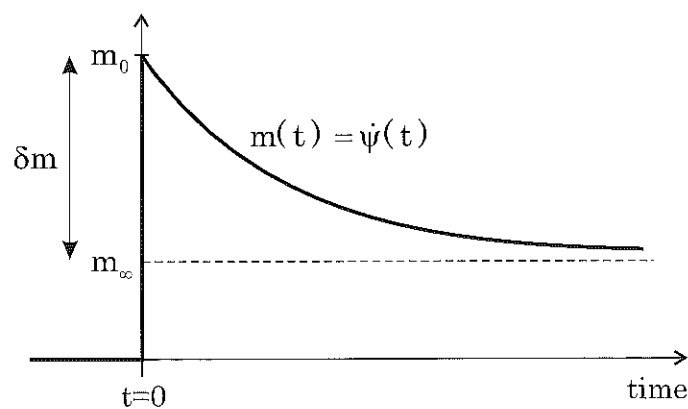


Fig. 2.13: Typical $m(t)$ function for a viscoelastic material.

Constitutive law in the spectral domain

From a mathematical point of view, Eq. (2.116) represents a convolution in time between m and ε . In the following, this relation will be written under the following condensed form:

$$\sigma(t) = m(t) * \varepsilon(t) \quad (2.118)$$

Considering time harmonic variations for the mechanical variables:

$$\sigma(t) = \sigma^*(\omega) \exp(i\omega t) \text{ and } \varepsilon(t) = \varepsilon^*(\omega) \exp(i\omega t) \quad (2.119)$$

equation (2.118) may be written in the frequency domain:

$$\sigma^*(\omega) = M(\omega) \varepsilon^*(\omega) \quad (2.120)$$

where $\sigma^*(\omega)$ and $\varepsilon^*(\omega)$ are the Fourier transforms of $\sigma(t)$ and $\varepsilon(t)$, $M(\omega)$ is the *complex viscoelastic modulus*, depending on frequency.

Starting from Eq.(2.117), $\psi(t)$ and $M(\omega)$ may be related as:

$$\psi(t) = \mathcal{F}^{-1} \left\{ \frac{M(\omega)}{i\omega} \right\} \quad (2.121)$$

where $\mathcal{F}^{-1}(f)$ is the inverse Fourier transform of function f .

In the case of an isotropic three-dimensional medium, the generalization of Eq.(2.114) is straightforward (Bourbié *et al.*, 1987):

$$\sigma_{ij}(t) = \int_{-\infty}^{+\infty} \left[\lambda(t-\tau) \frac{d}{dt} (\text{tr} \varepsilon) \delta_{ij} + 2\mu(t-\tau) \frac{d\varepsilon_{ij}}{dt} \right] d\tau \quad (2.122)$$

leading to the definition of complex Lamé parameters.

Characterization of $m(t)$ and $M(\omega)$

The function $m(t)$ (Eq.(2.118)) and the complex modulus $M(\omega)$ (Eq.(2.121)) characterize the viscoelastic behaviour of the material (Fig.2.13). Various parameters may be used to identify these functions:

- the *unrelaxed (elastic) modulus*⁶ m_0 which gives the instantaneous elastic response of the material, that is, in the time domain:

$$m_0 = \lim_{t \rightarrow 0} m(t) \quad (2.123)$$

or in the spectral domain:

$$m_0 = \lim_{\omega \rightarrow \infty} M(\omega) \quad (2.124)$$

- the *relaxed modulus* m_∞ which gives the response for the long term equilibrium of the material, that is, in the time domain:

$$m_\infty = \lim_{t \rightarrow \infty} m(t) \quad (2.125)$$

or in the spectral domain:

$$m_\infty = \lim_{\omega \rightarrow 0} M(\omega) \quad (2.126)$$

Quality factor and attenuation

The quality factor $Q(\omega)$ is derived from the complex modulus $M(\omega)$:

$$Q(\omega) = \frac{M_R(\omega)}{M_I(\omega)} \quad (2.127)$$

where M_R and M_I correspond to the real and imaginary parts of the complex modulus.

The inverse of the quality factor $Q^{-1}(\omega)$ is called *attenuation* and characterizes the damping properties of viscoelastic materials.

2.6.3 Rheological models

Constitutive laws

Rheological models are often used to describe the viscoelastic constitutive laws of dissipative materials. These allow the description of various types of attenuation-frequency dependencies (Bourbié *et al.*, 1987; Emmerich and Korn, 1987; Semblat, 1997; Semblat and Luong, 1998). As depicted in Fig.2.14, the rheological models considered for viscoelastic materials are composed of simple rheological cells: the *spring* and the *dashpot*. Figure 2.15 displays several classical viscoelastic models considering uniaxial traction/compression (σ being the uniaxial tensile/compressive stress and ε the corresponding uniaxial strain).

⁶In the field of geophysics, the unrelaxed modulus is often denoted M_U whereas the relaxed modulus is denoted M_R . The latter may be confusing when considering the real and imaginary parts of the complex modulus. It is thus avoided herein.

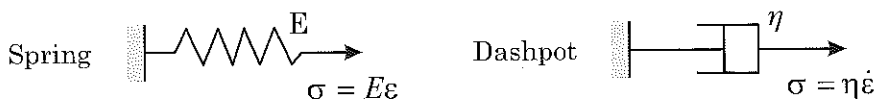


Fig. 2.14: Elementary rheological models in viscoelasticity.

The Maxwell model (Fig. 2.15) is composed of a spring (modulus E) and a dashpot (viscosity η) in series. For this model, considering cumulative uniaxial stresses in each cell, the constitutive law writes as follows:

$$\sigma + \frac{\eta}{E} \dot{\sigma} = \eta \dot{\epsilon} \quad (2.128)$$

The Kelvin-Voigt model (Fig. 2.15) is composed of a spring and dashpot associated in parallel (i.e. cumulative axial strains). For this model, the constitutive law is of the following form:

$$\sigma = E \left(\epsilon + \frac{\eta}{E} \dot{\epsilon} \right) \quad (2.129)$$

The Zener model (Fig. 2.15), also called the *three parameters model* or the *standard solid model* (Fung and Tong, 2001), is composed of a Kelvin-Voigt cell associated in series to a spring⁷. For this model, the constitutive law is as follows:

$$\sigma + \frac{\eta}{E + E_V} \dot{\sigma} = \frac{E E_V}{E + E_V} \left(\epsilon + \frac{\eta}{E_V} \dot{\epsilon} \right) \quad (2.130)$$

This relationship can be written under the general form⁸:

$$\sigma + \tau_\sigma \dot{\sigma} = m_\infty (\epsilon + \tau_\epsilon \dot{\epsilon}) \quad (2.131)$$

where m_∞ is the relaxed modulus, τ_σ is the stress relaxation time under constant strain and τ_ϵ is the strain relaxation time under constant stress.

Considering uniaxial shear, all previous constitutive laws can be written replacing the uniaxial tensile/compressive stress σ by the uniaxial shear stress τ , and the uniaxial longitudinal strain ϵ by the uniaxial shear strain γ . The shear viscoelastic properties are thus introduced (e.g. shear modulus μ instead of Young's modulus E).

Complex modulus

Considering a $e^{+i\omega t}$ time harmonic dependence, Eq.(2.131) may be written in the frequency domain:

$$(1 + i\omega\tau_\sigma)\sigma^*(\omega) = m_\infty(1 + i\omega\tau_\epsilon)\epsilon^*(\omega) \quad (2.132)$$

⁷ It may also be built with a Maxwell cell associated in parallel to a spring. It leads to a similar constitutive law.

⁸ The notations considered herein are similar to that used in the field of geophysics but are different from that considered in the field of continuum mechanics (Fung and Tong, 2001), that is generally: $\sigma + \tau_\epsilon \dot{\sigma} = m_\infty(\epsilon + \tau_\sigma \dot{\epsilon})$

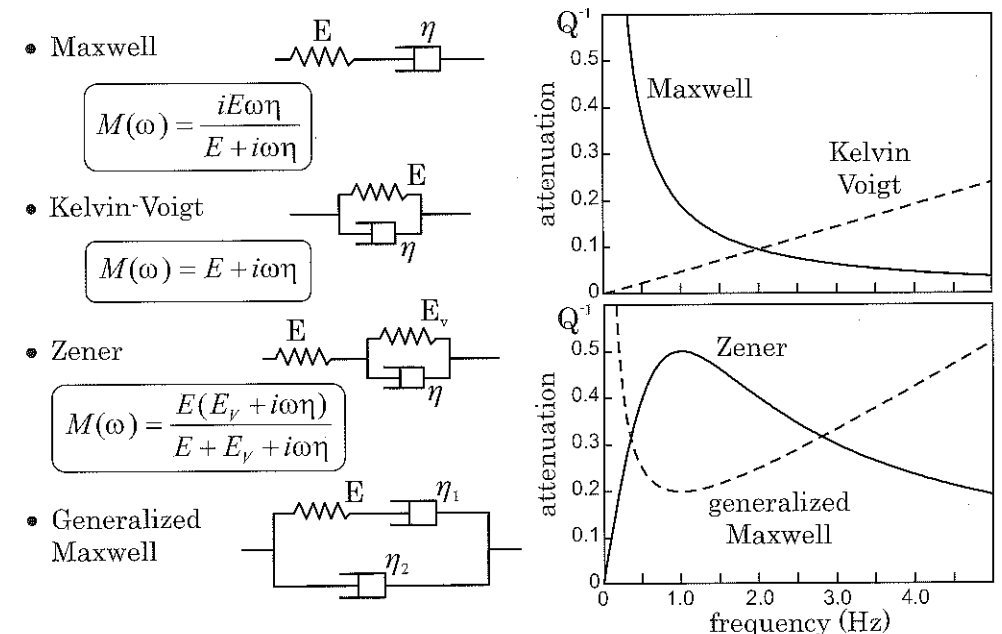


Fig. 2.15: Various rheological models: expressions of the complex moduli $M(\omega)$ and associated attenuation curves Q^{-1} .

allowing the determination of the general expression of the complex modulus $M(\omega)$:

$$M(\omega) = \frac{1 + i\omega\tau_\epsilon}{1 + i\omega\tau_\sigma} m_\infty \quad \text{thus: } |M(\omega)| = \sqrt{\frac{1 + \omega^2\tau_\epsilon^2}{1 + \omega^2\tau_\sigma^2}} m_\infty \quad (2.133)$$

As shown in Fig. 2.15, the complex modulus $M(\omega)$ for these rheological models is then:

$$\text{Maxwell : } M(\omega) = \frac{iE\omega\eta}{E + i\omega\eta} \quad (2.134)$$

$$\text{Kelvin-Voigt : } M(\omega) = E + i\omega\eta \quad (2.135)$$

$$\text{Zener : } M(\omega) = \frac{E(E_V + i\omega\eta)}{E + E_V + i\omega\eta} \quad (2.136)$$

For the generalized Maxwell model, the expression of $M(\omega)$ is a bit more complex:

$$M(\omega) = \frac{E\omega^2\eta_1^2 + i[E^2\omega(\eta_1 + \eta_2) + \omega^3\eta_1^2\eta_2]}{E^2 + \omega^2\eta_1^2} \quad (2.137)$$

The latter model will be also studied in Chapter 4 since it leads to a very convenient form of the quality factor (Semblat, 1997).

At large times (resp. low frequencies), the asymptotic value of the complex modulus for the Zener model is interesting:

$$\lim_{\omega \rightarrow 0} M(\omega) = \lim_{\omega \rightarrow 0} \left(\frac{1 + i\omega\tau_\varepsilon}{1 + i\omega\tau_\sigma} m_\infty \right) = m_\infty \quad (2.138)$$

with: $\frac{1}{m_\infty} = \frac{1}{E} + \frac{1}{E_V}$

In the Zener model, the complex modulus $M(\omega)$ tends to the relaxed modulus m_∞ at large times and the dashpot has then no effect on the response.

At short times (resp. high frequencies), the asymptotic value of the complex modulus for the Zener model is as follows:

$$\lim_{\omega \rightarrow +\infty} M(\omega) = \lim_{\omega \rightarrow +\infty} \left(\frac{1 + i\omega\tau_\varepsilon}{1 + i\omega\tau_\sigma} m_\infty \right) = \frac{\tau_\varepsilon}{\tau_\sigma} m_\infty = E = m_0 \quad (2.139)$$

For the Zener model, the complex modulus $M(\omega)$ tends to the unrelaxed (instantaneous) modulus m_0 at short times and the whole Kelvin cell has then no effect on the response (see also Fig.2.13).

Relaxation and creep functions

For a strain loading $\varepsilon(t)$ defined as a step function $H(t)$ (i.e. Heaviside in time), the solution of Eqs (2.128) to (2.130) allows the determination of the *relaxation functions* as follows (Bourbié *et al.*, 1987):

$$\text{Maxwell : } \psi(t) = E e^{-\frac{E}{\eta}t} H(t) \quad (2.140)$$

$$\text{Kelvin-Voigt : } \psi(t) = \eta \delta(t) + E H(t) \quad (2.141)$$

$$\text{Zener : } \psi(t) = m_\infty \left[1 - \left(1 - \frac{\tau_\varepsilon}{\tau_\sigma} \right) e^{-\frac{t}{\tau_\sigma}} \right] H(t) \quad (2.142)$$

where $\delta(t)$ is a Dirac function being always zero except for $t = 0$.

Similarly, for stress loading $\sigma(t)$ defined as a step function $H(t)$, the solution of Eqs (2.128) to (2.130) allows the determination of the *creep functions* under the following form:

$$\text{Maxwell : } \phi(t) = \left(\frac{1}{E} + \frac{1}{\eta} t \right) H(t) \quad (2.143)$$

$$\text{Kelvin-Voigt : } \phi(t) = \frac{1}{E} \left(1 - e^{-\frac{E}{\eta}t} \right) H(t) \quad (2.144)$$

$$\text{Zener : } \phi(t) = \frac{1}{m_\infty} \left[1 - \left(1 - \frac{\tau_\sigma}{\tau_\varepsilon} \right) e^{-\frac{t}{\tau_\varepsilon}} \right] H(t) \quad (2.145)$$

Quality factors and attenuation

Considering the definition of the quality factor (Eq.(2.127)), the expressions of attenuation for the linear viscoelastic models depicted in Fig.2.15 are the following:

$$Q_{Max}^{-1}(\omega) = \frac{E}{\omega\eta} \quad \text{and} \quad Q_{Kel}^{-1}(\omega) = \frac{\omega\eta}{E} \quad (2.146)$$

$$Q_{Zen}^{-1}(\omega) = \frac{\omega\eta E}{E_V(E + E_V) + \omega^2\eta^2} \quad (2.147)$$

$$Q_{GM}^{-1}(\omega) = \frac{E(\eta_1 + \eta_2)}{\eta_1^2} \frac{1}{\omega} + \frac{\eta_2}{E} \omega \quad (2.148)$$

for the Maxwell, the Kelvin-Voigt, the Zener and the generalized Maxwell models, respectively.

From Fig.2.15, these rheological models obviously have various attenuation-frequency dependencies. The Maxwell and generalized Maxwell models do not involve instantaneous elasticity (infinite attenuation at zero frequency). The Zener and the generalized Maxwell models show a band-cut and band-pass effects respectively. Some analytical wave propagation simulations will be considered in the following for these various models.

As in the previous subsection, the expression of the quality factor can also be determined under a general form derived from Eq.(2.133):

$$Q(\omega) = \frac{M_R(\omega)}{M_I(\omega)} = \frac{1 + \omega^2\tau_\varepsilon\tau_\sigma}{\omega(\tau_\varepsilon - \tau_\sigma)} \quad (2.149)$$

The maximum value of Q^{-1} corresponds to the largest attenuation and, for the Zener's model ($\tau_\varepsilon \neq 0$ et $\tau_\sigma \neq 0$), it is reached at frequency ω_m :

$$\omega_m = \frac{1}{\sqrt{\tau_\varepsilon\tau_\sigma}} \quad (2.150)$$

$$\text{and leads to: } \max_{\omega} Q^{-1}(\omega) = Q^{-1}(\omega_m) = \frac{\tau_\varepsilon - \tau_\sigma}{2\sqrt{\tau_\varepsilon\tau_\sigma}} \quad (2.151)$$

Defining the normalized frequency $\Omega = \omega/\omega_m$, Fig.2.16 depicts the variations of both $Q^{-1}(\Omega)$ and $|M(\Omega)|$ considering a semi-logarithmic scale⁹. Attenuation $Q^{-1}(\Omega)$ reaches its maximum at ω_m (*band-cut effect*), whereas $|M(\Omega)|$ tends to m_∞ at low frequencies (which is in good agreement with the definition of the complex modulus) and tends to $\frac{\tau_\varepsilon}{\tau_\sigma} m_\infty = m_0$ for higher frequencies.

⁹The $Q^{-1}(\Omega)$ curve is the same as in Fig.2.15 but, considering a semi-logarithmic scale (instead of a linear one), it yields a symmetric attenuation peak.

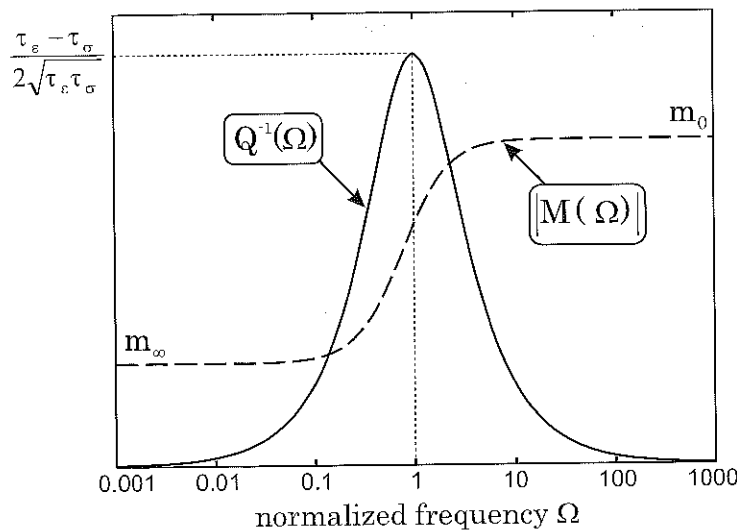


Fig. 2.16: Attenuation $Q^{-1}(\Omega)$ and complex modulus $|M(\Omega)|$ vs normalized frequency $\Omega = \omega/\omega_m$ for the Zener model.

2.7 Wave propagation in viscoelastic media

2.7.1 Dynamic equilibrium

The equilibrium of a uniaxial medium under longitudinal loadings writes:

$$(\underline{\nabla} \cdot \underline{\sigma}) \cdot \underline{n} = \frac{\partial \sigma(s, t)}{\partial s} = \rho \frac{\partial^2 u(s, t)}{\partial t^2} \quad (2.152)$$

where $\underline{\nabla}$ is the gradient vector ($\nabla_j = \partial/\partial x_j$), $\underline{\sigma}$ the Cauchy stress tensor and \underline{n} the normal to the cross-section.

This equation can be rewritten in the frequency domain under the following form:

$$\frac{\partial \sigma^*(s, \omega)}{\partial s} = -\rho \omega^2 u^*(s, \omega) \quad (2.153)$$

where $\sigma^*(s, \omega)$ and $u^*(s, \omega)$ are the Fourier transforms of $\sigma(s, t)$ and $u(s, t)$.

2.7.2 Viscoelastic behaviour

For a linear viscoelastic medium, the constitutive law (2.120) is combined with Eq.(2.153):

$$\frac{\partial \sigma^*(s, \omega)}{\partial s} = \frac{\partial}{\partial s} [M(\omega) \varepsilon^*(s, \omega)] = -\rho \omega^2 u^*(s, \omega) \quad (2.154)$$

yielding:

$$\frac{\partial \sigma^*(s, \omega)}{\partial s} = M(\omega) \frac{\partial^2 u^*(s, \omega)}{\partial s^2} = -\rho \omega^2 u^*(s, \omega) \quad (2.155)$$

2.7.3 Wave equation in viscoelastic media

The following differential equation in terms of displacement is obtained:

$$\frac{\partial^2 u^*(s, \omega)}{\partial s^2} = -\frac{\rho \omega^2}{M(\omega)} u^*(s, \omega) \quad (2.156)$$

The solutions of this equation are of the following form (Aki and Richards, 1980):

$$u^*(s, \omega) = U_0(\omega) \exp[-ik^*(\omega)s] \quad (2.157)$$

where k^* is a complex number such as:

$$(k^*(\omega))^2 = \frac{\rho \omega^2}{M(\omega)} \quad (2.158)$$

From Eq.(2.157), the displacement $u(s, t)$ solution of Eq.(2.152) is finally written as:

$$u(s, t) = U_0(\omega) \exp[i(\omega t - k^*(\omega)s)] \quad (2.159)$$

For a non-harmonic wave, the following expression is easily obtained¹⁰:

$$u(s, t) = \frac{1}{2\pi} \int_{-\infty}^{+\infty} U_0(\omega) \exp[i(\omega t - k^*(\omega)s)] d\omega \quad (2.160)$$

2.7.4 Complex wavenumber

$k^*(\omega)$ fully characterizes the propagation process and its dependency on the frequency governs attenuation. It is called the *complex wavenumber*. Denoting the real and imaginary parts of $k^*(\omega)$ under the form $k^*(\omega) = k(\omega) - i\alpha(\omega)$, it is possible to derive them as functions of the complex modulus M :

$$k(\omega) = \omega \sqrt{\frac{\rho(|M(\omega)| + M_R(\omega))}{2|M(\omega)|^2}} \quad (2.161)$$

$$\alpha(\omega) = \omega \sqrt{\frac{\rho(|M(\omega)| - M_R(\omega))}{2|M(\omega)|^2}} \quad (2.162)$$

where $|M|$ is the modulus of the complex variable M , that is $|M| = \sqrt{M_R^2 + M_I^2}$ (with M_R and M_I the real and imaginary parts of the complex modulus).

¹⁰For a $e^{-i\omega t}$ harmonic dependence, the expression would have been found as:

$$u(s, t) = \frac{1}{2\pi} \int_{-\infty}^{+\infty} U_0(\omega) \exp[i(k^*(\omega)s - \omega t)] d\omega$$

Both waves propagate toward the positive s since they are of the form $u(s - ct)$ defined in Fig.2.3.

The *real part* $k_R^* = k$ corresponds to the *real wavenumber* (characterizing a progressive wave) and the *imaginary part* $k_I^* = \alpha$ to the *attenuation factor*. $k^*(\omega)$ can then be derived under the following form:

$$k^*(\omega) = \frac{\omega}{c(\omega)} - i\alpha(\omega) \quad (2.163)$$

where ω is the frequency, $c(\omega)$ the phase velocity and $\alpha(\omega)$ the attenuation factor. These two terms (phase velocity, attenuation ratio) may depend on frequency. The dependence of the phase velocity $c(\omega)$ on frequency corresponds to the physical dispersion in the medium.

The solution of the wave equation in viscoelastic media may finally be written as follows:

$$u^*(s, \omega) = \exp(-ik^*(\omega)s) = \exp(-ik(\omega)s) \exp(-\alpha(\omega)s) \quad (2.164)$$

The $\alpha(\omega)$ variable thus characterizes the spatial decay of the wave.

When the viscous effects are small ($M_I \ll M_R$), it is possible to approximate the phase velocity, Eq.(2.161), as a function of the real part of the complex modulus as follows:

$$c(\omega) = \sqrt{\frac{M_R(\omega)}{\rho}} \quad (2.165)$$

This expression is similar to the wave velocity for an elastic medium.

2.7.5 Relationship between α and Q^{-1}

The attenuation Q^{-1} depending on the complex modulus under the following form:

$$Q^{-1} = \frac{M_I}{M_R} \quad (2.166)$$

the relationship between α and Q can be written:

$$\alpha = \frac{\omega}{\sqrt{2c}} \frac{\sqrt{\sqrt{1 + \frac{1}{Q^2}} - 1}}{\sqrt{1 + \frac{1}{Q^2}}} \quad (2.167)$$

In the case of weak attenuation ($Q^{-1} \ll 1$), the relation is simplified as:

$$Q^{-1} \simeq \frac{2\alpha c}{\omega} = \frac{\alpha c}{\pi f} \quad (2.168)$$

The solution $u^*(s, \omega)$ may then be expressed as a function of Q :

$$u^*(s, \omega) = U_0(\omega) \exp[-ik(\omega)s] \exp\left(-\frac{\pi f}{Qc}s\right) \quad (2.169)$$

Denoting $\Lambda = c/f$ the wavelength, it yields:

$$u^*(s, \omega) = U_0(\omega) \exp[-ik(\omega)s] \exp\left(-\frac{\pi s}{Q\Lambda}\right) \quad (2.170)$$

It gives a simple expression showing the influence of attenuation Q^{-1} on the spatial decay of the wavefield.

2.7.6 Dispersion laws

Wave propagation in dispersive media

In dispersive media, the wave velocity is frequency dependent (Aki and Richards, 1980; Bourbié *et al.*, 1987; Lighthill, 1965). To fully characterize wave propagation in dispersive media, two types of velocities are defined:

- the *group velocity* is the *velocity at which energy is carried*. The group velocity V_g is expressed under the following form:

$$V_g = \frac{d\omega}{dk} \quad (2.171)$$

that is under the form of the ratio between a frequency variation and a wavenumber variation.

- the *phase velocity* is the *velocity at which the points of constant phase propagate*, that is, generally, the velocity at which the peaks of the signal propagate. The phase velocity V_Φ has the following form:

$$V_\Phi = \frac{\omega}{k} \quad (2.172)$$

that is the ratio between a frequency and a wavenumber.

As depicted in Fig.2.17, the phase velocity at a given frequency may be estimated from a signal filtered around this frequency (individual peaks). For the group velocity, the envelope of the signal characterizes the velocity at which the energy is propagated (Fig.2.17).

Wave dispersion in viscoelastic media

For viscoelastic models, the determination of the phase velocity $c(\omega)$ as a function of frequency is simple since the complex wave number $k^*(\omega) = k(\omega) - i\alpha(\omega)$ can be directly expressed as a function of the complex modulus characterizing the rheological model considered.

Starting from the expressions given in Fig.2.15 and Eq.(2.163), it is possible to determine the attenuation factor and the phase velocity as functions of frequency, that is $\alpha(\omega)$ and $c(\omega)$. Figure 2.18 gives the variations of the phase velocity for various viscoelastic models (Maxwell, Kelvin and Zener):

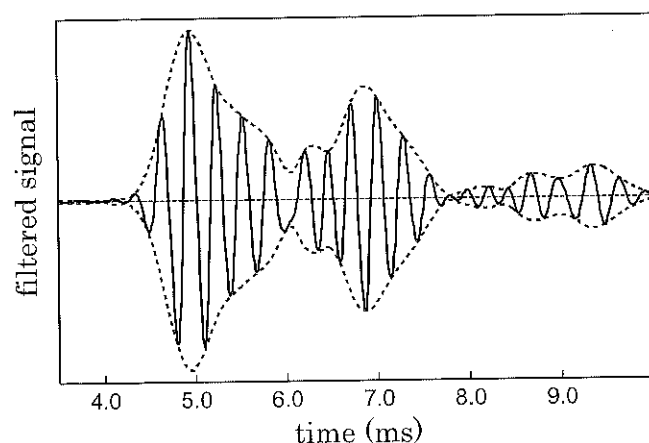


Fig. 2.17: Determination of the phase and group velocities from a filtered signal (solid) and its envelope (dotted).

- for the *Maxwell model*, the phase velocity decreases and reaches an asymptotic value $c_\infty = \sqrt{\frac{E}{\rho}}$,
- for the *Kelvin model*, the phase velocity increases rapidly starting from a minimum value $c_0 = \sqrt{\frac{E}{\rho}}$,
- for the *Zener model*, the phase velocity progressively increases from a minimum value $c_0 = \sqrt{\frac{m_\infty}{\rho}}$ to a maximum value $c_\infty = \sqrt{\frac{m_0}{\rho}}$.

The variations of the phase velocity are strongly dependent on the viscoelastic parameters of the model. This dependency is usually called *material dispersion*.

2.8 Examples of propagation in viscoelastic media

2.8.1 Example 1 : propagation of a triangular signal

Before considering actual signals, a synthetic signal may be chosen to illustrate the influence of the properties of the rheological models. It is thus possible to investigate the way the medium transmits slow or fast amplitude variations (zero frequency or infinite frequency). Considering a triangular signal and using Eq. (2.160), the curves displayed in Fig.2.19 depict the evolution of the initial shape of the wave during the propagation process.

The signals are referenced from an arbitrary origin, the first signal representing the excitation at a reference distance d_0 .

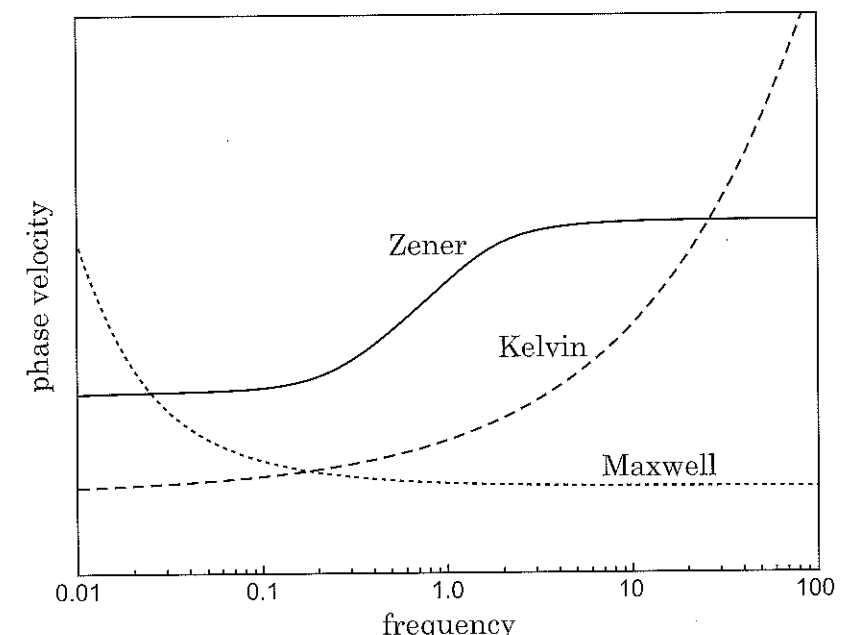


Fig. 2.18: Phase velocity as a function of frequency for various viscoelastic models (Maxwell, Kelvin-Voigt and Zener).

The simulations displayed in Fig.2.19 clearly illustrate in time domain the previous remarks on wave propagation. In a Maxwell linear viscoelastic medium (left):

- the *shape of the triangular signal is unchanged* during propagation: the *discontinuities (or high frequency components) are slightly attenuated* in a Maxwell medium (weak attenuation, Fig.2.15),
- the *peak amplitude decreases rapidly* during propagation: the *slow variations (or low frequency components) are strongly attenuated* in a Maxwell medium (strong attenuation, Fig.2.15).

For a Kelvin-Voigt medium, the propagation features are significantly different (Fig.2.19, right):

- the *peak shape is altered* during propagation: the *fast variations (or high frequency components) are quickly attenuated* in a Kelvin-Voigt medium,
- the *peak amplitude slowly decreases* during propagation: the *slow variations (or low frequency components) are weakly attenuated* in a Kelvin-Voigt medium.

Such differences between both rheological models are due to the fact that the attenuation is proportional to frequency for the Kelvin model whereas, for the Maxwell model, it is inversely proportional (see Fig.2.15). The asymptotic behaviour of attenuation is

thus very different in both cases. We may conclude that the viscoelastic properties of the medium as well as the frequency content of the propagating wave significantly influence the propagation features in terms of attenuation and spatial decay.

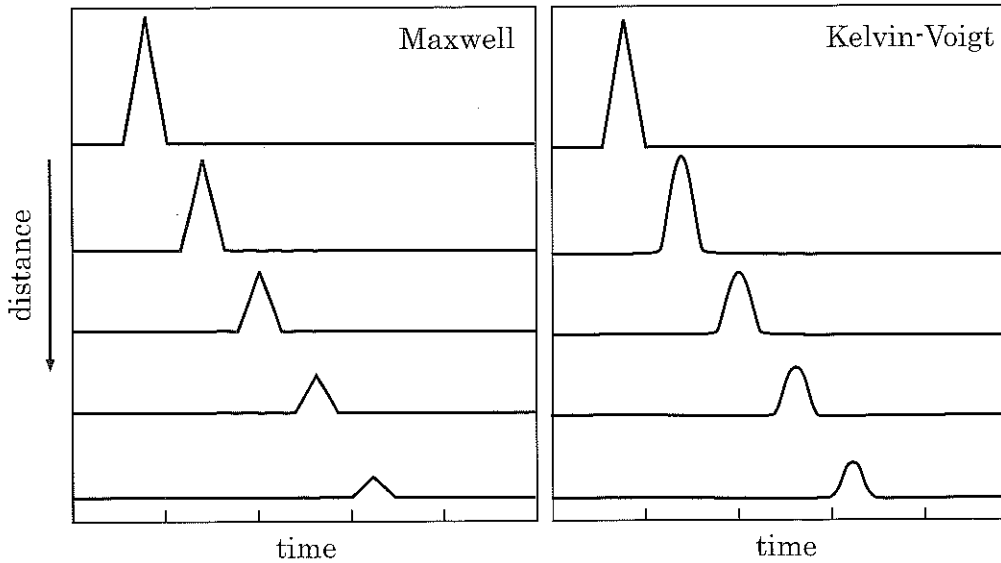


Fig. 2.19: Propagation of a triangular signal in a linear viscoelastic medium: Maxwell model (left) and Kelvin-Voigt model (right).

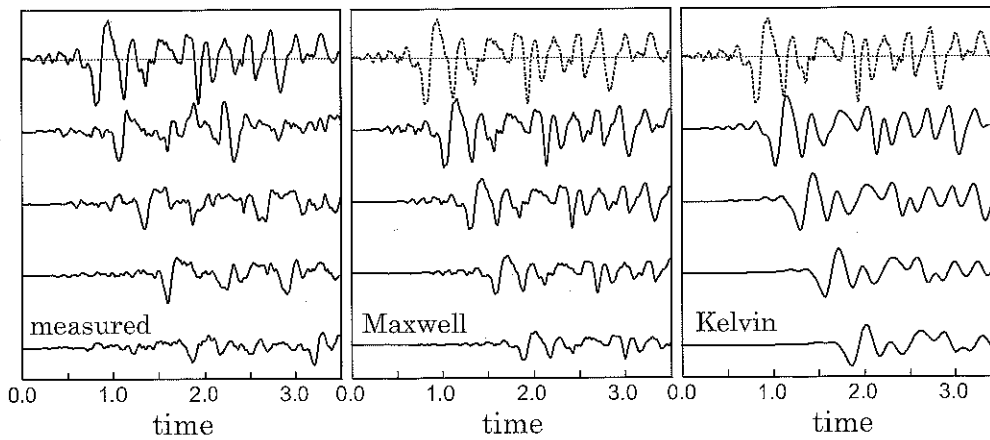


Fig. 2.20: Analytical simulations from centrifuge experiments (left) for two different rheological models (Maxwell: center, Kelvin: right).

2.8.2 Example 2 : propagation of a seismic wave.

We now consider seismic signals recorded in centrifuge tests (Semblat and Luong, 1998). The wavefield is nearly plane and mainly corresponds to longitudinal waves. The one-dimensional approximation is acceptable and the propagation process is the soil mass can be analyzed thanks to the rheological models presented earlier.

To simulate the propagation in the soil mass, one considers the acceleration signal measured at point A_i with abscissa x_i , denoted $a_{meas}(x_i, t)$, and one computes the signal propagated to point A_j at abscissa x_j , denoted $a_{sim}(x_j, t)$. We first write the relationship between the spectral components, $a_{meas}^*(x_i, \omega)$ and $a_{sim}^*(x_j, \omega)$, of these acceleration signals using expression (2.157):

$$a_{sim}^*(x_j, \omega) = a_{meas}^*(x_i, \omega) \exp [-ik^*(\omega)(x_j - x_i)] \quad (2.173)$$

From expression (2.173), the simulated acceleration $a_{sim}(x_j, t)$ is written as follows:

$$a_{sim}(x_j, t) = \frac{1}{2\pi} \int_{-\infty}^{+\infty} a_{meas}^*(x_i, \omega) \exp \{i[\omega t - k^*(\omega)(x_j - x_i)]\} d\omega \quad (2.174)$$

Figure 2.20 compares the signals recorded at different points (left) to the simulations performed with Kelvin-Voigt (center) and Maxwell models (right). The viscoelastic simulations are in good agreement with the experimental results. The Kelvin model nevertheless leads to overdamped higher frequency components. Simulations made with the Zener model are very close to those computed with the Maxwell model (Semblat and Luong, 1998).

2.9 Other linear and nonlinear models

Starting from the results of the previous sections, it is possible to develop more complex viscoelastic models with more realistic variations for the attenuation Q^{-1} . The interest of models built in such a way is first that they are simple and secondly that they fulfil the fundamental assumptions of continuum mechanics (causality among others). Some of them are presented in the following.

Many constitutive laws have also been proposed in the framework of elastoplasticity (Bonilla *et al.*, 2005; Critescu, 1974; Iai *et al.*, 1995; Kramer, 1996; Lade, 1977; Loret *et al.*, 1997; Matasovic and Vucetic, 1995; Mellal and Modaressi, 1998; Prevost, 1985; Pyke, 1979; Towhata, 2008). Since we mainly focus on wave propagation in the linear range, such models are not discussed herein.

2.9.1 Constant Q (CQ) model

Kjartansson (1979) proposed a frequency constant Q model having a complex modulus of the following form:

$$M(\omega) = M_0 \left(\frac{i\omega}{\omega_0} \right)^{2\gamma} \quad (2.175)$$

where M_0 is the modulus of $M(\omega)$ at the reference frequency ω_0 .

The quality factor is thus given as (Bourbié *et al.*, 1987):

$$Q^{-1} = \tan(\pi\gamma) \quad (2.176)$$

2.9.2 Frequency dependent Q model

Müller (1983) proposed a frequency dependent Q model expressed in the form of a power law:

$$Q(\omega) = Q(\omega_r) \left(\frac{\omega}{\omega_r} \right)^\gamma \quad (2.177)$$

where γ is an exponent chosen between -1 and +1 and the related complex modulus is given by (Müller, 1983):

$$M(\omega) = M(\omega_r) \exp \left\{ Q^{-1}(\omega_r) \left[\cot \left(\frac{\pi}{2} \gamma \right) - i \right] \left[1 - \left(\frac{\omega}{\omega_r} \right)^\gamma \right] \right\} \quad (2.178)$$

2.9.3 Nearly Constant Q (NCQ) model

Since the attenuation may often be considered as constant in a certain frequency range, Nearly Constant Q (NCQ) models were proposed by Lomnitz (1957), Liu *et al.* (1976) or Emmerich and Korn (1987). They are generally built as a combination of several simple rheological cells.

For a three parameter (Zener) rheological model, the constitutive law can be easily written for a sinusoidal disturbance (Liu *et al.*, 1976):

$$\varepsilon(t) = \frac{\sigma(t)}{m_\infty} \left\{ \left[1 - \frac{\omega^2 \tau_\varepsilon (\tau_\varepsilon - \tau_\sigma)}{1 + \omega^2 \tau_\varepsilon^2} \right] - i \left[\frac{\omega (\tau_\varepsilon - \tau_\sigma)}{1 + \omega^2 \tau_\varepsilon^2} \right] \right\} \quad (2.179)$$

Combining a finite number of rheological models (or relaxation mechanisms), the constitutive law can be generalized as follows:

$$\varepsilon(t) = \frac{\sigma(t)}{m_\infty} \left\{ \left[1 - \sum_{k=1}^N \frac{\omega^2 \tau_{\varepsilon k} (\tau_{\varepsilon k} - \tau_{\sigma k})}{1 + \omega^2 \tau_{\varepsilon k}^2} \right] - i \left[\sum_{k=1}^N \frac{\omega (\tau_{\varepsilon k} - \tau_{\sigma k})}{1 + \omega^2 \tau_{\varepsilon k}^2} \right] \right\} \quad (2.180)$$

In the case of a continuous spectrum (infinite number of mechanisms), we obtain an equivalent expression under an integral form.

Figure 2.21 displays the $Q^{-1}(\omega)$ curve corresponding to the combination of 12 mechanisms as proposed by Liu *et al.* (1976). The attenuation is nearly constant in a wide frequency band.

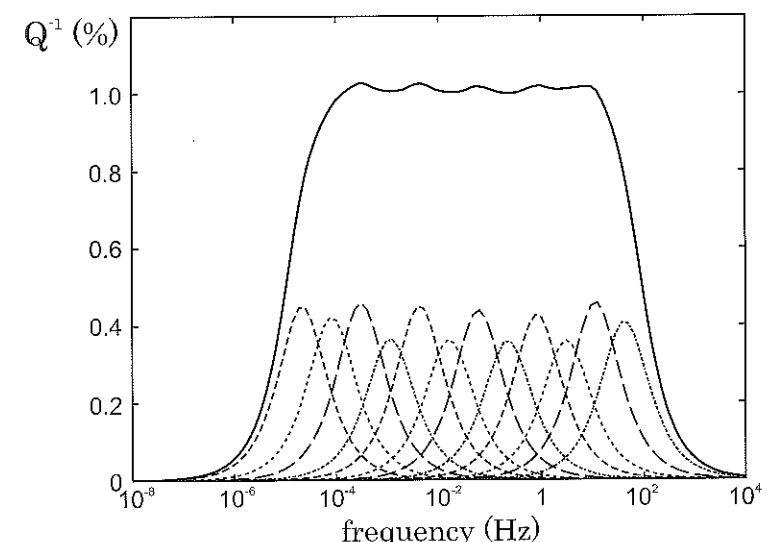


Fig. 2.21: Variation of attenuation Q^{-1} with frequency for the NCQ model ("A5") of Liu *et al.* (1976).

For the Liu model, the dispersion relationship is written:

$$\frac{c(\omega_1)}{c(\omega_2)} \simeq 1 + \frac{1}{\pi Q} \ln \frac{\omega_1}{\omega_2} \quad (2.181)$$

Lomnitz (1957) found a similar result by considering an experimental creep law of the form:

$$\phi_{NCQ}(t) = \begin{cases} 0 & t < 0 \\ \frac{1+q \ln(1+td)}{M_0} & t \geq 0 \end{cases} \quad (2.182)$$

where q , d and M_0 are constants determined experimentally.

Emmerich and Korn (1987) proposed a nearly constant Q model involving generalized Maxwell bodies. For n Maxwell cells, they found the attenuation Q^{-1} under the form:

$$Q^{-1}(\omega) = \frac{M_I(\omega)}{M_R(\omega)} = \frac{\delta m}{m_\infty} \frac{\sum_{j=1}^n a_j \frac{\omega/\omega_j}{1 + (\omega/\omega_j)^2}}{1 + \frac{\delta m}{m_\infty} \sum_{j=1}^n a_j \frac{(\omega/\omega_j)^2}{1 + (\omega/\omega_j)^2}} \quad (2.183)$$

To simplify this expression, they assume $\delta m \ll m_\infty$ yielding:

$$Q^{-1}(\omega) \simeq \frac{\delta m}{m_\infty} \sum_{j=1}^n a_j \frac{\omega/\omega_j}{1 + (\omega/\omega_j)^2} \quad (2.184)$$

They finally proposed a least-squares algorithm to optimize the Q^{-1} variations in the frequency band of interest. As discussed in §2.9.6, their model was recently generalized in the nonlinear range by Delépine *et al.* (2007)

2.9.4 Equivalent linear viscoelasticity

To analyze seismic wave propagation, it is often necessary to consider assumptions beyond the field of linear viscoelasticity. As shown by experimental results from cyclic tests (Fig.2.22) or resonant column tests (§2.10), the behaviour of soils can not always be described with a linear law. From the largest and the smallest loops depicted in Fig.2.22, the shear modulus decreases for larger excitations whereas damping strongly increases (area of the loops). Such properties are very important for loadings corresponding to large amplitude vibrations or strong earthquakes. One should thus consider more complex constitutive laws. The constitutive parameters (shear modulus, damping) may be determined from resonant column tests at various excitation levels (see §2.10).

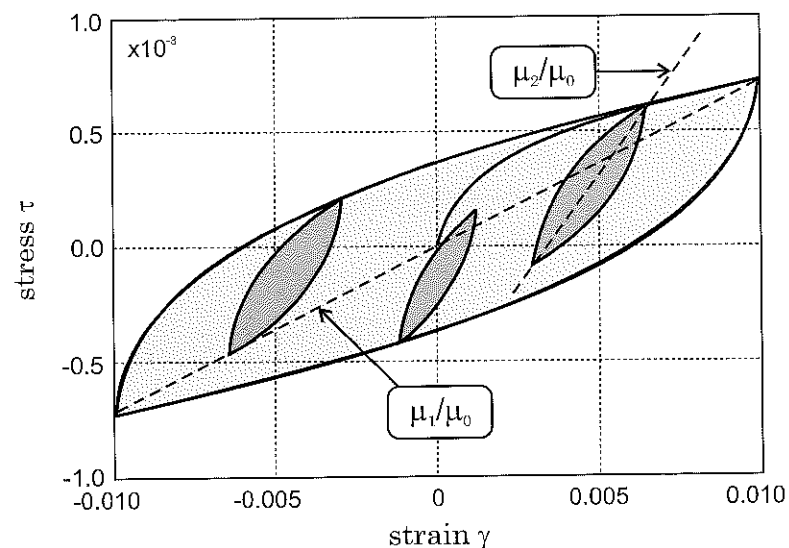


Fig. 2.22: Cyclic tests: hysteresis loops in the $\tau - \gamma$ diagram.

To approximate the nonlinear dynamic behaviour of soils, the *equivalent linear* approach consists in considering a linear viscoelastic model having its mechanical properties depending on the induced strain through an iterative procedure (Schnabel *et al.*, 1972). The equivalent linear approach is depicted in Fig.2.23:

- the viscoelastic constitutive parameters in each layer, $\{\mu_i(j), \xi_i(j)\}$ (shear modulus and damping ratio resp.), are firstly chosen from experimental results at low excitation levels,

- the average stresses and strains in each layer are then estimated ($\gamma_i^{eff}(j)$),
- the constitutive parameters are updated accordingly $\{\mu_{i+1}(j), \xi_{i+1}(j)\}$ starting an iterative process,
- if the new μ and ξ values are different from the previous ones ($\{\Delta\mu, \Delta\xi\} > \varepsilon$), a new stress/strain state is considered and the iterative process is resumed until a given tolerance is reached.

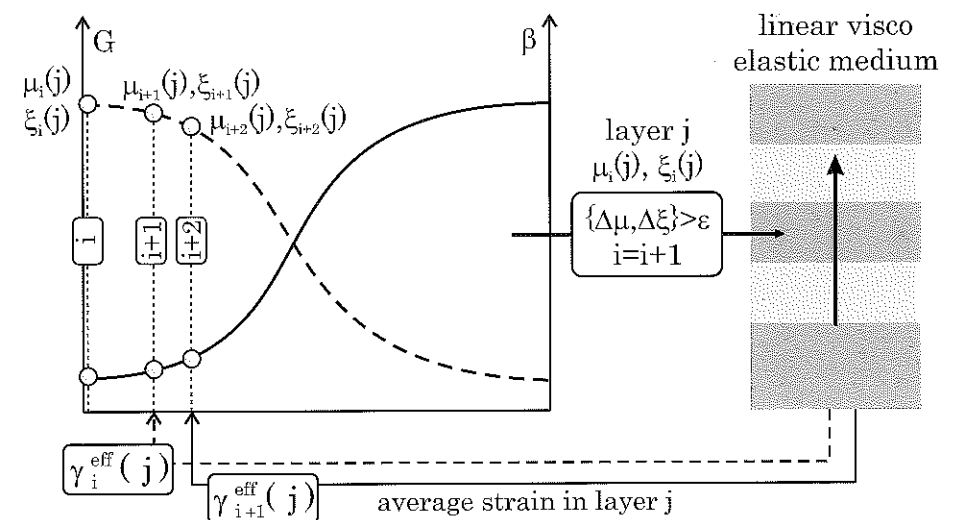


Fig. 2.23: Iterative procedure for the equivalent linear approach.

2.9.5 Frequency dependent models

The model proposed by Kausel and Assimaki (2002) is a viscoelastic model depending on frequency. It is a kind of generalization of the linear equivalent model. As shown by the curves in Fig.2.24, the modulus and the damping simultaneously depend on strain and frequency. This dependence corresponds to the higher frequency small loops and lower frequency large loops shown in Fig.2.22 (cyclic tests).

As shown in Fig.2.24, the shear modulus μ and damping ratio ξ are functions of both the strain γ and frequency ω . Simulations performed with such a strain/frequency dependent model are much better than those obtained with the equivalent linear approach (Kausel and Assimaki, 2002).

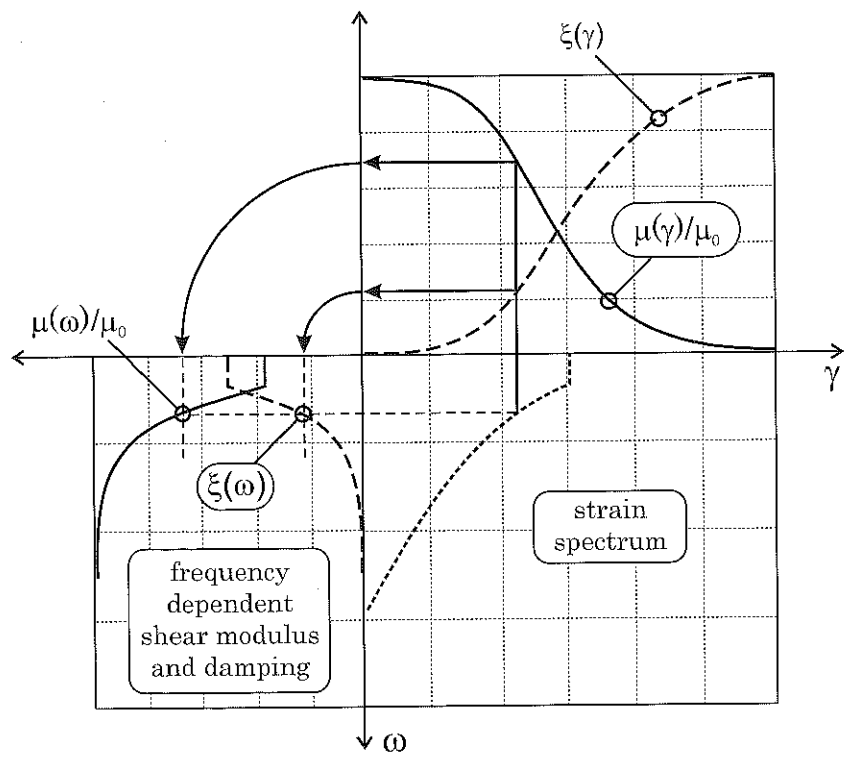


Fig. 2.24: Principles of the frequency dependent model (Assimaki *et al.*, 2000; Kausel and Assimaki, 2002).

2.9.6 Nonlinear viscoelastic models

Starting from the classical *Nearly Constant Q* model (Emmerich and Korn, 1987), Delépine *et al.* (2007) recently proposed a nonlinear model involving both nonlinear elasticity and nonlinear viscosity. The constitutive law of this model is the following:

$$s_{ij}(t) = 2m_0(J_2) \left[e_{ij}(t) - \sum_{l=1}^n \zeta_l(t, y_{l,0}) \right] \quad (2.185)$$

where s_{ij} and e_{ij} are the components of the deviatoric stress and strain tensors, J_2 is the second invariant of the strain tensor and ζ_l are relaxation parameters defined as:

$$\dot{\zeta}_l(t) + \omega_l \zeta_l(t) = \omega_l \frac{c(J_2)y_{l,0}}{1 + c(J_2) \sum_{l=1}^n y_{l,0}} e_{ij}(t) \quad (2.186)$$

As depicted in Fig. 2.25, the variations of attenuation for this nonlinear viscoelastic

model correspond to a nearly constant Q model in the frequency domain whereas attenuation increases for increasing shear strains. Since this model involves a very small number of parameters (Delépine *et al.*, 2007), it allows the analysis of strong seismic motion in large geotechnical models.

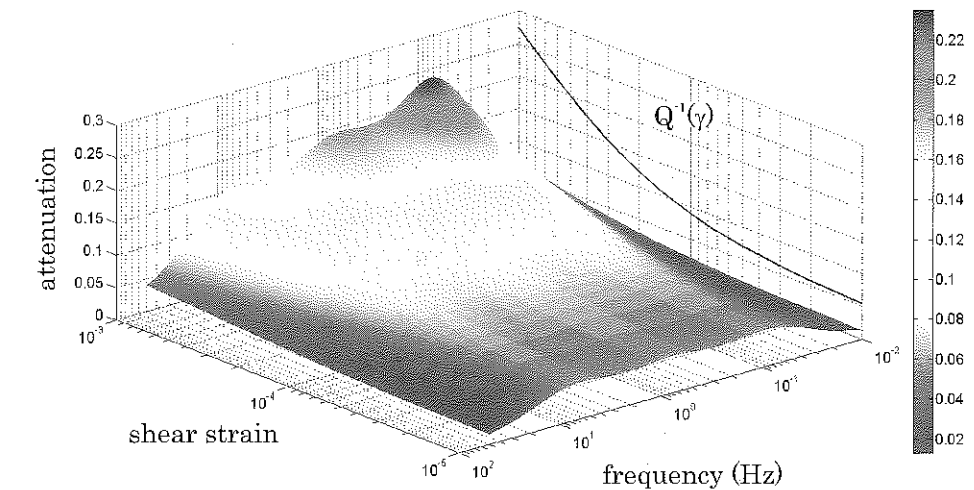


Fig. 2.25: Nonlinear viscoelastic model proposed by Delépine *et al.* (2007): variations of attenuation vs shear strain and frequency.

2.10 Application 1: dynamic characterization on resonant column

2.10.1 Principles of the test

The resonant column test is one of the most popular method to analyze the vibratory response of soils (Cascante *et al.*, 2005; Chung *et al.*, 1984; Drnevich and Richart, 1970; Luong, 1980; Saxena and Reddy, 1989). The quality of the tests mainly depends on the homogeneity of the stresses and strains in the specimen. As depicted in Fig. 2.26, the method consists in exciting a soil column with vibrations. One may apply longitudinal, transverse or torsional vibrations. The transverse vibrations are generally applied thanks to shaking tables. Longitudinal and torsional vibrations are exerted using resonant column devices. This test has been studied in details by Drnevich (1977). The same experimental device, depicted in Fig. 2.26, can be used for forced as well as free vibrations. Both methods allow the estimation of the shear modulus and the damping ratio of the soil specimen. For instance, Taylor and Larkin (1978) performed free vibration torsional experiments. For torsional tests, the hollow cylinder experiment is very interesting since it leads to a nearly constant tangential stress within the cylinder thickness.

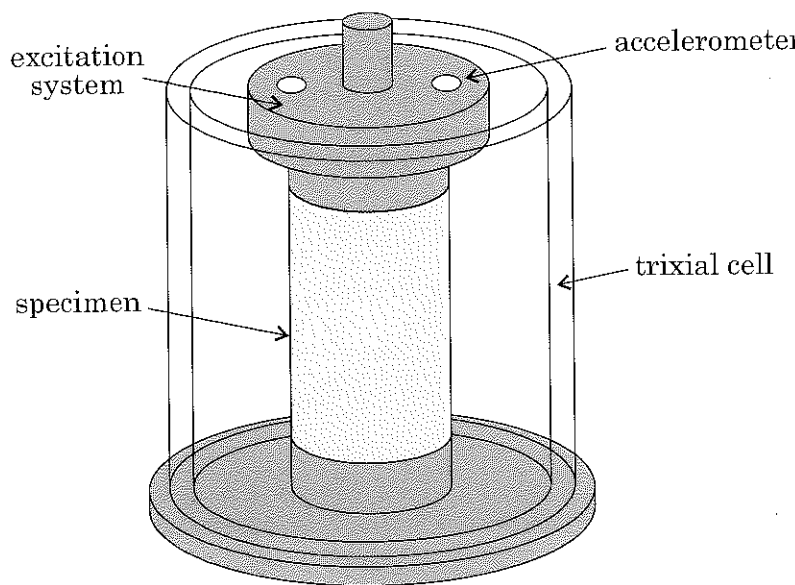


Fig. 2.26: Schematic of the resonant column device.

2.10.2 Description of the specimen motion

When this test is performed using forced vibrations, frequencies have to be tuned until the resonance of the soil specimen is achieved. The frequency of the electromagnetic loading system is adjusted to reach the first eigenmode of the specimen. The estimation of the eigenfrequency of the specimen and the associated eigenmode (generally the 1st one) allows the calculation of the soil shear modulus. It is also possible to perform free oscillations experiments by stopping the vibratory excitation instantaneously. For a torsional vibration of the specimen, the differential equation governing the motion is written as follows:

$$\frac{\partial^2 \theta}{\partial t^2} = V_S^2 \frac{\partial^2 \theta}{\partial x^2} \quad (2.187)$$

where θ is the rotation angle of the specimen cross-section located at distance x from the base and V_S the shear wave velocity. The general solution of Eq.(2.187) is written:

$$\theta = \left(C_1 \cos \frac{\omega x}{V_S} + C_2 \sin \frac{\omega x}{V_S} \right) (D_1 \cos \omega t + D_2 \sin \omega t)$$

that is: $\theta = \left(C_1 \cos \frac{\omega x}{V_S} + C_2 \sin \frac{\omega x}{V_S} \right) F(\omega t) \quad (2.188)$

where C_i and D_i ($i=1,2$) are integration constants depending on the boundary conditions as well as on the initial conditions.

In the configuration depicted in Fig.2.26 (zero displacement at the base and zero shear stress at the top), the boundary conditions are:

$$\begin{cases} \theta(x = 0) = 0 \\ T(x = l) = \mu I_P \frac{\partial \theta}{\partial x}(x = l) = 0 \end{cases} \quad (2.189)$$

where μ is the shear modulus, I_p the geometrical moment of inertia of a cross-section around the vertical axis of the specimen and T the applied torque. The eigenfrequencies are then given by (Eqs (2.188) and (2.189)):

$$\cos \frac{\omega l}{V_S} = 0 \quad (2.190)$$

$$\text{that is: } \omega_n = 2\pi f_n = (2n - 1) \frac{\pi}{2} \frac{V_S}{l} \quad (2.191)$$

The first eigenmode corresponds to a quarter wavelength resonance at frequency f_1 . The shear modulus μ has thus the following expression:

$$\mu = \rho V_S^2 = \rho (4f_1 l)^2 \quad (2.192)$$

The shear strain $\gamma(r, x)$ in the specimen, associated to the first eigenmode, is obtained through:

$$\gamma = r \frac{\partial \theta}{\partial x} = \frac{\pi}{2} \frac{\theta_0 r}{l} \cos \left(\frac{\pi x}{2l} \right) F \left(\frac{\pi V_S t}{2l} \right) \quad (2.193)$$

where θ_0 is the rotation amplitude at the top of the specimen. The shear strain is a function of the distance to the specimen axis and of the location of the considered cross-section. This inhomogeneous shear strain in the specimen makes the interpretation of the test difficult.

2.10.3 Actual resonant column test

In the actual resonant column device, the top of the specimen is not free in the sense of condition (2.189). The electromagnetic excitation system, as well as the sensors, are attached to the specimen head. Equation (2.189) is then replaced by the condition of continuity for forces and displacements at the interface between the specimen and the additional mass.

Denoting J_0 the moment of inertia of the mass m and accounting for the conditions of continuity, the dynamic equilibrium of the mass can be written as follows:

$$-J_0 \frac{\partial^2 \theta}{\partial t^2}(x = l) = G J_P \frac{\partial \theta}{\partial x}(x = l) \quad (2.194)$$

Then, substituting Eq.(2.188) and considering the condition (2.189):

$$\frac{J_P}{J_0} = \frac{\omega l}{V_S} \tan \left(\frac{\omega l}{V_S} \right) \quad (2.195)$$

where J_P denotes the mass moment of inertia of the specimen around the vertical axis.

Equation (2.195) gives the eigenfrequencies of the specimen. By choosing a high value for J_0/J_P , it is possible to have a strain state nearly independent of the cross-section location. Denoting $p = \omega l/V_S$ the first root of Eq.(2.195), and θ_0 the rotation at the top of the specimen, the strain can be expressed as:

$$\gamma = r \frac{\partial \theta}{\partial x} = r \frac{\theta_0}{l} \frac{p}{\sin p} \cos\left(\frac{px}{l}\right) F\left(\frac{pV_S}{l}t\right) \quad (2.196)$$

If J_0/J_P is high, p is small and:

$$\gamma = r \frac{\theta_0}{l} F\left(\frac{pV_S}{l}t\right) \quad (2.197)$$

The γ value generally retained is the average value in a cross-section. It leads to the following choice: $r = d/3$ where d is the specimen diameter.

As an illustration, Fig.2.27 displays the angular rotation associated to the first eigenmode for $J_0/J_P=0$ (no additional top mass) corresponding to a quarter wavelength vibration (left), and for $J_0/J_P=100$ corresponding to a typical commercial device (right).

Resonant column devices corresponding to other types of boundary conditions were also developed: finite stiffness at the base of the specimen (Woods, 1978). For practical situations, the device described previously is the most widely used (Drnevich, 1977).

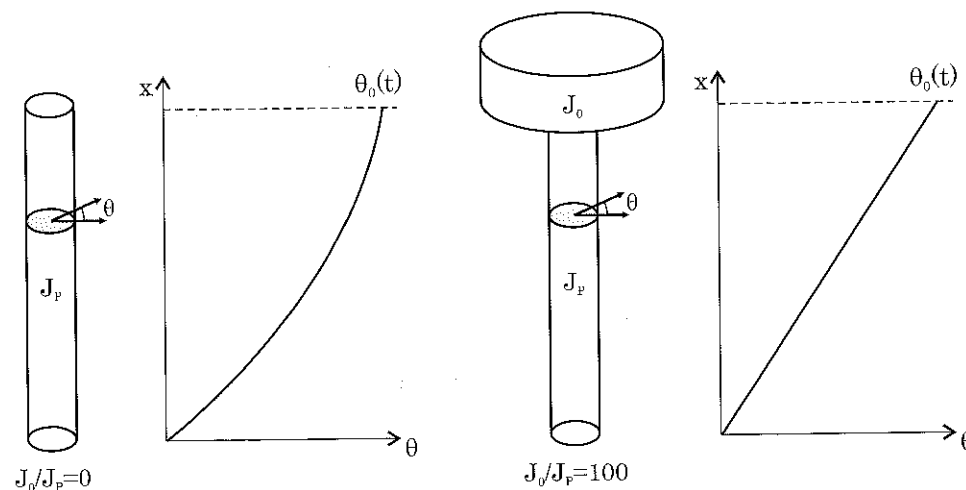
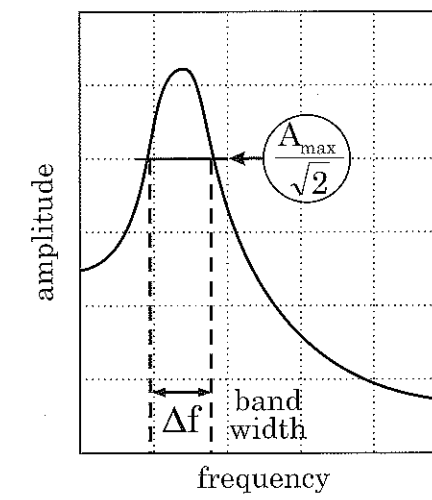


Fig. 2.27: Resonant column test: 1st eigenmode of the specimen without (left) and with (right) the additional top mass.

Forced vibrations



Free vibrations

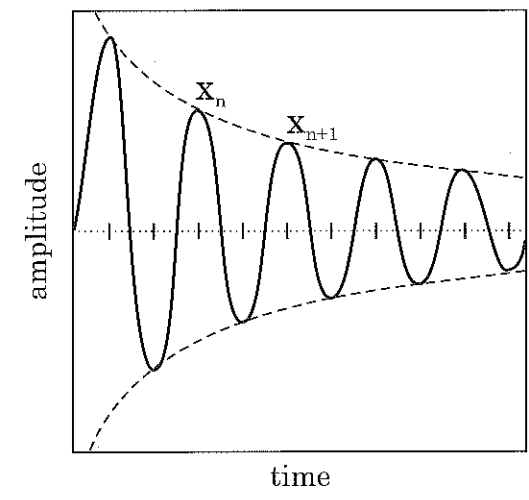


Fig. 2.28: Two types of resonant column tests: forced vibrations (left) and free vibrations (right).

2.10.4 Estimation of damping

To estimate material damping, resonant column tests may be performed considering either forced vibrations (Fig.2.28, left) or free vibrations (Fig.2.28, right). In each of these cases, the estimation of damping is thus performed in a different way:

- *forced vibrations*: one considers the band-width Δf of the resonance curve (Fig.2.28, left). The damping ratio is related to the band-width by the following expression:

$$\xi = \frac{\Delta f}{2f_0} \quad (2.198)$$

where f_0 is the eigenfrequency of the specimen.

- *free vibrations*: one considers the amplitude decay in time from which the logarithmic decrement δ can be estimated (Fig.2.28, right). The logarithmic decrement quantifies the amplitude decay between a given vibration cycle, n , and the following one, $n + 1$:

$$\delta = \ln \frac{x_{n+1}}{x_n} \quad (2.199)$$

These two quantities are related by:

$$\xi = \frac{\delta}{2\pi} \quad (2.200)$$

2.10.5 Results from resonant column tests

The resonant column experiment is as easy to perform as the triaxial test allowing control of drainage, measurement of the pore pressure, and the possibility to apply a wide range of static stresses. It allows the measurement of the dynamic properties of soils for strain amplitudes ranging from 10^{-6} to 5.10^{-4} for torsional tests, and even lower amplitudes in compression. Some experimental devices, such as the hollow cylinder system, allow to reach larger strains around 10^{-2} (Anderson, 1974). Such devices have the advantage of generating a uniform strain state in the specimen.

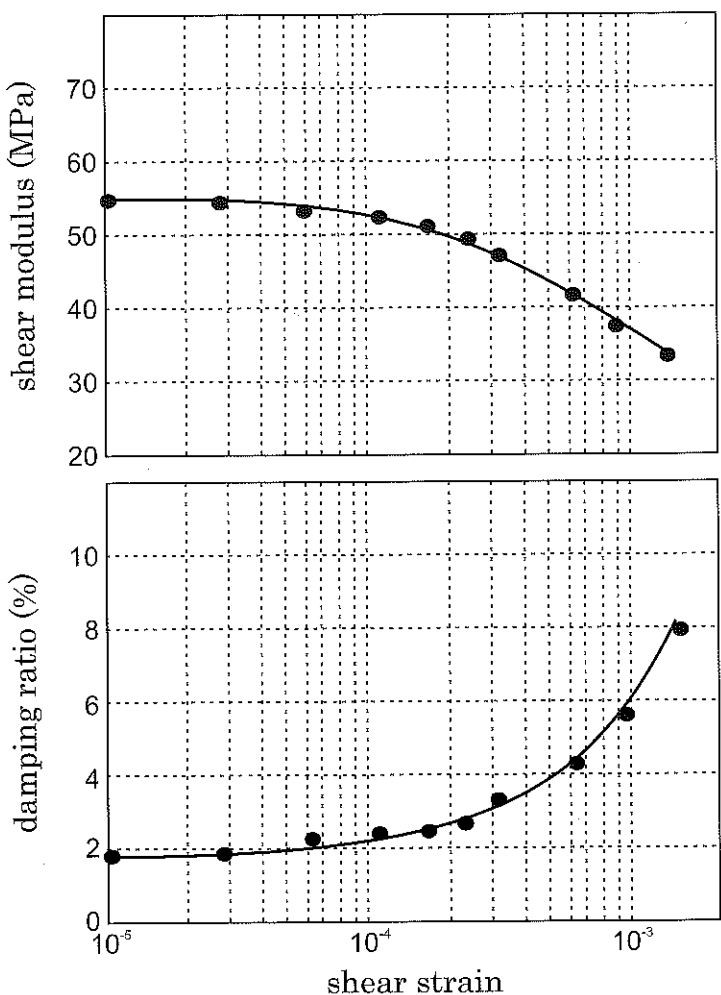


Fig. 2.29: Typical results from resonant column tests: degradation of the shear modulus (top), increasing damping ratio (bottom).

For excitations with amplitude lower than 10^{-4} , soils remain in the elastic range and the test is thus non destructive. It is then possible to obtain the maximum modulus which can be, in some cases, directly compared to that estimated from in situ geophysical measurements. To determine the maximum modulus, only the eigenfrequency and the geometrical configuration of the device are needed. No strain measurement is theoretically required, even if it is actually performed. The accuracy of the resonant column is thus larger than for tests with direct measurement of the applied force and induced strain.

Some results obtained from resonant column tests are displayed in Fig.2.29: the shear modulus (top) and the damping ratio (bottom) are given as functions of shear strain (Pecker and Dupas, 1981). For this test, made on a mud specimen, the dynamic properties have been measured for shear strains ranging from 2.10^{-6} to 3.10^{-4} . For strain below 10^{-4} , the behaviour of the soil remains elastic.

To conclude, one may notice that the resonant column test is reliable and reproducible. Skoglund *et al.* (1976) have shown a good agreement between results obtained in six different laboratories, using various devices, for experiments made on the same material under the same experimental conditions.

2.11 Application 2: dynamic characterization under fast loadings

In the field of fast dynamics (shocks, blasts, etc), wave propagation phenomena are often dominating. It is thus difficult to directly determine the dynamic behaviour of materials under fast loadings. A specific experimental device allows such a determination: the *Split Hopkinson Pressure Bar (SHPB)* (Davies and Hunter, 1963; Klepaczko *et al.*, 1991; Semblat *et al.*, 1999; Zhao *et al.*, 1997).

2.11.1 Split Hopkinson Pressure Bar test

The Split Hopkinson Pressure Bar device is designed to allow, under fast loadings, the longitudinal stress to quickly become uniform in the specimen. It is then possible to perform *behaviour experiments* at very high strain rates. In Hopkinson bar tests, the propagation phenomena are well controlled. Meunier (1974) and Semblat *et al.* in France (1999), Felice *et al.* (1987, 1991) and Veyera and Ross (1995) in the USA, Shibusawa and Oida (1992a,b) in Japan and Bragov and Lomunov (1994) in Russia performed Hopkinson bar tests to determine the response of soils under high strain rates. This method is very interesting since it allows reliable measurements of both displacements and forces at the specimen ends. However, performing such tests on soils raises specific difficulties. Since the mechanical properties of soils are generally weak (e.g. low moduli), it is necessary to adapt the classical device to this peculiar material. For instance, Meunier (1974) used nylon bars, Felice (1985) performed oedometric tests confining the specimen in a rigid cylinder and Zhao *et al.* (1997) used PMMA viscoelastic bars.

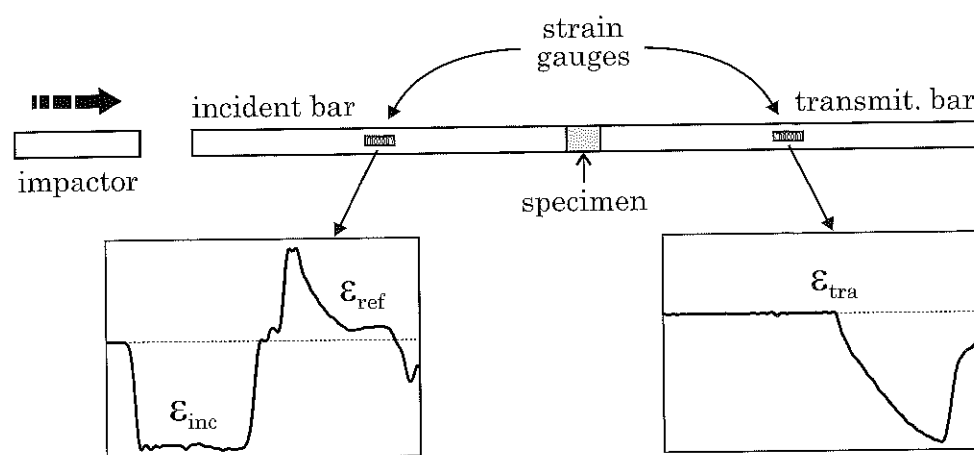


Fig. 2.30: Hopkinson bar dynamic experiment: "classical" device.

2.11.2 Experimental device

The classical experimental device is composed of two axial bars (an *incident bar* and a *transmitted bar*) and an impactor launched on the incident bar using a pressurized air system. Figure 2.30 gives a schematic of the classical Hopkinson device. It was originally composed of one single bar and has been improved by Kolsky (1949) to perform indirect measurements on both sides of the specimen.

As shown in Fig.2.30, the shock between the impactor and the incident bar generates a step wave composed of a loading wave and an unloading wave. These waves are nearly pure pressure waves since the bending of the bars is constrained thanks to several guides displayed all along their length. The duration of the step wave depends on the pressure wave velocity and the length of the impactor. The end of the transmitted bar is equipped with an energy absorbing device.

The measurements performed in the bars using strain gauges give the values of the incident (ε_{inc}), reflected (ε_{ref}) and transmitted (ε_{tra}) strains (Fig.2.30). From such measurements, it is possible to determine the forces and displacements in every cross-section of the bars (and especially at the bar-specimen interfaces) and at each time.

2.11.3 Stress wave in the specimen

The propagation of the stress wave in the bars and at the bar-specimen interfaces is a fundamental aspect of dynamic experiments on Hopkinson bars. At both bar-specimen interfaces, multiple reflected and transmitted waves appear. As discussed in §2.3.6, they are controlled by the mechanical parameters of the bars and the specimen.

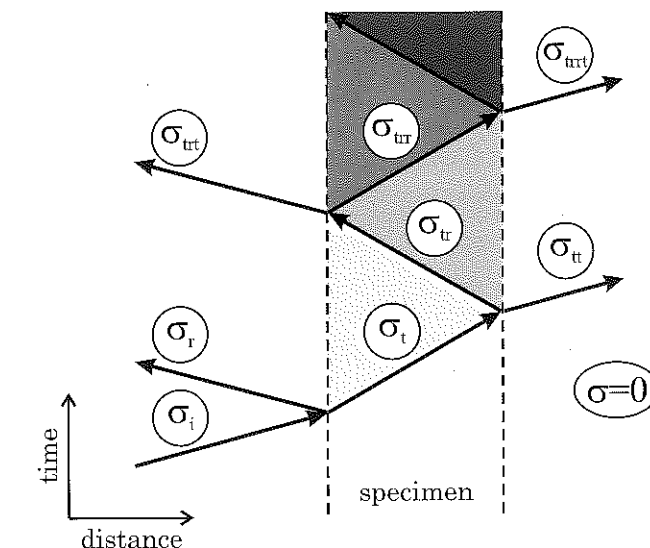


Fig. 2.31: Propagation of various reflected and transmitted stress waves through both bar-specimen interfaces.

Assuming the specimen to be purely elastic, it is possible to have a simple description of each reflection-transmission step. As shown in Fig.2.31, the different steps are as follows:

- the incident stress wave σ_i (compression) is partially reflected at the first interface. Since the modulus of the specimen is lower than that of the bars, a reflected stress wave σ_r (tension) and a transmitted stress wave σ_t (compression) simultaneously appear,
- at the second interface, the similar reflection-transmission process occurs and generates two compressive waves: a transmitted one σ_{tt} and a reflected one σ_{tr} .

The schematic given in Fig.2.31 displays several reflected and transmitted waves vs time and location. At each reflection-transmission step, the axial stress increases at a speed depending on the bar/specimen velocity ratio. After several steps, the axial stress in the specimen is very close to that of the incident stress wave. This phase of the experiment is called the *transient phase*: the propagation phenomena dominate. After this phase, the axial stress becomes progressively uniform in the specimen.

As shown in Fig.2.32, two different phases can generally be distinguished in Hopkinson bar dynamic tests:

- a *transient phase*: the first reflected and transmitted waves lead to an inhomogeneous stress state. The propagation phenomena strongly dominate in this transient

phase of the test. The incident force (Fig.2.32, continuous line) is much larger than the transmitted force (Fig.2.32, dotted line)

- a *fast quasi-static phase*: after several reflections and transmissions of the loading wave at both interfaces, the specimen reaches a stress equilibrium state. This step is called the *fast quasi-static phase* of the experiment: the axial stress is homogeneous in the whole specimen and the incident and transmitted forces are equal (Fig.2.32).

As shown in Fig.2.32, a transient phase occurs for both loading and unloading waves (phases number (1) and (3)). The time window considered in Hopkinson bar tests is generally the fast quasi-static phase (denoted (2) and (4) in Fig.2.32). Two equilibrium phases are possible in the specimen: for loading and for unloading. Original methods allow the detailed analysis of the transient phase of the Hopkinson bar tests (Zhao *et al.*, 1997).

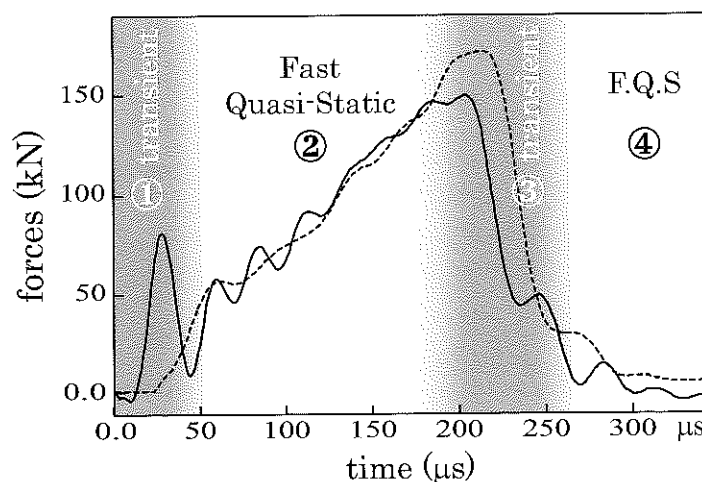


Fig. 2.32: Forces on both sides of the specimen showing the two loading (resp. unloading) phases (Semblat *et al.*, 1999).

2.11.4 Determination of the mechanical parameters

Mechanical parameters in the bars

In the bars, the parameters related to the behaviour and to wave propagation are expressed under a simple form. After correction of some dispersive phenomena due to the three dimensional geometry of the bars (Zhao *et al.*, 1997), the assumption of one-dimensional propagation is fully justified. The measurements performed along the bars should be propagated backward to the bar-specimen interfaces in order to determine the

forces and displacements at the specimen boundaries. Considering the results on pressure waves proposed in §2.3, the expressions of the axial stress and strain are the following:

$$\sigma_{ax}^{(b)} = \rho c v \quad (2.201)$$

$$\varepsilon_{ax}^{(b)} = \frac{v}{c} \quad (2.202)$$

where σ_{ax} is the axial stress, ε_{ax} the axial strain, ρ the mass density, v the particle velocity and c the pressure wave velocity in the bars.

These expressions are valid for any medium of propagation. For purely elastic bars, expression (2.201) yields:

$$\sigma_{ax}^{(b)} = \rho c^2 \varepsilon_{ax} \quad (2.203)$$

and the wave velocity c is expressed as follows:

$$c = \sqrt{\frac{E}{\rho}} \quad (2.204)$$

Stress and strain in the specimen

The strains being measured on the bars, the axial strain $\varepsilon_{ax}^{(s)}$ and the axial stress $\sigma_{ax}^{(s)}$ in the specimen may be determined from the incident ε_i , reflected ε_R and transmitted strains ε_T (Semblat, 1995; Zhao *et al.*, 1997).

The axial strain in the specimen is determined under the following form:

$$\varepsilon_{ax}^{(s)}(t) = \frac{1}{h} \int_0^t (v_{out}(\tau) - v_{in}(\tau)) d\tau \quad (2.205)$$

where *in* and *out* denote the first and second bar/specimen interfaces (respectively).

Considering Eq. (2.202), it leads to:

$$\varepsilon_{ax}^{(s)}(t) = \frac{1}{h} \int_0^t c(\varepsilon_{out}(\tau) - \varepsilon_{in}(\tau)) d\tau \quad (2.206)$$

Since $\varepsilon_{in}^{(s)}(t) = \varepsilon_i(t) - \varepsilon_R(t)$ and $\varepsilon_{out}^{(s)}(t) = \varepsilon_T(t)$, the axial strain in the specimen is finally expressed as:

$$\varepsilon_{ax}^{(s)}(t) = \frac{c}{h} \int_0^t (\varepsilon_T(\tau) + \varepsilon_R(\tau) - \varepsilon_i(\tau)) d\tau \quad (2.207)$$

To determine the axial stress, the normal force should be estimated at both bar-specimen interfaces. The following expressions are easily found:

$$\begin{cases} N_{in}(t) = ES_b [\varepsilon_i(t) + \varepsilon_R(t)] \\ N_{out}(t) = ES_b \varepsilon_T(t) \end{cases} \quad (2.208)$$

Finally, the axial stress is determined from:

$$\sigma_{ax}^{(s)} = \frac{N_{in}(t) + N_{out}(t)}{2S_s} \quad (2.209)$$

yielding the following expression in terms of measured axial strains:

$$\sigma_{ax}^{(s)} = \frac{S_b E}{2S_s} [\varepsilon_i(t) + \varepsilon_R(t) + \varepsilon_T(t)] \quad (2.210)$$

where S_b is the area of the bar cross-section and S_s the area of the specimen cross-section.

Previous expressions may be simplified if the forces at the bar/specimen interfaces are identical: $N_{in} = N_{out}$ (equilibrium). It corresponds to the fast quasi-static phase of the test. The simplified expressions are as follows:

- simplified axial strain:

$$\varepsilon_{ax}^{(s)}(t) = \frac{2c}{h} \int_0^t \varepsilon_R(\tau) d\tau \quad (2.211)$$

- simplified axial strain rate:

$$\dot{\varepsilon}_{ax}^{(s)}(t) = \frac{2c}{h} \varepsilon_R(t) \quad (2.212)$$

- simplified axial stress:

$$\sigma_{ax}^{(s)} = \frac{S_b E}{S_s} \varepsilon_T(t) \quad (2.213)$$

2.11.5 3D Split Hopkinson Pressure Bar test

Principles of the test

To apply a dynamic loading on soils, it is necessary to measure (or control) the axial and radial stresses. The dynamic response of the material may thus be analyzed considering three-dimensional stress paths. Semblat *et al.* (1999) performed dynamic oedometric tests on soils using a rigid confining cylinder. They also proposed an original experimental device: the *3D-Hopkinson pressure bar*. The use of a rigid confining cylinder avoids radial strain, but it is then possible to estimate the radial stress. A radial bar, in contact with the specimen through the confining cylinder, allows the measurement of the radial stress as a function of time (Semblat *et al.*, 1999). Figure 2.33 gives a schematic of the *3D-Hopkinson pressure bar*.

Experimental device

The special experimental device displayed in Fig. 2.33 involves three Hopkinson-type bars:

- two axial bars to measure the forces and displacements on both sides of the specimen (as for the classical device),

- one radial bar to evaluate the dynamic radial stress during the test.

For all the tests performed by Semblat *et al.* (1999), the specimens are made of dry Fontainebleau sand. The dynamic oedometric tests performed on the device of Fig. 2.33 are called *rigid confinement tests*: the rigid confining cylinder prevents the radial strain. The confining cylinder must be sufficiently rigid or thick to obtain a small radial strain. This has been checked from the measured radial stresses by Semblat *et al.* (1999).

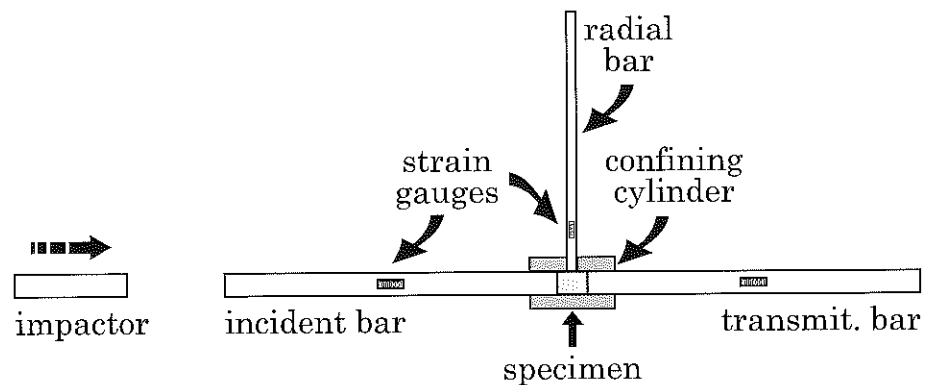


Fig. 2.33: 3D-Hopkinson pressure bar device (Semblat *et al.*, 1999).

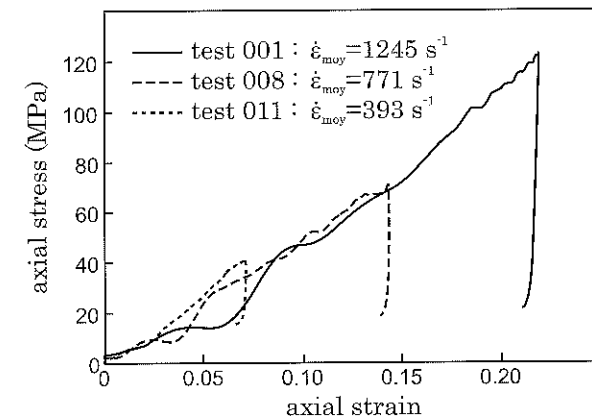


Fig. 2.34: Examples of dynamic axial responses on the 3D-Hopkinson bar device (Semblat *et al.*, 1999).

2.11.6 3D fast dynamic response of sand

Axial stress

Figure 2.34 displays the axial stress vs the axial strain for three oedometric tests (rigid confinement). These three tests correspond to identical specimen lengths ($l=10\text{mm}$) but various strain rates (see Fig.2.34 and (Semblat *et al.*, 1999)).

For the rigid confinement tests, the axial responses are nearly linear for loading as well as for unloading but with very different slopes in both cases. The behaviour of the material under dynamic oedometric loading is then strongly anelastic. However, the slopes for loading on one hand and for unloading on the other one are rather close for the three examples presented in Fig.2.34.

The elastic part of the response is then not really visible on the curves given in Fig.2.34. The response in the oedometric case is compared afterwards for various loading paths.

Measurement of the radial stress

The 3D-Hopkinson pressure bar device presented in Fig.2.33 allows the determination of both the axial stress and the radial stress. The two curves in Fig.2.35 display the variations of the axial and radial stresses with time. The radial stress σ_{rad} obviously changes with time since, for the results of this test, σ_{rad} reaches a maximum of 30 MPa at time $t=150\mu\text{s}$. Beyond this time value, the radial stress decreases whereas the axial stress is still increasing (Fig.2.35).

Taking into account the variations of the confining pressure (radial stress) in the dynamic oedometric tests is thus crucial since the variations of the radial stress during the axial loading are very important. This aspect of the problem is of great importance in the case of soils since their behaviour is strongly influenced by the three-dimensional loading path (Semblat *et al.*, 1999).

Dynamic loading: the three-dimensional point of view.

The 3D-Hopkinson bar device (Fig.2.33) gives the axial and radial stresses (denoted σ_{ax} and σ_{rad} respectively). Assuming a homogeneous radial stress around the specimen, it is possible to determine the three-dimensional loading paths in terms of mean stress p and deviatoric stress q : The mean and deviatoric stresses are defined by:

$$\begin{cases} p = \frac{\sigma_{ax} + 2\sigma_{rad}}{3} \\ q = \sigma_{ax} - \sigma_{rad} \end{cases} \quad (2.214)$$

where σ_{ax} and σ_{rad} are the axial and radial stresses respectively.

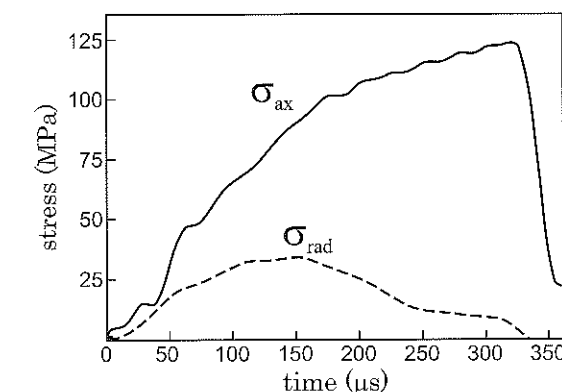


Fig. 2.35: Axial and radial stresses as functions of time (Semblat *et al.*, 1999).

As discussed by Semblat *et al.* (1999), Fig.2.36 clearly shows that, for a linear strain path ($\varepsilon_q/\varepsilon_v=2/3$ for the oedometric tests), the stress path is also linear. In Fig.2.36, the $p - q$ curves correspond to various specimen lengths: 10 mm (1), 15 mm (2) and 20 mm (3). For the shortest specimens (1,2), the loading and unloading slopes in the $p - q$ diagrams are very different. For the 20 mm long specimen (3), the loading and unloading slopes are very close (Fig.2.36). It shows that the structure of the specimen is different after the loading phase (due to the crushing of grains for instance). The unloading behaviour of the material is thus also different from the loading behaviour. From the curves displayed in Fig.2.36, this phenomenon is stronger for shorter specimens, that is when grain crushing is important (Semblat *et al.*, 1999).

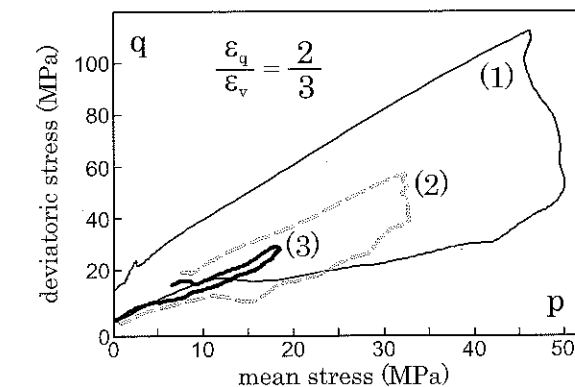


Fig. 2.36: $p-q$ diagrams: deviatoric stress vs mean stress for dynamic oedometric tests on sand (Semblat *et al.*, 1999).

Values of the dynamic "moduli"

The rigid confinement tests performed in the 3D-Hopkinson pressure bar by Semblat *et al.* (1999) cover a wide range of specimen sizes, strain rates, etc. For all these tests, the moduli of the stress-strain curves were determined in order to characterize the dynamic response of sand. The dynamic response of the material being strongly anelastic, the modulus considered by Semblat *et al.* (1999) corresponds to a hardening modulus. The larger values (800 MPa) correspond to the lowest strain rates (200 s^{-1}), whereas the lowest values (350-450 MPa) to the highest strain rates ($800\text{-}1200 \text{ s}^{-1}$). Semblat *et al.* (1999) concluded that *the modulus decreases when the strain rate increases*. It is nevertheless difficult to determine a quantitative relationship between the dynamic modulus and the strain rate due to the scatter of the results. Furthermore, it would be necessary to perform tests for various impactor lengths (that is loading phase of various durations) to clearly separate the effects of the stress level and the effects of the strain rate.

Semblat *et al.* (1999) also performed fast dynamic tests under 'soft confinement' (i.e. pressure cell) to compare the fast dynamic response of soils for various stress-strain paths.

2.12 Application 3: response of a heterogeneous soil profile

The approach proposed in this section is based on an analytical solution to the wave equation in a heterogeneous soil profile. The assumed soil constitutive behaviour is of the elastic perfectly plastic type, and is completely defined by the maximum shear stress and the yield strain at any depth. This methodology has been applied to parametric numerical analyses investigating seismic ground motion (Pecker, 2005).

2.12.1 Soil behaviour

It has long been recognized that soil behaviour is highly non-linear beyond very small strains, and that a complete description of the behaviour would require considerations of small as well as large strains. The result of a simple shear test carried out on an undisturbed sample of medium plasticity clay, shown in Fig.2.37, illustrates the previous statement. Within the context of the simplified approach developed herein, only the shear stress-shear strain curve is needed. The true stress-strain curve is then approximated by a bilinear curve corresponding to an elastic-perfectly plastic constitutive relationship (Fig.2.37); it is defined by two parameters, which may depend on the depth z : the shear strength $\tau_{max}(z)$ and the engineering shear strain at which yield occurs $\gamma_f(z)$.

The shear modulus is then given by $G(z) = \tau_{max}(z)/\gamma_f(z)$. The energy dissipated under cyclic loading does not explicitly appear in the formulation; it is taken into account in the analysis through an equivalent damping ratio (Pecker, 2005). Unlike the equivalent linear model, this model is robust and rather reliable because the shear strength is less affected by sample remolding than the shear modulus, it is easy to measure in the

laboratory or to derive from field tests through empirical correlations, and is routinely determined in any soil investigation. In the examples presented herein, a conservative value of 20% has been assumed.

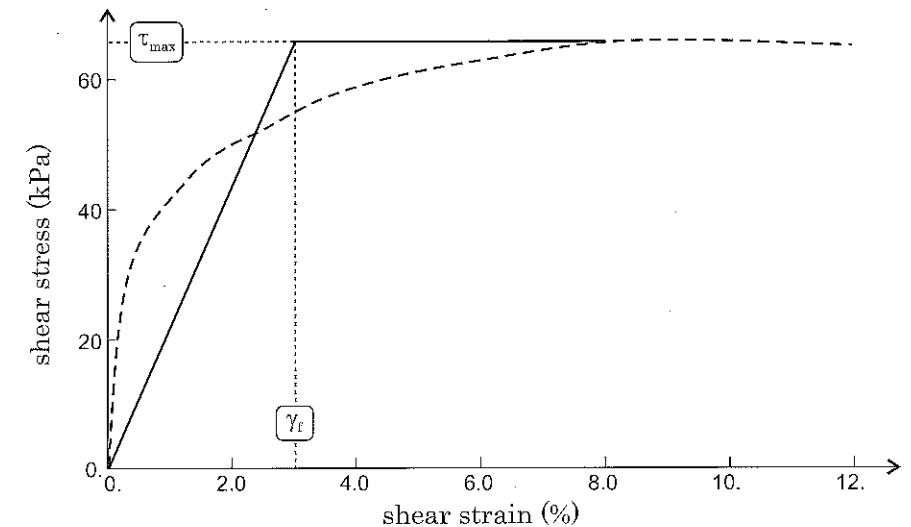


Fig. 2.37: Soil shear stress-shear strain curve: the dashed line represents laboratory measurements; the solid line represents the elasto-plastic idealization (Pecker, 2005).

2.12.2 Wave equation for a heterogeneous profile

Let us consider a soil layer of finite thickness overlying a stiffer halfspace (referred to as the bedrock in the following), which will be considered as a rigid boundary. The soil is assumed to be isotropic elastic, with a shear wave velocity increasing with depth according to some power law:

$$V(z) = V_S \left(\frac{z+d}{d+h} \right)^{\frac{p}{2}} \quad (2.215)$$

where z is measured from the ground surface, h is the layer thickness, p a real positive parameter smaller than 2 and V_S the shear wave velocity at depth h . d is a strictly positive parameter that can be chosen to fit Eq.(2.215) to the experimental data. As a particular case, this parameter can be set equal to zero giving a zero shear wave velocity at the ground surface. It is convenient to make a transformation and to define the new variables:

$$\zeta = \frac{z+d}{d+h} \quad \text{and} \quad H = d+h$$

The wave equation for a plane vertically incident shear wave is written as:

$$\frac{\partial \tau(z)}{\partial z} = \frac{\partial}{\partial z} \left(G(z) \frac{\partial U}{\partial z} \right) = \rho \frac{\partial^2 U}{\partial z^2} = \rho \left(\frac{\partial^2 u}{\partial t^2} + \ddot{v}_g(t) \right) \quad (2.216)$$

where ρ is the mass density, $\tau(z)$ is the horizontal shear stress, $G(z)$ the shear modulus related to the shear wave velocity by $G(z) = \rho V^2(z)$, U the absolute soil displacement, u is the horizontal displacement, relative to the bedrock, and v_g the bedrock displacement motion. With the change of variable $z \rightarrow \zeta$ defined above, Eq. (2.216) becomes:

$$\frac{V_S^2}{H^2} \frac{\partial}{\partial \zeta} \left(\zeta^p \frac{\partial u}{\partial \zeta} \right) = \frac{\partial^2 u}{\partial t^2} + \ddot{v}_g(t) \quad (2.217)$$

2.12.3 Boundary conditions

The boundary conditions express that the relative displacement at the bedrock interface and the shear stress at the ground surface are:

$$\begin{cases} \zeta = \frac{d}{H} = \zeta_0 : \tau(\zeta_0) = 0 \Rightarrow G(\zeta_0) \frac{\partial u}{\partial \zeta} \Big|_{\zeta=\zeta_0} = 0 \\ \zeta = 1 : u(1, t) = 0 \end{cases} \quad (2.218)$$

When the shear wave velocity is different from zero at the ground surface ($d > 0$), the first of the two boundary conditions reduces to:

$$\zeta = \frac{d}{H} = \zeta_0 : \frac{\partial u}{\partial \zeta} \Big|_{\zeta=\zeta_0} = 0 \quad (2.219)$$

When the shear wave velocity is equal to zero at the ground surface, the limit of the first boundary condition must be considered:

$$\zeta = 0 : \tau(\zeta = 0) = 0 \Rightarrow \lim_{\zeta \rightarrow 0} G(\zeta) \frac{\partial u}{\partial \zeta} = 0 \quad (2.220)$$

Considering the homogeneous equation, without the forcing term $\ddot{v}_g(t)$, and using the technique of separation of variables $u(\zeta, t) = X(\zeta)y(t)$; Eq. (2.217) becomes:

$$\frac{V_S^2}{H^2} \frac{d}{d\zeta} \left(\zeta^p \frac{dX}{d\zeta} \right) y(t) = X(\zeta) \ddot{y}(t) \quad (2.221)$$

which can be written:

$$\frac{V_S^2}{H^2} \frac{\frac{d}{d\zeta} \left(\zeta^p \frac{dX}{d\zeta} \right)}{X(\zeta)} = \frac{\ddot{y}(t)}{y(t)} = \text{cst} = -\omega^2 \quad (2.222)$$

The first equation gives the mode shapes:

$$\frac{d}{d\zeta} \left(\zeta^p \frac{dX}{d\zeta} \right) + \frac{H^2}{V_S^2} \omega^2 X(\zeta) = 0 \quad (2.223)$$

with the boundary conditions:

$$\begin{cases} \lim_{\zeta \rightarrow \zeta_0} \zeta^p X'(\zeta) = 0 \\ X(1) = 0 \end{cases} \quad (2.224)$$

A solution of the form $X(\zeta) = \zeta^\alpha Y(\zeta^q)$ is sought for Eq. (2.223) (Pecker, 2005). The following equation is easily obtained with the notation $\beta = \zeta^q$:

$$Y''(\beta) + \frac{2\alpha + q + p - 1}{q\beta} Y'(\beta) + \left[\frac{\alpha(\alpha - 1) + p\alpha}{q^2\beta^2} + \left(\frac{H\omega}{qV_S} \right)^2 \beta^{2q-p} \right] Y(\beta) = 0 \quad (2.225)$$

An appropriate choice of the parameters α and q reduces the previous equation to a Bessel equation provided the following choice is made:

$$\begin{cases} 2 - 2q - p = 0 & \Rightarrow q = \frac{2-p}{2} \\ 2\alpha + q + p - 1 = q & \Rightarrow \alpha = \frac{1-p}{2} \end{cases} \quad (2.226)$$

Eq. (2.225) becomes:

$$Y''(\beta) + \frac{1}{\beta} Y'(\beta) + \left[\left(\frac{2\omega H}{(2-p)V_S} \right)^2 - \frac{\nu^2}{\beta^2} \right] Y(\beta) = 0 \quad \text{with : } \nu = \frac{p-1}{2-p} \quad (2.227)$$

The general solution is obtained as:

$$X(\zeta) = \zeta^{\frac{1-p}{2}} \left[A J_\nu \left(\lambda \zeta^{\frac{2-p}{2}} \right) + B Y_\nu \left(\lambda \zeta^{\frac{2-p}{2}} \right) \right] \quad (2.228)$$

where J_ν and Y_ν are Bessel's function of the first kind and second kind and $\lambda = \frac{2\omega H}{(2-p)V_S}$.

Taking into account the recurrence formula (Abramowitz and Stegun, 1970):

$$C'_\nu(z) = -C_{\nu+1}(z) + \frac{\nu}{z} C_\nu(z) \quad (2.229)$$

in which C_ν represents either J_ν or Y_ν , the derivative of Eq.(2.228) can be expressed as:

$$X'(\zeta) = -\frac{2-p}{2} \lambda \zeta^{\frac{1-2p}{2}} \left[A J_{\nu+1} \left(\lambda \zeta^{\frac{2-p}{2}} \right) + B Y_{\nu+1} \left(\lambda \zeta^{\frac{2-p}{2}} \right) \right] \quad (2.230)$$

The boundary conditions (2.224) together with the two relationships (2.228) and (2.230) yield a system of two equations with two unknowns A and B . This system has a non-trivial solution if, and only if, its determinant is equal to zero. This condition provides the frequency equation, which possesses an infinite number of distinct real positive roots (Abramowitz and Stegun, 1970). To each of these roots is associated a mode

shape X_m , which is normalized to 1.0 at the surface for convenience; the solution $u(\zeta, t)$ is expanded in terms of the mode shapes:

$$u(\zeta, t) = \sum_{m=1}^{\infty} X_m(\zeta) y_m(t) \quad (2.231)$$

Given the orthogonality property of the mode shapes, the solution of the wave equation (2.217) is given by:

$$\ddot{y}_n(t) \int_{\zeta_0}^1 X_n^2(\zeta) d\zeta + \omega_n^2 y_n(t) \int_{\zeta_0}^1 X_n^2(\zeta) d\zeta = -\ddot{v}_g(t) \int_{\zeta_0}^1 X_n(\zeta) d\zeta \quad (2.232)$$

where ω_n is the n^{th} soil column circular frequency, which is solution of the frequency equation. Introducing the mode participation factor α_n :

$$\alpha_n = \frac{\int_{\zeta_0}^1 X_n(\zeta) d\zeta}{\int_{\zeta_0}^1 X_n^2(\zeta) d\zeta} \quad (2.233)$$

Equation (2.232) is finally written:

$$\ddot{y}_n(t) + \omega_n^2 y_n(t) = -\alpha_n \ddot{v}_g(t) \quad (2.234)$$

Equation (2.234) can be solved by any computational technique like Duhamel's integral. In the context of this section, only the maximum surface acceleration is sought and a spectral analysis is used. The maximum displacement response in each mode is given by:

$$u_i(\zeta) = \alpha_i S_d(\omega_i, \xi_i) X_i(\zeta) \quad (2.235)$$

where $S_d(\omega_i, \xi_i)$ is the spectral relative displacement of the input motion \ddot{v}_g for frequency ω_i and damping ratio ξ_i . The maximum ground surface acceleration due to the contribution of the first N modes is:

$$\ddot{u}_{max}(z=0) = \sqrt{\sum_{i=1}^N [\alpha_i S_d(\omega_i, \xi_i)]^2} \quad (2.236)$$

where $S_a(\omega_i, \xi_i) = \omega_i^2 S_d(\omega_i, \xi_i)$ is the pseudo acceleration. Equation (2.236) takes into account the fact that the mode shapes have been normalized to 1 at the ground surface ($X_i(\zeta_0) = 1$). The percentage of modal mass relative to the total mass of the soil column, which is an indicator of the number of modes N to retain, is:

$$m_n = \frac{1}{1 - \zeta_0} \frac{\left[\int_{\zeta_0}^1 X_n(\zeta) d\zeta \right]^2}{\int_{\zeta_0}^1 X_n^2(\zeta) d\zeta} \quad (2.237)$$

The shear strain at any depth within the profile is then expressed as:

$$\gamma_{max}(z) = \sqrt{\sum_{i=1}^N \left(\frac{\partial u_i(z)}{\partial z} \right)^2} = \frac{1}{H} \sqrt{\sum_{i=1}^N \left(\alpha_i \frac{S_a(\omega_i, \xi_i)}{\omega_i^2} X'_i(\zeta) \right)^2} \quad (2.238)$$

Zero shear wave velocity at the ground surface.

This situation arises when $d = 0$ in Eq.(2.215). For the mode shape to remain finite at the ground surface, $B = 0$ must be enforced in Eq.(2.228). The second boundary condition (2.224) yields the frequency equation:

$$J_{\frac{p-1}{2-p}}(\lambda) = 0 \quad (2.239)$$

which possesses an infinite number of distinct roots λ_i . The eigenfrequencies of the soil column are:

$$f_i = \lambda_i \frac{V_S(2-p)}{4\pi H} \quad (2.240)$$

and the mode shapes, normalized to 1.0 at the surface ($z = 0$), are:

$$X_i(\zeta) = \left(\frac{2}{\lambda_i} \right)^{\frac{p-1}{2-p}} \Gamma \left(\frac{1}{2-p} \right) \zeta^{\frac{1-p}{2}} J_{\frac{p-1}{2-p}} \left(\lambda_i \zeta^{\frac{2-p}{2}} \right) \quad (2.241)$$

where $\Gamma(\cdot)$ is the Gamma function. It is easily checked that, as long as $p < 2$, the first boundary condition (2.224) is satisfied because $X'_i(\zeta) \simeq \zeta^{\frac{1}{2}} J_{\frac{1}{2-p}} \left(\lambda_i \zeta^{\frac{2-p}{2}} \right)$ when ζ tends to zero.

Non-zero shear wave velocity at the surface.

The frequency equation is:

$$J_\nu(\lambda) Y_{\nu+1} \left(\lambda \zeta_0^{\frac{2-p}{2}} \right) - Y_\nu(\lambda) J_{\nu+1} \left(\lambda \zeta_0^{\frac{2-p}{2}} \right) = 0 \quad (2.242)$$

which possesses an infinite number of distinct roots λ_i . The frequencies of the soil column are still given by Eq.(2.240), and the mode shapes, normalized to 1.0 at the ground surface are:

$$X_i(\zeta) = \frac{\pi}{2} \lambda_i \sqrt{\zeta_0} \zeta^{\frac{1-p}{2}} \left[Y_{\frac{p-1}{2-p}} \left(\lambda_i \zeta^{\frac{2-p}{2}} \right) J_{\frac{1}{2-p}} \left(\lambda_i \zeta_0^{\frac{2-p}{2}} \right) - J_{\frac{p-1}{2-p}} \left(\lambda_i \zeta^{\frac{2-p}{2}} \right) Y_{\frac{1}{2-p}} \left(\lambda_i \zeta_0^{\frac{2-p}{2}} \right) \right] \quad (2.243)$$

The derivation of the previous equation takes advantage of the recurrence relationship (Abramowitz and Stegun, 1970):

$$J_{\nu+1}(x) Y_\nu(x) - J_\nu(x) Y_{\nu+1}(x) = \frac{2}{\pi x} \quad (2.244)$$

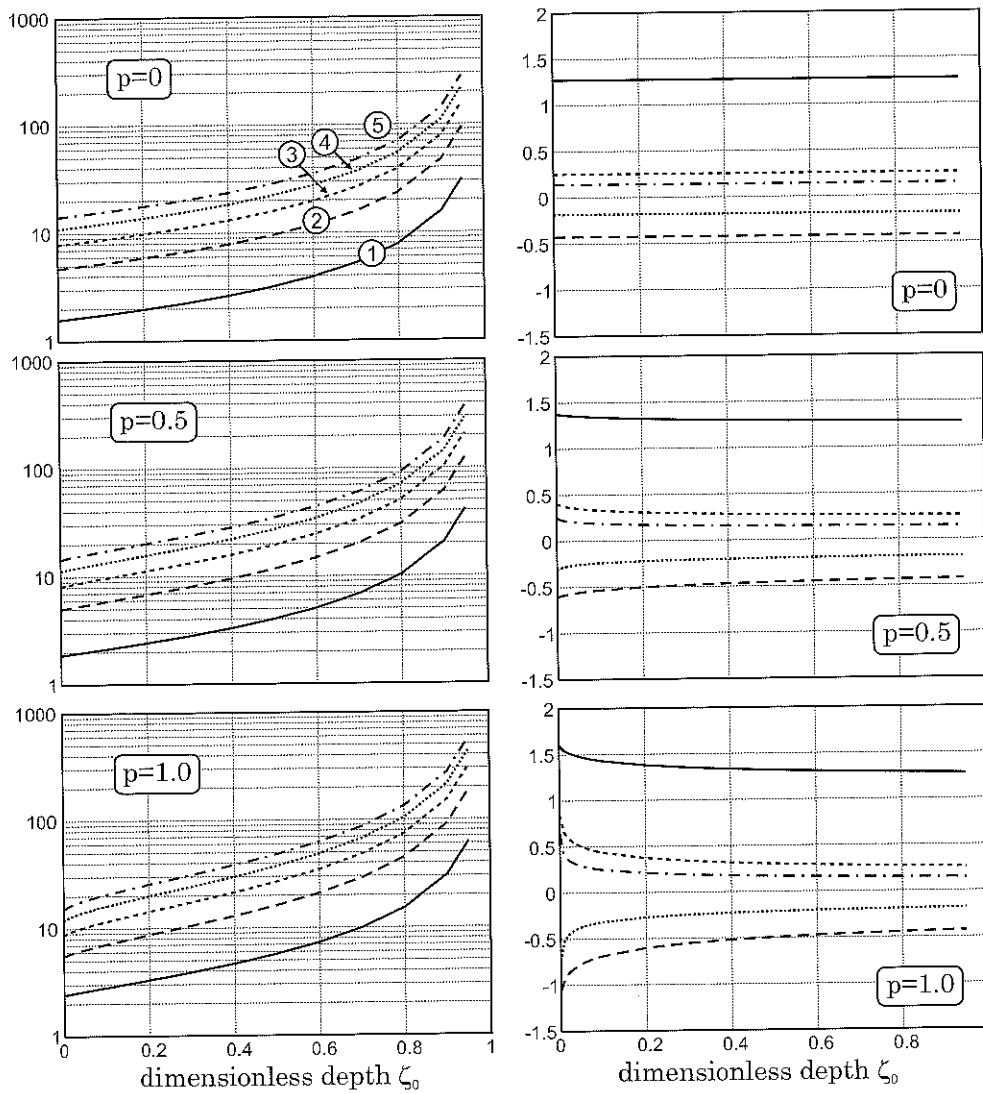


Fig. 2.38: Roots of the frequency equation (left) and mode participation factors (right) for the five first modes (numbered top-left) and three p -values: $p=0.00$ (top), $p=0.50$ (middle) and $p=1.00$ (bottom), from (Pecker, 2005).

2.12.4 Eigenfrequencies and mode participation factors

The solutions of Eqs (2.239) and (2.242) and the mode participation factors can be computed, once and for all, as a function of ζ_0 and p , the parameters defining the velocity profile (Pecker, 2005). The results are presented in Fig.2.38. For the special case $p = 0$,

corresponding to the homogeneous layer, given the relationships $J_{-\frac{1}{2}}(x) = \sqrt{\frac{2}{\pi}} \frac{\cos x}{\sqrt{x}}$ and $\Gamma(\frac{1}{2}) = \sqrt{\pi}$, the classical solution is retrieved from Eq. (26) to (28):

$$\lambda_i = (2i - 1) \frac{V_S}{4h} , \quad X(\zeta) = \cos(\lambda_i \zeta) = \cos\left(\frac{\omega_i z}{V_S}\right) \quad (2.245)$$

For $p \neq 0$, the eigenfrequencies (Fig.2.38, left) are found to be different from that of the homogeneous case and the mode participation factors are not constant with respect to dimensionless parameter ζ_0 .

2.13 Application 4: soil-structure interaction

2.13.1 Basic principles

Cone models were initially proposed by Meek and Wolf (1992) and allow the description of dynamic soil-structure interaction under a simplified form. This method considers a certain soil volume with a conical geometry to account for wave radiation in the soil. The schematic proposed in Fig.2.39 shows the basic principle of the method: a conical soil volume intersecting the base of the foundation is isolated and seismic wave propagation is then studied in this soil volume only (Pecker, 2008). It allows a simplified analysis of dynamic soil-structure interaction.

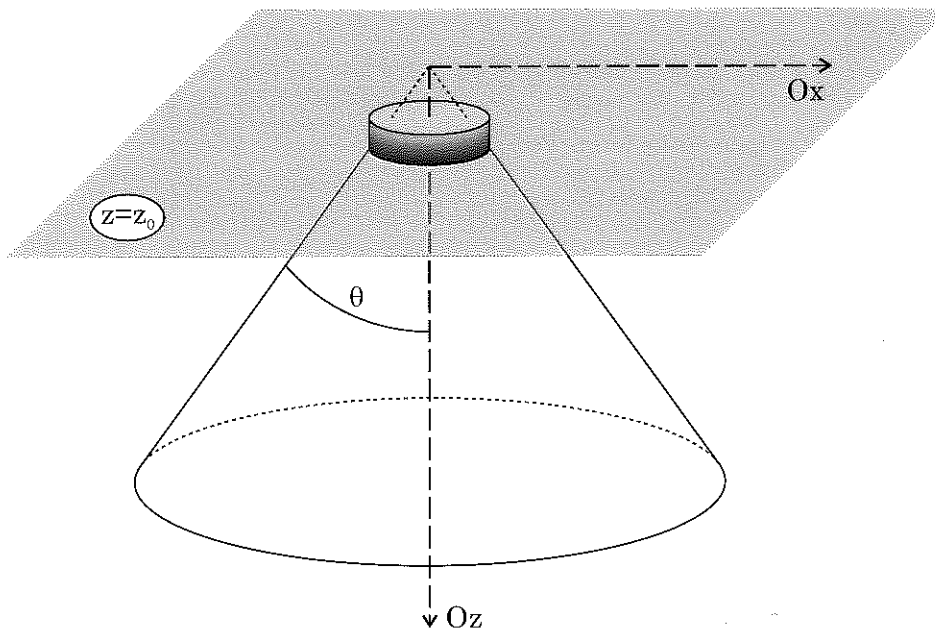


Fig. 2.39: Principle of cone models.

2.13.2 Equations of motion for the soil

One thus considers a conical soil column assumed as a one-dimensional bar having a variable cross-section with depth (area $S(z)$). The wavefield in the soil cone may then be derived from the 1D wave equations detailed in §2.5. For a purely horizontal motion, the following expression is obtained:

$$\frac{\partial V}{\partial z} = \rho S \frac{\partial^2 u_x}{\partial t^2} \quad (2.246)$$

where: $V = \mu S' \frac{\partial u_x}{\partial z}$ is the shear force (bending being neglected).

Furthermore:

$$S' = S(z) = \pi(z \tan \theta)^2 \quad (2.247)$$

hence:

$$\frac{\partial}{\partial z} \left(\mu S(z) \frac{\partial u_x}{\partial z} \right) = \rho S(z) \frac{\partial^2 u_x}{\partial t^2} \quad (2.248)$$

Since S depends on z , it leads to the following equation:

$$\frac{\partial S(z)}{\partial z} \frac{\partial u_x}{\partial z} + S(z) \frac{\partial^2 u_x}{\partial z^2} = \frac{\rho}{\mu} S(z) \frac{\partial^2 u_x}{\partial t^2} \quad (2.249)$$

the spatial derivative of the area of the cross-section is: $\frac{\partial S(z)}{\partial z} = 2\pi z \tan^2 \theta$, yielding:

$$\frac{2}{z} \frac{\partial u_x}{\partial z} + \frac{\partial^2 u_x}{\partial z^2} = \frac{\rho}{\mu} \frac{\partial^2 u_x}{\partial t^2} \quad (2.250)$$

The solution is then of the form (Pecker, 2008):

$$u_x(z, \omega) = \frac{u_x(z_0, \omega)}{z/z_0} \exp \left[-i \frac{\omega}{V_S} (z - z_0) \right] \exp(i\omega t) \quad (2.251)$$

The previous analysis performed for pure shear may be considered under a similar form for pure compression. The same expression holds for the vertical displacement u_z .

2.13.3 Case of a surface excitation

Considering a harmonic force $F(\omega)$ transmitted at the free surface by the foundation, the boundary condition fulfilled by the solution (2.251) reads:

$$F(\omega) = V(z_0) = -\mu S(z_0) \frac{\partial u_x}{\partial z} \quad (2.252)$$

$$\text{since: } \frac{\partial u_x}{\partial z} = -\frac{u_x(z_0, \omega)}{z^2/z_0} \exp \left[-i \frac{\omega}{V_S} (z - z_0) \right] \exp(i\omega t) \\ -i \frac{\omega}{V_S} \frac{u_x(z_0, \omega)}{z/z_0} \exp \left[-i \frac{\omega}{V_S} (z - z_0) \right] \exp(i\omega t)$$

$$\text{it implies: } \frac{\partial u_x(z_0, \omega)}{\partial z} = -u_x(z_0, \omega) \left(\frac{1}{z_0} + i \frac{\omega}{V_S} \right) \quad (2.253)$$

Hence:

$$F(\omega) = \mu \pi z_0 \tan^2 \theta \left(1 + i \frac{\omega z_0}{V_S} \right) u_x(z_0, \omega) \quad (2.254)$$

Considering that $R = z_0 \tan \theta$ and denoting $\bar{\omega} = \frac{\omega R}{c}$ and $K = \mu \pi R \tan \theta$, Eq.(2.254) becomes:

$$F(\omega) = K \left(1 + i \frac{\bar{\omega}}{\tan \theta} \right) u_x(z_0, \omega) \quad (2.255)$$

Using the static stiffness $K_{stat} = \frac{8\mu R}{2-\nu}$, θ may be identified:

$$K(\bar{\omega} = 0) = \mu \pi R \tan \theta = K_{stat}, \text{ that is: } \tan \theta = \frac{8}{(2-\nu)\pi} \quad (2.256)$$

The impedance of the foundation thus becomes:

$$K(\bar{\omega}) = K_{stat} \left[1 + i \frac{(2-\nu)\pi}{8} \bar{\omega} \right] \quad (2.257)$$

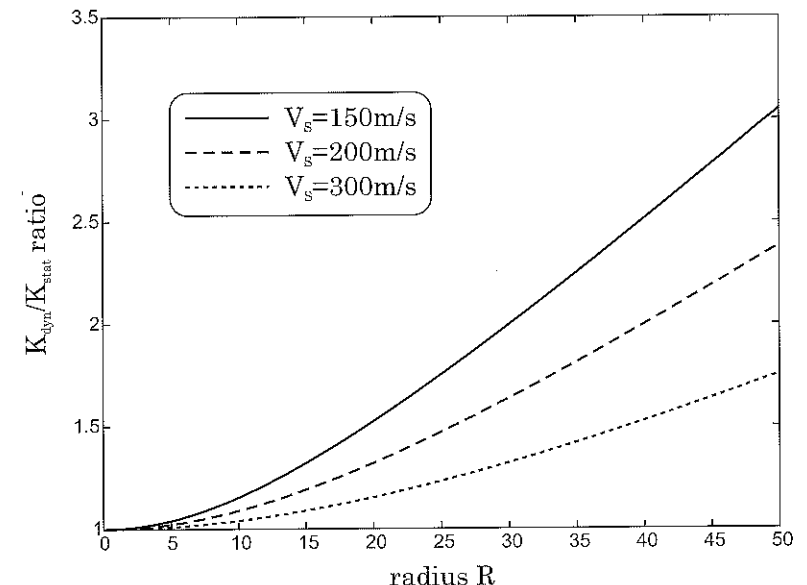


Fig. 2.40: K_{dyn}/K_{stat} ratio estimated through cone models as a function of the foundation radius R for various shear wave velocities: $V_s = 150$ m/s, $V_s = 200$ m/s and $V_s = 300$ m/s ($\nu = 0.25$, $\mu = 200$ MPa and $f = \frac{\omega}{2\pi} = 2$ Hz).

2.13.4 Influence of the wave velocity in the soil

To assess the influence of the foundation geometry as well as of the soil properties on the dynamic soil-structure interaction, the K_{dyn}/K_{stat} ratio, defined through Eq.(2.257), is plotted as a function of the foundation radius R for various values of the shear wave velocity in the soil V_S (Fig.2.40). The K_{dyn}/K_{stat} ratio is larger for lower shear wave velocities and larger foundation. The dynamic soil-structure interaction is thus stronger for large structures and soft soils.

2.14 Experimental estimation of damping

2.14.1 Various experimental methods

In addition to resonant column tests, several other methods are available for the experimental characterization of damping in soils. The main ones are discussed in this section.

Cyclic tests

For various types of experiments (triaxial tests, shear tests, hollow cylinder), the *energy loss per cycle* can be obtained from the hysteretic stress-strain curves for different loading and unloading cycles (Das, 1983; Kramer, 1996; Kokusho, 1980; Pecker, 1984). The *modulus* and the *damping* are estimated as functions of the strain level, the void ratio and, possibly, the number of cycles. As shown in Fig.2.22, the shear modulus decreases for an increasing strain level whereas the damping (related to the area of the loops) increases. At high frequencies and low strains, the direct measurement of the phase shift Φ is possible on rock specimens.

Resonant bar test

It is one of the most popular test for rock specimens. A rock bar is submitted to an harmonic excitation at one end, the displacement of the other end being measured to determine its eigenfrequency (Lucet, 1989).

The use of various bar lengths allows analyses at different frequencies corresponding to different modes. For strongly attenuating media ($Q < 3$), this method is no longer applicable since it is nearly impossible to reach resonance. Conversely, for weakly attenuating media, it is possible to consider a transient pulse and to analyze its decay.

Wave propagation based methods

Sonic or ultrasonic waves in rocks and soils. Ultrasonic tests are often used to study wave propagation in rocks. Several authors performed ultrasonic tests on soil specimens (Agarwal and Ishibashi, 1992; Blangy *et al.*, 1993; Koerner *et al.*, 1976; Stephenson, 1978). Various types of tests may be defined:

2.14 Experimental estimation of damping

- *acoustic emission*: measurement of acoustic signals emitted by the specimen during loading,
- *transmission tests*: excitation of the specimen by an ultrasonic source and measurement of the signal transmitted through the material.

Blangy *et al.* (1993) proposed some comparisons between various experimental approaches. The authors also analyze models proposed in various theories of propagation in porous media. Their main conclusions are the following:

- for *consolidated sands*: the shear modulus is proportional to porosity,
- for *loose sands*: there is an exponential dependence.

The ratio between the velocity of P -waves and that of S -waves is constant for clean sands ($V_P/V_S=1.5$) and depends on the porosity when the clay content increases. Furthermore, Blangy *et al.* (1993) define a *critical porosity* above which the specimen loses its shear resistance (grains in suspension).

Kolsky test. The Kolsky test (1949) is a dynamic experiment consisting in launching a mass directly on the specimen. As shown in Fig.2.41, the dynamic response is measured on the specimen itself, generally at two different points. The response of the material is analyzed from the observed propagation phenomena. The two measurements indeed characterize the way the perturbation propagates in the specimen. The Kolsky test may be considered for coherent and stiff materials (rocks, stiff clays, etc) and the excitation level should not be too large.

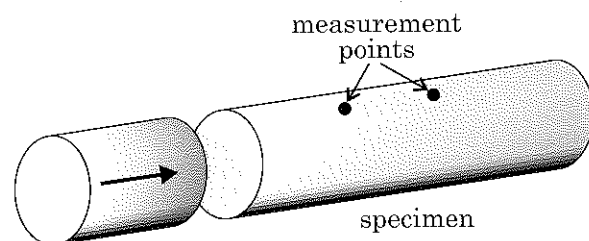


Fig. 2.41: Principle of the Kolsky test (Kolsky, 1949).

Propagation of plastic waves. Ultrasonic or Kolsky experiments involve low or moderate energy levels. Other types of tests at higher energy levels may be considered: it is for instance possible to generate plastic waves and to study their propagation in the material. Meunier (1974) performed such fast dynamic tests on clay specimens. Through fast image processing, such tests allow the analysis of the plastic wave propagation in the specimen.

All these tests may give a qualitative idea about the propagation phenomena occurring in the material: velocity, dispersion laws, etc. They generally do not allow a direct access to the behaviour of the material, whereas Hopkinson bar experiments do.

In situ methods

Many different surface or in-hole methods (reflection, refraction, logging) allow the analysis of in situ wave propagation. The excitation is generated by vibrating systems or by explosive sources. The wavelengths are such that the sampled soil depths are often heterogeneous.

These methods raise the need for sophisticated signal processing techniques to account for the velocity dispersion, the response spectrum of the sensors, etc. Since such techniques mainly involve 2D/3D wave propagation, they will be discussed in Chapter 3.

2.14.2 Methods for the estimation of attenuation

Rise time method

This method is based on the empirical relation proposed by Gladwin and Stacey (1974):

$$\tau = \tau_0 + C \int_0^T Q^{-1} dt \quad (2.258)$$

where τ is the rise time of the first peak (τ_0 at the source), T the travel time and C a constant depending on the source (for $Q > 10$).

This law is generally linear:

$$\tau = \tau_0 + \frac{CT}{Q} \quad (2.259)$$

On a $\tau = f(T)$ graph, the experimental rise times are obtained at different points (corresponding to different travel times T) and should theoretically allow the *determination of a line with a slope equal to C/Q* . The attenuation values can then be estimated from C (Bourbié *et al.*, 1987; Jongmans, 1991).

- *Advantages*: only the onset of the signal is considered; the effect of reflections is then reduced. This method is rather easy to use.
- *Drawbacks*: C and τ_0 depend on the source, but C also depends on the Q value. Furthermore, the method is not adapted to realistic seismic pulses (overestimation of Q) and unusable for low Q ($Q < 1$).

Spectral ratio method

For two measurement points M_1 and M_2 , assuming small variations of Q over the frequency range, the spectral amplitude ratio reads as follows:

$$\ln \frac{A_1(f, x_1)}{A_2(f, x_2)} = \frac{\pi}{QV} (x_2 - x_1) f + \ln \frac{G_1}{G_2} \quad (2.260)$$

The experimental measures give the $g(f) = \ln \frac{A_1}{A_2}$ curve which is nearly a line if the assumption is fulfilled. The slope of this line gives the attenuation value (Bourbié *et al.*, 1987).

- *Advantages*: This method is less sensitive to noise than the rise time method. Furthermore, it only requires two measurements.
- *Drawbacks*: to apply this method, a minimum signal duration is necessary. The influence of multiple reflections may be important. Q is generally underestimated (due to scattering effects).

"Propagation" methods.

Some authors (Badri and Mooney, 1987) use the *causal attenuation operator* due to Futtermann (1962). This method consists in simulating the propagation of a signal measured in purely elastic medium and to modify it by a filter satisfying the physical causality condition.

Q is then determined in order to optimize the agreement between the synthetic seismogram and the measured signal. Other synthesis methods may be considered.

- *Advantages*: the estimation of Q is independent of the source, the sensor and its environment.
- *Drawbacks*: the computations are generally carried out for plane waves, the actual geometrical attenuation must then be weak. The coupling with other methods is often necessary to determine the range of interest for Q .

2.14.3 Definitions of attenuation: synthesis

Various physical parameters allow the quantitative analysis of mechanical wave attenuation in solids: the *quality factor Q* , the *attenuation factor α* , the *logarithmic decrement δ* , the *phase difference $\Delta\Phi$* , etc (Aki and Richards, 1980; Bourbié *et al.*, 1987). These various parameters are compared hereafter:

- For a given loading/unloading cycle, the quality factor Q is defined by the following relation:

$$\frac{1}{Q(\omega)} = -\frac{\Delta W}{2\pi W} \quad (2.261)$$

where W is the *maximum elastic strain energy stored* in the considered volume and $-\Delta W$ is the energy lost in one cycle.

- the attenuation factor α : it corresponds to the *spatial amplitude decrease* of the wave (weakly attenuating medium). If the amplitude is known at two points, α may be written:

$$\alpha = \frac{1}{x_2 - x_1} \ln \left(\frac{A_1}{A_2} \right) \quad (2.262)$$

where $\Delta x = x_2 - x_1$ is the distance between both points.

- the logarithmic decrement δ : it corresponds to the *time amplitude decrease* for an harmonic wave (free vibrations) and it can be written:

$$\delta = \ln \left(\frac{A(t_n)}{A(t_{n+1})} \right) \quad (2.263)$$

- the phase difference Φ : given the complex modulus $M = M_R + iM_I$, the phase shift Φ between stresses and strains (forced harmonic vibrations) allows the characterization of attenuation:

$$\tan \Phi = \frac{M_I}{M_R} \quad (2.264)$$

- the width of the resonance peak Δf : on a resonance curve (see §2.10), the estimation of the peak band-width leads directly to the value of the quality factor:

$$\frac{1}{Q} = \frac{\Delta f}{f_r} \quad (2.265)$$

or to that of the damping ratio:

$$\xi = \frac{\Delta f}{2f_r} \quad (2.266)$$

Finally, all these parameters are related as follows:

$$\frac{1}{Q} = 2\xi = \frac{\alpha\Lambda}{\pi} = \frac{\delta}{\pi} = \frac{M_I}{M_R} = \tan \Phi = \frac{\Delta f}{f_r} \quad (2.267)$$

where Λ is the wavelength.

2.14.4 Variations of attenuation

This section gives several empirical results on the variations of attenuation for soils and rocks.

Influence of the strain amplitude

From the experiments performed by Hardin and Drnevich (1972a,b) in the laboratory on sand, at frequencies $f > 0.1\text{Hz}$, or Stoll (1979), at frequencies ranging from $f=10$ to $f=500\text{ Hz}$, the *attenuation strongly increases with the strain amplitude*. Saxena and Reddy (1989) even proposed the following empirical law:

$$Q^{-1} = A\varepsilon^{0.33} \quad (2.268)$$

where ε is the strain amplitude. This *increase is lower for a large confining pressure*.

Mavko (1979) and Stewart *et al.* (1983) showed experimentally and theoretically that, above a strain level of 10^{-6} or 10^{-5} , the *attenuation depends on the strain amplitude*. Thus, the attenuation increases rapidly with the strain amplitude.

Influence of the confining pressure

The *attenuation decreases for an increasing confining pressure*. Saxena and Reddy (1989) proposed the following empirical relation for soils:

$$D = KP^{-0.13}\varepsilon^{0.33} \quad (2.269)$$

where D is the attenuation and P is the confining pressure.

From the theoretical relation proposed by Stewart *et al.* (1983) for rocks, the attenuation $D = Q^{-1}$ can be written as follows:

$$Q^{-1} = \frac{k\zeta\varepsilon}{P^{4/3}} \quad (2.270)$$

where ζ is the density of cracks in the rock and k a coefficient inversely proportional to the contact radius a and the friction coefficient f .

From these relations, it is obvious that *Q^{-1} decreases when P increases* and that the variations are very different for soils and rocks. These laws will be compared in Chapter 4 to investigate seismic wave attenuation in centrifuged soils.

Influence of frequency

Most laboratory experiments on various types of soils and rocks show that the *attenuation is strongly dependent on frequency*. From the results obtained by Stoll on sand (1979) and Murphy on sandstone (Bourbié *et al.*, 1987), the *attenuation increases with frequency*.

Nevertheless, for soils in the frequency range of seismic waves, the attenuation slightly depends on frequency. From the results of Stoll (1979), the attenuation curves at low frequencies are very close.

Conversely, from in situ experiments on salt (1 to 200Hz), MacCartor and Wortman (1990) showed that the *attenuation decreases for increasing frequencies*.

2.14.5 Characterization of the various approaches

A synthesis of the various parameters characterizing each experimental method is proposed in Table 2.1. Seismic methods are also considered but are mainly dedicated to 2D/3D in situ characterization. The detailed analysis of such methods is proposed in Chapter 3.

2.14.6 Comparison of the governing parameters

To compare the practical problems and the investigation methods presented previously, three parameters are considered:

Table 2.1: Main parameters characterizing the various approaches.

Type of approach	Main mechanical parameters characterizing the approach		
cyclic tests	frequency 10 ⁻³ to 10 ⁻¹ Hz	strain from 10 ⁻⁵ to 10 ⁻²	dimensions cm, dm
resonant column	frequency from 10 to 500 Hz	strain 10 ⁻⁴ to 10 ⁻²	dimensions cm, dm
Hopkinson bars	strain rate from 50 to 1000 s ⁻¹	strain from 0.05 to 0.2 m/m	dimensions cm
seismic methods	frequency 1 to 100 Hz	strain 10 ⁻⁶ to 10 ⁻⁵ m/m	dimensions dam, hm, km
ultrasonic tests	frequency 100 kHz to 1 MHz	strain 10 ⁻⁷	dimensions cm, dm
plastic waves	strain rate 100 to 5000 s ⁻¹	strain 0.1 to 2.0 m/m	dimensions dm

- the frequency f ,
- the ratio between the wavelength and the characteristic dimension of the problem considered Λ/l_{char} ,
- the strain amplitude ε_0 .

The Λ/l_{char} ratio allows to distinguish situations where the propagation phenomena are dominating from cases where the analysis of behaviour may be directly performed:

- if the Λ/l_{char} ratio is large: the wavelength is large when compared to the characteristic dimensions of the problem. The *propagation phenomena are negligible*,
- if the Λ/l_{char} ratio is small: the dimensions of the problem are large when compared to the wavelength. The *propagation phenomena dominate*.

Figure 2.42 displays a 3D diagram showing the ranges of the following three parameters for dynamic experiments: *frequency*, Λ/l_{char} ratio and *strain*. The comparison between cyclic approaches and ultrasonic tests (Fig.2.42) clearly shows that:

- for *cyclic experiments* (top right), the frequencies are very low, the strain amplitudes are rather large and the Λ/l_{char} ratio is very high: the *propagation phenomena are negligible*,
- for *ultrasonic tests* (bottom left), the frequencies are very high, the strain amplitudes are extremely small and the Λ/l_{char} ratio is very small: the *propagation phenomena dominate*.

2.14 Experimental estimation of damping

The schematic proposed in Fig.2.42 allows a classification of the various approaches. Some other governing parameters may also be chosen, such as the *strain rate*. As explained previously, two types of approaches obviously appear in this classification. It is possible to directly analyze the *behaviour of the material* or to investigate the *propagation phenomena* generated in the material. These two types of approaches are discussed in this book:

- as discussed in this Chapter: the analysis of the soil behaviour under fast dynamic loadings is possible on a dynamic Hopkinson bar device,
- as it will be shown later (Chapter 3), propagation phenomena in soils may also be investigated through centrifuge experiments or analysis of surface waves in the field.

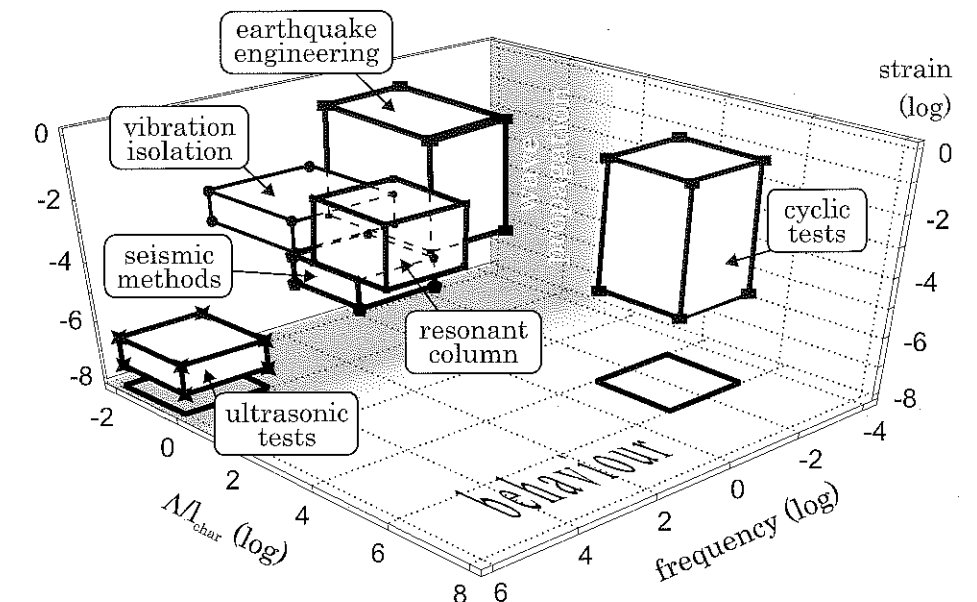


Fig. 2.42: Comparison of the characteristic parameters for various experimental approaches (Semblat *et al.*, 1999).

Chapter 3

2D/3D-wave propagation

Application to the dynamic characterization of soils

3.1 Introduction

The analysis of vibrations in beams, proposed in Chapter 2, allows to consider various wave types in 1D structures. Wave propagation in three-dimensional elastic solids corresponds to cases in which one dimension is not significantly larger than the others. It is often the case for wave propagation in soils: seismic wave propagation, impact due to explosions or dynamic compaction, vibrations due to traffic or pile driving.

All these phenomena have a common feature: their sources, located on the free-surface or at-depth, generate wavefields propagating in the soil layers. The main objective of this chapter is to analyze wave propagation considering 2D/3D heterogeneities or obstacles. Even if the soil has a dissipative (sometimes) nonlinear behaviour¹, we shall mainly consider linear elasticity and small strains. As evidenced in Chapter 2, the solutions for 2D/3D viscoelastic media may be easily derived from the elastic ones.

3.2 Dynamic equilibrium of a continuous medium

The first stage consists in writing the equilibrium equations starting from the *Principle of Virtual Work*. The equilibrium equations are then combined with the constitutive law of the medium in order to obtain expressions involving the displacement vector $\underline{u}(M)$ at every point M in the medium.

¹Several nonlinear models are discussed, or may be found through the citations, in §2.9

3.2.1 Equilibrium equation - principle of virtual work

Virtual rate of work by external forces

External forces are represented by a volumic density of force \underline{f} in the domain Ω and a surface density of force \underline{T}^d (Fig.3.1) on its boundary $\partial\Omega$. The rate of work by these forces considering a virtual velocity field $\hat{\underline{U}}(\underline{x})$, where \underline{x} denotes the position of a point M , writes as follows:

$$\mathcal{P}_e(\hat{\underline{U}}) = \int_{\Omega} \underline{f}(\underline{x}, t) \cdot \hat{\underline{U}}(\underline{x}) d\Omega + \int_{\partial\Omega} \underline{T}^d(\underline{x}, t) \cdot \hat{\underline{U}}(\underline{x}) da \quad (3.1)$$

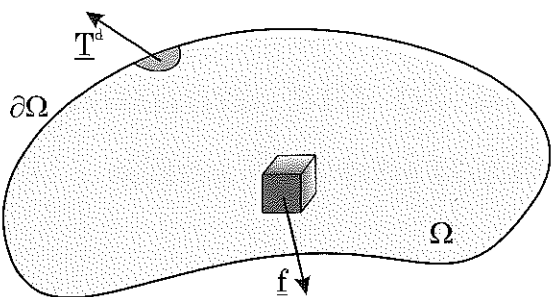


Fig. 3.1: External forces existing in domain Ω .

Virtual rate of work by internal forces

Considering that the rate of work by internal forces only depends on the virtual velocity field $\hat{\underline{U}}$ and its first gradient (Salençon, 2001), it is possible to show that:

$$\mathcal{P}_i(\hat{\underline{U}}) = - \int_{\Omega} \underline{\sigma} : \hat{\underline{d}}(\hat{\underline{U}}) d\Omega = - \int_{\Omega} \sum_{i,j} \sigma_{ij} \hat{d}_{ij}(\hat{\underline{U}}) d\Omega \quad (3.2)$$

in which $\underline{\sigma}$ is the Cauchy stress tensor, $\hat{\underline{d}}(\hat{\underline{U}}) = \frac{1}{2} \left({}^t \underline{\nabla} \hat{\underline{U}} + \underline{\nabla} \hat{\underline{U}} \right)$ is the strain rate tensor, $\underline{\nabla} \hat{\underline{U}}$ is the gradient of the virtual velocity field $\hat{\underline{U}}$ (see appendix A), that is in components: $\hat{d}_{ij}(\hat{\underline{U}}) = \frac{1}{2} \left(\frac{\partial \hat{U}_i}{\partial x_j} + \frac{\partial \hat{U}_j}{\partial x_i} \right)$.

Virtual rate of work by quantities of acceleration

The rate of work by quantities of acceleration is given by (Salençon, 2001):

$$\mathcal{A}(\hat{\underline{U}}) = \int_{\Omega} \rho \underline{a}(\underline{x}, t) \cdot \hat{\underline{U}}(\underline{x}) d\Omega \quad (3.3)$$

where ρ is the density and \underline{a} the acceleration vector.

3.2 Dynamic equilibrium of a continuous medium

Equilibrium equation

The equilibrium equation is obtained by expressing that the sum of the rate of work by external forces and the rate of work by internal forces is equal to the rate of work by quantities of acceleration (Salençon, 2001), that is:

$$- \int_{\Omega} \underline{\sigma} : \hat{\underline{d}}(\hat{\underline{U}}) d\Omega + \int_{\Omega} \underline{f} \cdot \hat{\underline{U}} d\Omega + \int_{\partial\Omega} \underline{T}^d \cdot \hat{\underline{U}} da = \int_{\Omega} \rho \underline{a} \cdot \hat{\underline{U}} d\Omega \quad (3.4)$$

Taking into account the symmetry of the stress tensor, the first term becomes:

$$\int_{\Omega} \underline{\sigma} : \hat{\underline{d}}(\hat{\underline{U}}) d\Omega = \int_{\Omega} \underline{\sigma} : \underline{\nabla} \hat{\underline{U}} d\Omega \quad (3.5)$$

and integrating by parts:

$$- \int_{\Omega} \underline{\sigma} : \hat{\underline{d}}(\hat{\underline{U}}) d\Omega = \int_{\Omega} (\underline{\nabla} \cdot \underline{\sigma}) \cdot \hat{\underline{U}} d\Omega - \int_{\partial\Omega} (\underline{\sigma} \cdot \underline{n}) \cdot \hat{\underline{U}} da \quad (3.6)$$

Introducing Eq.(3.6) in Eq.(3.4) and writing the equation for every virtual velocity field $\hat{\underline{U}}$, we obtain the equilibrium equations:

$$\underline{\nabla} \cdot \underline{\sigma} + \underline{f} = \rho \underline{a} \quad \text{in } \Omega \quad (3.7)$$

$$\underline{\sigma} \cdot \underline{n} = \underline{T}^d \quad \text{on } \partial\Omega \quad (3.8)$$

where $\underline{\sigma}$ is the Cauchy stress tensor, \underline{f} the body forces and \underline{T}^d the surface forces.

3.2.2 Constitutive equation

The isotropic linear elastic constitutive law in small strains is:

$$\underline{\sigma} = \lambda (\text{tr} \underline{\varepsilon}) \underline{\mathbb{I}} + 2\mu \underline{\varepsilon} \quad (3.9)$$

where λ and μ denote the Lamé constants, $\underline{\mathbb{I}}$ the unitary 2nd order tensor (i.e. its components are δ_{ij}), and $\underline{\varepsilon}$ the strain tensor related to the displacement field \underline{u} by:

$$\underline{\varepsilon} = \frac{1}{2} \left({}^t \underline{\nabla} \underline{u} + \underline{\nabla} \underline{u} \right) \quad (3.10)$$

that is, in terms of components:

$$\varepsilon_{ij} = \frac{1}{2} \left(\frac{\partial u_i}{\partial x_j} + \frac{\partial u_j}{\partial x_i} \right) \quad (3.11)$$

In Eq.(3.9), the term $\text{tr} \underline{\varepsilon}$ corresponds to the volumic strain:

$$\text{tr} \underline{\varepsilon} = \sum_{i=1}^3 \varepsilon_{ii} = \sum_{i=1}^3 \frac{\partial u_i}{\partial x_i} \quad (3.12)$$

The Lamé constants, λ and μ , fully define the isotropic linear elastic behaviour of the material. In Table 3.1, we recall the relations between λ , μ , the Young's modulus E , the Poisson's ratio ν and the bulk modulus K .

Table 3.1: Relationships between the parameters defining the isotropic linear elastic behaviour of the material.

E	ν	λ	$\mu = G$	K
E, ν	E	ν	$\frac{\nu E}{(1+\nu)(1-2\nu)}$	$\frac{E}{2(1+\nu)}$
λ, μ	$\frac{\mu(3\lambda+2\mu)}{\lambda+\mu}$	$\frac{\lambda}{2(\lambda+\mu)}$	λ	μ

3.2.3 Equilibrium equations in terms of displacements

Including the constitutive law (Eq.(3.9)) into the equilibrium equation (3.7), and taking into account the definition of the strain tensor (Eq.(3.10)), we obtain the equilibrium equation expressed as a function of the displacement field \underline{u} :

$$(\lambda + \mu) [\nabla(\nabla \cdot \underline{u})] + \mu \Delta \underline{u} = \rho \frac{\partial^2 \underline{u}}{\partial t^2} - \underline{f} \quad (3.13)$$

where the operators ∇ and Δ represent the gradient and the Laplacian respectively (see appendix A).

In terms of components, Eq.(3.13) yields:

$$(\lambda + \mu) \frac{\partial}{\partial x_i} \left(\sum_{j=1}^3 \frac{\partial u_j}{\partial x_j} \right) + \mu \sum_{j=1}^3 \frac{\partial^2 u_i}{\partial x_j^2} = \rho \frac{\partial^2 u_i}{\partial t^2} - f_i ; \quad i = 1, 3 \quad (3.14)$$

3.2.4 Decomposition of the displacement field

Considering Poisson's theorem, it is always possible to decompose a vectorial field \underline{u} as the sum of a gradient of a scalar potential ϕ and the rotational of a vectorial potential ψ :

$$\underline{u} = \nabla(\phi) + \nabla \wedge \underline{\psi} \quad (3.15)$$

that is, in terms of components:

$$u_i = \frac{\partial \phi}{\partial x_i} + \frac{\partial \psi_k}{\partial x_j} - \frac{\partial \psi_j}{\partial x_k} , \quad \text{circular permutation for } i, j, k \quad (3.16)$$

Examining Eq.(3.15) and starting from the three components of vector \underline{u} , we introduce four components by the decomposition into potentials: the scalar potential and the three components of the vectorial potential. It is then necessary to specify an additional condition. Such a condition is generally obtained by writing that the divergence of the vectorial potential $\underline{\psi}$ is zero:

$$\nabla \cdot \underline{\psi} = 0 \quad (3.17)$$

It means that the vectorial potential $\underline{\psi}$ does not lead to any volume change.

3.2.5 Uncoupled wave equations

Including Eq.(3.15) into the equilibrium equation (Eq.(3.13)) and taking into account Eq.(3.17), we obtain the following equations for the potentials:

$$\Delta(\phi) = \frac{1}{V_P^2} \frac{\partial^2 \phi}{\partial t^2} - F \quad (3.18)$$

$$\Delta(\underline{\psi}) = \frac{1}{V_S^2} \frac{\partial^2 \psi}{\partial t^2} - G \quad (3.19)$$

in which we consider the notations:

$$V_P = \sqrt{\frac{\lambda + 2\mu}{\rho}} \quad \text{and} \quad V_S = \sqrt{\frac{\mu}{\rho}} \quad (3.20)$$

and we apply Poisson's theorem to f :

$$f = V_P^2 \nabla(F) + V_S^2 \nabla \wedge G \quad (3.21)$$

In terms of components, Eqs (3.18) and (3.19) may be written:

$$\sum_{j=1}^3 \frac{\partial^2 \phi}{\partial x_j^2} = \frac{1}{V_P^2} \frac{\partial^2 \phi}{\partial t^2} - F \quad (3.22)$$

$$\sum_{j=1}^3 \frac{\partial^2 \psi_i}{\partial x_j^2} = \frac{1}{V_S^2} \frac{\partial^2 \psi_i}{\partial t^2} - G_i ; \quad i = 1, 3 \quad (3.23)$$

3.2.6 Body waves

Omitting the boundary conditions, Eqs (3.18) and (3.19) govern the propagation of two different waves propagating at velocities V_P and V_S . These waves are called *body waves* and are of two types:

- equation (3.18) governs the propagation of the *pressure wave* which is also called a *P-wave*,
- equation (3.19) governs the propagation of the *shear wave* which is also called an *S-wave*.

The polarization of these waves is illustrated in the following section for plane waves.

The comparison of Eqs (3.20) shows that the *P*-wave velocity V_P is larger than the *S*-wave velocity V_S . The V_P/V_S ratio can be easily expressed as a function of Poisson's ratio:

$$\frac{V_P}{V_S} = \sqrt{\frac{2-2\nu}{1-2\nu}} \quad (3.24)$$

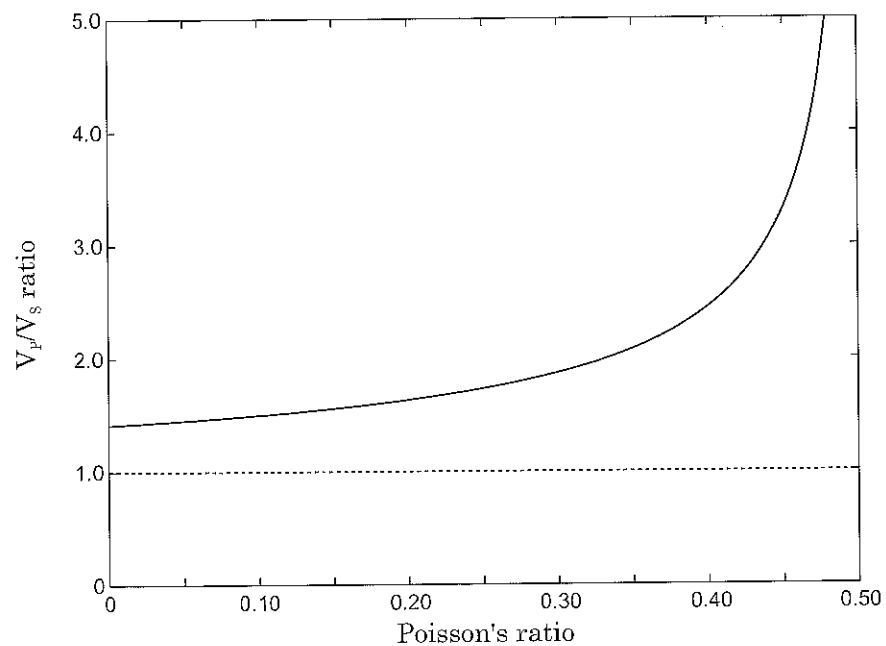


Fig. 3.2: Ratio between the P -wave velocity and the S -wave velocity.

Figure 3.2 displays the variations of the ratio between the P -wave velocity and the S -wave velocity. The P -wave velocity is always larger than the S -wave velocity and the ratio fastly increases for Poisson's ratios above 0.4.

Table 3.2 gives several values of the V_P and V_S velocities for various types of soils (soft, stiff, intermediate).

Table 3.2: Typical values of the P and S -wave velocities for different types of soils.

Material	V_S (m/s)	V_P (m/s)
Clay	100-200	1500
Sand above watertable	200-400	400-800
Sand below watertable	200-400	1500-1700
Marl	400-600	1500-2000
Rock	> 800	> 2 000

3.2.7 Wave propagation in anisotropic media

In the case of linear elasticity in small strains, the constitutive law has the following form:

$$\underline{\sigma} = \underline{\underline{C}} : \underline{\underline{\varepsilon}} \quad (3.25)$$

where $\underline{\sigma}$ is the stress tensor, $\underline{\underline{C}}$ is the fourth order elasticity tensor and $\underline{\underline{\varepsilon}}$ is the strain tensor.

In the isotropic case, the elasticity tensor leads to the same expression as in Eq.(3.9) since it can be expressed as:

$$C_{ijkl} = \lambda \delta_{ij} \delta_{kl} + \mu (\delta_{ik} \delta_{jl} + \delta_{il} \delta_{jk}) \quad (3.26)$$

For an anisotropic medium, $\underline{\underline{C}}$ may have up to 21 independent components. Geological media are often considered as *orthotropic* media (also called *transversely anisotropic* media). Assuming the orthotropy axis as e_z , all the directions in the planes perpendicular to e_z are then equivalent. Among the 21 components of the elasticity tensor, only five are independent: $C_{xxxx} = C_{yyyy}$, C_{zzzz} , C_{xxyy} , $C_{yyzz} = C_{xxzz}$ and $C_{xzxz} = C_{yzzy}$ (Bourbié *et al.*, 1987). All other components are zero except C_{xyxy} which is written:

$$C_{xyxy} = \frac{1}{2} (C_{xxxx} - C_{xxyy}) \quad (3.27)$$

We finally obtain four independent velocity values (Bourbié *et al.*, 1987):

- for P -waves:

$$\begin{cases} V_P = \sqrt{\frac{C_{zzzz}}{\rho}} \\ V_P = \sqrt{\frac{C_{xxxx}}{\rho}} = \sqrt{\frac{C_{yyyy}}{\rho}} \end{cases} \quad (3.28)$$

- for S -waves:

$$\begin{cases} V_S = \sqrt{\frac{C_{yyzz}}{\rho}} = \sqrt{\frac{C_{xzxz}}{\rho}} \\ V_S = \sqrt{\frac{C_{xyxy}}{\rho}} \end{cases} \quad (3.29)$$

In the case of anisotropic media, the wave velocity is thus depending of the direction of propagation. Its characterization may be performed by using field measurements (Aki and Richards, 1980) or laboratory tests (Nguyen *et al.*, 2008).

3.3 Wave propagation in unbounded media

3.3.1 Wave equations for plane waves

Assuming the propagation of *P* and *S* waves to take place along one direction only, denoted \underline{e}_1 , the variables involved in the wave equations only depend on x_1 . Equation (3.15) is then reduced to:

$$\underline{u} = \frac{\partial \phi}{\partial x_1} \underline{e}_1 - \frac{\partial \psi_3}{\partial x_1} \underline{e}_2 + \frac{\partial \psi_2}{\partial x_1} \underline{e}_3 \quad (3.30)$$

that is, in terms of displacements (Eq. (3.13)):

$$\frac{\partial^2 u_1}{\partial x_1^2} = \frac{1}{V_P^2} \frac{\partial^2 u_1}{\partial t^2} \quad (3.31)$$

$$\text{and } \frac{\partial^2 u_j}{\partial x_1^2} = \frac{1}{V_S^2} \frac{\partial^2 u_j}{\partial t^2} ; \quad j = 2, 3 \quad (3.32)$$

This situation of one-dimensional propagation is also encountered in the case of curvilinear media for which the geometry of the medium constrains the direction of propagation (see Chapter 2). Equation (3.31) then represents the equation of longitudinal vibrations of a beam in which we considered $E = \rho V_P^2$ and equations (3.32) that of the transverse vibrations of beams in which we have taken $\mu S' = \rho S V_S^2$ and neglected the bending strains when compared to shear strains ($ES \gg \mu S'$).

We can also find these wave types in the case of a two or three-dimensional medium. For instance, in the case of an isotropic infinite solid, a point source will generate a spherical wavefield because of the symmetry of the problem. Far away from the source, the wavefront may be considered, due to its expansion, as a plane (the plane tangent to the wavefront of the spherical wave, Fig.3.3).

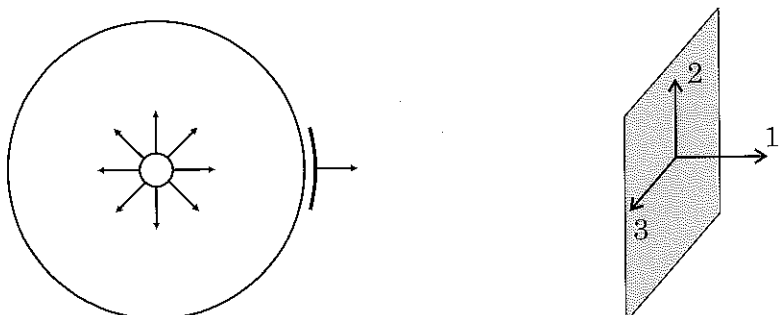


Fig. 3.3: Nearly plane waves generated at large distances from a spherical source.

In the case of a pure plane wave, the pressure wave governed by Eq.(3.31) generates a vibration oriented along the direction of propagation (Fig.3.4, top). The pressure wave is thus polarized along the direction of propagation. Conversely, the shear wave governed by Eq.(3.32) generates a vibration in the plane perpendicular to the direction of propagation (Fig.3.4, bottom). The shear wave is thus polarized perpendicularly to the direction of propagation (tangent plane). Two types of shear waves, having the same velocity V_S , may be distinguished:

- *SV-waves* polarized perpendicularly to the direction of propagation but with the induced motion located in a vertical plane,
- *SH-waves* polarized perpendicularly to the direction of propagation but with the induced motion located in a horizontal plane (for horizontally propagating waves).

As it will be evidenced later, for general 3D cases involving oblique incidences, the polarization of *SV-waves* is not vertical but located in a vertical plane including the direction of propagation (i.e. direction of polarization of *P-waves*). Similarly, the polarization of *SH-waves* is not horizontal but located in a plane which is perpendicular to the (oblique) direction of propagation.

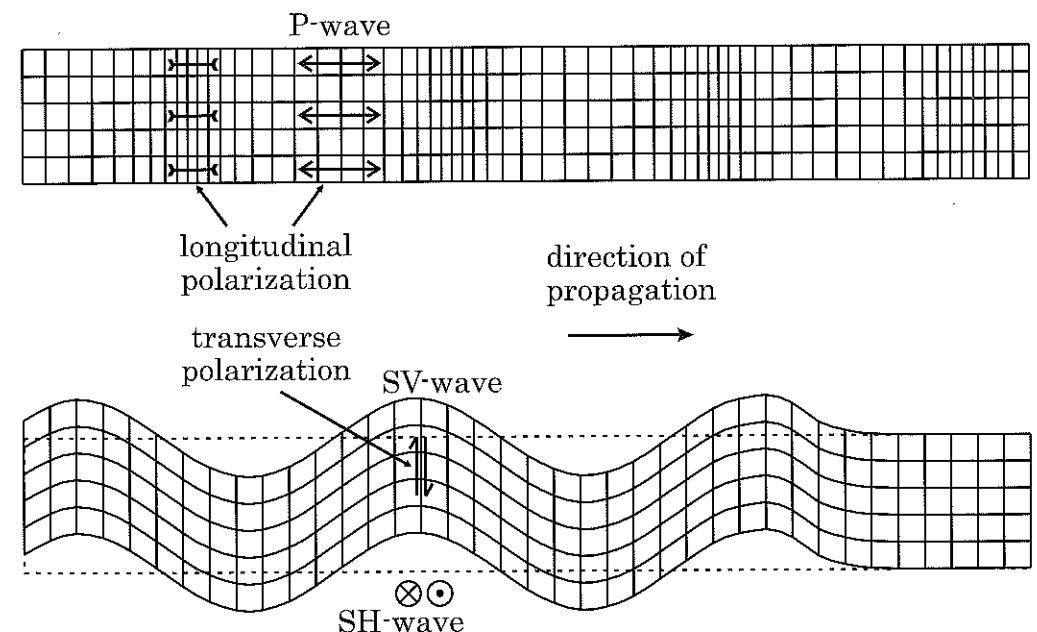


Fig. 3.4: Plane pressure waves (top) and shear waves (bottom).

3.3.2 Plane monochromatic waves

Solutions in terms of potentials

The expression of potentials ϕ and ψ for a plane monochromatic wave at frequency ω , is obtained as the solution of the equations of propagation (3.18) and (3.19). We look for solutions of the form $\mathcal{H}(M)e^{-i\omega t}$, point M belonging to a plane of fixed direction². We thus obtain:

$$\phi = A \exp \left[\frac{i\omega}{V_P} (l_x x + l_y y + l_z z - V_P t) \right] \quad (3.33)$$

$$\psi = B \exp \left[\frac{i\omega}{V_S} (l_x x + l_y y + l_z z - V_S t) \right] \quad (3.34)$$

where \underline{l} is the normalized wave vector defined, from the wave vector \underline{k} , by:

$$\underline{l} = \frac{\underline{k}^{(j)}}{\|\underline{k}^{(j)}\|} \quad \text{with: } \underline{k}^{(j)} = \frac{\omega}{V_j} \underline{l} \quad (j = P, S) \quad (3.35)$$

and Eqs (3.33) and (3.34) involve the following product:

$$\underline{k}^{(j)} \cdot \underline{x} = \frac{\omega}{V_j} \underline{l} \cdot \underline{x} = \frac{\omega}{V_j} (l_x x + l_y y + l_z z) \quad (j = P, S) \quad (3.36)$$

When the components of vector \underline{l} are all real, it corresponds to the vector of the cosine directions of the propagation axis for the *body waves* with velocity V_P and V_S . It should be noticed that the polarization of the *S*-wave along \underline{B} corresponds to the plane perpendicular to \underline{l} (i.e. $\underline{l} \cdot \underline{B} = 0$).

When a component of \underline{l} , for instance l_z , is purely imaginary and the other components are real, the solution potentials (Eqs (3.33) and (3.34)) thus represent a wave propagating in the $(x - y)$ plane with an exponentially decaying amplitude along z . Such waves are called *surface waves* and will be studied later in this chapter (§3.5.2).

Solutions in terms of displacements

The displacements associated to the potentials ϕ and ψ are derived from Eq.(3.15). Denoting:

$$f_P = \exp \left[\frac{i\omega}{V_P} (l_x x + l_y y + l_z z - V_P t) \right] \quad (3.37)$$

$$\text{and } f_S = \exp \left[\frac{i\omega}{V_S} (l_x x + l_y y + l_z z - V_S t) \right] \quad (3.38)$$

²As already discussed in Chapter 2, solutions of the form $u(s - ct)$ are equivalent to solutions of the form $u(ct - s)$. However, considering solutions of the form $u(s - ct)$ leads to spectral components estimated by inverse Fourier transform instead of direct Fourier transforms for solutions of the form $u(ct - s)$.

They are expressed as:

$$\underline{u} = -\frac{i\omega}{V_P} f_P \underline{A} \underline{l} + \frac{i\omega}{V_S} f_S \underline{B} \wedge \underline{l} \quad (3.39)$$

Under this form, we notice the *P*-wave, with velocity V_P , leading to a displacement along the direction of propagation \underline{l} ; the *S*-wave with velocity V_S leading to a displacement in the plane perpendicular to the direction of propagation (Fig.3.4). The latter motion may be decomposed into a component located in a horizontal plane and a component in a vertical plane. Denoting A_{SH} and A_{SV} the amplitudes of the related displacements, Eq.(3.39) yields:

$$u_{SH} = A_{SH} f_S = \frac{i\omega}{V_S} \frac{B_z}{\sqrt{l_x^2 + l_y^2}} f_S \quad (3.40)$$

$$u_{SV} = A_{SV} f_S = \frac{i\omega}{V_S} \frac{l_x B_y - l_y B_x}{\sqrt{l_x^2 + l_y^2}} f_S \quad (3.41)$$

Proof. The displacement vector for transverse waves is given by the second term of Eq.(3.39). For *SH*-waves, we look for a horizontal component of \underline{U} .

Denoting \underline{t} the horizontal unit vector in the plane perpendicular to \underline{l} and $(\underline{e}_1, \underline{e}_2, \underline{e}_3)$ a Cartesian orthonormal frame, we get the following relations:

$$\underline{t} \cdot \underline{e}_3 = 0 ; \quad \underline{t} \cdot \underline{l} = 0 ; \quad \|\underline{l}\| = 1 \quad (3.42)$$

Neglecting the multiplicative scalar terms, the horizontal component of \underline{U} writes:

$$\underline{A} = (\underline{B} \wedge \underline{l}) \cdot \underline{t} \quad (3.43)$$

thus, developing and taking into account the relations giving t_1 and t_2 obtained from Eq.(3.42):

$$t_1 = \frac{-l_y}{\sqrt{l_x^2 + l_y^2}}, \quad t_2 = \frac{-l_x}{\sqrt{l_x^2 + l_y^2}} \quad (3.44)$$

$$\underline{A} = \frac{-(B_y l_z - B_z l_y) l_y + (B_z l_x - B_x l_z) l_x}{\sqrt{l_x^2 + l_y^2}} \quad (3.45)$$

Considering that $\underline{l} \cdot \underline{B} = 0$, we have $-B_y l_z l_y - B_x l_z l_x = B_z l_z^2$ and including in Eq.(3.45), the following relation is derived:

$$\underline{A} = \frac{B_z}{\sqrt{l_x^2 + l_y^2}} \quad (3.46)$$

from which we obtain expression (3.40). The same type of proof stands for the calculation of A_{SV} by choosing to project \underline{U} on the vector \underline{n} defined by $\underline{n} = \underline{l} \wedge \underline{t}$.

Keeping the general meaning of the previous relations, it is possible to choose the global coordinate system in order to have the direction of propagation included in the $(x - z)$ plane. Thus, it comes that $l_y = 0$ (Fig.3.5) and that relations (3.39) and (3.40) can be written:

$$\begin{cases} u_x &= A_P f_P l_x + A_{SV} f_S l_z \\ u_y &= A_{SH} f_S \\ u_z &= A_P f_P l_z - A_{SV} f_S l_x \end{cases} \quad (3.47)$$

Equations (3.47) show that, in the case of plane waves, the displacement along Oy is uncoupled from displacements along Ox and Oz . It is only due to the propagation of shear waves with horizontal polarization, which are called SH -waves. The displacements along directions x and z result from the propagation of P -waves as well as S -waves with vertical polarization, which are called SV -waves (Fig.3.5). Furthermore, if the direction of propagation is vertical, parallel to Oz ($l_x = l_y = 0$, $l_z = 1$), the problem becomes one-dimensional: each component of the motion is uncoupled from the others:

$$\begin{cases} u_x &= A_{SV}f_S \\ u_y &= A_{SH}f_S \\ u_z &= A_Pf_P \end{cases} \quad (3.48)$$

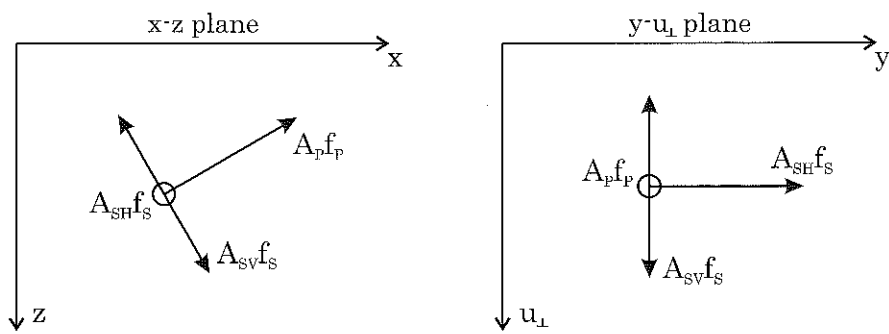


Fig. 3.5: Polarization of P , SV and SH -waves displayed in the $(x - z)$ and $(y - u_\perp)$ planes.

3.3.3 Reflection-refraction of plane waves at an interface

General form of the various waves

We now consider an incident plane wave (Fig.3.6) propagating across an interface between two half-spaces having the following mechanical properties: $(\lambda_1, \mu_1, \rho_1)$ and $(\lambda_2, \mu_2, \rho_2)$. This incident wave will generate reflected waves propagating in the medium from which the incident wave is originated, and refracted waves crossing the interface and propagating in the second medium. In the general case, Fig.3.6 (right), we can demonstrate that an incident wave gives rise to:

- two reflected waves,
- two refracted waves.

The amplitude, the incidence and the nature of the reflected and refracted waves are easily obtained writing the continuity of the displacement vector \underline{u} and the stress vector $\underline{\tau} = \underline{\sigma} \cdot \underline{n}$ at the interface.

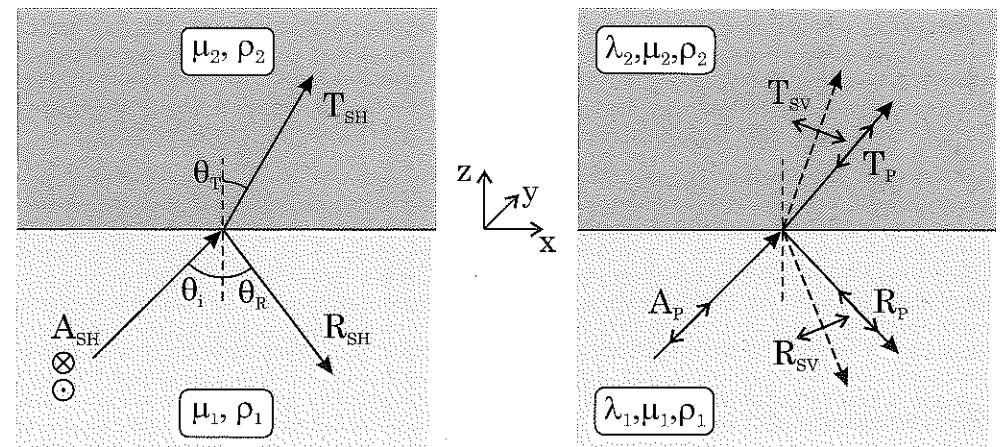


Fig. 3.6: Reflection-refraction of plane waves at a plane interface: SH -waves (left), P/SV -waves (right).

In the following, we analyze in great details the reflection-refraction of a plane SH , P and SV -waves respectively.

The variables related to the incident wave are denoted with an (i) index, those related to the reflected waves with an (R) index and those related to the transmitted (or refracted) waves with a (T) index.

The displacements of the incident waves can be written under the general form:

$$\underline{u}_n = A_n \underline{d}^{(n)} \exp \left[\frac{i\omega}{V_n} (x l_x^{(n)} + z l_z^{(n)} - V_n t) \right] \quad (3.49)$$

relation in which index (n) identifies the various wave types, (l_x, l_z) are the cosine directions of the *propagation axis* (normalized wave vector). Vector \underline{d} is the unit vector giving the direction of the displacement, that is the *direction of polarization* of the wave. These different parameters are detailed hereafter for various wave types.

- | | |
|---|--|
| Incident wave:
• SH-wave:
• P-wave:
• SV-wave: | $l_x^{(i)} = \sin \theta_i ; \quad l_z^{(i)} = \cos \theta_i$ $\begin{cases} V_S = V_{S1} \\ d_i^{(SH)} = \{0, 1, 0\} \end{cases}$ $\begin{cases} V_P = V_{P1} \\ d_i^{(P)} = \{\sin \theta_i^P, 0, \cos \theta_i^P\} \end{cases}$ $\begin{cases} V_S = V_{S1} \\ d_i^{(SV)} = \{\cos \theta_i^{SV}, 0, -\sin \theta_i^{SV}\} \end{cases}$ |
|---|--|

Reflection-refraction of a SH-wave between two media

Reflected and transmitted waves. We seek a solution under the form of a reflected SH-wave, with amplitude R_{SH} , and a transmitted (or refracted) SH-wave, with amplitude T_{SH} (Fig. 3.6, left). The directions of propagation and polarization of these waves are defined as follows:

- Reflected SH-wave:
$$\begin{cases} V_S = V_{S_1} \\ \underline{d}_R^{(SH)} = \{0, 1, 0\} \\ \underline{l}_R^{(SH)} = \{\sin \theta_R, 0, -\cos \theta_R\} \end{cases}$$
- Transmitted SH-wave:
$$\begin{cases} V_S = V_{S_2} \\ \underline{d}_T^{(SH)} = \{0, 1, 0\} \\ \underline{l}_T^{(SH)} = \{\sin \theta_T, 0, \cos \theta_T\} \end{cases}$$

The displacements related to the incident, reflected and transmitted waves are thus given by:

$$\begin{cases} u_y^{(i)} = A_{SH} \exp \left[\frac{i\omega}{V_{S_1}} (x \sin \theta_i + z \cos \theta_i - V_{S_1} t) \right] \\ u_y^{(R)} = R_{SH} \exp \left[\frac{i\omega}{V_{S_1}} (x \sin \theta_R - z \cos \theta_R - V_{S_1} t) \right] \\ u_y^{(T)} = T_{SH} \exp \left[\frac{i\omega}{V_{S_2}} (x \sin \theta_T + z \cos \theta_T - V_{S_2} t) \right] \end{cases} \quad (3.50)$$

the other components (x and z) being zero for all waves.

Equations of continuity

Continuity of displacement. Choosing the origin $z=0$ at the interface, the equations of continuity for displacements require:

$$u_y^{(i)} + u_y^{(R)} = u_y^{(T)} \quad (3.51)$$

Including relations (3.50) into Eqs (3.51) and writing that, for $z = 0$, the derived identities are valid for all values of x and t , we obtain the following relations, to be satisfied by θ_j and V_{S_k} :

$$\frac{\sin \theta_i}{V_{S_1}} = \frac{\sin \theta_R}{V_{S_1}} = \frac{\sin \theta_T}{V_{S_2}} \quad (3.52)$$

One recognizes in relations (3.52) the Snell-Descartes laws from classical optics.

The equation of continuity for displacement thus leads to a first relation between R_{SH} and T_{SH} :

$$A_{SH} + R_{SH} = T_{SH} \quad (3.53)$$

3.3 Wave propagation in unbounded media

Continuity of traction. Only the xy and yz components of the strain tensor are non zero. Its trace is zero and the stress tensor has only non zero components along xy and yz . The vector normal to the interface being $\underline{n} = \underline{e}_z$, the equations of continuity for the stress vector $\underline{\sigma} \cdot \underline{n}$ thus involve the component σ_{yz} :

$$\sigma_{yz}^{(i)} + \sigma_{yz}^{(R)} = \sigma_{yz}^{(T)} \quad (3.54)$$

$$\text{yielding: } \mu_1 \left(\frac{\partial u_y^{(i)}}{\partial z} + \frac{\partial u_y^{(R)}}{\partial z} \right) = \mu_2 \frac{\partial u_y^{(T)}}{\partial z} \quad (3.55)$$

Starting from Eq.(3.55), this equation can be rewritten under the form:

$$\mu_1 A_{SH} \frac{\cos \theta_i}{V_{S_1}} - \mu_1 R_{SH} \frac{\cos \theta_R}{V_{S_1}} = \mu_2 T_{SH} \frac{\cos \theta_T}{V_{S_2}} \quad (3.56)$$

Amplitudes of the reflected and transmitted waves. Equations (3.53) and (3.56) allow the determination of the amplitudes of the reflected wave R_{SH} and the transmitted wave T_{SH} as functions of the amplitude of the incident wave A_{SH} :

$$\begin{cases} \frac{R_{SH}}{A_{SH}} = \frac{\mu_1 V_{S_2} \cos \theta_i - \mu_2 V_{S_1} \cos \theta_T}{\mu_1 V_{S_2} \cos \theta_i + \mu_2 V_{S_1} \cos \theta_T} \\ \frac{T_{SH}}{A_{SH}} = \frac{2 \mu_1 V_{S_2} \cos \theta_i}{\mu_1 V_{S_2} \cos \theta_i + \mu_2 V_{S_1} \cos \theta_T} \end{cases} \quad (3.57)$$

in which μ_j and V_{S_j} are linked by Eq.(3.20).

Denoting $\chi_S = V_{S_2}/V_{S_1}$ the shear wave velocity ratio and assuming that $\rho_1 \simeq \rho_2$, the amplitudes of the reflected and transmitted waves can be derived as functions of χ_S and the incidence angle θ_i only:

$$\begin{cases} \frac{R_{SH}}{A_{SH}} = \frac{\cos \theta_i - \chi_S \sqrt{1 - \chi_S^2 \sin^2 \theta_i}}{\cos \theta_i + \chi_S \sqrt{1 - \chi_S^2 \sin^2 \theta_i}} \\ \frac{T_{SH}}{A_{SH}} = \frac{2 \cos \theta_i}{\cos \theta_i + \chi_S \sqrt{1 - \chi_S^2 \sin^2 \theta_i}} \end{cases} \quad (3.58)$$

since Eq. (3.52) yields $\cos^2 \theta_T^2 = 1 - \chi_S^2 \sin^2 \theta_i$.

The normalized amplitudes R_{SH}/A_{SH} and T_{SH}/A_{SH} are displayed in Fig.3.7 as functions of the incidence angle θ_i for two values of the velocity ratio $\chi_S = V_{S_2}/V_{S_1}$: $\chi_S = 0.8$ (top, softer upper medium) and $\chi_S = 2.0$ (bottom, stiffer upper medium).

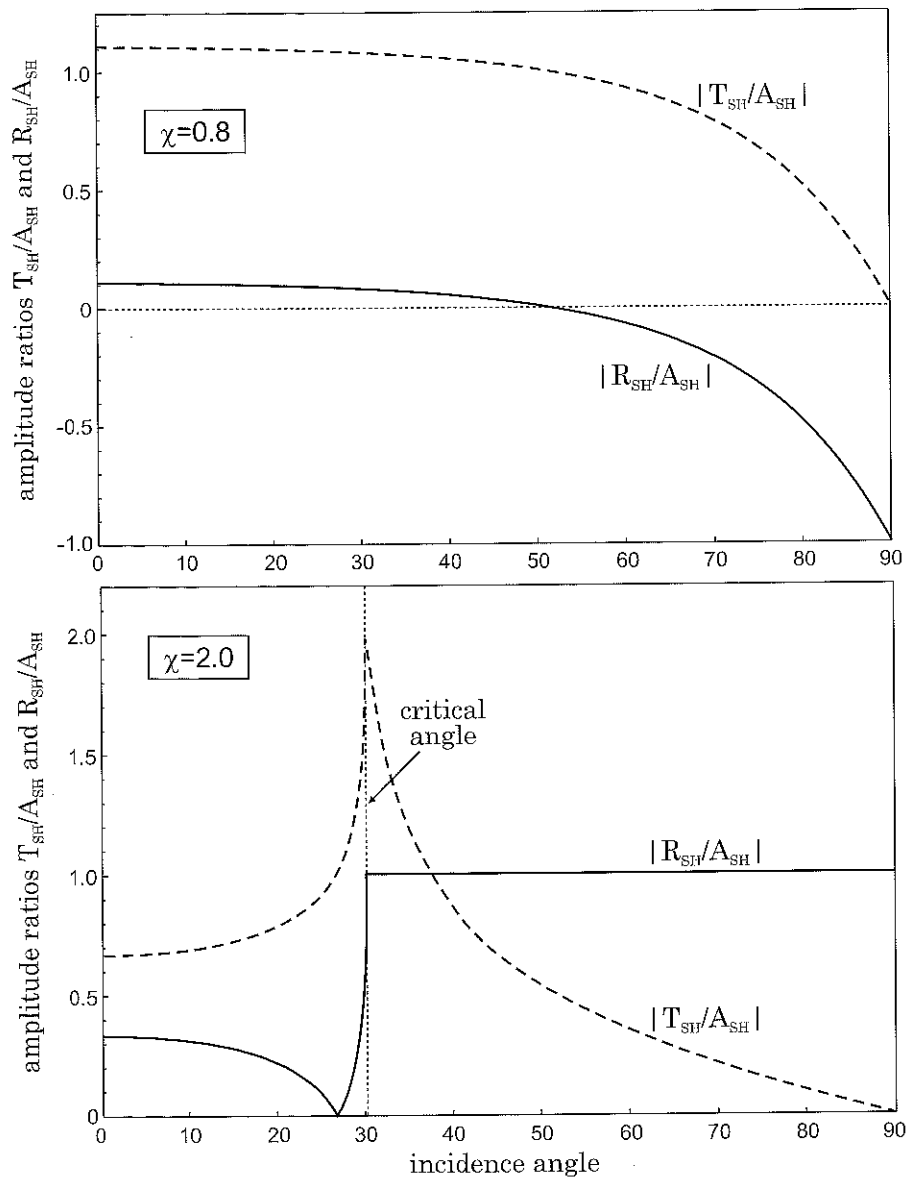


Fig. 3.7: Amplitudes of the reflected (solid) and transmitted (dashed) waves at a plane interface for two values of the velocity ratio $\chi = V_{S_2}/V_{S_1}$: $\chi = 0.8$ (top), $\chi = 2.0$ (bottom).

The curves displayed in Fig.3.7 lead to the following remarks:

- if the upper medium is softer ($\chi_S = 0.8$, top), the transmission coefficient is larger

than unity. Conversely, for a stiffer upper medium ($\chi_S = 2.0$, bottom), the transmission coefficient is lower than one.

- the incident SH -wave is fully refracted ($R_{SH}=0$) when the following condition is fulfilled:

$$\mu_1 V_{S_2} \cos \theta_i = \mu_2 V_{S_1} \cos \theta_T \quad (3.59)$$

A specific combination of the mechanical properties of both media thus leads to no reflected wave ($\chi_S = 0.8$, top). Removing θ_T in relations (3.52) and (3.59), this expression becomes:

$$\left(\frac{\mu_1}{\mu_2} \right)^2 \cos^2 \theta_i + \sin^2 \theta_i = \left(\frac{V_{S_1}}{V_{S_2}} \right)^2 \quad (3.60)$$

- if the term $(V_{S_2}/V_{S_1}) \sin \theta_i$ is larger than unity, $\cos \theta_T$ is then purely imaginary and the transmitted wave is expressed as:

$$u_y^{(T)} = T_{SH} e^{-\bar{\chi}_S z} \exp \left[\frac{i\omega}{V_{S_2}} (x \sin \theta_T - V_{S_2} t) \right] \quad (3.61)$$

in which $\bar{\chi}_S$ corresponds to:

$$\bar{\chi}_S = \frac{\omega}{V_{S_1}} \sqrt{\chi_S^2 \sin^2 \theta_i - 1} \quad (3.62)$$

The transmitted wave is then an *interface wave* which amplitude exponentially decreases with the distance to the interface. Furthermore, Eq.(3.58) shows that the R_{SH}/A_{SH} ratio corresponds to two conjugated complex variables, since $\cos \theta_T$ is purely imaginary ; the amplitude of the reflected wave is equal to the amplitude of the incident wave with a $\pi/2$ phase shift ($\chi_S = 2.0$, bottom).

- if $\mu_2 = V_{S_2} = 0$, the wavefield propagates in a half-space (medium 1) and is reflected on the free-surface (this case will be examined in the next sections).

Reflection-refraction of a P -wave at an interface

Reflected and transmitted waves. Since P -waves have two components of displacement (along x and z), the continuity conditions for both displacement and traction thus lead to four equations (instead of two for SH -waves). If, as in the case of SH -wave, we only consider two unknowns R_P and T_P , the system will be overdetermined. An incident P -wave actually generates reflected and refracted P -waves as well as reflected and refracted SV -waves (Fig.3.6, right). The equations of displacements associated to the various waves types are given by Eqs (3.49) considering the adequate parameters, that is:

- Reflected P -wave:

$$\begin{cases} V_P = V_{P_1} \\ d_R^{(P)} = \{\sin \theta_R^P, 0, -\cos \theta_R^P\} \\ l_R^{(P)} = d_R^{(P)} \end{cases}$$

- Reflected SV-wave:
$$\begin{cases} V_S = V_{S_1} \\ \underline{d}_R^{(SV)} = \{\cos \theta_R^{SV}, 0, \sin \theta_R^{SV}\} \\ \underline{l}_R^{(SV)} = \{\sin \theta_R^{SV}, 0, -\cos \theta_R^{SV}\} \end{cases}$$
- Refracted P-wave:
$$\begin{cases} V_P = V_{P_2} \\ \underline{d}_T^{(P)} = \{\sin \theta_T^P, 0, \cos \theta_T^P\} \\ \underline{l}_T^{(P)} = \underline{d}_T^{(P)} \end{cases}$$
- Refracted SV-wave:
$$\begin{cases} V_S = V_{S_2} \\ \underline{d}_T^{(SV)} = \{-\cos \theta_T^{SV}, 0, \sin \theta_T^{SV}\} \\ \underline{l}_T^{(SV)} = \{\sin \theta_T^{SV}, 0, \cos \theta_T^{SV}\} \end{cases}$$

The displacements due to the different waves are such as $u_y^{(j)} = 0 (\forall j)$ and:

- incident wave, $\underline{u}^{(i-P)}$:

$$\begin{cases} u_x^{(i-P)} = A_P \sin \theta_i^P \exp \left[\frac{i\omega}{V_{P_1}} (x \sin \theta_i^P + z \cos \theta_i^P - V_{P_1} t) \right] \\ u_z^{(i-P)} = A_P \cos \theta_i^P \exp \left[\frac{i\omega}{V_{P_1}} (x \sin \theta_i^P + z \cos \theta_i^P - V_{P_1} t) \right] \end{cases} \quad (3.63)$$

- reflected waves, $\underline{u}^{(R-P)}$ and $\underline{u}^{(R-SV)}$:

$$\begin{cases} u_x^{(R-P)} = R_P \sin \theta_R^P \exp \left[\frac{i\omega}{V_{P_1}} (x \sin \theta_R^P - z \cos \theta_R^P - V_{P_1} t) \right] \\ u_z^{(R-P)} = -R_P \cos \theta_R^P \exp \left[\frac{i\omega}{V_{P_1}} (x \sin \theta_R^P - z \cos \theta_R^P - V_{P_1} t) \right] \end{cases} \quad (3.64)$$

$$\begin{cases} u_x^{(R-SV)} = R_{SV} \cos \theta_R^{SV} \exp \left[\frac{i\omega}{V_{S_1}} (x \sin \theta_R^{SV} - z \cos \theta_R^{SV} - V_{S_1} t) \right] \\ u_z^{(R-SV)} = R_{SV} \sin \theta_R^{SV} \exp \left[\frac{i\omega}{V_{S_1}} (x \sin \theta_R^{SV} - z \cos \theta_R^{SV} - V_{S_1} t) \right] \end{cases} \quad (3.65)$$

- transmitted (or refracted) waves, $\underline{u}^{(T-P)}$ and $\underline{u}^{(T-SV)}$:

$$\begin{cases} u_x^{(T-P)} = T_P \sin \theta_T^P \exp \left[\frac{i\omega}{V_{P_2}} (x \sin \theta_T^P + z \cos \theta_T^P - V_{P_2} t) \right] \\ u_z^{(T-P)} = T_P \cos \theta_T^P \exp \left[\frac{i\omega}{V_{P_2}} (x \sin \theta_T^P + z \cos \theta_T^P - V_{P_2} t) \right] \end{cases} \quad (3.66)$$

$$\begin{cases} u_x^{(T-SV)} = -T_{SV} \cos \theta_T^{SV} \exp \left[\frac{i\omega}{V_{S_2}} (x \sin \theta_T^{SV} + z \cos \theta_T^{SV} - V_{S_2} t) \right] \\ u_z^{(T-SV)} = T_{SV} \sin \theta_T^{SV} \exp \left[\frac{i\omega}{V_{S_2}} (x \sin \theta_T^{SV} + z \cos \theta_T^{SV} - V_{S_2} t) \right] \end{cases} \quad (3.67)$$

Equations of continuity

Continuity of displacement. At the interface ($z = 0$), the equations of continuity for displacement can be written under the following form:

$$u_j^{(i-P)} + u_j^{(R-P)} + u_j^{(R-SV)} = u_j^{(T-P)} + u_j^{(T-SV)} \quad j = x, z \quad (3.68)$$

These relations must be valid for all values of x and t . It thus leads to the conditions:

$$\frac{\sin \theta_i^P}{V_{P_1}} = \frac{\sin \theta_R^P}{V_{P_1}} = \frac{\sin \theta_R^{SV}}{V_{S_1}} = \frac{\sin \theta_T^P}{V_{P_2}} = \frac{\sin \theta_T^{SV}}{V_{S_2}} \quad (3.69)$$

Starting from the system of equations (3.68), we obtain two equations relating the amplitudes R_j and T_j ($j = P, SV$) of the reflected and transmitted waves to the amplitude of the incident wave A_P :

$$\begin{cases} \text{along } x : (A_P + R_P) \sin \theta_i^P + R^{SV} \cos \theta_R^{SV} = T_P \sin \theta_T^P - T_{SV} \cos \theta_T^{SV} \\ \text{along } z : (A_P - R_P) \cos \theta_i^P + R^{SV} \sin \theta_R^{SV} = T_P \cos \theta_T^P + T_{SV} \sin \theta_T^{SV} \end{cases} \quad (3.70)$$

Continuity of traction. For each wavefield ($j = i-P, R-P, R-SV, T-P, T-SV$), the stress vector is written as follows:

$$\underline{\sigma}^{(j)} \cdot \underline{n} = \sigma_{xz}^{(j)} \underline{e}_x + \sigma_{zz}^{(j)} \underline{e}_z \quad (3.71)$$

$$\text{that is: } \sigma_{kz}^{(i-P)} + \sigma_{kz}^{(R-P)} + \sigma_{kz}^{(R-SV)} = \sigma_{kz}^{(T-P)} + \sigma_{kz}^{(T-SV)} \quad k = x, z \quad (3.72)$$

It thus leads to the system of equations:

$$\begin{cases} \text{along } x : (A_P - R_P) \sin 2\theta_i^P - R^{SV} \chi_1 \cos 2\theta_R^{SV} = \\ \qquad T_P \frac{\chi_1}{\chi_2} \chi_S \sin 2\theta_T^P - T_{SV} \chi_1 \chi_S \cos 2\theta_T^{SV} \\ \text{along } z : (A_P + R_P) \chi_1 \cos 2\theta_R^{SV} - R^{SV} \sin 2\theta_R^{SV} = \\ \qquad T_P \chi_2 \chi_S \cos 2\theta_T^{SV} + T_{SV} \chi_S \sin 2\theta_T^{SV} \end{cases} \quad (3.73)$$

$$\text{with: } \chi_S = \frac{V_{S_2}}{V_{S_1}} ; \chi_j = \frac{V_{P_j}}{V_{S_j}} \quad j = 1, 2$$

$$\text{and: } \frac{\lambda_1 + 2\mu_1 \cos^2 \theta_i^P}{\mu_1} = \chi_1^2 \cos 2\theta_R^{SV} ; \frac{\lambda_2 + 2\mu_2 \cos^2 \theta_T^P}{\mu_2} = \chi_2^2 \cos 2\theta_T^{SV}$$

Amplitudes of the reflected and transmitted waves

Variable incidence: Considering a variable incidence, we obtain the following system of four equations with four unknowns:

$$\begin{pmatrix} -\sin \theta_i^P & -\cos \theta_i^{SV} & \sin \theta_T^P & -\cos \theta_T^{SV} \\ \cos \theta_i^P & -\sin \theta_i^{SV} & \cos \theta_T^P & \sin \theta_T^{SV} \\ \sin 2\theta_i^P & \chi_1 \cos 2\theta_R^{SV} & \frac{\chi_1}{\chi_2} \chi_S \sin 2\theta_T^P & -\chi_1 \chi_S \cos 2\theta_T^{SV} \\ -\chi_1 \cos 2\theta_R^{SV} & \sin 2\theta_R^{SV} & \chi_2 \chi_S \cos 2\theta_T^{SV} & \chi_S \sin 2\theta_T^{SV} \end{pmatrix} \begin{Bmatrix} R_P \\ R_{SV} \\ T_P \\ T_{SV} \end{Bmatrix} = A_P \begin{Bmatrix} \sin \theta_i^P \\ \cos \theta_i^P \\ \sin 2\theta_i^P \\ \chi_1 \cos 2\theta_R^{SV} \end{Bmatrix} \quad (3.74)$$

Conversely to the case of *SH*-waves, for an incident *P*-wave, two critical angles can be defined:

- *critical angle 1*: the transmitted *P*-wave becomes an interface wave if:

$$\sin \theta_{i_{cr1}}^P = \frac{1}{\chi_P} \leq 1 \quad (\text{that is, when } V_{P2} \geq V_{P1})$$

- *critical angle 2*: the transmitted *SV*-wave becomes an interface wave if:

$$\sin \theta_{i_{cr2}}^P = \frac{\chi_1}{\chi_S} \leq 1 \quad (\text{that is, when } V_{S2} \geq V_{P1})$$

For two values of the velocity ratio χ , we then obtain the results displayed in Figs 3.8 and 3.9 corresponding to various cases with or without critical incidence. As in the case of *SH*-waves, the transmission coefficient of *P*-waves is larger than unity when the upper medium is stiffer (and less than one in the opposite case).

Normal incidence: Considering a normal incidence at the interface ($\theta_i^P=0$), we can easily show that relations (3.74) become:

$$\begin{cases} R_{SV} = T_{SV} = 0 \\ \frac{R_P}{A_P} = \frac{\rho_2 V_{P2} - \rho_1 V_{P1}}{\rho_2 V_{P2} + \rho_1 V_{P1}} \\ \frac{T_P}{A_P} = \frac{2\rho_1 V_{P1}}{\rho_2 V_{P2} + \rho_1 V_{P1}} \end{cases} \quad (3.75)$$

Equations (3.75) show that, if the incidence of the *P*-wave is perpendicular to the interface, there is neither reflected *SV*-wave nor transmitted *SV*-wave. When the two media in contact have the same *mechanical impedance* ($=\rho V_P$), no reflected *P*-wave appears for normal incidence, which is in agreement with intuition.

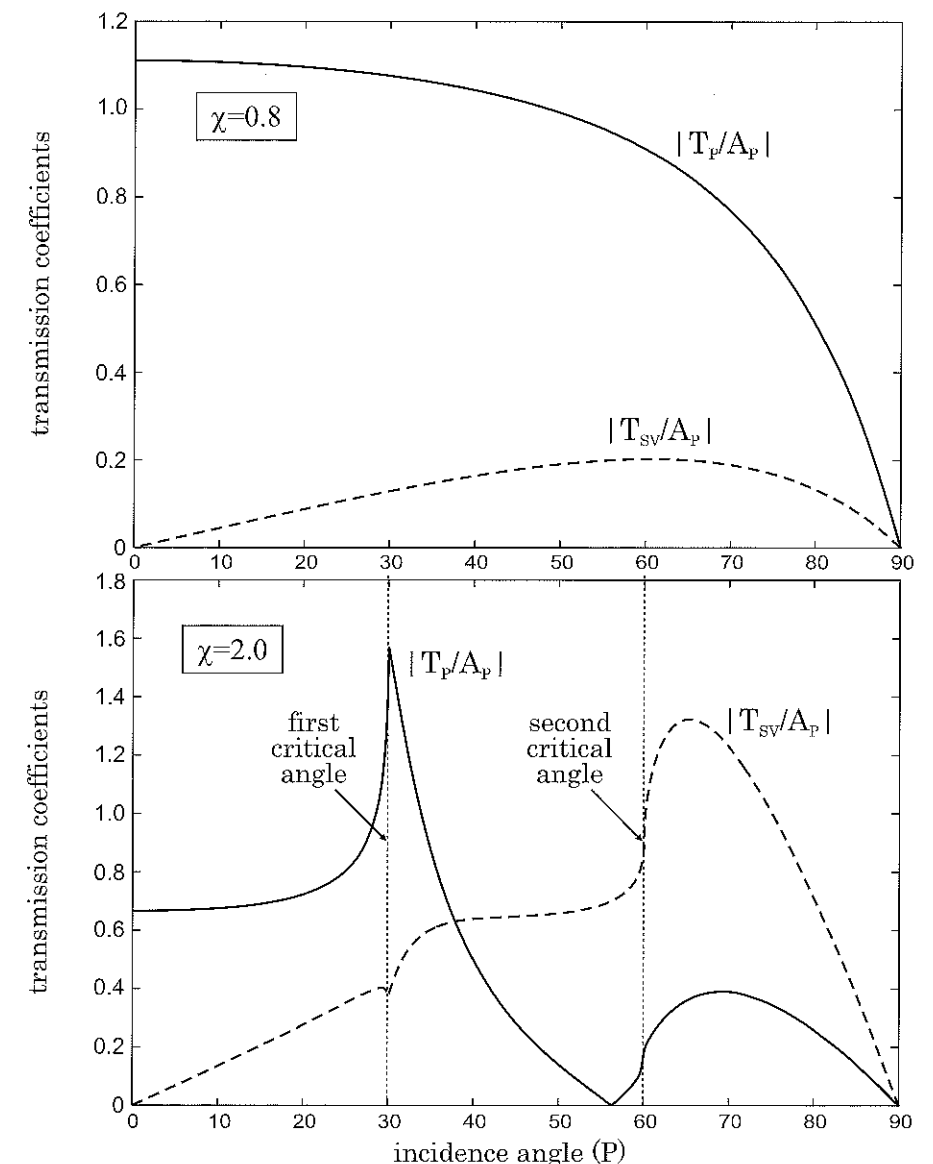


Fig. 3.8: Amplitudes of transmitted *P* and *SV*-waves at a plane interface for an incident *P*-wave and for two values of the velocity ratio $\chi = V_{P2}/V_{P1}$: $\chi = 0.8$ (top), $\chi = 2.0$ (bottom).

Reflection-refraction of a SV-wave at an interface

The same method as in the previous section leads to similar results for an incident SV-wave:

$$\frac{\sin \theta_i^{SV}}{V_{S_1}} = \frac{\sin \theta_R^P}{V_{P_1}} = \frac{\sin \theta_R^{SV}}{V_{S_1}} = \frac{\sin \theta_T^P}{V_{P_2}} = \frac{\sin \theta_T^{SV}}{V_{S_2}} \quad (3.76)$$

The solution can be derived by considering a system of four equations with four unknowns similar to system (3.74):

$$\begin{pmatrix} \cos \theta_i^{SV} & \sin \theta_R^P & \cos \theta_T^{SV} & \sin \theta_T^P \\ \sin \theta_i^{SV} & -\cos \theta_R^P & -\sin \theta_T^{SV} & \cos \theta_T^P \\ -\cos 2\theta_i^{SV} & -\frac{1}{\chi_1} \sin 2\theta_R^P & \chi_S \cos 2\theta_T^{SV} & -\frac{\chi_S}{\chi_2} \sin 2\theta_T^P \\ -\sin 2\theta_i^{SV} & \chi_1 \cos 2\theta_R^{SV} & -\chi_S \sin 2\theta_T^{SV} & -\chi_2 \chi_S \cos 2\theta_T^{SV} \end{pmatrix} \begin{Bmatrix} R_{SV} \\ R_P \\ T_{SV} \\ T_P \end{Bmatrix} = A_{SV} \begin{Bmatrix} \cos \theta_i^{SV} \\ -\sin \theta_i^{SV} \\ \cos 2\theta_i^{SV} \\ -\sin 2\theta_i^{SV} \end{Bmatrix} \quad (3.77)$$

As illustrated in Fig.3.9 (bottom), in the case of an incident SV-wave, we may have at least one and up to three different critical angles:

- *critical angle 1*: the reflected P-wave becomes an interface wave if:

$$\sin \theta_{i_{cr1}}^{SV} = \frac{1}{\chi_1} \leq 1 \quad (\text{that is, when } V_{P_1} \geq V_{S_1} \text{ (always true)})$$

- *critical angle 2*: the transmitted SV-wave becomes an interface wave if:

$$\sin \theta_{i_{cr2}}^{SV} = \frac{1}{\chi_S} \leq 1 \quad (\text{that is, when } V_{S_2} \geq V_{S_1})$$

- *critical angle 3*: the transmitted P-wave becomes an interface wave if:

$$\sin \theta_{i_{cr3}}^{SV} = \frac{1}{\chi_P \chi_1} \leq 1 \quad (\text{that is, when } V_{P_2} \geq V_{S_1})$$

3.3.4 Plane waves in layered media: vibration isolation

Vibration isolation by screens or trenches: simplified analysis

As already discussed in Chapter 1, vibration isolation may be performed by screens or trenches in the soil. Using previous theoretical results, we shall now consider a simplified analysis involving an infinite vertical layer of constant thickness h embedded in a free-space. As depicted in Fig.3.10, the mechanical properties of the layer are different from that of the soil. For sake of simplicity, the free-surface is disregarded and the efficiency of the isolation system is studied as a function of the velocity ratio between the soil and the layer.

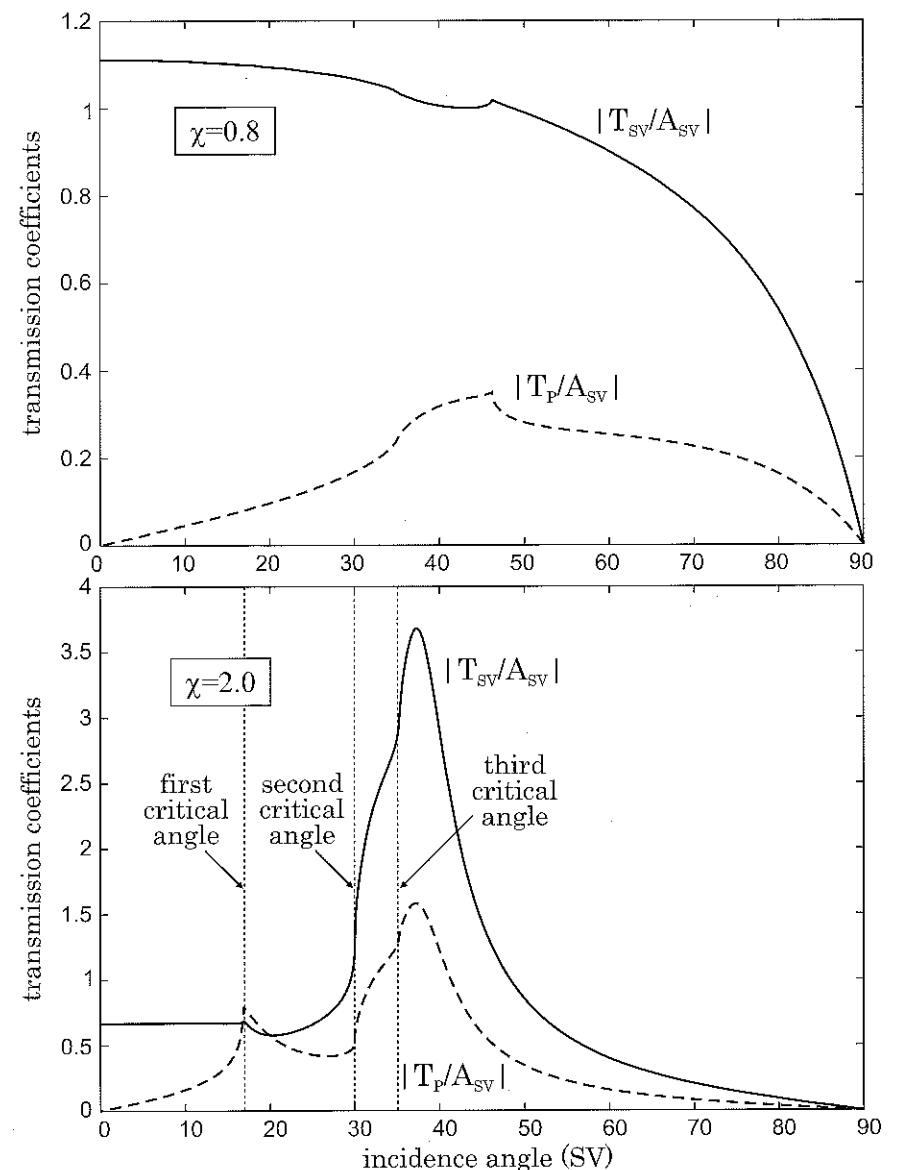


Fig. 3.9: Amplitudes of transmitted P and SV-waves at a plane interface for an incident SV-wave and for two values of the velocity ratio $\chi = V_{S_2}/V_{S_1}$: $\chi = 0.8$ (top), $\chi = 2.0$ (bottom).

Transmittivity of a plane SH -wave through a single layer

Displacements and tractions. As depicted in Fig.3.10, we shall now consider an infinite layer of constant thickness embedded in an infinite elastic homogeneous isotropic medium. The propagation of a harmonic plane wave across such a layer can be described easily. Only the continuity of displacements and tractions at the interfaces are needed. As shown in Fig.3.11, we first consider the case of a normally incident plane SH -wave (amplitude A_{SH}): there are two reflected (amplitudes R_{SH} and R'_{SH}) and two transmitted waves (amplitudes T_{SH} and T'_{SH}).

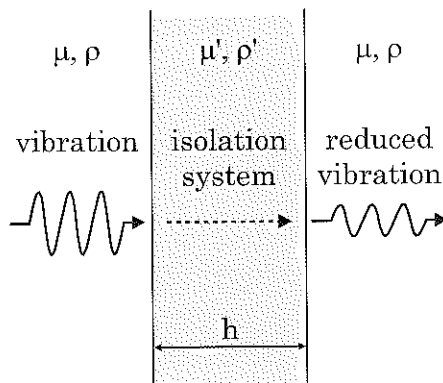


Fig. 3.10: Simplified analysis of vibration isolation by screens and trenches.

For such a plane SH -wave, the expression of the displacement field is the following:

$$\begin{cases} u_x = 0 \\ u_y = A_{SH} \exp\left[\frac{i\omega}{V_S}(x - V_S t)\right] \\ u_z = 0 \end{cases} \quad (3.78)$$

where V_S is the shear wave velocity.

Equations of continuity. Considering the expression of the displacement field, Eq.(3.78), the only non zero component of the stress tensor is:

$$\sigma_{yx} = \mu \frac{\partial u_y}{\partial x} \quad (3.79)$$

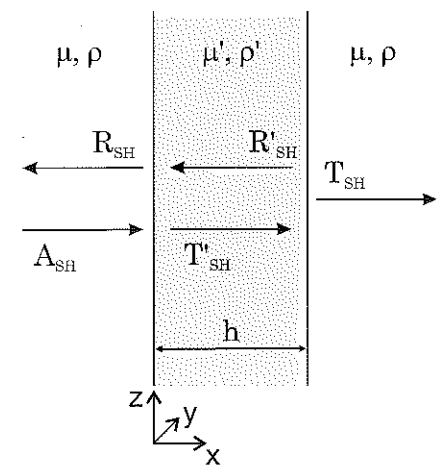


Fig. 3.11: Propagation of a normally incident plane SH -wave through a single infinite layer.

The equations of continuity are thus written:

- first interface:

- displacement:

$$A_{SH} + R_{SH} = T'_{SH} + R'_{SH} \quad (3.80)$$

- traction:

$$\mu \frac{A_{SH}}{V_S} - \mu \frac{R_{SH}}{V_S} = \mu' \frac{T'_{SH}}{V'_S} - \mu' \frac{R'_{SH}}{V'_S} \quad (3.81)$$

- second interface:

- displacement:

$$T'_{SH} \exp\left(\frac{i\omega}{V'_S} h\right) + R'_{SH} \exp\left(-\frac{i\omega}{V'_S} h\right) = T_{SH} \exp\left(\frac{i\omega}{V_S} h\right) \quad (3.82)$$

- traction:

$$\frac{\mu'}{V'_S} \left[T'_{SH} \exp\left(\frac{i\omega}{V'_S} h\right) - R'_{SH} \exp\left(-\frac{i\omega}{V'_S} h\right) \right] = \frac{\mu}{V_S} T_{SH} \exp\left(\frac{i\omega}{V_S} h\right) \quad (3.83)$$

We shall also consider the approximation $\rho \simeq \rho'$, leading to a simple expression of the ratio $\frac{\mu' V_S}{\mu V'_S}$ using the shear wave velocity contrast χ_S as follows:

$$\frac{\mu' V_S}{\mu V'_S} = \sqrt{\frac{\mu' \rho'}{\mu \rho}} \simeq \frac{V'_S}{V_S} = \chi_S \quad (3.84)$$

The following system is thus derived:

$$\left\{ \begin{array}{l} 1 + \frac{R_{SH}}{A_{SH}} - \frac{T'_{SH}}{A_{SH}} - \frac{R'_{SH}}{A_{SH}} = 0 \\ 1 - \frac{R_{SH}}{A_{SH}} - \chi_S \frac{T'_{SH}}{A_{SH}} + \chi_S \frac{R'_{SH}}{A_{SH}} = 0 \\ e^+ \frac{T'_{SH}}{A_{SH}} + e^- \frac{R'_{SH}}{A_{SH}} = T_{SH} \\ e^+ \frac{T'_{SH}}{A_{SH}} - e^- \frac{R'_{SH}}{A_{SH}} = \frac{T_{SH}}{\chi_S} \end{array} \right. \quad (3.85)$$

where $e^+ = \exp\left(\frac{i\omega}{V'_S}h\right)$, $e^- = \exp\left(-\frac{i\omega}{V'_S}h\right)$ and the transmission coefficient T is:

$$T_{SH} = \frac{T_{SH}}{A_{SH}} \exp\left(\frac{i\omega}{V'_S}h\right)$$

Transmission coefficient. The solution of Eqs (3.85) leads to the expression of the transmission coefficient T_{SH} :

$$T_{SH} = \frac{4\chi_S}{(1 + \chi_S)^2 e^- - (1 - \chi_S)^2 e^+} \quad (3.86)$$

where χ_S is the shear wave velocity ratio such as:

$$\chi_S = \frac{V'_S}{V_S} \quad (3.87)$$

Influence of the velocity ratio on transmission. The transmission coefficient T_{SH} is complex valued and includes one term related to the amplitude and another one related to the phase. Both terms are influenced by the propagation through the layer. In order to assess the amplitude reduction through the layer, the modulus of the transmission coefficient will now be derived.

Considering the complex exponentials e^+ and e^- under a simple form: $e^+ = a + ib$ and $e^- = a - ib$, the modulus of the transmission coefficient can be written as:

$$|T_{SH}| = \frac{2\chi_S}{\sqrt{4a^2\chi_S^2 + b^2(1 + \chi_S^2)^2}} \quad (3.88)$$

Taking into account the fact that $a^2 + b^2 = 1$, the previous expression can be further simplified:

$$|T_{SH}| = \left[a^2 + \frac{1-a^2}{4} \left(\frac{1}{\chi_S} + \chi_S \right)^2 \right]^{-\frac{1}{2}} \quad (3.89)$$

where χ_S is the velocity ratio and $a = \cos(\frac{\omega}{V'_S}h)$.

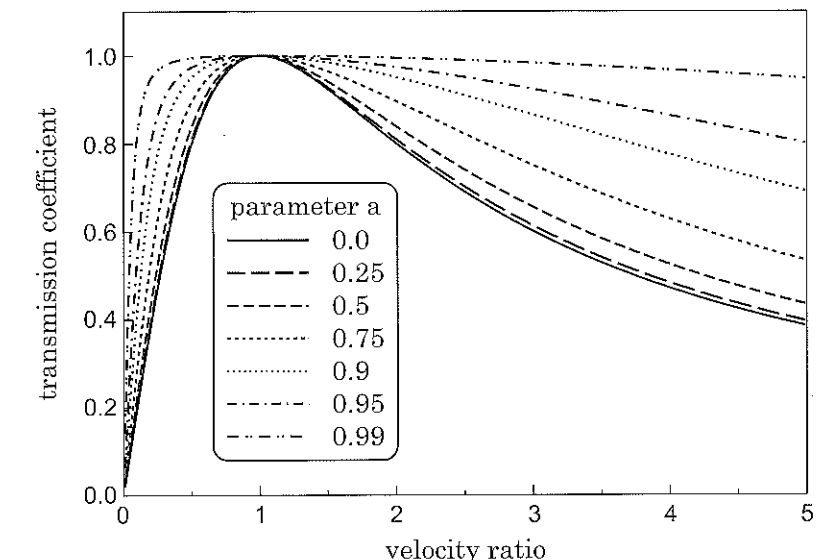


Fig. 3.12: Transmission coefficient of a plane SH -wave through a single layer: influence of the velocity ratio.

From Eq.(3.89), the influence of the velocity ratio on the transmission coefficient is obvious. Since the velocity ratio and its inverse are directly combined in Eq.(3.89), the transmission coefficient may be the same if the layer is stiffer than the infinite medium, $V'_S = \chi_S V_S > V_S$ ($\chi_S > 1$), or if the layer is softer than the infinite medium, $V'_S = \chi_S V_S < V_S$ ($\chi_S < 1$). The various curves displayed in Fig.3.12 correspond to different values of a (0.0, 0.25, 0.5, 0.75, 0.9, 0.95 and 0.99 resp.). The maximum value of the transmission coefficient, $|T_{SH}| = 1$, is reached for a velocity ratio $\chi_S = 1$ (leading to $V'_S = V_S$). Starting from $\chi_S = 1$, the transmission coefficient decreases for both a decreasing or increasing velocity ratio. This decay is much faster for small values of a : the minimum values of $|T_{SH}|$ are 0.8 for $\chi_S = 2.0$ and 0.6 for $\chi_S = 3.0$. The velocity ratio has a strong influence on the transmission coefficient. Nevertheless, for values of a close to 1, the transmission coefficient is not far from 1 and there is nearly no decay. The parameter a also has a significant influence on the transmission coefficient. It is mainly related to the layer thickness h and will be discussed in details in the next paragraph.

Optimal layer thickness. The transmission coefficient is now displayed as a function of the layer thickness/wavelength ratio for three different values of the velocity ratio: $\chi_S = 1.5$, $\chi_S = 2.0$ and $\chi_S = 3.0$ (Fig.3.13). For a very thin layer, the transmission coefficient is nearly 1. The minimum transmission is for a layer thickness equivalent to a quarter of the wavelength $h = \Lambda'/4$ with $\Lambda' = V'_S/f$ (f : frequency). Whereas for $h = \Lambda'/2$ (parameter $a = 1$ in Eq.(3.89)), the transmission coefficient is constant $|T_{SH}| = 1$. In such a case, the incident wave is totally transmitted through the layer

whatever the velocity ratio. As shown in Fig.3.13, the transmission coefficient is periodic with period $\Lambda'/2$ and the isolation efficiency is similar for thicker layers.

The transmission coefficient is thus minimum for an optimal layer thickness corresponding to a quarter wavelength. For this thickness, related to $a = 0$, Eq.(3.89) may be simplified in the following form:

$$|T_{SH}| = f(\chi_S) = \frac{2\chi_S}{1 + \chi_S^2} \quad (3.90)$$

This expression is useful for applications in vibration isolation (minimum transmission coefficient). As already mentioned previously, the isolation efficiency is the same for a stiff layer with a velocity ratio χ_S and a soft layer with a velocity ratio $1/\chi_S$. It is due to the fact that:

$$f(\chi_S) = f\left(\frac{1}{\chi_S}\right) \quad (3.91)$$

However, the corresponding optimal layer thicknesses, $h = \Lambda'/4$, are different in both cases since the wavelength is larger for the softer layer.

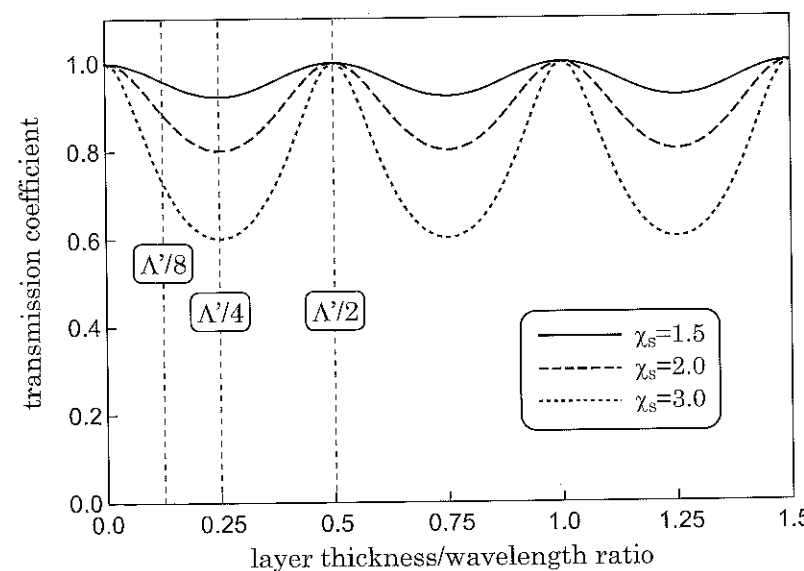


Fig. 3.13: Transmission coefficient of a plane SH -wave through a single layer: influence of the layer thickness as a fraction of the wavelength.

Influence of incidence on transmission. For a SH -wave with a non normal incidence (Fig.3.14), the expression of the displacement field is now as follows:

$$\begin{cases} u_x = 0 \\ u_y = A_{SH} \exp \left[\frac{i\omega}{V_S} (x \cos \theta + z \sin \theta - V_S t) \right] \\ u_z = 0 \end{cases} \quad (3.92)$$

where V_S is the shear wave velocity and θ the angle of incidence.

The only non zero component of the traction at the interface is the following:

$$\sigma_{yx} = \mu \frac{\partial u_y}{\partial x} \quad (3.93)$$

The Snell-Descartes equation can be written:

$$\frac{\sin \theta}{V_S} = \frac{\sin \theta'}{V'_S} \quad (3.94)$$

The same type of equations as in the case of normal incidence are obtained. The ratio $\mu'V_S/\mu V'_S$ is nevertheless replaced by the following ratio:

$$\frac{\mu'V_S \cos \theta'}{\mu V'_S \cos \theta} \simeq \chi_S \frac{\cos \theta'}{\cos \theta} = \frac{\chi_S}{\cos \theta} \sqrt{1 - \chi_S^2 \sin^2 \theta} \quad (3.95)$$

This ratio will then be denoted $\bar{\chi}_S$.

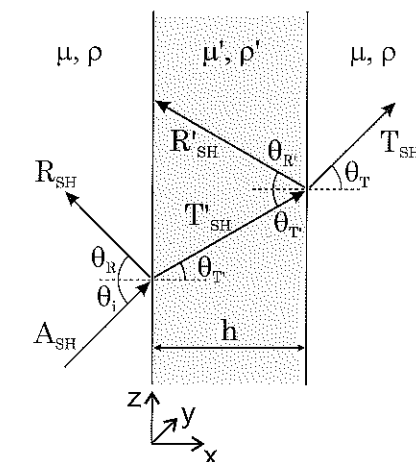


Fig. 3.14: Propagation of a plane SH -wave with oblique incidence in a single infinite layer.

Equation (3.95) is expressed as a function of the incidence angle θ . A critical incidence angle is obtained for $\sin \theta = 1/\chi_s$. In Fig. 3.15, for three different velocity ratios ($\chi_s=1.5$, $\chi_s=2.0$ and $\chi_s=3.0$), the transmission coefficient increases below the critical incidence (ranging from 40 to 20 degrees resp.), reaches its maximum value $|T_{SH}|=1$, and decreases very rapidly above the critical incidence. As shown in Fig. 3.15, the velocity ratio has a strong influence on the results:

- the transmission coefficient for a normal incidence ranges from 0.92 for $\chi_s=1.5$ down to 0.6 for $\chi_s=3.0$,
- above the critical incidence, the transmission coefficient decay is much faster for the largest velocity ratio values.

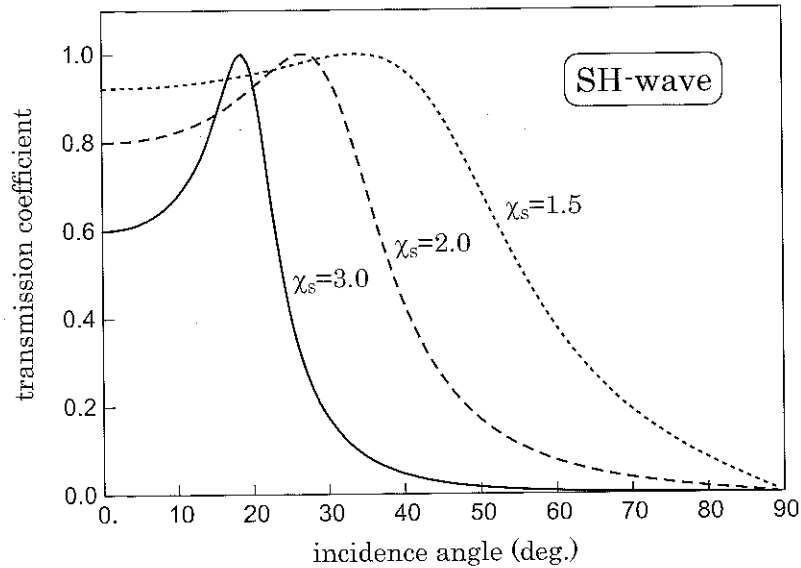


Fig. 3.15: Transmission coefficient as a function of incidence for different velocity ratios: $\chi_s=1.5$, $\chi_s=2.0$ and $\chi_s=3.0$ (single-layer case, SH-wave).

Transmittivity of a plane P -wave through a single layer

For a normal incidence, the results with P and SV -waves are identical to the previous ones. In Fig. 3.15, the transmission coefficient estimated for a normally incident SH -wave ($|T|=0.6$ for $\chi_s=3.0$) will be the same for a normally incident P -wave (velocity ratio nevertheless expressed in V_P). However, the velocity ratio is different for a P -wave (the velocity involving a $\lambda + 2\mu$ term instead of μ only for shear waves).

Displacement and traction. As shown in Fig. 3.16, for an oblique incident P -wave, the wavefield is converted into two wave types: P -wave and SV -wave. The displacement fields are the following:

- incident P -wave:

$$\begin{cases} u_x^{(i-P)} = A_P \cos \theta_i^P \exp \left[\frac{i\omega}{V_P} (x \cos \theta_i^P + z \sin \theta_i^P - V_P t) \right] \\ u_y^{(i-P)} = 0 \\ u_z^{(i-P)} = A_P \sin \theta_i^P \exp \left[\frac{i\omega}{V_P} (x \cos \theta_i^P + z \sin \theta_i^P - V_P t) \right] \end{cases} \quad (3.96)$$

where V_P is the P wave velocity and θ_i^P the incidence angle of the P -wave.

- resulting (reflected) SV -wave:

$$\begin{cases} u_x^{(R-SV)} = R_{SV} \sin \theta_R^{SV} \exp \left[\frac{i\omega}{V_S} (x \cos \theta_R^{SV} - z \sin \theta_R^{SV} - V_{St} t) \right] \\ u_y^{(R-SV)} = 0 \\ u_z^{(R-SV)} = R_{SV} \cos \theta_R^{SV} \exp \left[\frac{i\omega}{V_S} (x \cos \theta_R^{SV} - z \sin \theta_R^{SV} - V_{St} t) \right] \end{cases} \quad (3.97)$$

where V_S is the shear wave velocity and θ_R^{SV} the incidence angle of the SV -wave.

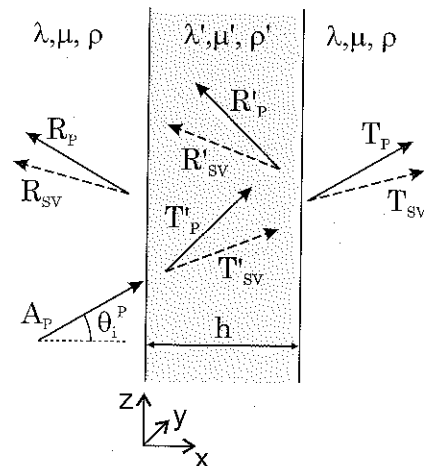


Fig. 3.16: Propagation of a P -wave with oblique incidence in a single infinite layer model.

Considering the expression of the displacement field (P -wave), the traction at the interface is the following:

$$\underline{\underline{\sigma}}^{(i-P)} \cdot \underline{n} = \begin{Bmatrix} 2i\mu \frac{\omega}{V_P} \cos \theta_i^P u_x^{(i-P)} + i\lambda \left(\frac{\omega}{V_P} \cos \theta_i^P u_x^{(i-P)} + \frac{\omega}{V_P} \sin \theta_i^P u_z^{(i-P)} \right) \\ 0 \\ i\mu \left(\frac{\omega}{V_P} \sin \theta_i^P u_x^{(i-P)} + \frac{\omega}{V_P} \cos \theta_i^P u_z^{(i-P)} \right) \end{Bmatrix} \quad (3.98)$$

Similar expressions are also obtained for other wavefields.

Equations of continuity. The Snell-Descartes equations can be written:

$$\frac{\sin \theta_i^P}{V_P} = \frac{\sin \theta_R^P}{V_S} = \frac{\sin \theta_R^{SV}}{V_S} = \frac{\sin \theta_{T'}^P}{V'_P} = \frac{\sin \theta_{T'}^{SV}}{V'_S} = \frac{\sin \theta_T^P}{V_P} = \frac{\sin \theta_T^{SV}}{V_S} \quad (3.99)$$

The equations of continuity yield:

- first interface:

- first component of displacement:

$$(A_P - R_P) \cos \theta_i^P + R_{SV} \sin \theta_R^{SV} = (T'_P - R'_P) \cos \theta_{T'}^P + (T'_{SV} + R'_{SV}) \sin \theta_{T'}^{SV} \quad (3.100)$$

- third component of displacement:

$$(A_P + R_P) \sin \theta_i^P + R_{SV} \cos \theta_R^{SV} = (T'_P + R'_P) \sin \theta_{T'}^P - (T'_{SV} - R'_{SV}) \cos \theta_{T'}^{SV} \quad (3.101)$$

- first component of traction:

$$\begin{aligned} A_P (\lambda + 2\mu \cos^2 \theta_i^P) + \frac{R_P}{V_P} (\lambda + 2\mu \cos^2 \theta_R^P) - \frac{R_{SV}}{V_S} \mu \sin 2\theta_R^{SV} = \\ \frac{T'_P}{V'_P} (\lambda' + 2\mu' \cos^2 \theta_{T'}^P) - \frac{T'_{SV}}{V'_S} \mu' \sin 2\theta_{T'}^{SV} \\ + \frac{R'_P}{V'_P} (\lambda' + 2\mu' \cos^2 \theta_{R'}^P) - \frac{R'_{SV}}{V'_S} \mu' \sin 2\theta_{R'}^{SV} \end{aligned} \quad (3.102)$$

- third component of traction:

$$\begin{aligned} \mu \frac{A_P}{V_P} \sin 2\theta_i^P - \mu \frac{R_P}{V_P} \sin 2\theta_R^P - \mu \frac{R_{SV}}{V_S} \cos 2\theta_R^{SV} = \\ \mu' \frac{T'_P}{V'_P} \sin 2\theta_{T'}^P - \mu' \frac{T'_{SV}}{V'_S} \cos 2\theta_{T'}^{SV} \\ - \mu' \frac{R'_P}{V'_P} \sin 2\theta_{R'}^P - \mu' \frac{R'_{SV}}{V'_S} \cos 2\theta_{R'}^{SV} \end{aligned} \quad (3.103)$$

- second interface:

- first component of displacement:

$$T_{P'} \cos \theta_{T'}^P e_P^+ - R_{P'} \cos \theta_{R'}^P e_{P'}^- + T'_{SV} \sin \theta_{T'}^{SV} e_{SV'}^+ + R'_{SV} \sin \theta_{R'}^{SV} e_{SV'}^- = T_P \cos \theta_T^P e_P^+ + T_{SV} \sin \theta_T^{SV} e_{SV}^+ \quad (3.104)$$

- third component of displacement:

$$T_{P'} \sin \theta_{T'}^P e_P^+ + R_{P'} \sin \theta_{R'}^P e_{P'}^- - T'_{SV} \cos \theta_{T'}^{SV} e_{SV'}^+ + R'_{SV} \cos \theta_{R'}^{SV} e_{SV'}^- = T_P \sin \theta_T^P e_P^+ - T_{SV} \cos \theta_T^{SV} e_{SV}^+ \quad (3.105)$$

- first component of traction:

$$\begin{aligned} \frac{T'_P}{V'_P} (\lambda' + 2\mu' \cos^2 \theta_{T'}^P) e_P^+ + \frac{R'_P}{V'_P} (\lambda' + 2\mu' \cos^2 \theta_{R'}^P) e_{P'}^- \\ + \frac{T'_{SV}}{V'_S} \mu' \sin 2\theta_{T'}^{SV} e_{SV'}^+ - \frac{R'_{SV}}{V'_S} \mu' \sin 2\theta_{R'}^{SV} e_{SV'}^- = \\ \frac{T_P}{V_P} (\lambda + 2\mu \cos^2 \theta_T^P) e_P^+ + \frac{T_{SV}}{V_S} \mu \sin 2\theta_T^{SV} e_{SV}^+ \end{aligned} \quad (3.106)$$

- third component of traction:

$$\begin{aligned} \mu' \frac{T'_P}{V'_P} \sin 2\theta_{T'}^P e_P^+ - \mu' \frac{R'_P}{V'_P} \sin 2\theta_{R'}^P e_{P'}^- \\ - \mu' \frac{T'_{SV}}{V'_S} \cos 2\theta_{T'}^{SV} e_{SV'}^+ - \mu' \frac{R'_{SV}}{V'_S} \cos 2\theta_{R'}^{SV} e_{SV'}^- = \\ \mu \frac{T_P}{V_P} \sin 2\theta_T^P e_P^+ - \mu \frac{T_{SV}}{V_S} \cos 2\theta_T^{SV} e_{SV}^+ \end{aligned} \quad (3.107)$$

where e_j^+ , $e_{j'}^+$, e_j^- and $e_{j'}^-$ are the same notations as e^+ and e^- for SH -wave but involving V_j for index j and V'_j for index j' ($j = P, S$).

Transmission coefficients. For an incident P -wave, Fig.3.17 gives two types of results: $|T_P|$ transmission coefficient for P -waves (top) and $|T_{SV}|$ transmission coefficient for SV -waves (bottom). Three curves are displayed in each graph corresponding to three different velocity ratios: $\chi_P=1.5$, $\chi_P=2.0$ and $\chi_P=3.0$. For a normal incidence ($\theta_i^P=0$), $|T_{SV}|$ is always zero. For an oblique incidence, as shown in Fig.3.17 (top), the values of $|T_P|$ exhibit very different variations:

- for the largest velocity ratio ($\chi_P=3.0$), the transmission coefficient $|T_P|$ is always below 0.6,
- for the lowest velocity ratio ($\chi_P=1.5$), the transmission coefficient $|T_P|$ is above 0.6 for incidences up to 45 degrees,

- for $\chi_P=2.0$, the transmission coefficient $|T_P|$ is generally in between the previous cases. Its is nevertheless lower than the $\chi_P=3.0$ case between 30 and 50 degrees but higher than the $\chi_P=1.5$ case for all incidences above 50 degrees.

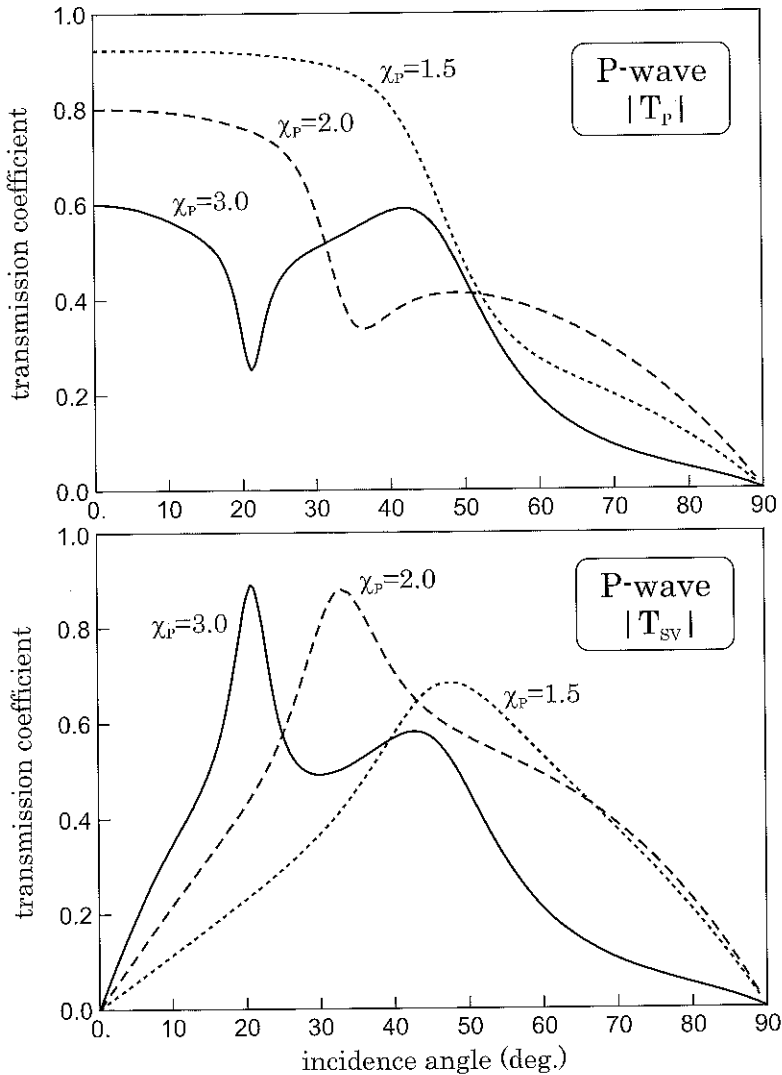


Fig. 3.17: Transmission coefficients: $|T_P|$ (top) and $|T_{SV}|$ (bottom) vs incidence for different velocity ratios: $\chi_P=1.5$, $\chi_P=2.0$ and $\chi_P=3.0$ (single-layer case, incident P-wave).

It is even more complicated for $|T_{SV}|$, the transmission coefficient of SV-waves (Fig. 3.17, bottom). For instance, the lowest velocity ratio ($\chi_P=1.5$) leads to the lowest transmission coefficient for incidences below 40 degrees. Since the amount of transmitted P-waves is larger in this case, the contribution of converted SV-waves is much lower. To investigate the optimal configurations, both transmission coefficients $|T_P|$ and $|T_{SV}|$ should be simultaneously considered.

Transmittivity of a plane SV-wave through a single layer

Displacement and traction. As shown in Fig. 3.18, for an oblique incident SV-wave, the wavefield is converted into two wave types: P-wave and SV-wave. The displacement fields are the following:

- incident SV-wave:

$$\begin{cases} u_x^{(i-SV)} = A_{SV} \sin \theta_i^{SV} \exp \left[\frac{i\omega}{V_S} (x \cos \theta_i^{SV} + z \sin \theta_i^{SV} - V_S t) \right] \\ u_y^{(i-SV)} = 0 \\ u_z^{(i-SV)} = A_{SV} \cos \theta_i^{SV} \exp \left[\frac{i\omega}{V_S} (x \cos \theta_i^{SV} + z \sin \theta_i^{SV} - V_S t) \right] \end{cases} \quad (3.108)$$

where V_S is the shear wave velocity and θ_i^{SV} the incidence angle of the SV-wave.

- resulting (reflected) P-wave:

$$\begin{cases} u_x^{(R-P)} = R_P \cos \theta_R^P \exp \left[\frac{i\omega}{V_P} (x \cos \theta_R^P - z \sin \theta_R^P - V_P t) \right] \\ u_y^{(R-P)} = 0 \\ u_z^{(R-P)} = R_P \sin \theta_R^P \exp \left[\frac{i\omega}{V_P} (x \cos \theta_R^P - z \sin \theta_R^P - V_P t) \right] \end{cases} \quad (3.109)$$

where V_P is the P wave velocity and θ_i^P the incidence angle of the P-wave.

Equations of continuity. At the second interface, the continuity conditions for both displacements and tractions are the same as in the case of an incident P-wave. One must rewrite the continuity conditions at the first interface only, thus:

- first interface:

– first component of displacement:

$$-R_P \cos \theta_R^P + (A_{SV} + R_{SV}) \sin \theta_i^{SV} = (T'_P - R'_P) \cos \theta_{T'}^P + (T'_{SV} + R'_{SV}) \sin \theta_{T'}^{SV} \quad (3.110)$$

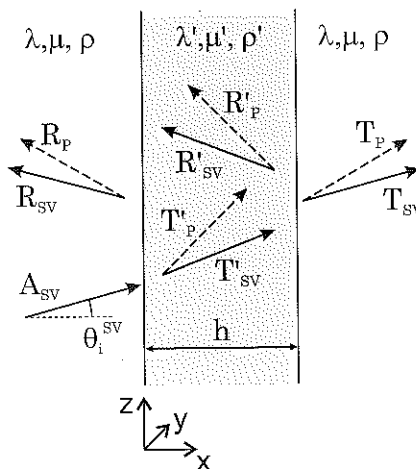


Fig. 3.18: Propagation of a SV-wave with oblique incidence in a single infinite layer model.

– third component of displacement:

$$\begin{aligned} R_P \sin \theta_R^P + (-A_{SV} + R_{SV}) \cos \theta_i^{SV} = \\ (T'_P + R'_P) \sin \theta_{T'}^P - (T'_{SV} - R'_{SV}) \cos \theta_{T'}^{SV} \end{aligned} \quad (3.111)$$

– first component of traction:

$$\begin{aligned} \frac{A_{SV}}{V_S} \mu \sin 2\theta_i^{SV} + \frac{R_P}{V_P} (\lambda + 2\mu \cos^2 \theta_R^P) - \frac{R_{SV}}{V_S} \mu \sin 2\theta_R^{SV} = \\ \frac{T'_P}{V'_P} (\lambda' + 2\mu' \cos^2 \theta_{T'}^P) - \frac{T'_{SV}}{V'_S} \mu' \sin 2\theta_{T'}^{SV} \\ + \frac{R'_P}{V'_P} (\lambda' + 2\mu' \cos^2 \theta_{R'}^P) - \frac{R'_{SV}}{V'_S} \mu' \sin 2\theta_{R'}^{SV} \end{aligned} \quad (3.112)$$

– third component of traction:

$$\begin{aligned} -\mu \frac{A_{SV}}{V_S} \cos 2\theta_i^{SV} - \mu \frac{R_P}{V_P} \sin 2\theta_R^P - \mu \frac{R_{SV}}{V_S} \cos 2\theta_R^{SV} = \\ \mu' \frac{T'_P}{V'_P} \sin 2\theta_{T'}^P - \mu' \frac{T'_{SV}}{V'_S} \cos 2\theta_{T'}^{SV} \\ - \mu' \frac{R'_P}{V'_P} \sin 2\theta_{R'}^P - \mu' \frac{R'_{SV}}{V'_S} \cos 2\theta_{R'}^{SV} \end{aligned} \quad (3.113)$$

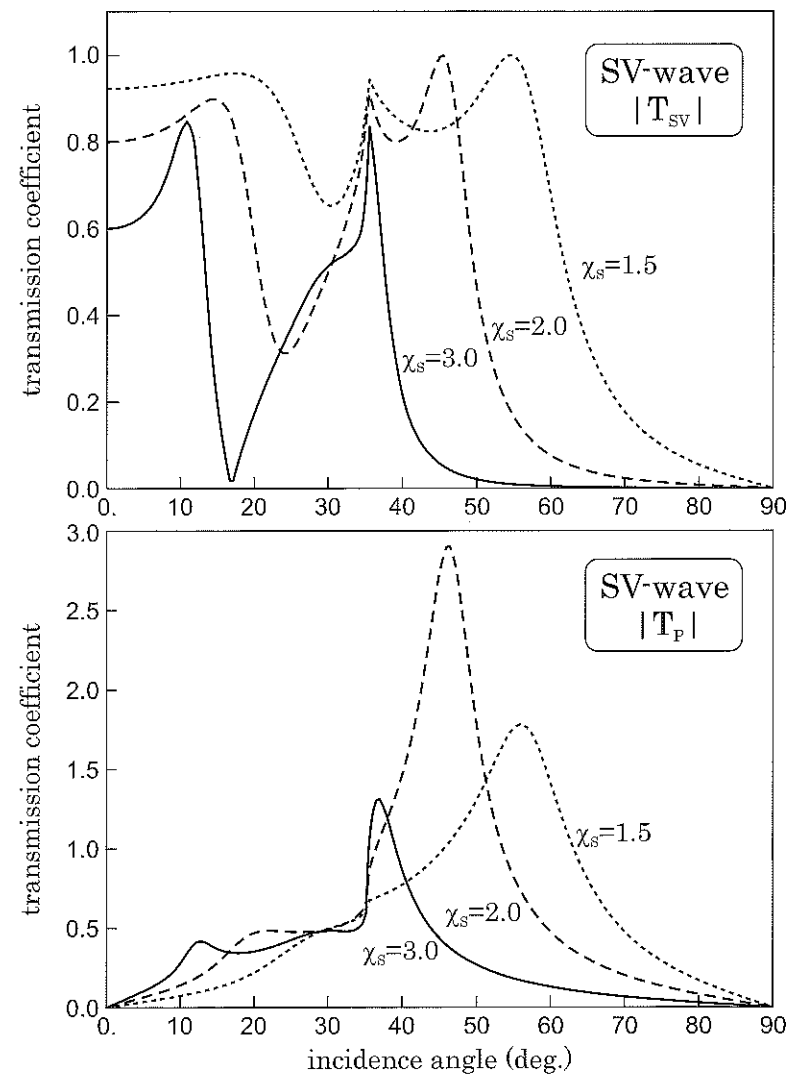


Fig. 3.19: Transmission coefficient: $|T_{SV}|$ (top) and $|T_P|$ (bottom) vs incidence for different velocity ratios: $\chi_s=1.5$, $\chi_s=2.0$ and $\chi_s=3.0$ (single layer case, incident SV-wave).

Transmission coefficients. For an incident SV-wave, Fig.3.19 gives two types of results: $|T_{SV}|$ transmission coefficient for SV-waves (top) and $|T_P|$ transmission coefficient for P-waves (bottom). For a normal incidence ($\theta_i^{SV}=0$), $|T_P|$ is always zero. For an oblique incidence, the values of $|T_{SV}|$ show very strong variations (Fig.3.19, top). It is due to the fact that, for an incident SV-wave, the P-wave incidence is larger than the SV-

wave incidence and a critical angle thus appears. It leads to an inhomogeneous P -wave (i.e. interface wave) propagating vertically and a very large transmission coefficient $|T_P|$ for P -waves (Fig.3.19, bottom). Depending on the velocity ratio, the maximum value of $|T_P|$ ranges from 1.3 ($\chi_S=3.0$) to nearly 3.0 ($\chi_S=2.0$). Such transmission coefficients larger than 1 are nevertheless valid from an energetic point of view since the refracted P -wave does not actually propagate beyond the layer since its direction of propagation is vertical (exponential decay in the horizontal direction). For applications in vibratory isolation, such conclusions (local "amplification" but strong spatial decay) should be taken into account.

Transmittivity in the multilayered case

Various configurations. The case of an infinite single layer is very simple to solve since it is governed by two parameters only: the velocity ratio χ and the layer thickness h . In the multilayered case, several velocity ratios and layer thicknesses have to be considered. One has to determine the optimum layers arrangement depending on the isolation level required. In this section, different multilayered cases are compared to the one-layer case. As shown in Fig.3.20, we shall especially consider two alternative configurations involving two layers.

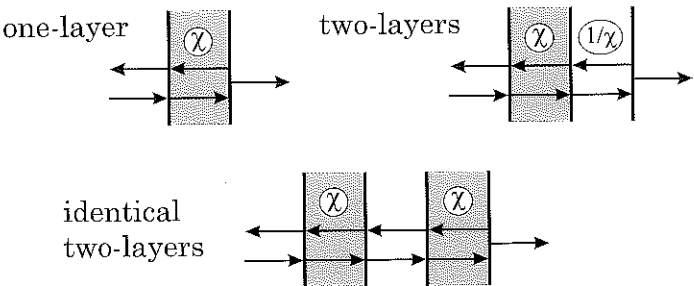


Fig. 3.20: Various multilayered configurations: one-layer (top left), two-layers (top right) and identical two-layers (bottom).

Two-layers case. In the two-layers case (Fig.3.20), we consider a normally incident SH -wave in a free-space including two infinite layers of constant thickness:

- the first layer having a shear wave velocity V_1 , the velocity ratio with the free-space is $\chi_S = V_1/V_0$. Its thickness is denoted h_1 ,
- the second layer having a shear wave velocity V_2 , the velocity ratio with the free-space is chosen as $\chi'_S = 1/\chi_S$ leading to $V_2 = 1/V_1$. Its thickness is denoted h_2 .

If the first layer is stiffer than the infinite medium (larger velocity), the second one will be softer (lower velocity). The aim is then to have a higher contrast between both layers

3.3 Wave propagation in unbounded media

(χ_S^2) than between the infinite medium and the first layer (χ_S). It should lead to a lower transmission coefficient than the one-layer case.

To solve the two-layer case, the equations of continuity for displacements and tractions must now be written at all three interfaces (Semblat, 1989):

- first interface:

$$\begin{cases} \text{displacement: } A_{SH} + R_{SH} = T'_{SH} + R'_{SH} \\ \text{traction: } A_{SH} - R_{SH} = \chi_S T'_{SH} - \chi_S R'_{SH} \end{cases} \quad (3.114)$$

- second interface:

$$\begin{cases} \text{displacement: } e_1^+ T'_{SH} + e_1^- R'_{SH} = e_2^+ T''_{SH} + e_2^- R''_{SH} \\ \text{traction: } e_1^+ T'_{SH} - e_1^- R'_{SH} = \frac{e_2^+}{\chi_S} T''_{SH} - \frac{e_2^-}{\chi_S} R''_{SH} \end{cases} \quad (3.115)$$

- third interface:

$$\begin{cases} \text{displacement: } e_2^+ T''_{SH} + e_2^- R''_{SH} = e^+ T_{SH} \\ \text{traction: } e_2^+ T''_{SH} - e_2^- R''_{SH} = \chi_S e^+ T_{SH} \end{cases} \quad (3.116)$$

where $e_1^+ = \exp(i\omega \frac{h_1}{V_1})$, $e_2^+ = \exp(i\omega \frac{h_1+h_2}{V_2})$, $e_{21}^+ = \exp(i\omega \frac{h_1}{V_2})$ and $e^+ = \exp(i\omega \frac{h_1+h_2}{V_0})$ (similarly for e_1^- , e_2^- and e_{21}^-).

For the second interface, we obtain a factor $1/\chi_S^2$ due to the velocity ratio between both layers which is larger than in the one-layer case. The definition of the transmission coefficient T_{SH} being now the following:

$$T_{SH} = \frac{T_{SH}}{A_{SH}} e^+$$

its expression is obtained by solving the equations of continuity at the three interfaces:

$$T_{SH} = \frac{4\chi_S^2(f_1(\chi_S) + 1)e_1^+ e_2^+}{(1 - \chi_S^2)(\chi_S^2 f_1(\chi_S) - 1)e_2^{2+} e_{21}^- + (1 + \chi_S)^2(\chi_S^2 f_1(\chi_S) + 1)e_{21}^+} \quad (3.117)$$

$$\text{with } f_1(\chi_S) = \frac{(\chi_S + 1)e_1^- - (\chi_S - 1)e_1^+}{(\chi_S + 1)e_1^- + (\chi_S - 1)e_1^+} \quad (3.118)$$

For a normally incident SH -wave, the transmission coefficient T_{SH} is minimum for the following layers thicknesses: $h_1 = \Lambda_1/4$ and $h_2 = \Lambda_2/4$. It may then be expressed under a simplified form:

$$|T_{SH}| = g(\chi_S) = \frac{2\chi_S^2}{1 + \chi_S^4} \quad (3.119)$$

The function $g(\chi_S)$ has the same property as the function $f(\chi_S)$ (defined by Eq.(3.91)), that is: $g(\chi_S) = g(1/\chi_S)$. The two-layers case leads to the same results with the first

layer having a velocity ratio χ_S ($1/\chi_S$ for the second layer resp.) or the first layer having a velocity ratio $1/\chi_S$ (χ_S for the second layer resp.). Furthermore, the velocity ratio between both layers being $1/\chi_S^2$, the isolation efficiency should be much larger in the two-layers than in the one-layer case. Considering the expressions of the functions f and g (Eqs (3.91) and (3.119)), this velocity ratio directly appears when comparing both functions:

$$g(\chi_S) = f(\chi_S^2) = f\left(\frac{1}{\chi_S^2}\right) \quad (3.120)$$

For a normally incident SH -wave and a given velocity ratio, it means that the isolation efficiency in the one-layer case is much smaller than in the two-layers case. The f and g functions are displayed in Fig.3.21 to assess the influence of the velocity ratio in both cases.

The results of the two-layers case for an oblique incidence are displayed in Fig.3.22. They correspond to the following layer thicknesses: $h_1 = \Lambda_1/8$ et $h_2 = \Lambda_2/8$ (where Λ_j are the wavelengths in both layers). The comparison with other cases will be discussed in the following.

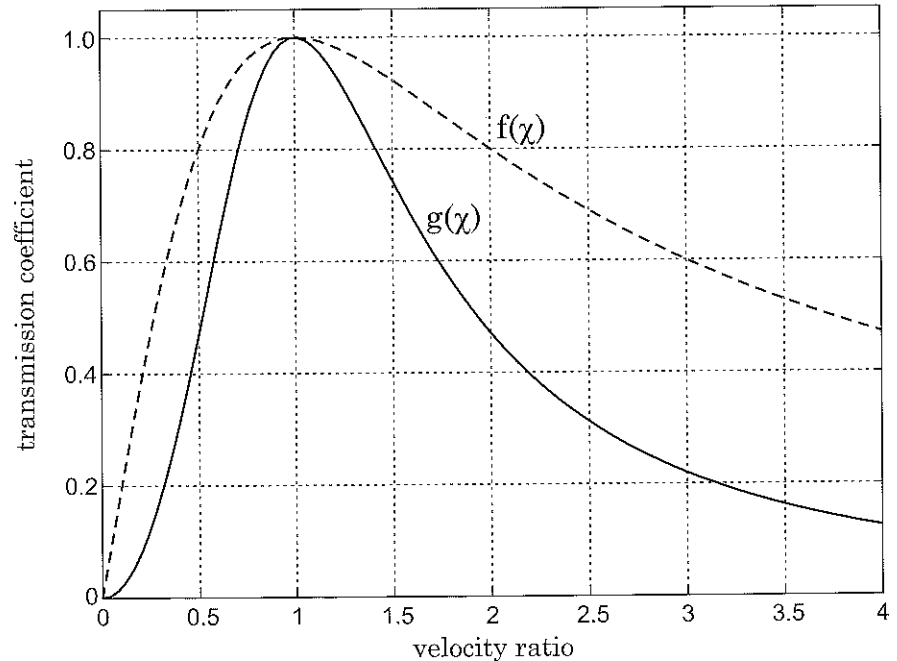


Fig. 3.21: Comparison between the one-layer (dashed) and the two-layers (solid) cases for a normally incident SH -wave: functions f and g vs velocity ratio χ .

Identical two-layers case. In the "identical two-layers" case (Fig.3.20, bottom), we consider two identical layers embedded in a free-space. The two layers are separated by an infinite layer having the same properties as the free-space. The main objective is now to assess the efficiency of a configuration involving two layers with identical properties and to perform a comparison with the two-layers case studied previously.

The equations of continuity will now be considered at the four interfaces:

- first interface:

$$\begin{cases} \text{displacement: } A_{SH} + R_{SH} = T'_{SH} + R'_{SH} \\ \text{traction: } A_{SH} - R_{SH} = \chi_S T'_{SH} - \chi_S R'_{SH} \end{cases} \quad (3.121)$$

- second interface:

$$\begin{cases} \text{displacement: } e_{11}^+ T'_{SH} + e_{11}^- R'_{SH} = e_1^+ T''_{SH} + e_1^- R''_{SH} \\ \text{traction: } e_{11}^+ T'_{SH} - e_{11}^- R'_{SH} = \frac{e_1^+}{\chi_S} T''_{SH} - \frac{e_1^-}{\chi_S} R''_{SH} \end{cases} \quad (3.122)$$

- third interface:

$$\begin{cases} \text{displacement: } e_2^+ T''_{SH} + e_2^- R''_{SH} = e_{12}^+ T'''_{SH} + e_{12}^- R'''_{SH} \\ \text{traction: } e_2^+ T''_{SH} - e_2^- R''_{SH} = \chi_S e_{12}^+ T'''_{SH} - \chi_S e_{12}^- R'''_{SH} \end{cases} \quad (3.123)$$

- fourth interface:

$$\begin{cases} \text{displacement: } e_{13}^+ T'''_{SH} + e_{13}^- R'''_{SH} = e_3^+ T_{SH} \\ \text{traction: } e_{13}^+ T'''_{SH} - e_{13}^- R'''_{SH} = \frac{e_3^+}{\chi_S} T_{SH} \end{cases} \quad (3.124)$$

where $e_{11}^+ = \exp(i\omega \frac{h_1}{V_1})$, $e_{12}^+ = \exp(i\omega \frac{h_1+h_2}{V_1})$, $e_{13}^+ = \exp(i\omega \frac{h_1+h_2+h_3}{V_1})$, $e_1^+ = \exp(i\omega \frac{h_1}{V_0})$, $e_2^+ = \exp(i\omega \frac{h_1+h_2}{V_2})$ and $e_3^+ = \exp(i\omega \frac{h_1+h_2+h_3}{V_0})$ (similarly for e_{11}^- , e_{12}^- , e_{13}^- , e_1^- and e_2^-).

The expression of the transmission coefficient T_{SH} for the identical two-layers case is the following:

$$T_{SH} = \frac{2\chi_S \frac{f_1(\chi_S) - 1}{f_1(\chi_S) - \chi_S} e_{12}^- e_{11}^+ e_1^- e_2^+ e_3^- \left(1 + f_2(\chi_S) \frac{1 - \chi_S}{1 + \chi_S}\right)}{(\chi_S + 1) e_{13}^- e_1^+ - (\chi_S - 1) f_2(\chi_S) e_{12}^{2-} e_{13}^+} \quad (3.125)$$

$$\text{with } f_2(\chi_S) = \frac{\frac{f_1(\chi_S) + \chi_S}{f_1(\chi_S) - \chi_S} (\chi_S + 1) e_1^{2-} e_2^+ + (\chi_S - 1) e_1^-}{\frac{f_1(\chi_S) + \chi_S}{f_1(\chi_S) - \chi_S} (\chi_S - 1) e_1^{2-} e_2^+ + (\chi_S + 1) e_1^-} \quad (3.126)$$

The results of the identical two-layers are displayed in Fig.3.22 for the following values of the layers thicknesses: $h_1 = \Lambda_1/8$, $h_2 = \Lambda_2/4$ and $h_3 = \Lambda_3/8$ respectively.

Comparison of the multilayered cases

Incident SH-wave. The results shown in Fig.3.22 assess the better efficiency of the two-layers case when compared to the one-layer and the identical two-layers cases. Only for very large incidences does the two-layers case give larger transmission coefficients. For very small incidences, the identical two-layers case is more efficient than the one-layer case. At other incidences there is a slight difference between both cases.

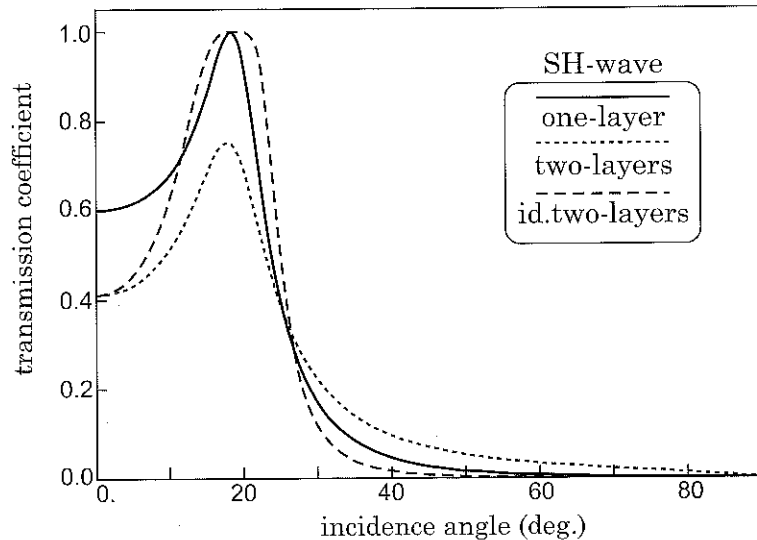


Fig. 3.22: Transmission coefficient vs incidence for various multilayered configurations (incident SH-wave).

Incident P-wave. We also considered the multilayered cases for an incident *P*-wave. As shown in Fig.3.23, the two-layers case is much more efficient than both other cases (except for large incidences). The identical two-layers case has a complex behaviour since, for large incidences, it leads to lower transmission coefficients for *P*- and *SV*-waves than the one-layer case. For small incidences, it leads to close results for *SV*-waves and lower or larger results for *P*-waves depending on the incidence range.

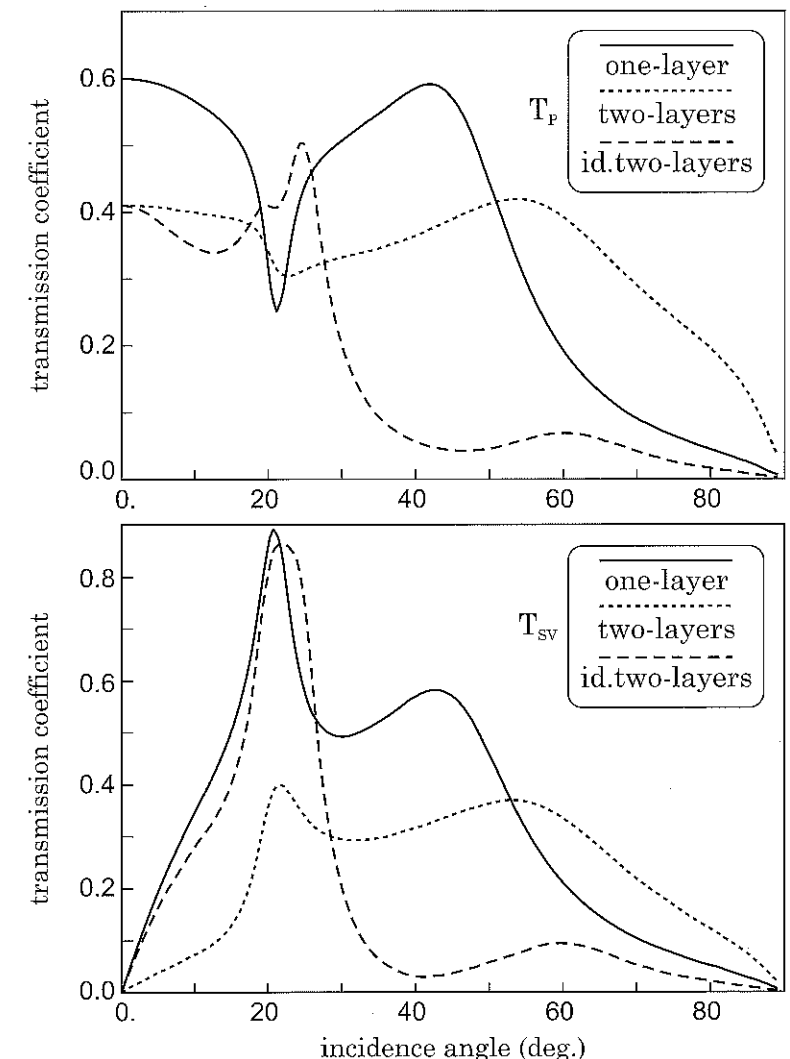


Fig. 3.23: Transmission coefficients $|T_P|$ (top) and $|T_{SV}|$ (bottom) vs incidence for various multilayered configurations (incident *P*-wave).

3.4 Spherical waves

3.4.1 Wave equation

From a practical point of view, the case of plane waves studied in the previous sections is very useful since, for the far-field, it is possible to assume a plane wavefront. However, for the analysis of near-field propagation, this approximation is no longer valid. The solution then depends on the nature of the displacement (or stress) field induced by the source. In this section, we consider the case for which the emitted waves have a spherical symmetry.

Under this assumption, the only displacement component is, due to the symmetry, the radial one denoted u_r . Considering a spherical coordinate system, the equations of propagation are thus reduced to:

$$\frac{\partial^2 u_r}{\partial r^2} + \frac{2}{r} \frac{\partial u_r}{\partial r} - \frac{2u_r}{r^2} = \frac{1}{V_P^2} \frac{\partial^2 u_r}{\partial t^2} \quad (3.127)$$

The equation governing the potential is expressed under a similar form:

$$\frac{\partial^2 \phi}{\partial r^2} + \frac{2}{r} \frac{\partial \phi}{\partial r} = \frac{1}{V_P^2} \frac{\partial^2 \phi}{\partial t^2} \quad (3.128)$$

Choosing the new variable $\varphi = r\phi$, Eq.(3.128) may be simplified:

$$\frac{\partial^2 \varphi}{\partial r^2} = \frac{1}{V_P^2} \frac{\partial^2 \varphi}{\partial t^2} \quad (3.129)$$

3.4.2 Solution wavefield

The previous equation corresponds to the wave equation of longitudinal waves leading to a general solution of the form:

$$\phi(r, t) = \frac{\varphi(r, t)}{r} = \frac{1}{r} [f(r - V_P t) + g(r + V_P t)] \quad (3.130)$$

In this equation, the two terms correspond to waves propagating away from the source and waves converging to the source respectively. In a free-space, no wave reflection occurs and no wave converging to the source may appear: the $g(r + V_P t)$ is thus zero. This condition is known as the Sommerfeld radiation condition. The displacement is now given by:

$$u_r(r, t) = \frac{\partial \phi}{\partial r} = -\frac{1}{r^2} f(r - V_P t) + \frac{1}{r} f'(r - V_P t) \quad (3.131)$$

In the case of a monochromatic wave, expressions similar to Eqs (3.130) and (3.131) are derived:

$$\phi(r, \omega) = \frac{A}{r} \exp \left[\frac{i\omega}{V_P} (r - V_P t) \right] \quad (3.132)$$

3.4 Spherical waves

$$u_r(r, \omega) = A \left(-\frac{1}{r^2} + \frac{i\omega}{r V_P} \right) \exp \left[\frac{i\omega}{V_P} (r - V_P t) \right] \quad (3.133)$$

The quantities $f(\cdot)$ or A are determined through the initial and the boundary conditions of the problem. Thus, in the case of a spherical cavity of radius R loaded by a radial pressure, $p(t)$, we get $\sigma_{rr}(R, T) = -p(t)$. Knowing the displacement field, we may derive the stresses originating in the medium considering its constitutive law (linear elasticity herein). We recall that, for spherical symmetry, the only non zero components of the stress tensor are σ_{rr} , $\sigma_{\theta\theta}$ and $\sigma_{\varphi\varphi}$. These variables have the following expression:

$$\begin{cases} \sigma_{rr} = (\lambda + 2\mu) \frac{\partial u_r}{\partial r} + 2\lambda \frac{u_r}{r} \\ \sigma_{\theta\theta} = \sigma_{\varphi\varphi} = \lambda \frac{\partial u_r}{\partial r} + 2(\lambda + \mu) \frac{u_r}{r} \end{cases} \quad (3.134)$$

The σ_{rr} component corresponds to the radial effect whereas the $\sigma_{\theta\theta}$ and $\sigma_{\varphi\varphi}$ components are related to purely tangential effects.

Considering these results, we can for instance determine the eigenmodes of the entire Earth assuming a homogeneous elastic sphere³.

3.4.3 Geometrical damping

Equations (3.132) and (3.133) show that the wavefront, location of the points with constant ϕ , corresponds to a sphere centered at the source. The wavefront expands during propagation and the amplitude of displacement decreases because of the conservation of energy. The expansion of the wavefront thus induces an amplitude decay; this decay, similar to the effect of damping, is called geometrical damping. It is important to notice that it is not related to damping that could be due to the dissipative properties of the medium. In this section, the medium is non dissipative but the geometrical damping leads to a spatial amplitude decay only due to the expansion of the wavefront.

As shown in Eq.(3.133), the amplitude decay in terms of displacement has two different forms:

- a fast decaying term ($1/r^2$) corresponding to near-field (i.e. near source) effects,
- a slower decay ($1/r$ term) corresponding to far-field effects.

³Realistic Earth models are available from various teams. The corresponding analyses generally involve both rotating and self-gravitating assumptions which lead to much more complicated equations (Chaljub *et al.*, 2003).

3.5 Waves in a homogeneous or heterogeneous half-space

3.5.1 Surface waves: SH case

As depicted in Fig.3.24, we shall now consider the case of a plane monochromatic *SH*-wave reflected at the free-surface of the soil (assumed as a homogeneous half-space). The incident displacement field reads as follows:

$$\begin{cases} u_y^{(i)} = A_{SH} \exp\left[\frac{i\omega}{V_S}(x \sin \theta_i + z \cos \theta_i - V_S t)\right] \\ u_x^{(i)} = u_z^{(i)} = 0 \end{cases} \quad (3.135)$$

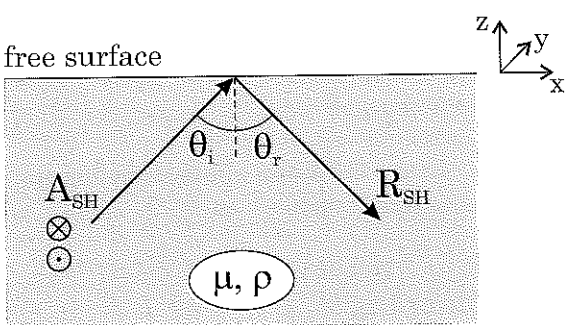


Fig. 3.24: Reflection of a plane *SH*-wave at a free-surface.

Accounting for the uncoupling of *SH*-waves, the reflected wave must be defined by a pure *SH*-wave related to an antiplane displacement such as:

$$u_y^{(R)} = R_{SH} \exp\left[\frac{i\omega}{V_S}(x \sin \theta_R - z \cos \theta_R - V_S t)\right] \quad (3.136)$$

The free-surface condition can be derived considering that, for $z=0$, the traction is zero:

$$\underline{t} = \underline{t}^{(i)} + \underline{t}^{(R)} \quad (3.137)$$

At the free-surface ($z=0$), the traction $\underline{t} = \underline{\sigma} \cdot \underline{n}$ has the following components: $\{\sigma_{xz}, \sigma_{yz}, \sigma_{zz}\}$. Considering the constitutive law and the expression of the displacement field, these components are reduced to: $\{0, \sigma_{yz}, 0\}$ where:

$$\sigma_{yz} = \mu \frac{\partial u_y}{\partial z} \quad (3.138)$$

From Eqs (3.136) and (3.138), we obtain that, at the free-surface $z=0$:

$$\begin{cases} \underline{t}^{(i)} = \mu A_{SH} \frac{i\omega}{V_S} \cos \theta_i \exp\left[\frac{i\omega}{V_S}(x \sin \theta_i - V_S t)\right] \\ \underline{t}^{(R)} = -\mu R_{SH} \frac{i\omega}{V_S} \cos \theta_R \exp\left[\frac{i\omega}{V_S}(x \sin \theta_R - V_S t)\right] \end{cases} \quad (3.139)$$

Introducing this expressions in Eq.(3.137) and writing that this condition must remain valid at every time t and every location x , we thus derive:

$$\theta_R = \theta_i \quad , \quad A_{SH} = R_{SH} \quad (3.140)$$

The displacement resulting from the superposition of the incident and reflected waves has the following expression:

$$u_y = u_y^{(i)} + u_y^{(R)} = 2A_{SH} \cos\left(\frac{\omega z \cos \theta_i}{V_S}\right) \exp\left[\frac{i\omega}{V_S}(x \sin \theta_i - V_S t)\right] \quad (3.141)$$

The reflected wave has the same amplitude as the incident wave and the angle of reflection is equal to the angle of incidence. At a depth z , the total amplitude of the motion is:

$$|u_y| = 2A_{SH} \cos\left(\frac{\omega z \cos \theta_i}{V_S}\right) \quad (3.142)$$

3.5.2 Surface waves: P/SV case

We already mentioned that other wave types than body waves may propagate in semi-infinite media. Such waves, called *surface waves*, correspond to the case where one of the components of the normalized wave vector \underline{l} , characterizing the direction of propagation, becomes purely imaginary. These waves are characterized by an exponential decay of displacement away from the free-surface.

Form of the wavefield

Considering the case of a plane wave propagating in the $x-z$ plane, such that l_z is purely imaginary. In such conditions, the potentials ϕ and ψ can be written as follows:

$$\phi = A e^{az} \exp\left[\frac{i\omega}{V_R}(x - V_R t)\right] \quad (3.143)$$

$$\psi = B e^{bz} \exp\left[\frac{i\omega}{V_R}(x - V_R t)\right] \quad (3.144)$$

where V_R is the velocity of the surface wave. The potentials given by the previous equations must fulfil the corresponding wave equations. As a result, the constants a , b , V_R must satisfy the relations:

$$a^2 = \frac{\omega^2}{V_R^2} - \frac{\omega^2}{V_P^2} \quad (3.145)$$

$$b^2 = \frac{\omega^2}{V_R^2} - \frac{\omega^2}{V_S^2} \quad (3.146)$$

The displacement field may thus be derived under the following form:

$$\begin{cases} u_x = \frac{\partial \phi}{\partial x} - \frac{\partial \psi_2}{\partial z} = \left(\frac{i\omega}{V_R} A e^{az} - b B_2 e^{bz} \right) \exp \left[\frac{i\omega}{V_R} (x - V_R t) \right] \\ u_y = \frac{\partial \psi_1}{\partial z} - \frac{\partial \psi_3}{\partial x} = \left(b B_1 - \frac{i\omega}{V_R} B_3 \right) e^{bz} \exp \left[\frac{i\omega}{V_R} (x - V_R t) \right] \\ u_z = \frac{\partial \phi}{\partial z} + \frac{\partial \psi_2}{\partial x} = \left(a A e^{az} + \frac{i\omega}{V_R} B_2 e^{bz} \right) \exp \left[\frac{i\omega}{V_R} (x - V_R t) \right] \end{cases} \quad (3.147)$$

Free-surface condition

The free-surface condition implies the nullity of the traction in the $z=0$ plane. It is thus straightforward ($\sigma_{yz}=0$) that the displacement u_y is always zero. Taking into account the constitutive law, the nullity of the traction, of components σ_{xz} and σ_{zz} , leads to the following relations:

$$\sigma_{zz}(z=0) = \lambda \frac{\partial u_x}{\partial x} + (\lambda + 2\mu) \frac{\partial u_z}{\partial z} = A \left[(\lambda + 2\mu)a^2 - \frac{\omega^2}{V_R^2} \lambda \right] + 2i\mu \frac{\omega}{V_R} b B_2 = 0 \quad (3.148)$$

$$\sigma_{xz}(z=0) = \mu \left(\frac{\partial u_x}{\partial z} + \frac{\partial u_z}{\partial x} \right) = 2iAa \frac{\omega}{V_R} - \left(b^2 + \frac{\omega^2}{V_R^2} \right) B_2 = 0 \quad (3.149)$$

Equations (3.148) and (3.149) have a non trivial solution in A and B_2 if, and only if, the determinant of the linear system is zero. Denoting $\beta^2 = \mu/(\lambda+2\mu)$ and $\chi_R = V_R/V_S$, we obtain the following equation:

$$\chi_R^6 - 8\chi_R^4 + (24 - 16\beta^2)\chi_R^2 + 16(\beta^2 - 1) = 0 \quad (3.150)$$

This equation is known as the Rayleigh equation. It is possible to show that it has a solution V_R satisfying the inequality $0 < V_R < V_S$ (Achenbach, 1973). This solution depends on the β ratio that is on the Poisson's ratio of the medium since, considering the relations given in Table 3.1, $\beta^2 = (1 - 2\nu)/(2 - 2\nu)$. In Table 3.3, the values of the V_R/V_S ratio are given for Poisson's ratios ranging from 0.0 to 0.5.

It should be noticed that the velocity V_R in a homogeneous half-space does not depend on the frequency ω ; the Rayleigh waves are then non dispersive. As it will be discussed for methods of analysis of surface waves (§3.7), this feature is no longer valid in a layered medium.

To estimate the velocity of Rayleigh waves V_R , a useful approximation is given by:

$$V_R = \frac{0.862 + 1.14\nu}{1 + \nu} V_S \quad (3.151)$$

Table 3.3: Velocities of Rayleigh waves for various Poisson's ratios.

Poisson's ratio	V_R/V_S
$\nu=0.00$	0.862
$\nu=0.25$	0.919
$\nu=0.33$	0.932
$\nu=0.50$	0.955

Solution wavefield

Considering Eqs (3.148) and (3.149), the displacements (3.147) are derived in the following form:

$$\begin{cases} u_x = \frac{i\omega}{V_R} A \left(e^{az} - \frac{2ab}{b^2 + \omega^2/V_R^2} e^{bz} \right) \exp \left[\frac{i\omega}{V_R} (x - V_R t) \right] \\ u_z = a A \left(e^{az} - \frac{2\omega^2/V_R^2}{b^2 + \omega^2/V_R^2} e^{bz} \right) \exp \left[\frac{i\omega}{V_R} (x - V_R t) \right] \end{cases} \quad (3.152)$$

The wavefields fulfilling the previous relations are called Rayleigh waves, from the name of Lord Rayleigh who evidenced such waves first. The imaginary term i in the expression of the horizontal displacement shows that this component has a 90° phase shift from the vertical displacement. As depicted in Fig.3.25, the motion of the material points follows retrograde ellipses in the $x-z$ plane. One should notice that the amplitude of displacement decreases faster with depth for shorter wavelengths $\Lambda = 2\pi V_R/\omega$.

Rayleigh waves

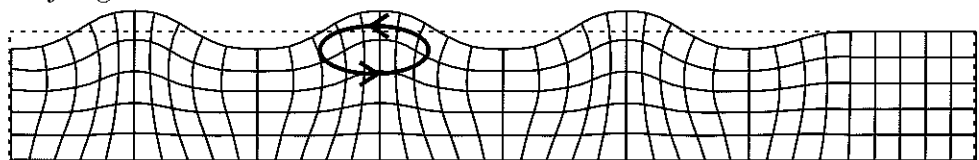


Fig. 3.25: Wavefield due to surface waves showing the elliptic motion near the free-surface.

For $\nu=0.25$, Fig.3.26 displays the variations of the horizontal and vertical displacements with depth. In this figure, the surface horizontal displacement is normalized to 1.0.

When the motion is perpendicular to the propagation plane ($u_x = u_z = 0, u_y \neq 0$), surface waves are called Love waves (Fig.3.27). The velocity of Love waves is equal to that of shear waves (V_S). Waves having an exponential decay with depth do not only occur at a free-surface, but may also appear at the interface between two media with different mechanical properties. It is for instance possible to have surface waves at the

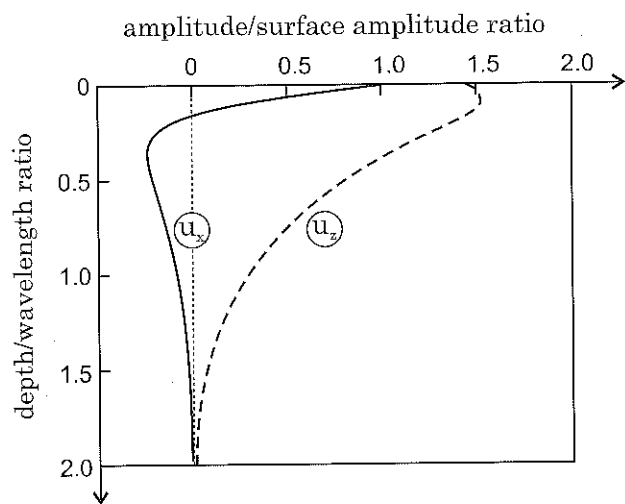


Fig. 3.26: Horizontal and vertical displacements due to Rayleigh waves in an elastic half-space ($\nu=0.25$).

interface between a solid and a fluid or at the interface between two solids (Aki and Richards, 1980). Such waves, for which the motion is located in the propagation plane ($u_x \neq 0, u_y = 0, u_z \neq 0$), are called *Stoneley waves*.

3.5.3 Propagation of a plane SH-wave in a surface layer

We have just shown that, in the case of plane monochromatic waves, the horizontal displacement in the direction perpendicular to the propagation plane was uncoupled from the other components of displacement and may be written as:

$$u = A \exp \left[\frac{i\omega}{V_S} (x \sin \theta + z \cos \theta - V_S t) \right] \quad (3.153)$$

To simplify the notation, the indices have been omitted: the displacement u denotes the u_y component of displacement (for a propagation in the $x - z$ plane), and A is the amplitude of the *SH*-wave.

Layer over a half-space

Considering a layer of constant thickness overlying a half-space (Fig. 3.28), we can calculate the motion in the surficial layer and in the half-space. The solution corresponding to this configuration can be obtained by using the same methodology as in the previous sections (continuity of displacement and traction at the interface, free-surface condition).

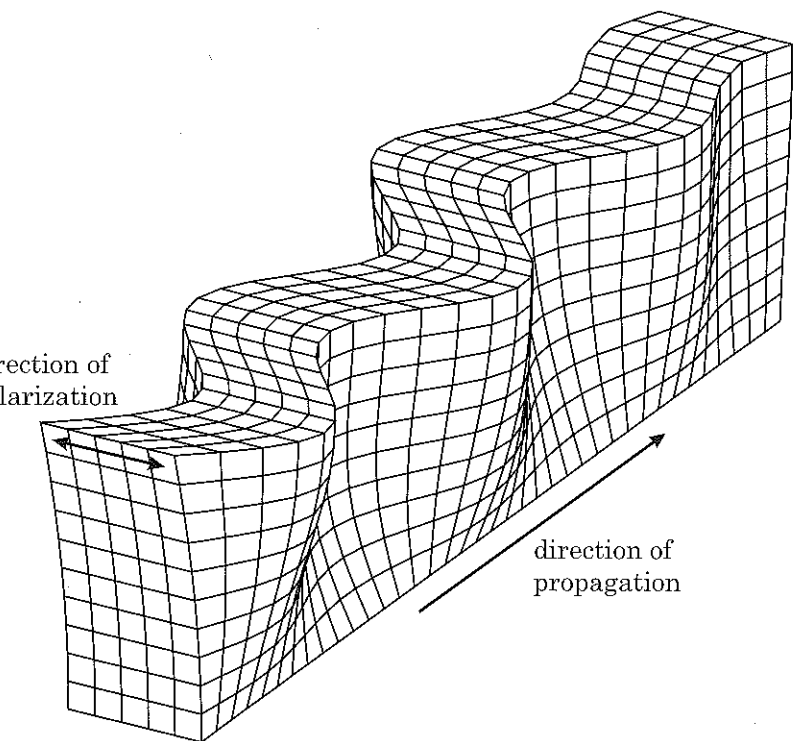


Fig. 3.27: Displacements due to Love waves in an elastic half-space.

In each medium, the total motion resulting from the superposition of the waves propagating in the upwards direction ($z > 0$) and the downward direction ($z < 0$) is written choosing the origin of the z axis at the top of each medium:

$$u_n = [A_n \exp(ik_{z_n} z_n) + A'_n \exp(-ik_{z_n} z_n)] f_n(x, t) \quad (3.154)$$

where k_{z_n} is the vertical wavenumber in medium n defined as:

$$k_{z_n} = \frac{\omega \cos \theta_n}{V_{S_n}} \quad (3.155)$$

$$f_n(x, t) = \exp \left[\frac{i\omega}{V_{S_n}} (x \sin \theta_n - V_{S_n} t) \right] \quad (3.156)$$

The index n is used to identify each medium: $n = 1$ for the surficial layer and $n = 2$ for the half-space. A_n and A'_n are the amplitudes of the waves propagating in the directions $z > 0$ and $z < 0$ respectively.

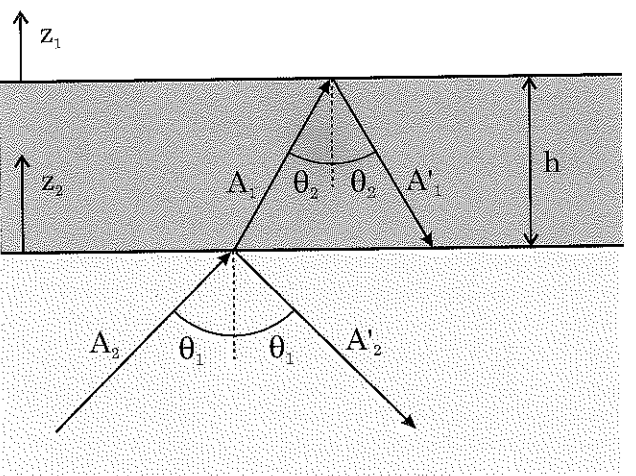


Fig. 3.28: Plane SH -wave in a layer of constant thickness h over an elastic half-space.

Conditions at the interfaces

The free-surface condition (§3.5.1) yields:

$$A_1 = A'_1 \quad (3.157)$$

The compatibility conditions at the interface thus leads to:

- continuity of displacement $u_1(z = -h) = u_2(z = 0)$, that is:

$$A_1 (e^{-ik_{z_1}h} + e^{+ik_{z_1}h}) f_1(x, t) = (A_2 + A'_2) f_2(x, t) \quad (3.158)$$

from which, the relation being valid for all x and all t , we derive:

$$\frac{\sin \theta_1}{V_{S_1}} = \frac{\sin \theta_2}{V_{S_2}} \quad (3.159)$$

$$A_1 (e^{-ik_{z_1}h} + e^{+ik_{z_1}h}) = (A_2 + A'_2) \quad (3.160)$$

- continuity of traction $\sigma_{yz}^{(1)}(z = -h) = \sigma_{yz}^{(2)}(z = 0)$, that is:

$$A_1 \mu_1 k_{z_1} (e^{-ik_{z_1}h} - e^{+ik_{z_1}h}) = \mu_2 k_{z_2} (A_2 - A'_2) \quad (3.161)$$

Solution of the problem

Introducing the impedance ratio between both media:

$$\bar{\chi} = \sqrt{\frac{\mu_1 \rho_1}{\mu_2 \rho_2} \cos \theta_1 \cos \theta_2} \quad (3.162)$$

the relations (3.160) and (3.161) allows to determine the amplitudes of the various waves:

$$\begin{cases} A_2 = \frac{1}{2} A_1 [(1 + \bar{\chi}) e^{-ik_{z_1}h} + (1 - \bar{\chi}) e^{+ik_{z_1}h}] \\ A'_2 = \frac{1}{2} A_1 [(1 - \bar{\chi}) e^{-ik_{z_1}h} + (1 + \bar{\chi}) e^{+ik_{z_1}h}] \end{cases} \quad (3.163)$$

Equations (3.163) are derived assuming the amplitude of the surface motion to be known. It is generally an input data for the analysis of seismic motion. When the surface motion is not represented by a monochromatic wave but by an actual time variation of the displacement (or velocity, or acceleration), the solution may be found, for linear constitutive laws, as the superposition of various monochromatic waves (using direct and inverse Fourier transforms). It is thus interesting to consider the *transfer function* of the layer.

Transfer function

By definition, the transfer function between two points of the layer is the ratio between the motion amplitudes at these two points expressed in the frequency domain. If one of the points is chosen as the point where the displacement is known, the product of the transfer function by the Fourier transform⁴ of this displacement represents the spectral response at the second point. The inverse Fourier transform allows the determination of the time-domain response.

Alternative definitions. Considering the points defined in Fig.3.29, the transfer function of a wave through a soil layer may be defined by various means:

- Transfer function $T(\omega)$: it is defined as the spectral ratio between the surface motion (point A) and the motion at the layer/half-space interface (point B),
- Transfer function $\bar{T}(\omega)$: it is defined as the spectral ratio between the surface motion (point A) and the motion at the surface of the half-space without the layer (point B'); B' is known as the outcrop of the half-space.

To use the first definition, it is necessary to know the in-depth motion whereas the second one involves the motion at a reference point B' (Fig.3.29 right), located at the free-surface, which may correspond to a bedrock outcrop (e.g. reference station).

⁴Or inverse Fourier transform depending on the harmonic dependence chosen for the wavefield ($e^{+i\omega t}$ or $e^{-i\omega t}$).

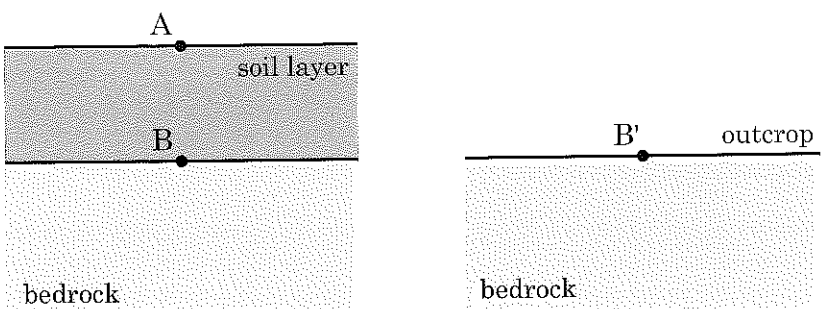


Fig. 3.29: Points allowing the calculation of the transfer function through a soil layer.

Ratio between surface motion and motion at the interface. For the system depicted in Fig.3.29 (left), the transfer function $T(\omega)$ between the soil surface (point A) and the interface with the half-space (point B) may be expressed as:

$$T(\omega) = \frac{u_A}{u_B} \quad \text{thus:} \quad |T(\omega)| = \left| \frac{u_A}{u_B} \right| = \frac{2A_1}{A_2 + A'_2} \quad (3.164)$$

Taking into account relations (3.163) :

$$|T(\omega)| = \frac{1}{\cos(k_{z_1}h)} \quad (3.165)$$

This function is infinite for the following frequency values:

$$\omega_n = \frac{(2n-1)\pi}{2} \frac{V_{S_1}}{h \cos \theta_1} \quad (3.166)$$

The eigenfrequencies given by Eq.(3.166) represent the eigenfrequencies of the soil layer of thickness h . It is straightforward to check this proposal by seeking the classical periodic solutions of the wave equation, under the following boundary conditions: zero displacement at the base and zero stress vector at the free-surface.

Figure 3.30 displays the transfer function of a 20m deep layer having a shear wave velocity $V_S=200$ m/s, a mass density $\rho=2$ t/m³ and considering a normally incident plane SH-wave ($\theta_1=0$). It is obvious from Eq.(3.165) that the features of the half-space are not involved in this expression of the transfer function.

Ratio between the surface motion and the outcrop motion. The transfer function $\bar{T}(\omega)$ between the soil surface (point A) and the bedrock motion (point B': surface of the half-space outcrop) is such that:

$$\bar{T}(\omega) = \frac{u_A}{u_{B'}} = \frac{2A_1}{2A_2} = \frac{1}{\cos k_{z_1}h + i\bar{\chi} \sin k_{z_1}h} \quad (3.167)$$

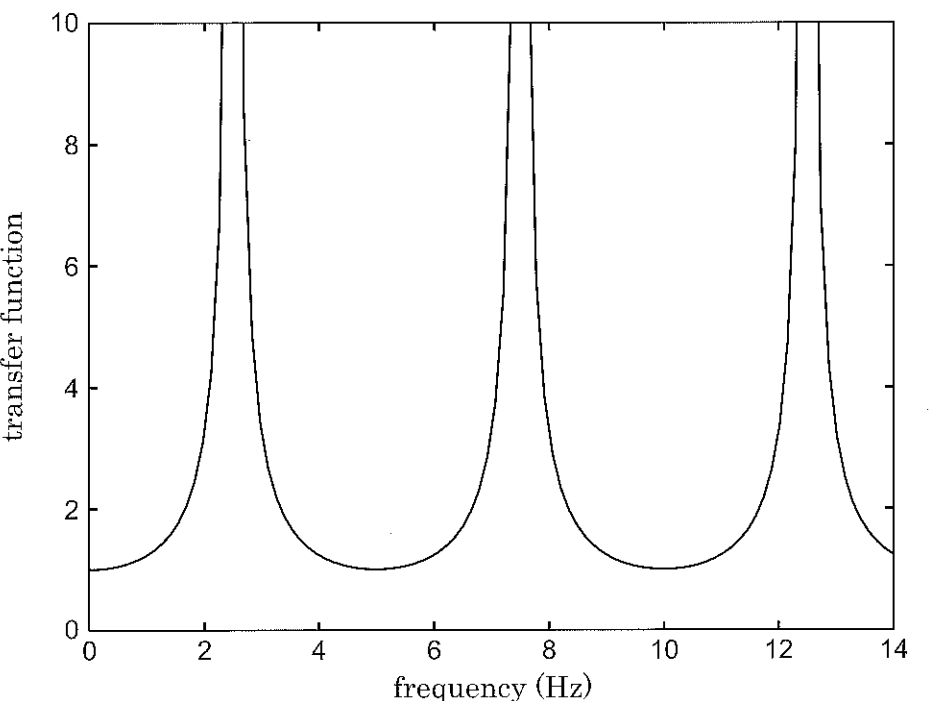


Fig. 3.30: Transfer function $T(\omega)$ of an elastic soil layer.

$$\text{where: } \bar{\chi} = \sqrt{\frac{\mu_1 \rho_1}{\mu_2 \rho_2}} \frac{\cos \theta_1}{\cos \theta_2}$$

$$\text{thus: } |\bar{T}(\omega)| = (\cos^2 k_{z_1}h + \bar{\chi}^2 \sin^2 k_{z_1}h)^{-1/2} \quad (3.168)$$

This alternative definition leads to a very different expression of the transfer function since:

- transfer function $\bar{T}(\omega)$ depends on the features of both media (parameter $\bar{\chi}$),
- the peaks have a finite amplitude ($1/\bar{\chi}$), it is due to the fact that the energy is partially absorbed by the reflected wave A'_2 (radiative damping). It is no more the case for very large $\bar{\chi}$ values.

Keeping the same shear wave velocity in the soil layer as in the previous case (i.e. $V_{S_1}=200$ m/s), Fig. 3.31 displays a comparison of both transfer functions for various sets of properties for the bedrock (i.e. half-space):

- case 1 : $V_{S_2}=5000$ m/s, $\rho_2=2500$ kg/m³,
- case 2 : $V_{S_2}=2000$ m/s, $\rho_2=2200$ kg/m³,

- case 3 : $V_{S_2}=800\text{m/s}$, $\rho_2=2000\text{kg/m}^3$.

The influence of the velocity ratio between both media clearly appears since, for case 3, the maximum value of the transfer function is lower than 2. Conversely, for a very low $\bar{\chi}$ value, the transfer function $\bar{T}(\omega)$ leads to values very close to that of $T(\omega)$ (case 1).

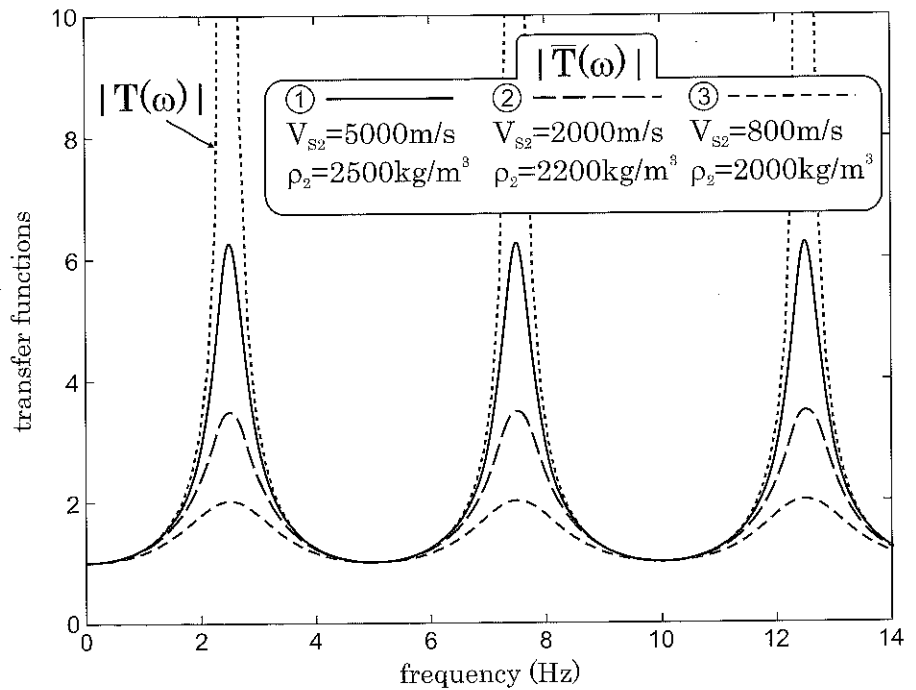


Fig. 3.31: Transfer functions $\bar{T}(\omega)$ and $T(\omega)$ of an elastic soil layer: modulus vs frequency for various bedrock properties.

3.5.4 Amplification of seismic waves in layered media

Transfer function between layers

In the more general case of a layered medium with n layers, the relation (3.163) can be generalized under the following form:

$$\begin{cases} A_{j+1} = \frac{1}{2} A_j (1 + \bar{\chi}_j) e^{-ik_{z_j} h_j} + \frac{1}{2} A'_j (1 - \bar{\chi}_j) e^{+ik_{z_j} h_j} \\ A'_{j+1} = \frac{1}{2} A_j (1 - \bar{\chi}_j) e^{-ik_{z_j} h_j} + \frac{1}{2} A'_j (1 + \bar{\chi}_j) e^{+ik_{z_j} h_j} \end{cases} \quad (3.169)$$

$$\text{where: } \bar{\chi}_j = \sqrt{\frac{\mu_j \rho_j}{\mu_{j+1} \rho_{j+1}}} \frac{\cos \theta_j}{\cos \theta_{j+1}}$$

A recursive method thus allows the determination of the displacement amplitudes in layer j as a function of the displacements amplitudes at the free-surface:

$$\begin{cases} A_j = f_j(\omega) A_1 \\ A'_j = g_j(\omega) A_1 \end{cases} \quad (3.170)$$

We can thus express the transfer function between layers j and k as follows:

$$T_{j,k}(\omega) = \frac{f_k(\omega) + g_k(\omega)}{f_j(\omega) + g_j(\omega)} \quad (3.171)$$

Comparison for the one-layer and two-layer cases

In order to estimate the influence of the soil stratification on the amplification of seismic waves, a comparison between the one-layer case and several two-layers cases is now proposed. The one-layer case (case 1) corresponds to a single layer of thickness $h_1=20\text{m}$ and velocity $V_{S_1}=200\text{m/s}$, overlying a half-space. The transfer function is displayed in Fig.3.32 (it is similar to the curves displayed in Fig.3.31).

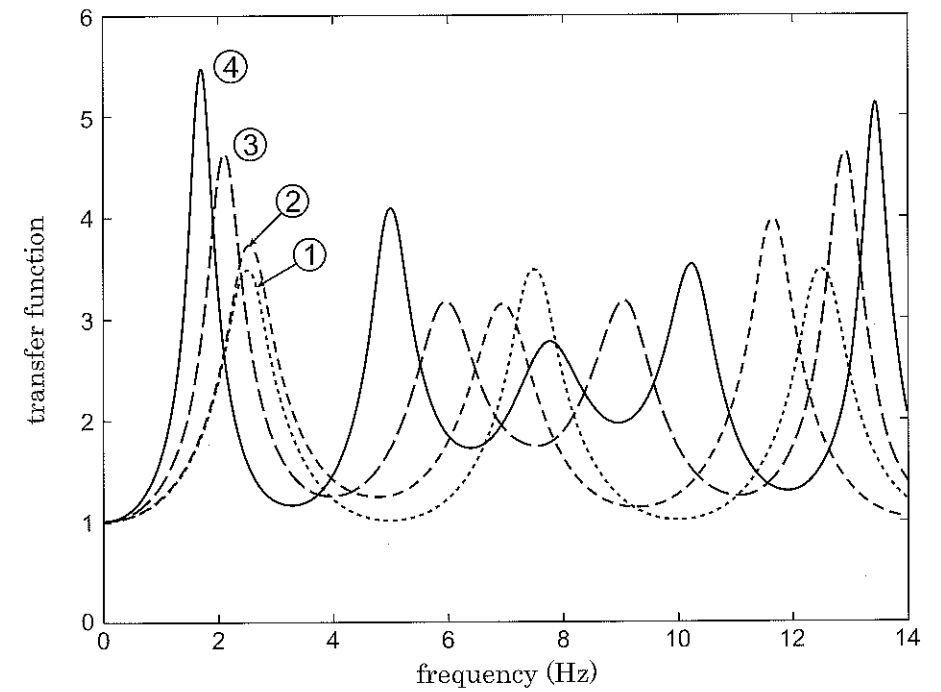


Fig. 3.32: Transfer function through an elastic soil layer (case 1) or through two elastic layers with different velocities (cases 2, 3 and 4).

In the two-layers cases (cases 2, 3 and 4), we chose two 10m thick layers corresponding to the same total layer thickness than in the previous case. The velocities in each layer are determined in order to progressively increase the velocity ratio between both layers and simultaneously keeping the same equivalent velocity (i.e. $\frac{V_1+V_2}{2}=200\text{m/s}$ as in case 1):

- case 2 : $V_{S_1}=150\text{m/s}$; $V_{S_2}=250\text{m/s}$,
- case 3 : $V_{S_1}=100\text{m/s}$; $V_{S_2}=300\text{m/s}$,
- case 4 : $V_{S_1}=75\text{m/s}$; $V_{S_2}=325\text{m/s}$.

The results displayed in Fig.3.32 show that, for an identical total layer thickness, the two-layers cases lead to a stronger amplification than the one-layer case. Furthermore, the larger the velocity ratio between both layers, the stronger the amplification. Finally, the frequency of maximum amplification decreases as the velocity ratio increases.

3.6 Application 1: waves in centrifuged models

3.6.1 Historical summary

For wave propagation problems, the main interest of reduced scale experiments (e.g. centrifuge) is to allow the analysis of complex wavefields for small experimental configurations under well controlled conditions. It is useful for two types of problems: seismic wave propagation or vibrations induced in soils. In 1869, E. Phillips presented at the french Academy of Sciences the idea of reduced scale experiments on centrifuged models (Phillips, 1869). Phillips proposed to use the centrifuge forces to study problems for which gravity is an essential governing factor of equilibrium. The first scaling laws established by Phillips (see hereafter) were rediscovered and finally applied in the early 30's simultaneously in USA and in Soviet Union. But it was mainly in the 70's, thanks to researches performed in Great Britain, that centrifuge modelling was widely developed.

The main experimental applications concerned problems of structural stability (applications to dams and embankments), of slope stability and of bearing capacity of foundations. Afterwards, experiments on soil liquefaction under seismic loadings were developed and set the path for dynamic centrifuge tests.

3.6.2 Equivalence principle

Centrifuge tests allow simulation, at a reduced scale, of the response of actual geotechnical structures (Luong, 1993). Generating artificial gravity forces makes the reduced scale model equivalent, from a mechanical point of view, to a large actual structure under natural gravity. This equivalence is governed by the laws of mechanics under the form of *scaling factors*. For a mechanical parameter w , the scaling factor \tilde{w} represents the ratio between w_m , value of w for the reduced scale model, and w_p , the value of w for the

3.6 Application 1: waves in centrifuged models

prototype (actual structure). The scaling factor \tilde{w} is thus written:

$$\tilde{w} = \frac{w_m}{w_p} \quad (3.172)$$

3.6.3 Calculation of the scaling factors

Denoting u_i the displacement components, l the length scale, σ_{ij} the components of the stress tensor, ρ the mass density, t the time, g_i the components of the gravity forces, we consider the related scaling factors: \tilde{u} , \tilde{l} , $\tilde{\sigma}$, $\tilde{\rho}$, \tilde{t} , \tilde{g} . These factors can be calculated thanks to the equations of mechanics. Considering for instance the equilibrium equations, that is:

$$\frac{\partial \sigma_{ij}}{\partial x_j} + \rho \left(g_i - \frac{\partial u_i}{\partial t^2} \right) = 0 \quad (3.173)$$

if these scales are modified, the first term is multiplied by $\tilde{\sigma} \tilde{l}^{-1}$, the second one by $\tilde{\rho} \tilde{g}$ and the third one by $\tilde{\rho} \tilde{u} \tilde{t}^{-2}$. To satisfy the equilibrium equations, it implies that:

$$\tilde{\sigma} = \tilde{\rho} \tilde{g} \tilde{l} \quad \text{and} \quad \tilde{u} = \tilde{g} \tilde{t}^2 \quad (3.174)$$

To fulfil the "rheological scaling", it is necessary that $\tilde{\rho}=1$ (same material) and $\tilde{g}=1$ (same behaviour). From Eq.(3.174), we thus derive: $\tilde{g} \tilde{l}=1$. In centrifuge experiments, \tilde{g} is chosen in order to have $\tilde{g} = g_m/g_p = N$. The scaling factor for the length scale is thus: $\tilde{l}=1/N$. The model dimensions are related to the prototype (actual) dimensions as follows: $l_m = l_p/N$. Centrifuging a scale model at N g simulates the behaviour, at 1g, of an actual structure N times larger. For dynamic problems, the scaling factors of the various mechanical parameters are synthetized in Table 3.4.

Table 3.4: Scaling factor for several mechanical parameters.

mechanical parameter	scaling factor	value
length	\tilde{l}	$1/N$
time	\tilde{t}	$1/N$
stress	$\tilde{\sigma}$	1
velocity	\tilde{v}	1
mass density	$\tilde{\rho}$	1
force	\tilde{F}	$1/N^2$
frequency	\tilde{f}	N
acceleration	\tilde{a}	N

3.6.4 Dynamic experiments in the centrifuge

Many geotechnical centrifuges are available in different teams around the world (Adalier and Elgamal, 2002; Arulanandan *et al.*, 1982; Brennan and Madabhushi, 2002; Chazelas *et al.*, 2001; Cheney *et al.*, 1990; Luong, 1993; Ng *et al.*, 2004; Takahashi and Takemura, 2005). As shown in Fig.3.33, various types of experimental devices are used. The related maximum acceleration level and reduction scale are thus different from one device to the other. Generating dynamic or seismic loadings is also a crucial issue in such experiments (Chazelas *et al.*, 2001; Cheney *et al.*, 1990; Coe *et al.*, 1985; Luong, 1993).

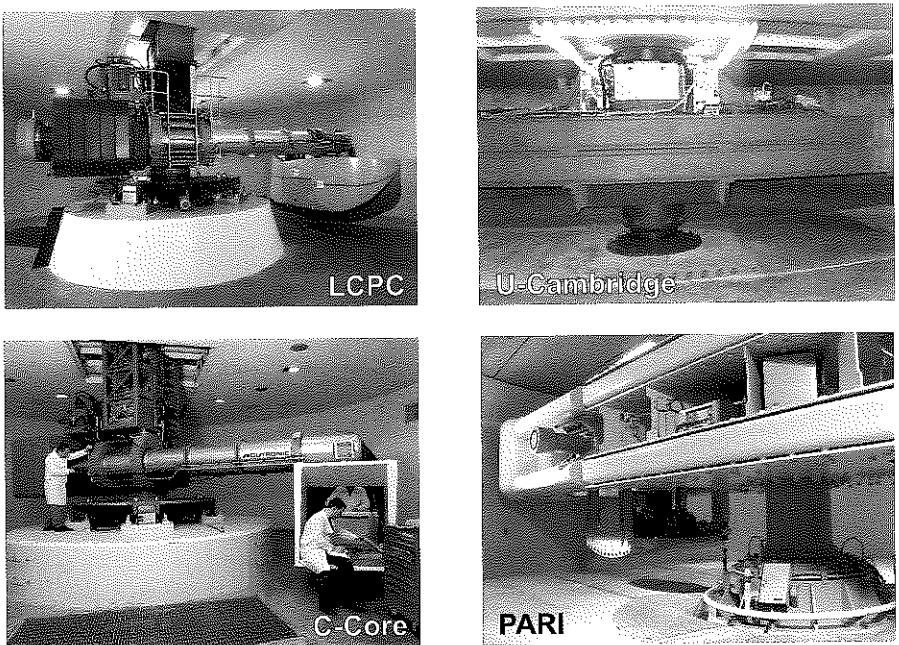


Fig. 3.33: Geotechnical centrifuges at several research centers: LCPC-Paris (top left), University of Cambridge (top right), C-Core-St-John (bottom left) and PARI-Kanagawa (bottom right).

Dynamic and seismic loadings

To perform dynamic tests in the centrifuge (e.g.: seismic loadings or vibrations), it is necessary to apply a dynamic loading at the bottom of the model, at the free-surface or on a structure founded on the soil (Brennan and Madabhushi, 2002; Chazelas *et al.*, 2001; Cheney *et al.*, 1990; Luong, 1993). The first method is very interesting to analyze seismic wave propagation in soils, but it raises important technological difficulties.

3.6 Application 1: waves in centrifuged models

The accelerograms displayed in Fig.3.34 correspond to dynamic experiments performed in the Cambridge University geotechnical centrifuge (Brennan and Madabhushi, 2002). A shaking table is installed at the bottom of the soil container and a shear wave is generated. The upward propagating shear waves allow the analysis of the propagation phenomena as well as of dynamic soil structure interaction.

To have realistic earthquake simulations in the centrifuge, it is necessary to apply a dynamic loading to the whole soil model. It is for instance possible to design shaking tables efficient even under large artificial gravities (Finn, 2007). To retrieve actual seismic excitations with such devices, it may be necessary to consider non rigid containers to allow the soil model to deform during the dynamic excitation (e.g. *equivalent shear beam system*).

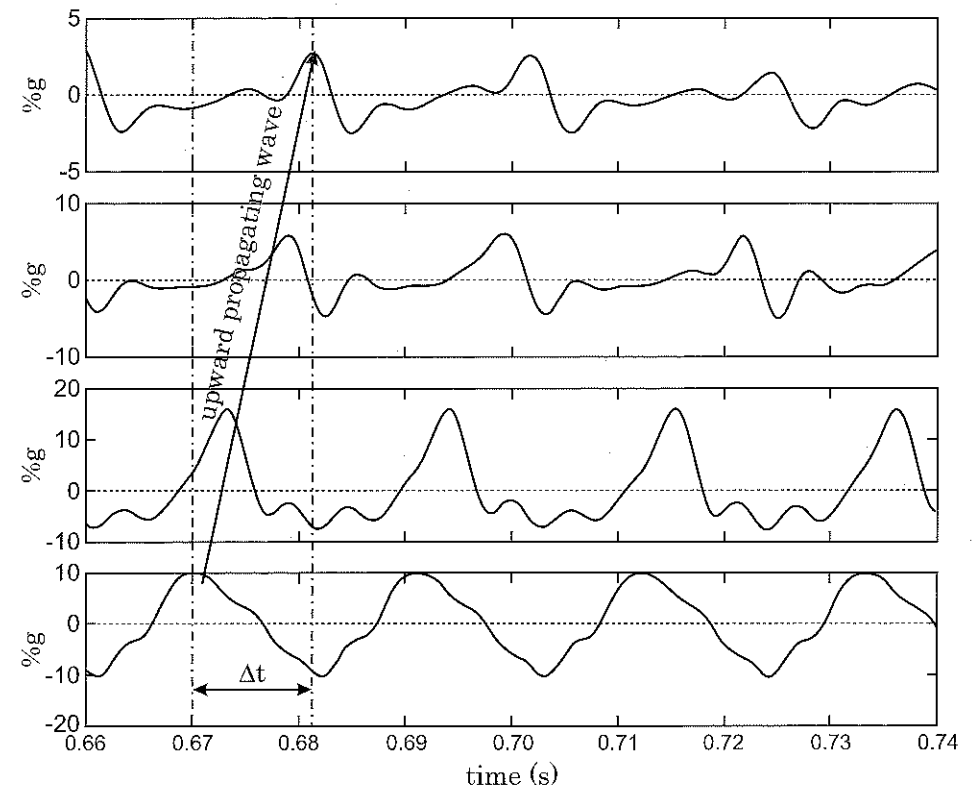


Fig. 3.34: Shear wave propagation in the Cambridge University geotechnical centrifuge (Brennan and Madabhushi, 2002).

3.6.5 Examples of dynamic centrifuge experiments

Centrifuge experiments by Semblat and Luong (1998)

The experiments presented herein were performed in a French geotechnical centrifuge (CEA-CESTA) on sand by Semblat and Luong (1998). For all the tests, the soil model was centrifuged in order to reach *artificial gravity forces* equivalent to $100g$ where g stands for the natural gravity constant.

In the framework of these experiments, the dimensions of the scaled model are as follows: length $L_m = 1.30\text{m}$, height $h_m = 0.35\text{m}$ and width $l_m = 0.80\text{m}$ (see Fig.3.35). The scaling factor for the length scale being $\bar{l} = l_m/l_p = 1/100$, the dimensions of the model correspond to an actual prototype of dimensions: length $L_p = 130\text{m}$, depth $h_p = 35\text{m}$ and width $l_p = 80\text{m}$.

Two excitation sources were used by Semblat and Luong (1998): an earthquake simulator and a surface wave generator (falling mass).

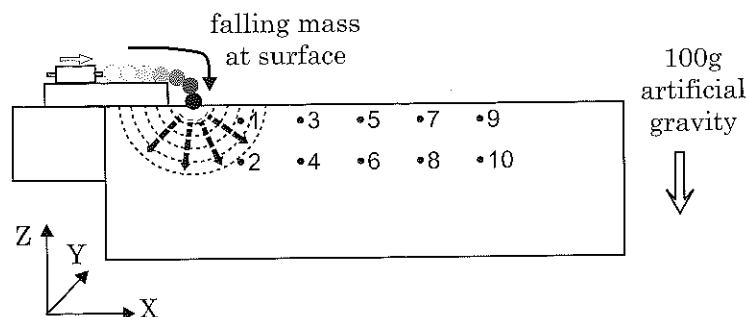


Fig. 3.35: Schematic of the centrifuge experiments performed by Semblat and Luong (1998).

Earthquake simulator

Earthquake simulators are useful to analyze seismic wave propagation or dynamic soil structure/soil-pile interaction (Finn, 2007). It may be a shaking table or an explosive system. The latter was used by Semblat and Luong (1998). With such a system, it is possible to simulate earthquakes of various durations and intensities. Nevertheless, as it was detailed previously, the scaling factor for the time scale is $\bar{t} = 1/N$ for a centrifuge model at Ng . The excitations must then be N times faster than for an actual earthquake. A typical seismic signal measured with such an earthquake simulator is displayed in Fig.3.36 (Semblat and Luong, 1998).

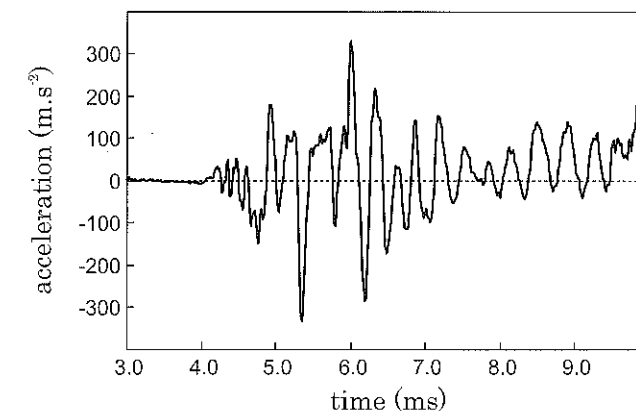


Fig. 3.36: Typical seismic signal measured in the centrifuge with an earthquake simulator (Semblat and Luong, 1998).

Surface wave generator

The classical devices used to analyze wave propagation in the centrifuge (explosives, electromagnetic vibrators, etc) do not allow an easy control of the signal duration. A simple idea was proposed (Semblat and Luong, 1998) to generate nearly-spherical surface waves having a short duration. The experimental arrangement consists in a pneumatic system dropping, during the flight, a mass on the soil surface. The system is thus called *drop-ball arrangement*. Figure 3.35 gives a schematic of the experimental arrangement: a spherical ball, initially at rest, is pushed by a pneumatic system and finally falls on the soil surface. As shown in Fig.3.37, the dynamic loading has thus a short duration.

Several authors studied in great details similar systems mainly dedicated to surface waves (Chazelas *et al.*, 2001). The work of Abe *et al.* (1990) for instance presents the various features (in time and frequency domains) of a system generating seismic waves by using a spherical mass falling on a plate. They made a parametric study considering different masses, densities, falling heights, etc. They analyzed in details their influence on the generated wavefield.

Two wave types

Thanks to the earthquake simulator, the wavefield generated in the soil model may be assumed as plane waves. Whereas, for the drop-ball arrangement, we nearly have a point source leading to a spherical wavefield (Semblat and Luong, 1998). The geometrical features of the wavefield are fundamental to analyze the geometrical, as well as physical, attenuation of the waves in the soil. They change the basic assumptions for further theoretical or numerical analyses of the observed phenomena.

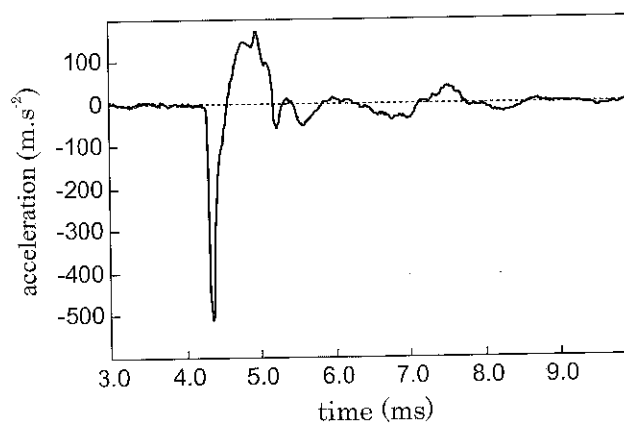


Fig. 3.37: Typical signal measured in the centrifuge with a drop-ball arrangement (Semblat and Luong, 1998).

3.6.6 Analysis of the threedimensional wavefield

The acceleration measurements performed by Semblat and Luong (1998) were made in the three directions of space X , Y and Z . The threedimensional measurements of acceleration allow the identification of the acceleration vector at the point considered. For the *earthquake simulator*, the acceleration vector describes a very complex path which is very difficult to characterize. Conversely, for the *drop-ball tests*, the acceleration vector follows a rather simple path.

Drop-ball experiments

Considering the symmetry of the problem, the Y transversal component should be zero. It is nearly the case even if some very small accelerations are found along this axis (Semblat and Luong, 1998). The experimental findings indeed show that the mass does not exactly fall along the X -axis corresponding to the sensors alignment (it is probably due to the Coriolis forces). The acceleration amplitude along Y -axis is nevertheless very small and may be neglected. Only the measurements along X (horizontal) and Z (vertical) will finally be taken into account.

The drop-ball experiments leading to simpler signals, they will be chosen for the analysis of the acceleration vector polarization. For this type of loading system, the excitation is short enough to avoid wave reflections to be combined with direct waves. It is thus possible to estimate the acceleration amplitude along the X and Z axes and to deduce the acceleration vector in this plane. As shown in Fig.3.38, the components of the acceleration vector along X and Z allows the calculation, for sensor i , of the angle with the horizontal axis, denoted θ_i (Semblat and Luong, 1998). This calculation will be made in the next paragraph.

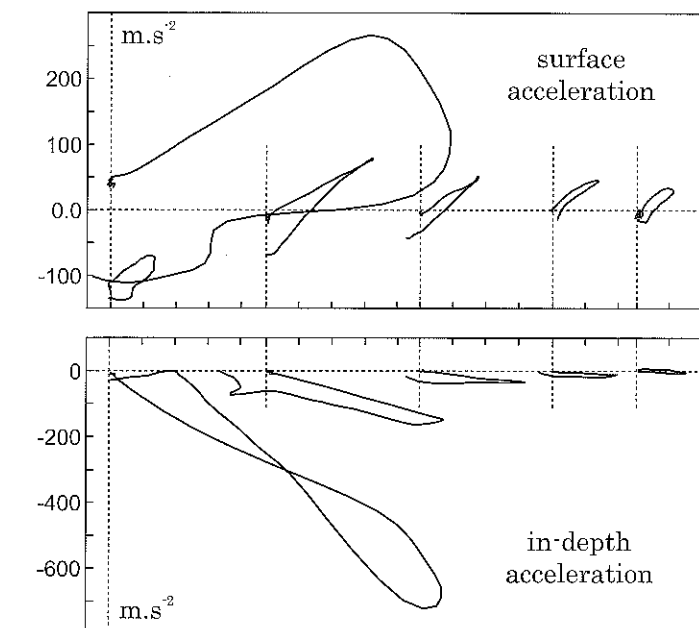


Fig. 3.38: Accelerations measured in the XZ plane for surface and in-depth sensor (drop-ball experiments), from Semblat and Luong (1998).

Identification of the wave polarization

Semblat and Luong (1998) compared the angles of the acceleration vectors, θ_i , and the angles of incidence at the different sensors, denoted θ'_i . The values of the θ_i angles are determined from the acceleration curves in the XZ plane (Fig.3.38). The locations of the sensors allow the determination of the incidence angles θ'_i . The values of the θ'_i are given in Table 3.5.

From Table 3.5, the angles θ_i are found to coincide with the angles θ'_i for the in-depth sensors (even numbers). It means that, in the XZ plane, for all in-depth sensors, the *direction of the acceleration vector coincides with the direction of incidence*. The acceleration vector having no transverse component along Y , the drop-ball arrangement is found to generate *pressure waves at depth* (i.e. P -waves). At the free-surface, the angles θ_i and θ'_i do not coincide: several wave types are present (including surface waves).

Figure 3.39 displays, for all sensors, the acceleration vectors (maximum acceleration) deduced from these results. The directions of the acceleration vectors for the in-depth sensors obviously coincide with the incidence directions at these sensors. The vectors

Table 3.5: Values of the theoretical angles of incidence at the various sensors (Semblat and Luong, 1998).

In-depth sensors	surface sensors
#2	$\theta'_2 = 52^\circ$
#4	$\theta'_4 = 32^\circ$
#6	$\theta'_6 = 22^\circ$
#8	$\theta'_8 = 17^\circ$
#10	$\theta'_{10} = 13^\circ$
	$\#1 \quad \theta'_1 = 16^\circ$
	$\#3 \quad \theta'_3 = 7.2^\circ$
	$\#5 \quad \theta'_5 = 4.7^\circ$
	$\#7 \quad \theta'_7 = 3.4^\circ$
	$\#9 \quad \theta'_9 = 2.7^\circ$

lengths show that the acceleration amplitude fastly decreases (Fig.3.39).

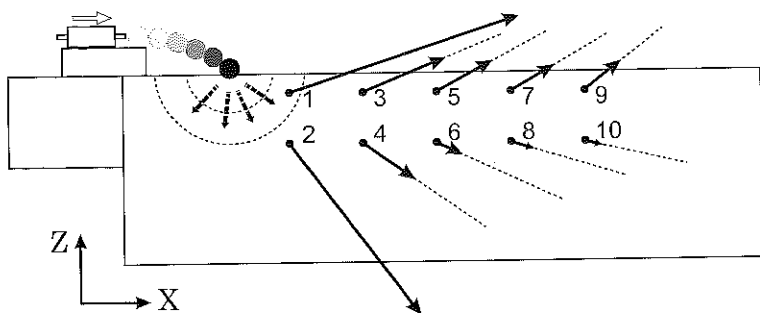


Fig. 3.39: Acceleration vectors in the XZ plane showing pressure waves at depth and various wave types at the free-surface (Semblat and Luong, 1998).

3.6.7 Modelling propagation in dissipative soils

Attenuation and dissipative phenomena

To assess the attenuation properties of the soil in the centrifuge experiments, it is necessary to model wave propagation in attenuating soils and to identify the dissipative properties of the soil used for the tests. The definitions of attenuation given in Chapter 2 correspond to various approaches. The governing parameters of cyclic, vibratory or propagation tests are linked by the following relations:

$$\frac{1}{Q} = \frac{\alpha\Lambda}{\pi} = \frac{\delta}{\pi} = \frac{M_I}{M_R} = \tan \phi = \frac{\Delta f}{f_r} \quad (3.175)$$

where Q is the quality factor, α the attenuation factor, Λ the wavelength, δ the logarithmic decrement, M_R and M_I the real and imaginary parts of the complex modulus, ϕ the

3.6 Application 1: waves in centrifuged models

phase shift and Δf the bandwidth in the resonance curve.

Preliminary simulations from the experiments

Geometrical damping. For a spherical wave, we may consider that, far away from the source, the geometrical damping is inversely proportional to the distance to the source. We shall thus disregard the $1/r^2$ near field term obtained in §3.4. Only considering the geometrical damping, the comparison of the acceleration amplitudes at two points M_i and M_j may be written as follows:

$$A_j = A_i \frac{r_i}{r_j} \quad (3.176)$$

Simplified material attenuation. From the centrifuge experiments performed by Rivière and Luong in the 80's (Rivière, 1983), the attenuation factor α was assumed to be constant:

$$A(x) = A_0 \exp(-\alpha x) \text{ with: } \alpha = 1.10 \quad (3.177)$$

This estimation of attenuation is rough but it allows a direct analysis of the propagation process in the soil. For the drop-ball experiments performed by Semblat and Luong (1998), the wavefield being spherical, we have to take into account the geometrical damping together with material damping. Comparing the acceleration amplitudes at two points M_i and M_j leads to:

$$A_j = A_i \frac{r_i}{r_j} \exp[-\alpha(r_j - r_i)] \quad (3.178)$$

This expression allows, from a signal measured at point M_i to calculate the acceleration at point M_j . The r_i/r_j ratio takes into account the geometrical damping (expansion of the wavefront) whereas the $\exp[-\alpha(r_j - r_i)]$ factor stands for the material attenuation between M_i and M_j . It is also necessary to account for the propagation term considering a constant velocity (directly estimated from peak to peak delays).

Figure 3.40 gives an example of simulations for drop-ball experiments (Semblat and Luong, 1998), α being assumed constant as suggested by Rivière and Luong (Rivière, 1983). These simulations involve both geometrical damping (spherical waves) and material attenuation. As shown in Fig.3.40, the agreement between the measured and the simulated signals is not very good. It is thus necessary to investigate more complex models in order to retrieve the experimental results in terms of attenuation.

Spherical wave in a viscoelastic medium

Propagation and mechanical behaviour. To simulate propagation phenomena in dissipative soils, it is necessary to write the wave equations as well as the constitutive

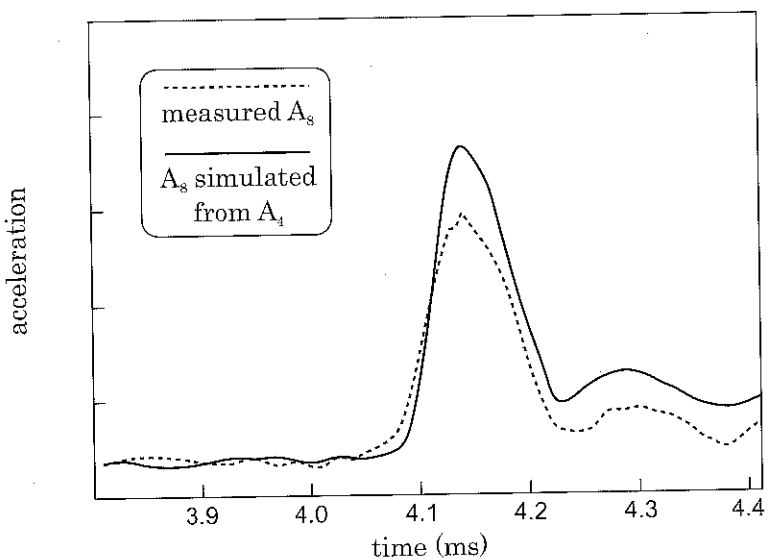


Fig. 3.40: Time domain simulation with a constant attenuation factor for drop-ball experiments: modulus of the acceleration vector at sensors #8 (measured and simulated from signal at sensor #4), from Semblat (1995).

behaviour of the material. The propagation phenomena are accounted for using the equilibrium equation. As shown in Chapter 2, the constitutive equations allows replacement of stress components by strain components in the equilibrium equation. The differential equation thus obtained generally allows the determination of the solution. For soils, the constitutive laws adapted to wave propagation considering weak motions generally involve linear viscoelastic behaviour.

Equilibrium equation in spherical coordinates. For the drop-ball experiments performed by Semblat and Luong (1998), the directions of the acceleration vector being identical to the incidence directions, the wavefield propagating at depth is spherical and only radial components have to be considered. It is thus possible to use the solution of the spherical wave equation determined in §3.5.2, that is, for a monochromatic wave:

$$u_r(r, \omega) = A \left(-\frac{1}{r^2} + \frac{i\omega}{rV_P} \right) \exp \left[\frac{i\omega}{V_P}(r - V_P t) \right] \quad (3.179)$$

Viscoelastic models. In order to solve the problem of propagation in a dissipative medium, the soil behaviour is supposed to be linear viscoelastic. Such models are often used to analyze wave propagation in dissipative soils. Indeed, they allow linking of the stress terms to the strain terms considering the complex spectra of the mechanical variables. We shall consider three linear viscoelastic models already studied in Chapter 2:

3.6 Application 1: waves in centrifuged models

Maxwell, Kelvin-Voigt and Zener. In the one-dimensional case, the solution of the wave equation in viscoelastic media was (see Chapter 2)⁵:

$$u^*(x, \omega) = U_0(\omega) \exp [ik^*(\omega)x] \quad (3.180)$$

where u^* is the spectral transform of the displacement, k^* is the complex wavenumber depending on ω and expressed as a function of the complex modulus $M(\omega)$ under the form:

$$(k^*(\omega))^2 = \frac{\rho\omega^2}{M(\omega)} \quad (3.181)$$

The *real part* of the complex wavenumber $k^*(\omega)$ corresponds to the *real wavenumber* k and its *imaginary part* to the *attenuation factor* α ⁶. The expressions of the complex modulus $M(\omega)$ corresponding to the three viscoelastic models are given in Chapter 2.

The solution (3.180) of the wave equation in viscoelastic media is now combined with the solution (3.179) of the spherical wave equation (only keeping, for sake of simplicity, the $1/r$ term). We thus obtain the radial displacement solution of the wave equation for spherical waves in viscoelastic media:

$$u^*(r, \omega) = \frac{B}{r} \exp [ik^*(\omega)r] \quad (3.182)$$

where B is determined by the boundary conditions of the problem.

Finally, the attenuation is expressed through two different terms:

- the *geometrical damping* accounting for the spherical propagation is inversely proportional to r (simplified solution in far field), but independent of frequency,
- the *material damping* characterized by the imaginary part of $k^*(\omega)$ and thus depending on frequency.

Expression (3.182) fully characterizes the propagation of longitudinal spherical waves in a linear viscoelastic soil. Considering the experimental results obtained in the centrifuge by Semblat and Luong (1998), it is thus possible to simulate the propagation of spherical waves in the soil and to identify the mechanical parameters of the viscoelastic models.

3.6.8 Simulations for drop-ball experiments

Computation for a transient wave

The measurements performed by Semblat and Luong (1998) in the centrifuge experiments lead to 3C-accelerograms. The solution in terms of spectral components of acceleration,

⁵Since a $e^{-i\omega t}$ harmonic dependence has been chosen in the present chapter, the sign in this equation is different from that in the equivalent expression in Chapter 2 ($e^{+i\omega t}$ harmonic dependence).

⁶For a $e^{-i\omega t}$ harmonic dependence, the complex wavenumber is expressed as $k^*(\omega) = k(\omega) + i\alpha(\omega)$ (the sign is different from that given in Chapter 2 for a $e^{+i\omega t}$ harmonic dependence).

$a^*(r, \omega)$, may indeed be written under a similar form as the solution in displacement given by Eq.(3.182). It is due to the fact that, in the frequency domain, the complex spectra in displacement and acceleration are directly proportional: $a^*(r, \omega) = -\omega^2 u^*(r, \omega)$. This expression being valid for all frequency values ω , it is possible to transform the signals in the time domain as long as the superposition principle is fulfilled (linear behaviour). The acceleration $a(r, t)$ in the time domain is thus obtained with the following expression⁷:

$$a(r, t) = \frac{1}{2\pi} \int_{-\infty}^{+\infty} a^*(r, \omega) \exp(-i\omega t) d\omega \quad (3.183)$$

The complete expression of acceleration, as a function of r and t , is then:

$$a(r, t) = \frac{1}{2\pi r} \int_{-\infty}^{+\infty} -\frac{B\omega^2}{r} \exp[ik^*(\omega)r] \exp(-i\omega t) d\omega \quad (3.184)$$

The simulations are thus performed using the complex spectra in the frequency domain. The time domain solution is computed afterwards considering Eq.(3.184).

For the Maxwell and Kelvin-Voigt models, the parameters characterizing the behaviour are the *Young's modulus E* and the *viscosity η*. For the Zener model, the parameters are three instead of two: two moduli (E and E_v) and the viscosity η .

Simulations from experimental results

The simulations are performed for the drop-ball experiments (Semblat and Luong, 1998) since the wavefield at-depth corresponds to pure longitudinal waves. In the XZ plane, the acceleration vector is characterized by its modulus $a_m = \sqrt{a_x^2 + a_z^2}$. It is possible to simulate the propagation at several distances from the source considering the first measured signal as the reference signal used for the viscoelastic simulations.

Considering the acceleration moduli for sensors i and j , that is $a_m(r_i, t)$ and $a_m(r_j, t)$, respectively located at distances r_i and r_j from the source, the ratio of the acceleration amplitudes in the frequency domain, $a_m^*(r_j, \omega)/a_m^*(r_i, \omega)$ can be easily written thanks to expression (3.182), adapted to acceleration components under the following form:

$$\frac{a_m^*(r_j, \omega)}{a_m^*(r_i, \omega)} = \frac{r_i}{r_j} \exp[ik^*(\omega)(r_j - r_i)] \quad (3.185)$$

If the acceleration is known at distance r_i from the source, the acceleration at distance r_j can be computed by using a viscoelastic simulation. From expression (3.185), the simulated acceleration $a_m^{sim}(r_j, t)$ is written, in the frequency domain, under the form:

$$a_m^{sim}(r_j, t) = \frac{1}{2\pi} \int_{-\infty}^{+\infty} a_m^*(r_i, \omega) \frac{r_i}{r_j} \exp[ik^*(\omega)(r_j - r_i)] \exp(-i\omega t) d\omega \quad (3.186)$$

⁷Inverse Fourier transforms have to be used for a $e^{-i\omega t}$ harmonic dependence (instead of direct transforms in Chapter 2).

For the Maxwell and Kelvin-Voigt models, the Lamé constants λ, μ being identified (e.g. wave velocity), the values of η should be estimated considering the experimental results. The agreement between the measured and simulated signals will be assessed from the first acceleration peak. In the following, only the simulations obtained with these two models are discussed. The simulations computed with the Zener model will be presented later.

To compare the viscoelastic simulations to the measured accelerations, we shall choose a reference signal from which the acceleration at a distance r will be simulated. The simulations are compared afterwards to the acceleration signals given by the sensor located at the same distance r from the reference sensor. The *values of viscosity* for different models are *tuned in order to retrieve the amplitude of the first acceleration peak*. After the first peak, the direct and reflected waves are combined. This is the reason why it is more difficult to identify the parameters from the signals measured for the earthquake simulator experiments (Semblat and Luong, 1998).

The values of η leading to the best fit for the first acceleration peak are the following:

- $\eta=150000$ Pa.s for the Maxwell model,
- $\eta=1000$ Pa.s for the Kelvin-Voigt model.

The acceleration signals obtained with these viscosity values are displayed in Fig.(3.41). The acceleration signal (modulus of the acceleration vector in the XZ plane) given by sensor #4 is the reference signal. The accelerations computed at a distance $r = r_6 - r_4$ from the reference sensor are compared to the acceleration measured by sensor #6.

From the curves displayed in Fig.3.41, the values chosen for η lead to simulated acceleration curves very close to the measured acceleration. The simulations performed are satisfactory, but their respective features are different:

- the *Maxwell model* leads to an acceleration signal very close to the measured signal since the *simulation fits the acceleration amplitude* but also the *shape of the first peak*,
- the *Kelvin-Voigt model* gives a *correct simulation* in amplitude but it *does not exactly fit the shape of the measured signal*. The higher frequency components of the signal vanish whereas the lower frequency components are weakly attenuated: the first acceleration peak tends to smoothen during the propagation.

To precisely assess this frequency dependence of attenuation, the analysis of the variations of k^* as a function of frequency will be made in the following.

Optimization process for the Maxwell and Zener models

For the Maxwell and Kelvin-Voigt models, assuming the velocity to be slightly dependent on the viscosity, the parameter identification is easy since only the viscosity has

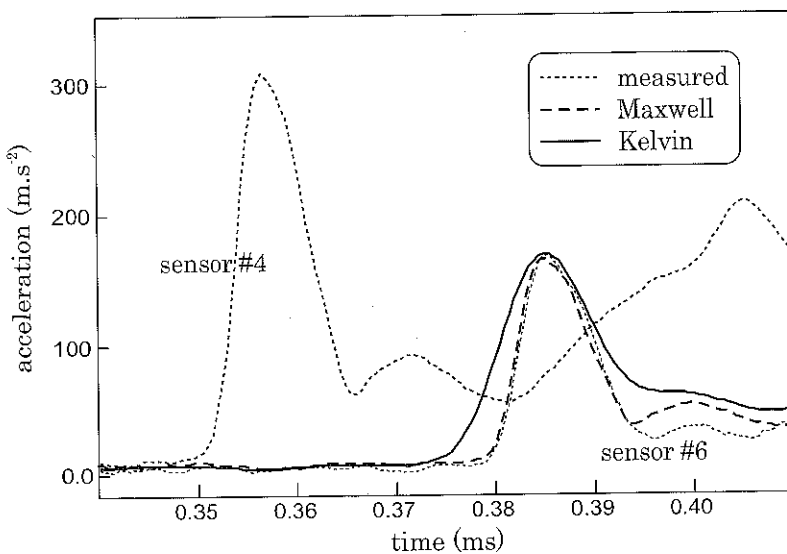


Fig. 3.41: Accelerations computed with linear viscoelastic models: modulus in the XZ plane (drop-ball experiments), from Semblat and Luong (1998).

to be estimated. Furthermore, the identification process is an amplitude fitting method between the peaks of the simulated and measured signals. For the Zener model, the value of the elastic modulus being fixed, *two parameters still have to be determined*. The estimation of these parameters is more complex than for Maxwell and Kelvin-Voigt models.

To estimate the optimal mechanical parameters for various types of models, it is necessary to quantify the quality of the viscoelastic simulation. It is for instance possible to estimate the quadratic error between the simulation a_m^{sim} and the measured signal $a_m(r_j)$. Considering a time interval $[t_1; t_2]$ corresponding to the first acceleration peak, the functional $J(\eta)$ defines the quadratic error for the Maxwell model under the following form:

$$J_{Max}(\eta) = \frac{1}{J_0} \int_{t_1}^{t_2} (a_m(r_j) - a_m^{sim}(r_j))^2 dt \quad \text{with} \quad J_0 = \int_{t_1}^{t_2} a_m^2(r_j) dt \quad (3.187)$$

The minimization of $J_{Max}(\eta)$ leads to the optimal viscosity η_{opt} . The curve displayed in Fig. 3.42 gives the values of $J_{Max}(\eta)$ for $\eta \in [130; 160 \text{ kPa.s}]$ (calculation performed for sensors #4 and 6). As shown in Fig. 3.42, the optimal viscosity is $\eta_{opt} = 144 \text{ kPa.s}$. The fit between the first peak of the simulated and measured signals is then very good.

To estimate the optimal E_v and η parameters for the Zener model (see Chapter 2),

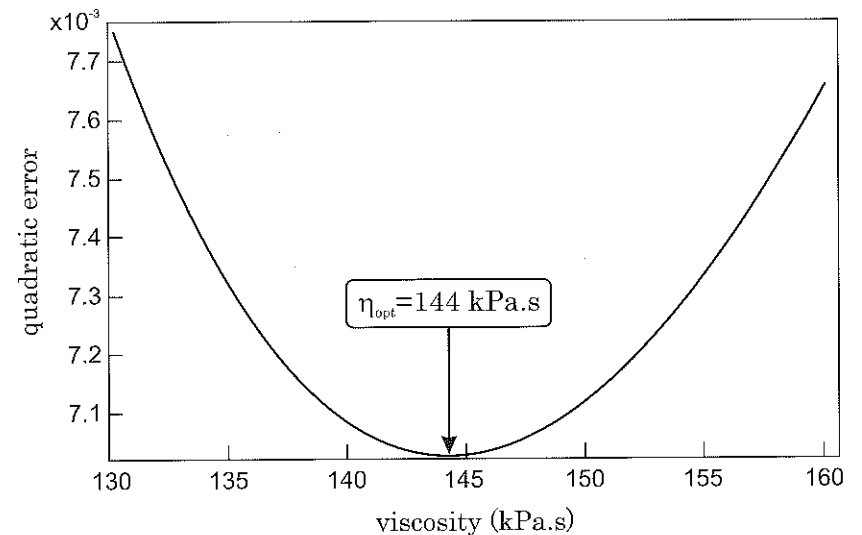


Fig. 3.42: Determination of the optimal viscosity for the Maxwell model: minimization of the quadratic error (sensors #4 and 6).

the quadratic error is now defined by the functional $J_{Zen}(E_v, \eta)$ as follows:

$$J_{Zen}(E_v, \eta) = \frac{1}{J_0} \int_{t_1}^{t_2} (a_m(r_j) - a_m^{sim}(r_j))^2 dt \quad \text{with} \quad J_0 = \int_{t_1}^{t_2} a_m^2(r_j) dt \quad (3.188)$$

The functional $J_{Zen}(E_v, \eta)$ has been calculated to determine the optimal (E_v, η) parameters. The curve displayed in Fig. 3.43 gives the $J_{Zen}(E_v, \eta)$ for $E_v \in [0; 50 \text{ MPa}]$ and $\eta \in [130; 160 \text{ kPa.s}]$ (simulations between sensors #4 and 6). The *minimum quadratic error* is obtained for $E_v = 25.5 \text{ MPa}$ and $\eta = 146 \text{ kPa.s}$. The optimal viscosity η_{opt} determined for the Zener model is very close to that of the Maxwell model.

Another type of "objective function" may be considered to optimize the rheological parameters. It is for instance possible to compare, in the frequency domain, the attenuation values Q^{-1} . The expression of such an objective function could take the following form:

$$J = \frac{1}{J_0} \int_{\omega_1}^{\omega_2} (Q_{exp}^{-1}(\omega) - Q_{sim}^{-1}(\omega))^2 d\omega \quad \text{with:} \quad J_0 = \int_{\omega_1}^{\omega_2} (Q_{exp}^{-1}(\omega))^2 d\omega \quad (3.189)$$

3.6.9 Influence of frequency on attenuation factor

From expression (3.181), the complex wavenumber k^* is a function of ω . Its real and imaginary parts characterize the phase-shift and the attenuation respectively. These two

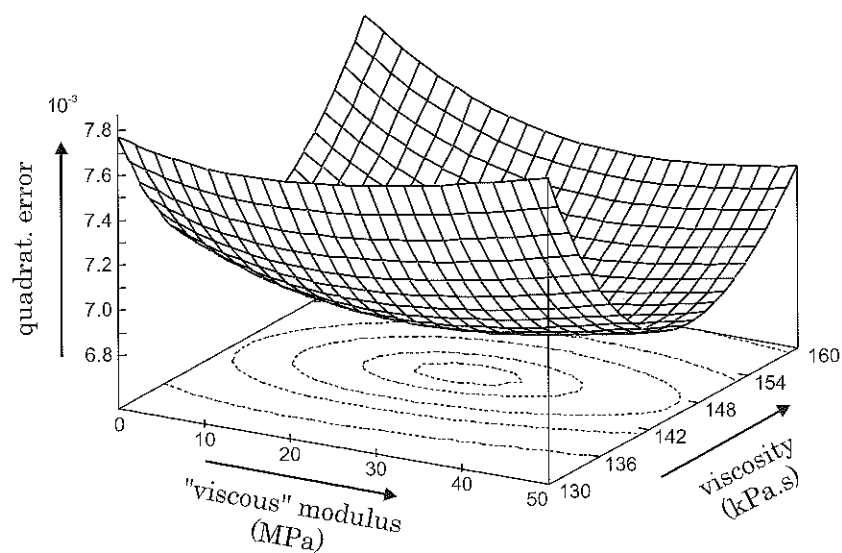


Fig. 3.43: Optimal mechanical parameters for the Zener model: minimization of the quadratic error (Semblat and Luong, 1998).

parameters depend on frequency but this dependence is different from one model to another.

Figure 3.44 displays the attenuation factor α as a function of frequency for the Maxwell and Kelvin-Voigt models. The η values considered correspond to the previous simulations ($\eta_{Max} = 150000$ Pa.s et $\eta_{Kel} = 1000$ Pa.s).

The attenuation factor estimated by Rivière (1983) is in the range of the values obtained in Fig.3.44 with viscoelastic models. The attenuation factor derived from the viscoelastic simulations ranges from 0 to 2 m^{-1} in the considered frequency band. The attenuation factor appears to be larger than the value proposed by Rivière (1983) which was previously seen to under-estimate the dissipation (Fig.3.40). The curves displayed in Fig.3.44 clearly show why, for the Kelvin-Voigt model, the higher frequency components are more attenuated than lower frequency components.

3.6.10 Numerical modelling of centrifuge experiments

Several numerical results obtained by finite element simulations are shown in Fig.3.45. They illustrate the main features of the propagation process in the centrifuged model: wave type, reflections at the bottom of the model, etc. Considering the spherical source, these computations were performed using a axisymmetrical model (CESAR-LCPC FEM/BEM code), from Semblat and Luong (1998).

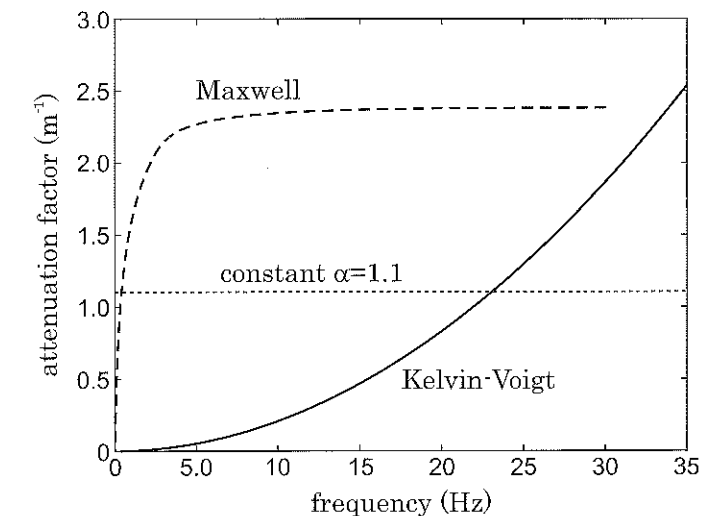


Fig. 3.44: Attenuation factor as a function of frequency for the Maxwell and Kelvin-Voigt models (Semblat, 1995). Comparison with the constant attenuation factor estimated by Rivière and Luong (Rivière, 1983).

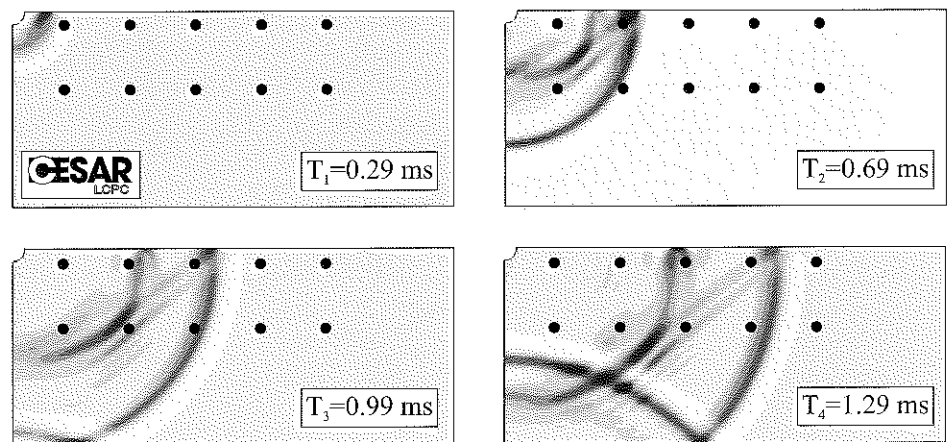


Fig. 3.45: Numerical modelling (FEM, CESAR-LCPC) of wave propagation in a centrifuge model (Semblat and Luong, 1998).

The results displayed in Fig.3.45 correspond to four different time steps:

- *time T₁*: beginning of the propagation process, the various wave types can not be distinguished yet,
- *time T₂*: clear separation of the longitudinal waves (the fastest) from the shear waves and the surface waves,
- *time T₃*: beginning of the reflection of longitudinal waves at the bottom of the model,
- *time T₄*: the direct longitudinal and shear waves keep propagating in the model whereas the reflected P-wave propagates towards the free-surface.

As shown in Fig.3.39, only longitudinal waves are characterized by in-depth accelerometers. Conversely, the experimental results and the numerical simulations (Figs 3.39 and 3.45) show that various wave types are present near the free-surface.

3.6.11 Removing reflections by homomorphic filtering

The homomorphic filtering technique, described in the appendices (§E), is now considered to remove reflections on the container boundaries from the direct wavefield. For the acceleration signals measured in the drop-ball experiments, Fig.3.46 shows that homomorphic filtering allows to remove waves reflected at the bottom of the model. It is even possible for signals having long durations (see §E).

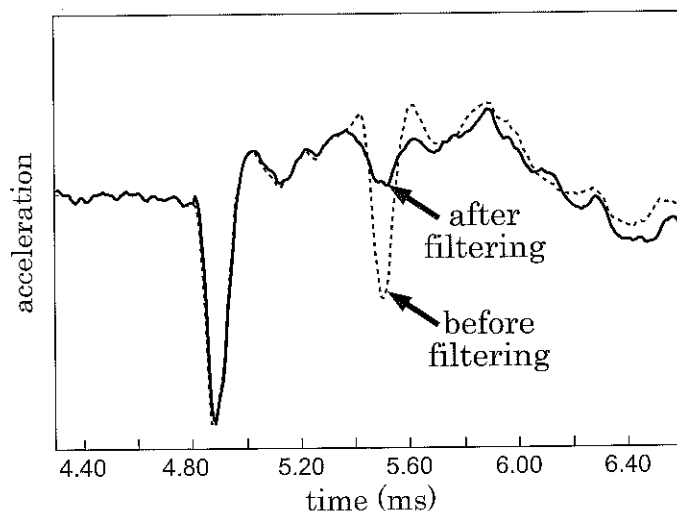


Fig. 3.46: Echo removal by homomorphic filtering (Semblat and Luong, 1998).

3.6.12 Analysis of dispersion

A wavelet method was considered by Semblat and Luong (1998) to analyze the propagation in various frequency bands. It is thus possible to estimate the phase velocity by comparing, for different sensors, the signals analyzed in different frequency bands (see Fig.3.47). Various filtering techniques are presented in (Scherbaum, 2006) and (Mari *et al.*, 1999) and several issues are briefly discussed in Appendix C.

For the centrifuge tests performed by Semblat and Luong (1998), a geometrical dispersion due to the model boundaries is characterized at low frequencies whereas a lower physical dispersion due to the dissipative properties of the soil is observed at higher frequencies. As shown in Fig.3.47, the direct and reflected waves are well separated at higher frequencies but not at low frequencies (these frequencies are given at the model scale and a factor 1/N must be considered to derive the prototype frequencies).

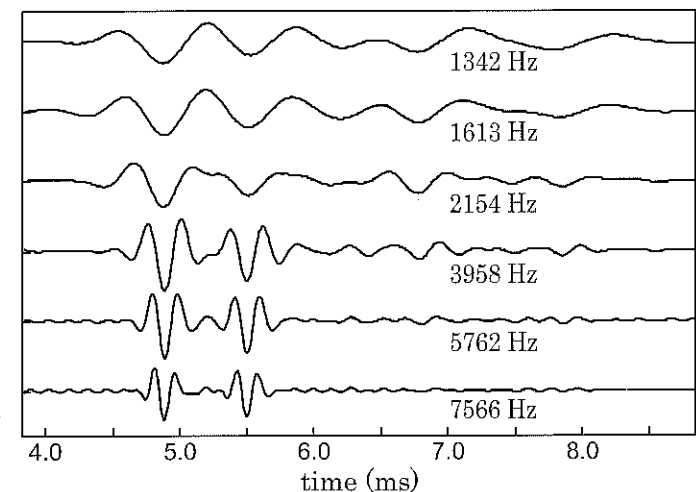


Fig. 3.47: Acceleration signals filtered in different frequency bands given at the model scale (Semblat, 1995).

3.7 Application 2: Spectral Analysis of Surface Waves and in situ tests

Various types of in situ tests are available to identify the dynamic properties of soils. The Spectral Analysis of Surface Waves (or SASW) investigates the dispersive nature of surface waves in layered soils (Achenbach, 1973; Aki and Richards, 1980; Bodet *et al.*, 2005; Foti, 2000, 2003; Lai *et al.*, 2002). As it will be shown in this section, it is possible to link such dispersive properties to the geotechnical features of the site under investigation.

3.7.1 Dispersion of Love waves in a single-layered half-space

Model and wavefields

As depicted in Fig.3.48, we consider a surface (Love) wave propagating horizontally, along the x axis, in a soil layer (thickness h) overlaying an elastic half-space. The wavefields in each medium are only polarized along the y axis and fulfil the following equations of propagation:

$$\begin{aligned}\frac{\partial^2 u_y}{\partial t^2} &= \frac{\mu_1}{\rho_1} \left(\frac{\partial^2 u_y}{\partial x^2} + \frac{\partial^2 u_y}{\partial z^2} \right) && \text{for } -h \leq z \leq 0 \\ \frac{\partial^2 u_y}{\partial t^2} &= \frac{\mu_2}{\rho_2} \left(\frac{\partial^2 u_y}{\partial x^2} + \frac{\partial^2 u_y}{\partial z^2} \right) && \text{for } z \leq -h\end{aligned}\quad (3.190)$$

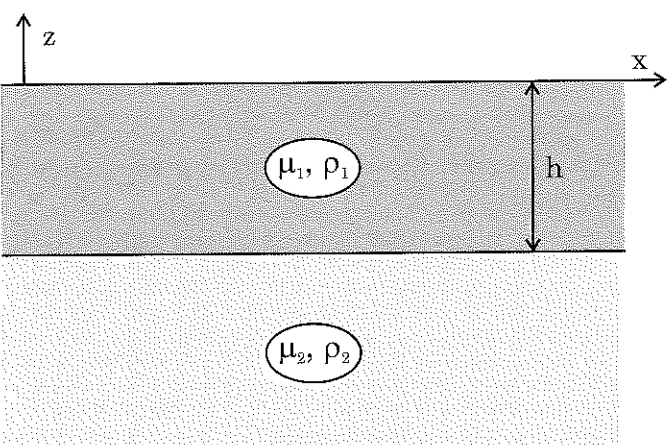


Fig. 3.48: Dispersion of surface waves in a single-layered half-space: schematic of the problem.

Considering Fig.3.48 and the results from §3.5.2, the expression of the wavefield is:

$$\begin{aligned}u_y &= (A_1 e^{b_1 z} + A'_1 e^{-b_1 z}) \exp \left[\frac{i\omega}{V_R} (x - V_R t) \right] && \text{for } -h \leq z \leq 0 \\ u_y &= A_2 e^{b_2 z} \exp \left[\frac{i\omega}{V_R} (x - V_R t) \right] && \text{for } z \leq -h\end{aligned}\quad (3.191)$$

with, similarly to Eq.(3.146), the expression of b_i :

$$b_i^2 = \frac{\omega^2}{V_R^2} - \frac{\omega^2}{V_{S_i}^2} \quad (3.192)$$

$$\text{and } V_{S_i} = \sqrt{\frac{\mu_i}{\rho_i}} \quad (3.193)$$

Free-surface and continuity conditions

The free-surface condition yields:

$$\frac{\partial u_y}{\partial z} = 0 \Rightarrow A_1 = A'_1 \quad (3.194)$$

The continuity equations at the interface ($z = -h$) are thus as follows:

$$\begin{aligned}2A_1 \cos(ib_1 h) &= A_2 e^{-b_2 h} \\ 2i\mu_1 b_1 A_1 \sin(ib_1 h) &= \mu_2 b_2 A_2 e^{-b_2 h}\end{aligned}\quad (3.195)$$

The following equation is finally derived:

$$\tan(ib_1 h) = \frac{\mu_2 b_2}{i\mu_1 b_1} \quad (3.196)$$

Dispersion law

From the previous results, the equation of dispersion of a surface (Love) wave is the following (Aki and Richards, 1980):

$$\tan \left[\omega h \sqrt{\frac{1}{V_{S_1}^2} - \frac{1}{V_R^2(\omega)}} \right] = \frac{\mu_2}{\mu_1} \sqrt{\frac{1}{V_R^2(\omega)} - \frac{1}{V_{S_2}^2}} \quad (3.197)$$

where $V_R(\omega)$ is the velocity of surface waves (depending on frequency).

Each term of the previous equation is displayed in Fig.3.49 as a function of hb_1 . A graphical method may then be used to determine the roots of Eq.(3.197) in terms of eigenvalues (Aki and Richards, 1980).

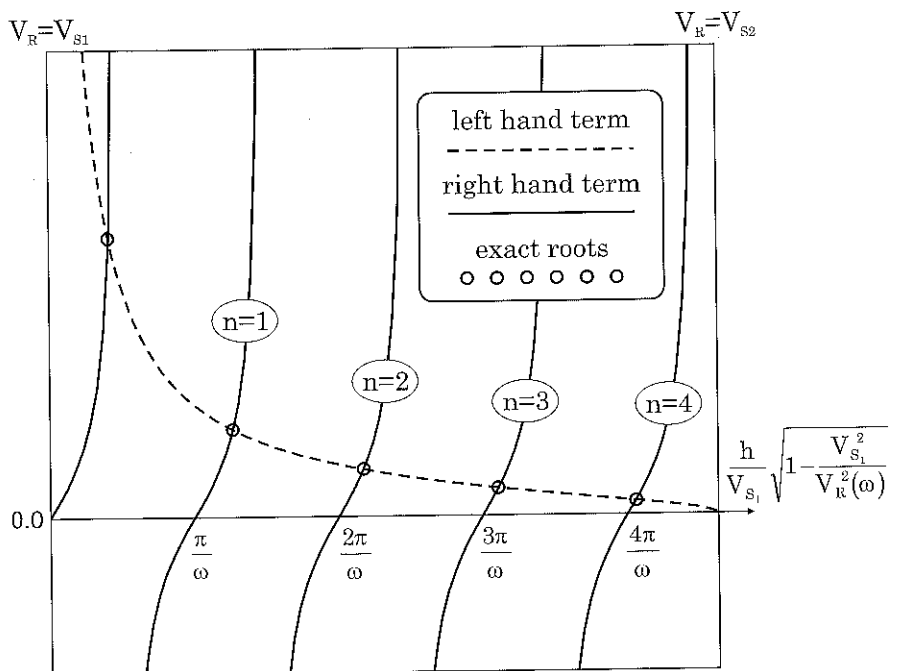


Fig. 3.49: Dispersion of surface waves (Love waves) in a surficial layer: graphical comparison of both terms of Eq.(3.197) to estimate its eigenvalues.

Finally, the eigenfunctions corresponding to the previous eigenvalues are as follows (Aki and Richards, 1980):

$$\begin{aligned}
 u_y^{(n)}(x, z, t) &= 2A_1 \cos \left[\omega \sqrt{\frac{1}{V_{S1}^2} - \frac{1}{V_R^2(\omega_n)} z} \right] \\
 &\quad \exp \left[\frac{i\omega}{V_R(\omega_n)} (x - V_R(\omega_n)t) \right] \quad -h \leq z \leq 0 \\
 &= 2A_1 \cos \left[\omega \sqrt{\frac{1}{V_{S1}^2} - \frac{1}{V_R^2(\omega_n)} h} \right] \\
 &\quad \exp \left[-\omega \sqrt{\frac{1}{V_R^2(\omega_n)} - \frac{1}{V_{S2}^2}} (h - z) \right] \\
 &\quad \exp \left[\frac{i\omega}{V_R(\omega_n)} (x - V_R(\omega_n)t) \right] \quad z \leq -h
 \end{aligned} \tag{3.198}$$

As shown by Eq.(3.198), the eigenfunctions involve sinusoidal oscillation in the surficial layer whereas they have an exponential decay in the half-space.

Application for a given soil layering

Soil model and number of modes. We shall now consider a single layer with the following parameters: $h=50\text{m}$, $V_{S1}=400\text{m/s}$ and $V_{S2}=800\text{m/s}$. Applying the previous method, for three given frequencies (5Hz, 10Hz and 15Hz), we obtain various numbers of eigenvalues displayed in Fig.3.50. The number of eigenvalues ranges from 2 at 5Hz to 4 at 15Hz. The curves being drawn as functions of hb_1 , it is necessary to find the roots of Eq.(3.197) and compute the corresponding velocity values (Love waves) for each frequency.

Velocity values for each mode. Considering the curves displayed in Fig.3.50, one can compute the eigenvalues of Eq.(3.197) at each frequency. The roots are firstly determined in terms of hb_1 and then converted into surface wave velocities using the expression of b_1 , Eq.(3.192). All these values are detailed in Table 3.6 for $f=5\text{Hz}$, 10Hz and 15Hz . The number of modes depends on the frequency level:

- for $f=5\text{Hz}$: only two modes are obtained with velocities close to that of the layer ($n=0$) and that of the half-space ($n=1$) respectively,
- for $f=10\text{Hz}$: a third mode ($n=2$) is reached at this frequency and mode $n=1$ now leads to a velocity in between V_{S1} and V_{S2} ,
- for $f=15\text{Hz}$: a fourth mode ($n=3$) is now reached and modes $n=1$ and $n=2$ have velocities in between V_{S1} and V_{S2} .

Table 3.6: Number of modes at three different frequencies and corresponding hb_1 values and surface wave velocities ($h=50\text{m}$, $V_{S1}=400\text{m/s}$ and $V_{S2}=800\text{m/s}$).

frequency values	mode $n=0$	mode $n=1$	mode $n=2$	mode $n=3$
5 Hz: hb_1 velocity	0.0462564	0.1080292	no	no
	430.56524	795.08442	no	no
10 Hz: hb_1 velocity	0.0240927	0.0715505	0.1074094	no
	407.64347	487.82181	781.99225	no
15 Hz: hb_1 velocity	0.0162638	0.0486718	0.0804589	0.1065728
	403.42933	434.27302	522.66928	765.41439

Dispersion curves for two soil models. We shall now consider two soil models and compute the dispersion curves for each of them. Both models involve a single layer with the following parameters:

- $h=50\text{m}$, $V_{S1}=400\text{m/s}$ and $V_{S2}=800\text{m/s}$,

- $h'=30m$, $V_{S_1}=400m/s$ and $V_{S_2}=800m/s$.

The velocities in the layer and the half-space are then identical and both configurations are only differing through the layer depth.

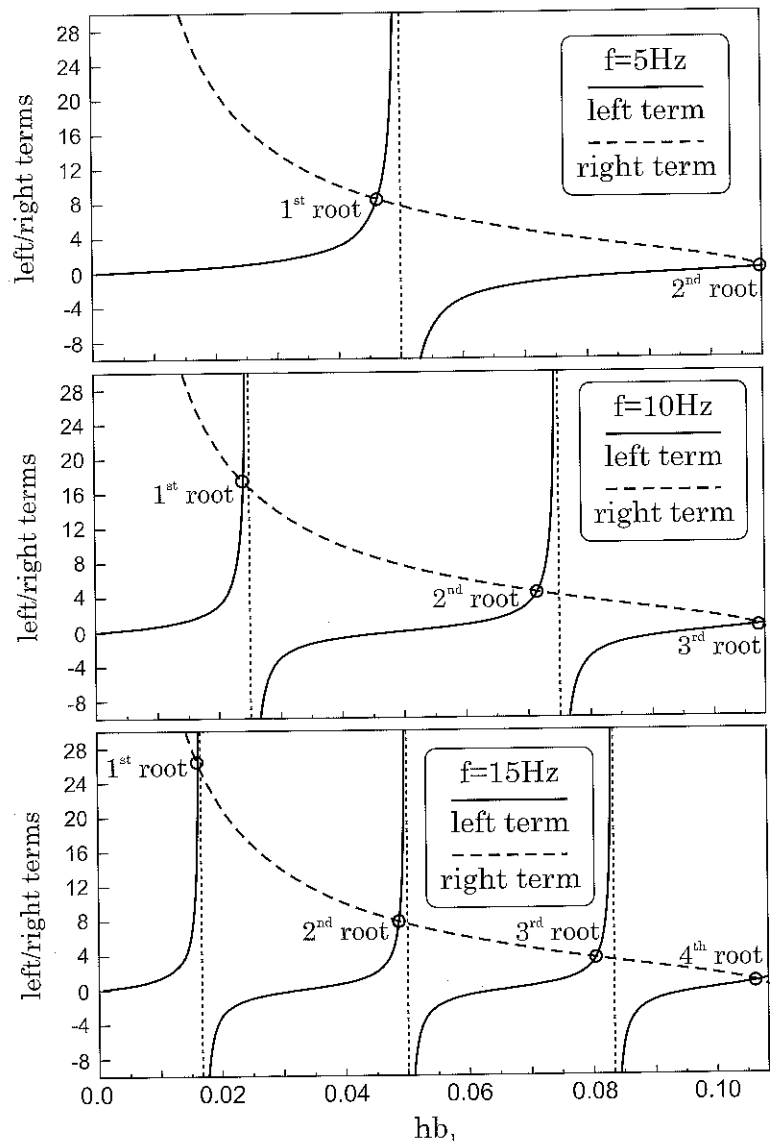


Fig. 3.50: Number of modes at three different frequencies: 5, 10 and 15Hz ($h=50m$, $V_{S_1}=400m/s$ and $V_{S_2}=800m/s$).

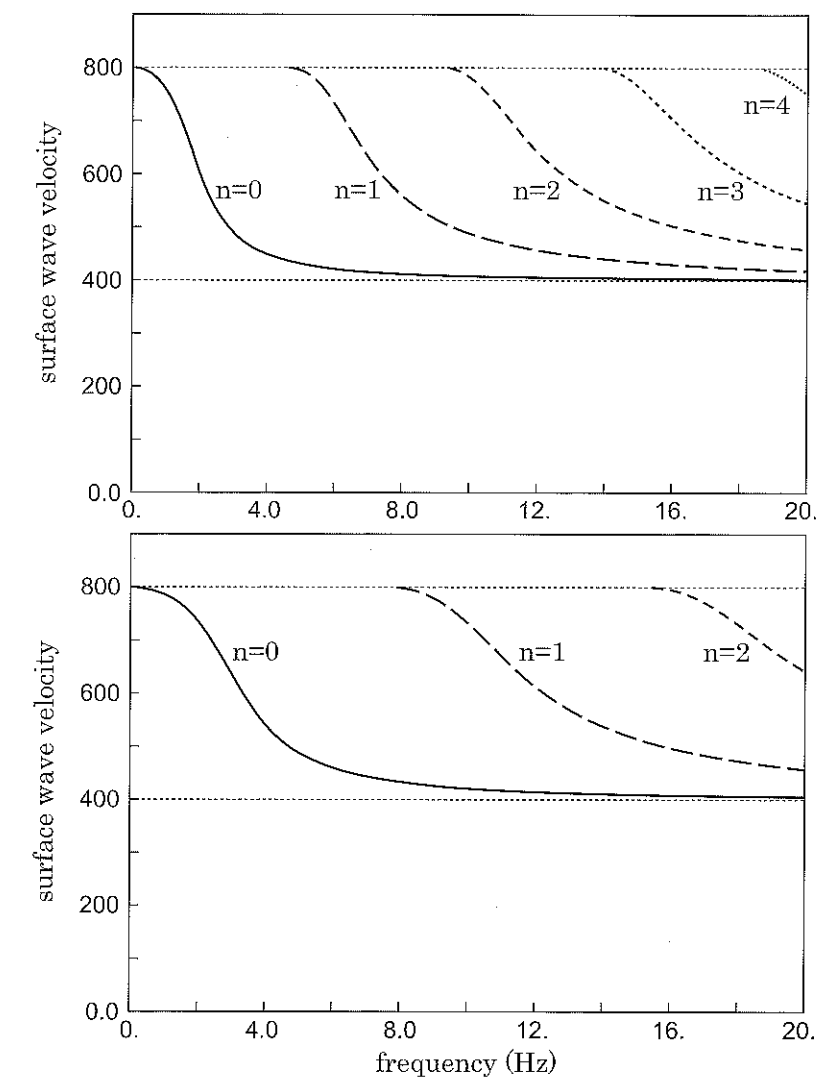


Fig. 3.51: Dispersion curves (Love waves) between 0 and 20Hz for the two soil models: $h=50m$ (top), $h'=30m$ (bottom).

Applying the previous method, we shall compute, for each soil model, the roots of Eq.(3.197) for various frequencies in the range [0,20Hz]. As shown in Fig.3.51, the number of modes increases with frequency: new modes progressively appear at some specific frequency values. Comparing both soil models, the number of modes is larger (in the same frequency range) for the deepest layer. For a given mode, the velocity is close to the half-space velocity $V_{S_2}=800m/s$ at low frequencies and converges to the layer veloc-

ity $V_{S_1}=400\text{m/s}$ for higher frequencies (Fig.3.51). The surface wave velocity decreases rapidly for $h=50\text{m}$, whereas for $h=30\text{m}$, the decay is much slower (wider frequency range).

Considering these theoretical results, it will now be possible to characterize the various modes at some specific site thanks to experimental methods. A way of separating different modes is for instance to record them at various distances. Lower order modes are related to large distances (long wavelengths) whereas higher order modes can be characterized on small distances (short wavelengths). It is thus possible, using inversion techniques, to find out what are the soil profile characteristics at the specific site considered. This is the basis of an investigation method called the *Spectral Analysis of Surface Waves* (Bodet *et al.*, 2005; Foti, 2000, 2003).

3.7.2 Dispersion of surface waves in a heterogeneous half-space

Heterogeneous half-space

We shall now consider a heterogeneous half-space having its mechanical properties defined as functions of the vertical coordinate z : $\lambda(z)$, $\mu(z)$ and $\rho(z)$ (Fig.3.52). Surfaces waves propagating horizontally, along the x axis, will be investigated (Aki and Richards, 1980).

Theoretical analysis for Love waves

Model and wavefields. For Love waves, the expression of the wavefield is:

$$\begin{aligned} u_x &= 0 \\ u_y &= \mathcal{L}_1(V_R, z, \omega) \exp \left[\frac{i\omega}{V_R} (x - V_R t) \right] \\ u_z &= 0 \end{aligned} \quad (3.199)$$

The related stress components are the following:

$$\begin{aligned} \sigma_{xx} &= \sigma_{yy} = \sigma_{zz} = \sigma_{zx} = 0 \\ \sigma_{yz} &= \mu \frac{\partial \mathcal{L}_1}{\partial z} \exp \left[\frac{i\omega}{V_R} (x - V_R t) \right] \\ \sigma_{xy} &= \frac{i\omega}{V_R} \mu \mathcal{L}_1 \exp \left[\frac{i\omega}{V_R} (x - V_R t) \right] \end{aligned} \quad (3.200)$$

The equation of motion is thus:

$$-\omega^2 \rho(z) \mathcal{L}_1 = \frac{\partial}{\partial z} \left(\mu(z) \frac{\partial \mathcal{L}_1}{\partial z} \right) - \frac{\omega^2}{V_R^2} \mu(z) \mathcal{L}_1 \quad (3.201)$$

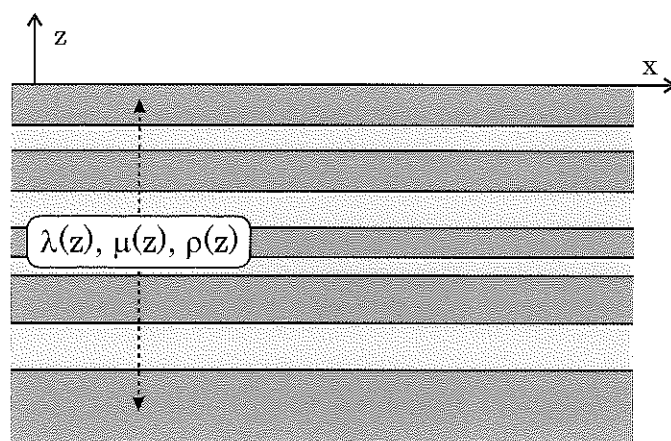


Fig. 3.52: Dispersion of surface waves in a heterogeneous half-space: schematic of the problem.

Free-surface and continuity conditions. The displacements and tractions must be continuous at any interfaces $z = z_0$. The z dependence of the stress component σ_{yz} being rewritten as:

$$\sigma_{yz} = \mathcal{L}_2(V_R, z, \omega) \exp \left[\frac{i\omega}{V_R} (x - V_R t) \right] \quad (3.202)$$

equations (3.200) and (3.201) thus yield:

$$\begin{aligned} \frac{\partial \mathcal{L}_1}{\partial z} &= \frac{\mathcal{L}_2}{\mu(z)} \\ \frac{\partial \mathcal{L}_2}{\partial z} &= \left[\frac{\omega^2}{V_R^2} \mu(z) - \omega^2 \rho(z) \right] \mathcal{L}_1 \end{aligned} \quad (3.203)$$

that is, under a matrix form (Aki and Richards, 1980):

$$\frac{\partial}{\partial z} \begin{Bmatrix} \mathcal{L}_1 \\ \mathcal{L}_2 \end{Bmatrix} = \begin{pmatrix} 0 & \frac{1}{\mu(z)} \\ \frac{\omega^2}{V_R^2} \mu(z) - \omega^2 \rho(z) & 0 \end{pmatrix} \begin{Bmatrix} \mathcal{L}_1 \\ \mathcal{L}_2 \end{Bmatrix} \quad (3.204)$$

The boundary conditions at the free-surface and at infinity lead to:

$$\begin{aligned} \lim_{z \rightarrow -\infty} \mathcal{L}_1 &= 0 \\ \mathcal{L}_2(z = 0) &= 0 \end{aligned} \quad (3.205)$$

Similarly to the case of Love waves in a single-layered half-space, combining Eq.(3.204) and Eq.(3.205) leads to an eigenvalue problem requiring a numerical solution method (e.g. Runge-Kutta algorithm).

Theoretical analysis for Rayleigh waves

Model and wavefields. For Rayleigh waves, the expression of the wavefield is (Aki and Richards, 1980):

$$\begin{aligned} u_x &= \mathcal{R}_1(V_R, z, \omega) \exp\left[\frac{i\omega}{V_R}(x - V_R t)\right] \\ u_y &= 0 \\ u_z &= i\mathcal{R}_2(V_R, z, \omega) \exp\left[\frac{i\omega}{V_R}(x - V_R t)\right] \end{aligned} \quad (3.206)$$

The related stress components are the following:

$$\begin{aligned} \sigma_{xy} &= \sigma_{yz} = 0 \\ \sigma_{xx} &= i \left[\lambda \frac{\partial \mathcal{R}_2}{\partial z} + \frac{\omega}{V_R} (\lambda + 2\mu) \mathcal{R}_1 \right] \exp\left[\frac{i\omega}{V_R}(x - V_R t)\right] \\ \sigma_{yy} &= i \left(\lambda \frac{\partial \mathcal{R}_2}{\partial z} + \lambda \frac{\omega}{V_R} \mathcal{R}_1 \right) \exp\left[\frac{i\omega}{V_R}(x - V_R t)\right] \\ \sigma_{zz} &= i \left[(\lambda + 2\mu) \frac{\partial \mathcal{R}_2}{\partial z} + \lambda \frac{\omega}{V_R} \mathcal{R}_1 \right] \exp\left[\frac{i\omega}{V_R}(x - V_R t)\right] \\ \sigma_{zx} &= \mu \left(\frac{\partial \mathcal{R}_1}{\partial z} - \frac{\omega}{V_R} \mathcal{R}_2 \right) \exp\left[\frac{i\omega}{V_R}(x - V_R t)\right] \end{aligned} \quad (3.207)$$

Free-surface and continuity conditions. The displacements and tractions must be continuous at any interfaces $z = z_0$. The z dependence of the stress component σ_{zx} and σ_{zz} yields similar notations as in the case of Love waves:

$$\begin{aligned} \sigma_{zx} &= \mathcal{R}_3(V_R, z, \omega) \exp\left[\frac{i\omega}{V_R}(x - V_R t)\right] \\ \sigma_{zz} &= i\mathcal{R}_4(V_R, z, \omega) \exp\left[\frac{i\omega}{V_R}(x - V_R t)\right] \end{aligned} \quad (3.208)$$

We thus obtain the following matrix system (Aki and Richards, 1980):

$$\frac{\partial}{\partial z} \begin{Bmatrix} \mathcal{R}_1 \\ \mathcal{R}_2 \\ \mathcal{R}_3 \\ \mathcal{R}_4 \end{Bmatrix} = \begin{Bmatrix} 0 & \frac{\omega}{V_R} & \frac{1}{\mu(z)} & 0 \\ -\frac{\omega}{V_R} \frac{\lambda(z)}{\lambda(z) + 2\mu(z)} & 0 & 0 & \frac{1}{\lambda(z) + 2\mu(z)} \\ \frac{\omega^2}{V_R^2} \frac{4\mu(z)(\lambda(z) + \mu(z))}{\lambda(z) + 2\mu(z)} - \omega^2 \rho(z) & 0 & 0 & \frac{\omega}{V_R} \frac{\lambda(z)}{\lambda(z) + 2\mu(z)} \\ 0 & -\omega^2 \rho(z) & \frac{\omega}{V_R} & 0 \end{Bmatrix} \begin{Bmatrix} \mathcal{R}_1 \\ \mathcal{R}_2 \\ \mathcal{R}_3 \\ \mathcal{R}_4 \end{Bmatrix} \quad (3.209)$$

The boundary conditions at the free-surface and at infinity lead to:

$$\begin{aligned} \lim_{z \rightarrow -\infty} \mathcal{R}_1 &= 0 \quad \text{and} \quad \lim_{z \rightarrow -\infty} \mathcal{R}_2 = 0 \\ \mathcal{R}_3(z = 0) &= 0 \quad \text{and} \quad \mathcal{R}_4(z = 0) = 0 \end{aligned} \quad (3.210)$$

The eigenvalue problem thus obtained needs some numerical method of solution. Lai (1998) proposed a comprehensive presentation of the various approaches.

Solution methods for the eigenvalue problem

Propagator-matrix method. The Propagator-matrix method was originally introduced in seismology by Gilbert and Backus (1966). A special formulation of this method was proposed by Thomson and Haskell (Thomson, 1950; Haskell, 1953). In this formulation, the solutions of eigenproblem (3.209) are found considering the Rayleigh dispersion equation (Eq.(3.150)) at various frequencies. The roots of the Rayleigh dispersion equation give the wavenumber corresponding to the modes of propagation of Rayleigh waves at each frequency. The eigenfunctions may thus be computed yielding the dependence of the wavefield with depth (Lai, 1998). Haskell also proposed some asymptotic expansions for short and long wavelengths. Nevertheless, the original Thomson-Haskell method is not fully stable at higher frequencies (Schwab and Knopoff, 1970).

Reflection and transmission coefficients method. Kennett (1974) proposed a method considering the reflection and transmission coefficients for a multilayered medium. The method is very efficient and was further improved by other researchers (Hisada, 1995). Furthermore, it also gives a direct insight of the various interferences occurring in surface soil layers.

Dynamic stiffness matrix method. Starting from the Thomson-Haskell approach, Kausel and Roessel (1981) derived a finite element formulation using layer stiffness matrices similar to those considered in structural dynamics. It thus allows the use of standard

structural analysis techniques such as substructuring. This formulation simultaneously solves the eigenproblem and the inhomogeneous elastodynamic problem. The use of closed forms was also proposed by Kausel (2000) leading to a very efficient method ("Thin Layer Method").

Other numerical methods. In addition to the finite element method, other numerical methods may also be considered to solve the eigenvalue as well as propagation problems: the finite difference method, the boundary element method or the spectral element method. These methods will be presented in the next Chapter.

3.7.3 Steady State Rayleigh method

This method consists in generating Rayleigh waves at a given frequency f . Their wave velocity, denoted V_R , may be written as: $V_R = f\Lambda$ where Λ is the wavelength. As shown in Fig.3.53, for each frequency f_i , it is possible to determine Λ_i using the relation $\Lambda_i = x/k_i$. The Rayleigh wave velocity V_R is known for each frequency. The shear wave velocity V_S is close to that of the Rayleigh waves ($V_S \approx V_R$). Furthermore, Rayleigh waves have a *significant effect down to a depth of one wavelength*. The velocity V_S is thus known for every frequency f_i , allowing the *characterization of a soil layer having a mean depth of $\Lambda_i/2$* .

Heitz and Bonnet (Heitz, 1992) considered a nonlinear constitutive law to analyze such harmonic tests. They could investigate the influence of the excitation level on the characterization of the dynamic soil properties.

3.7.4 Spectral Analysis of Surface Waves: experiments

Experimental set-up and principle

This method represents an extension, and an improvement, of the harmonic vibration of a block foundation resting on the ground surface (Stokoe and Nazarian, 1985). In this older method, the wavelength Λ_R of a Rayleigh wave generated by the block foundation vibrating at frequency f is measured with a geophone moved on the ground surface. In a homogeneous soil profile, this velocity is frequency independent. As shown in the previous sections, in a layered profile, the wave propagation is frequency dependent and the relationship between frequency and wave velocity is called the dispersion curve. This phenomenon arises from waves with different wavelengths propagating in different layers: high frequency waves (short wavelengths) propagate near the layers interfaces; low frequency waves propagate in shallow and deep layers. Altering the vibration frequency allows to sample different depths and to derive a Rayleigh wave velocity profile and, if Poisson's ratio is known or estimated, a shear wave velocity profile.

The SASW method takes advantage of a more refined analysis of the records for the layered profile and of an easier and faster implementation. As shown in Fig.3.54, the generation of Rayleigh waves is produced by an impulse loading at the ground surface.

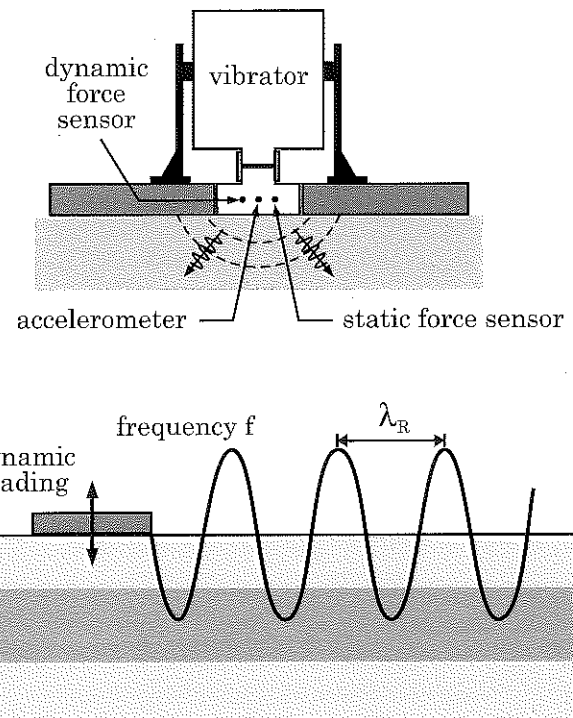


Fig. 3.53: Principle of the Steady State Rayleigh method.

Recorded signals are digitized and transferred into the frequency domain, the phase shift $\Delta\phi$ between two recorded signals is determined, from which the propagation time and the wave propagation velocity are computed. Repeating these steps for different frequencies, the dispersion curve can be established.

Analysis of dispersion from recorded signals

Computing the dispersion. Considering a large number of sensors in the experimental set-up (Fig.3.54), the medium is described in the time-distance plane ($t - x$) through either wave velocities or slownesses (Foti, 2000). The dispersion is not easily characterized in this plane whereas it is in the wavenumber-frequency plane ($k - \omega$). First, the signal must be corrected from geometrical damping. It is then necessary to transform the recordings from the $x - t$ domain to $k - \omega$ domain. This can be done using the $f - k$ transform, also called the two-dimensional Fourier transform (Bodet *et al.*, 2005):

$$s(k, \omega) = \iint s(x, t) e^{i(kx - \omega t)} dx dt \quad (3.211)$$

This expression must be considered in a discrete form with:

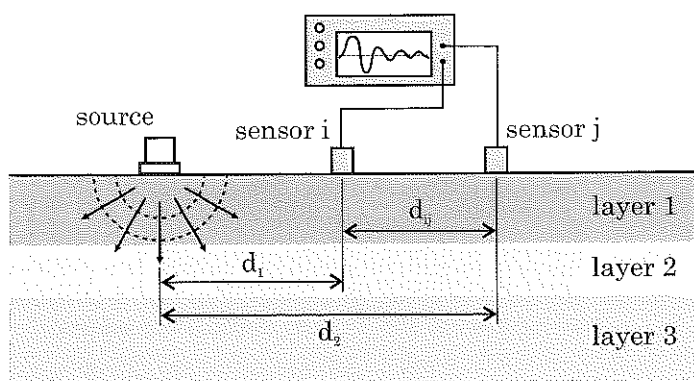


Fig. 3.54: Schematic of surface wave experiments (SASW).

- the frequency sampling related to the time sampling:

$$\Delta f = \frac{1}{t_{max}} = \frac{1}{N_t \Delta t} \quad (3.212)$$

- the wavenumber sampling related to the spatial sampling:

$$\Delta k = \frac{1}{x_{max}} = \frac{1}{N_x \Delta x} \quad (3.213)$$

The distance d_{ij} between the sensors is thus an important parameter since it may induce, as the time sampling, spectral aliasing. It governs the minimum wavelength to which the dispersion may be investigated (Foti, 2000). The number of sensors is also important since the longer the distance the better the resolution in frequency. A longer sensor network thus leads to a higher (spatial) resolution of dispersion.

Inversion of the dispersion data The dispersion phenomena being characterized, inverse methods are needed to estimate the velocity profile of the layered soil. However, as shown by Backus and Gilbert (1967), the inverse problem is nonlinear and there is no unique solution. Various methods are available (Tarantola, 1987; Hunaidi, 1998; Lai, 1998; Beaty *et al.*, 2002; Wathelet *et al.*, 2004). One of the main limitations is that the direct problem is generally assumed to be 1D. As it will be shown in the next paragraph, this assumption is not always valid and the influence of 2D/3D effects may be significant.

Experimental results

Analysis in the lab on model structures. On model structures, Bodet *et al.* (2005) investigated the influence of 2D effects on the analysis of surface wave propagation. They considered a dipping PMMA layer on an aluminum plate (Fig.3.55) and recorded the wavefields at different distances from the source. As shown in Fig.3.56, the results are

significantly different for both areas (*line 8* and *line 7*) and correspond to an average flat layered medium at each location. Such differences illustrate the influence of the layers geometry (depth, inclination, etc) on the reliability of the SASW technique.

Simulated data for three different profiles. Several synthetic data are now proposed to compare different geotechnical profiles depicted in Fig.3.57. As shown in Fig.3.58, the analysis in terms of *frequency-slowness* (in "s/m") is very close to the frequency-wavenumber transform. Foti (2000) simulated the data corresponding to the three different profiles displayed in Fig.3.57. From the frequency-slowness curves, the dispersion may be easily assessed and inversion procedures may lead to the corresponding velocity profile if unknown.

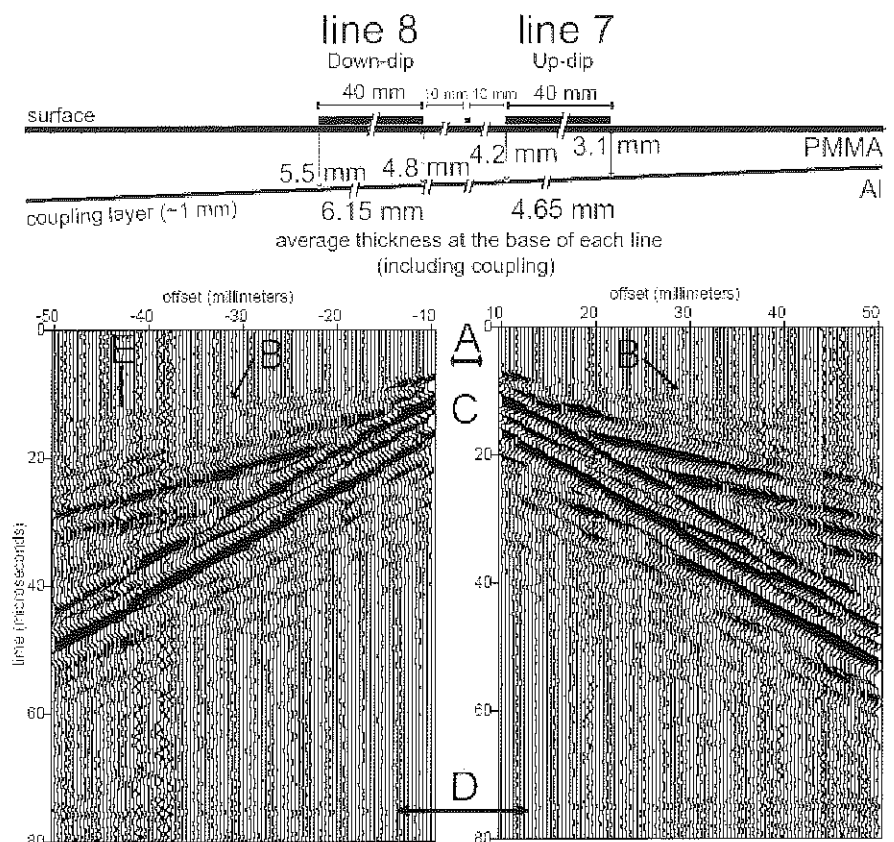


Fig. 3.55: SASW: experimental configuration for a PMMA dipping layer (top) and recorded signals (bottom), from Bodet *et al.* (2005).

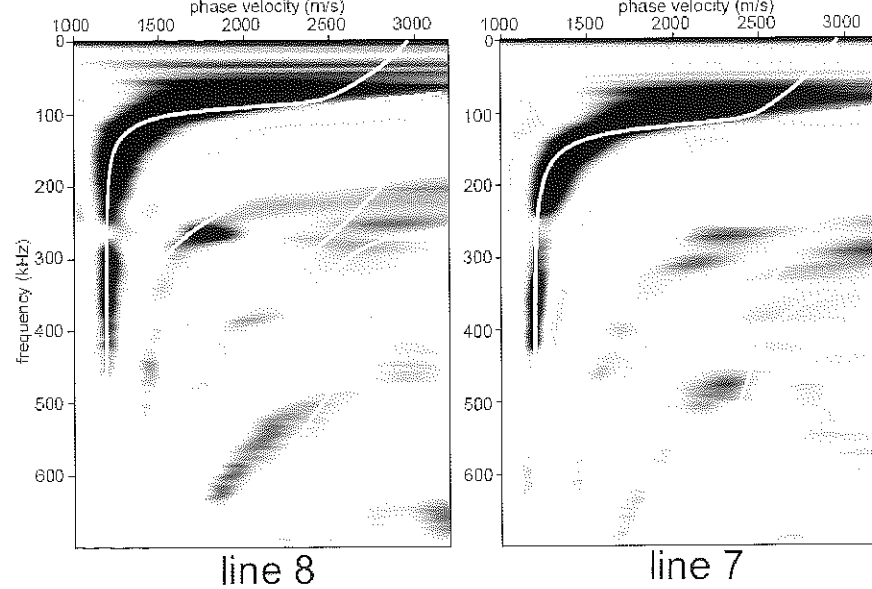


Fig. 3.56: SASW: example of measured dispersion curves in a PMMA dipping layer (from Bodet *et al.*, 2005).

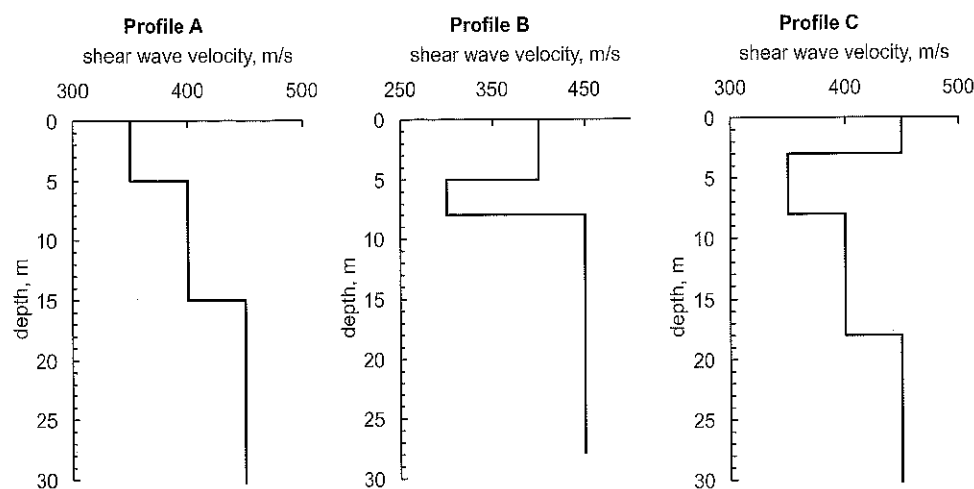


Fig. 3.57: Description of the three different profiles considered by Foti (2000).

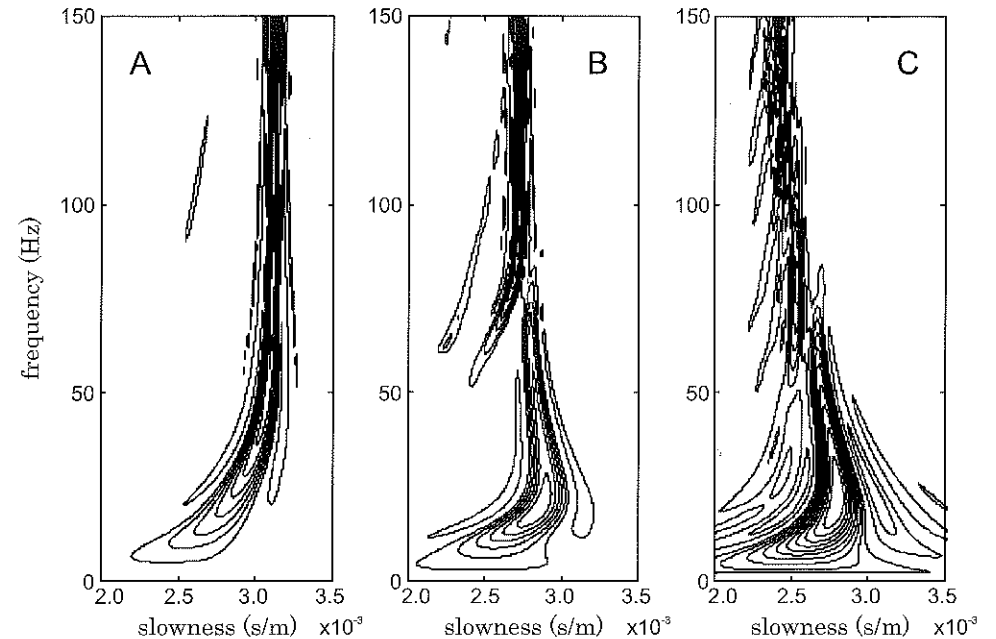


Fig. 3.58: Slowness curves for three different profiles (Foti, 2000).

Foti (2000) proposed a simplified procedure to invert the velocity profile from the frequency-slowness curves. As shown in Fig. 3.59, for three different lengths, the inverted velocity profiles are well correlated to the actual ones. Nevertheless, for profiles *B* and *C*, since the velocity does not follow a monotonic increase with depth, the inversion is less satisfactory. This is generally the main difficulty when performing velocity profile inversions.

Analysis in the field on actual soils. Figure 3.60 presents a dispersion curve constructed from the SASW method (Stokoe and Hoar, 1978). The theoretical curve is compared to the experimental one and the wave velocity profile is altered until a good agreement is reached between both curves. The wave velocity profile computed at the last iteration is deemed to represent the actual velocity profile. This procedure is illustrated in Fig. 3.60 (Stockoe and Hoar, 1978) which shows the evolution of the velocity profile with the iterations and the measured dispersion curve. The final wave velocity profile has been compared to measurements from a nearby cross-hole test, validating the results. However, the SASW method yields a stepped wave velocity profile as opposed to the more continuous variation obtained from a cross-hole test; this arises from the sampling method which is more global in the SASW method.

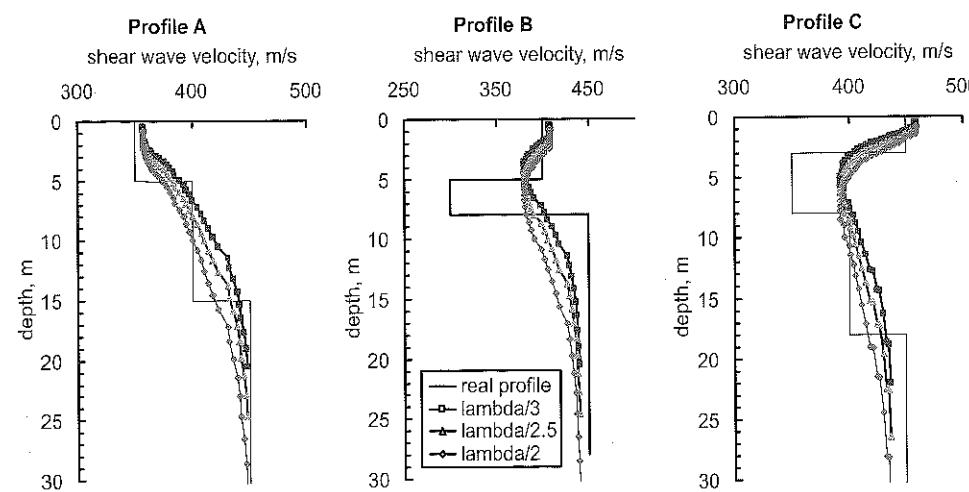


Fig. 3.59: Approximated inversion for three different profiles (Foti, 2000).

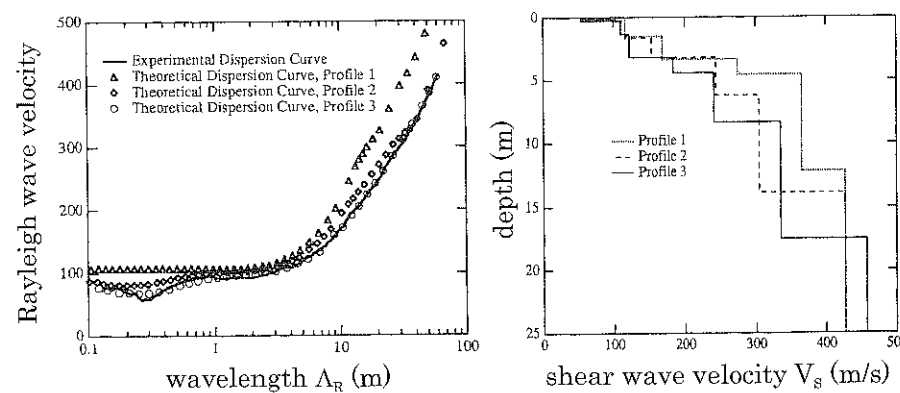


Fig. 3.60: SASW: example of measured dispersion curves in soils (from Stokoe and Hoar, 1978).

3.7.5 Seismic refraction

This method is well suited for preliminary site investigations but its implementation may be difficult. Theory and exploration techniques are well known and have been described in details in textbooks (Richart *et al.*, 1970). As shown in Fig.3.61, the method consists in determining the propagation time of body waves (P or S) generated by a surficial source to a linearly aligned network of receivers. According to the soil profile beneath the receivers, the waves propagate either directly towards the receivers, or along refracted

paths at interfaces between layers. For a three layers soil profile (two soil layers overlying a bedrock), the refraction paths are depicted in Fig.3.61 (top). As discussed earlier in this Chapter, the critical incidences may be estimated from the Snell-Descartes law (i.e. from the velocity ratio between the soil layers).

The slopes of the straight lines obtained by plotting the propagation time versus the distance are equal to the wave velocities (Fig.3.61, bottom). Such plots are obtained from more complex experimental traces. Such signals recorded by (Guéguen *et al.*, 2007) are displayed in Fig.3.62. The source should preferably give rise to shear waves, which is achieved by horizontally hitting a block laid on the ground. With this technique, an almost pure shear wave propagates perpendicularly to the source. Interpretation of the tests is done assuming that the wave velocity increases with depth. If this condition is not satisfied, significant errors can affect the interpretation. Likewise, the presence of a soft layer (with a smaller wave velocity) entrapped between two stiff layers cannot be detected. Finally, in this method, the waves propagate near the layers interfaces; it is therefore impossible to sample an average wave velocity for the layer under consideration.

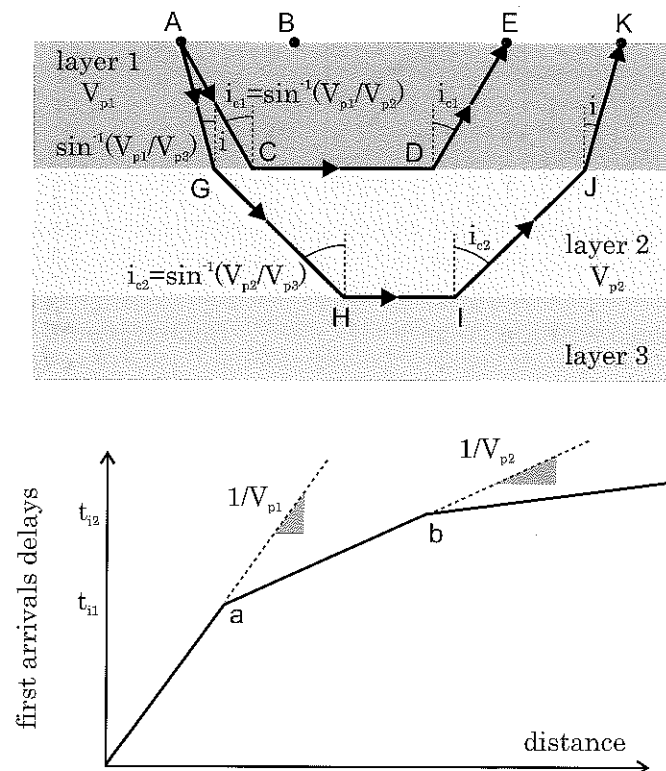


Fig. 3.61: Principle of the seismic refraction method: source and receivers arrangement (top), first arrivals curve (bottom).

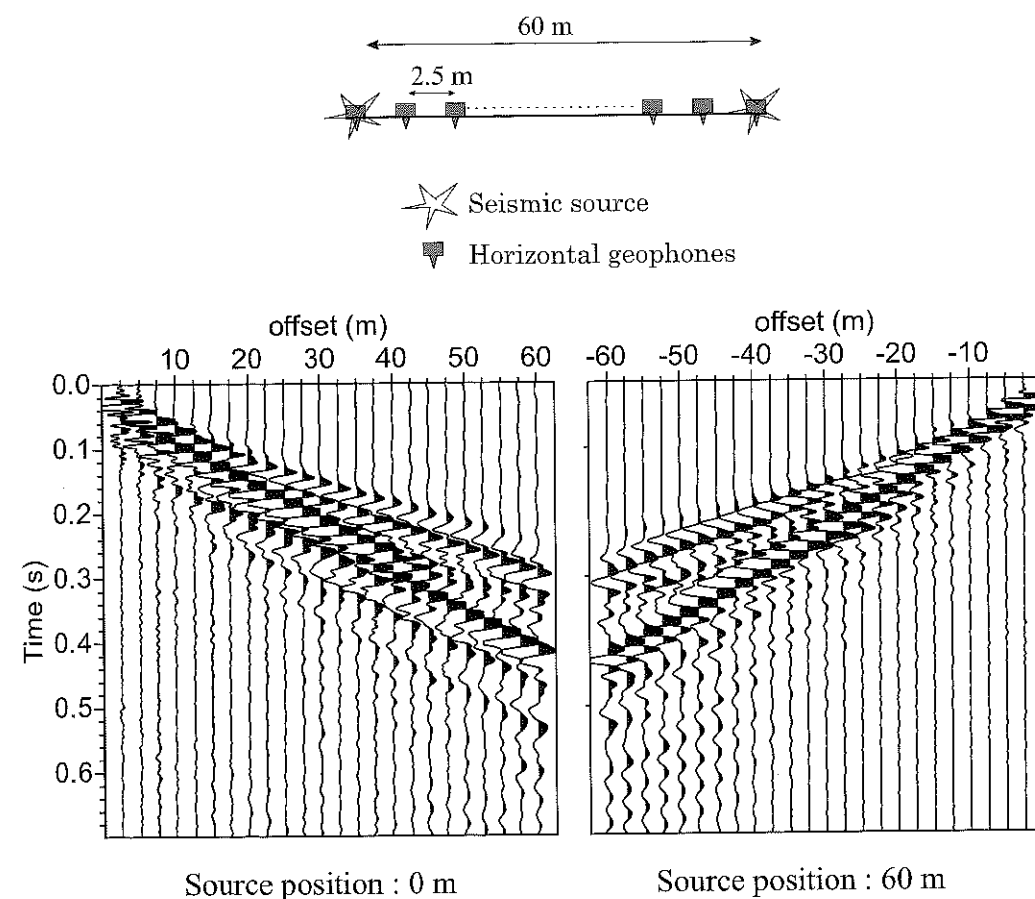


Fig. 3.62: Traces measured in a seismic refraction test with a source located successively at both ends of the network (Guéguen *et al.*, 2007).

3.7.6 In-hole tests

In-hole tests can be grouped into two categories: those requiring a prior drilling of bore hole(s) in which measuring devices are lowered down (cross-hole, down-hole, suspension logging) and those for which the measuring device is lowered with the drilling tool (seismic cone). For the first category, tubing of the hole with a PVC casing is required and the annular space between the casing and the hole must be grouted to ensure a good coupling with the surrounding soil. These operations are time-consuming and costly; in addition, it is absolutely required to measure the holes inclinations.

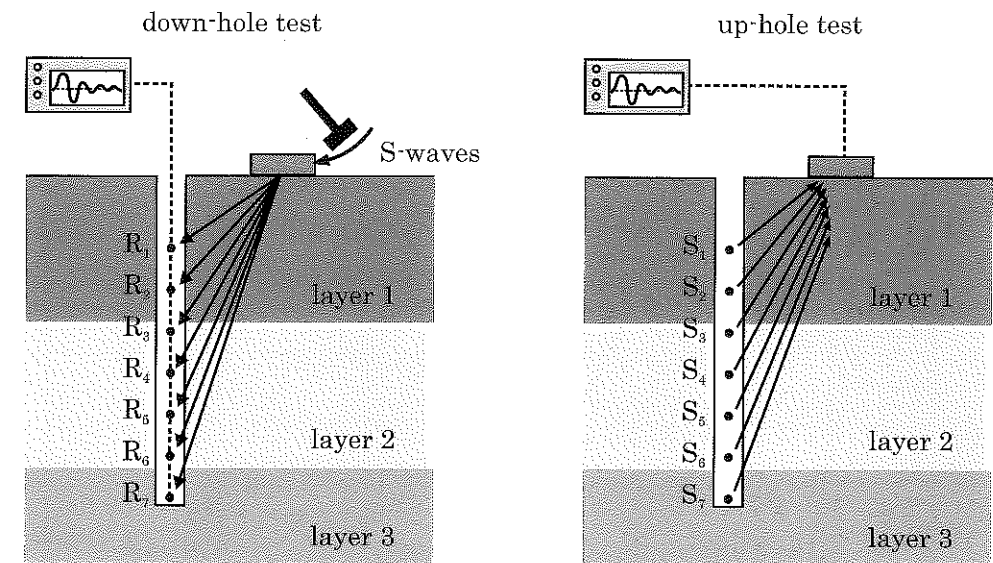


Fig. 3.63: Schematic of down-hole and up-hole tests.

Down-hole tests

The measurement of the wave propagation velocity is performed along one hole (Fig. 3.63). The source is placed at the ground surface and the receivers are placed inside the casing. The use of adequate sources (horizontal impact of a block foundation) gives rise to predominant shear waves. In its simplest version, only one receiver is used and lowered in the hole at successive depths. More elaborate techniques take advantage of a set of receivers clamped on the same frame which allow for a simultaneous recording of some input signal. The accuracy in the determination of the wave velocity is better because the distances between receivers are perfectly known and because the signals are originated from the same impulse. Velocities measured in a down-hole test correspond to values along the vertical side of the hole, for a vertically propagating wave. In-plane variations of these velocities cannot be assessed. On the other hand, with a sufficiently small spacing between the receivers, it is possible to sample layers with lower characteristics, even if they are entrapped in between two stiffer layers. This is one of the major advantages of the method. Figure 3.64 presents an example of a down-hole record showing the way wave velocities may be estimated.

Suspension logging

This method, for the measurements of P and S wave velocities, uses only one, preferably uncased, hole. The borehole is filled with water or drilling mud. The receivers and the source are clamped on the same frame and lowered down at the same time (Fig. 3.65).

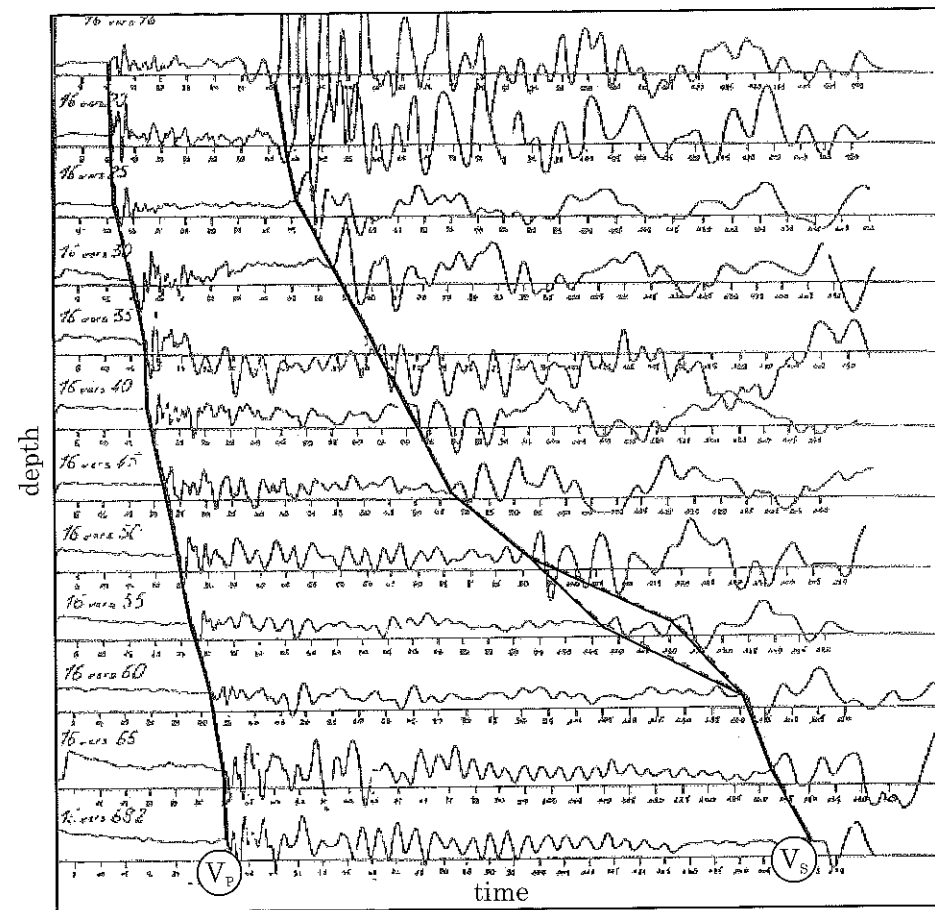


Fig. 3.64: Typical signals recorded in a down-hole test.

The source, with the capability of inverting the wave polarity, is made of a horizontally oriented solenoid which generates a pressure wave in the fluid. When hitting the borehole wall, this pressure wave induces a radial displacement in the soil which gives rise to radially and vertically propagating body waves in the soil. The propagation and displacement of the boreholes wall in turn induce pressure waves in the fluid which are recorded by biaxial geophones. The separating distance between two geophones is 1 m which permits an accurate resolution of the signal. The frame with a total length of 7 m is suspended with a wire line from the ground surface; this test set-up makes possible the investigation at great depths, in excess of 100 m (Nigbor and Imai, 1994).

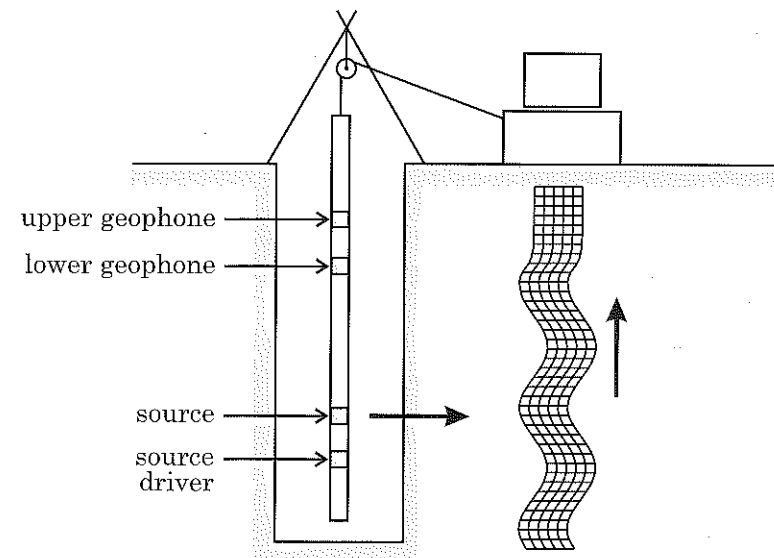


Fig. 3.65: Suspension logging test set-up.

Seismic cone

This is the only in-hole measuring technique which does not require the prior drilling of a borehole. The equipment is similar to the one used for the cone penetration tests (CPT); in addition to the gages for measuring the tip resistance, the skin friction, eventually the excess pore pressure, the cone is provided with a piezo-resistive gage for the detection of seismic waves and with inclinometers for the measurement of verticality (Campanella and Stewart, 1992). The seismic wave is generated at the ground surface by any appropriate mechanical device which favours the generation of shear waves. Recordings of the signals are made at stops during penetration, every 0.5m or 1m. In order to compare the amplitudes of the signals at various depths and to compute the material damping, the source must be capable of generating reproducible signals. The test interpretation is straightforward and resorts to the computation of the propagation time of the wave between two successive positions of the receiver.

The major advantage of the test is, besides its low cost and quick realization, to allow within the same test the determination of different parameters which can be used to characterize the site from a geotechnical standpoint: tip resistance, friction ratio, pore pressure ratio, permeability, and wave velocities. The limitations of the test are similar to those of the down-hole test: good definition of the velocity profile only along the hole, limitation of the sampled depth because of the limiting capacity of the source.

Cross-hole test

Principle of the test. Unlike the other in-hole techniques, the cross-hole tests require the drilling of at least two cased boreholes equipped with PVC tubings, grouted to the soil. To improve the test quality, it is better to use three, or more, aligned boreholes (Fig. 3.66), spaced by a few meters (typically 3m to 10m). The impulse is imparted in the emitting borehole and the generated waves are recorded in the receiving boreholes with triaxial geophones located at the same depth as the source. The source and the receivers are lowered in the holes and clamped to the casing with pneumatic or hydraulic packers.

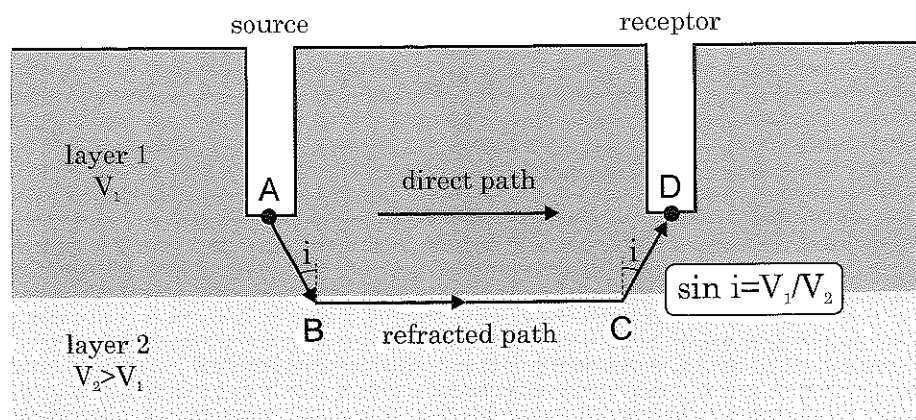


Fig. 3.66: Cross-hole test set-up: direct and refracted waves.

The most commonly used sources are mechanical hammers with a vertically oriented stroke imparting a shear displacement to the borehole wall; this stroke gives primary rise to shear waves propagating horizontally in the soil. This type of sources allows an inversion of the direction of the stroke which modifies the polarity of the shear waves; in addition, it is possible to sum up the signals from different, reproducible, strokes. Use of at least two receiving holes present many advantages:

- the propagation time is computed from differential measurements between receiving holes, when with a two holes set-up, it is computed between the source and the receiver; the coupling between the emitting source and the casing being weaker than the coupling between the geophones and the casing, the determination of the initial time (time zero) may be subjected to errors. When only two holes are required, it is mandatory to have a geophone attached to the source;
- identification of refraction paths in stiffer layers located at shallow depths below the measuring depth is possible. As shown in Fig. 3.66, refraction paths in stiffer layers are a common source of error in cross-hole tests (Stokoe and Hoar, 1978).

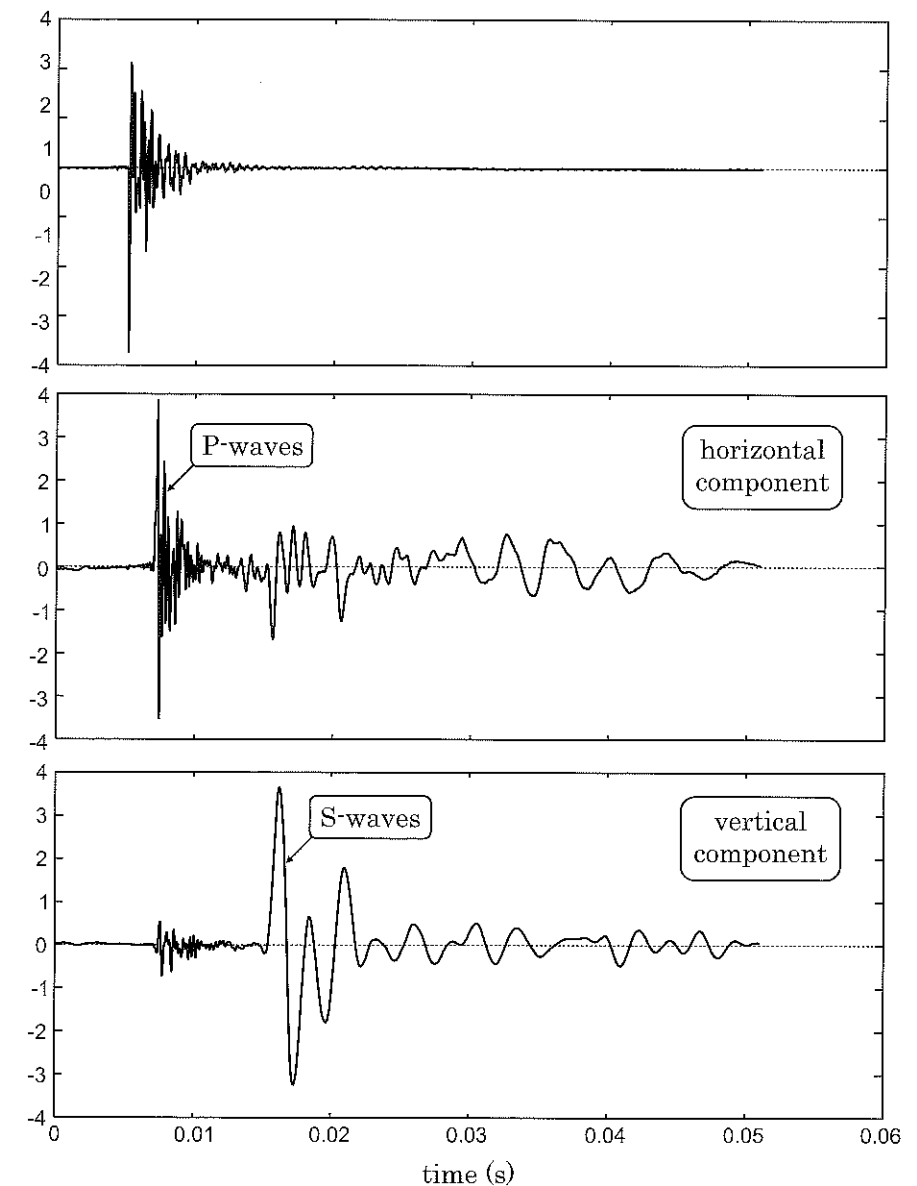


Fig. 3.67: Typical signals from a cross-hole test: emitter (top), horizontal component at receiver 1 (middle) and vertical component at receiver 1 (bottom).

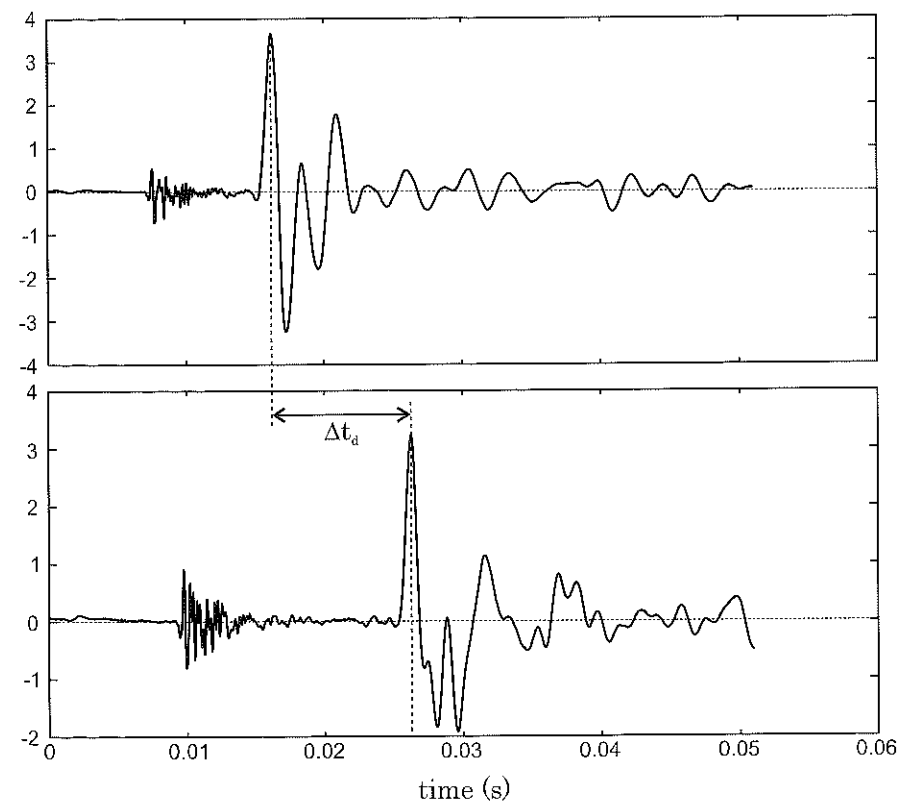


Fig. 3.68: Typical signals from a cross-hole test at two different locations: receiver 1 (top) and receiver 2 (bottom).

The major advantage of cross-hole tests with respect to other in-hole measuring techniques is the possibility of obtaining mechanical characteristics within a horizontal plane and not along a borehole. Owing to the geological deposition of sedimentary deposits, the variation of soil characteristics is more pronounced in the vertical direction than in the horizontal one and the cross-hole test is therefore well-suited. If the receiving boreholes are arranged along different azimuthal directions (usually two mutually perpendicular directions), it is possible to measure the in-plane anisotropy of a layer; this possibility might be interesting in highly tectonized rock deposits.

The cross-hole test, owing to its high versatility, and despite its relatively high cost, is the most powerful used test for important structures. Depths as deep as 100m can easily be reached in cross-hole tests. Typical signals from a cross-hole test are displayed in Fig.3.67: the horizontal (radial) component at the receiver (middle) is mainly composed of P -waves propagating faster than S -waves characterized by the vertical component (bottom).

To estimate the wave velocity in the soil, it is possible to compare the signals at two receivers. As shown in Fig.3.68, the maximum amplitude is reached at $t_1=0.01620s$ for receiver 1 and $t_2=0.02625s$ for receiver 2. The travel time between both receivers is thus $\Delta t_d=0.01005s$.

From these signals, we may compute the cross-correlation as displayed in Fig.3.69 (see Appendix D for its theoretical expression). From this curve, the travel time is found to be $\Delta t_c=0.01015s$ which is very close to the travel time directly estimated from the time signals. Nevertheless, the estimation by the cross-correlation is more reliable since it also takes into account the shape of the signal and not only one single peak.

Misinterpretation in cross-hole tests. Cross-hole tests are very efficient but several types of errors may lead to significant misinterpretations of the test: poor estimation of the arrival time of shear waves, bad quality of the reference time (description of the source), influence of refracted waves in stiff layers, variability of the soil properties, etc.

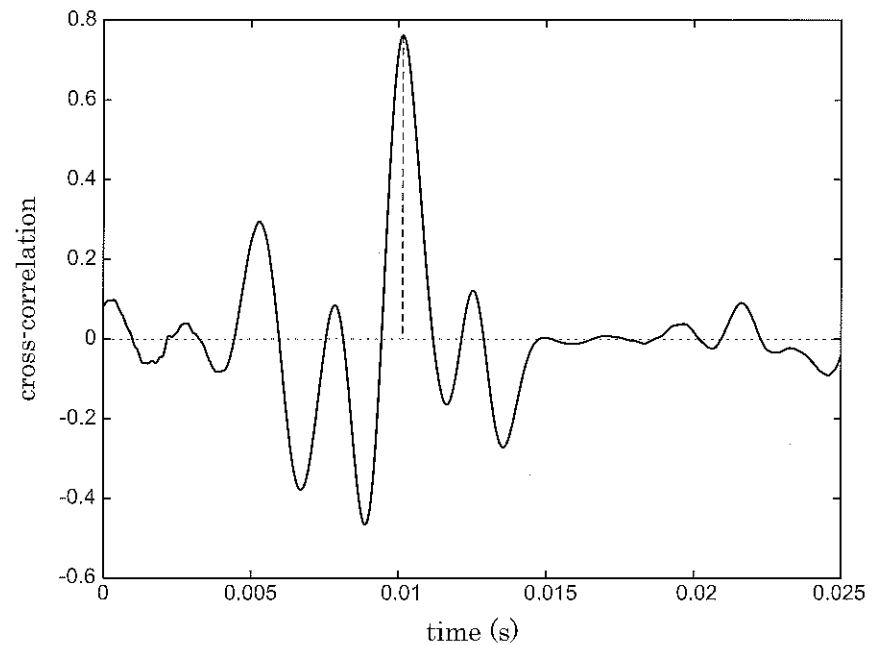


Fig. 3.69: Cross-correlation of two cross-hole test signals showing the travel time (see Appendix D).

The influence of shallow stiff layers may be large since waves refracted by such layers may influence the interpretation of the cross-hole test (Stokoe and Hoar, 1978). As depicted in Fig.3.66, the refracted wave may reach the receiver before the direct wave. The interpretation of the test would thus be biased because of a shorter estimated travel time. The refraction in a deeper stiff layer may be found under the following condition:

$$\frac{x}{H} \geq \frac{2(V_1 + V_2)}{\sqrt{V_2^2 - V_1^2}} \quad (3.214)$$

where x is the distance between both holes, H is the vertical distance between the stiff layer and the bottom of the holes, V_1 and V_2 the wave velocities in the soil and in the stiff layer respectively.

From this condition, the admissible zone for cross-hole tests are determined and displayed in Fig.3.70. The shaded area corresponds to the situations where refraction may not occur thus avoiding misinterpretation of the cross-hole test due to such phenomena.

The variations of the soil properties with depth may also influence the interpretation of cross-hole tests. Since the shear modulus increases with depth (faster near the free-surface), the wave path may not be linear. The ratio between the actual velocity V_{act} and the estimated one V_{est} may thus differ from unity.

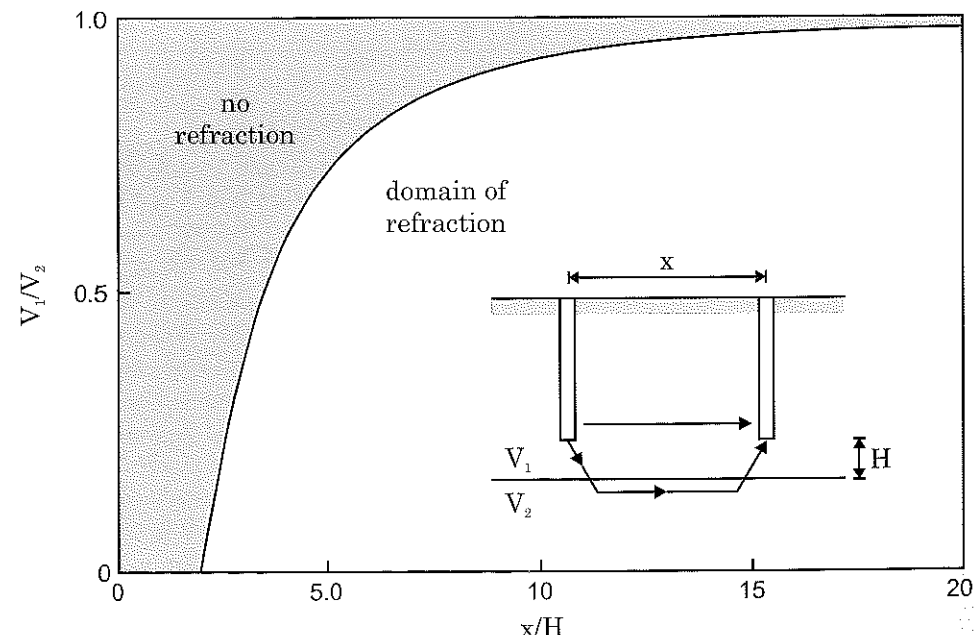


Fig. 3.70: Admissible zones for cross-hole tests.

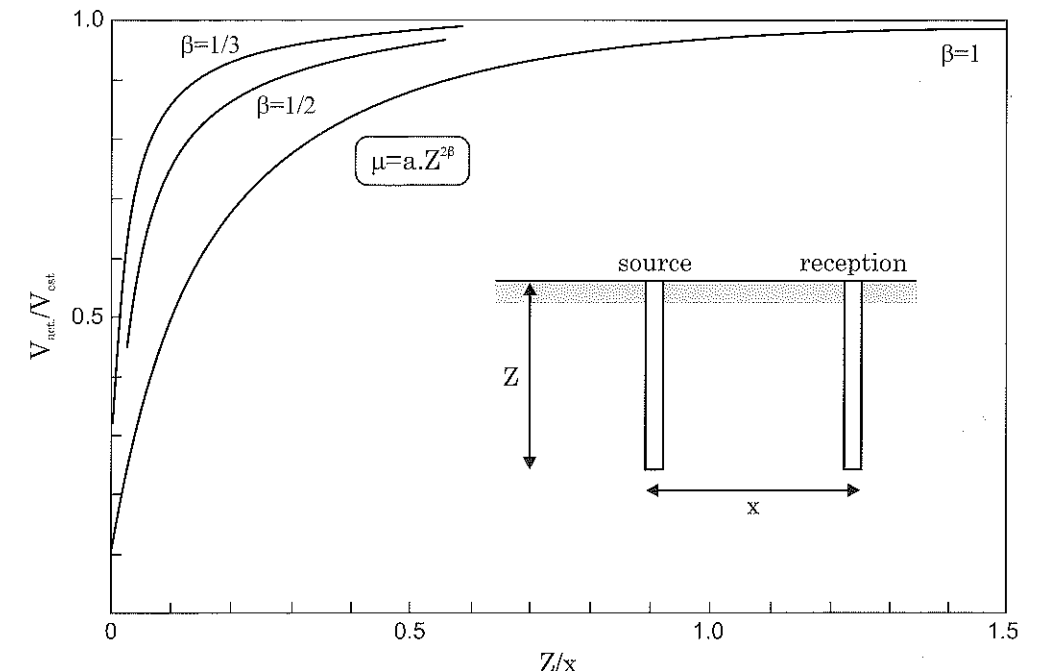


Fig. 3.71: Influence of variable soil properties on cross-hole tests.

To estimate the potential error, we assume a power law for the variations of the shear modulus with depth:

$$\mu(z) = \mu_0 z^{2\beta} \quad (3.215)$$

For such a dependency, the velocity error V_{act}/V_{est} is displayed for several β values in Fig.3.71. For a classical experimental configuration (distance between two holes $x=10$ m), the velocity error is less than 5% for a measurement depth larger than 3 m ($\beta=1/3$) or 4.5 m ($\beta=1/2$). Closer from the free-surface, the velocity error may thus be significant.

3.7.7 Microtremor methods

The microtremor method consists in recording ambient vibrations due to human activities, to the wind, etc (Bonnefoy *et al.*, 2004; Cornou *et al.*, 2003; Duval, 1996). As shown in Fig. 3.72, both the horizontal and vertical components of the motion, denoted $h(t)$ and $v(t)$, are recorded. We then determine the Fourier spectra of the time signals, denoted $H(f)$ and $V(f)$. The calculation of the spectral ratio $H(f)/V(f)$ allows the characterization of the fundamental mode of the geotechnical structures (sharp peak around the fundamental frequency f_0). This spectral ratio is called *H/V microtremor ratio*.

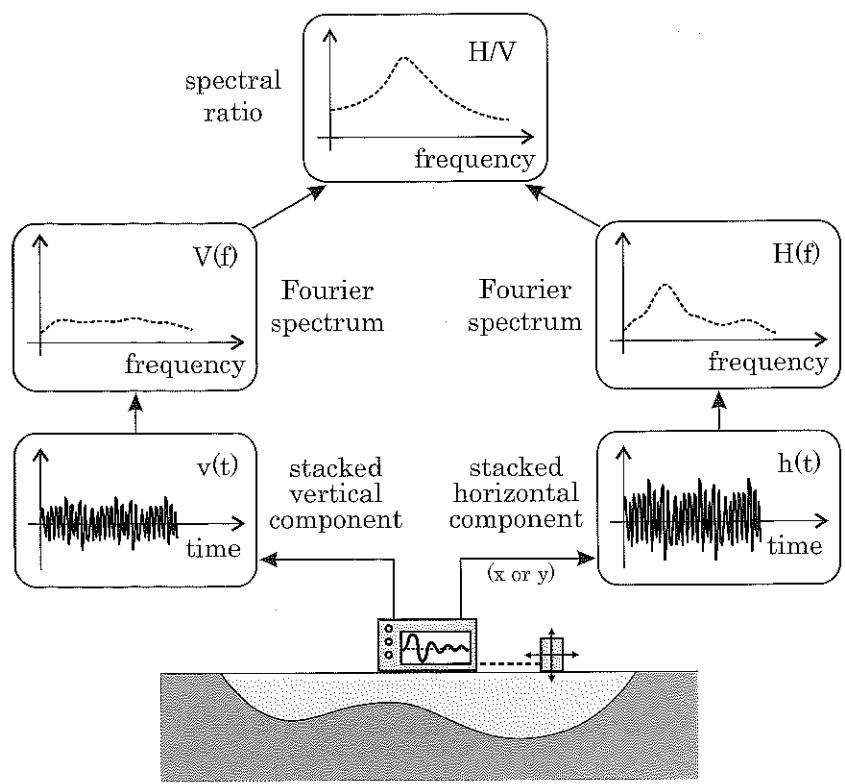


Fig. 3.72: Principle of the microtremor method.

The microtremor ratio may be computed for each of the horizontal components of the motion: $H_x(f)/V(f)$ et $H_y(f)/V(f)$ (denoting Oxy the free-surface plane). An example will be shown in Chapter 5 to investigate the modal features of an alluvial deposit (Scmblat *et al.*, 2000).

3.7.8 Conclusions on field tests

All the previously described field techniques require, for a reliable interpretation, an accurate knowledge of the soil profile: for the cross-hole tests, it prevents from mistakes in the interpretation; for SASW, it gives an initial guess for the iterative calculations; for all the tests, it helps defining a measuring depth increment adapted to the soil profile. It is therefore of paramount importance, for an accurate interpretation of the tests, to have a continuous log of a borehole close to the test. For the down-hole or suspension logging tests, it can be the testing hole; for the cross-hole test, it can be one of the holes.

In-situ testing techniques differ by the possibilities they offer and the information they provide. On the one hand, depths reached with geophysical tests performed from the ground surface (seismic refraction, SASW, down-hole, seismic cone) are limited, typically of the order of 50m; on the other hand, techniques in which the source is lowered in the hole, maintaining a limited distance between the source and the receiver (suspension logging, cross-hole), may sample larger depths, in excess of 100m.

Techniques involving only one hole (suspension logging, down-hole, seismic cone) give only local information on the soil characteristics, those of the soil in the immediate vicinity of the hole; however, they allow an accurate definition of the profile. Seismic refraction or SASW tests provide global information on the medium, but do not allow an accurate definition of the soil profile. Cross-hole tests are a good compromise giving average in-plane characteristics, at a scale of approximately 10m, while maintaining a good accuracy for the definition of the soil profile.

The main limitation of field tests, besides their inability, in the present state of practice, to induce large strains in the soils and therefore to test the soil behaviour beyond its elastic range, lies in the fact that the characteristics are evaluated under the stress field prevailing in the soil profile at the time of testing. More often, constructions involve significant modifications to the stress field in the soil: these variations are related to excavations, backfills, modification of the hydraulic regime, stress increase due to buildings, etc. Since elastic soil properties (shear modulus, for instance) depend upon the effective stresses supported by the soil, these modifications to the initial stress field lead to significant variations of the soil mechanical properties which must be assessed. It is therefore necessary to evaluate the in-situ stress field at the time of realization of the tests and complement the tests with laboratory tests in which variable stress fields can be imposed to the sample. For projects of secondary importance, with a limited budget, the variation with stress of the soil properties can be assessed on the basis of the classification tests, together with experimental published correlations on similar materials.

Finally, it is mandatory to complement the in-situ geophysical tests with an accurate description of the materials and with laboratory tests including, as a minimum, classification tests (water content, dry unit weight, grain size distribution, Atterberg limits,...) and, better, tests characterizing the general soil behaviour (compressibility tests, triaxial tests) and the cyclic and dynamic behaviour. In addition, the geophysical investigation should give an estimate of the horizontal and vertical effective stresses in the soil at the time of the survey to allow a correct interpretation of the tests and an extrapolation of the results to other stress conditions.

Chapter 4

Modelling wave propagation

4.1 Numerical methods for wave propagation

4.1.1 Modelling wave propagation

As discussed in the previous chapters, wave propagation problems are characterized by various phenomena (Aki and Richards, 1980; Bourbié *et al.*, 1987): dispersion, scattering, attenuation, wave conversion, etc. The governing parameters of all these phenomena can not always be estimated experimentally. It is often necessary to perform model experiments (model materials (Bodet *et al.*, 2005), reduced scale model (Chazelas *et al.*, 2001; Coe *et al.*, 1985), etc). As shown in Chap.2, Hopkinson bar tests for instance allow to control the fast dynamic response of a material through indirect measurements of the waves at both sides of the specimen (Semblat *et al.*, 1999; Zhao *et al.*, 1997). One may also consider numerical models and/or inverse methods in order to characterize the material and the waves propagating through it (Lai *et al.*, 2002; Foti, 2000, 2003).

The various numerical methods allowing modelling of wave propagation (finite differences, finite elements, boundary elements, etc) have different advantages and drawbacks. The finite element method is for instance convenient to have a reliable description of the material behaviour, but does not allow an easy modelling of wave propagation in media having an infinite extension. Furthermore, the finite difference or the finite element methods induce a dependence of the propagation features on some algorithmic parameters (time integration scheme, spatial discretization, etc) (Bamberger *et al.*, 1980; Ihlenburg and Babuška, 1995; Scmblat and Brioist, 2000). Other numerical methods (boundary elements, spectral elements) eliminate or limit such phenomena (Bonnet, 1999; Beskos, 1997; Faccioli *et al.*, 1997; Komatitsch and Vilotte, 1998). It is thus necessary to discuss the advantages and drawbacks of each numerical method.

4.1.2 Numerical Modelling in Elastodynamics

To analyze 3D elastodynamic problems, various numerical methods are available:

- the *finite element method* which efficiently deals with complex geometries and numerous heterogeneities (Chammas *et al.*, 2003), even for inelastic constitutive models (Delépine *et al.*, 2007). It has nevertheless several drawbacks such as numerical dispersion (and damping) (Deraemaeker *et al.*, 1999; Ihlenburg and Babuška, 1995; Semblat and Brioist, 2000) and (consequently) numerical cost in 3D elastodynamics,
- the *finite difference method* which is very accurate in elastodynamics but is mainly adapted to simple geometries and linear constitutive models (Frankel and Vidale, 1992; Graves, 1996; Moczo *et al.*, 2002, 2004; Saenger *et al.*, 2000; Virieux, 1986),
- the *boundary element method* which allows a very good description of the radiation conditions but tends to be limited to weak heterogeneities and linear constitutive models (Banerjee *et al.*, 1988; Beskos, 1997; Beskos *et al.*, 1986; Bonnet, 1999; Dangla, 1988; Sánchez-Sesma and Luzón, 1995; Yokoi, 2003),
- the *spectral element method* which has been increasingly considered to analyse 2D/3D wave propagation in linear media (Faccioli *et al.*, 1996, 1997; Komatitsch and Vilotte, 1996, 1998),
- the *Aki-Larner method* which takes advantage of the frequency-wavenumber decomposition but is limited to simple geometries (Aki and Larner, 1970; Bouchon *et al.*, 1989; Kawase, 1988),
- *series expansions of wave functions* which give a semi-analytical estimation of the scattered wavefield for simple geometries (Lee, 1984; Moeen-Vaziri and Trifunac, 1985; Sánchez-Sesma, 1983).

Each method has specific advantages and drawbacks. It is consequently often more interesting to combine two methods to take advantage of their peculiarities. One common method in elastodynamics is to couple FEM and BEM allowing an accurate description of the near field (FEM model including complex geometries, heterogeneities and constitutive behaviours) and a reliable estimation of the far-field (BEM model involving radiation conditions), (Dangla, 1988).

In this chapter, two methods will be mainly discussed: the Finite Element Method and the Boundary Element Method.

4.1.3 Time domain vs frequency domain

Numerical modelling of waves and vibrations in soils may be performed either by time domain integration or by frequency domain solution methods. In the field of structural dynamics, modal methods, including superposition, are often used but are not fully

4.1 Numerical methods for wave propagation

adapted to analyze wave propagation (Clough and Penzien, 1993). However, a simplified modal approach adapted to the analysis of geological structures will be discussed in Chapter 5.

Time integration methods allow an easier implementation of time-dependent constitutive laws as well as nonlinear constitutive laws. They consist in a numerical estimation of the solution at various times starting from the initial conditions and the time variations of the loading. These methods involve assumptions allowing the approximation of the time derivatives of displacement. For linear constitutive laws, the solution is obtained by solving a linear set of equations. For nonlinear problems, it is generally necessary to implement numerical iterative procedures at each time step. Many time integration algorithms can be considered (Hughes, 1987), some of them will be discussed in the following. Frequency domain solution methods are widely used in Boundary Element approaches (Bonnet, 1999). They are very powerful in the field of dynamics/wave propagation since the equation of motion may be easily derived in the frequency domain (time derivatives expressed as simple products by a factor $\pm i\omega$). As shown in Chapter 2, they are also convenient in accounting for attenuation.

4.1.4 Actual or synthetic signals

Numerical modelling of wave propagation phenomena raises the need for the estimation of the dynamic properties of the medium, but also the features of the loading. Various types of loadings may be considered depending on the aim of the analysis (design, parametric study, etc):

- actual seismic signals or vibrations recorded at a site which may be used (directly or after deconvolution) as a loading/input in a numerical model,
- synthetic signals computed from standard spectra of the site,
- purely synthetic signals determined from simple analytical expressions.

Several types of wavelets are presented hereafter; several others are detailed in appendix B.

Original Ricker wavelet

In the latter class of signals, Ricker (1943, 1953) proposed complex synthetic wavelets to model wave propagation due to a shot pulse. He considered the wave equation in dissipative media, as first proposed by Stokes:

$$\nabla^2 \left(u + \frac{1}{\omega_0} \frac{\partial u}{\partial t} \right) = \frac{1}{c^2} \frac{\partial^2 u}{\partial t^2} \quad (4.1)$$

where u is a component of the displacement field \underline{u} and ω_0 is a constant.

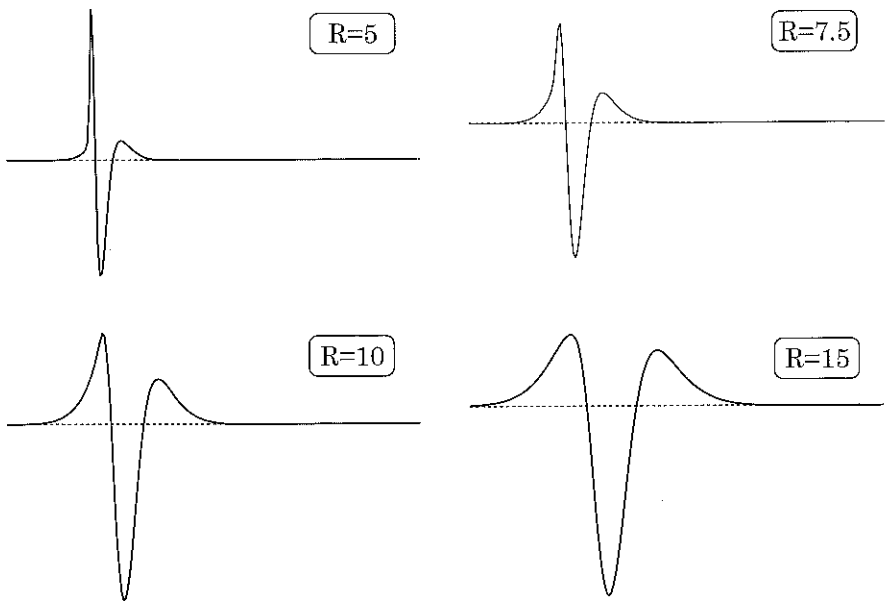


Fig. 4.1: Time variations of the original Ricker wavelets for various dimensionless distances $R=5, 10, 15$ and 20 (Ricker, 1943, 1953).

The expression of the seismic wavelet proposed by Ricker (1953), in terms of velocity, is the following:

$$\dot{u} = -\frac{2}{R} \int_0^\infty \beta^2 \exp \left[-R\beta(1+\beta^2)^{-1/4} \sin \left(\frac{\arctan \beta}{2} \right) \right] \cos \left[R\beta(1+\beta^2)^{-1/4} \cos \left(\frac{\arctan \beta}{2} \right) - \beta T \right] d\beta \quad (4.2)$$

where $R = \omega_0 r / c$ and $T = \omega_0 t$ with r the true radial distance, c the wave velocity and t the time. R and T are dimensionless parameters called the numerical distance and numerical time respectively.

The velocity wavlet defined in Eq.(4.2) is now computed for various dimensionless distances R . The corresponding curves are displayed in Fig.4.1:

- For $R=5$: the wavelet is strongly asymmetrical with a very sharp positive peak followed by a smoother negative peak. This shape fits well the main features of near field seismic waves in anelastic media.
- For $R=7.5$: the wavlet is still asymmetrical but a bit smoother than in the previous case. The shape variations from $R = 5$ to $R = 7.5$ are related to the properties of seismic waves in anelastic media.

- For $R=10$: the wavelet is much smoother than in both previous cases.
- For $R=15$: the wavelet is nearly symmetrical with a main negative peak and two secondary positive peaks. This shape is close to the simplified Ricker wavelet defined in the next paragraph.

Many various types of seismic wavelets were recently discussed by Mavroelidis and Papageorgiou (2003): they are mainly due to Gabor, Berlage, Küpper or Ricker (see appendix B). In this paper, these authors also proposed their own analytical model and performed extensive identification studies from actual seismological data.

Simplified Ricker wavelet

In the Ricker class of wavelets, simplified Ricker wavelets are often used in geophysics and seismology (Bard and Bouchon, 1985; Bisch *et al.*, 1999). This family of Ricker wavelets is derived from a gaussian and the signals consequently have a strong decay in both time and frequency domains (see Fig.4.2). At order 2, the expression of the Ricker wavelet is as follows (Mavroelidis and Papageorgiou, 2003):

$$R_2(t) = A_0 \left(2\pi^2 \frac{(t-t_s)^2}{t_p^2} - 1 \right) \exp \left[-\pi^2 \frac{(t-t_s)^2}{t_p^2} \right] \quad (4.3)$$

where t_s is the time related to the maximum amplitude of the wavelet and t_p is the fundamental period of the signal.

As shown in Fig.4.2, it is also possible to define the Ricker wavelet breadth t_b as (Ryan, 1994):

$$t_b = \frac{\sqrt{6}t_p}{\pi} \simeq 0.78t_p \quad (4.4)$$

t_b corresponds to the time delay between both secondary peaks of the 2nd order Ricker wavelet. There is consequently a significant difference between the fundamental period t_p and the wavelet breadth t_b .

The interest of the 2nd order Ricker wavelet is that it is well localized in both time and frequency domain (see appendix B). It is thus easy to control the signal duration and its frequency content.

Double- M wavelet

Other types of synthetic signals are considered in the field of train induced vibration. Such a synthetic signal may be used either for numerical simulations or experimental models. For instance, the double- M wavelet characterizing the excitation induced by the bogie is depicted in Fig.4.3 (Al Shaer *et al.*, 2008). It is defined as a combination of two gaussians (Ricker signals at order zero):

$$F(t, Q, v) = \frac{QY}{2} \left[X^{\frac{(vt-a)^2}{d^2}} + X^{\frac{(vt-a-L)^2}{d^2}} \right] \quad (4.5)$$

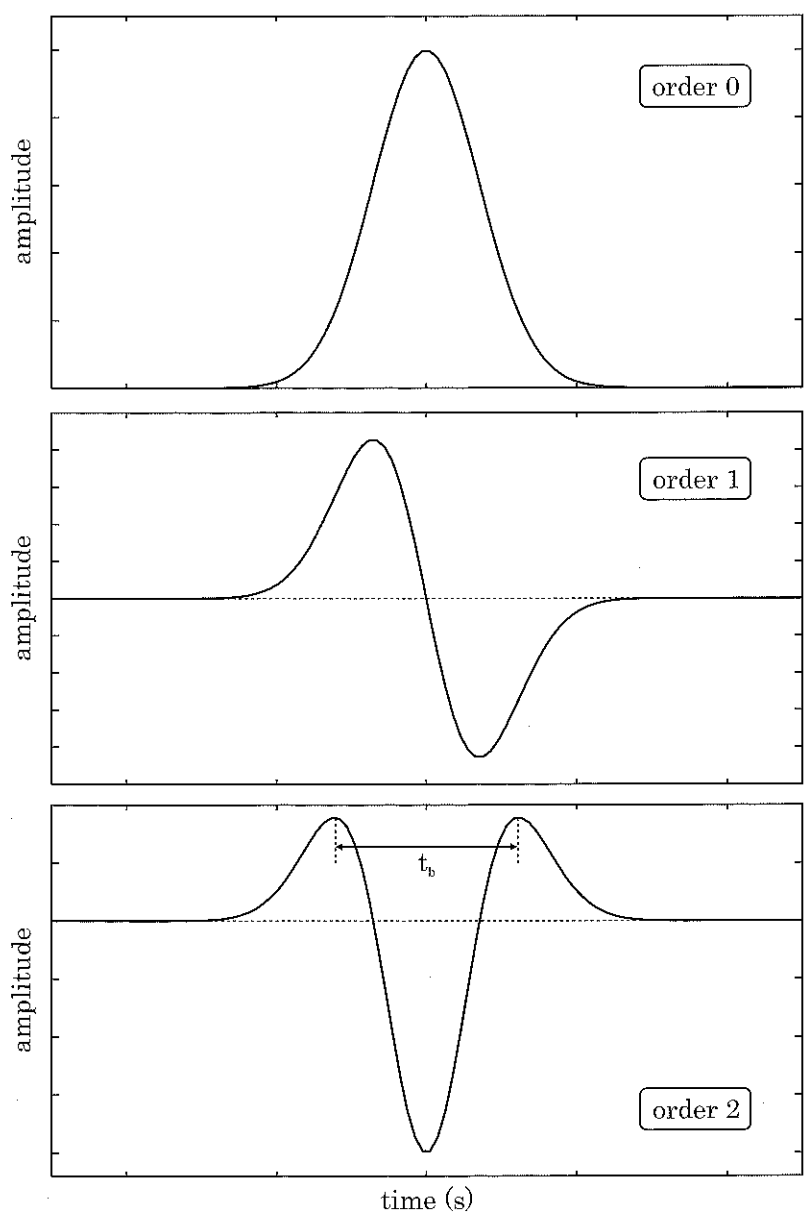


Fig. 4.2: Time variations of a 0th (top), 1st (middle) and 2nd order (bottom) Ricker wavelet and definition of the wavelet breadth t_b .

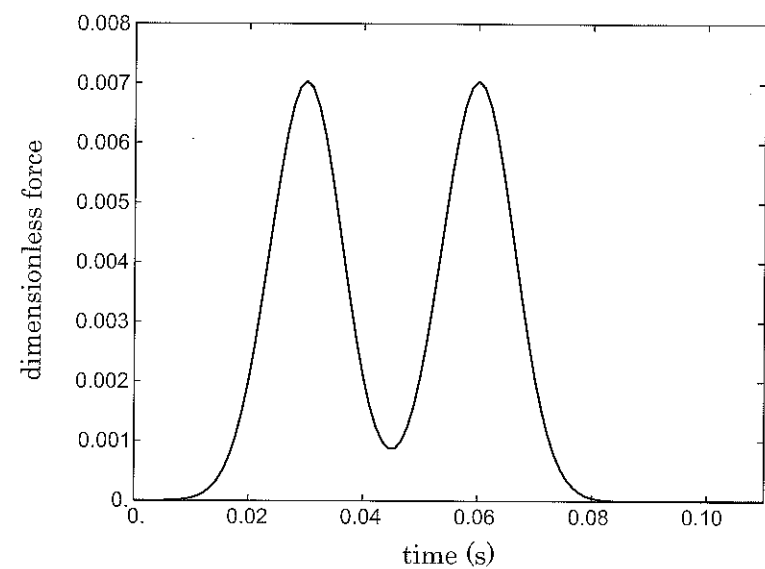


Fig. 4.3: Time variations of the double- M wavelet (dimensionless load F/Q) considered to model dynamic loadings by trains (Al-Shaer *et al.*, 2008).

Q denotes the load supported by the axle, v the train speed, t the time, d the distance between two sleepers, a a critical distance, L the distance between two axles of a bogie, X and Y are dimensionless variables depending on the elasticity modulus of the soil.

Such wavelets have been identified from field measurements (under and along tracks) and some typical values of X and Y are proposed in (Al Shaer *et al.*, 2008).

Synthetic seismograms

In the case of seismic excitations, the computation of realistic accelerograms usually requires a detailed knowledge of the source, path, and site effects.

Some empirical models were proposed by various authors (Pousse *et al.*, 2006; Sabetta and Pugliese, 1996). The method proposed by Pousse *et al.* (2006) models the time-domain accelerogram based on the assumption that the phase is random and that the time envelope can be represented by a lognormal distribution for P and S -waves combined with an algebro-exponential function representing the envelope of coda waves. In addition, the frequency content of the signal is nonstationary and follows a modified ω -square model.

The wave envelope proposed by Pousse *et al.* (2006) is displayed in Fig.4.4 showing the various parts of the signal: P -waves, S -waves and coda waves. This method depends on four common indicators in earthquake engineering.

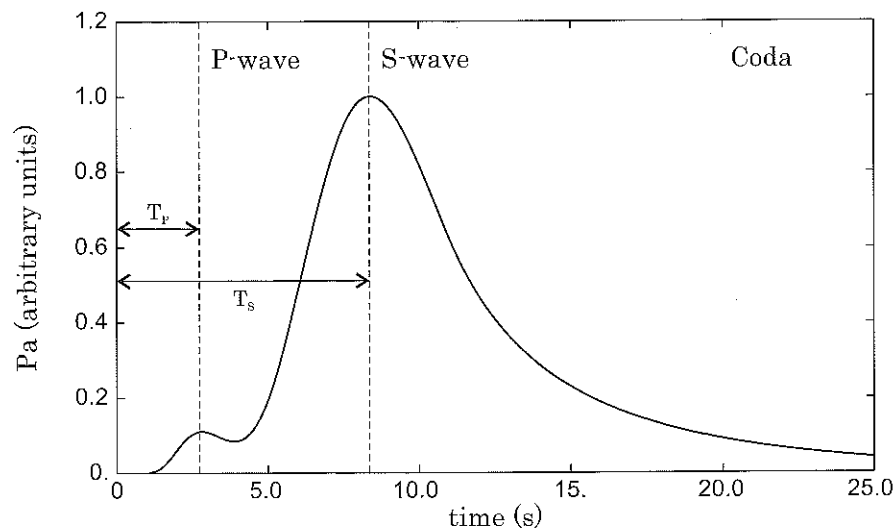


Fig. 4.4: Envelope of the synthetic seismogram proposed by Pousse *et al.* (2006).

These indicators (peak ground acceleration, strong-motion duration, Arias intensity, and central frequency, see Appendix D) were calibrated by Pousse *et al.* (2006) using Japanese data recorded by the K-net array.

4.2 The Finite Element Method

The main interest of the Finite Element Method in the field of dynamics is that it can be used to model complex geometries and constitutive laws, strong heterogeneities (Hughes, 1987; Curnier, 1993). Furthermore, it is well-adapted to simulate dynamic soil-structure interaction (Clough and Penzien, 1993).

4.2.1 Strong formulation

For a bounded domain Ω (see Fig.3.1), the strong formulation corresponds to the analysis of the local equilibrium in an exact way such as (Salençon, 2001):

$$\underline{\nabla} \cdot \underline{\sigma} + \underline{f} = \rho \underline{a} \quad \text{in } \Omega \quad (4.6)$$

$$\underline{\sigma} \cdot \underline{n} = \underline{T}^d \quad \text{on } \partial\Omega \quad (4.7)$$

where $\underline{\nabla}$ is the gradient vector (Appendix A), $\underline{\sigma}$ the Cauchy stress tensor, \underline{f} the body forces, \underline{a} the acceleration vector and \underline{T}^d the surface forces.

4.2 The Finite Element Method

The continuity of tractions at any interface also has to be satisfied:

$$[\underline{\sigma}]_{\Sigma} \cdot \underline{n} = \underline{t} = 0 \quad \text{on } \Sigma \quad (4.8)$$

where $[\cdot]_{\Sigma}$ denotes the jump across a surface of discontinuity Σ , \underline{n} is the vector normal to Σ and \underline{t} is the stress vector.

As already shown in Chap.3, considering the Principle of Virtual Work (Salençon, 2001), the global equilibrium may be written for any virtual velocity field $\hat{\underline{U}}$ as:

$$-\int_{\Omega} \underline{\sigma} : \hat{\underline{d}}(\hat{\underline{U}}) d\Omega + \int_{\Omega} \underline{f} \cdot \hat{\underline{U}} d\Omega + \int_{\partial\Omega} \underline{T}^d \cdot \hat{\underline{U}} da = \int_{\Omega} \rho \underline{a} \cdot \hat{\underline{U}} d\Omega \quad (4.9)$$

where $\hat{\underline{d}}$ is the strain rate tensor (see Chapter 3).

It may also be expressed under an equivalent form involving virtual displacements $\hat{\underline{u}}$ instead of virtual velocities (Salençon, 2001):

$$-\int_{\Omega} \underline{\sigma} : \hat{\underline{\varepsilon}}(\hat{\underline{u}}) d\Omega + \int_{\Omega} \underline{f} \cdot \hat{\underline{u}} d\Omega + \int_{\partial\Omega} \underline{T}^d \cdot \hat{\underline{u}} da = \int_{\Omega} \rho \underline{a} \cdot \hat{\underline{u}} d\Omega \quad (4.10)$$

with $\hat{\underline{\varepsilon}}$ the strain tensor (see Eq.(3.10)).

4.2.2 Weak formulation

For an isotropic linear elastic medium in small strains, the constitutive law is written as the classical Hooke's law:

$$\underline{\sigma} = \underline{\underline{C}} : \underline{\varepsilon} = \lambda (\text{tr} \underline{\varepsilon}) \underline{\mathbb{I}} + 2\mu \underline{\varepsilon} \quad (4.11)$$

or, in terms of components:

$$\sigma_{ij} = \lambda \left(\sum_{i=1}^3 \varepsilon_{ii} \right) \delta_{ij} + 2\mu \varepsilon_{ij} \quad (4.12)$$

The constitutive law may be recast into Eq.(4.9) to obtain the *weak form* of the equilibrium of the medium (Le Tallec, 2007; Salençon, 2001):

$$\begin{aligned} -\int_{\Omega} \underline{\varepsilon}(\hat{\underline{u}}) : \underline{\underline{C}} : \underline{\varepsilon}(\hat{\underline{u}}) d\Omega + \int_{\Omega} \underline{f} \cdot \hat{\underline{u}} d\Omega + \int_{\partial\Omega} \underline{T}^d \cdot \hat{\underline{u}} da \\ - \int_{\Omega} \rho \frac{\partial^2 \hat{\underline{u}}}{\partial t^2} \cdot \hat{\underline{u}} d\Omega = 0 \end{aligned} \quad (4.13)$$

for any displacement field $\hat{\underline{u}} \in \mathcal{S}$, \mathcal{S} being the space of all kinematically admissible fields, and with the following initial conditions on \underline{u} : $\underline{u}(\underline{x}, 0) = u_0(\underline{x})$ and $\dot{\underline{u}}(\underline{x}, 0) = v_0(\underline{x})$ ($\underline{x} \in \Omega$).

Instead of searching for the exact solution of the problem, we may try to estimate an approximate solution by minimizing the left scalar term in Eq.(4.13), denoted $\mathcal{W}(\hat{\underline{u}})$, in the space of kinematically admissible fields $\hat{\underline{u}}$. Equation (4.13) is called the *weak formulation* of the problem.

4.2.3 Approximate minimization: Galerkin method

The main idea of the Galerkin approximation is to minimize the left term in Eq.(4.13) not in the space of all kinematically admissible fields \mathcal{S} but in a finite-dimension sub-space (Bonnet and Frangi, 2007; Le Tallec, 2007; Salençon, 2001). The approximation thus consists in defining the sub-space \mathcal{S}^h , for instance:

$$\mathcal{S}^h = \{\underline{\hat{u}}^h = \sum_{i=1}^n a_i \underline{N}_i + \underline{u}_d, a_i \in \mathbb{R}^n\} \subset \mathcal{S} \quad (4.14)$$

where $\underline{\hat{u}}^h$ may be expressed from any given displacement \underline{u}_d satisfying the boundary conditions and n functions \underline{N}_i explicitly given in the space of the displacements being zero on the boundaries where the displacement is prescribed. The n scalar parameters a_i should be identified by the following minimizing process:

$$\min_{\underline{\hat{u}}^h \in \mathcal{S}^h} \mathcal{W}(\underline{\hat{u}}^h) \quad (4.15)$$

This formulation is called the *semi-discretized* variational formulation since the time derivatives are still continuous and also have to be approximated considering a time discretization (Hughes, 1987; Reddy, 2004; Zienkiewicz and Taylor, 2005).

4.2.4 Finite elements

Discretization of the domain

Through the Galerkin method, the space of all kinematically admissible displacement fields \mathcal{S} is approximated by the sub-space \mathcal{S}^h . As shown in Fig.4.5 (2D case), a convenient way to do so consists in approximating the exact domain Ω by a set of triangular or quadrilateral areas Ω_e (spatial discretization) such as:

$$\Omega \simeq \sum_{e=1}^{n_e} \Omega_e \quad (4.16)$$

Such small geometrical areas are called finite elements and their average dimension will be denoted Δh in the following. In the 3D case, 3D elements may be considered: tetrahedra, pentahedra or hexahedra for instance (Bathe, 1995; Hughes, 1987).

Various types of finite elements

Various interpolation orders. As shown in Fig.4.5, we generally consider the nodal displacements to define the displacement field in a given triangular finite element:

$$\underline{u}^h(x) = N_i(x)\underline{u}_i + N_j(x)\underline{u}_j + N_k(x)\underline{u}_k \quad (4.17)$$

The shape functions may be linear, that is in two dimensions:

$$N_l(x_1, x_2) = a_l + b_l x_1 + c_l x_2 \quad l = i, j, k \quad (4.18)$$

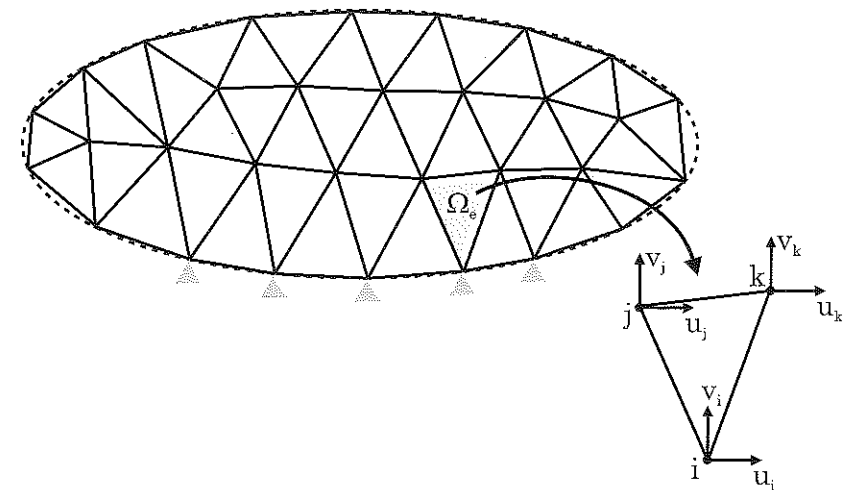


Fig. 4.5: Discretization of domain Ω by finite elements Ω_e and description of nodal displacements (2D case).

It is also possible to choose quadratic or even higher order shape functions (Hughes, 1987; Reddy, 2004; Zienkiewicz and Taylor, 2005). For a quadrilateral element, linear and quadratic shape functions are compared in Fig.4.6. The linear and quadratic shape functions are defined as follows:

- Linear quadrilateral element (4 nodes):

$$\begin{cases} N_1(r, s) = \frac{1}{4}(1-r)(1-s) \\ N_2(r, s) = \frac{1}{4}(1+r)(1-s) \\ N_3(r, s) = \frac{1}{4}(1+r)(1+s) \\ N_4(r, s) = \frac{1}{4}(1-r)(1+s) \end{cases} \quad (4.19)$$

- Quadratic quadrilateral element (8 nodes):

$$\begin{cases} N_1(r, s) = \frac{1}{4}(1-r)(1-s)(-1-r-s) \\ N_2(r, s) = \frac{1}{4}(1+r)(1-s)(-1+r-s) \\ N_3(r, s) = \frac{1}{4}(1+r)(1+s)(-1+r+s) \\ N_4(r, s) = \frac{1}{4}(1-r)(1+s)(-1-r+s) \\ N_5(r, s) = \frac{1}{4}(1-r^2)(1-s) \\ N_6(r, s) = \frac{1}{4}(1-s^2)(1+r) \\ N_7(r, s) = \frac{1}{4}(1-r^2)(1+s) \\ N_8(r, s) = \frac{1}{4}(1-s^2)(1-r) \end{cases} \quad (4.20)$$

As shown in Fig.4.6, each shape function is zero at all nodes but one. Because of the higher degree of the shape functions in the quadratic case (bottom), it is possible to retrieve faster variations in a quadratic element than in a linear element. This remark will be particularly important for the simulation of wave propagation.

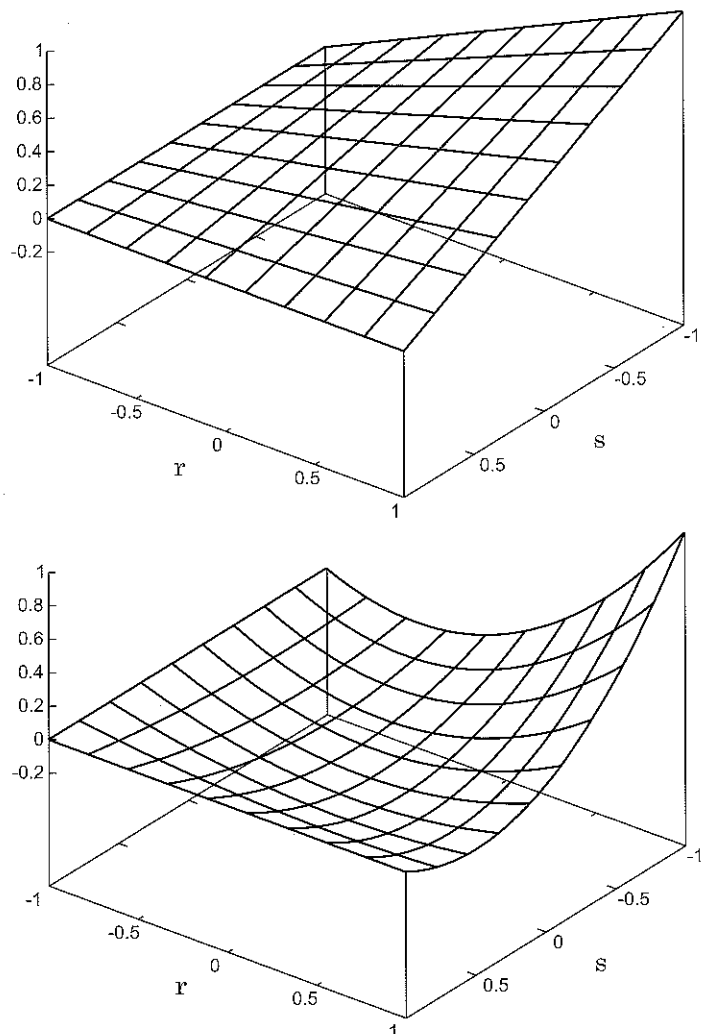


Fig. 4.6: Shape functions for a linear (top) and a quadratic (bottom) quadrilateral finite element.

Reference finite element. In addition to the interpolation of the displacement field within each finite element, it is convenient to consider a reference element, fixed normalized geometry, to perform the basic calculations always the same way (Bathe, 1995; Hughes, 1987). As depicted in Fig.4.7, the quadrilateral reference element is a square and any quadrilateral geometry may be defined by a simple transformation between the actual elements and the reference one. The Jacobian matrix of this transformation must be calculated since the element integrals have to be transformed the same way. For each finite element, it will thus be necessary to interpolate both the displacement field and the geometry. An easy way to perform both interpolations is the consider the same shape functions: such finite elements are called *isoparametric elements* (Reddy, 2004; Zienkiewicz and Taylor, 2005).

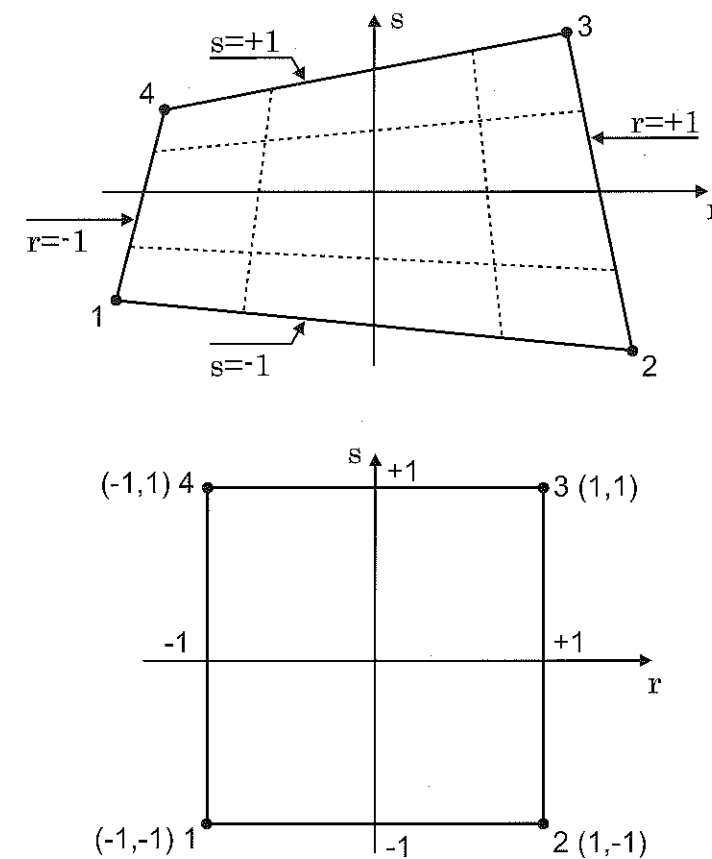


Fig. 4.7: Intrinsic coordinates for quadrilateral finite elements: distorted element (top) defined from the reference element (bottom).

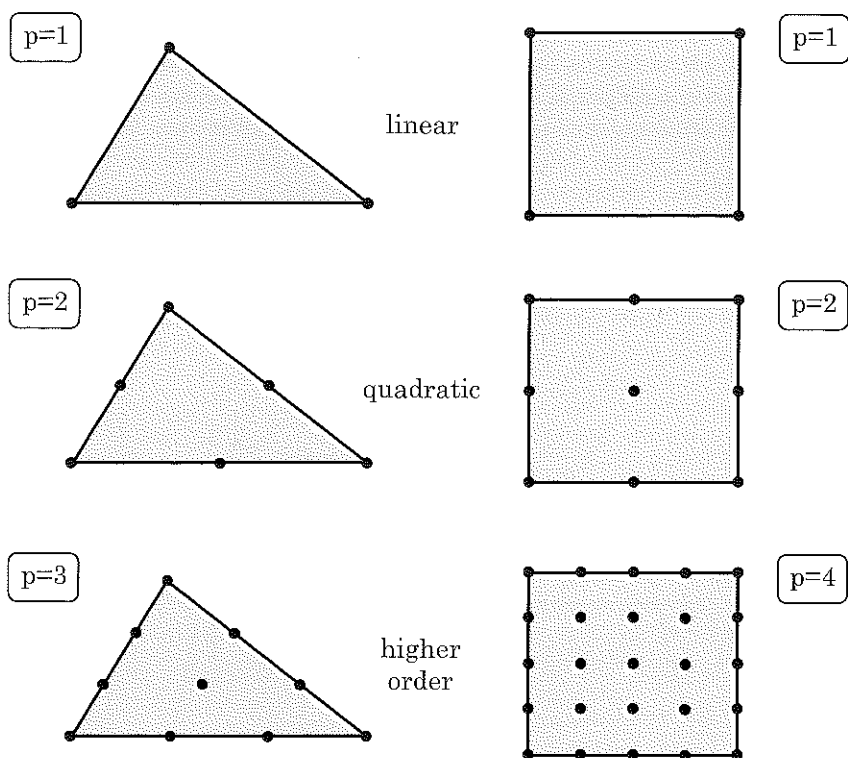


Fig. 4.8: Various types of finite elements at different orders p .

Different types of triangular and quadrilateral isoparametric elements, at various orders p (Hughes, 1987), are depicted in Fig.4.8. Linear (top) and quadratic (middle) finite elements are first shown for both the triangular and the quadrilateral cases. Higher order elements are also described in Fig.4.8: a 3rd order triangular element (bottom left) and a 4th order quadrilateral element (bottom right). The accuracy of such finite elements will be considered in the following in the case of wave propagation simulations.

Equation of motion

The estimation of all integrals in each finite element (Bathe, 1995; Reddy, 2004) yields the equation of motion in the following matrix form:

$$[M]\{\ddot{U}(t)\} + [K]\{U(t)\} = \{F(t)\} \quad (4.21)$$

where $[K]$ is the stiffness matrix deriving from the elastic energy, $[M]$ the mass matrix derived from the kinetic energy, $\{U\}$ and $\{\ddot{U}\}$ the vectors of unknown displacements and accelerations (respectively) and $\{F\}$ is the vector of nodal forces. The classical form of

the mass (distributed mass) leads to a consistent mass matrix (Hughes, 1987; Reddy, 2004). Alternative forms for this matrix will be discussed afterwards in the framework of elastodynamics.

4.2.5 Time integration algorithms

The semi-discretized variational formulation only concerns the spatial discretization. It is also necessary to consider a time discretization to approximate the time derivatives. We shall thus consider $m+1$ discrete times t_n such as: $t_n = n\Delta t$, $n = 0, m$. The time step Δt is defined as $\Delta t = t_{max}/m$ where t_{max} is the maximum time of the simulation. Starting from the initial conditions, $(\{U_0\}, \{\dot{U}_0\})$, time-integration algorithms then proceed to the computations of the approximate solutions at each time step, namely $(\{U_n\}, \{\dot{U}_n\}, \{\ddot{U}_n\})$. Various time integration schemes are available: explicit, implicit, multistep algorithm, and sub-stepping methods, etc (Hughes, 1987; Zienkiewicz and Taylor, 2005). We will only discuss some of the classical time integration schemes and their properties (advantages and drawbacks) in the field of dynamics and wave propagation.

The central difference method

The central difference method is a simple explicit time integration scheme (Bathe, 1995; Reddy, 2004). The velocity and the acceleration are expressed under a simple form:

$$\begin{aligned} \{\dot{U}_{n+1}\} &= \frac{1}{2\Delta t} (\{U_{n+1}\} - \{U_{n-1}\}) \\ \{\ddot{U}_n\} &= \frac{1}{\Delta t^2} (\{U_{n+1}\} - 2\{U_n\} + \{U_{n-1}\}) \end{aligned} \quad (4.22)$$

It thus yields a classical second order approximation of the acceleration vector. If we consider a lumped mass matrix (see §4.3), the expression of the central difference algorithm is fully explicit. Nevertheless, we shall see later that this algorithm is only conditionally stable.

The Newmark method

The Newmark method is a second-order accurate approach widely used in the field of dynamics (Hughes, 1987; Zienkiewicz and Taylor, 2005). It is a two-parameters algorithm (β, γ) defined as follows:

$$\begin{aligned} [M]\{\ddot{U}_{n+1}\} + [C]\{\dot{U}_{n+1}\} + [K]\{U_{n+1}\} &= \{F_{n+1}\} \\ \{U_{n+1}\} &= \{U_n\} + \Delta t \{\dot{U}_n\} + \frac{\Delta t^2}{2} \left[(1 - 2\beta)\{\ddot{U}_n\} + 2\beta\{\ddot{U}_{n+1}\} \right] \\ \{\dot{U}_{n+1}\} &= \{\dot{U}_n\} + \Delta t \left[(1 - \gamma)\{\ddot{U}_n\} + \gamma\{\ddot{U}_{n+1}\} \right] \end{aligned} \quad (4.23)$$

The stability conditions of the algorithm are the following:

- unconditional stability:

$$\frac{1}{2} \leq \gamma \leq 2\beta \quad (4.24)$$

- conditional stability:

$$\gamma \geq \frac{1}{2} ; \beta < \frac{\gamma}{2} ; \omega^h \Delta t \leq \Omega_{crit} \quad (4.25)$$

where ω^h is the approximated circular frequency for finite elements of average size Δh and Ω_{crit} is the critical frequency, such as:

$$\Omega_{crit} = \frac{\xi(\gamma - \frac{1}{2}) + \sqrt{\frac{\gamma}{2} - \beta + \xi^2(\gamma - \frac{1}{2})^2}}{\frac{\gamma}{2} - \beta} \quad (4.26)$$

where ξ is the damping ratio.

Classical choices for the algorithm parameters are:

- average acceleration* method: the parameters are $\beta = \frac{1}{4}$ and $\gamma = \frac{1}{2}$. The algorithm is thus implicit and is unconditionally stable.
- linear acceleration* method: the parameters are $\beta = \frac{1}{6}$ and $\gamma = \frac{1}{2}$. The algorithm is thus implicit and is conditionally stable with $\Omega_{crit} = 2\sqrt{3}$.
- central difference* method: choosing $\beta = 0$ and $\gamma = \frac{1}{2}$ in the Newmark scheme leads to the central difference method. The algorithm is thus explicit and is conditionally stable with $\Omega_{crit} = 2$.

For other values of the parameters β and γ , the stability conditions are depicted in Fig.4.9 with respect to A_1 and A_2 defined as (Curnier, 1993; Hughes, 1987):

$$A_1 = 1 - \frac{[\xi\Omega + \frac{\Omega^2}{2}(\gamma + \frac{1}{2})]}{1 + 2\gamma\xi\Omega + \beta\Omega^2} \quad (4.27)$$

$$A_2 = 1 - \frac{[2\xi\Omega + \Omega^2(\gamma - \frac{1}{2})]}{1 + 2\gamma\xi\Omega + \beta\Omega^2} \quad (4.28)$$

with $\Omega = \omega^h \Delta t$.

Outside the triangle ($\gamma < 1/2$ and $2\beta - \gamma < 0$), the Newmark scheme is unstable (Curnier, 1993). In the triangle, it may be unconditionally stable ($\gamma \geq 1/2$ and $2\beta - \gamma \geq 0$) or conditionally stable ($\gamma \geq 1/2$ and $2\beta - \gamma < 0$). The corresponding ranges for the spectral radius ρ (Curnier, 1993; Reddy, 2004) are also given in Fig.4.9.

Multistep methods

Among multistep methods, the α -method proposed by Hilber, Hughes and Taylor (Hughes, 1987) has the following form:

$$\begin{aligned} [M]\{\ddot{U}_{n+1}\} + (1+\alpha)[C]\{\dot{U}_{n+1}\} - \alpha[C]\{\dot{U}_n\} \\ + (1+\alpha)[K]\{U_{n+1}\} - \alpha[K]\{U_n\} = \{F(t_{n+\alpha})\} \end{aligned} \quad (4.29)$$

with: $t_{n+\alpha} = (1+\alpha)t_{n+1} - \alpha t_n = t_{n+1} + \alpha\Delta t$

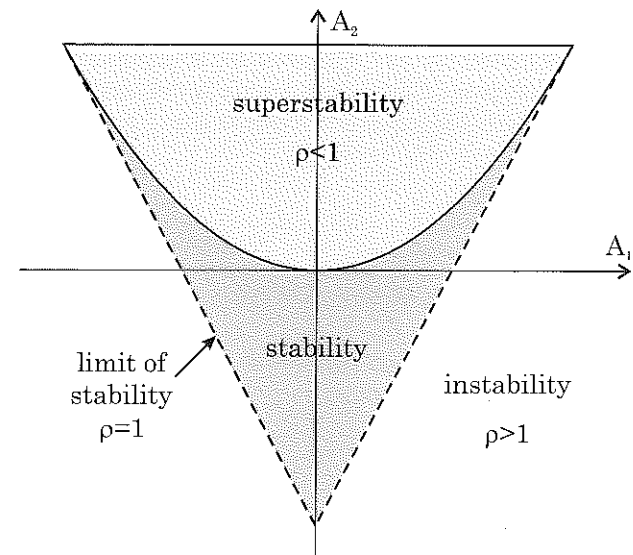


Fig. 4.9: Stability conditions of the Newmark time-integration scheme (Curnier, 1993; Hughes, 1987).

which corresponds to the Newmark algorithm for $\alpha=0$.

This method is often called the α -HHT method. It is unconditionally stable when $-\frac{1}{3} < \alpha < 0$, $\gamma = \frac{1-2\alpha}{2}$ and $\beta = \frac{(1-\alpha)^2}{4}$. Its main interest is that it can easily suppress spurious high frequency components (using *algorithmic damping*).

Another method of this type was proposed by Wood *et al.* (1981). In this method, only the inertial term is modified yielding:

$$(1 - \alpha_B)[M]\{\ddot{U}_{n+1}\} + \alpha_B[M]\{\ddot{U}_n\} + [C]\{\dot{U}_{n+1}\} + [K]\{U_{n+1}\} = \{F_{n+1}\} \quad (4.30)$$

This method is unconditionally stable for $\alpha_B \leq \frac{1}{2}$, $\beta \geq \frac{\gamma}{2} \geq \frac{1}{4}$, $\alpha_B + \gamma \geq \frac{1}{2}$.

It is also possible to consider higher order time-integration schemes using for instance sub-stepping procedures. The accuracy of computed dynamic responses appears to be improved by such procedures (Fung, 1997). Various other time integration schemes have been proposed in the field of dynamics: Wilson, Park, Houbolt, etc (Bathe, 1995; Hughes, 1987; Zienkiewicz and Taylor, 2005).

4.2.6 Spectral elements

The spectral element method uses the flexibility of the finite element method and the high accuracy of spectral methods (Patera, 1984; Faccioli *et al.*, 1996, 1997; Komatitsch

and Vilotte, 1996, 1998). Spectral elements are sub-parametric since they involve lower order interpolants for the geometry and higher order interpolants for the field variable (Meza-Fajardo and Papageorgiou, 2008). The higher order interpolants may be chosen as Legendre polynomial (Meza-Fajardo and Papageorgiou, 2008) leading to integration points defined, in the 1D case, as the roots of:

$$(1 - x^2)P'_N(x) = 0 \quad (4.31)$$

where $P_N(x)$ is the Legendre polynomial at order N .

They may be also chosen as Chebyshev functions (Dauksher and Emery, 1999) leading to integration points defined as:

$$x_j = \cos \theta_j \quad \text{with: } \theta_j = \frac{\pi j}{N} \quad (j = 0, \dots, N) \quad (4.32)$$

In the 2D or 3D cases, a tensorial interpolation operator should be introduced (Chaljub *et al.*, 2003, Komatitsch and Vilotte, 1998).

As shown in Fig. 4.10 at order 4, such higher order interpolants yield a non regular node spacing in the spectral elements (right) when compared to the finite elements (left). Considering the smallest node-to-node distance, it may thus lead to smaller time step than for a regular spacing (Delavaud, 2007). Nevertheless, the accuracy of spectral elements is excellent for wave propagation simulations, especially in terms of *numerical dispersion*.

The spectral element method often involves higher order interpolants up to order 8 (Faccioli *et al.*, 1996, 1997; Komatitsch and Vilotte, 1996, 1998). To illustrate the way the field variables are interpolated in such cases, the Lagrange polynomials related to the Gauss-Lobatto-Legendre points at order 8 are displayed in Fig. 4.10.

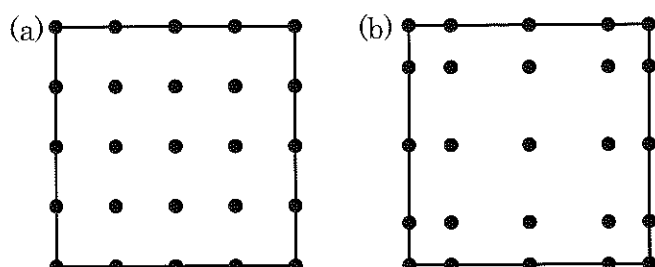


Fig. 4.10: Fourth order finite (left) and spectral (right) elements.

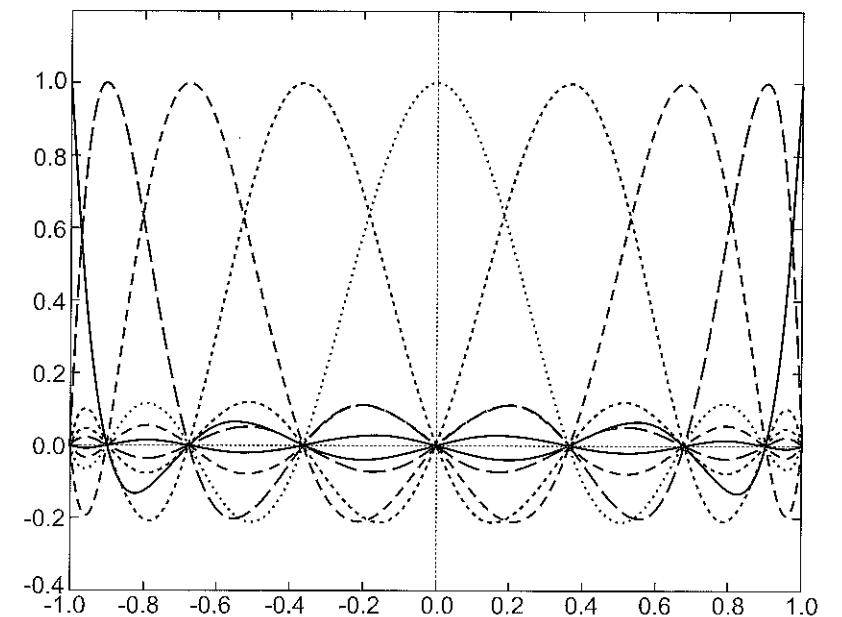


Fig. 4.11: Lagrange polynomials related to the Gauss-Lobatto-Legendre points at order 8 (Komatitsch, 1997).

4.3 Numerical dispersion

4.3.1 Physical dispersion and attenuation

As discussed in Chapter 2, in a linear viscoelastic medium, the one-dimensional wave equation may be derived in the frequency domain under the following form:

$$\frac{\partial^2 u^*(x, \omega)}{\partial x^2} + \frac{\rho\omega}{M(\omega)} u^*(x, \omega) = 0 \quad (4.33)$$

where u^* is the Fourier transform of the displacement, x the distance, ω the circular frequency, ρ the mass density and $M(\omega)$ the complex modulus (Aki and Richards, 1980; Bourbié *et al.*, 1987).

The problem solution may thus take the form (Semblat and Luong, 1998):

$$u^*(x, \omega) = U_0(\omega) \exp[-ik^*(\omega)x] \quad (4.34)$$

where $k^*(\omega)$ is the complex wavenumber such as:

$$k^*(\omega) = \frac{\omega}{c(\omega)} - i\alpha(\omega) \quad (4.35)$$

with $c(\omega)$ is the frequency dependent wave velocity and $\alpha(\omega)$ the attenuation factor.

In addition to this first classical term of phase shift, this complex wavenumber also involves an imaginary term related to damping. Both terms (phase shift, damping) generally depend on frequency. The dependency between the phase velocity $c(\omega)$ and the frequency is related to the material dispersion in the medium.

From a numerical point of view, both properties have their counterparts which are generally called *numerical dispersion* and *numerical damping* (Hughes, 1987; Semblat, 1998; Stewart and Hughes, 1998). Numerical dispersion makes the wave velocity depend on the model features (time integration scheme, element size, element type, etc). Numerical damping corresponds to the same type of dependency for the wave amplitude. Both numerical errors are discussed in the following.

4.3.2 Numerical errors for wave propagation

In the field of structural dynamics, two types of numerical error occur (Hughes, 1987). As depicted in Fig.4.12, the *relative period error* is linked to the estimation of the fundamental period of the structure. *Algorithmic damping* corresponds to an artificial amplitude reduction due to a purely numerical damping. It is possible to analyze and quantify such numerical errors.

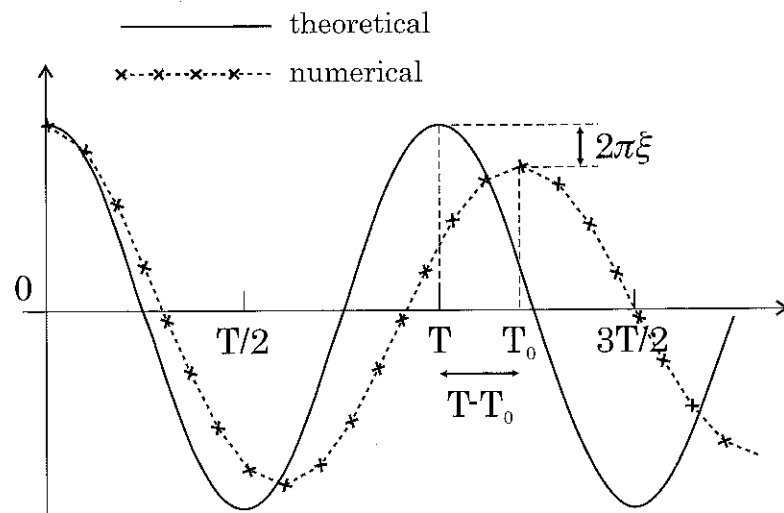


Fig. 4.12: Relative period error and algorithmic damping as defined by Hughes (1987).

The relative period error is different from one time-integration scheme to another (Fig.4.13). The α -HHT method, Eq.(4.29), leads to some of the lowest period errors ($\alpha=-0.3$ and -0.05). For wave propagation problems, the relative period error appears through the estimation of the wave velocity. The propagation of a wave in a given numerical scheme depends on the element size, the integration scheme, the element type, etc. This phenomenon is called numerical dispersion with reference to physical dispersion (Eq.(4.35)) making the wave velocity dependent on frequency (Hughes *et al.*, 2008; Ihlenburg and Babuška, 1995; Semblat and Luong, 1998; Semblat and Brioist, 2000).

It may thus be difficult to simulate wave propagation phenomena because in the finite difference or the finite element methods the numerical error may increase during the propagation of the wave. As shown in Fig.4.6, higher order interpolants may yield more accurate solutions in the framework of the finite element or spectral element method. The comparison of lower order and higher order finite elements with respect to numerical dispersion will be discussed in the following.

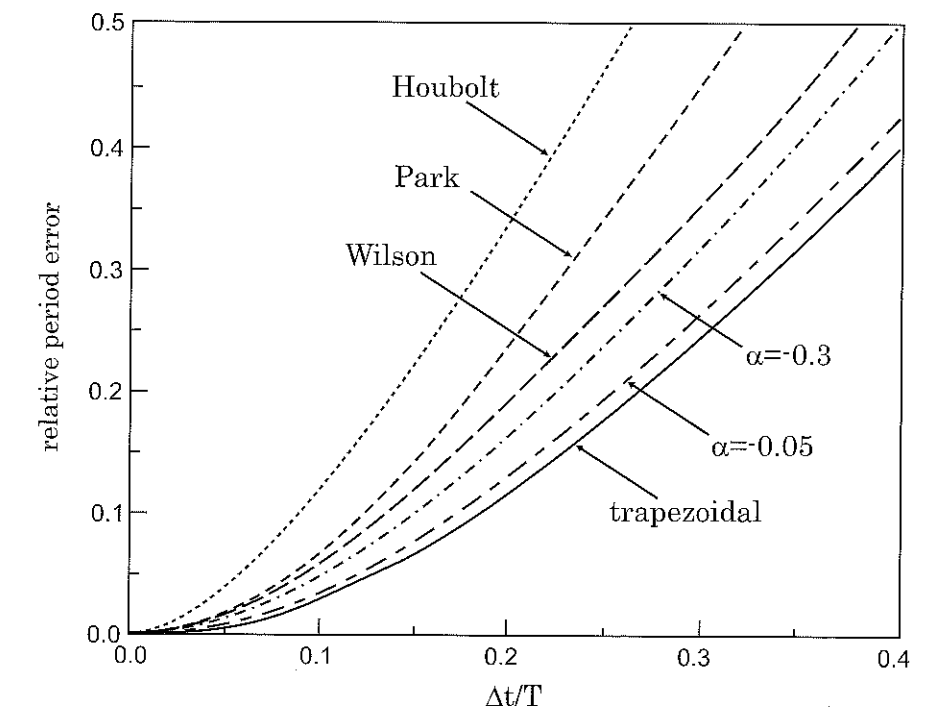


Fig. 4.13: Relative period error for various time integration schemes (Hughes, 1987).

4.3.3 Theoretical numerical dispersion

One-dimensional analysis

The numerical solution of Eq.(4.33) may take a form similar to that of the theoretical solution (Eq.4.34):

$$u^h(x, \omega) = U_0(\omega) \exp(-ik^h(\omega)x) \quad (4.36)$$

where u^h and k^h are the approximate displacement and wavenumber respectively.

Several theoretical works concern the analysis of the error in the numerical estimation of the approximate wavenumber k^h when compared to the exact/theoretical wavenumber k (Bamberger *et al.*, 1980; Hu *et al.*, 1998; Hughes *et al.*, 2008; Ihlenburg & Babuška, 1995). In the case of linear finite elements, Ihlenburg and Babuška (1995) proposed the following relation:

$$\cos k^h \Delta h = \frac{1 - \frac{K^2}{3}}{1 + \frac{K^2}{6}} \quad (4.37)$$

where K is the normalized frequency such as $K = k\Delta h = \omega\Delta h/c$.

Expression (4.37) shows that the numerical solution of Eq.(4.33) is related to propagation phenomena only for normalized frequencies below a given cut-off frequency K_0 , Fig.4.14 (Ihlenburg & Babuška, 1995). However, for such frequency values, the numerical wave propagates faster or slower than the theoretical solution. It is thus necessary to analyze the numerical dispersion of waves and to quantify the related numerical error.

For higher order elements, the error on the wavenumber is derived by Ihlenburg and Babuška (1995), if $k\Delta h/p < 1$, as follows:

$$|k^h - k| = \frac{kC_1}{4\sqrt{\pi p}} \left(\frac{e}{4} \right)^{2p} \left(\frac{k\Delta h}{2p} \right)^{2p} \quad (4.38)$$

where C_1 is a constant, p the interpolant order, Δh the element size.

This analytical result shows that the decrease of the phase difference is even stronger for larger p . Hughes *et al.* (2008) recently proposed a unified theoretical analysis comparing higher order classical finite elements and NURBS¹ approximations.

In the framework of the classical Finite Element Method, the comparison of interpolants of various orders will be considered in the following through numerical examples involving wave propagation in soils.

Two-dimensional analysis

Assessing numerical wave dispersion is rather simple in the one-dimensional case. In two dimensions, such phenomena are more difficult to analyze. As demonstrated by Bamberger *et al.* (1980), it is necessary to take into account the properties of the medium, the

¹non-uniform rational B-splines.

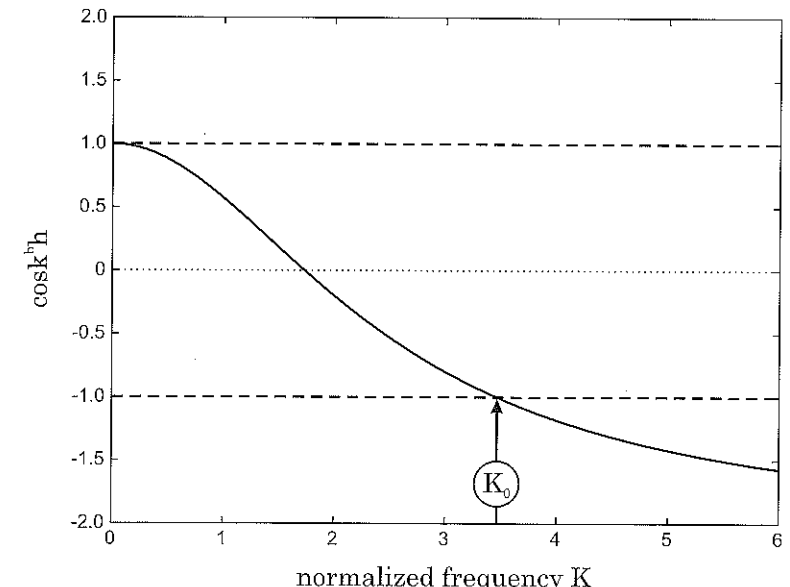


Fig. 4.14: Theoretical error on the approximate wavenumber k^h for linear finite elements and cut-off frequency K_0 (Ihlenburg and Babuška, 1995).

wave type, the angle of incidence, the type and size of finite elements (triangles, quadrilaterals, etc). Some dispersion relations are proposed for various numerical schemes by Bamberger *et al.* (1980) or Ihlenburg and Babuška (1995). The analytical expressions of the phase and group velocities of the numerical waves are calculated for various wave types (Bamberger *et al.*, 1980). Some of them are discussed in the following.

Considering linear finite element, the dimensionless numerical phase velocities for P and S waves are found to be (Bamberger *et al.*, 1980):

$$V_P^\phi = \frac{\sqrt{3}}{2\pi H \bar{\Delta t} \zeta} \arccos \left[1 - \bar{\Delta t}^2 \frac{6\zeta^2(1 - \beta_1\beta_2) + (1 - \beta_1)(1 - \beta_2)}{2(\beta_1 + 2)(\beta_2 + 2)} \right] \quad (4.39)$$

$$V_S^\phi = \frac{\sqrt{3}}{2\pi H \bar{\Delta t} \sqrt{1 - \zeta^2}} \arccos \left[1 - \bar{\Delta t}^2 \frac{7 - 5\beta_1\beta_2 - \beta_1 - \beta_2 - 6\zeta^2(1 - \beta_1\beta_2)}{2(\beta_1 + 2)(\beta_2 + 2)} \right]$$

where: $\beta_1 = \cos(2\pi H \cos \theta)$; $\beta_2 = \cos(2\pi H \sin \theta)$; θ is the incidence angle of the numerical wave; $H = \Delta h/\Lambda$ (with Δh the element size and Λ the wavelength); $\bar{\Delta t} = \frac{\Delta t}{\Delta t^*}$ (Δt being the time step considered in the computation; $\Delta t^* = \frac{\Delta h}{\sqrt{V_P^2 + V_S^2}}$, V_P and V_S the wave velocities of P and S -wave respectively); $\zeta^2(\nu) = \frac{V_P^2}{V_P^2 + V_S^2} = \frac{2-2\nu}{3-4\nu}$ (thus $\frac{2}{3} \leq \zeta \leq 1$).

These relations fully characterize 2D numerical dispersion and lead to some of the curves displayed in Fig.4.15. These curves give the dimensionless phase velocities of P and S -waves for a two-dimensional mesh. The dimensionless phase velocity is the ratio between the velocity of the numerical waves and the theoretical phase velocity. Figure 4.15 corresponds to quadrilateral (top) and triangular (middle and bottom) finite elements having a linear interpolation. These results allow the quantification of the numerical error as a function of the element size to wavelength ratio for various values of the angle of incidence.

All the results displayed in Fig.4.15 are given for a Poisson's ratio $\nu=0.25$ and a time-step ratio $\Delta t=1$. From Fig.4.15, it is possible to make several remarks for such various configurations:

- the numerical dispersion (and thus the numerical error) is stronger for a larger element size (i.e., larger element size to wavelength ratios);
- the error is generally maximum for a normal incidence ($\theta = 0^\circ$) and minimum for a 45° incidence (for this specific numerical scheme) except for triangular elements when $\theta < 0$;
- for quadrilateral elements (top) and small values of the element size, P -waves are more sensitive to the angle of incidence than S -waves. Whereas, for triangular elements (middle and bottom), S -waves are strongly dispersed with either larger or smaller wave velocities than the theoretical waves.

For triangular elements (right angled triangles), the influence of incidence is different for positive or negative angles (there is no symmetry). In the case of P -waves, there is no numerical dispersion for a 45° incidence (constant phase velocity). The angles of incidence leading to the lowest numerical dispersion are different for P and S -waves (Bamberger *et al.*, 1980; Semblat, 1998).

Several other theoretical studies have been made on the numerical dispersion of waves among which:

- Joly (1982) studied numerical Rayleigh waves and demonstrated that their numerical dispersion is slightly larger for low order finite elements than with finite differences. Nevertheless, the Finite Difference Method may generate artificial surface wave components.
- Cohen *et al.* (1994) performed extensive analyses on the accuracy of higher order finite elements considering mass condensation.
- Kim *et al.* (1999) proposed numerical models to simulate cross-hole tests in isotropic and anisotropic soils. They studied the influence of numerical dispersion on the arrival-time estimation.

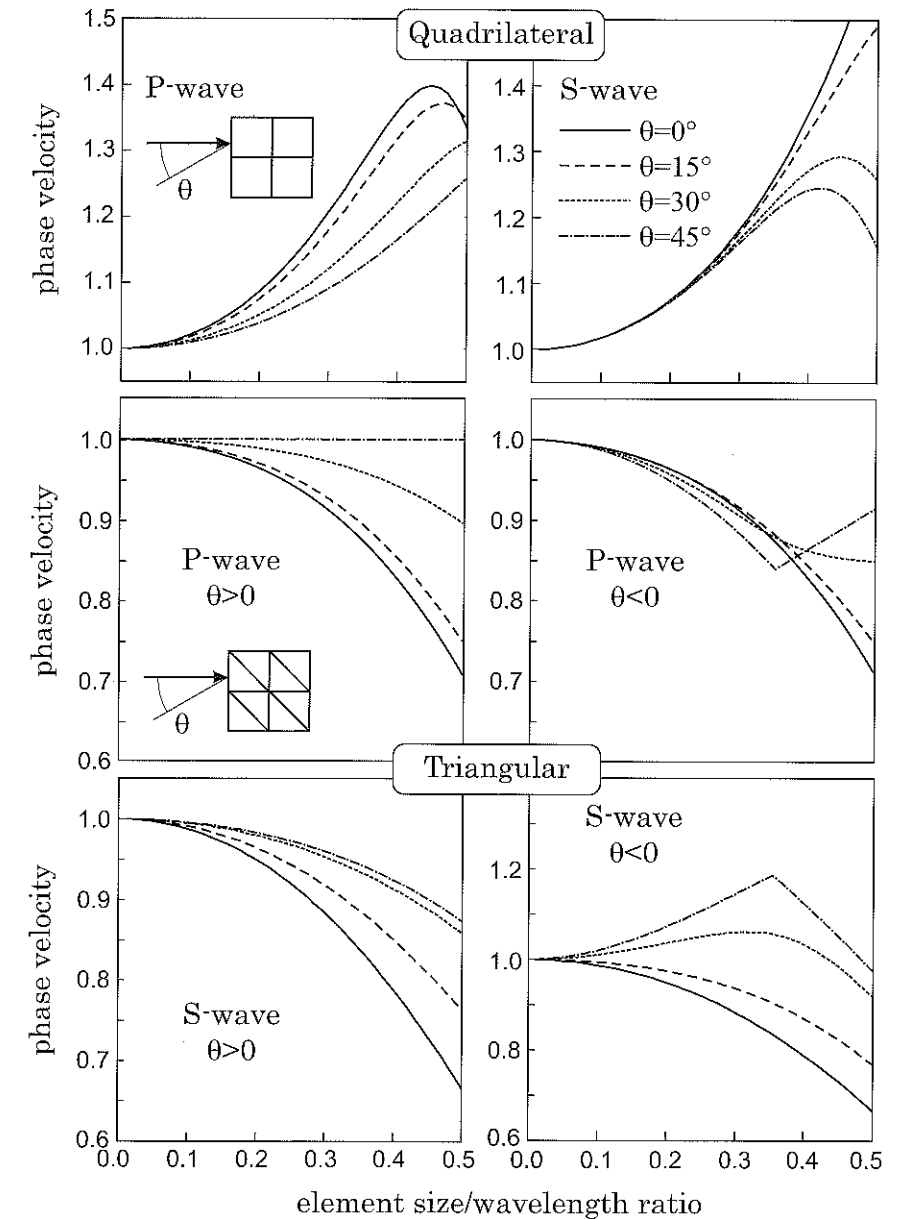


Fig. 4.15: Numerical dispersion for a 2D numerical scheme as estimated by Bamberger *et al.* (1980), Eq.(4.39), for $\nu = 0.25$ and $\Delta t = 1$: P -waves (left) and S -waves (right), quadrilateral elements (top) and triangular elements (middle and bottom).

4.3.4 Time-step estimates for some simple cases

As shown by Hughes (1987) for a plane pressure wave in a bar, the critical time step for the central-difference method, that is Newmark method with $\beta = 0$ and $\gamma = \frac{1}{2}$, is:

$$\Delta t \leq \frac{2}{\omega_{max}^h} = \frac{\Delta h}{c} \quad \text{for a lumped mass matrix} \quad (4.40)$$

$$\Delta t \leq \frac{\Delta h}{\sqrt{3}c} \quad \text{for a consistent mass matrix} \quad (4.41)$$

where c is the pressure wave velocity in the bar: $c = \sqrt{E/\rho}$.

Thus, consistent mass matrices tend to yield smaller critical time steps than lumped mass matrices.

For a rectangular 2D element (dimensions Δh_1 and Δh_2), Flanagan and Belytschko (1981) have shown that, for the central-difference method, the critical time-step is:

$$\Delta t \leq \frac{1}{V_P \sqrt{\frac{1}{\Delta h_1^2} + \frac{1}{\Delta h_2^2}}} \quad (4.42)$$

where V_P is the P -wave velocity.

The choice for the critical time-step depends on the time-integration scheme as well as on the element size and type (Hughes, 1987). In the following paragraphs, the influence of the latter on numerical dispersion will be investigated.

4.3.5 Numerical dispersion for low order elements

To assess the numerical error for wave propagation problems, we firstly consider a one-dimensional case with a linear elastic isotropic medium (no physical dispersion). As depicted in Fig.4.16, a 2nd order Ricker wavelet (Eq.(B.3)) propagates through a 1D model of variable refinement. Table 4.1 gives the number of elements for each model and the corresponding element size Δh . In the last line, the $\Delta h/\Lambda$ ratio characterizes the element size normalized to the wavelength Λ .

Table 4.1: Mesh refinement and element size to wavelength ratio for the various 1D cases studied.

Number of elements	50	100	200	300	400	800
Element size Δh	2 m	1 m	0.5 m	0.333 m	0.25 m	0.125 m
$\Delta h/\Lambda$ ratio	2/5	1/5	1/10	1/15	1/20	1/40

The waveforms computed at different times are displayed in Fig.4.17 for each numerical model detailed in Table 4.1. These curves clearly show that the element size

4.3 Numerical dispersion

strongly influences the numerical error. The coarse meshes lead to numerical results under-estimating the amplitudes but overestimating the velocities (group and phase). It illustrates the practical meaning of numerical dispersion which may be limited by choosing an element size adapted to the wavelength of the problem. The element size is classically chosen as one tenth or one twentieth of the wavelength. However, as shown in Fig.4.17 in cases 3 (200 elements, $\Delta h/\Lambda=1/10$) and 5 (400 elements, $\Delta h/\Lambda=1/20$), the numerical error becomes significant beyond a propagation distance of approximately 5Λ or 10Λ (respectively).

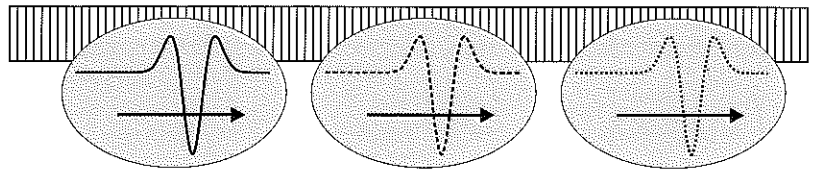


Fig. 4.16: Finite element mesh and Ricker wavelet considered for the analysis of 1D numerical dispersion.

4.3.6 Influence of the geometrical arrangement

Since we shall analyse later the accuracy of different finite element orders, we only consider two types of 2D spatial arrangements. The influence on numerical dispersion of these 2D element patterns, depicted in Fig.4.18, will now be investigated. The first one is a regular set of triangles called "half-square" pattern (a). The second one combines all possible orientations to get a more isotropic pattern called "square-diamond" (b). In the following, we shall analyse the efficiency of both 2D patterns with respect to numerical dispersion for a particular problem (seismic waves originated by a vibrating foundation).

To assess the influence of the spatial arrangement, one considers the particular problem of seismic waves generated by foundation vibration and propagating in a centrifuged soil mass. The complete description of the experiments is given in (Chazelas *et al.*, 2001). Figure 4.19 shows the foundation above the soil mass and displays the force vs time curve considered herein. The time step is $\Delta t=0.05$ s and the time integration algorithm is a Newmark non dissipative one ($\beta = 1/4$, $\gamma = 1/2$). The element size is $\Delta h=0.01$ m. The mechanical properties of the soil are the following : mass density $\rho=1600\text{kg/m}^3$, Young's modulus $E=100\text{MPa}$ and Poisson's ratio $\nu=0.24$. The numerical analysis is performed with the FEM/BEM code CESAR-LCPC (Humbert *et al.*, 2005).

The two element patterns depicted in Fig.4.18 are compared with respect to numerical dispersion considering the propagation problem of Fig.4.19. The horizontal displacement along the soil surface is displayed in Fig.4.20. The square-diamond pattern (SD) appears to be more accurate than the half-square pattern (HS) since the numerical dispersion is stronger with the latter (velocity increase).

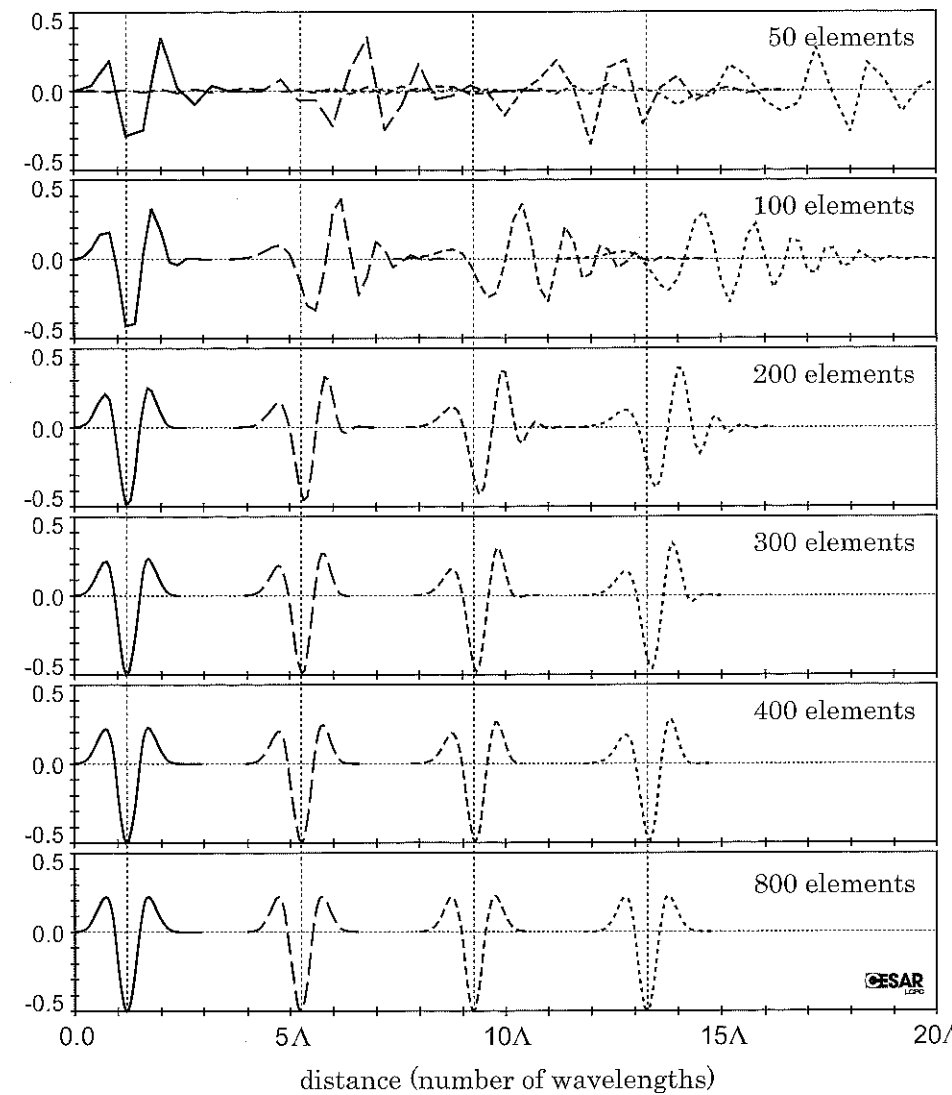


Fig. 4.17: Analysis of the one-dimensional numerical dispersion (waveforms at different times) for wave propagation problems computed by the FEM (lower order elements).

The SD pattern being much more "isotropic" than the HS pattern, this result is logical. In the following, we shall consider the square-diamond pattern to investigate the numerical accuracy for different finite element orders.

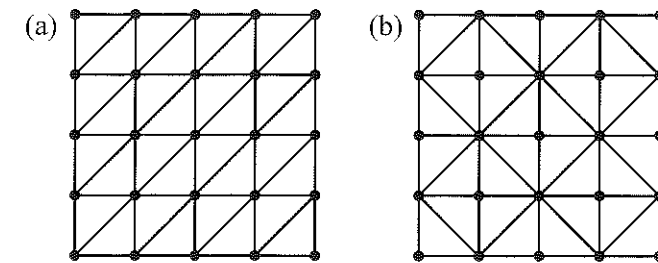


Fig. 4.18: Types of 2D element pattern considered : half-square (a) and square-diamond (b).

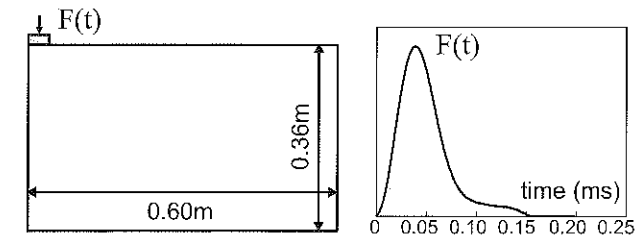


Fig. 4.19: Model for the analysis of waves generated by foundation vibration in the centrifuge (Chazelas *et al.*, 2001).

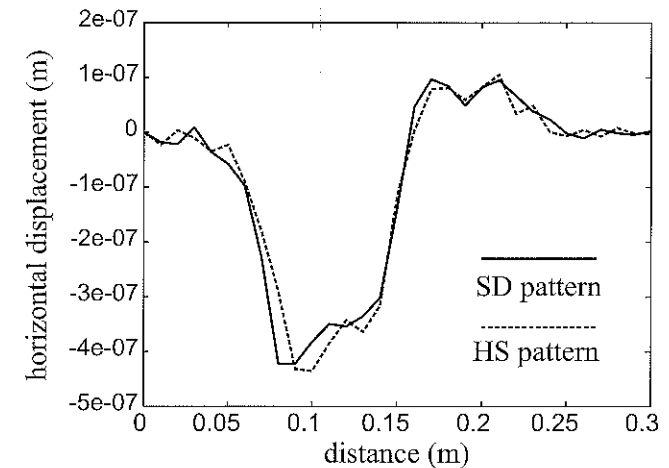


Fig. 4.20: Horizontal displacement along the surface at time $t=0.75\text{ms}$: comparison of both element patterns (SD: square-diamond, HS: half-square).

4.3.7 Influence of mass matrix formulation

The numerical dispersion also depends on the mass matrix formulation. As shown in Fig.4.21, the numerical error is different for a consistent or a lumped mass matrix formulation (Hughes, 1987). In the previous one-dimensional example (Fig.4.17), the mass matrix formulation is a consistent one. To limit the numerical dispersion, it may be interesting to consider alternative mass matrix formulations. Two formulations will be now compared: a lumped formulation and a mixed consistent/lumped formulation.

The efficiency of both formulations in terms of numerical dispersion will now be assessed. To derive a lumped mass matrix, a simple method consists in replacing the diagonal term by the sum of the terms of the line and the non diagonal terms by zero values. This method is called the "sum of the row" method (Hughes, 1987; Reddy, 2004). Both types of formulation (consistent and lumped) are now compared in terms of dispersion through a one-dimensional example (propagation of a Ricker wavelet). The curves displayed in Fig.4.22 show that the consistent mass matrix formulation overestimates the wave velocity (signal in advance on the reference curve) whereas the lumped mass matrix formulation obtained by summing the row terms underestimates the wave velocity (signal delayed from the reference curve). As already shown in Fig.4.21, both formulations lead to numerical errors with equivalent levels but opposite effects (overestimation for the consistent mass, underestimation for the lumped mass).

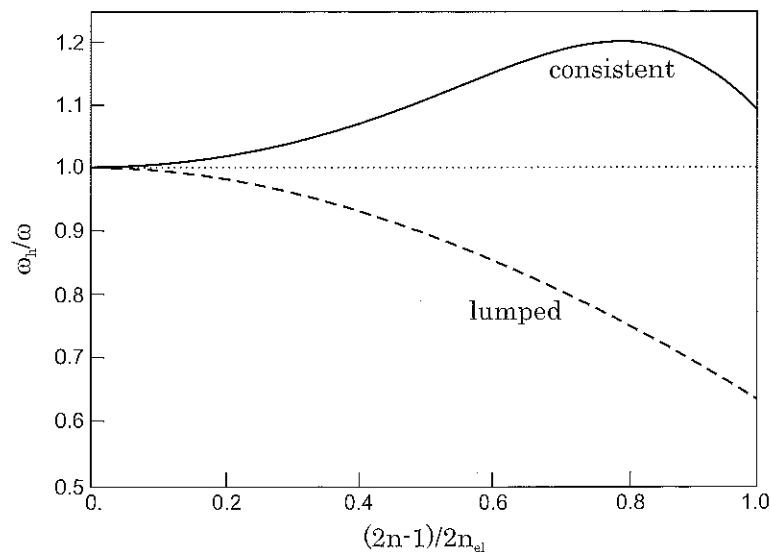


Fig. 4.21: Comparison between a consistent mass matrix and a lumped mass matrix in the case of the identification of the eigenmodes of a cantilever beam (Hughes, 1987).

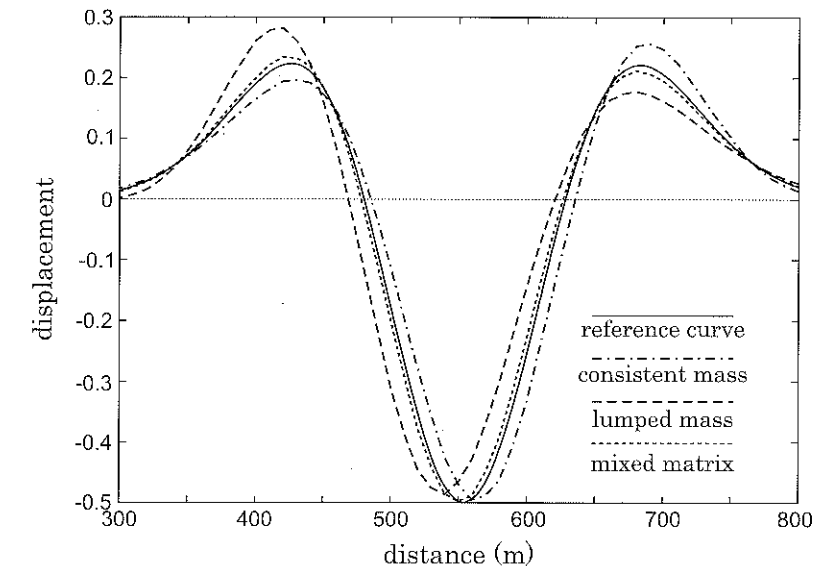


Fig. 4.22: Comparison of the numerical dispersions obtained from a consistent mass matrix (dotted-dashed), a lumped mass matrix (dashed) and a mixed formulation (dotted).

Considering the results obtained with both formulations, Lysmer (1970), as well as Hansson and Sandberg (1997), proposed a mixed formulation considering a linear combination of the consistent mass matrix $[M]_c$ and the lumped mass matrix $[M]_l$ as follows:

$$[M]_m = a[M]_c + (1-a)[M]_l \quad (4.43)$$

In Fig.4.22, the result obtained with the mixed formulation and a coefficient $a=0.5$ is displayed. The mixed formulation leads to numerical results very close to those of the reference case. It is thus much better in terms of numerical dispersion than the consistent and lumped formulations. Similar formulations may be considered for higher order finite elements (Cohen *et al.*, 1994, 2001).

4.3.8 Efficiency of higher order elements

1D analysis

Numerical dispersion is also influenced by the order of the polynomial interpolants considered in the finite element formulation. Higher order finite elements are known to be very accurate for computations in elastoplasticity (Molenkamp and Kay, 1997; Sloan and Randolph, 1982). For wave propagation, several theoretical works have proposed some theoretical results to assess the numerical error in terms of dispersion (Bamberger *et al.*, 1980; Hughes *et al.*, 2008; Ihlenburg and Babuška, 1995). Higher order finite elements

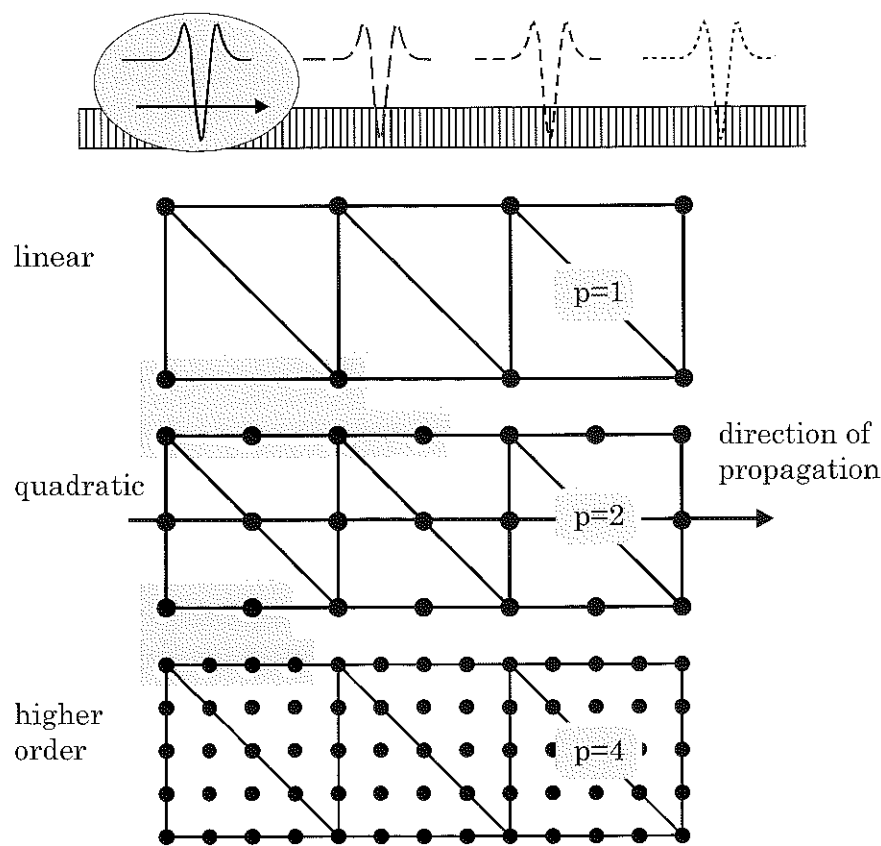


Fig. 4.23: Numerical dispersion for various types of finite elements: one-dimensional problem and arrangement of the elements.

seem to lead to a lower numerical dispersion.

In order to compare the efficiency of finite elements at different order of interpolation, a one-dimensional wave propagation problem is now studied. As shown in Fig.4.23, three different types of (triangular) elements are considered: three-noded linear elements, six-noded quadratic elements and 15-noded fourth order elements (Hughes, 1987). For a meaningful comparison, the number of elements in each finite element mesh is chosen in order to keep the number of nodes in the direction of propagation constant for all element types (Semblat and Brioist, 2000). It turns out that the proportionality of the number of elements corresponds to the ratio between the interpolants orders for the three element types. The three meshes indeed involve 80 linear elements for the first one (linear interpolants), 40 elements for the second (quadratic interpolants) and 20 elements for the third (4th order interpolants). A mesh involving elements with an interpolant order

two times larger will have two times less elements for an identical number of nodes in the direction propagation (Fig.4.23).

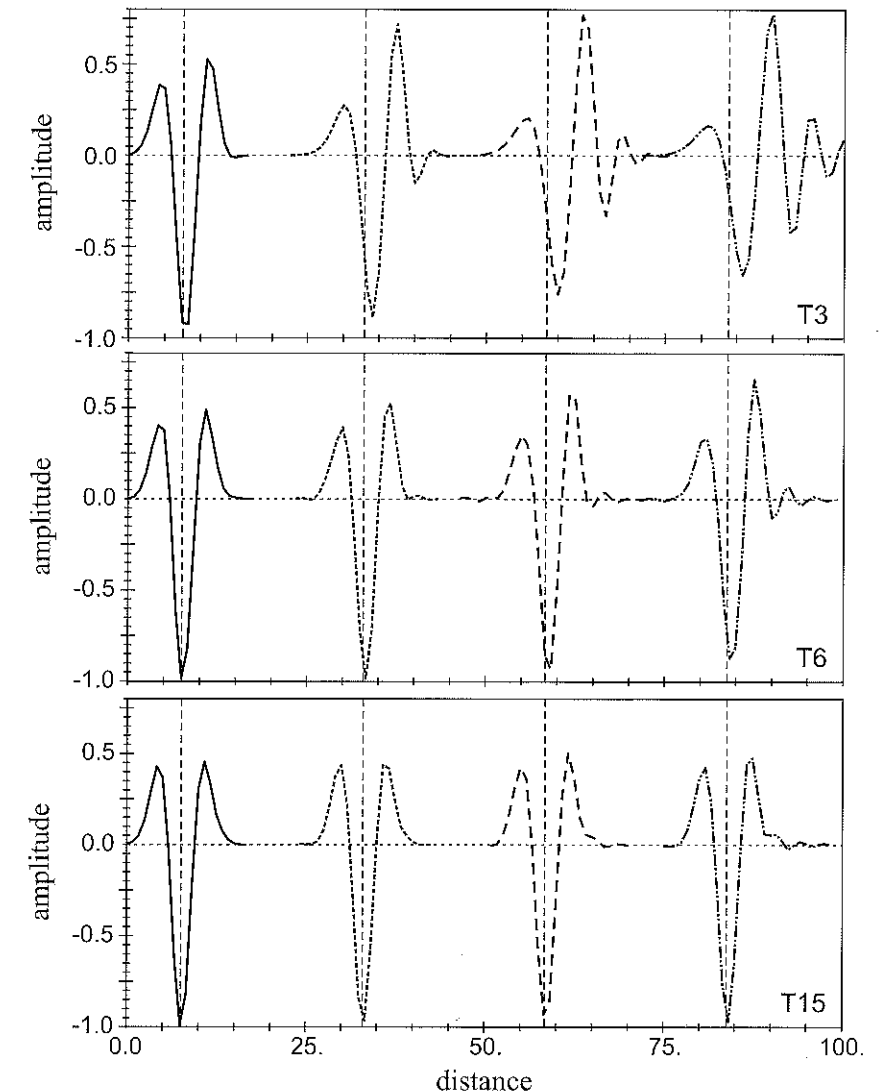


Fig. 4.24: Numerical dispersion for various types of finite elements: 3-noded (top), 6-noded (middle) and 15-noded (bottom) elements. Waveforms at different times and expected theoretical propagation delays (vertical dashed lines).

The results obtained for each mesh are displayed in Fig.4.24. The different element types are denoted $T3$ for the linear three-noded elements, $T6$ for the quadratic six-noded elements and $T15$ for the fourth order 15-noded elements. Figure 4.24 shows that, for linear elements ($T3$), the numerical dispersion is very strong (the expected theoretical propagation delays are displayed as vertical dashed lines). For the quadratic elements ($T6$), the results are much better, but, at a certain distance, the cumulative error becomes significant (third and fourth signals). In the case of higher order elements ($T15$), the numerical dispersion is very small. For an identical number of nodes in the direction of propagation, the simulation involving such higher order elements thus gives very good results. The accuracy of higher order finite elements in terms of numerical dispersion seems excellent. More detailed results are discussed in (Hughes *et al.*, 2008; Semblat and Brioist, 2000).

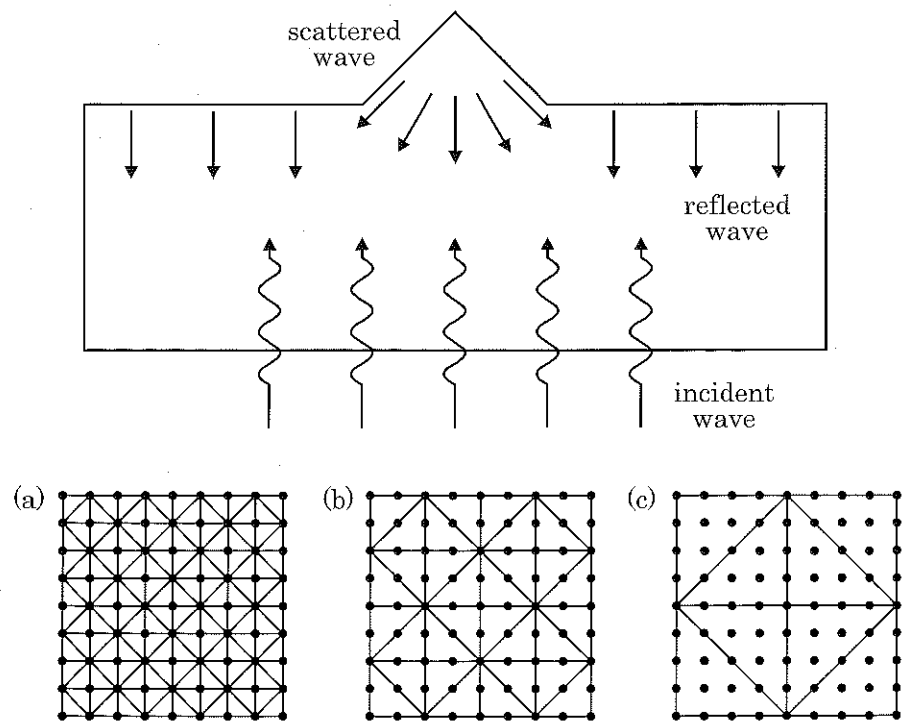


Fig. 4.25: Scattering of a plane seismic wave by a topographic irregularity to analyze 2D numerical dispersion for finite elements at different orders: linear (left), quadratic (centre) and fourth-order (right).

Higher order elements in 2D

As shown by the results displayed in Fig.4.15, numerical dispersion is also influenced by the 2D features of the model. For instance, the angle of incidence of the wave on the mesh has a strong influence on the numerical error. For higher order elements, 2D numerical dispersion will be discussed considering a model involving a topographic irregularity submitted to a seismic excitation. The goal is to estimate the influence of numerical dispersion on the seismic wavefield scattered at the surface for various element types.

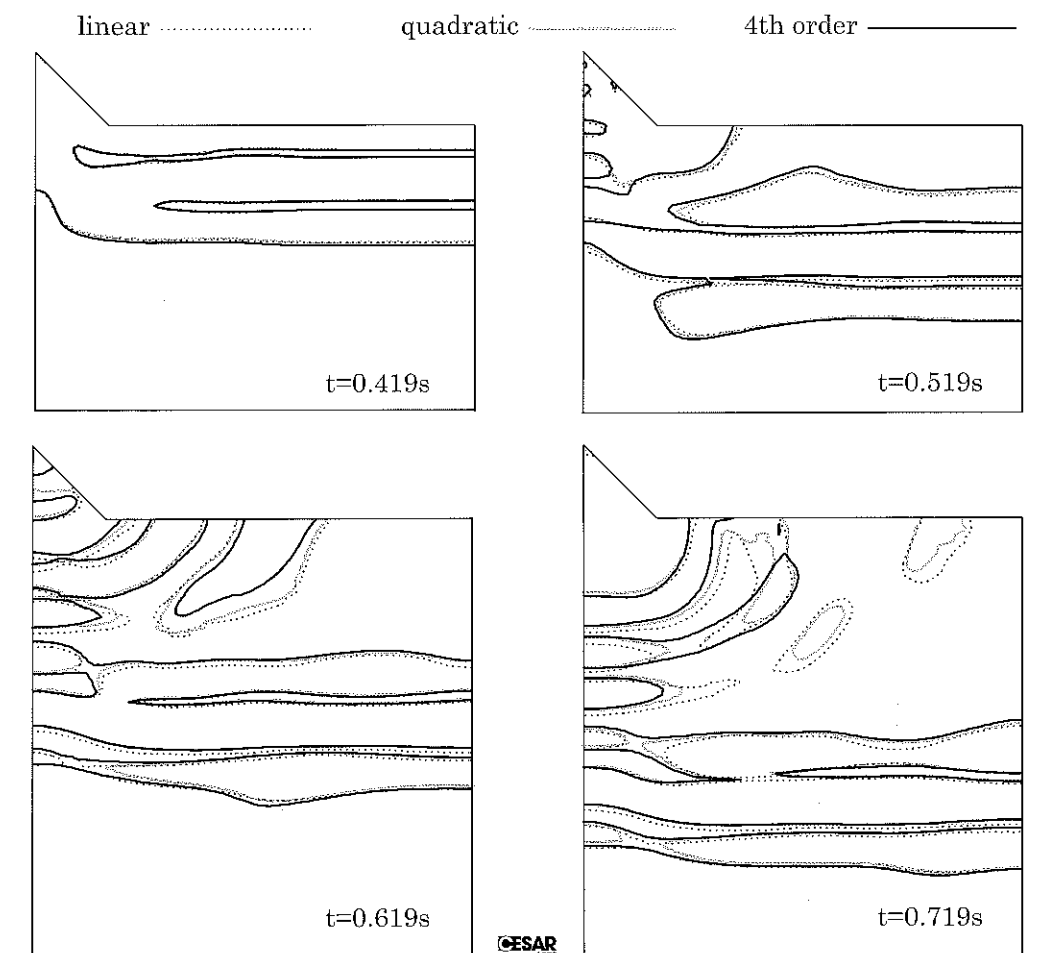


Fig. 4.26: 2D numerical dispersion of the scattered wavefield for various finite element types.

As shown in Fig.4.25, the geometrical arrangement of the triangular finite elements is chosen in order to avoid any particular orientation for the propagation (Semblat and Brioist, 2001). The basic patterns of the model involve various types of triangular finite element types: linear 3-noded elements (a), quadratic 6-noded (b) and 4th order 15-noded (c). All these models involve the same number of degrees of freedom.

2D numerical dispersion being influenced by the wave incidence and the spatial arrangement of the elements, it is interesting to estimate the effect on the estimation of the scattered wavefield. The computed scattered wavefield is displayed in Fig.4.26 for various finite element types at different times. For the first time value, the effect of numerical dispersion is very small. It becomes significant for the second time value and is strong for the two last graphs. Following a vertical line starting from the top of the hill, the effect of numerical dispersion is rather small for all element types. Whereas, for other directions, the scattered wavefield and the surface waves are strongly influenced by numerical dispersion (Semblat and Brioist, 2001).

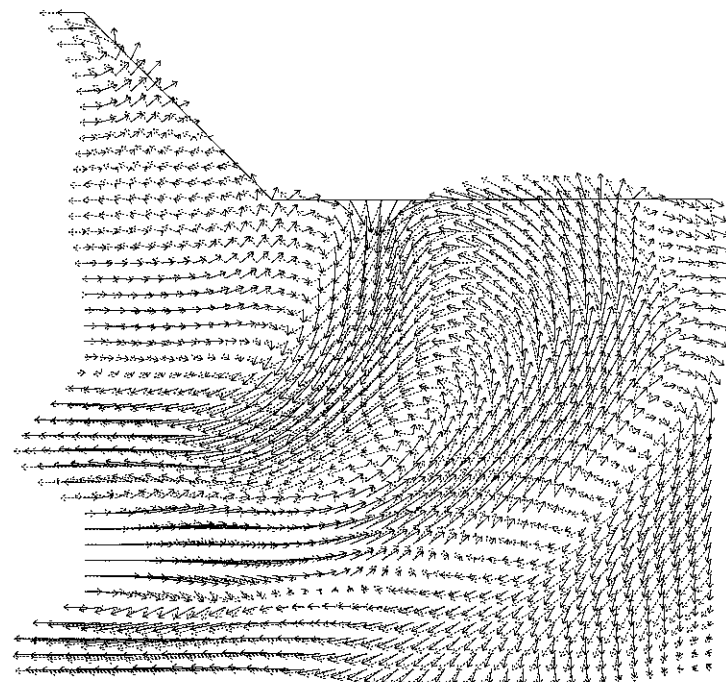


Fig. 4.27: 2D numerical dispersion at $t=0.719\text{s}$: comparison of the displacements and the polarizations for linear and higher order ($p=4$) finite elements.

The scattered wavefield displayed in Fig.4.27 shows that 2D numerical dispersion is influenced by the numerical anisotropy of the model, that is by the simultaneous effects of the wave incidence, the spatial arrangement and the shape of the elements. Several areas corresponding to small or large numerical errors can be distinguished in Fig.4.26. However, as shown in (Semblat and Brioist, 2001), the best numerical accuracy in terms of 2D numerical dispersion is obtained with the higher order elements.

4.4 Physical and numerical damping

As discussed in Chapter 2, the attenuating properties of soils are very important since they govern the amplitude variations during the propagation process. Various types of methods are available to model wave attenuation in soils: empirical models, rheological models, constitutive models, etc. In this section, several approaches dedicated to the numerical modelling of damping will be presented. The influence of the numerical scheme will be also discussed since it may modify the wave amplitude through purely numerical damping.

4.4.1 Rayleigh and Caughey damping

A convenient way to model damping consists in the formulation proposed by Rayleigh (Clough and Penzien, 1993). The Rayleigh formulation considers a damping matrix $[C]$ proportional to the mass $[M]$ and stiffness $[K]$ matrices under the following form:

$$[C] = a[M] + b[K] \quad (4.44)$$

A more general formulation derived from the Rayleigh one has been proposed by Caughey (Clough and Penzien, 1993) and is expressed as follows:

$$[C] = [M] \sum_{j=0}^{m-1} a_j ([M]^{-1}[K])^j \quad (4.45)$$

For $m=1$, the Caughey formulation is equivalent to the Rayleigh one. The Rayleigh and Caughey formulations are widely used in structural dynamics and allow an easy computation through modal methods. They indeed both lead to damping matrices that are diagonal in the real eigenmodes base.

The Rayleigh formulation leads to a damping ratio ξ involving a first term proportional to frequency and a second term inversely proportional to frequency (Clough and Penzien, 1993), that is:

$$\xi = \frac{a}{2\omega} + \frac{b\omega}{2} \quad (4.46)$$

As shown in Chapter 2, the attenuation Q^{-1} has a simple expression in terms of damping ratio, yielding:

$$Q^{-1} = 2\xi = \frac{a}{\omega} + b\omega \quad (4.47)$$

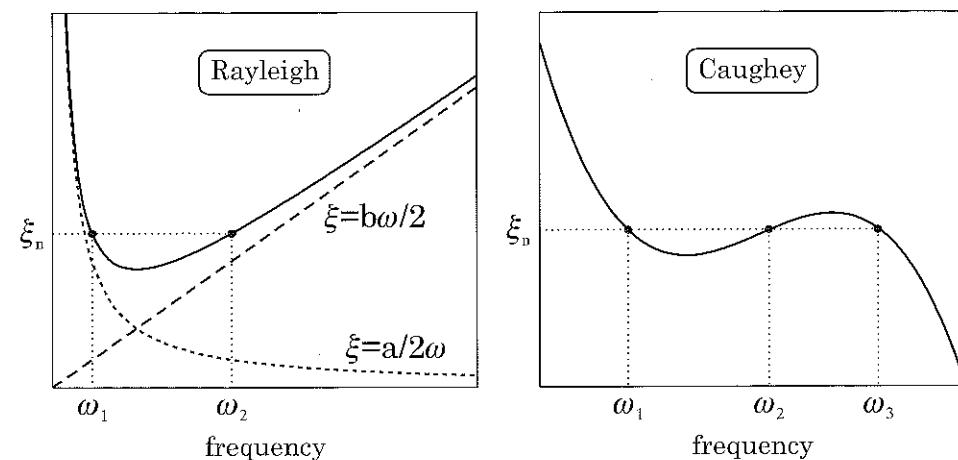


Fig. 4.28: Damping ratio vs frequency for the Rayleigh and the Caughey formulations.

As shown in Fig.4.28, for the Rayleigh formulation (left), the damping ratio is infinite at zero frequency and infinite at infinite frequency. It reaches a minimum value in an intermediate frequency range. For the Caughey formulation (Fig.4.28, right), the variations of damping are more complex depending on the number of terms in the series (Eq.(4.45)).

4.4.2 Rheological interpretation of Rayleigh damping

To use the Rayleigh formulation, it is necessary to have realistic values of both a and b coefficients in Eq.(4.44). The experimental estimation of these parameters raises the need for a physical interpretation of the Rayleigh formulation. As shown in Fig.4.29, a generalized Maxwell model leads to the same expression of attenuation as the Rayleigh formulation (Semblat, 1997):

$$Q_{GM}^{-1} = \frac{M_I}{M_R} = \frac{E(\eta_1 + \eta_2)}{\eta_1^2} \frac{1}{\omega} + \frac{\eta_2 \omega}{E} \quad (4.48)$$

Rayleigh damping is thus equivalent to a generalized Maxwell model as depicted in Fig.4.29. This equivalence is valid for moderate values of the damping ratio ξ ($\xi < 20\%$), that is when the approximation $Q^{-1} \approx 2\xi$ is justified and material dispersion is weak (Semblat, 1997).

To assess such an equivalence for various damping values, wave propagation simulations are performed considering the Rayleigh formulation. They are compared to semi-analytical results obtained using the generalized Maxwell model and directly solving the 1D wave equation in the frequency domain (see Chap.2). The comparisons

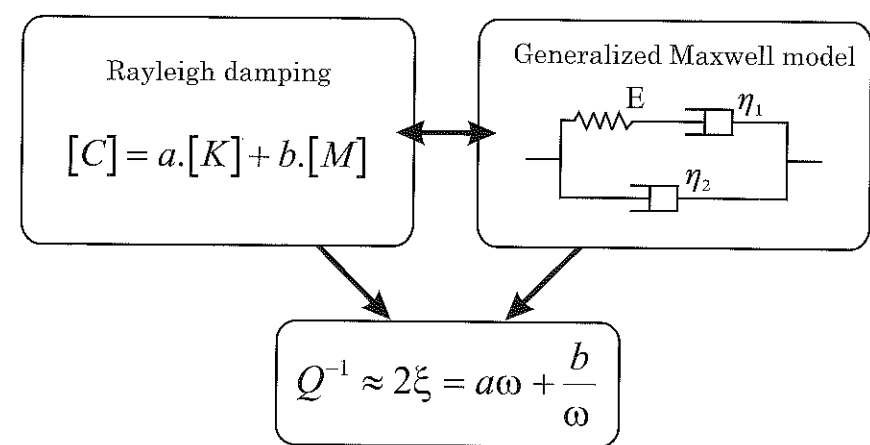


Fig. 4.29: Equivalence between Rayleigh damping and generalized Maxwell model (Semblat, 1997).

between numerical and analytical results are displayed in Fig.4.30. They show an excellent agreement between both approaches for low to moderate damping values. For larger damping values, the approximation $Q^{-1} \approx 2\xi$ is no longer justified and the results disagree (Semblat, 1997).

4.4.3 Attenuation models for geomaterials

Experimental results on geomaterials clearly show that various factors influence the attenuating properties of soils: frequency, mean stress, number of cycles, etc (see Chapter 2). More complex damping models than the previous ones are necessary to include such various dependencies.

Viscoelastic models

Various attenuation models are already discussed in Chapter 2 and may be considered for the numerical analysis with finite elements (Bourbié *et al.*, 1987; Lucet, 1989; Semblat, 1997, 1998). It is nevertheless necessary to incorporate some dissipative terms in the variational formulation through a fully reliable mechanical formulation. Another key point is the accuracy and the cost of the computations. Since attenuation models generally involve memory variables, the computational cost may be large (depending of the considered range for the relaxation time). Various approaches were proposed by different authors ranging from Padé's approximants (Day and Minster, 1984), coarse-grained memory variables (Day, 1998) to parallel 3D viscoelastic finite difference formulations (Bohlen, 2002). Thanks to such models, it is possible to obtain satisfactory results in the linear range (Emmerich and Korn, 1987; Semblat, 1997; Semblat and Luong, 1998) as well as in the nonlinear range (Delépine *et al.*, 2007).

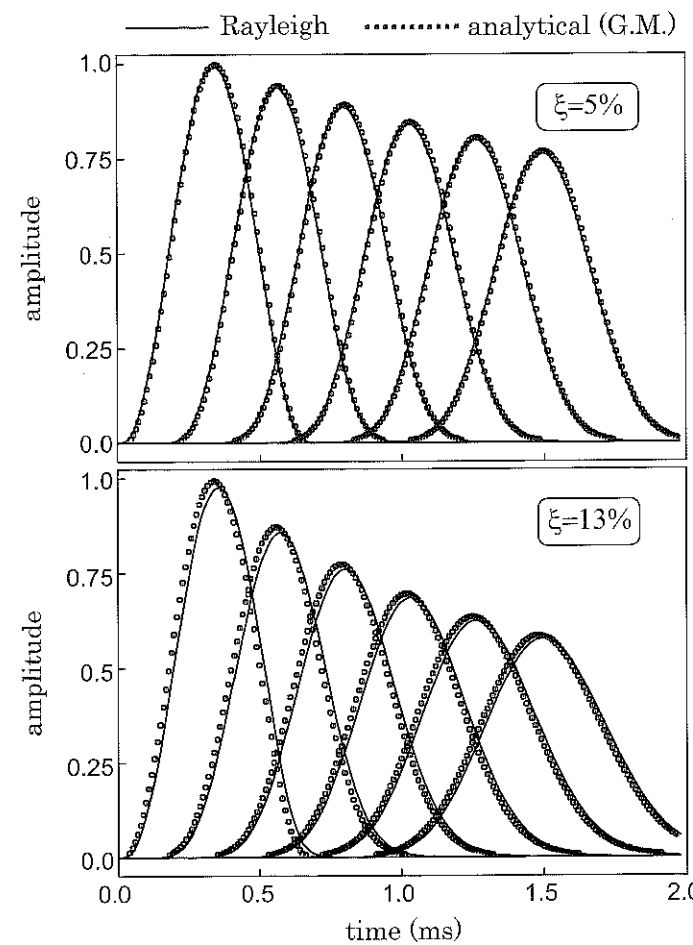


Fig. 4.30: Agreement between analytical results derived from the generalized Maxwell model (symbols) and numerical simulations considering the Rayleigh formulation (solid).

Other finite element formulations are also available such as fractional derivatives viscoelastic models as proposed in the fields of structural dynamics (Sorrentino and Fasana, 2007).

Rayleigh damping for wave propagation problems

The use of Rayleigh damping for wave propagation problems is possible, but it is rather limited since it does not account for the complex anelastic properties of soils.

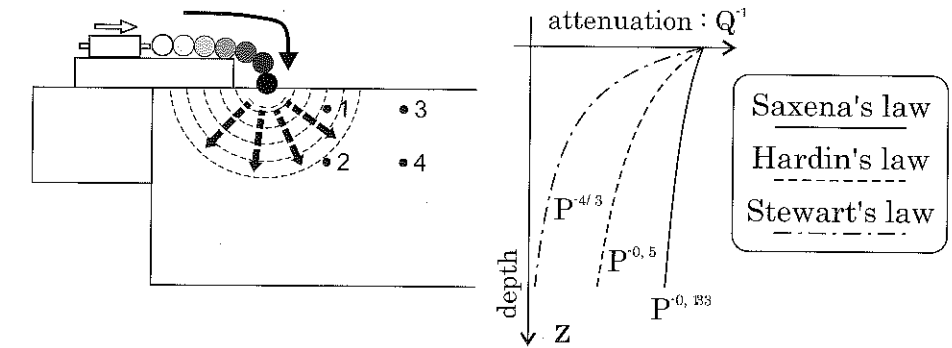


Fig. 4.31: Various damping profiles for wave propagation tests in the centrifuge (see Chapter 3).

Nevertheless, a first attempt may be to model attenuation using Rayleigh damping but considering an inhomogeneous damping profile (Idriss *et al.*, 1974; Semblat and Brioist, 1998). To do so, it is necessary to define a damping submatrix $[C]_e$ for each finite element e as follows (Idriss *et al.*, 1974):

$$[C]_e = a_e [M]_e + b_e [K]_e \quad (4.49)$$

where $[M]_e$, $[C]_e$ and $[K]_e$ are the mass, damping and stiffness submatrices (resp.) and a_e and b_e depend on the damping properties of element e at an average depth z_e .

It is thus possible to simulate seismic wave propagation from a inhomogeneously damped soils. Semblat and Brioist (1998) performed numerical simulations considering various damping profiles. As depicted in Fig. 4.31, centrifuge tests (already presented in Chapter 3) are analyzed considering three different damping profiles:

- *Saxena's law*: Saxena and Reddy (1989) proposed the following attenuation dependence:

$$Q^{-1} = KP^{-0.13}\varepsilon^{0.33} \quad (4.50)$$

where K is a constant, P is the mean stress and ε is the strain.

- *Hardin's law*: Hardin (1965) proposed a specific relationship for sands:

$$Q^{-1} = 9\gamma_{\theta_x}^{0.2}P^{-0.5} \quad (4.51)$$

where γ_{θ_x} is the shear strain and P is the mean stress.

- *Stewart's law:* Stewart *et al.* (1983) assumes another kind of relation for rocks:

$$Q^{-1} = \frac{K\zeta\varepsilon}{P^{4/3}} \quad (4.52)$$

where ζ is the crack density in the specimen.

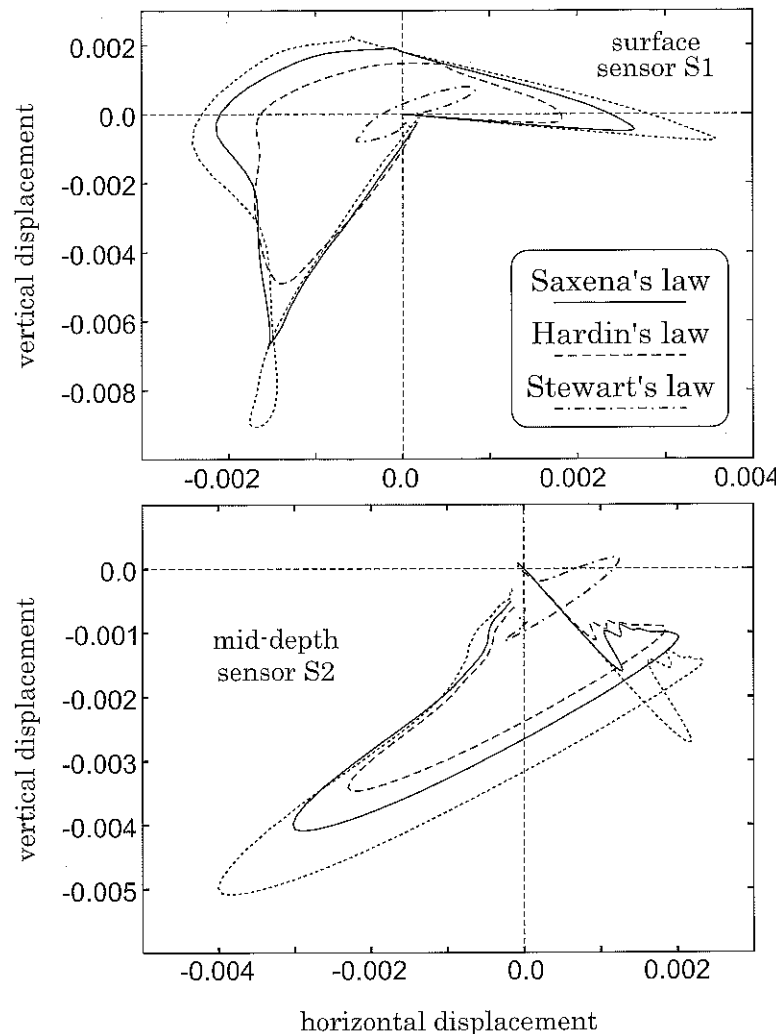


Fig. 4.32: Soil response in the centrifuge for various damping profiles: FEM simulations using variable Rayleigh damping (Semblat and Brioist, 1998).

The damping profiles derived from these laws for the centrifuge experiments discussed in Chapter 3 are displayed in Fig.4.31 (right). The case of homogeneous damping is also considered. It can be noticed that the damping profile derived from Stewart's law leads to very strong variations of attenuation with depth. This law was proposed for rocks and is probably not well-adapted for soils.

FEM simulations considering these four damping profiles were performed by Semblat and Brioist (1998). The results are displayed in Fig.4.32 for both a surface and a deep sensor location. The motion computed with the Stewart's law is very small and this law is not reliable for soils. Conversely, the results derived from the Hardin's law seem to be very interesting when compared to experimental results (Semblat and Brioist, 1998). Finally, for the Saxena's law, the numerical results are very close to the homogeneous damping case and do not allow to retrieve the damping to mean stress dependence observed experimentally (Semblat and Luong, 1998).

From these results, it may be concluded that, to simulate wave propagation in soils, some simple numerical models, involving more or less realistic damping profiles, may be performed using the Rayleigh damping assumption. Nevertheless, for more complex situations, truly viscoelastic, or even elastoplastic, models are necessary (Day, 1998; Delépine *et al.*, 2007; Emmerich and Korn, 1987; Sorrentino and Fasana, 2007).

4.4.4 Numerical damping

In addition to numerical dispersion previously discussed (and mainly depending on the spatial discretization of the model), time integration schemes also involve numerical damping phenomena. Such phenomena lead to an artificial amplitude decay of the wave due to purely numerical errors (see Fig.4.12). This amplitude decay is generally named *algorithmic or numerical damping* (Hughes, 1987).

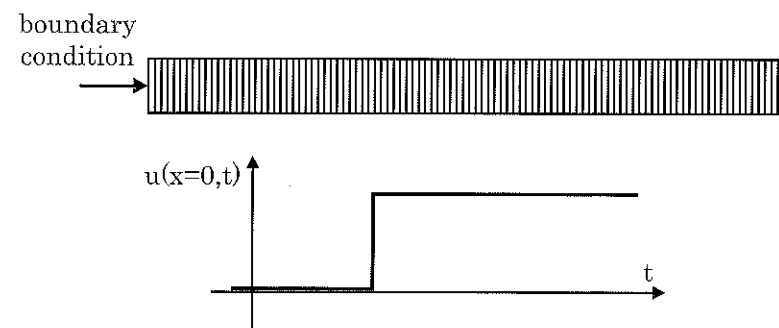


Fig. 4.33: Effect of numerical damping on the propagation of a steep signal: schematic of the model.

Hughes (1987) and Curnier (1993) derived various results for classical time integration schemes. Numerical damping is more or less sensitive depending on the chosen algorithm. The Newmark type algorithms may, for some values of the controlling parameters, involve no numerical damping at all (for instance if the 2nd parameter of the Newmark scheme is 0.5). If well controlled, numerical damping may allow the attenuation of spurious oscillations at high frequencies.

As depicted in Fig.4.33, the influence of numerical damping is now estimated considering a step wavefront generated at the end of a one-dimensional model (linear elements or quadratic elements). The Newmark algorithm considered herein involves either no numerical damping ($\beta=0.25$ and $\gamma=0.5$) or a significant numerical damping ($\beta=0.3$ and $\gamma=0.6$).

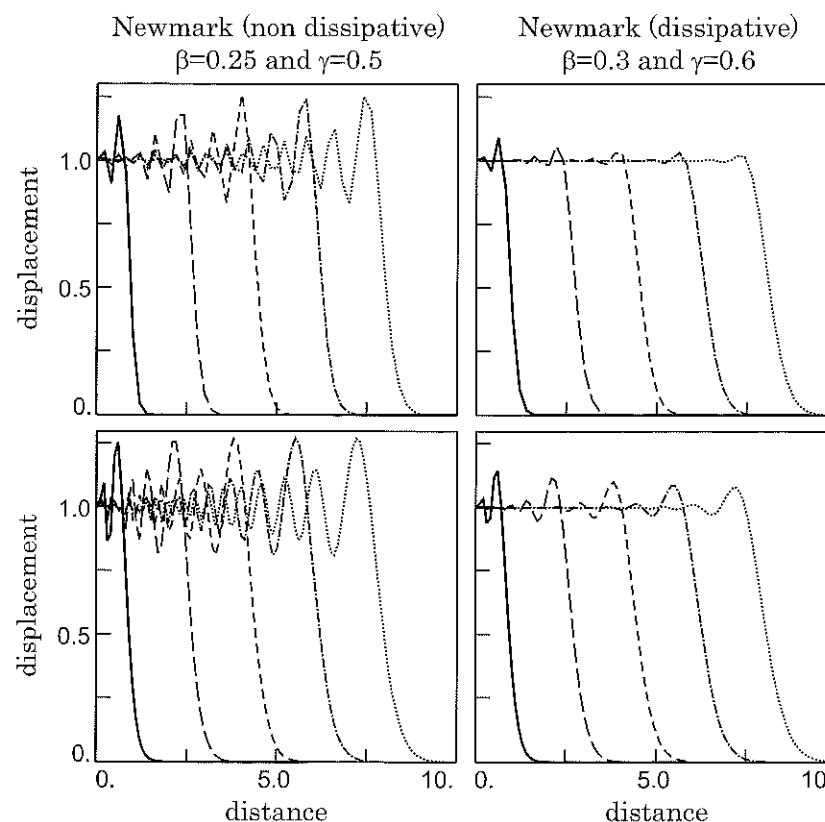


Fig. 4.34: Effect of numerical damping on the propagation of a step wavefront: waveforms at different times for linear elements (top) and quadratic elements (bottom) using a non dissipative (left) or a dissipative (right) Newmark integration scheme.

As shown in Fig.4.34, numerical damping attenuates the amplitude of spurious oscillations in the seismic wave. Such oscillations are artificial and are simply due to the fact that the excitation includes higher frequency components. Such components cannot propagate correctly in a discrete undamped medium, since the element size should be extremely small (Hughes, 1987). The observed oscillations are larger for quadratic elements (bottom) since these elements are more sensitive to the fast variations of the wave.

As shown through the curves displayed in Fig.4.34, numerical damping allows removal of spurious oscillations in the case of fast varying excitations (pulse, Heaviside, etc) or nonlinear wave propagation including, or generating, higher frequency components (Delépine *et al.*, 2007). Another solution to avoid this problem consists in using excitations having slower variations, as is generally the case for actual signals.

4.5 Modelling wave propagation in unbounded media

Modelling wave propagation in (semi-)infinite media may be difficult depending on the numerical method considered. As it will be shown at the end of this Chapter, boundary integral equation methods allow an accurate description of wave propagation in unbounded media (Bonnet, 1999). With the finite or spectral element method, it is necessary to avoid artificial wave reflections on the mesh boundaries. Various techniques which solve this problem will be discussed in the following: absorbing boundaries, infinite elements and absorbing layers (Givoli, 1992; Meza-Fajardo and Papageorgiou, 2008; Festa and Nielsen, 2003; Modaressi and Benzenati, 1992).

4.5.1 Absorbing boundaries in 1D

As already demonstrated in Chapter 2 in the 1D case (§2.3.7), it is possible to remove wave reflections at the model boundaries by adding a dashpot having an adequate viscosity depending on the mechanical properties of the medium (Fig.4.35). The parameters of the absorbing elements must compensate the influence of the reflected wave (free-surface condition). From Chapter 2, the optimal viscosity of the dashpot is $\eta = \rho c$ (ρ : mass density, c : wave velocity). As it will be shown in the next section, the analysis is more complicated in the 2D case.

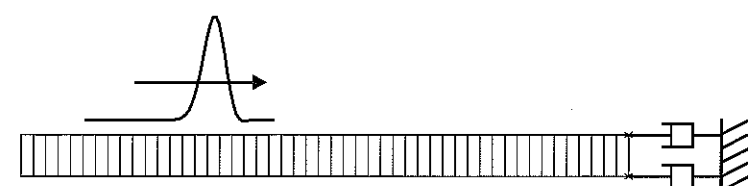


Fig. 4.35: Absorbing elements in the one-dimensional case.

4.5.2 Absorbing boundaries in 2D

In 2D cases, the theoretical solution for the optimal absorbing conditions is not as simple as in the 1D case (§2.3.7). A 2D example will now be considered to design absorbing boundary conditions: a cylindrical domain is modelled by a quarter of a disk discretized with finite elements (plane strain).

As shown in Fig.4.36, discrete elements are connected at the domain boundary. The goal is to have a theoretical determination of the optimal features of the absorbing elements in order to minimize or fully remove spurious wave reflections.

This example was for instance proposed by Dubreucq and Piau (see Bisch *et al.*, 1999) to analyse soil-structure interaction. The first step consists in deriving the equation of propagation for cylindrical waves (Bisch *et al.*, 1999). The medium is assumed elastic, linear and isotropic in the framework of small strains. The displacement field is supposed to depend on the radial distance r only.

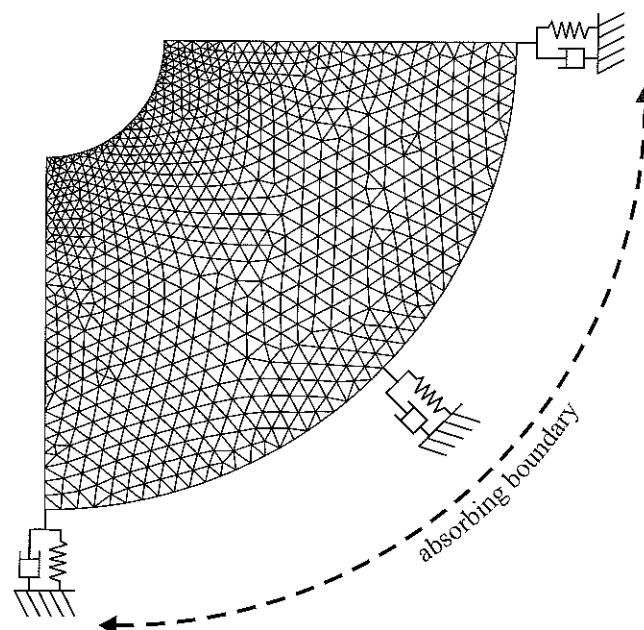


Fig. 4.36: 2D mesh with dashpots and springs at its boundary (Bisch *et al.*, 1999).

The components of the Cauchy stress tensor in cylindrical coordinates are thus:

$$\left\{ \begin{array}{l} \sigma_{rr} = (\lambda + 2\mu) \frac{\partial u_r}{\partial r} + \lambda \frac{u_r}{r} \\ \sigma_{r\theta} = \mu \left(\frac{\partial u_\theta}{\partial r} - \frac{u_\theta}{r} \right) \\ \sigma_{\theta\theta} = \lambda \frac{\partial u_r}{\partial r} + (\lambda + 2\mu) \frac{u_r}{r} \end{array} \right. \quad (4.53)$$

From the equilibrium equations in cylindrical coordinates and assuming pure body waves at a distance from the source, the following differential equations corresponding to the two body wave types (P and S -waves) are obtained:

- for P -waves:

$$\frac{\partial^2 u_r}{\partial r^2} + \frac{1}{r} \frac{\partial u_r}{\partial r} - \frac{1}{r^2} u_r = \frac{1}{V_P^2} \frac{\partial^2 u_r}{\partial t^2} \quad (4.54)$$

- for S -waves:

$$\frac{\partial^2 u_\theta}{\partial r^2} + \frac{1}{r} \frac{\partial u_\theta}{\partial r} - \frac{1}{r^2} u_\theta = \frac{1}{V_S^2} \frac{\partial^2 u_\theta}{\partial t^2} \quad (4.55)$$

The idea of the method is to evaluate the stress components at a certain radial distance R_e (mesh boundary) and to design adequate absorbing boundary conditions using springs and dashpots. For that purpose, we need to express the stress components as functions of the displacement components and their time derivatives. From the expression of the stress components, Eq.(4.53), the spatial derivatives may be easily converted into time derivatives as follows (see Chapter 2):

$$\frac{\partial u_k}{\partial r} = -\frac{1}{V_k} \dot{u}_k \quad ; \quad k = P, S \quad (4.56)$$

At radial distance R_e , the components of the stress tensor may be easily derived as functions of the displacement components and their time derivatives:

- for P -waves:

$$\sigma_{rr} = -\frac{\lambda + 2\mu}{V_P} \dot{u}_r + \frac{\lambda}{R_e} u_r \quad (4.57)$$

- for S -waves:

$$\sigma_{r\theta} = -\frac{\mu}{V_S} \dot{u}_\theta - \frac{\mu}{R_e} u_\theta \quad (4.58)$$

with R_e the external radius of the cylindrical domain, V_P and V_S the P and S wave velocities (resp.).

The coefficients of the displacement terms and of the time derivatives of displacement represent the lineic stiffnesses and lineic dampings:

- the $-\frac{\lambda+2\mu}{V_P}$ and $-\frac{\mu}{V_S}$ terms are the longitudinal and transverse viscous damping coefficients respectively,

- the $\frac{\lambda}{R_e}$ and $-\frac{\mu}{R_e}$ terms correspond to the lineic stiffnesses for each wave type.

It is also necessary to determine the characteristic features of the springs and dashpots in the framework of a finite element formulation (depending on the element type) and take into account the discretization of the boundary (Bisch *et al.*, 1999).

For a given finite element discretization and excitation (*P* or *S* wave), it is thus possible to determine the optimal stiffness and damping values to remove the spurious reflections at the domain boundaries. One should nevertheless notice that these optimal values are determined assuming the radius of the cylindrical domain, R_e , to be large and the simplification of the stress components thus obtained (Eqs (4.57) and (4.58)) does not account for the influence of frequency. These results appear as a generalization of the 1D results obtained in Chapter 2 (§2.3.7).

4.5.3 Infinite elements

The first researches on *infinite elements* were proposed in the early 70's by Zienkiewicz *et al.* (1985). The goal of this method is to artificially extend the medium towards infinity, by coupling infinite elements at its boundaries (Chadwick *et al.*, 1999). It allows a reduction of the model size as well as of the computational time. More recent works were also performed in the 90's (Autenzio, 1997; Bettess, 1992; Lagrouche, 1996).

First approach of the method

The basic principle consists in keeping the functions for the geometrical transformation of the finite elements and to chose shape functions with a weighting function modelling the decay at infinity. By this means, one tries to approximate the actual physical process. The domain of interest, as well as the local variable(s) characterizing the system geometry, is thus extended to infinity (see Fig.4.37).

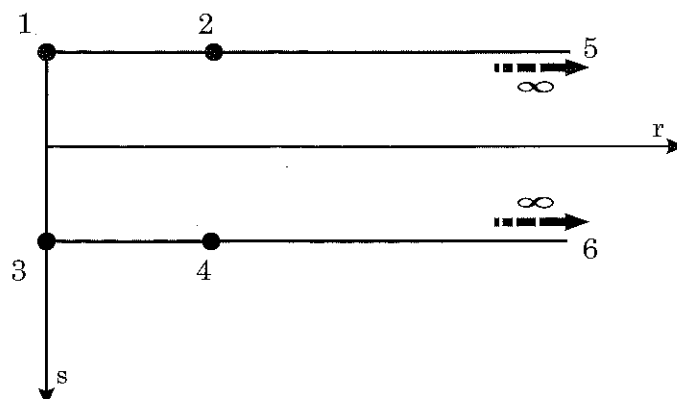


Fig. 4.37: Infinite elements and decay function ($r \rightarrow \infty$).

Second approach

In this case, the domain of interest remains bounded and the local variables, depending on the number of directions extending to infinity, range between -1 and +1. We thus transform the infinite geometry of the real domain in a bounded domain by using mapping functions involving the reciprocal function of the considered decay. For this type of element, we thus keep the shape functions of the classical finite elements (see Fig.4.38).

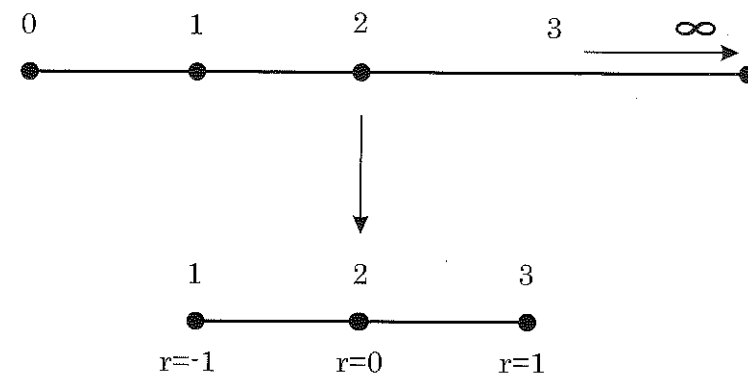


Fig. 4.38: Mapped infinite element ($-1 \leq r \leq 1$).

Comparison of both approaches

The major advantage of the first method is its natural approach and its easy implementation in a computer program (a simple multiplication between a polynomial function and the weighting function is only necessary). Its main drawback is the computation of the element matrices involving generalized integral along infinite directions.

The second method leads to integrals over finite limits and involves polynomial shape functions. The main difficulty is the calculation of the Jacobian of the transformation, the integration being performed in local variables. The derivatives of the reciprocal functions are thus needed. In order to avoid complex computations, it is necessary to chose decay laws having the most regular analytical expression as possible. For this method, classical integration methods such as Gauss quadrature may be used (Chadwick *et al.*, 1999; Lagrouche, 1996).

Both methods are actually equivalent since, through a change of variables, we can show that the integrals computed by each method are identical. The Jacobian of the geometrical transformation indeed allows us to retrieve the same expression (Bettess, 1992).

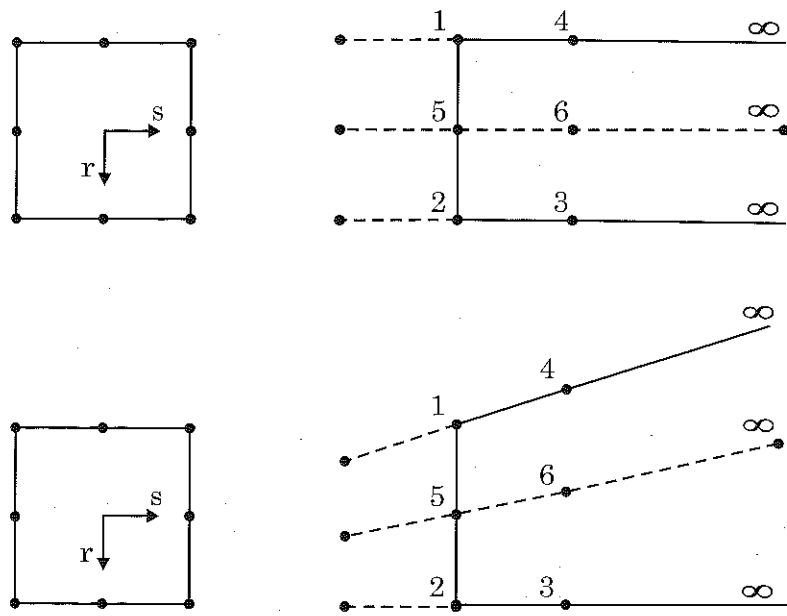


Fig. 4.39: Schematic of a 2D infinite elements along one direction (top) or two directions (bottom).

Two-dimensional case

In 2D, the principle of the method is the same as in 1D and the 2D element may be infinite along one or two directions. Figure 4.39 (top) displays a 2D infinite element along one direction only. In this case, Chadwick *et al.* (1999) proposed a radially infinite element with the following mapping functions:

$$\begin{aligned}
 M_1 &= \left(-\frac{2s}{1-s} \right) \left(-\frac{1}{2}r(1-r) \right) \\
 M_2 &= \left(\frac{1+s}{1-s} \right) \left(-\frac{1}{2}r(1-r) \right) \\
 M_3 &= \left(-\frac{2s}{1-s} \right) (1+r)(1-r) \\
 M_4 &= \left(\frac{1+s}{1-s} \right) (1+r)(1-r) \\
 M_5 &= \left(-\frac{2s}{1-s} \right) \frac{1}{2} r(1+r) \\
 M_6 &= \left(\frac{1+s}{1-s} \right) \frac{1}{2} r(1+r)
 \end{aligned} \tag{4.59}$$

The infinite elements depicted in Fig.4.39 (top) may thus be related to standard finite elements through such transformations.

In the case of an infinite element along two directions (Fig.4.39, bottom), previous expressions may be easily generalized (Bettess, 1992).

Infinite elements in dynamics

Depending on the chosen method, the weighting functions in the shape functions or the mapping functions depend on the type of decay considered in the analysis. The choice of the decay is related to the physical problem studied: cylindrical geometry, spherical geometry, anelastic media, etc. Furthermore, these decay laws depend on the wave type considered. The work of Medina and Taylor (1983) gives the analytical expressions of the geometrical transformation functions. A damping factor, denoted ξ , is taken into account in these functions under the form of a complex exponential $\exp(i\xi)$. The final form of the functions accounts for the type of decay and the damping factor. The method proposed by Medina and Taylor (1983) has been considered for the analysis of traffic induced vibrations in soils by Laghrouche (1996). The numerical results obtained by this author show the efficiency of such a method for wave propagation problems.

Some other works in the field of dynamics were dedicated to the formulation of infinite elements (Gerdes, 1998; Yerli *et al.*, 1999).

4.5.4 Absorbing layers (PML)

The absorbing layers method is different from the absorbing boundaries technique since the idea is now to avoid spurious reflections at the medium boundaries using layers having specific attenuation properties. It is for instance the case for the *Perfectly Matched Layer* method briefly presented in the following.

Perfectly Matched Layer method

The method proposed by Basu and Chopra (2003) is presented for a semi-infinite rod on elastic foundation subjected to an harmonic displacement at one end. The time-harmonic displacement in the rod is governed by the following equations:

$$\begin{aligned}
 \frac{d\sigma}{dx} - \frac{k_g}{S} u &= -\omega^2 \rho u \\
 \sigma &= E\varepsilon \\
 \varepsilon &= \frac{du}{dx}
 \end{aligned} \tag{4.60}$$

where σ and ε are the scalar, axial stress and strain in the rod, E and S are the Young's modulus and the cross-sectional area of the rod, ρ the mass density and k_g the stiffness per unit length of the foundation.

The space coordinate x is then replaced by a stretched coordinate \tilde{x} such as (Basu and Chopra, 2003):

$$\tilde{x} = \int_0^x \lambda(s) ds \quad (4.61)$$

where λ is the coordinate *stretching function*. It is assumed continuous and complex-valued thus leading to:

$$\frac{d\tilde{x}}{dx} = \lambda(x) \quad (4.62)$$

The system of equations (4.60) can be rewritten as:

$$\begin{aligned} \frac{1}{\lambda(x)} \frac{d\sigma}{dx} - \frac{k_g}{S} u &= -\omega^2 \rho u \\ \sigma &= E\varepsilon \\ \varepsilon &= \frac{1}{\lambda(x)} \frac{du}{dx} \end{aligned} \quad (4.63)$$

As depicted in Fig.4.40, for *Perfectly Matched Medium (PMM)*, the λ functions may be chosen with identical values at the interface between two media (no reflected wave) and the solutions of Eq.(4.63) are similar to those of Eq.(4.60). For $a_0 < 1$, evanescent-wave-type solutions are of the form (Basu and Chopra, 2003):

$$u(x) = \exp\left(-\sqrt{1-a_0^2}\frac{\tilde{x}}{r_0}\right) \text{ and } u(x) = \exp\left(+\sqrt{1-a_0^2}\frac{\tilde{x}}{r_0}\right) \quad (4.64)$$

whereas, for $a_0 > 1$, Eq.(4.63) yields propagating-wave-type solutions:

$$u(x) = \exp\left(-i\sqrt{a_0^2-1}\frac{\tilde{x}}{r_0}\right) \text{ and } u(x) = \exp\left(+i\sqrt{a_0^2-1}\frac{\tilde{x}}{r_0}\right) \quad (4.65)$$

For $a_0 > 1$, the stretching function λ may be chosen as:

$$\lambda(x) = 1 - i \frac{f(x)}{\sqrt{a_0^2 - 1}} \quad (4.66)$$

$$\text{then: } \frac{\tilde{x}}{r_0} = \frac{x}{r_0} - i \frac{\bar{F}\left(\frac{x}{r_0}\right)}{\sqrt{a_0^2 - 1}} \text{ where: } \bar{F}(\tilde{x}) = \int_0^{\tilde{x}} \bar{f}(\xi) d\xi \quad (4.67)$$

with $\bar{\xi} = \xi/r_0$ and $\bar{f}(\bar{\xi}) = f(r_0\bar{\xi}) = f(\xi)$ (f is a real-valued continuous function).

The solution is thus:

$$u(x) = \exp\left[-\bar{F}\left(\frac{x}{r_0}\right)\right] \exp\left(-i\sqrt{a_0^2-1}\frac{x}{r_0}\right) \quad (4.68)$$

corresponding, for $\bar{F}(\frac{x}{r_0}) > 0$, to a propagating wave attenuated in the x direction.

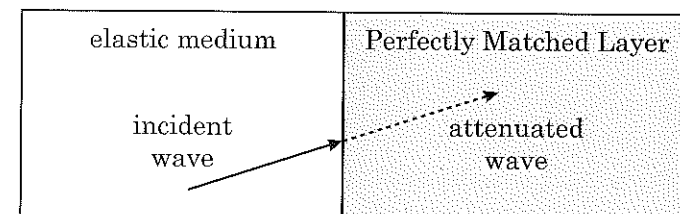


Fig. 4.40: Principle of Perfectly Matched Layer formulations.

This property is the main interest of PMM: it may be used to model wave propagation in an unbounded domain. A Perfectly Matched Layer (PML of finite length L) is then considered (Fig.4.40). The parameters of the PML must be chosen in order to have sufficient attenuation in a finite distance.

The PML generally very efficiently avoids reflections of body waves. Nevertheless, as discussed in the next paragraphs, the effect of the PML technique is not optimal for grazing incidences and may even turn as a drawback for surface waves.

Filtering PML formulation

As shown by Festa *et al.* (2005), denoting the coordinate change as:

$$\tilde{x} = x + \frac{\Sigma(x)}{i\omega} \quad (4.69)$$

a plane wave $\Phi(x, z, t) = A e^{i(\omega t - k_x x - k_z z)}$ becomes in the PML area:

$$\tilde{\Phi}(x, z, t) = \Phi(x, z, t) e^{-\frac{k_x}{\omega} \Sigma} \quad (4.70)$$

where Σ is an arbitrary function decaying from the medium/layer interface to the external boundary of the layer and thus leading to an exponential decay of $\tilde{\Phi}(x, z, t)$.

In the case of Rayleigh waves, we consider the plane wave decomposition as follows:

$$\Psi(x, z, t) = e^{-i(\omega t - k_x x)} (A_P e^{-\omega \tilde{\eta}_P z} + A_S e^{-\omega \tilde{\eta}_S z}) \quad (4.71)$$

where $\tilde{\eta}_i^2 = \frac{1}{V_R^2} - \frac{1}{V_i^2}$ ($i = P, S$) and (A_P, A_S) are constants (see Chapter 3).

If the Rayleigh wave has some interaction with the bottom PML in the model, the geometrical transformation yields:

$$\tilde{\Psi}(x, z, t) = e^{-i(\omega t - k_x x)} (A_P e^{-\omega \tilde{\eta}_P z} e^{i\tilde{\eta}_P \Sigma} + A_S e^{-\omega \tilde{\eta}_S z} e^{i\tilde{\eta}_S \Sigma}) \quad (4.72)$$

For $\omega \rightarrow 0$, the Rayleigh wave becomes a body wave and the vertical wavenumber is controlled by Σ which is an increasing function of depth (Festa and Nielsen, 2003).

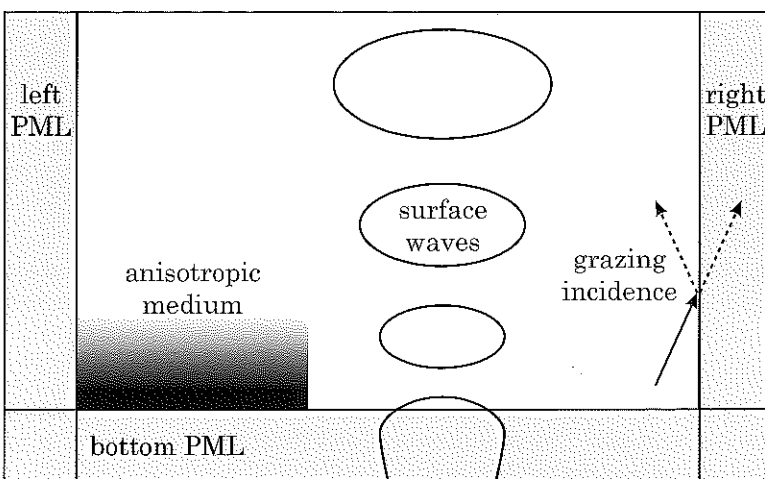


Fig. 4.41: Various configurations leading to significant numerical errors in the PML formulation.

As depicted in Fig.4.41, the surface waves may then be amplified at depth leading to a significant numerical error. Festa *et al.* (2005) proposed an enhanced PML method: the *Filtering PML* (FPML).

In the frequency domain, transformation (4.69) has a pole at $\omega = 0$. As proposed by Festa *et al.* (2005), it can be moved along the imaginary axis as follows:

$$\tilde{x} = x + \frac{\Sigma(x)}{i\omega + \omega_c} \quad (4.73)$$

where ω_c is a constant.

Using transformation (4.73) instead of (4.69), the body wave now decreases in the PML, yielding:

$$\tilde{\Phi}(x, z, t) = \Phi(x, z, t) \exp \left(\frac{k_x}{\omega} \frac{\omega^2 - i\omega\omega_c}{\omega^2 + \omega_c^2} \Sigma \right) \quad (4.74)$$

The exponential decay is now frequency dependent: the layer corresponds to an elastic medium at low frequencies and to an attenuating layer at higher frequencies.

For surface waves propagating vertically, the $e^{-\omega\eta z}$ term in Eq.(4.72) becomes:

$$\exp(-\omega\eta z) \rightarrow \exp \left(-\omega\eta z - \Sigma(z) \frac{\omega\omega_c}{\omega^2 + \omega_c^2} \eta + i\Sigma(z) \frac{\omega^2}{\omega^2 + \omega_c^2} \eta \right) \quad (4.75)$$

The first term retains the exponential decay of surface waves and the second term is also a decreasing term (tending to 0 for $\omega \rightarrow 0$).

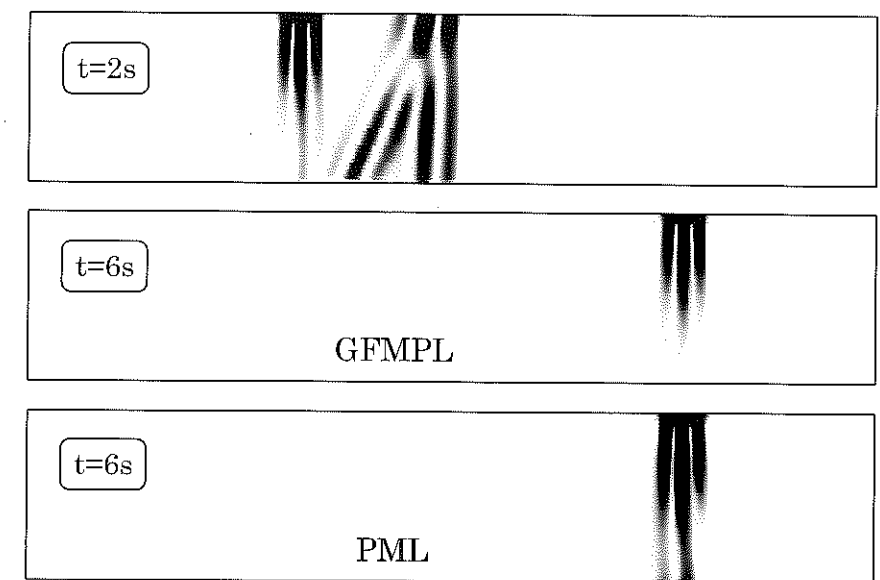


Fig. 4.42: Comparison between the filtering PML formulation (middle) and the classical PML formulation (bottom) leading to an artificial amplification of surface waves (Festa *et al.*, 2005).

This transformation thus retains the features of a surface wave at low frequencies without spurious effects in the PML (Delavaud, 2007). As shown in Fig.4.42, the filtering PML formulation (middle) avoids the problem of artificial surface wave amplification with the classical PML (bottom). Nevertheless, as depicted in Fig.4.41, there are still some numerical instabilities with the PML for grazing incidences (Festa *et al.*, 2005; Komatitsch and Martin, 2007) or anisotropic media (Bécache *et al.*, 2003). Meza-Fajardo and Papageorgiou (2008) proposed a multidirectional PML formulation to overcome this difficulty.

Multidirectional PML formulation

To deal with the numerical instabilities of PML for grazing incidences (Festa *et al.*, 2005; Komatitsch and Martin, 2007) or anisotropic media (Bécache *et al.*, 2003), Meza-Fajardo and Papageorgiou (2008) proposed a multidirectional PML formulation (Fig.4.43). In the classical PML approach, the maximum attenuation is always in the direction of one coordinate (generally x). As depicted in Fig.4.41, for waves entering the PML at grazing incidences, the wavenumber k_x is nearly zero (i.e., wave vector nearly perpendicular to the direction of attenuation) and the attenuation is thus minimal.

The basic idea of Meza-Fajardo and Papageorgiou (2008) is hence to consider various laws of attenuation along the three space coordinates. The coordinate stretching

approach is thus generalized as follows:

$$\begin{cases} \tilde{x} = x + \frac{1}{i\omega} \alpha_x^{(x)} x \\ \tilde{y} = y + \frac{1}{i\omega} \alpha_y^{(x)} y \\ \tilde{z} = z + \frac{1}{i\omega} \alpha_z^{(x)} z \end{cases} \quad (4.76)$$

where the functions $\alpha_i^{(x)}$ are related to the damping profiles $d_i^{(x)}$ through:

$$\begin{cases} \alpha_x^{(x)}(x) = \frac{1}{x} \int_0^x d_x^{(x)}(\xi) d\xi \\ \alpha_y^{(x)}(x) = d_y^{(x)}(x) \\ \alpha_z^{(x)}(x) = d_z^{(x)}(x) \end{cases} \quad (4.77)$$

In the classical PML approach, $\alpha_y^{(x)}=0$ and $\alpha_z^{(x)}=0$ and the maximum attenuation is always in the direction of the x -coordinate. For the M-PML, similar expressions may be obtained in layers having their damping profile controlled by the y or the z coordinates. The treatment of corner regions is similar to that of the classical PML, the properties of the overlapping layers being superimposed (Meza-Fajardo and Papageorgiou, 2008).

The M-PML plane-wave solutions are derived under the following form:

$$\begin{aligned} \underline{u} &= A \exp(-\underline{\alpha} \cdot \underline{x}) \exp[-i(\underline{k} \cdot \underline{x} - \omega t)] \\ \underline{\alpha} &= \frac{|\underline{k}|}{\omega} \left\{ n_x \alpha_x^{(x)} \quad n_y \alpha_y^{(x)} \quad n_z \alpha_z^{(x)} \right\}^T \end{aligned} \quad (4.78)$$

where T denotes the transpose of a vector/matrix.

The real-valued vector $\underline{\alpha}$ can be interpreted as an attenuation vector similar to the case of viscoelastic materials (Chapter 2). In the M-PML, the attenuation does not depend on frequency and the formulation thus corresponds to a non dispersive medium. Conversely to the classical PML, the M-PML allows an optimal choice of vector $\underline{\alpha}$: its components may be related to those of the wave vector \underline{k} . The direction of maximum attenuation may thus be closely related to the direction of propagation. As shown by Meza-Fajardo and Papageorgiou (2008), the M-PML is consequently more efficient for grazing incidence than the classical PML. Meza-Fajardo and Papageorgiou (2008) also proposed dispersion relations and reflection coefficients for M-PML in the case of isotropic media modelled by the spectral element method. They also defined a general procedure for constructing stable M-PML terminations for any anisotropic media. The stability of this formulation is compared to that of the classical PML in Fig.4.43 for an orthotropic medium (Meza-Fajardo and Papageorgiou, 2008). For the longest time ($t=400\mu s$), the classical PML formulation is found to be unstable (Fig.4.43, bottom left) whereas the M-PML formulation remains stable (Fig.4.43, bottom right).

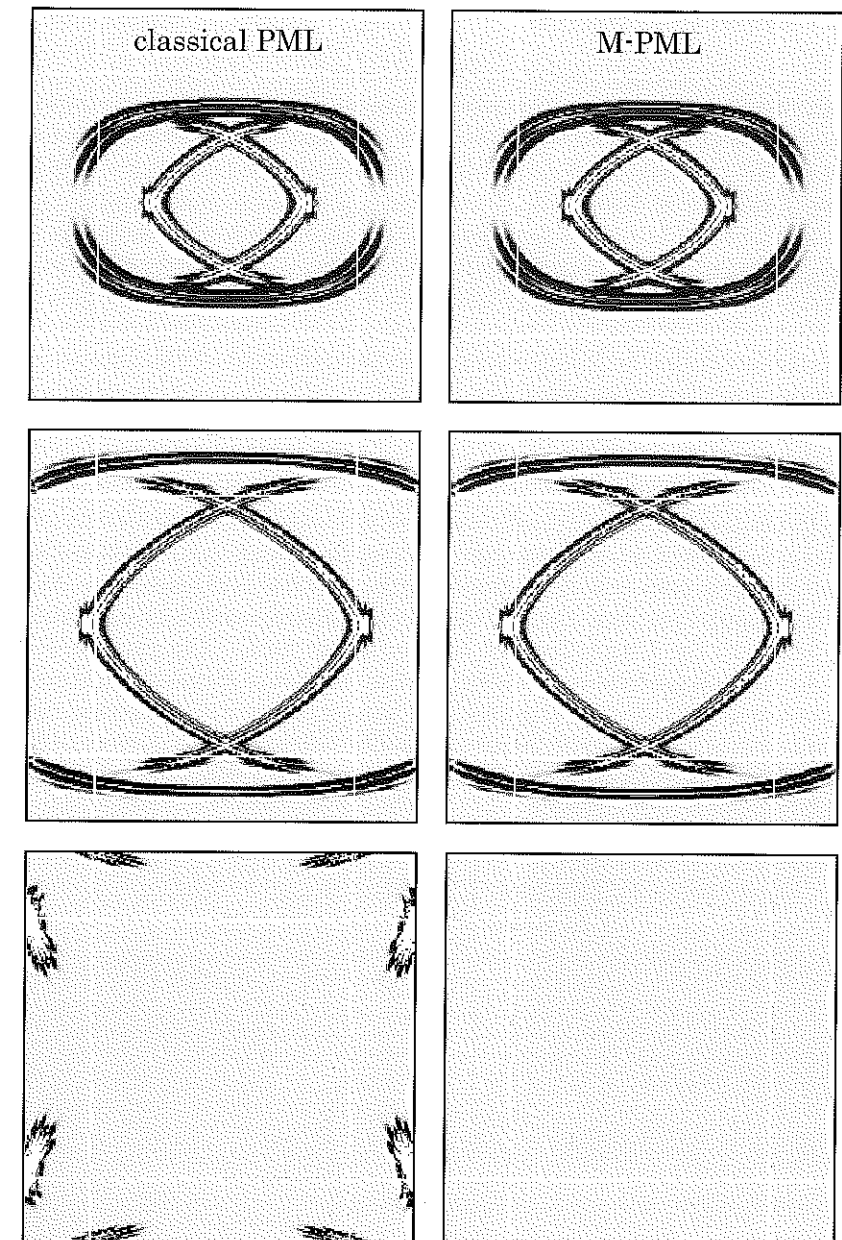


Fig. 4.43: Snapshots of propagation of the velocity magnitude in orthotropic elastic medium at $t = 35\mu s$ (top), $t = 60\mu s$ (middle) and $t = 400\mu s$ (bottom): classical PML (left) and M-PML (right), with $p^{(y/x)} = p^{(x/y)} = 0.15$, as proposed by Meza-Fajardo and Papageorgiou (2008).

4.5.5 Coupled approaches

In addition to the absorbing boundaries/layers, others techniques may also be considered to deal with wave propagation in unbounded domains. It is possible to couple different numerical methods (FEM/BEM, FEM/FDM, etc.) or scale models with various spatial resolutions. Two approaches will be briefly discussed in the following: the FEM/BEM coupling and the *Domain Reduction Method*.

FEM/BEM coupling

To deal with wave propagation in unbounded media, it is possible to couple the Finite Element Method and the Boundary Element Method (Bonnet, 1999; Dangla, 1988). As it will be seen in the following, the Boundary Element Method allows an exact description of the radiation conditions at infinity and is thus a very interesting alternative to FEM approaches.

Since the Finite Element Method is very flexible and allows modelling of complex constitutive laws as well as realistic civil engineering structures, whereas the Boundary Element Method does not, it is interesting to combine both methods. As shown in Fig.4.44, the propagation near the free-surface and the dynamic soil-structure interaction is modelled by the Finite Element Method (*near field*). The propagation at long distances, *far field*, is preferably modelled by the Boundary Element Method since the radiation conditions are exactly accounted for thus avoiding such techniques as absorbing boundaries/layers. At the interface between both domains, the degrees of freedom of the FEM model are condensed and coupled to those of the BEM model (Bonnet, 1999; Dangla, 1988).

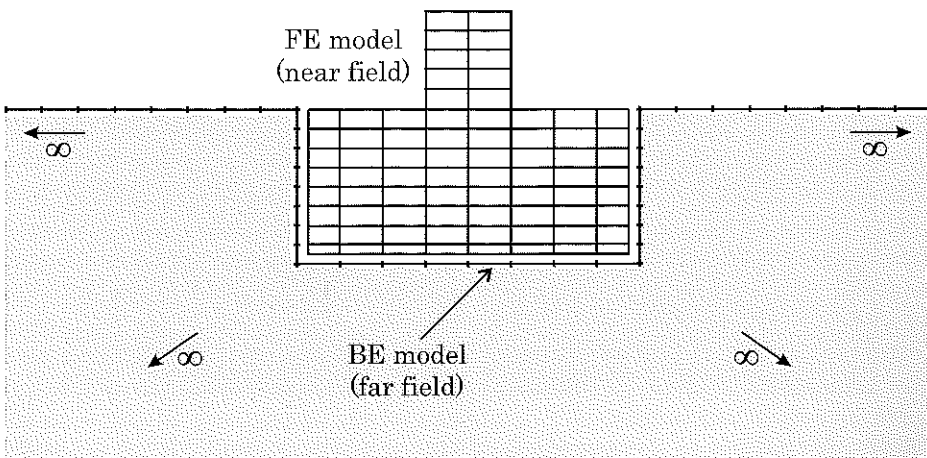


Fig. 4.44: Principle of FEM/BEM coupling in elastodynamics.

Domain Reduction Methods

Another alternative is for instance the *Domain Reduction Method* investigated by Bielak *et al.* (2003). The main idea is to model wave propagation using the finite-element methodology but considering highly heterogeneous localized regions with large contrasts in wavelengths. The target is then complex geological structures (sedimentary basins, ridges) that are far away from the earthquake source. Bielak *et al.* (2003) proposed to subdivide the original problem into two simpler ones. The first is an auxiliary problem that simulates the earthquake source and propagation path effects forgetting the detailed surface geology. The second problem models local amplification in surface layers (see also Chapter 5). The basic idea consists in choosing a set of equivalent localized forces derived from the first step as the input for the second problem. The domain size in the second step may thus be drastically reduced. If the subsurface geological structure is simple, one can replace the finite-element method in the first step with an alternative efficient method. The Domain Reduction Method, proposed in (Bielak *et al.*, 2003), is illustrated in another paper by the same authors (Yoshimura *et al.*, 2003) dealing with 3D problems such as wave amplification in the Los Angeles Basin. In this paper, as illustrated in Fig.4.45, Yoshimura *et al.* (2003) also applied the method to the analysis of the seismic response of a weathered hill. The Domain Reduction Method may thus be considered at various scales and in different frequency ranges.

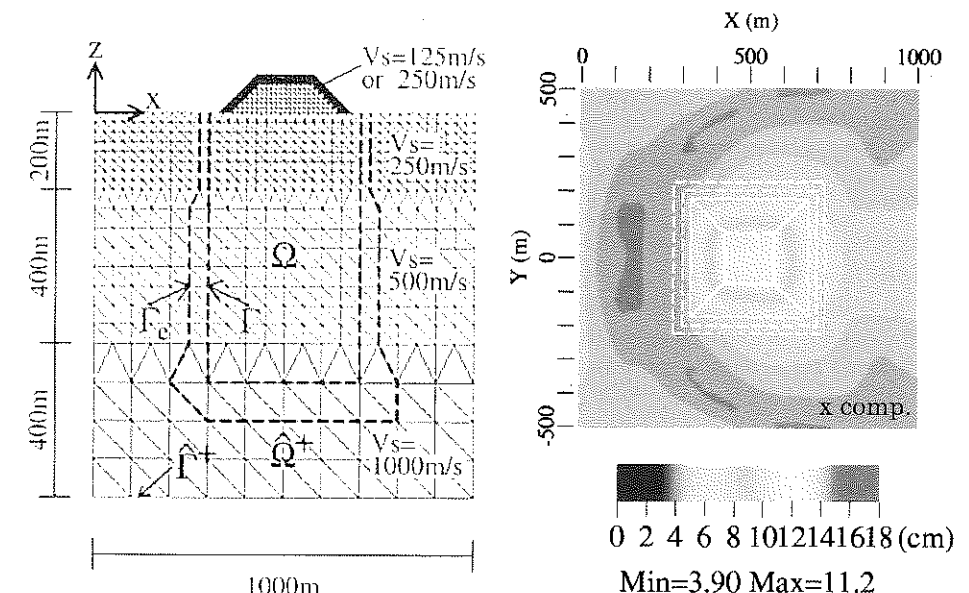


Fig. 4.45: Response of a weathered hill modelled by the Domain Reduction Method in the framework of the FEM (Yoshimura *et al.*, 2003).

4.6 The Boundary Element Method

4.6.1 Interest of the method in dynamics

In addition to the Finite Element Method, such methods as the Boundary Element Method are particularly suitable to model wave propagation problems. This method avoids spurious reflections at the model boundaries since it directly includes exact radiation conditions (Aubry and Clouteau, 1991; Bonnet, 1999; Dangla, 1988). Nevertheless, it is mainly adapted to media having a linear behaviour. As the Finite Element Method, the Boundary Element Method is also sensitive to the element size considered, but there are no similar cumulative errors during the propagation process (numerical dispersion). Furthermore, this method is suitable to model various seismic sources such as plane waves or extended as well as point sources.

4.6.2 Maxwell-Betti theorem

The classical way to derive the Boundary Integral Equations (*BIE*) from the equations of continuum mechanics is not linked to variational approaches. The main idea is to consider the Maxwell-Betti theorem as follows. For sake of simplicity, we will firstly write the equations in the case of linear elastostatics. In that case, the principle of virtual work leads to:

$$\int_{\Omega} \underline{\underline{\sigma}} : \underline{\underline{\varepsilon}}(\hat{u}) d\Omega - \int_{\partial\Omega} (\underline{\underline{\sigma}} \cdot \underline{n}) \cdot \hat{u} dS - \int_{\Omega} f \cdot \hat{u} d\Omega = 0 \quad (4.79)$$

All elastostatic states $\{(u^1, \underline{\underline{\sigma}}^1, f^1), (u^2, \underline{\underline{\sigma}}^2, f^2)\}$ in Ω satisfies the *Maxwell-Betti reciprocity theorem*:

$$\int_{\partial\Omega} [(\underline{\underline{\sigma}}^1 \cdot \underline{n}) \cdot u^2 - (\underline{\underline{\sigma}}^2 \cdot \underline{n}) \cdot u^1] dS = \int_{\Omega} [f^2 \cdot u^1 - f^1 \cdot u^2] d\Omega = 0 \quad (4.80)$$

To derive the Boundary Integral Equations, the basic idea is to chose a particular elastostatic state $(u^2, \underline{\underline{\sigma}}^2, f^2)$ corresponding to a simple reference problem (e.g. point load in an infinite space). The solutions of this problem are called *fundamental solutions* and will be used to solve Eq.(4.80). For time-harmonic problems, The Maxwell-Betti theorem leads to a similar equation. In the transient case, we shall nevertheless see several differences afterwards (§4.6.9)

4.6.3 Integral equations in elastodynamics

Equation of propagation

We will now consider isotropic elastodynamics for time-harmonic problems of circular frequency ω . For any given body force distribution $f_i(\underline{x})$ over Ω , the governing equations which must be verified by any displacement and stress fields, $u_i(\underline{x})$ and $\sigma_{ij}(\underline{x})$ are:

$$\sigma_{ij} = \lambda u_{k,k} \delta_{ij} + \mu(u_{i,j} + u_{j,i}) \quad (4.81)$$

$$\sigma_{ij,j} + \rho \omega^2 u_i + f_i = 0 \quad (4.82)$$

where $u_{i,j}$ and $\sigma_{ij,j}$ are condensed notations for the spatial derivative $\partial/\partial x_j$.

4.6 The Boundary Element Method

Fundamental solutions

The fundamental solutions, in time-harmonic elastodynamics, are defined by a force of unit amplitude applied at a fixed point \underline{y} along a fixed direction k : $f_i(\underline{x}) = \delta(\underline{x} - \underline{y}) \delta_{ik}$. For unbounded domains, the fundamental solution, denoted by $u_i(\underline{x}) = U_i^k(\underline{x}, \underline{y}; \omega)$, is known as the Helmholtz fundamental solution and is given by (Eringen and Suhubi, 1975):

$$U_i^k(\underline{x}, \underline{y}; \omega) = \frac{1}{4\pi\mu} \left[\frac{1}{k_S^2} \frac{\partial^2}{\partial x_i \partial x_k} \left(\frac{e^{ik_S r}}{r} - \frac{e^{ik_P r}}{r} \right) + \frac{e^{ik_S r}}{r} \delta_{ik} \right] \quad (4.83)$$

where $r^2 = (\underline{x} - \underline{y})^2$ and where $k_P = \omega\sqrt{\rho/(\lambda + 2\mu)}$ and $k_S = \omega\sqrt{\rho/\mu}$ are the longitudinal and transverse wave numbers respectively. The stress tensor associated with $U_i^k(\underline{x}, \underline{y}; \omega)$, defined by (4.81), is denoted by $\Sigma_{ij}^k(\underline{x}, \underline{y}; \omega)$ while the stress vector applied to the surface boundary of Ω is $T_i^k(\underline{x}, \underline{y}; \omega) = \Sigma_{ij}^k(\underline{x}, \underline{y}; \omega) n_j$.

The fundamental solutions are generally known as the Green's functions of the problem. In the 2D case, the fundamental solutions are defined as Hankel functions (Dangla, 1988; Bonnet, 1999). A compendium of fundamental solutions in elastodynamics was recently published by Kausel (2006).

Integral representation formula

For sake of simplicity let us consider no body force from now on. Application of the Maxwell-Betti reciprocity theorem, Eq.(4.80), leads to the following displacement integral representation at point $\underline{y} \in \mathbb{R}^3$ (Bonnet, 1999), with $\kappa = 1$ ($\underline{y} \in \Omega$) or $\kappa = 0$ ($\underline{y} \notin \Omega$):

$$\kappa(\underline{y}) u_k(\underline{y}) = \int_{\partial\Omega} [t_i(\underline{x}) U_i^k(\underline{x}, \underline{y}; \omega) - u_i(\underline{x}) T_i^k(\underline{x}, \underline{y}; \omega)] dS_x \quad (4.84)$$

The integral representation formula thus allows the determination of the solution at any interior point \underline{y} only knowing the solution at the medium boundary $\partial\Omega$. A comparison with the Finite Element Method is proposed in Fig.4.46. As shown in Fig.4.46c, the solution will only be determined at the model boundary.

Integral equation

Let \underline{y} denote a fixed point on the boundary surface $\partial\Omega$. As depicted in Fig.4.47, for a given small $\varepsilon > 0$, we introduce a spherical shaped neighbourhood $v_\varepsilon(\underline{y})$ of \underline{y} , called an exclusion neighbourhood (Dangla *et al.*, 2005; Guiggiani *et al.*, 1992). The domain $\Omega_\varepsilon(\underline{y}) = \Omega - v_\varepsilon(\underline{y})$ obtained by removing $v_\varepsilon(\underline{y})$ from Ω is such that the point \underline{y} is exterior to $\Omega_\varepsilon(\underline{y})$. Its boundary is $\partial\Omega_\varepsilon = (\partial\Omega - e_\varepsilon) + s_\varepsilon$, where $e_\varepsilon = \partial\Omega \cap v_\varepsilon$, $s_\varepsilon = \Omega \cap \partial v_\varepsilon$.

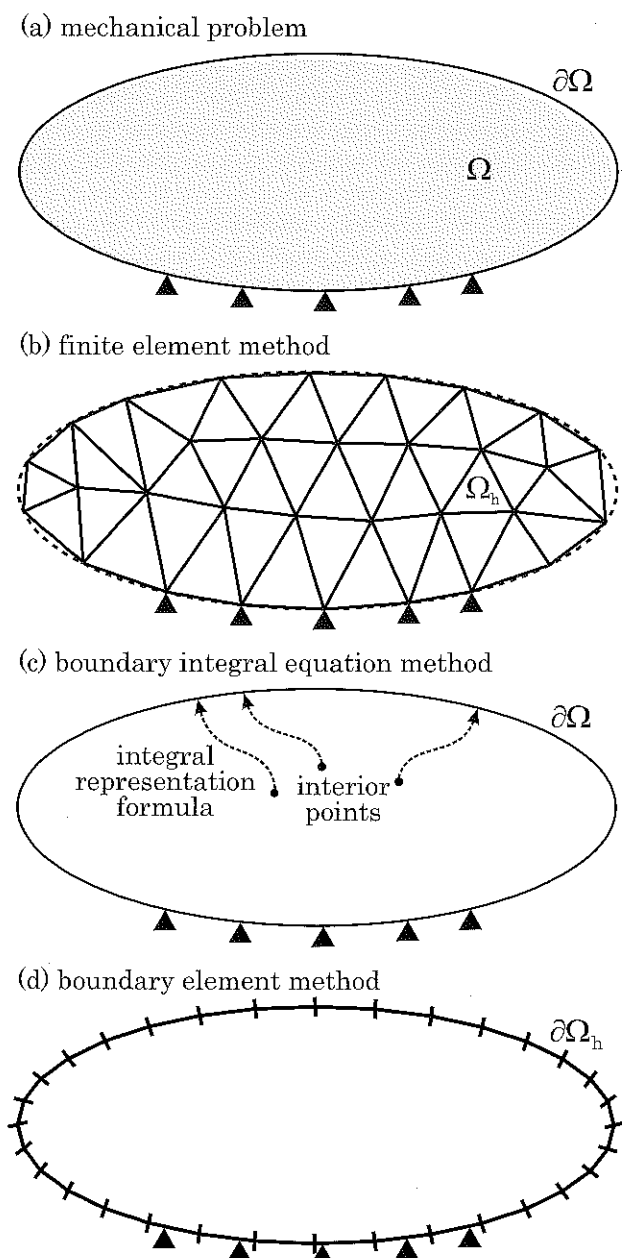


Fig. 4.46: Modelling a mechanical problem (a) by the Finite Element Method (b), the Boundary Integral Equation Method (c) and the Boundary Element Method (d).

The classical form of the integral equation consists in taking the limit $\varepsilon \rightarrow 0$ in the representation formula (4.84) taken for the domain Ω_ε (Bonnet, 1999; Dangla *et al.*, 2005). The limiting expression thus obtained is known as the *Somigliana identity*:

$$C_i^k(\underline{y}) u_i(\underline{y}) = \int_{\partial\Omega} [t_i(x) U_i^k(\underline{x}, \underline{y}; \omega) - u_i(x) T_i^k(\underline{x}, \underline{y}; \omega)] dS_x \quad (4.85)$$

The notation \int stands for the *Cauchy principal value* of a singular integral, i.e. the limit:

$$\int_{\partial\Omega} (\cdot) = \lim_{\varepsilon \rightarrow 0} \int_{(\partial\Omega - e_\varepsilon)} (\cdot) \quad (4.86)$$

The *free term* $C_i^k(\underline{y})$ appearing in Eq.(4.85), is defined by:

$$C_i^k(\underline{y}) = \lim_{\varepsilon \rightarrow 0} \int_{S_\varepsilon} T_i^k(\underline{x}, \underline{y}; \omega) dS_x \quad (4.87)$$

It is found to be equal to $1/2\delta_{ik}$ when Ω is smooth at \underline{y} .

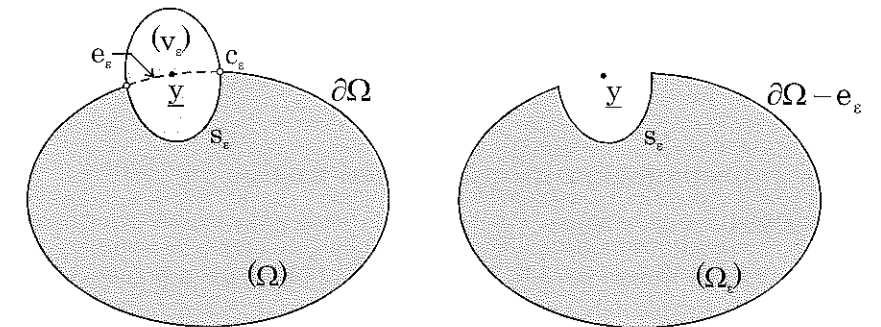


Fig. 4.47: Exclusion neighbourhood considered to apply the limiting process and derive the integral equations (Bonnet, 1999).

4.6.4 Discretization and regularization principle

Regularization of Boundary Integral Equations

In contrast to other discretization methods, the Boundary Element Method involves singular integrals (Bonnet, 1999; Dangla *et al.*, 2005). There are three different kinds of singularities: weak singularity, strong singularity or hyper-singularity. Strong and hyper-singular integrals have to be converted into regular ones in the regularization of the BEM formulations (Tanaka *et al.*, 1994; Sladec and Sladek, 1996, 1998). From the point of view of numerical integrations, one should devote great attention to the evaluation of these integrals because standard integration quadratures fail in accuracy (Lachat and

Watson, 1976; Sladek *et al.*, 1997, 2001; Manolis and Beskos, 1988). Therefore each type of singularity has to be treated by appropriate techniques.

Most of the researches has dealt with strong (Bonnet and Bui, 1993) and hyper-singularities. Some methods have been proposed in the literature to treat these singular integrals (Sladek and Sladek, 1998; Niu and Zhou, 2004; Guiggiani, 1994; Guiggiani *et al.*, 1992; Chen and Hong, 1999; Bonnet, 1999; Bui *et al.*, 1985; Aubry and Clouteau, 1991). It is notable that the regularization can be performed either before or after the discretization, i.e. in the global or local (intrinsic) coordinate space, as observed in some papers mentioned above. A comprehensive review of BEM in dynamic analysis has been proposed by Beskos (Beskos, 1997).

Analytical method

Dangla *et al.* (2005) proposed an analytical regularization method taking advantage of an assumed three-noded triangle element for the discretization of three-dimensional problems. Thanks to this simple shaped element, one can perform analytical evaluations of the Cauchy principal value of the singular integrals. Such an approach has been previously applied for 2D elastodynamic problems in (Dangla, 1988, 1989). The efficiency and accuracy of such a regularization method will be illustrated numerically hereafter in 3D elastodynamics.

4.6.5 Wave propagation in unbounded media

Exterior problems

The Boundary Integral Equation (4.85) has been established for a bounded domain Ω . We may consider the complementary to Ω , denoted Ω_C , and try to write the integral equations for such an exterior problem. To do so, a bounded sphere Ω_R such as $\Omega \subset \Omega_R \subset \Omega_C$ is considered (Fig.4.48). Thanks to a limiting process ($R \rightarrow +\infty$), it is possible to generalize the Boundary Integral Equation if there are no sources at infinity.

The conditions on the decay of the wavefield at infinity is then:

$$\begin{cases} \underline{u}_P \cdot \underline{n} = o(1) & \underline{u}_P \cdot \underline{\tau} = o(R^{-1}) \\ \underline{u}_S \cdot \underline{n} = o(R^{-1}) & \underline{u}_S \cdot \underline{\tau} = o(1) \end{cases} \quad (4.88)$$

for longitudinal and transverse waves respectively, $\underline{\tau}$ being the tangent vector such as $\underline{n} \cdot \underline{\tau} = 0$.

An expression on Ω is then obtained (Bonnet, 1999) which is close to that given in Eq.(4.85) but with normals directed outward (Fig.4.48). Considering exterior problem formulations, wave propagation in infinite or semi-infinite media can thus be easily modelled by Boundary Integral Equations. However, the integral equations associated to exterior problems may have a non-unique solution for some specific frequencies which

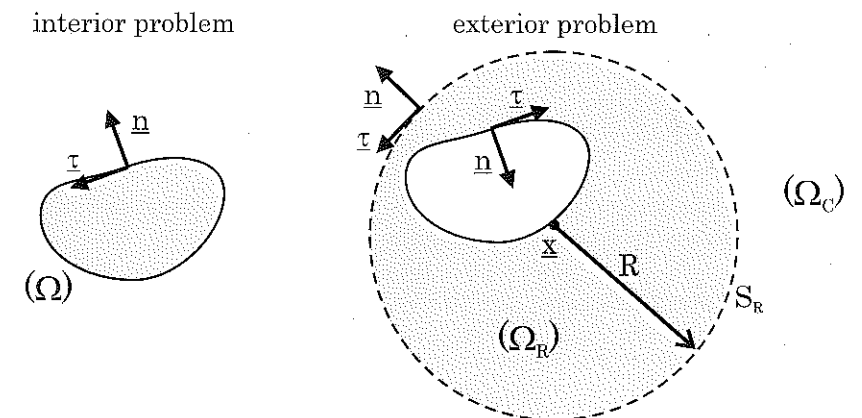


Fig. 4.48: Description of interior and exterior problems for the derivation of the corresponding Boundary Integral Equations.

correspond to the eigenvalues of a certain interior problem (Bonnet, 1999). Such frequencies are called *fictitious eigenvalues* and may be avoided using *indirect BIE* formulations (Bonnet, 1999; Pedersen *et al.*, 1995).

Radiation conditions

Using the formulation of the exterior problem, it is possible to account exactly for the conditions at infinity considering the exterior of a bounded domain Ω . The radiation conditions may be derived as follows (Bonnet, 1999):

$$\begin{cases} t_P - i\omega\rho V_P u_P = o(R^{-1}) \\ t_S - i\omega\rho V_S u_S = o(R^{-1}) \end{cases} \quad (4.89)$$

for longitudinal and transverse waves respectively (t_k being the stress vector components for each wave type).

As it will be shown afterwards, it is then possible to accurately model wave propagation in an unbounded domain considering only the boundary $\partial\Omega$ of the bounded domain Ω . It is particularly interesting to model seismic wave propagation or vibrations in the environment.

4.6.6 Numerical Implementation

Both boundary and unknowns are discretized and interpolation techniques initially developed for the Finite Element Method are considered (Bonnet, 1999). Using for instance three-noded flat triangles, the discretization of the geometry and the unknowns is thus

written, respectively, as follows (Dangla *et al.*, 2005):

$$\underline{x}(\xi) = \sum_{k=1}^3 N_k(\xi) \underline{x}^k \quad a(\underline{x}) = \sum_{k=1}^3 N_k(\xi) a^k \quad (4.90)$$

with \underline{x}^k : the node coordinates, N_k : the linear interpolation functions and a^k : the *nodal values* of the displacement or traction unknowns.

Thus, the set of scalar equations resulting from the discretization of equations (4.85), enforced at the nodes of the mesh, has the following matrix structure:

$$[A]\{u\} + [B]\{t\} = 0 \quad (4.91)$$

where $[A]$ and $[B]$ are fully populated non symmetric matrices; $\{u\}$ and $\{t\}$ are the 'vectors' containing the nodal values of $u_i(y)$ and $t_i(y)$, respectively.

The incorporation of the boundary conditions consists in substituting the prescribed nodal values of (u_i, t_i) into $\{\{u\}; \{t\}\}$ in Eq. (4.91). The columns of this matrix equation are reordered so as to have a matrix equation of the form:

$$[K]\{v\} = \{f\} \quad (4.92)$$

where the vector $\{v\}$ consists of the unknown components of $\{u\}, \{t\}$.

The matrix $[K]$ contains the columns of $[A], [B]$ associated with those unknown components while the right-hand side $\{f\}$ results from the multiplication of the known components of $\{u\}, \{t\}$ by the corresponding columns of the matrices $[A], [B]$. As shown in the following for unbounded media, the right hand side $\{f\}$ may also involve a contribution due to an incident wavefield. The results shown hereafter have been computed by Dangla *et al.* (2005) using the computer code CESAR-LCPC (Humbert *et al.*, 2005) of the Laboratoire Central des Ponts et Chaussées (French Public Works Research Laboratory, Paris, France).

4.6.7 Validation and influence of the regularization

Spherical cavity under harmonic internal pressure

The first example (Fig.4.49) concerns a spherical cavity of radius R in a full elastic isotropic space undergoing an internal harmonic pressure (Chaillat *et al.*, 2008). The cavity mesh includes 320 triangular boundary elements (that is 162 nodes) and a special generation process is considered to have a regular triangular mesh of the sphere starting from an icosahedron (Edouard *et al.*, 1996). Using the regularization method proposed by Dangla *et al.* (2005), the displacement field around the cavity is computed at various (normalized) frequencies.

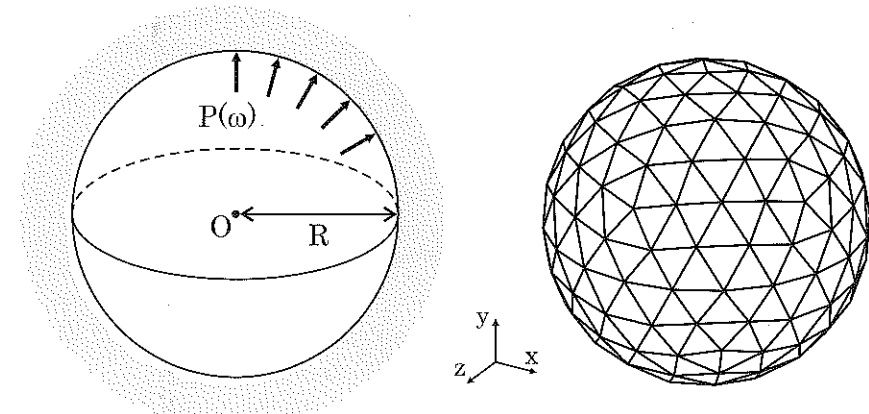


Fig. 4.49: Cavity under harmonic internal pressure: model description.

The validation of the numerical results is made by considering the analytical solution in terms of radial displacement $u(r, \omega)$ given by Eringen and Suhubi (1975) as follows:

$$u(r, \omega) = -\frac{P(\omega)R^3(ik_P - 1/r)\exp(ik_P(r - R))}{4\mu r(1 - ik_P R - k_S^2 R^2/4)} \quad (4.93)$$

where k_P and k_S are the longitudinal and transverse wavenumbers.

This equation may be rewritten using normalized distance $\bar{r} = r/R$, normalized frequency $\eta_P = k_P R/\pi$ (that is $\eta_P = 2R/\Lambda_P$, Λ_P being the longitudinal wavelength) and considering $\bar{u}(\bar{r}, \eta_P) = \frac{4\mu u(r, \omega)}{P(\omega)R}$. It leads to:

$$\bar{u}(\bar{r}, \eta_P) = -\frac{(i\pi\bar{r}\eta_P - 1)\exp(i\pi\eta_P(\bar{r} - 1))}{(1 - i\pi\eta_P - \pi^2\zeta^2\eta_P^2/4)\bar{r}^2} \quad (4.94)$$

with $\zeta = k_S/k_P = \sqrt{(2 - 2\nu)/(1 - 2\nu)} = \sqrt{3}$ (for $\nu=0.25$).

Comparisons between numerical and analytical results

In Fig.4.50, the real part of the normalized radial displacement $\bar{u}(\bar{r}, \eta_P)$ defined by equation (4.94) is displayed vs normalized distance \bar{r} for both analytical and numerical solutions at normalized frequencies $\eta_P=0.01, 0.50, 1.00$ and 2.00 . For the nearly static case ($\eta_P=0.01$) as well as the full dynamic cases, the agreement between the numerical results and the analytical ones is very good at all normalized distances. From this first simple example, the reliability and accuracy of the proposed method for analyzing propagation in unbounded media appear very good.

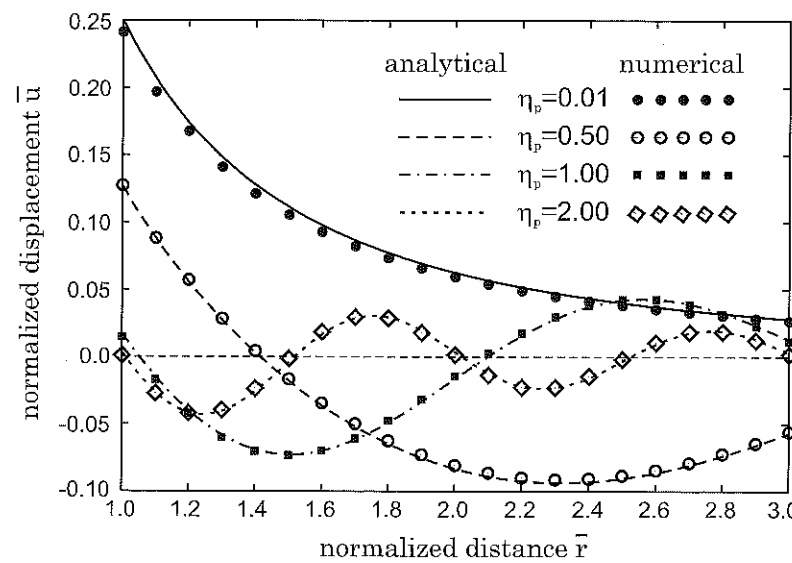


Fig. 4.50: Normalized radial displacement $\bar{u}(\bar{r}, \eta_p)$ (real part) vs normalized distance \bar{r} : comparison between numerical and analytical results for normalized frequencies $\eta_p=0.01, 0.50, 1.00$ and 2.00 (Dangla *et al.*, 2005).

4.6.8 Advanced formulation: the Fast Multipole Method

The standard BEM formulation leads to fully populated non symmetric matrices in Eq.(4.92). It is thus very difficult to model problems involving more than about 10^4 DOFs. It is possible to overcome this difficulty by considering an alternative formulation called the *Fast Multipole Method* (Fujiwara, 1998, 2000; Greengard *et al.*, 1998).

The goal of the FMM is to speed up the matrix-vector product computation required for each iteration of the iterative solver applied to the BEM-discretized equations arising from (4.92). Moreover, the governing matrix is never explicitly formed, which leads to a storage requirement well below the $O(N^2)$ memory required for holding the whole BEM matrix. The FM-accelerated BEM therefore achieves substantial savings in both CPU time and memory (Chaillat *et al.*, 2008).

The main idea behind the FMM is to reformulate the fundamental solutions in terms of products of functions of \underline{x} and of \underline{y} . This allows to reuse integrations with respect to \underline{y} when the collocation point \underline{x} is changed, a strategy which is not feasible in the traditional BEM, based on expression (4.83). Such fundamental solutions may be written as linear combinations of the Green's function for the Helmholtz equation, for which such a reformulation is known from earlier works, e.g. (Nishimura, 2002; Darve, 2000). The position vector $\underline{r} = \underline{y} - \underline{x}$ can be decomposed as $\underline{r} = (\underline{x}_0 - \underline{x}) + (\underline{y}_0 - \underline{x}_0) - (\underline{y}_0 - \underline{y}) = \tilde{\underline{x}} + \underline{r}_0 - \tilde{\underline{y}}$, where \underline{x}_0 and \underline{y}_0 are two poles. Application of the Gegenbauer addition theorem (Darve,

4.6 The Boundary Element Method

2000) permits to write the Helmholtz Green's function as:

$$\frac{\exp(ik|\underline{y} - \underline{x}|)}{|\underline{y} - \underline{x}|} = \frac{ik}{4\pi} \lim_{L \rightarrow \infty} \int_{\tilde{\underline{s}} \in S} e^{ik\tilde{\underline{s}} \cdot \tilde{\underline{x}}} \mathcal{G}_L(\tilde{\underline{s}}; \underline{r}_0) e^{-ik\tilde{\underline{s}} \cdot \tilde{\underline{y}}} d\tilde{\underline{s}}, \quad (4.95)$$

where S is the unit sphere of \mathbb{R}^3 and the *transfer function* $\mathcal{G}_L(\tilde{\underline{s}}; \underline{r}_0)$ is defined by:

$$\mathcal{G}_L(\tilde{\underline{s}}; \underline{r}_0) = \sum_{0 \leq l \leq L} (2l+1)i^\ell h_\ell^{(1)}(k|\underline{r}_0|) P_\ell(\cos(\tilde{\underline{s}}, \underline{r}_0)) \quad (4.96)$$

in terms of the Legendre polynomials P_ℓ and of the spherical Hankel functions of the first kind $h_\ell^{(1)}$. Then, the elastodynamic fundamental solution (4.83) is easily seen to admit representations of the form (4.95) with \mathcal{G}_L replaced with suitably-defined (tensor) transfer functions $\mathcal{U}_{i,L}^k$ and $\mathcal{T}_{i,L}^k$ (Chaillat *et al.*, 2008).

Formula (4.95) with $L = O(k_S |\underline{r} - \underline{r}_0|)$ is suitably accurate whenever $|\underline{r} - \underline{r}_0|/|\underline{r}_0| \leq 2/\sqrt{5}$ (Darve, 2000). Guided by this consideration, a 3D cubic grid of linear spacing d embedding the whole boundary $\partial\Omega$ is introduced. The above condition is then automatically satisfied whenever \underline{x} and \underline{y} belong to non-adjacent cubic cells, the poles \underline{x}_0 and \underline{y}_0 being chosen as the cell centers, while it may be violated otherwise. The one-level FMM basically consists of using decomposition (4.95) whenever \underline{x} and \underline{y} belong to non-adjacent cubic cells (Chaillat *et al.*, 2008).

As depicted in Fig.4.51, the interactions between remote points are computed once for all at the centre of each cell. It leads to much lower computational costs and memory requirements. If \underline{x} and \underline{y} belong to adjacent cells, the corresponding terms are computed by standard BEM. Thanks to the FMM, it is then possible to compute problems involving up to 10^6 DOFs on a single-processor computer (Chaillat *et al.*, 2008).

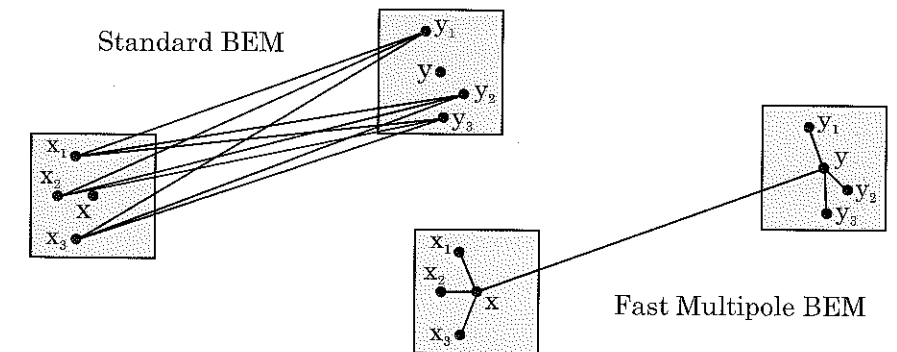


Fig. 4.51: Comparison between the classical BEM and the Fast Multipole method.

4.6.9 Elastodynamics in time domain

For transient problems, the BEM formulation may also be written in the time domain (Schanz and Antes, 1997; Takahashi *et al.*, 2003). Considering the scalar wave equation in time domain (Bonnet, 1999):

$$\Delta u - \frac{1}{c^2} \ddot{u} + F = 0 \quad \forall (y, t) \in \Omega \times [0, T] \quad (4.97)$$

For transient problems, it is also necessary to account for the initial conditions:

$$u(y, 0) = u_0(y) \quad \text{and} \quad \dot{u}(y, 0) = v_0(y) \quad (4.98)$$

The reciprocity theorem thus takes the following form:

$$\begin{aligned} & \int_{\partial\Omega} [(q^1 * u^2)(y, t) - (q^2 * u^1)(y, t)] dS_y = \\ & \int_{\Omega} [(F^2 * u^1)(y, t) - (F^1 * u^2)(y, t)] d\Omega_y \\ & + \int_{\Omega} \frac{1}{c^2} [v_0^2(y)u^1(y, t) - v_0^1(y)u^2(y, t)] d\Omega_y \\ & + \int_{\Omega} \frac{1}{c^2} [u_0^2(y)\dot{u}^1(y, t) - u_0^1(y)\dot{u}^2(y, t)] d\Omega_y \end{aligned} \quad (4.99)$$

where $q = \nabla u \cdot n$ and $**$ denotes the convolution product.

This expression involves convolution products, instead of multiplications in the frequency domain, and includes two additional integrals when compared to Eq.(4.80) (Maxwell-Betti theorem in elastostatics or time-harmonic elastodynamics). To deal with these convolution products, Schanz and Antes (1997) proposed a BEM formulation in the Laplace domain. They also developed a *convolution quadrature method* to approximate the convolution integrals numerically. Their formulations have also been generalized to viscoelastodynamics (Gaul and Schanz, 1999).

4.7 Applications to wave propagation in soil

4.7.1 Diffraction of a plane wave in unbounded media

2D unbounded medium

The diffraction of a plane wave by a cylindrical cavity may be fully characterized through theoretical approaches. For such a problem, the comparison with the Boundary Element Method will evidence the capabilities of the method to model wave propagation in unbounded domains (Semblat and Dangla, 2005). In the case of a plane *SH*-wave, the wavefield calculated analytically (Eringen and Suhubi, 1975) is displayed in Fig.4.52 (dotted line) for various radial directions around the cavity. In Fig.4.52, the numerical

results computed by the Boundary Element Method are represented by symbols (Semblat and Dangla, 2005). Since this numerical approach involves an exact description of the radiation conditions, the analytical and numerical results are in very good agreement.

Such a comparison would be more difficult with the Finite Element Method since it would raise the need for specific numerical techniques such as absorbing boundaries or absorbing layers (see §4.5). The validation in complex configurations (geometry, characteristics of the excitation, etc) may thus be difficult with such methods.

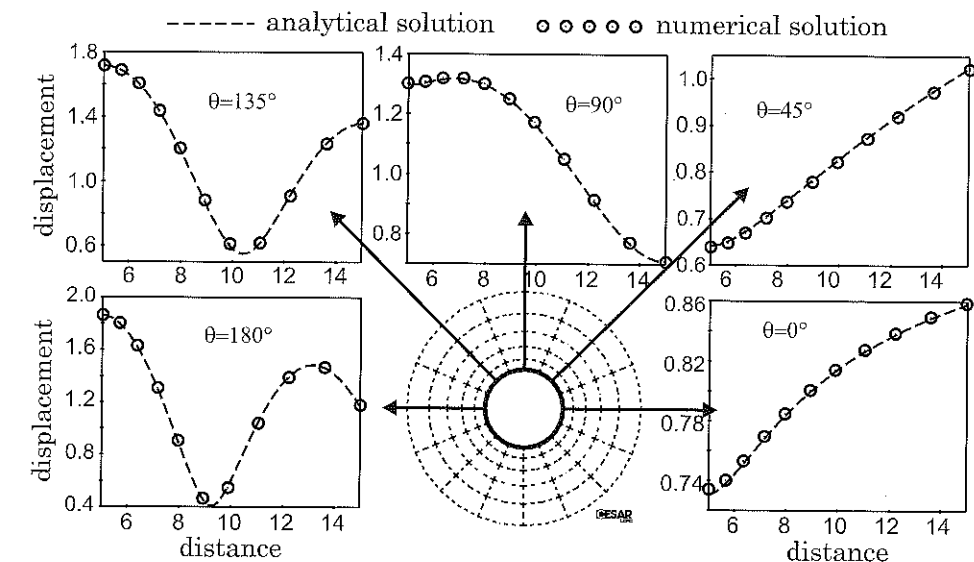


Fig. 4.52: Diffraction of a plane *SH*-wave by a cylindrical cavity: comparison between analytical (dotted) and numerical results (symbols), (Semblat and Dangla, 2005).

3D unbounded medium

The second example deals with the diffraction, by a spherical cavity, of a plane P-wave propagating along x axis and defined by:

$$\underline{u}_{inc} = U_0 \exp[i(\omega t - k_P x)] \underline{e}_x \quad \text{with } U_0 = 1$$

The numerical results are firstly computed in frequency domain and compared with analytical results (Dangla *et al.*, 2005). They are afterwards converted into time domain to characterize the scattered wavefield.

The wavefield computed around the cavity for various directions is shown in Fig.4.53. The boundary element mesh of the cavity (2562 nodes) is generated the same way as in

the case of the pressurized cavity (Edouard *et al.*, 1996). However, this mesh has been refined since the wavefield has strong variations especially at grazing incidences. The analytical solution in terms of radial displacement u_r is given by Pao and Mow (1973) as well as Eringen and Suhubi (1975).

The results are computed for various azimuths ($\theta_i = (i - 1) \times 45^\circ$, $1 \leq i \leq 5$) and Fig.4.53 displays the real part of the radial displacement vs normalized distance $\bar{r} = r/R$ ($1 \leq \bar{r} \leq 3$) at two different normalized frequencies $\eta_P=1.00$ and $\eta_P=2.00$ (Dangla *et al.*, 2005). The analytical results are plotted with lines (dotted for $\eta_P=1.00$ and solid for $\eta_P=2.00$) and the numerical results with symbols (circles for $\eta_P=1.00$ and bullets for $\eta_P=2.00$). The agreement between the numerical and analytical results is very good for all azimuths at $\eta_P=1.00$. For $\theta_3 = 90^\circ$, some slight differences can be noticed at $\eta_P=2.00$ near the cavity wall. This is probably due to the fact that there is a grazing incidence at this point.

In Fig.4.54, the numerical results are also displayed as displacement isovalues on the cavity wall and on an horizontal area embedded in the domain. It can be noticed that, at the grazing incidence, the interferences between the wavefield and the cavity are very strong.

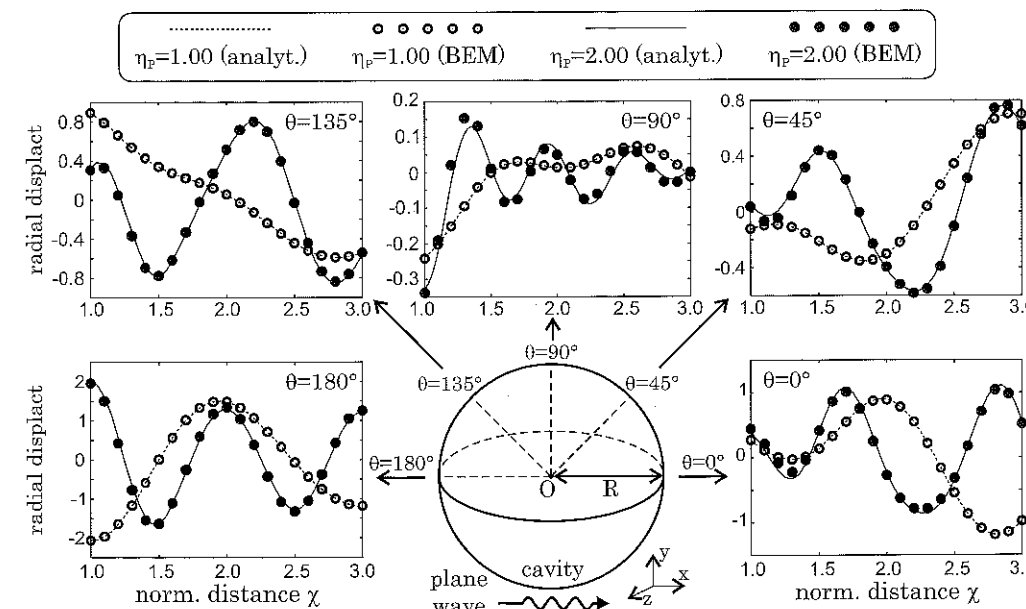


Fig. 4.53: Diffraction of a plane wave by a spherical cavity: comparison with analytical results for various azimuths at normalized frequencies $\eta_P=1.00$ and $\eta_P=2.00$ (Dangla *et al.*, 2005).

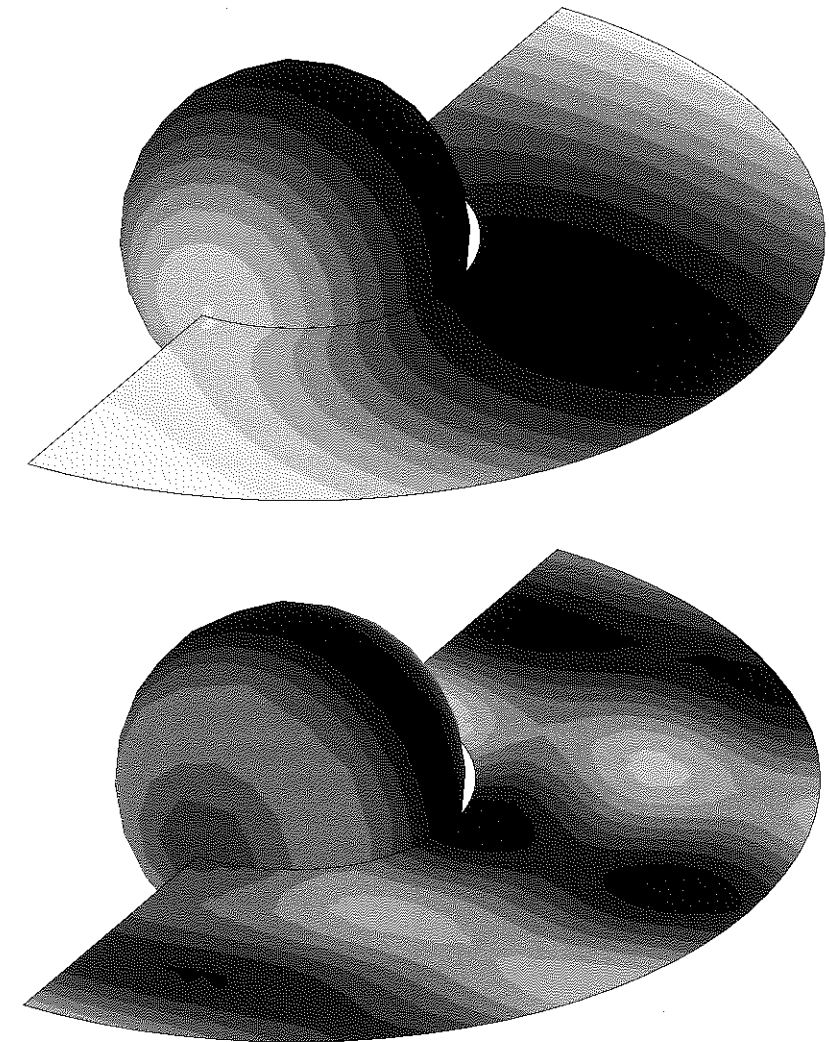


Fig. 4.54: Diffraction of a plane wave by a spherical cavity: wavefield computed by the BEM for two normalized frequencies $\eta_P=0.25$ (top) and $\eta_P=0.50$ (bottom).

4.7.2 Vibrations of a foundation

The example depicted in Fig.4.55 deals with the analysis of the wavefield generated by a vibrating foundation. The analysis is performed by the Finite Element Method and the features of the model are the following:

- a circular foundation (radius 1m) is submitted to a dynamic vertical load whose variations are given in Fig.4.55,
- the foundation being circular, the finite element model is axisymmetrical (radius 8m),
- the model includes 2600 quadrilateral elements and the dynamic computations involves 100 time steps (unconditionally stable/non dissipative Newmark time-integration scheme).

The results displayed in Fig.4.56 correspond to two different times T_1 (left) and T_2 (right). Displacement isovalue diagrams are given at the top and the corresponding wavefield is drawn as vectors at the bottom. At time T_2 , the isovalue diagrams clearly show the pressure waves propagating faster than the shear wave ($V_S < V_P$). In Fig.4.56, the results in terms of displacement wavefield (bottom right) show that, as predicted by the theory of surface waves in Chapter 3, the motion describes an ellipse close to the free-surface. This type of motion is due to Rayleigh waves the amplitude of which decreases rapidly with depth.

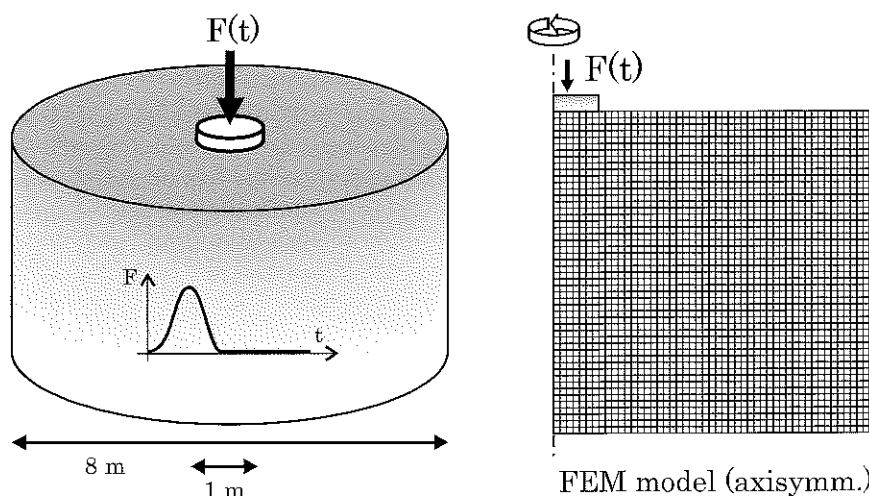


Fig. 4.55: Vibration of a foundation and idealization of the problem.

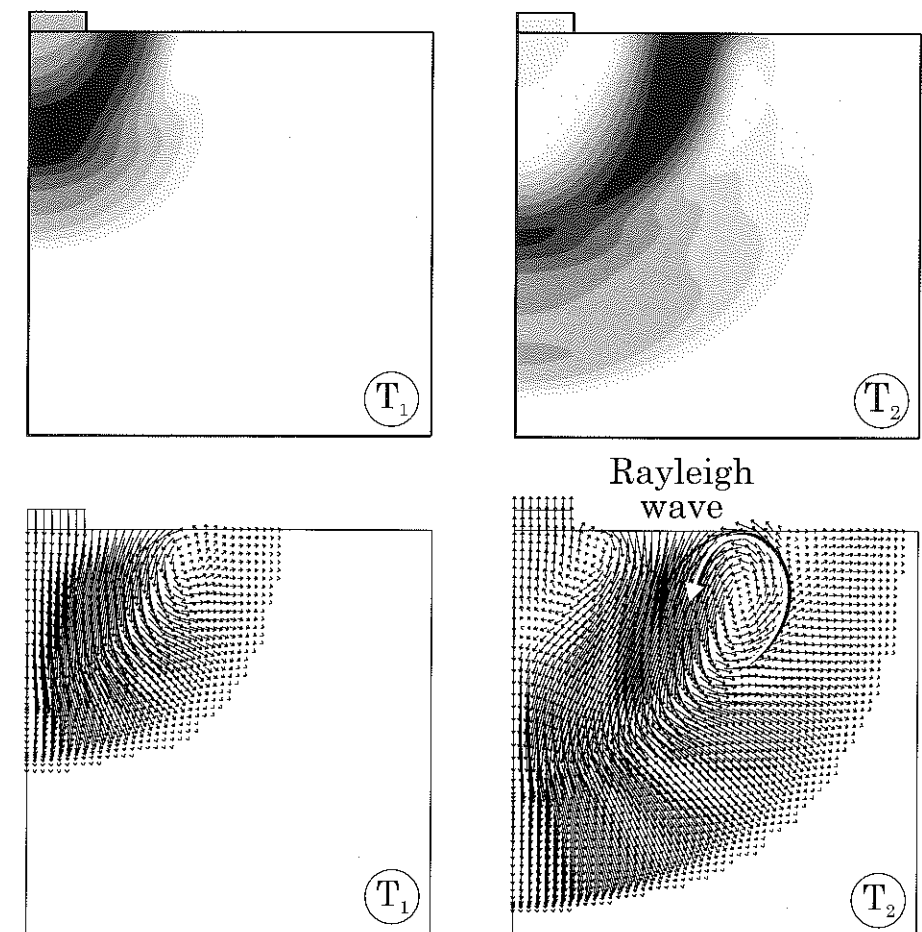


Fig. 4.56: Wavefield generated in the soil by the vibration of a foundation (Finite Element model): displacement isovalue (top) and displacement wavefield (bottom).

4.7.3 Vibration isolation using piles or trenches

As discussed in Chapter 1, vibratory isolation is a crucial issue since annoyances due to traffic induced or construction works generated vibrations may be strong. In Chapter 2, we analyzed the influence of a rigid layer (embedded in an infinite medium) on the propagation and transmission of a plane wave. We shall now try to study numerically the efficiency of cylindrical inclusions embedded in a free-space (2D model). The 3D case will also be investigated for piles and trenches. The main goal is to assess and illustrate the efficiency of various types of isolation systems.

Influence of cylindrical piles/holes

Various authors have studied the influence of piles as isolation barriers (Aviles and Sánchez-Sesma, 1983; Liao and Sangrey, 1978). The piles may act as scatterers leading, if arranged adequately, to a reduction of the wave amplitude in the soil. The interest of piles is mainly in terms of durability since systems involving trenches may be easily damaged.

Description of the problem. In this paragraph, we shall consider a 2D model using the Boundary Element Method. The influence of cylindrical holes on mechanical wave propagation is investigated considering various configurations (Fig.4.57). The radius of the cylindrical holes being a , the distance between two holes is denoted S and various values of the dimensionless spacing S/a are considered ($S/a = 0.5, 1, 2$).

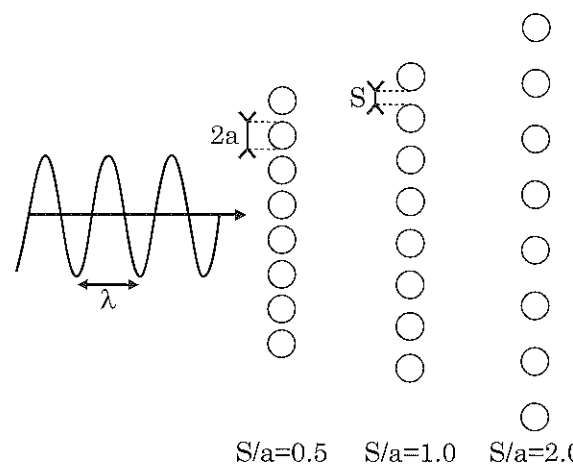


Fig. 4.57: Vibratory isolation with cylindrical inclusions and variable spacings: model description.

Efficiency of the isolation system (2D). From the model depicted in Fig.4.57, various BEM simulations were performed in the frequency domain. A normalized frequency η , related to the size of the cylindrical holes, is defined as follows:

$$\eta = \frac{2a}{\Lambda} \quad (4.100)$$

where Λ is the wavelength in the soil.

The amplitude reduction factor computed for a dimensionless spacing $S/a=1$ is displayed in Fig.4.58 for the following normalized frequencies: $\eta_1 = 0.089$, $\eta_2 = 0.115$,

$\eta_3 = 0.140$, $\eta_4 = 0.166$, $\eta_5 = 0.191$. These results show that the efficiency of the isolation system is very small for η_1 and η_2 (less than 12 to 25%) and is much better for higher frequencies. The area having the largest amplitude reduction is located at the center of the isolation system and strong edge effects are found (wave scattered at the boundaries of the isolation system). For η_5 , the lowest transmission coefficient is around 0.5 and the geometrical arrangement in this case at this frequency appears to be very efficient. This frequency nearly corresponds to a quarter wavelength configuration where the isolation effect should be optimal (as shown in Chapter 3).

Several dimensionless spacings, S/a , are now considered to assess the influence of this geometrical parameters on the efficiency of the isolation system.

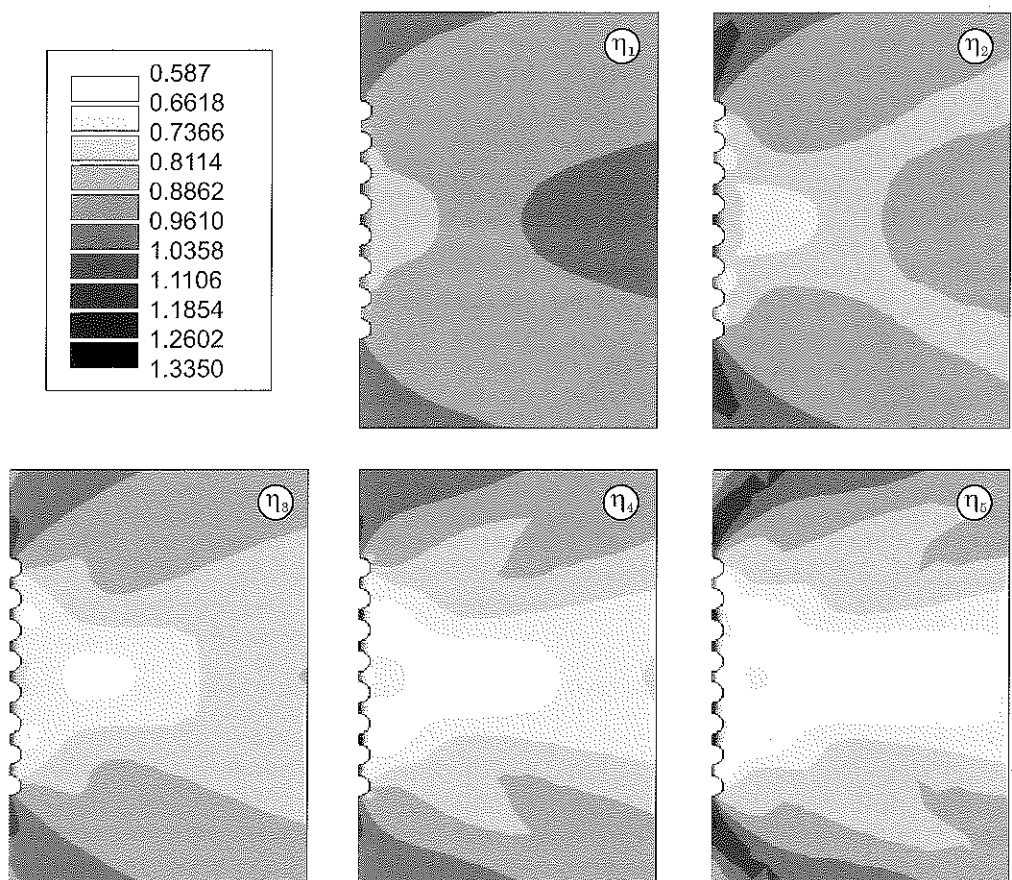


Fig. 4.58: Vibratory isolation by cylindrical inclusions at various frequencies: amplitude reduction factor at various normalized frequencies for a dimensionless spacing $S/a=1$.

As depicted in Fig.4.59, at normalized frequency $\eta_5=5.23$, the transmission coefficient is minimum for $S/a=0.5$ ($T_{min} = 0.4$), whereas it is never below 0.6 for $S/a=1$ and 0.8 for $S/a=2$. Since the number of cylindrical holes remains constant, it can also be noticed in Fig.4.59 that the extension of the isolated area is smaller when the holes are closer.

The results are now displayed as a function of the distance to the isolation system (Fig.4.60). The amplitude progressively decreases beyond the isolation system until it reaches its minimum value. Afterwards, far from the inclusions, it increases until the reduction factor reaches 1 (no influence of the isolation system at long distances). The maximum efficiency is reached for $S/a=0.5$ (top) with a reduction factor reaching 0.4 whereas it remains above 0.8 for $S/a=2$ (bottom).

The influence of frequency also appears in Fig.4.60. The amplitude reduction is larger at higher frequencies since the radius to wavelength ratio, a/Λ , is thus larger. The distance at which the maximum amplitude reduction is reached also depends on frequency.

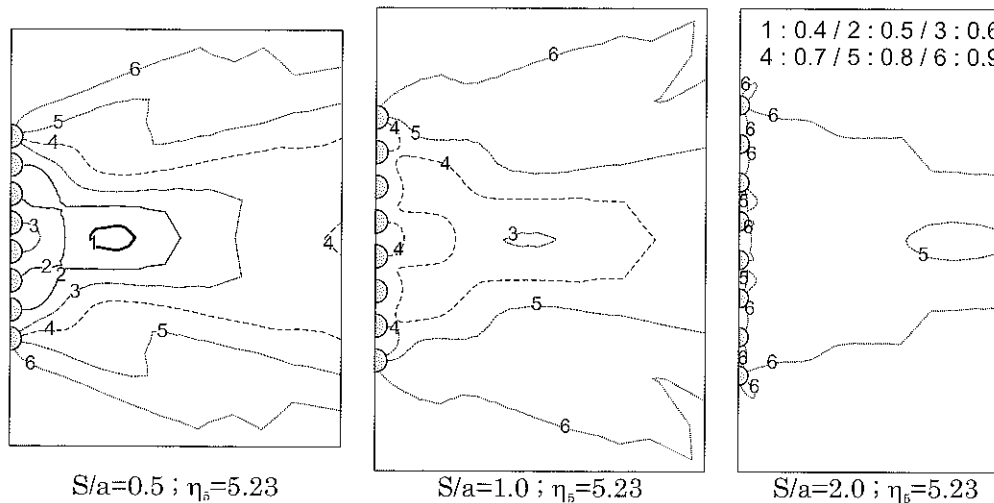


Fig. 4.59: Displacement isovales for various dimensionless spacings S/a .

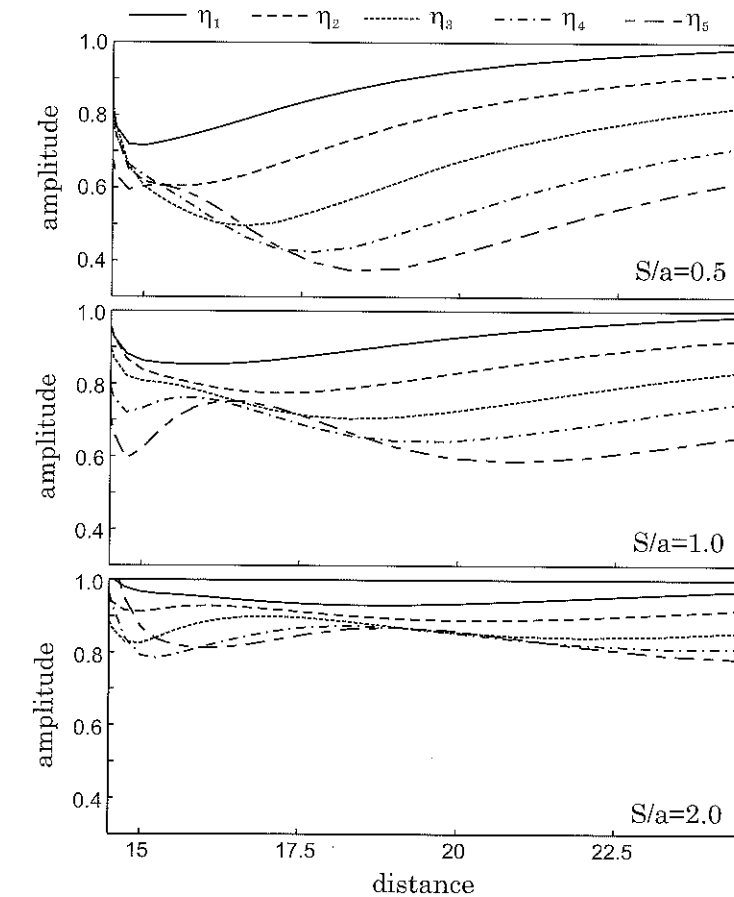


Fig. 4.60: Amplitude reduction factor as a function of the distance to the isolation system for various dimensionless spacings ($S/a=0.5$, $S/a=1.0$ and $S/a=2.0$) and different dimensionless frequencies ($\eta_1 = 0.089$, $\eta_2 = 0.115$, $\eta_3 = 0.140$, $\eta_4 = 0.166$, $\eta_5 = 0.191$).

Efficiency of the isolation system in 3D. Kattis *et al.* (1999) also modelled an isolation system involving a row of cylindrical holes in the 3D configuration (free-space). Using the Boundary Element Method, they computed the surface displacement around the isolation system. As depicted in Fig.4.61, the efficiency of the system is good since the amplitude reduction factor is around 0.45 beyond the inclusions.

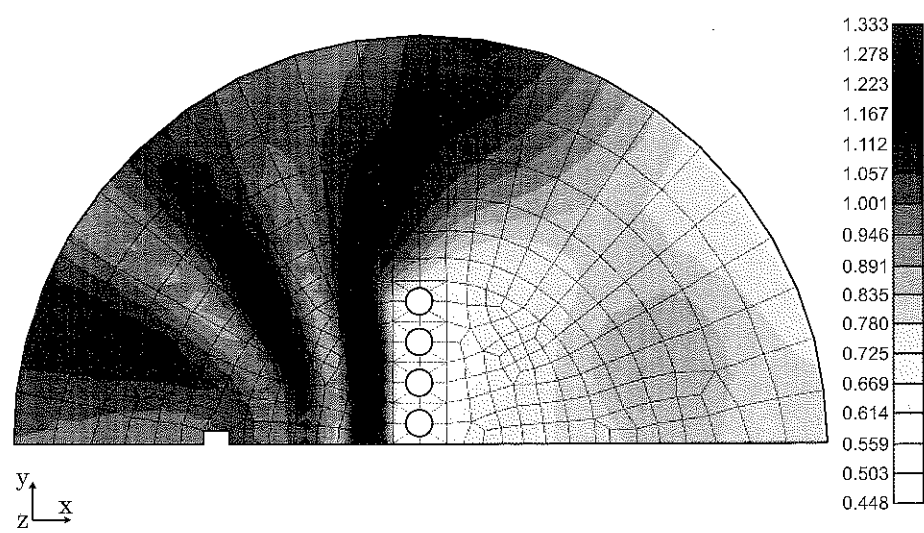


Fig. 4.61: 3D wavefield scattered by a row of 8 cylindrical holes: numerical BEM results from Kattis *et al.* (1999).

For stiff 3D piles of square cross-section, Gao *et al.* (2006) modelled the propagation of Rayleigh waves by the Boundary Integral Equation Method. As shown in Fig.4.62 (top left), they considered various configurations for the isolation system involving from one to three pile rows. Their numerical results are displayed in Fig.4.62 for each configuration. For the single pile row, the reduction factor is around 0.94 and the system is actually not efficient. For two rows of piles, the reduction factor is nearly 0.60 and the efficiency is satisfactory. Finally, for three pile rows, the amplitude is reduced by two thirds and the influence of combined pile rows appears to be beneficial.

Vibration isolation using trenches

As depicted in Fig.4.63, two problems involving trenches as wave barriers are considered: a half-circle trench (left) and a rectangular trench (right). As shown in Chapter 1, such cases have already been studied experimentally by Richart *et al.* (1970). Some 2D computations were performed by Segol *et al.* (1978). Banerjee *et al.* (1988) carried out 3D simulations using the Boundary Element Method. Their numerical results are displayed in Fig.4.63 (bottom) and compared² to the experimental results from Woods (1968). The following geometrical parameters are chosen for the trench:

²It should be noticed that the experimental results are displayed using a single isovalue scale whereas numerical results from Banerjee *et al.* (1988) correspond to different scales for the half-circle and the rectangular trenches.

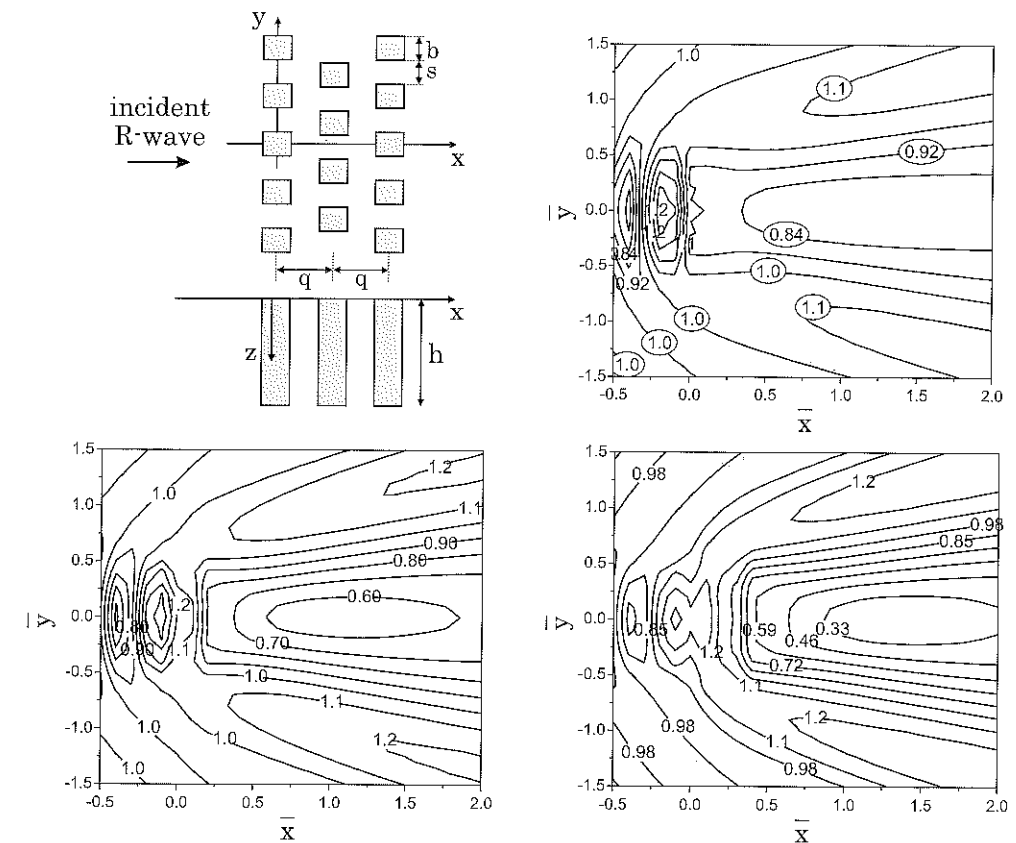


Fig. 4.62: Vibration isolation by pile rows: schematic of the problem and amplitude reduction factor fo various configurations involving 1 to 3 rows from Gao *et al.* (2006).

- *half-circle trench*: dimensionless trench depth $H/\Lambda_R = 0.596$ and circle radius $R/\Lambda_R = 0.596$;
- *rectangular trench*: dimensionless trench depth $H/\Lambda_R = 1.19$, trench width $L/\Lambda_R = 1.79$ and distance to the source $R/\lambda_R = 2.97$.

where Λ_R is the Rayleigh wavelength.

As shown in Fig.4.63, the BEM solutions predict the amplitude reduction factor reasonably well. As discussed by Banerjee *et al.* (1988), the lack of symmetry of the experimental results reflects the influence of the inhomogeneous properties of the actual soil.

However, for the half-circle trench, the main isolated area computed by the BEM is found to be similar to that found experimentally: it is bounded by two radial lines at 45 degrees from each end of the trench.

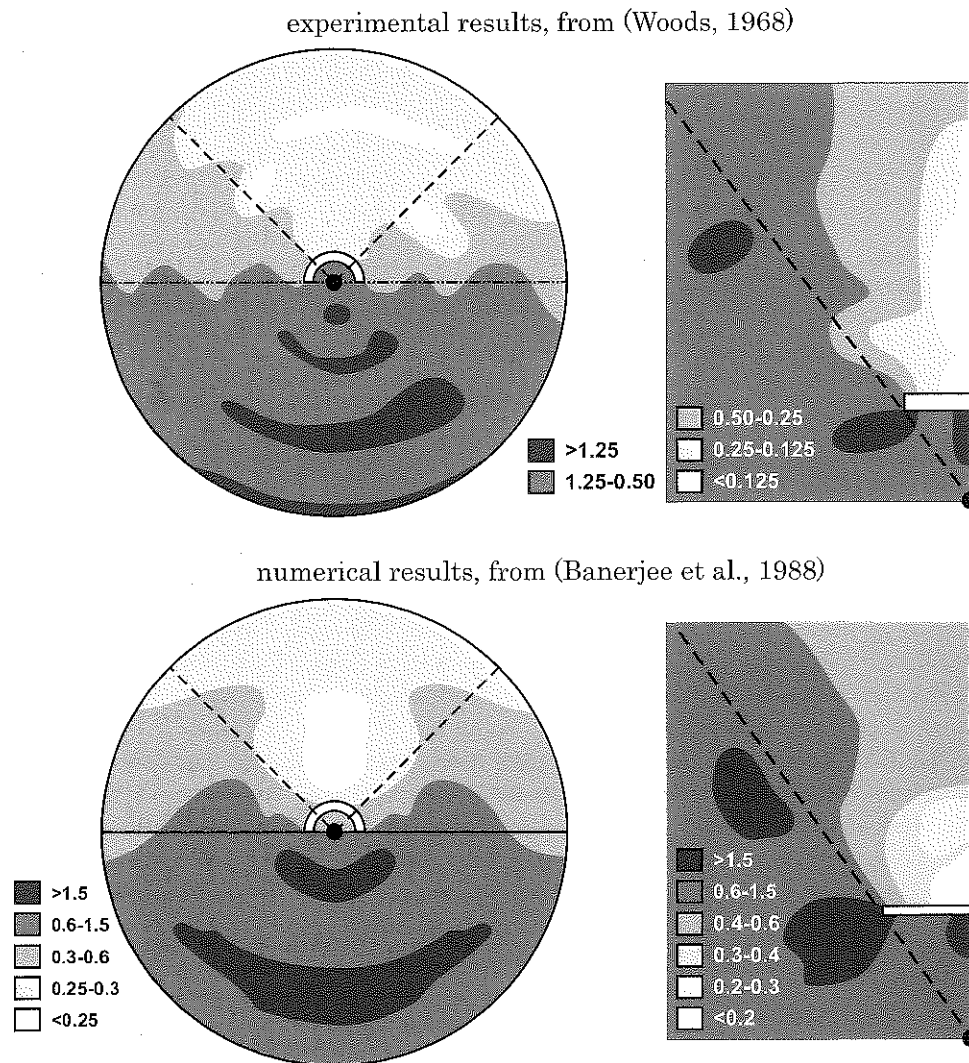


Fig. 4.63: Vibration isolation by trenches: comparison between experimental results from Woods (1968, top) and 3D BEM results obtained by Banerjee *et al.* (1988, bottom).

4.7.4 Traffic induced vibrations in railway tunnels

Dangla and van Hoove (1988) analyzed the influence of traffic induced vibrations in railway tunnels. Considering a single tunnel, the numerical results computed by the Boundary Element Method are displayed in Fig.4.64 in terms of displacement isovalues (Semblat and Dangla, 2005). As shown by these results, the solution is strongly dependent on the frequency content of the loading.

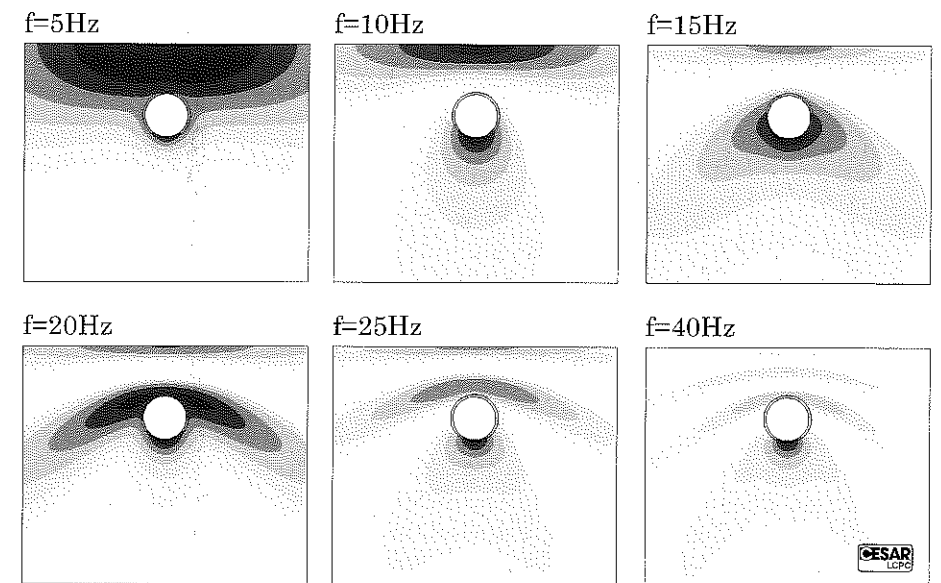


Fig. 4.64: Traffic induced vibrations in a railway tunnel: displacement isovalues at various frequencies computed by the Boundary Element Method (Semblat and Dangla, 2005).

Dangla and van Hoove (1988) also performed some experiments on site using a dynamic loading device called *Dynaplaque*. They measured the vertical displacement at the top of the hill above the railway tunnel. Some interesting comparisons between their experimental and numerical results are proposed in Fig.4.65 (Semblat and Dangla, 2005).

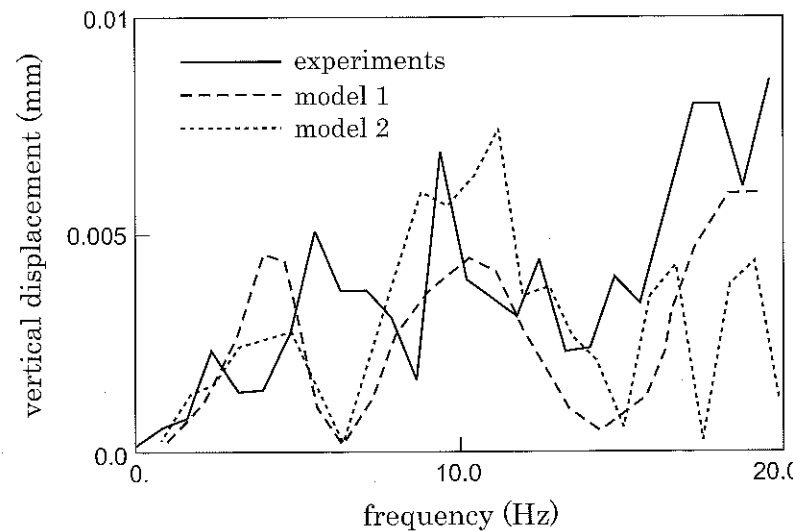


Fig. 4.65: Vertical displacement induced by dynamic loadings in a railway tunnel: comparisons between numerical and experimental results, from (Dangla and van Hoove, 1988).

Chapter 5

Seismic wave propagation and amplification

5.1 Introduction

The seismic ground motion is strongly influenced by the source and path effects, but propagation and amplification of seismic waves in surficial soil layers is also a key issue (Boore, 2004). As discussed in Chapter 3, the reflection and refraction of seismic waves at the interface between layers having different velocities may lead to larger amplitudes at the free-surface (Bard and Bouchon, 1985; Chávez-García *et al.*, 1999, 2000; Kawase, 2003; Moeen-Vaziri and Trifunac, 1988; Pitilakis *et al.*, 1999a; Sánchez-Sesma and Luzón, 1995). Hence, it is necessary to estimate, through experimental as well as numerical approaches, the *amplification factor* at a specific site and the corresponding frequency range. Characterizing the seismic ground motion is mandatory to assess the seismic risk in a particular area.

As it will be shown in this Chapter, the amplification factor may be estimated experimentally through various techniques. The analysis may also be performed through different numerical approaches investigating the propagation process in complex geological structures such as alluvial deposits. The Spectral Element Method and the Boundary Element Method are very useful techniques for modelling seismic wave propagation and amplification. They allow the analysis of various earthquake scenarios and the assessment of the seismic hazard at a specific site.

Simple and extensive experimental methods, such as the measurement of ambient vibrations, are also available. They give very interesting results allowing a simplified characterization of alluvial deposits. From a theoretical point of view, it is also possible to consider simplified approaches such as the modal method to be discussed herein. It leads to a fast and reliable estimation of the fundamental frequency of sedimentary basins. Finally, the characterization of the soil properties directly on site or in the laboratory is

also a key issue to quantify seismic ground motion in alluvial deposits. It is especially the case for strong events for which various (anelastic) constitutive parameters are needed.

5.2 Seismic wave amplification

5.2.1 Main governing phenomena

Site effects: some examples

The propagation of seismic waves in surficial geological structures may often lead to strong motion amplifications due to the velocity contrast between alluvial deposits and the bedrock. Such phenomena, named *site effects*, may considerably increase the impact of an earthquake (Baise *et al.*, 2003; Bard and Bouchon, 1980a,b, 1985; Kham *et al.*, 2002a; Raptakis *et al.*, 2000; Sommerville, 1998). One of the first large earthquakes to show the importance of this issue was the Michoacan 1985 earthquake in Mexico (Fig.5.1) (Fäh *et al.*, 1994; Kawase and Aki, 1989; Singh *et al.*, 1988). The maximum acceleration at sixty kilometers from the epicentre was around 0.28 g. It reached 0.2 g in the centre of Mexico city located much farther (400 kilometers). As shown in Fig.5.1 in terms of velocity, the Peak Ground Velocity was even larger in the Mexico basin (*SCT* station) than at the Campos station located nearby the epicenter. In the city itself, the intensity variations were very large. The thick clay deposit in the lake-bed area nearby the volcanic belt amplified up to a factor 5 the seismic motions when compared to the bedrock (maximum acceleration in time domain).

In the case of areas with moderate seismicity, the site effect influence is also very important. As depicted in Fig.5.2, for alpine valleys, deep and narrow alluvial deposits may lead to complex propagation patterns. In this figure, the 500m deep Grenoble basin (French alps) is schematized. The reference bedrock site is called *OGMU* (top left) and other stations are located at the surface of the deposit. These stations are part of the French accelerometric network (*RAP*). The Grenoble basin strongly amplifies the seismic motion due to multiple reflections and diffractions at the basin edges (Chaljub, 2006; Delépine and Semblat, 2006). An international numerical benchmark was organized to estimate seismic wave amplification in this alpine valley (Chaljub, 2006).

Seismic wave amplification may also occur in very large basins such as that of Los Angeles, Fig.5.3 (Komatitsch *et al.*, 2004). This numerical model involving the spectral element method allows a detailed analysis of the amplification process (main amplification areas, effect on duration, frequency range, etc) as well as of the source and path effects. Other sites, such as the Ashigara valley in Japan, have also been extensively studied (Kawase and Sato, 1992; Pitarka *et al.*, 1994; Scherbaum *et al.*, 1994; Uetake and Kudo, 2005; Zahradník *et al.*, 1994).

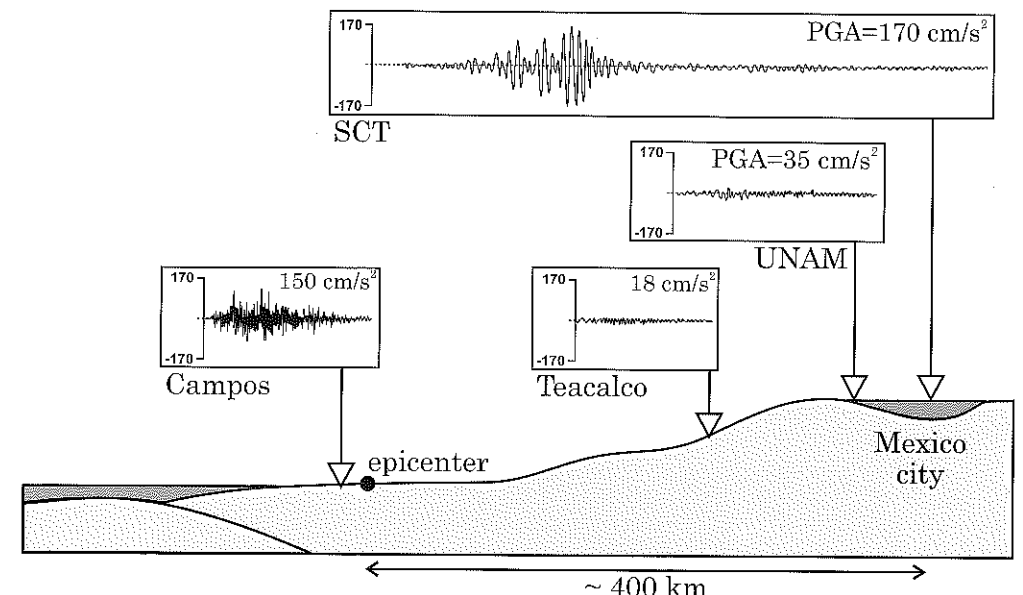


Fig. 5.1: Propagation of seismic waves for the Michoacan 1985 earthquake in Mexico (adapted from P.Moczo, Comenius University, Bratislava).

Site effects and seismic risk

From these examples, it is apparent that the assessment of seismic wave amplification is a crucial issue. It is not only useful for the quantification of the seismic hazard but also for seismic risk purposes.

Such a coincidence occurred during the 1967 Caracas earthquake which was strongly amplified by the alluvial deposit in the centre of the city (Duval *et al.*, 1998). As it will be discussed herein, the fundamental frequency of a basin is linked to the geometrical configuration as well as the velocity contrast in the various soil layers. For Caracas, this frequency was around 0.6 Hertz for the most damaged blocks (Declavaud, 2007; Semblat *et al.*, 2002b). It has been shown that the three buildings that collapsed during the earthquake were structures including more than 14 storeys leading to eigen frequencies close to 0.6 Hertz. In the case where the amplification of the seismic motion may be large, it is then necessary to characterize the local seismic response of the soil to scale the features of the reference earthquake considered for the design of the buildings in this area. The case of Caracas will be discussed herein since it also involves a significant influence of the topography in the propagation/amplification process.

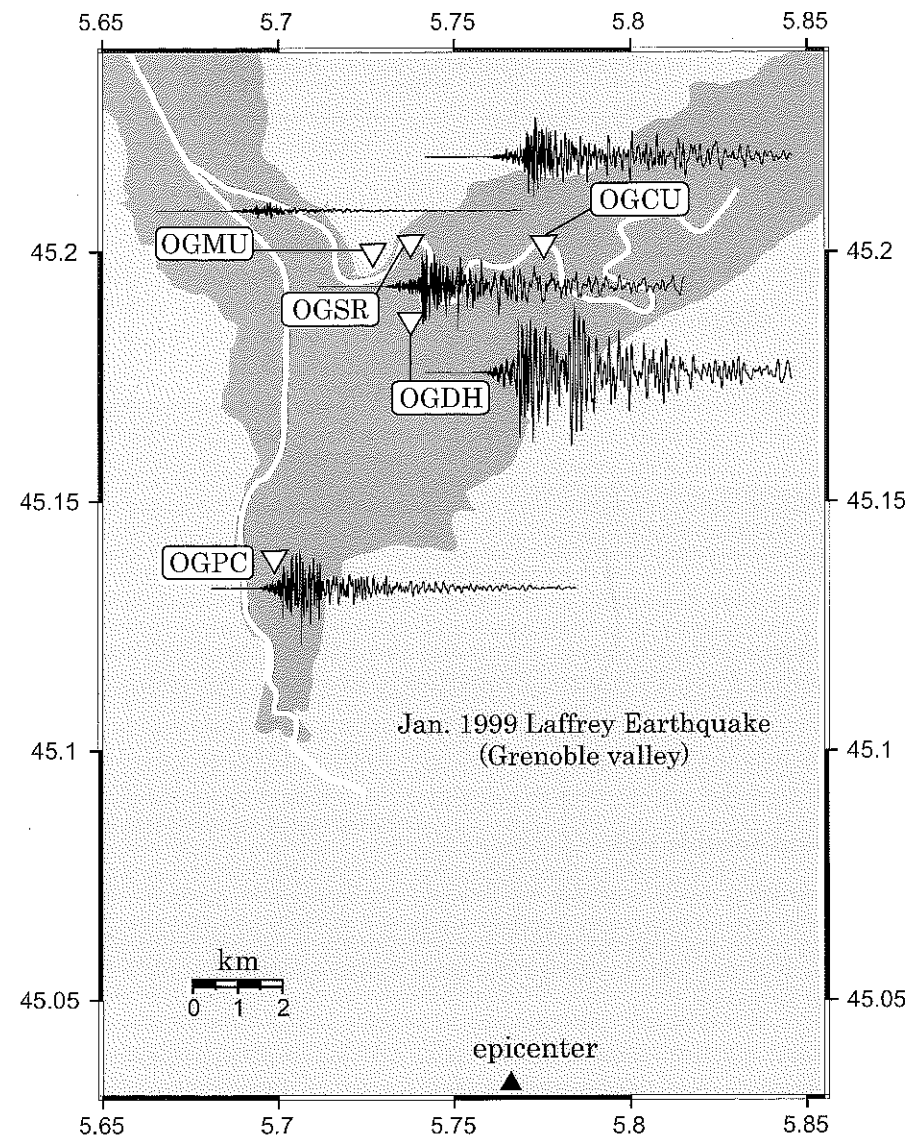


Fig. 5.2: Velocities ($N-S$ component) recorded at various locations in the city of Grenoble during the 1999 Laffrey earthquake (data: French accelerometric network, www-rap.obs.ujf-grenoble.fr, reference: (Lebrun *et al.*, 2001)).

Site effects: 1D, 2D or 3D analysis

As already shown in Chapter 3, the amplification of seismic waves in an alluvial deposit is strongly influenced by the mechanical properties of the layers. Indeed, the velocity

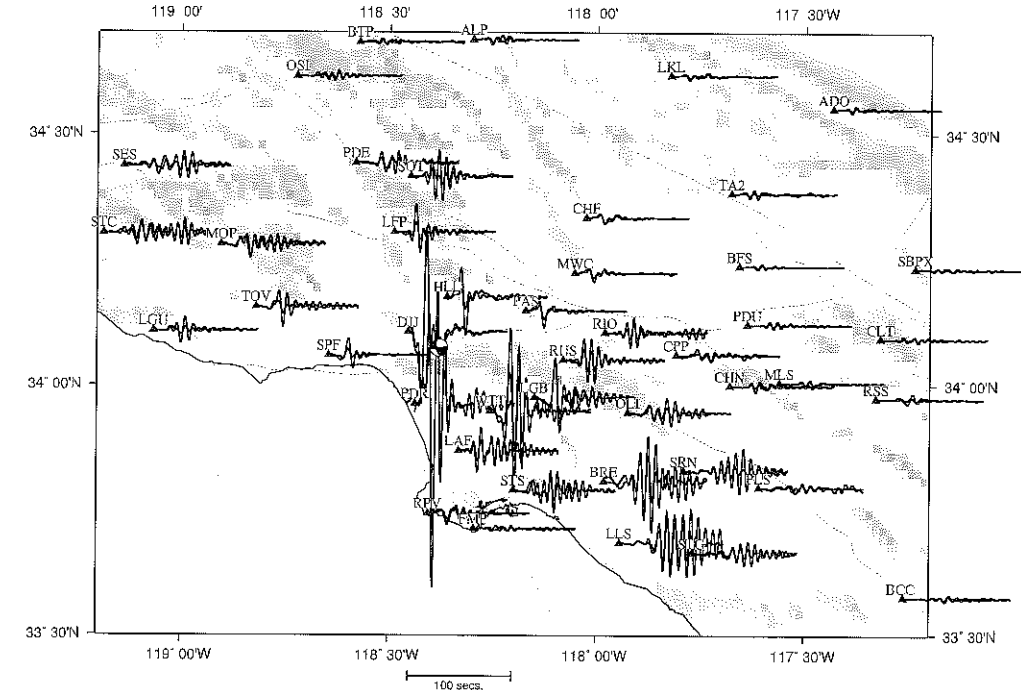


Fig. 5.3: Seismic wave amplification in the Los Angeles area: numerical simulations by the Spectral Element Method (Komatitsch *et al.*, 2004).

contrast between the soil layers (vertical heterogeneities) modifies the motion amplification at the free-surface. As depicted in Fig.5.4 (left), it is mainly a 1D effect. The geometry of the deposit is also a governing factor (Fig.5.4, right). It may be characterized by an average depth or by a detailed form for a sedimentary basin. In the latter case (lateral heterogeneities), the seismic waves are trapped in the basin leading to a larger amplification than through the 1D assumption. In the case where only the average depth of the layers is considered (one-dimensional case), the amplification factor can be estimated theoretically (Chapter 3). The estimation of the seismic ground motion in the codes is mainly performed through such simplified approaches (Pitilakis *et al.*, 1999b). Whereas, when the lateral heterogeneities are large, it is necessary to investigate seismic wave propagation in two or three dimensions (Bard and Bouchon, 1985).

5.2.2 Experimental characterization

To characterize seismic wave amplification experimentally, it is necessary to perform measurements of the ground motion at the considered alluvial site, denoted $S^{(i)}$, and to compare it to unamplified motions. It is thus mandatory to choose a *reference station*,

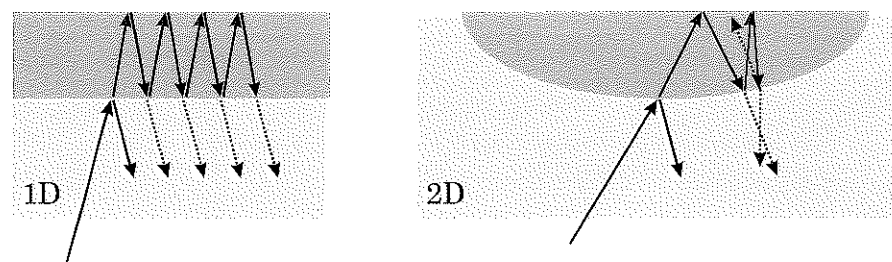


Fig. 5.4: Seismic wave amplification: main phenomena in 1D (left) and 2D/3D (right) geological structures.

denoted R , located in a quiet area free of topographic irregularities as well as sedimentary deposits (e.g., an outcropping bedrock). The measurement performed at R is then used as a reference to which the signals measured at $S^{(i)}$ can be compared. Figure 5.5 describes the methodology for such analyses: the Fourier spectra of the time signals $r(t)$ at R and $s^{(i)}(t)$ at $S^{(i)}$ are computed in order to estimate the site/reference spectral ratio $S^{(i)}(f)/R(f)$. When the reference station is well chosen, the site/reference ratio allows the assessment of the amplification phenomena in the frequency domain (Theodoulidis and Bard, 1995). One can either characterize the amplification due to a relief (Fig.5.5, site $S^{(1)}$) or that due to an alluvial deposit (Fig.5.5, site $S^{(2)}$). As shown by Chávez-García *et al.* (2002), the choice of the reference bedrock station is crucial to estimate the amplification factor.

The measurements performed at R and $S^{(i)}$ may involve the horizontal components of the ground motion or the vertical ones. For three-dimensional measurements, three different site/reference spectral ratios are hence available: $(S_x^{(i)}(f)/R_x(f))$, $(S_y^{(i)}(f)/R_y(f))$ and $(S_z^{(i)}(f)/R_z(f))$ allowing the analysis of the ground motion amplification for each of these components.

5.3 Seismic wave amplification in layered media

5.3.1 From transfer function to time-domain response

As discussed in Chapter 3, in the case of a harmonic wave, the amplification of the seismic motion in a single layer medium may be quantified through a 1D transfer function:

$$\bar{T}(\omega) = \frac{u_A^*}{u_{B'}^*} = \frac{2A_1}{2A_2} = \frac{1}{\cos k_{z_1} h + i\bar{\chi} \sin k_{z_1} h} \quad (5.1)$$

$$\text{where: } k_{z_i} = \frac{\omega \theta_i}{V_{S_i}}$$

$$\text{and: } \bar{\chi} = \sqrt{\frac{\mu_1 \rho_1}{\mu_2 \rho_2}} \cos \theta_1$$

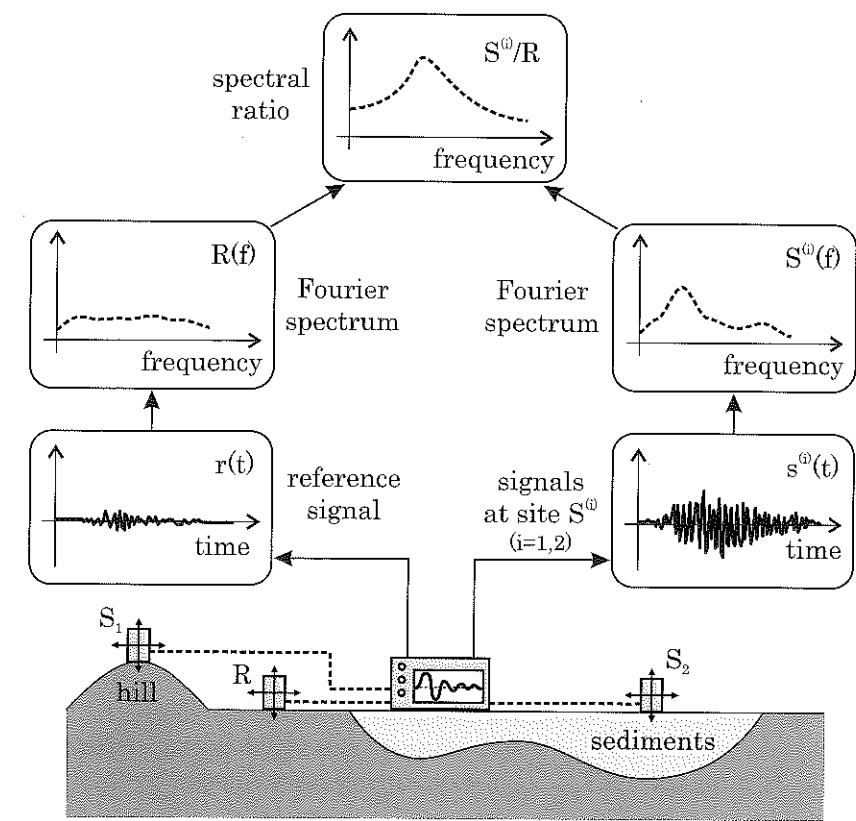


Fig. 5.5: Amplification of the seismic motion through site/reference spectral ratios.

Considering the definitions given in Fig.5.5, u_A corresponds to the ground motion at the alluvial site S whereas $u_{B'}$ is the reference motion at the reference site R .

Since such transfer functions correspond to complex-valued spectral ratios, it is possible to consider the time-domain amplification through inverse Fourier transforms. If we consider the time-domain response at the surface of the layer, namely $u_A(t)$, it may be related to the response at B' through the following relation:

$$u_A(t) = \frac{1}{2\pi} \int_{-\infty}^{+\infty} \bar{T}(\omega) u_{B'}^*(\omega) e^{i\omega t} d\omega = \frac{1}{2\pi} \int_{-\infty}^{+\infty} \left(\frac{u_{B'}^*(\omega)}{\cos p_1 h + i\bar{\chi} \sin p_1 h} \right) e^{i\omega t} d\omega \quad (5.2)$$

The unamplified wavefield $u_{B'}(t)$ corresponds to the double of the incident wavefield u_{inc} (due to the free-surface condition). Knowing the transfer function $\bar{T}(\omega)$ and the Fourier transform of the reference motion $u_{B'}^*(\omega)$ (or, alternatively, the incident motion if the free-surface effects are removed), it is thus possible to compute the amplified

wavefield $u_A(t)$ through Eq.(5.2). As discussed hereafter, the time-domain analysis of the amplification process may be performed directly using this method.

5.3.2 Amplification in single-layered media

As already studied in Chapter 3 (Fig.3.31), a single layer medium is considered first. It corresponds to a 20m deep layer having a shear wave velocity $V_S=200$ m/s, mass density $\rho=2$ t/m³. A vertically incident plane SH -wave is considered. The ground response is computed using expression (5.2) and considering a 2nd order Ricker wavelet, with central frequency f_R , as the incident wavefield (see definition in Chapter 4 and Appendix B).

Ricker wavelet at maximum amplification

The central frequency of the Ricker wavelet, f_R , is first chosen at the fundamental frequency of the layer: $f_R = f_s$. This case corresponds to the maximum amplification. As already proposed in Chapter 3, three different layer/bedrock velocity ratios $\{\chi_1, \chi_2, \chi_3\}$ are considered (see values in Fig.3.31). The incident wavefield is displayed in Fig.5.6 (top) together with the amplified wavefields for each velocity ratio. For the largest velocity ratio χ_1 , the maximum amplitude is increased by a factor of 2. This value may be compared to the maximum spectral amplification (around 6) obtained, in Chapter 3, at the fundamental frequency of the layer (Fig.3.31). Even if the central frequency of the Ricker wavelet coincides with the fundamental frequency of the layer, the time-domain amplification is much lower than the spectral one. This is due to the fact that the Ricker wavelet has a short duration whereas the spectral analysis assumes sinusoidal signals with infinite durations. This difference is thus crucial when comparing spectral amplifications and time-domain amplification.

Comparing the amplified signals displayed in Fig.5.6, it should be noticed that the influence of the velocity ratio is huge: the lower the velocity ratio the smaller the amplification. These results also show that the amplification process in time-domain leads to different signal durations. Finally, the time-domain amplification is much lower than the spectral one but the effect in time-domain also concerns the motion duration. In the following, such conclusions will also stand for actual seismic motions in geological structures. Beauval *et al.* (2003) for instance evidenced the ground motion lengthening at the Volvi Euroseistest site.

Ricker wavelet at $f_R = f_s/2$

Another Ricker wavelet is now considered at a lower central frequency: $f_R = f_s/2$. As shown in Fig.3.31 (Chapter 3), the spectral amplification is not maximum at this frequency and the time-domain amplification should follow the same trend. The lower frequency Ricker wavelet is displayed in Fig.5.7 together with the amplified signals. Compared to Fig.5.6, the amplification in the time-domain is significantly lower and the duration is increased less than in the previous case. A lower spectral amplification thus lead to a lower time-domain amplification and a smaller duration increase.

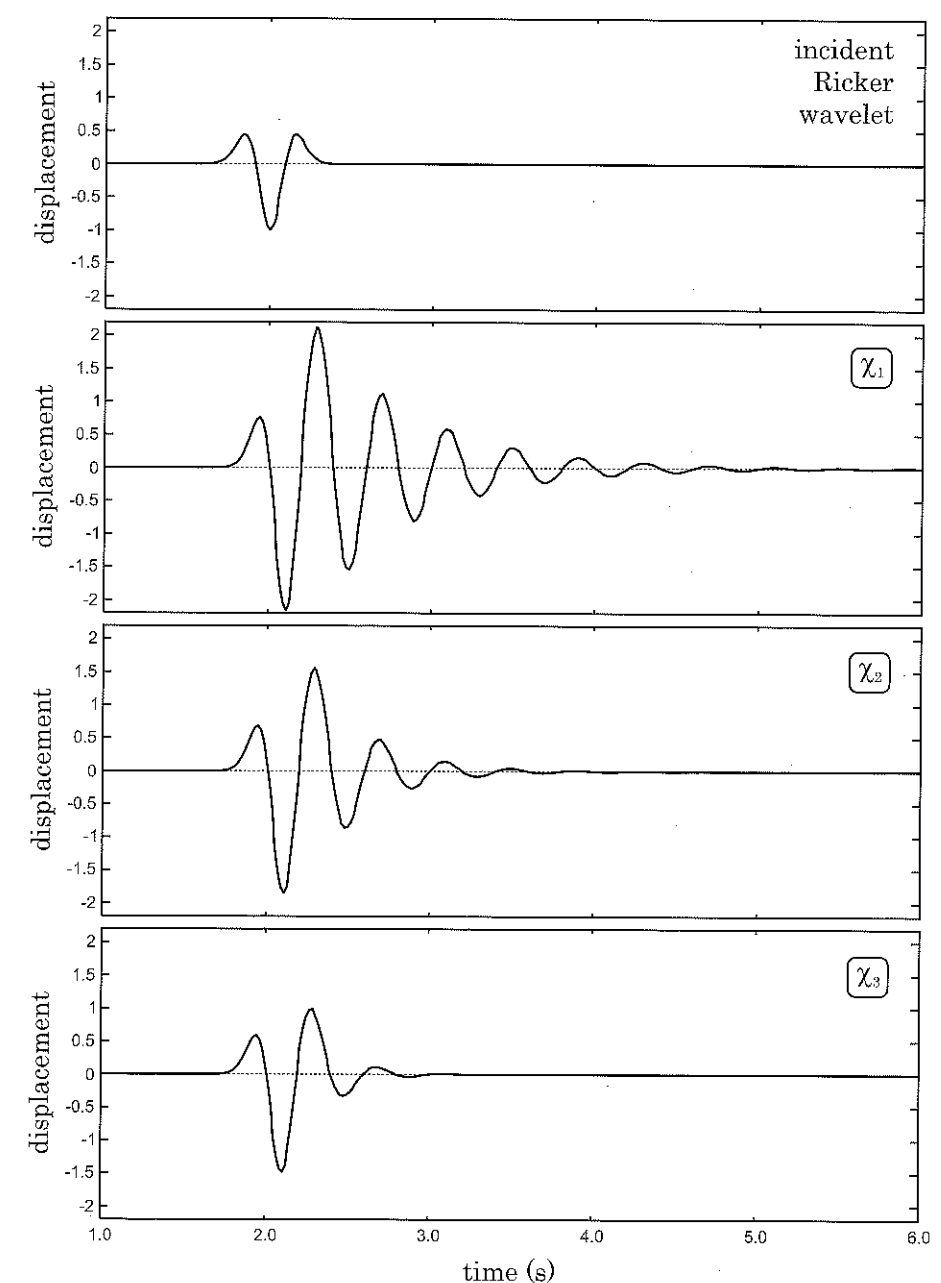


Fig. 5.6: Amplification of a Ricker wavelet ($f_R = f_s$) in a single-layered medium for various velocity contrasts (χ_1, χ_2, χ_3).

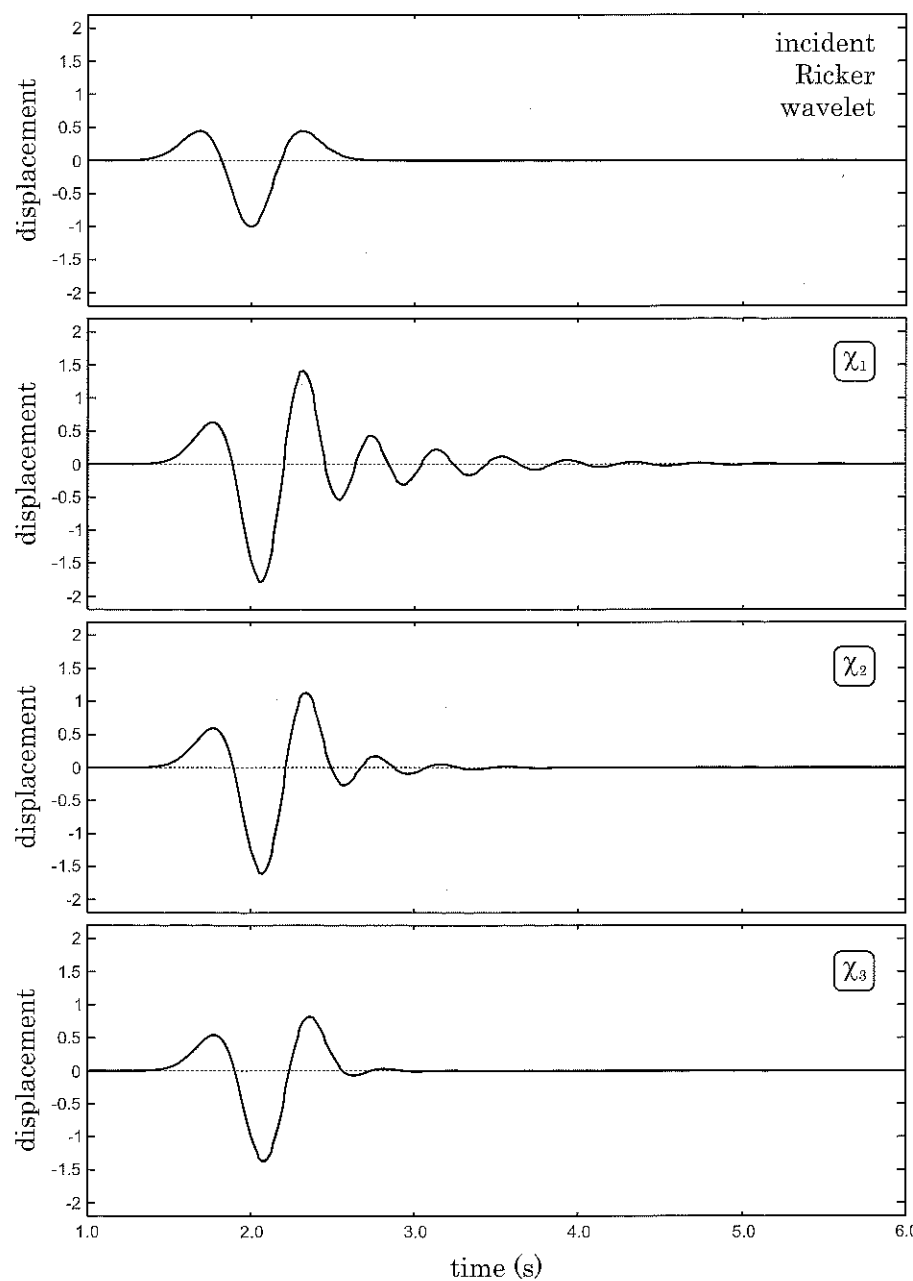


Fig. 5.7: Amplification of a Ricker wavelet ($f_R = f_s/2$) in a single-layered medium for various velocity contrasts (χ_1, χ_2, χ_3).

5.3.3 Amplification in multi-layered media

As discussed in Chapter 3, the case of multi-layered media may be easily derived from the case of single-layered media. The transfer function between layers j and k is easily expressed as:

$$T_{j,k}(\omega) = \frac{f_k(\omega) + g_k(\omega)}{f_j(\omega) + g_j(\omega)} \quad (5.3)$$

If the time-domain motion is known in one layer j , it is then possible to compute the time-domain response in any other layer k using the transfer function between layers j and k , $T_{j,k}$, and the Fourier transform of the motion in j , $u_j^*(\omega)$ (see Eq.(5.2)). The analysis may be performed for any kind of seismic motion. However, as it will be discussed in the following, the amplification estimated from 1D analyses is often much lower than the actual one due to specific 2D or 3D effects (Fig.5.4).

5.4 Amplification due to the topography

5.4.1 Main phenomena and simplified analysis

Topographical site effects

As evidenced for various actual sites (Ma *et al.*, 2007; Paolucci, 2002), the influence of topography on seismic wave propagation may be significant. It is the case for crests, hills, canyons and any type of steep topographic irregularity (Boore, 1972; Gaffet and Bouchon, 1989; Kouch-Bille *et al.*, 1991). As depicted in Fig.5.8, a simple interpretation of topographic site effects may be to consider the constructive interferences due to various wave paths focusing at the same point. The amplification process may then be influenced by different parameters: the wave type (through wave conversion effects), the geometry (namely the aspect ratio) and possibly the heterogeneities within the profile.

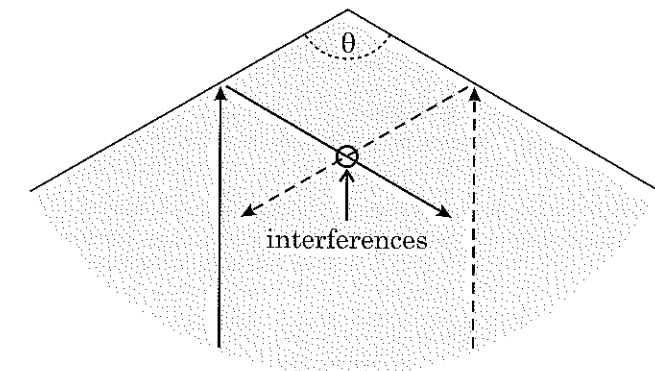


Fig. 5.8: Constructive interferences due to a simple topographic irregularity.

Simplified analysis for 2D topographies

Basic principles. Bouchon (1985) proposed a simplified method to assess the influence of 2D topographies on the seismic motion. In the case of plane *SH*-waves, he considered a simplified 2D topography ($x, z = \zeta(x)$) as depicted in Fig.5.9.

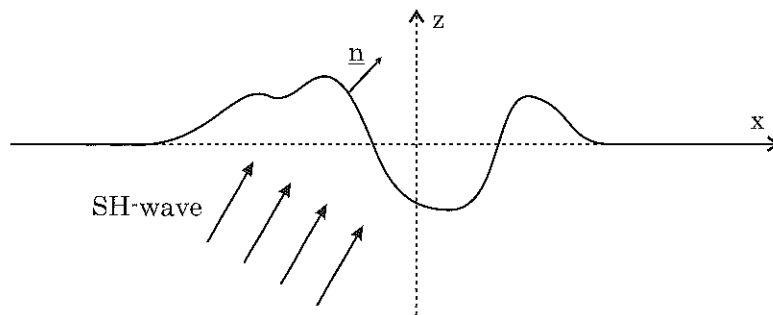


Fig. 5.9: Simplified topographic model proposed by Bouchon (1985).

Considering the notations given in Fig.5.9, the following time-harmonic displacement field may be written:

$$u(x, z) = \exp i(k_x x + k_z z) \quad (5.4)$$

The resulting incident (shear) stress along the surface is then:

$$\sigma(x, z) = \mu \left(n_x \frac{\partial u}{\partial x} + n_z \frac{\partial u}{\partial z} \right) = i\mu(n_x k_x + n_z k_z) \exp i(k_x x + k_z \zeta(x)) \quad (5.5)$$

Simplified method. The simplified method proposed by Bouchon (1985) consists in finding the force distribution along the surface which cancels the incident stress. The displacement field produced at (x, z) by a line force $Q(x_0, z_0)$ acting in the direction normal to the (x, z) plane (i.e. *SH*-wave) can be written:

$$v(x, z; x_0, z_0) = \frac{Q(x_0, z_0)}{4\pi i \mu} \int_{-\infty}^{+\infty} \frac{1}{k_z} \exp ik_z(z - \zeta(x_0)) \exp ik_x(x - x_0) dk \quad (5.6)$$

To transform this integral into a discrete summation, Bouchon (1985) introduced a periodicity in the surface shape: $\zeta(x + nL) = \zeta(x)$ with L the periodicity interval and n an integer. It yields:

$$v(x, z; x_0, z_0) = \frac{Q(x_0, z_0)}{2i\mu L} \sum_{n=-\infty}^{+\infty} \frac{1}{k_{z_n}} \exp ik_{z_n}|z - \zeta(x_0)| \exp ik_{x_n}(x - x_0) \quad (5.7)$$

By integration along the *x*-axis, it is then possible to evaluate the displacement field produced by the total force distribution:

$$u(x, z) = \frac{1}{2i\mu L} \sum_{n=-\infty}^{+\infty} \int_{-L/2}^{L/2} Q(x_0, z_0) \frac{1}{k_{z_n}} \exp ik_{z_n}|z - \zeta(x_0)| \exp ik_{x_n}(x - x_0) dx_0 \quad (5.8)$$

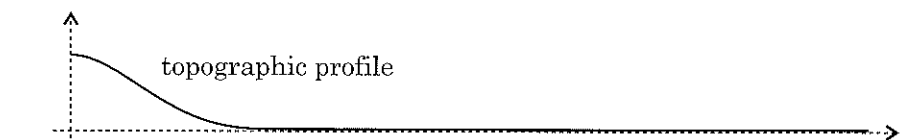
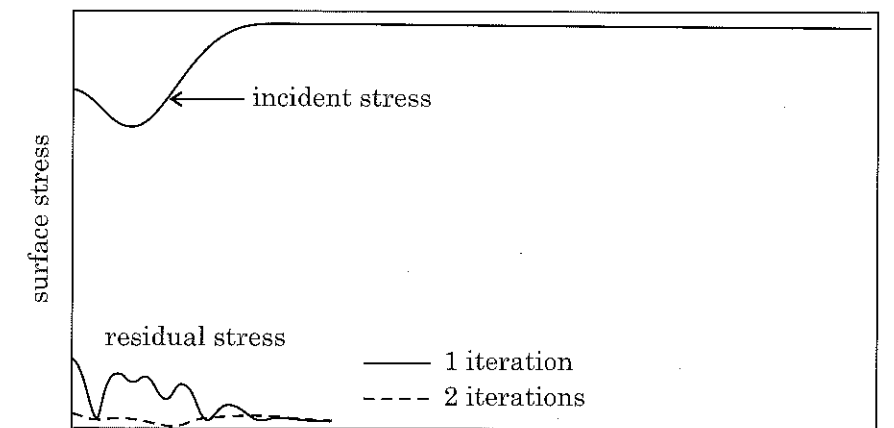
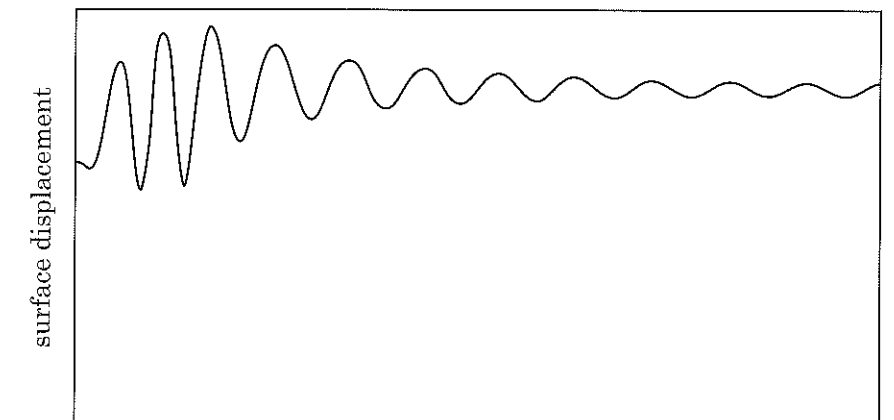


Fig. 5.10: Geometry of the topographic profile considered (bottom), final surface displacement (top) and evolution of the residual surface stress (middle) as investigated by Bouchon (1985).

Discretizing the surface (interval Δx), the discrete Fourier transform over the x coordinate arises and the solution may thus be estimated by inverse discrete Fourier transform:

$$u(x_j, z) = \frac{1}{2i\mu N} \sum_{m=-M}^M Q_m \sum_{p=-M}^M \frac{1}{k_{zp}} \exp ik_{zp}|z - \zeta(m\Delta x)| \\ \times \exp \left(i \frac{2\pi}{N} pj \right) \exp \left(i \frac{2\pi}{N} pm \right) \quad (5.9)$$

The linear system of equations (5.9) leads to the force distribution which cancels the stress produced by the incident wavefield along the surface. A fast iterative procedure was also proposed by Bouchon (1985).

Approximate solution. The iterative procedure proposed by Bouchon (1985) consists in choosing the following force distribution as a preliminary assumption:

$$Q_m = 2\sqrt{t_m^2 + 1} \sigma_{0m} \quad (5.10)$$

where σ_{0m} denotes the surface incident stress at x_m and t_m is the surface slope.

This distribution creates a stress discontinuity across the surface which cancels the incident stress field. However, the radiated stress field yields a non-zero resulting stress at the surface. Equation (5.9) is then used to evaluate the residual stress σ_{1m} at the surface points. Hence, a new force distribution is defined using these values:

$$Q_m = 2\sqrt{t_m^2 + 1}(\sigma_{0m} + \sigma_{1m}) \quad (5.11)$$

The new residual stress is evaluated and the process is continued until it becomes negligible. The resulting displacement field being computed, the effect of surface periodicity may be removed using the method proposed by Bouchon and Aki (1977).

Some results computed by Bouchon (1985) using this iterative procedure are displayed in Fig.5.10. The residual stress for each iteration is given: it is nearly zero at the third iteration. Bouchon (1985) also investigated the case of a triangular profile for which the residual stress is found to be large around the discontinuities of the surface slope.

5.4.2 Amplification by crests and hills

Amplification at a hill crest

For step-like slope topographies, some analyses were performed in the late 60's in the case of earthbanks (Idriss *et al.*, 1967). Recently Bouckovalas and Papadimitriou (2005) studied in great details such topographies in order to propose code provisions. As depicted in Fig.5.11, they computed the seismic ground motion around step-like slope topographies for various geometrical features. They assessed the effect of the slope in terms of topography aggravation factors defined as $A_v = a_v/a_{v,ff}$ for the vertical component and

5.4 Amplification due to the topography

$A_h = a_h/a_{h,ff}$ for the horizontal one (where a_j and $a_{j,ff}$ denote the j th acceleration component at each point of the ground surface and ff the similar variable for the free-field case). The topography aggravation factors computed by Bouckovalas and Papadimitriou (2005) are displayed in Fig.5.11. They show that the amplitude is reduced at the bottom of the slope and is enhanced at its top.

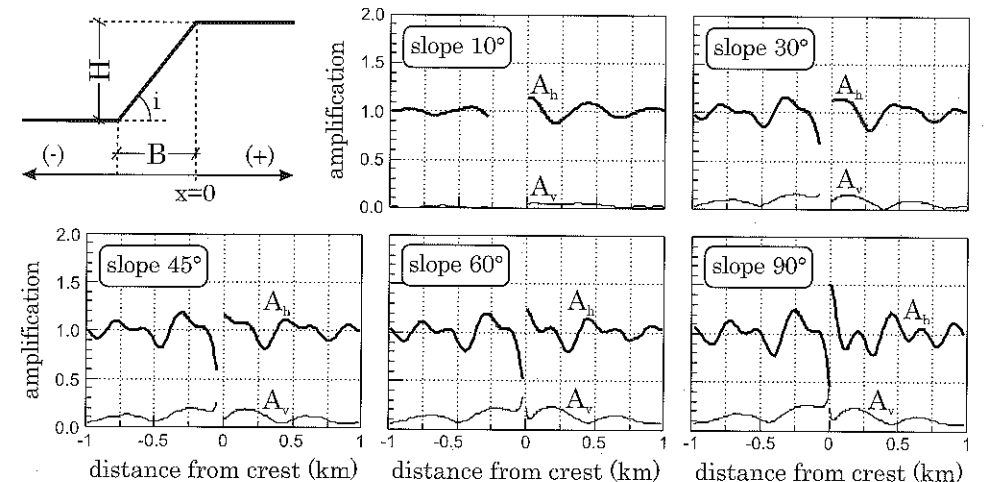


Fig. 5.11: Amplification of seismic wave around a crest for various inclinations of the topography (Bouckovalas and Papadimitriou, 2005).

Bouckovalas and Papadimitriou (2005) performed extensive parametric studies to assess the influence of such topographies on the seismic ground motion. From these results, they derived the following expression for the amplification of the horizontal component:

$$A_{h,max} = 1 + F_{Ah} \left(\frac{H}{\Lambda} \right) G_{Ah}(I) H_{Ah}(\xi) J_{Ah}(N) \quad (5.12)$$

where functions F , G , H and J are chosen as:

$$F \left(\frac{H}{\Lambda} \right) = \left(\frac{H}{\Lambda} \right)^{0.4} \\ G(I) = \frac{I^2 + 2I^6}{I^3 + 0.02} \\ H(\xi) = \frac{1}{1 + 0.9\xi} \\ J(N) = 0.225 \quad (5.13)$$

where H is the crest height, Λ the wavelength, $I = i/90$ the normalized incidence, ξ the

damping ratio in the soil and N the number of significant excitation cycles.

In (Bouckovalas and Papadimitriou, 2005), the amplification of the vertical component $A_{v,max}$ is analyzed as well. For both components, the variations of $A_{h,max}$ and $A_{v,max}$ are displayed in Fig.5.12 vs two parameters: the dimensionless height H/λ and the normalized incidence $I = i/90$. Bouckovalas and Papadimitriou (2005) compared their predictions to the code provisions from European EC-8 and from the French PS-92. They concluded that the 20 to 40% increase of the horizontal ground motion estimated numerically is similar to the provisions of both codes. Nevertheless, their numerical results lead to a significant parasitic vertical component (Fig.5.12) which is not accounted for in the seismic codes. Bouckovalas and Papadimitriou (2005) also proposed distances from the crest to the free-field that are larger than in the codes.

Amplification by a hill

Approximate fundamental frequency. Paolucci (2002) proposed a simplified method using the Rayleigh approximation to estimate the fundamental frequency of hills defined by two different slopes (Fig.5.13). This method will be presented later in the case of alluvial basins.

For steep hills and plane SH -waves, the fundamental frequency as derived by Paolucci (2002) has the following form:

$$\hat{f}_0 = 0.38 \frac{V_S}{L} \frac{\sin(\theta_1 + \theta_2)}{\cos \theta_2} \sqrt{\left[1 + \ln^2 \left(\frac{R_2}{R_1} \right)^{1/(\theta_1 + \theta_2)} \right] \frac{2 \ln(R_2/R_1)}{(R_2/R_1)^2 - 1}} \quad (5.14)$$

It may be expressed as a function of the slopes on both sides of the hill, namely H/L_1 and H/L_2 . From this expression, Paolucci (2002) found that, for aspect ratios below 0.5, the fundamental frequency may be approximated as follows:

$$\hat{f}_0 \simeq 0.7 \frac{V_S}{L} \quad (5.15)$$

In the case of plane SV -waves, the approximate method proposed by Paolucci (2002) yields the fundamental frequency as:

$$\begin{aligned} \hat{f}_0 &= 0.38 \frac{V_S}{L} \frac{\sin(\theta_1 + \theta_2)}{\cos \theta_2} \sqrt{\frac{\kappa}{(R_2/R_1)^2 - 1}} \\ &\times \left\{ (\kappa^2 + 1) \left(3 + \frac{\lambda}{\mu} \right) (\theta_1 + \theta_2) \right. \\ &\left. + \left(1 + \frac{\lambda}{\mu} \right) \left[(\kappa^2 - 1) \frac{\sin 2\theta_2 + \sin 2\theta_1}{2} + \kappa(\cos 2\theta_2 - \cos 2\theta_1) \right] \right\}^{-1/2} \end{aligned} \quad (5.16)$$

$$\text{where: } \kappa = \frac{1}{\theta_1 + \theta_2} \ln \frac{R_2}{R_1}$$

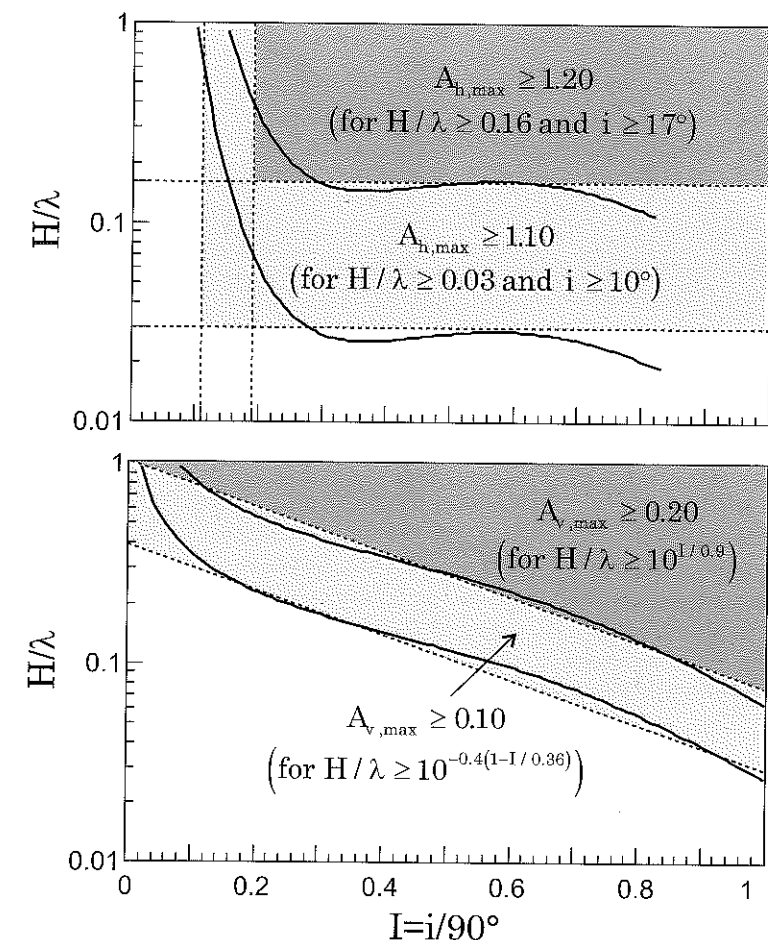


Fig. 5.12: Aggravation factors for the horizontal (top) and vertical (bottom) motion components with respect to the topographical features: normalized height H/λ and slope I (Bouckovalas and Papadimitriou, 2005).

Through this formula, Paolucci (2002) found that the fundamental frequency in the SV case is 30% larger than in the SH case. As also demonstrated by Géli *et al.* (1988), these theoretical results show that the fundamental frequency for both SH and SV -waves corresponds to wavelengths that are significantly longer than the hill width. Paolucci (2002) also studied actual steep topographies and one of these examples will be shown later on.

Simulations for a triangular hill. As shown in Fig.5.8, the amplification by a hill may be due to the focusing of various upcoming waves. In Chapter 4, we considered

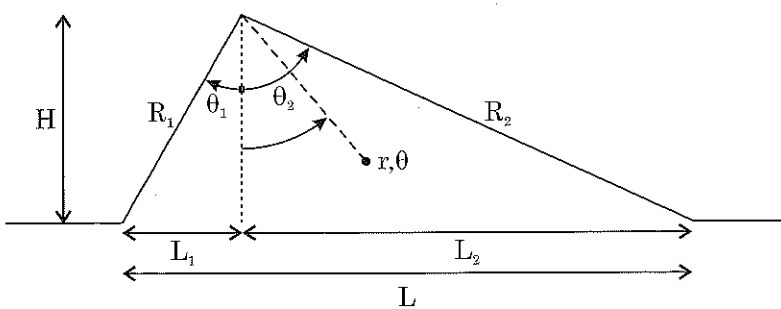


Fig. 5.13: Geometrical description of the theoretical topography proposed by Paolucci (2002).

a triangular hill to discuss the accuracy of numerical methods (Fig.4.25). The same example is now used to analyze seismic wave scattering (vertically incident plane wave) by a hill in terms of topographic site effect. The displacement field is computed by the finite element method and displayed in Fig.5.14 vs time and distance. The amplification is maximum at the hill top. At other locations, the radiated wavefields lead to longer motion duration. Conversely, a slight amplitude decrease may be noticed at the base of the hill. As previously shown, the interaction depends on the ratio between the hill dimensions and the wavelength. Similar effects will be shown later in realistic cases.

Géli *et al.* (1988) studied the influence of the topography combined with that of a soil layering along the slope (i.e. *ridge subsurface layering*). The former lead to significant amplification/deamplification phenomena (similar to that depicted in Fig.5.14) whereas the latter may generally be neglected.

5.4.3 Amplification by canyons

The case of canyons is close to the case of alluvial valleys. Topographic effects are nevertheless dominating since the soil is generally assumed homogeneous. However, as it will be discussed at the end of this section, such purely geometrical effects may be combined with the influence of the velocity contrast.

2D canyons

Triangular canyons. Sánchez-Sesma and Rosenblueth (1979) studied the response of canyons of arbitrary shape under plane waves (Fig.5.15). They formulated the problem in terms of a Fredholm integral equation and solved it numerically. They analyzed the influence of the angle of incidence θ as well as the canyon slope h/a . Triangular and cosine-shaped canyons were considered. Sánchez-Sesma and Rosenblueth (1979) discussed the results for given values of the normalized frequency η defined as:

$$\eta = \frac{ka}{\pi} = \frac{2a}{\Lambda} \quad (5.17)$$

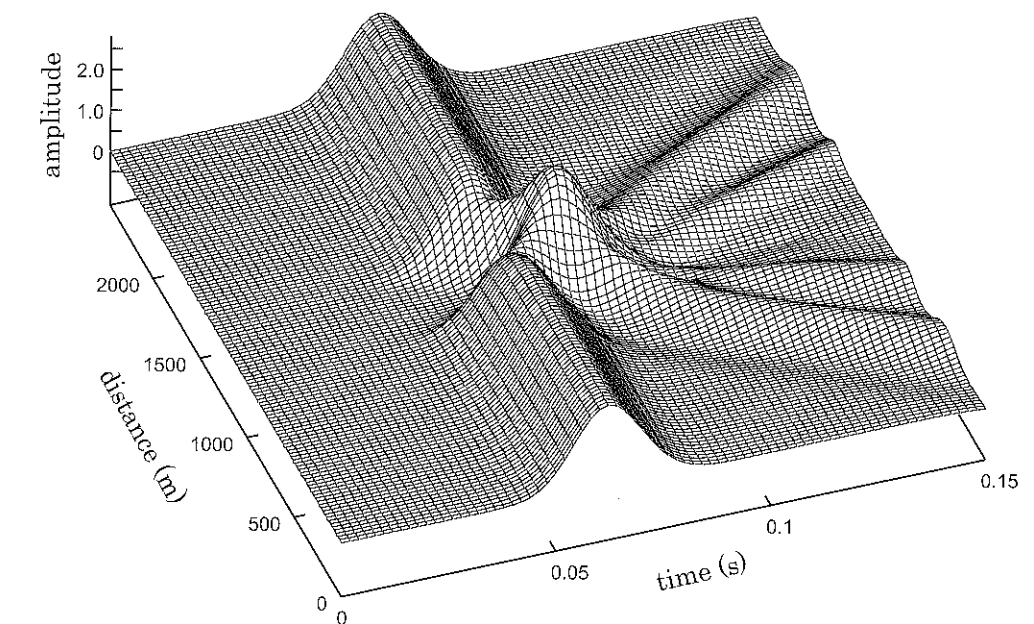


Fig. 5.14: Amplification of the seismic motion at the surface of a topographic irregularity: FEM results.

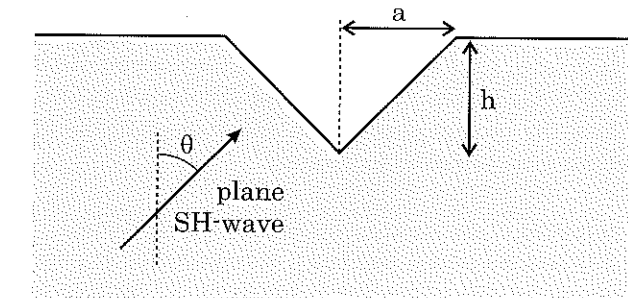


Fig. 5.15: Triangular canyon considered by Sánchez-Sesma and Rosenblueth (1979) to analyze the scattering of plane *SH*-waves.

where k is the wavenumber, a is the canyon half-width and Λ the wavelength.

As depicted in Fig.5.16 in the case of a triangular canyon at normalized frequency $\eta = 0.5$, larger incidences lead to stronger amplifications on the upstream part of the canyon. Conversely, the amplification on the left part of the canyon is lower for increasing incidence angles.

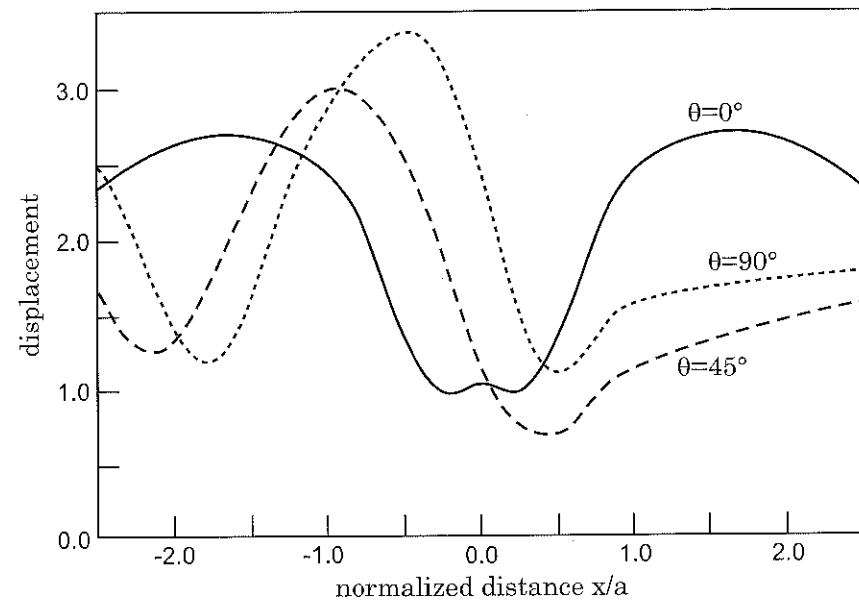


Fig. 5.16: Surface motion for a triangular canyon (slope 45°) and an oblique SH -wave, Sánchez-Sesma and Rosenblueth (1979).

Another interesting issue is the location of the maximum amplification: it is around $x/a = 1.75$ for $\theta = 0$, $x/a = 1.0$ for $\theta = 45^\circ$ (that is the canyon slope) and $x/a = 0.75$ for $\theta = 90^\circ$. For plane SH -waves, the maximum amplification may thus be located along the free-surface or along the canyon slope. As it will be seen in the following, the time-domain analysis leads to more complicated results.

In Fig. 5.17, the influence of the canyon slope h/a is now studied. The wavelength is kept constant ($\Lambda = 5h$) and a vertical incidence is considered. For the steepest slope, a strong deamplification of the ground motion is found at the bottom of the canyon. The maximum amplification is above 1.25 (free-surface effects being removed) and is located near the basins edges.

Circular canyons. For two-dimensional canyons and plane SH -waves, Trifunac (1973) derived the closed-form solution in terms of Hankel and Bessel functions. He obtained the scattered wavefield under the following form:

$$u_z^R = \sum_{n=0}^{\infty} [a_n H_{2n}^{(2)}(kr) \cos 2n\theta + b_n H_{2n+1}^{(2)}(kr) \sin(2n+1)\theta] \quad (5.18)$$

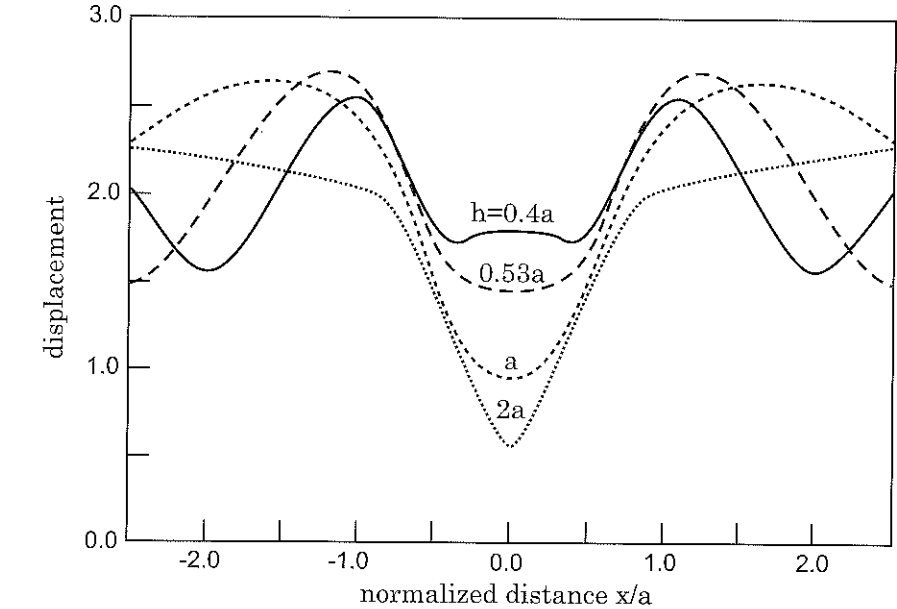


Fig. 5.17: Surface motion for a triangular canyon and various slopes h/a (plane vertical SH -wave), from Sánchez-Sesma and Rosenblueth (1979).

where $H_p^{(2)}$ is the Hankel function of the second kind and, denoting J_k the Bessel functions of the first kind, the following expressions:

$$\begin{aligned} a_0 &= -2 \frac{J_1(ka)}{H_1^{(2)}(ka)} \\ b_0 &= 4i \sin \gamma \frac{ka J_0(ka) - J_1(ka)}{ka H_0^{(2)}(ka) - H_1^{(2)}(ka)} \end{aligned} \quad (5.19)$$

and for $n \neq 0$:

$$\begin{aligned} a_n &= -4(-1)^n \cos 2n\gamma \frac{ka J_{2n-1}(ka) - 2n J_{2n}(ka)}{ka H_{2n-1}^{(2)}(ka) - 2n H_{2n}^{(2)}(ka)} \\ b_n &= 4i(-1)^n \sin(2n+1)\gamma \frac{ka J_{2n}(ka) - (2n+1) J_{2n+1}(ka)}{ka H_{2n}^{(2)}(ka) - (2n+1) H_{2n+1}^{(2)}(ka)} \end{aligned} \quad (5.20)$$

After determination of these parameters, the total wavefield may be determined:

$$u_z^T = u_z^i + u_z^r + u_z^R \quad (5.21)$$

where u_z^i and u_z^r are the incident and the reflected wavefields respectively.

From this closed-form solution, Trifunac (1973) studied the scattering of plane SH -waves and concluded that the surface topography has prominent effects when the wavelengths are short compared to the radius of the canyon. He found that the amplification factor is always less than two.

3D canyons

Vertical plane waves. 3D canyons are now considered for various wave types. Different canonical 3D models were studied in the framework of the *QSHA*¹ research project considering various numerical methods (see <http://qsha.obs.ujf-grenoble.fr> for data and results). As depicted in Fig.5.18, the scattering of a plane P -wave by a semi-spherical canyon is first considered. The Fast Multipole formulation, formulated in the framework of the Boundary Element Method (see Chapter 4), is used for the computations in the frequency domain (Chaillat *et al.*, 2008).

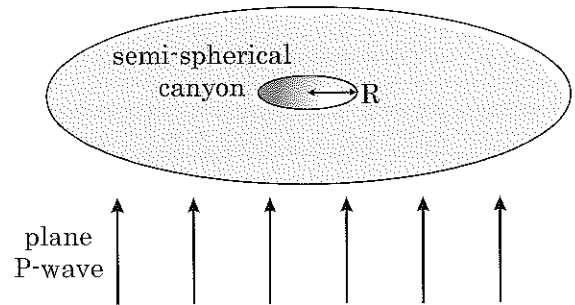


Fig. 5.18: Diffraction of a plane P -wave by a semi-spherical canyon: schematic of the problem (Sánchez-Sesma, 1983).

In Fig.5.19, the FM-BEM results, computed for a normalized frequency $\eta = 0.50$, are compared to those published by Sánchez-Sesma (1983) and Reinoso *et al.* (1997). They are displayed as a function of the distance along the canyon surface, denoted s , normalized with respect to the canyon radius. The agreement between all these results in terms of both vertical and horizontal components is excellent. A strong deamplification is observed at the centre of the canyon. A slight amplification is found near the canyon edges.

Oblique plane waves. The case of oblique plane waves is now considered. Various authors analyzed the scattering of plane oblique waves due to irregular topographies such as canyons (Eshraghi and Dravinski, 1989; Reinoso *et al.*, 1997; Mossessian and Dravinski, 1990). For an oblique P -wave, Reinoso *et al.* (1997) computed the surface displacements

¹Quantitative Seismic Hazard Assessment

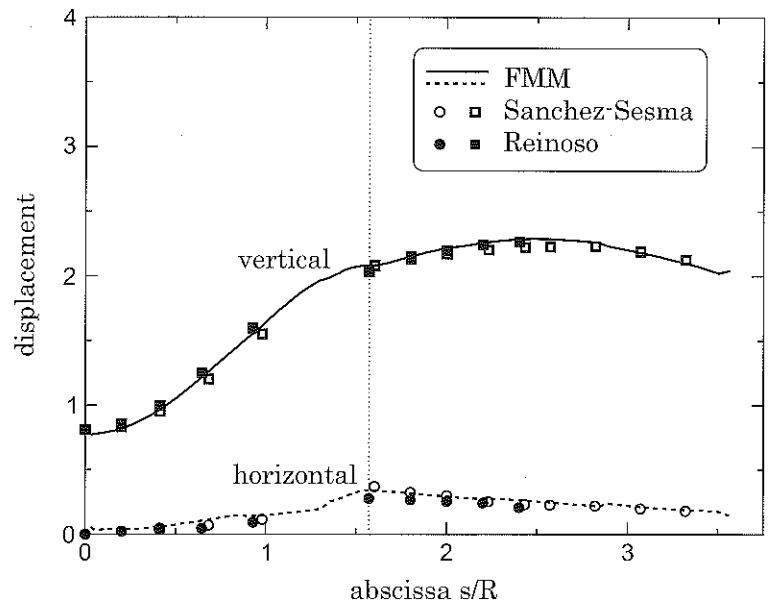


Fig. 5.19: Diffraction of a plane P -wave by a semi-spherical canyon: comparison of the FM-BEM results with previous results by Sánchez-Sesma (1983) and Reinoso *et al.* (1997) at normalized frequency $\eta_P=0.50$ (Chaillat *et al.*, 2007).

at a normalized frequency $\eta=0.5$. Their results are displayed in Fig.5.20 (top) in terms of vertical and horizontal displacements. These curves are strongly assymmetrical with a larger vertical displacement on the left side (incident wave) but a smaller horizontal component due to lower wave conversion at this side.

For an oblique SV -wave, Reinoso *et al.* (1997) computed the surface displacements at the normalized frequency $\eta=0.5$. Their results are displayed in Fig.5.20 (bottom) in terms of vertical and horizontal displacements. These curves are strongly assymmetrical with a very sharp peak. The amplification of the vertical component on the left side of the canyon (incident wave) is larger than for an incident P -wave.

5.4.4 Amplification on actual topographies

Many different areas in the world are affected by topographic site effects. In some cases, small cities are located in such areas and may suffer from ground motion amplification (Paolucci, 2002) or induced landslides (Bourdeau and Havenith, 2008). We shall recall some results for two specific sites: Caracas, Venezuela and a very steep site in Italy (Bagnoregio). It will be also shown that topographic site effects may also influence the stability of natural slopes such as in Las Colinas, Salvador (Bourdeau, 2005).

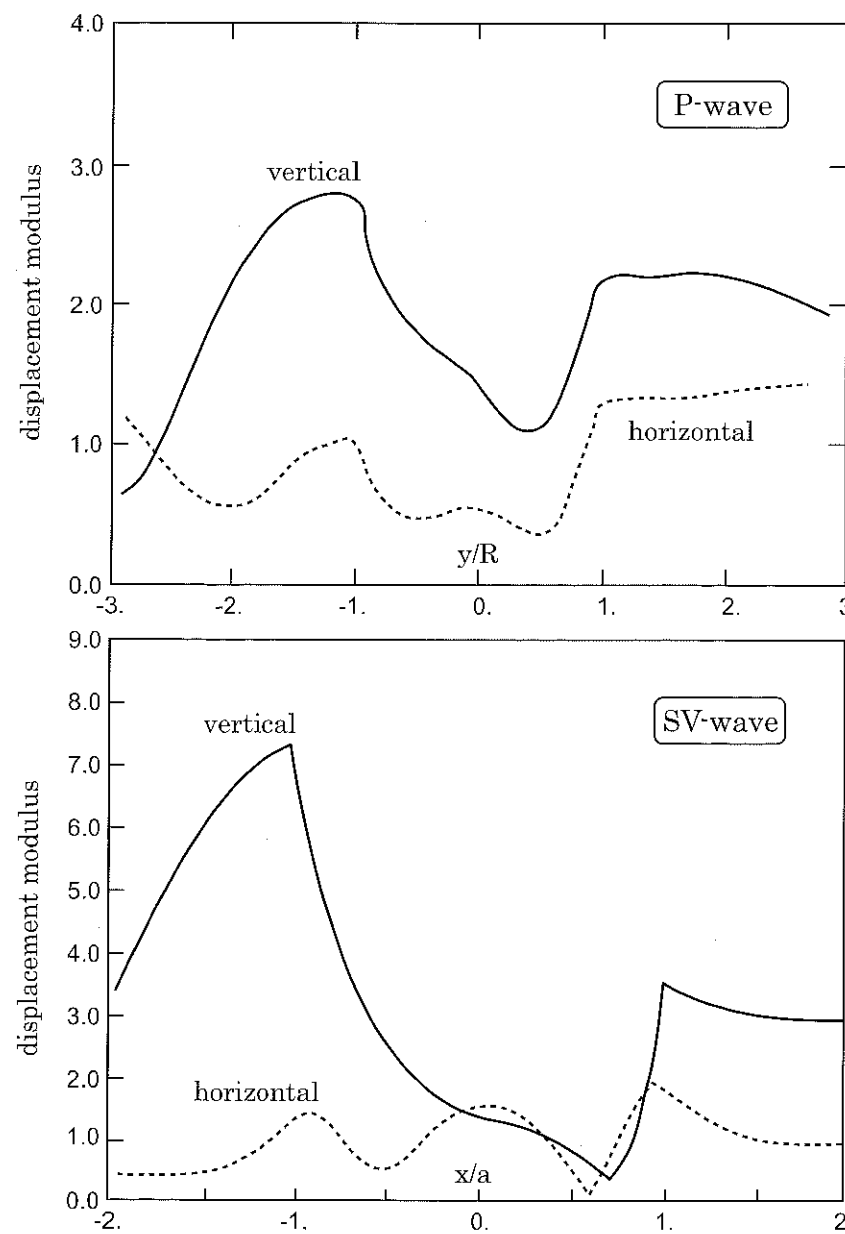


Fig. 5.20: Surface motion for a semi-spherical canyon computed by Reinoso *et al.* (1997) for an oblique P -wave (top) and an oblique SV -wave (bottom) at the normalized frequency $\eta = 0.5$.

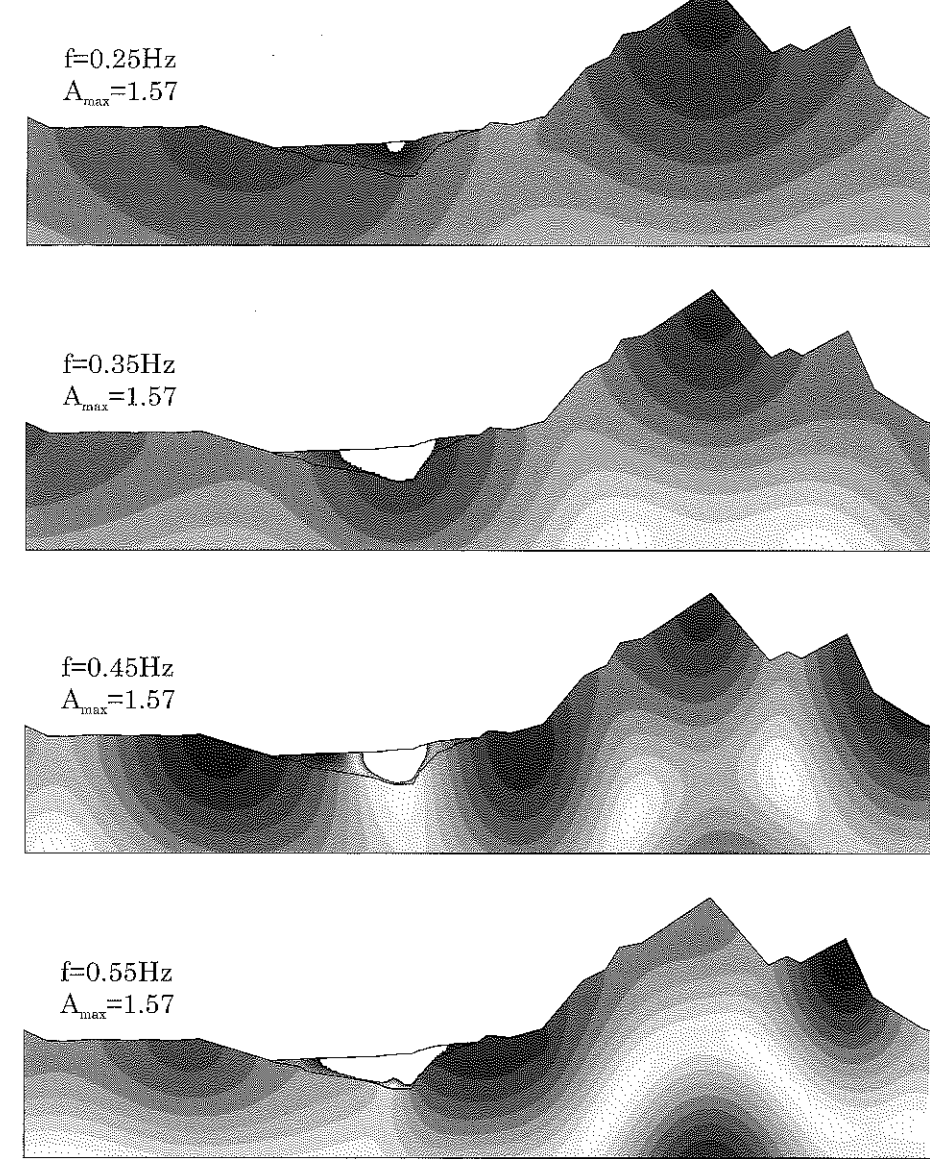


Fig. 5.21: Topographic amplification of seismic waves around the city of Caracas, maximum amplification values given by A_{\max} (vertical scale exaggerated by a factor of 2).

Amplification in Caracas

Description of the site. The city of Caracas, Venezuela, is founded on a very deep alluvial basin surrounded by high mountains. The analysis of seismic site effects in Caracas has been performed by various teams through experimental (Duval *et al.*, 1998) as well as numerical approaches (Delavaud, 2007; Papageorgiou and Kim, 1991; Semblat *et al.*, 2002a,b). Site effects in Caracas are dominated by the amplification in the deep alluvial basin, whereas topographic effects are only significant at very low frequencies (Semblat *et al.*, 2002b).

Topographic amplification. The topography is modelled by the Boundary Element Method considering a 10km long geological profile. The topographic amplification of plane SH -waves was computed for several low frequency values: 0.25, 0.35, 0.45 and 0.55 Hz. The numerical results are displayed in Fig.5.21 all along the profile with a fixed grey scale for the amplification level. At very low frequencies ($f=0.25$ Hz), the topographic amplification is prominent when compared to that due to the alluvial basin. The largest amplification is found at the top of the highest mountain and reaches $A_{topo}=1.57$, the free-surface effect being removed. For $f=0.35$ Hz, the amplification is larger in the basin (out of scale) than along the topography. For the highest frequency ($f=0.55$ Hz), the main topographic amplification area is located at the top of a smaller and narrower mountain, due to the shortest wavelength in this case.

Comparison with previous results. In order to compare with previous results derived for simplified geometries, we selected three points along the topography (Fig.5.22): at the top of the two mountains (points 1 and 2 resp.) and in between at the lowest local height (point 3). The topographic amplification at these three points is displayed in Fig.5.22 as a function of frequency. For point 3, the ground motion is generally deamplified with values of A_{topo} ranging from 0.5 to 1.0. At the top of the mountains, the amplification is significant since $A_{topo}=1.64$ at $f=0.43$ Hz for point 1 and $A_{topo}=2.12$ at $f=0.78$ Hz for point 2. Paolucci (2002) also found topographic amplification factors larger than 2 for very steep sites.

The present results are in agreement with the conclusions of the canonical topographies: the ground motion is amplified at the top of the mountains/crests whereas it is deamplified at the bottom locations. As it can be seen in Fig.5.22, the free-surface effect being removed, the amplification may even be larger than 2 in some locations. Nevertheless, in the case of Caracas, the amplification factor in the basin is much larger than the topographic effect (Semblat *et al.*, 2002b). As concluded by experimental studies, the maximum amplification areas in the city of Caracas are located at places and for frequency ranges where the buildings were mostly damaged during the 1967 earthquake (Duval *et al.*, 1998).

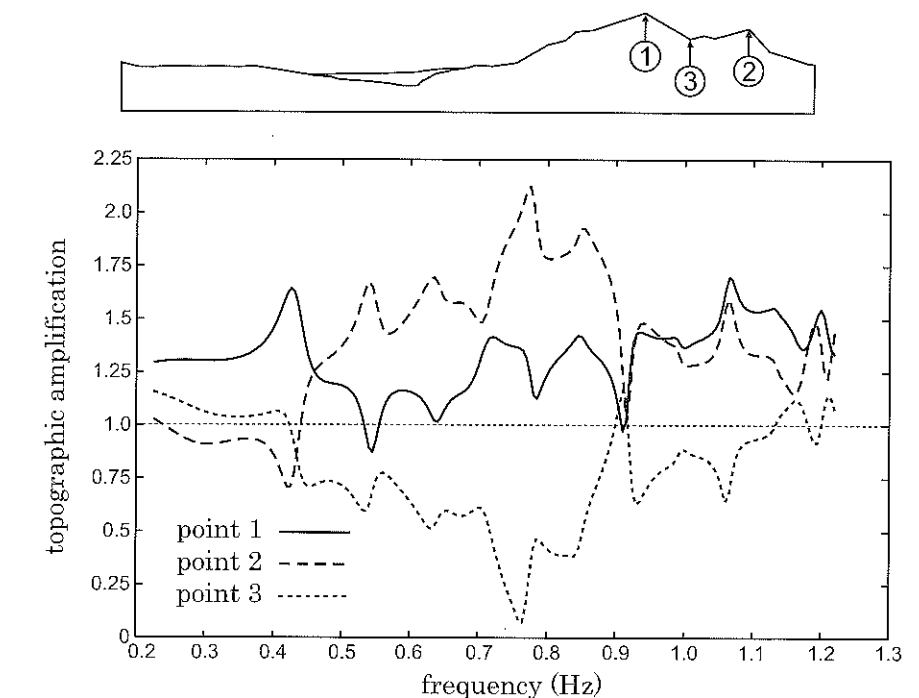


Fig. 5.22: Amplification and deamplification at different locations along the topography around Caracas.

Amplification for steep narrow hills (Italy)

Description of the site. Rovelli *et al.* (2001) and Paolucci (2002) investigated topographic site effects for various steep Italian sites. One of those is called Civita di Bagnoregio and is located on a steep isolated hill (Fig.5.23). The hill is about 110 m high and was hit by a strong earthquake in 1695 (local intensities ranging from IX to X). The enormous damage in Civita may suggest a significant topographic amplification. For this site, Paolucci (2002) performed numerical simulations using the Spectral Element Method.

Topographic amplification. For an EW cross-section, the results computed by Paolucci (2002) at four receivers are displayed in Fig.5.24: a Ricker wavelet was considered for time-domain analysis (top) and the spectral amplification was also estimated (middle). From the displacement time-histories, the topographic effect is found to increase both the amplitude and the motion duration. In the frequency domain, a prominent peak at about 1 Hz appears in all transfer functions at the hill top. Paolucci (2002) compared this fundamental frequency of the hill to the values computed by a simplified

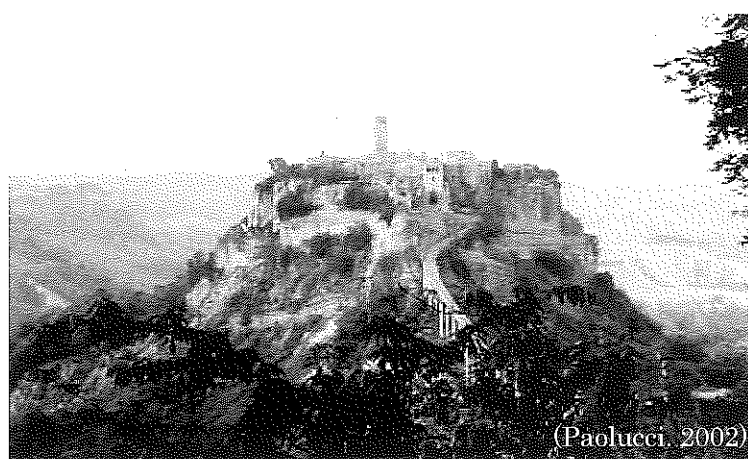


Fig. 5.23: Picture of Civita de Bagnoregio (Italy) where topographic site effects were studied by Paolucci (2002).

modal approach (this method will be presented herein for alluvial basins).

Comparison with previous results. Paolucci (2002) computed the 3D topographic amplification all around the hill as illustrated in Fig.5.25: the displacement peaks from the numerical analysis (EW polarization, with $f_p = 1$ Hz) are depicted with dots of variable size. As already noticed in the previous sections, the larger values occur at the top of the hill. However, Paolucci (2002) showed that for other frequencies (e.g. $f_p=2$ Hz) the amplification due to resonance is smaller, while that due to the convexity of the profile becomes prominent. Similarly to previous results, significant deamplification is found at the base of the hill. These results are in good agreement with the theoretical formula proposed by Paolucci (2002) for such concave wedges.

Effect on slope stability

The previous paragraphs only considered the amplification of the seismic motion at the top of crests or hills. The influence of this phenomenon may also induce instabilities in slopes. The analysis of both phenomena was for instance performed by Bourdeau (2005) for the Las Colinas site (Salvador) and by Bozzano *et al.* (2008) for the Salcito landslide (Italy). For the Las Colinas site, a large landslide was observed after the 2001 earthquake. The numerical back-analysis of this earthquake (Bourdeau, 2005) evidenced the fact that the landslide was induced by the amplification of the seismic motion at the top of the slope. Such phenomena are very complex since they also depend on the nonlinear constitutive laws of the various materials, their initial stress state, their water content, etc.

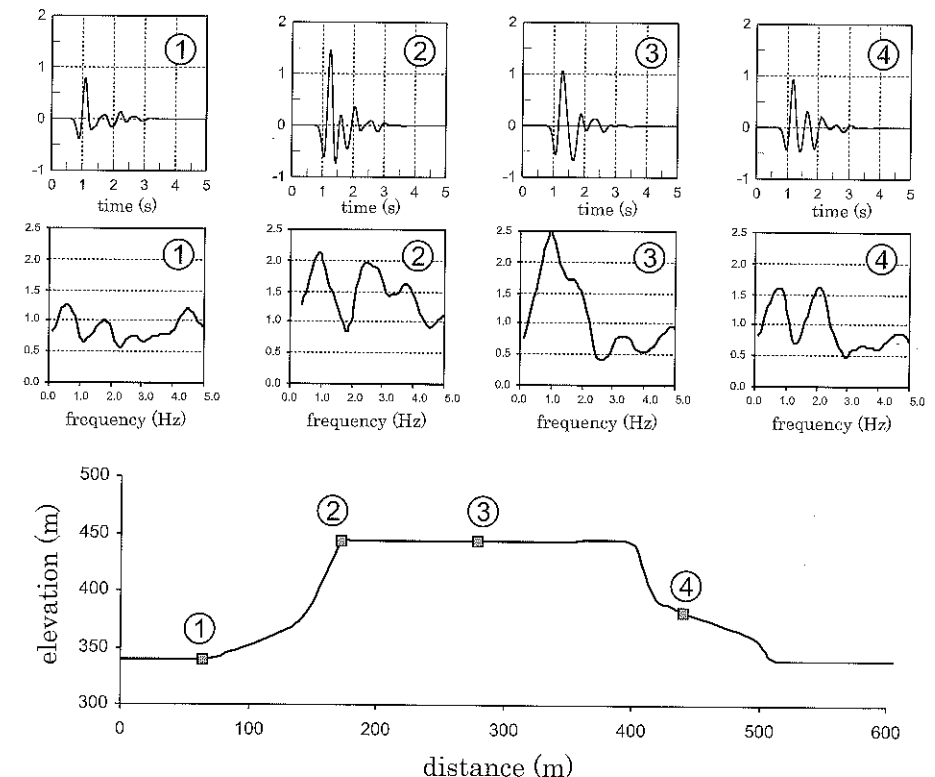


Fig. 5.24: Analysis of topographic site effects in Civita de Bagnoregio (Italy): results from Paolucci (2002) by the Spectral Element Method.

5.5 Amplification of seismic waves in 2D alluvial basins

Amplification of seismic waves may be due to soil layering or topographic irregularities. As previously depicted in Fig.5.4, the amplification process may strongly differ between the 1D (horizontal layering) and the 2D/3D cases (Moczo and Bard, 1993). The influence of dipping layers or alluvial basins having simple geometries will be discussed in this section (2D) as well as in the following one (3D). The case of actual alluvial deposits will be investigated later.

5.5.1 Amplification by wedges

Some analytical results were derived by various authors for simple geometries (Sánchez-Sesma, 1985). The case of semi-infinite layers is investigated first. Alluvial basins with finite geometrical extents will be discussed in the next section.

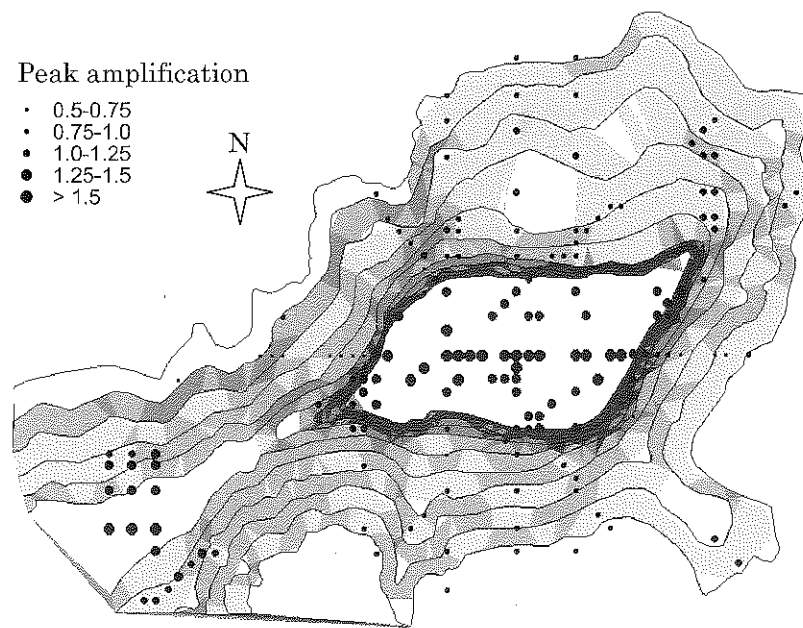


Fig. 5.25: Analysis of topographic site effects in Civita de Bagnoregio (Italy): results from Paolucci (2002).

Infinite dipping layer

Description and solution of the problem. Sánchez-Sesma and Velazquez (1987) for instance analyzed the case of an infinite dipping layer depicted in Fig.5.27. For plane SH -waves, they derived, from geometrical considerations, the solution under the following form:

$$\text{harmonic excitations: } \frac{v}{v_0} = \sum_{j=0}^M \varepsilon_{M-j} (-1)^j \exp(-ikx \cos \theta_j) \quad (5.22)$$

$$\text{transient excitations: } \frac{v}{v_0} = \sum_{j=0}^M \varepsilon_{M-j} (-1)^j f \left(t - \frac{x}{V_S} \cos \theta_j \right)$$

where $\theta_j = \frac{[N-(2j+1)]\pi}{2N}$, $M = \frac{N-1}{2}$ and ε_n is the Neumann factor defined as:

$$\varepsilon_n = \begin{cases} 1, & \text{if } n = 0, \\ 2, & \text{if } n \geq 0 \end{cases} \quad (5.23)$$

Dravinski and Mossessian (1987) also studied the scattering of various wave types by dipping layers of arbitrary shape.

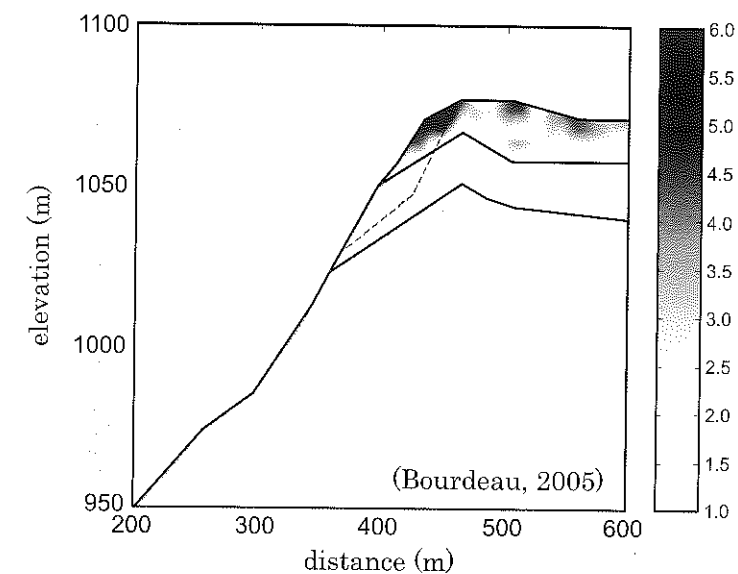


Fig. 5.26: Topographic amplification at the Las Colinas site (Bourdeau, 2005).

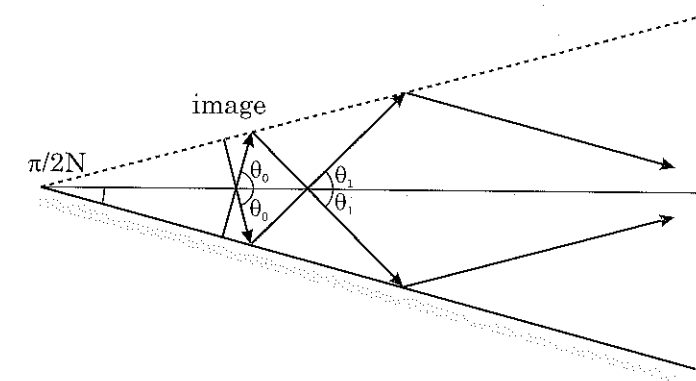


Fig. 5.27: Seismic wave propagation in a dipping layer: description of the problem (Sánchez-Sesma and Velazquez, 1987).

Spectral amplification. The spectral amplification was computed by Sánchez-Sesma and Velazquez (1987) for various angles $\frac{\pi}{2N}$. The results displayed in Fig.5.28 for $N=3,5,7$ lead to the following conclusions:

- the first amplification peak is located at a distance $x = \Lambda$ for $N=3$ and at $x \simeq 2\Lambda$ for $N=7$ (Λ : wavelength),

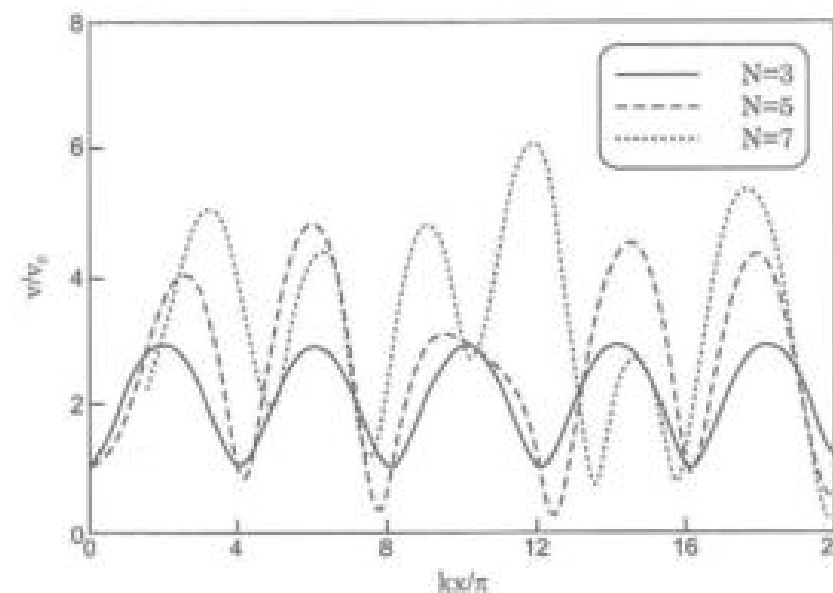


Fig. 5.28: Seismic wave propagation in a dipping layer: amplification for various angles $\pi/2N$ (Sánchez-Sesma and Velazquez, 1987).

- the spectral amplification is larger (up to a factor of 2) for smaller angles,
- the maximum amplification may be found far away from the edge of the layer (e.g. at $x = 6A$ for $N=7$).

It should nevertheless be noticed that the above spectral amplification is computed for a non attenuating medium. Sánchez-Sesma and Velazquez (1987) also proposed some results in the frequency domain for various quality factor values. The influence of attenuation is strong since, in this case, the maximum amplification is reached close to the layer edge. Time-domain results will now be investigated in the damped case.

Time-domain amplification. Considering a 2nd order Ricker wavelet as the incident wavefield (characteristic period t_p), the surface motion was computed at several points by Sánchez-Sesma and Velazquez (1987). The dipping angle is $\pi/14$ and the layer is assumed viscoelastic with a quality factor $Q=20$. The locations of these points and the computed time-histories are displayed in Fig.5.29.

From Fig.5.29, the amplification is found to be large near the layer edge (point 2), whereas the amplitude at other locations is only slightly increased with respect to the incident motion. However, the duration of the seismic motion is much larger at points 3 or 5. These effects are due to the two-dimensional geometry of the layer and may not be found in one-dimensional layers.

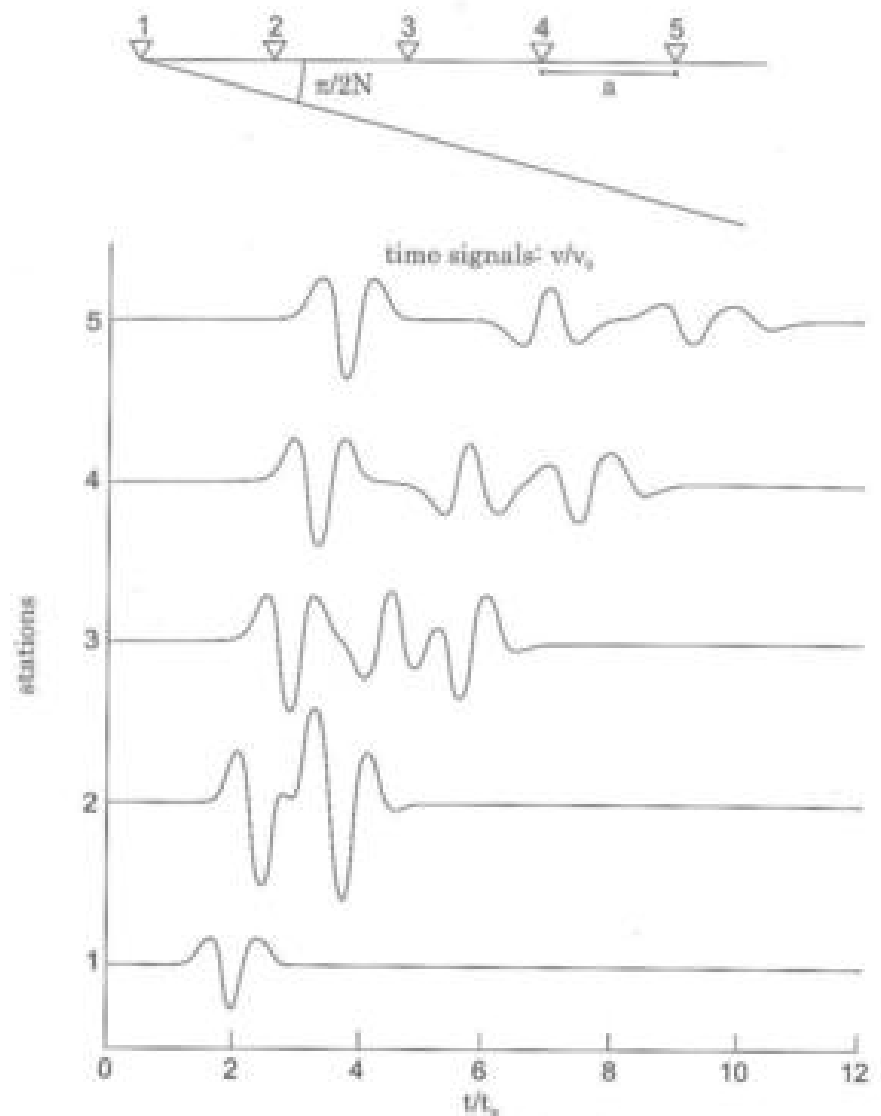


Fig. 5.29: Seismic wave propagation in a dipping layer: time-domain amplification for $N=7$ and $Q=20$ (Sánchez-Sesma and Velazquez, 1987).

Wall-layer system

As depicted in Fig.5.30, the wall-layer system corresponds to a semi-infinite horizontal layer (constant depth). It was firstly studied by Sánchez-Sesma et al. (2000), but recent results were also proposed by Pashucci and Mostabili (2006).

The transfer function derived by Sánchez-Sesma *et al.* (2000) has the following form:

$$V(\omega) = \frac{4}{\pi} \sum_{m=0}^{\infty} \frac{(-1)^m}{2m+1} (\Omega_m^2 - \omega^2 \exp(-ik_m x)) \frac{1}{\Omega_m^2 - \omega^2} \cos \frac{\Omega_m z}{V_S^*} \quad (5.24)$$

where: $\Omega_m = \frac{(2m+1)\pi V_S^*}{2H}$; $k_m = \sqrt{\frac{\omega^2 - \Omega_m^2}{V_S^*}}$; $V_S^* = V_S \left(1 + \frac{i}{2Q}\right)$

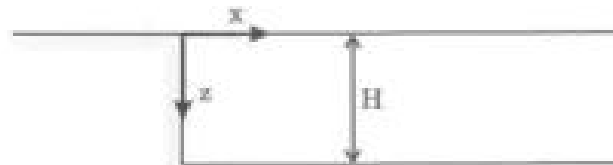


Fig. 5.30: Seismic wave propagation in a wall-layer system: description of the problem (Sánchez-Sesma *et al.*, 2000).

Paolucci and Mostabili (2006) computed the transfer function for various values of the normalized distance, x/Λ , and the normalized frequency, f/f_0 , where f_0 is the fundamental frequency of the 1D layer. They found that the peak responses occur close to the layer edge at normalized distances up to 0.5 or 0.7. The corresponding frequencies are slightly higher than the 1D fundamental frequency due to the lateral confinement of the layer (Paolucci and Mostabili, 2006). These authors also proposed some aggravation factors for both the wedge and wall-layer cases. These aggravation factors were estimated from response spectra with a maximum of about 1.5 for the most severe case (Paolucci and Mostabili, 2006).

5.5.2 Theoretical basins

Since alluvial deposits often have limited geometrical extent, theoretical cases involving two edges will now be investigated. The amplification of seismic waves in such alluvial basins leads to complex propagation patterns due to the influence of both edges.

Rectangular basin

Several authors analyzed the case of rectangular basins considering plane SH -waves. As depicted in Fig.5.31, the rectangular soft layer is embedded in a rigid half-space (depth H , width $2w$). Bard and Bouchon (1985) analyzed the modal features of such a basin and Rodríguez-Zúñiga *et al.* (1995) derived the exact transfer function.

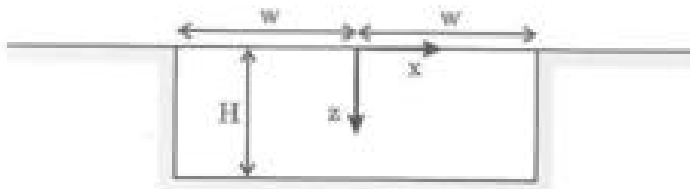


Fig. 5.31: Seismic wave propagation in a rectangular basin: description of the problem (Bard and Bouchon, 1985; Rodríguez-Zúñiga *et al.*, 1995).

Fundamental frequency. Bard and Bouchon (1985) analyzed the anti-plane eigenmodes of the rectangular basin to estimate its modal features. For anti-plane motion, they derived eigenmodes having the following form:

$$u(x, z, t) = \cos(\gamma_m z) \sin(k_n(x + w)) \exp(2i\pi f t) \quad (5.25)$$

$$\text{where: } k_n = \frac{(n+1)\pi}{2w} \\ \text{and: } \gamma_m = \frac{(2m+1)\pi}{2H} \\ k_n^2 + \gamma_m^2 = \frac{4\pi^2 f^2}{V_S^*}$$
(5.26)

The resonant frequencies are therefore (Bard and Bouchon, 1985):

$$f_{n,m} = f_H \sqrt{(2m+1)^2 + (n+1)^2 \frac{H^2}{w^2}} \quad (5.27)$$

$$\text{with: } f_H = \frac{V_S}{4H}$$

The eigenfrequencies defined by Eq.(5.27) depend on the vertical aspect ratio $\kappa_v = H/w$. For the same depth, the fundamental frequency of a narrower basin is then larger than that of a wider basin.

The related mode shapes are depicted in Fig.5.32 in terms of vertical interferences (index m) and horizontal interferences (index n). There are symmetric and antisymmetric modes. In the case of P or SV -waves, which corresponds to in-plane motion, the vertical and horizontal displacements are coupled and the eigenfrequencies may not be expressed in a simple form. Bard and Bouchon (1985) proposed to identify the dependence of the fundamental frequency on the aspect ratio by identification from parametric studies on sine-shaped basins. Choosing a basin half-width L equivalent to $2w$, the identification is very good for anti-plane motion. For in-plane motion, Bard and Bouchon (1985) considered a similar assumption and derived the following approximations:

$$f_0^P = f_H^P \sqrt{1 + \left(\frac{H}{L}\right)^2} \quad (5.28)$$

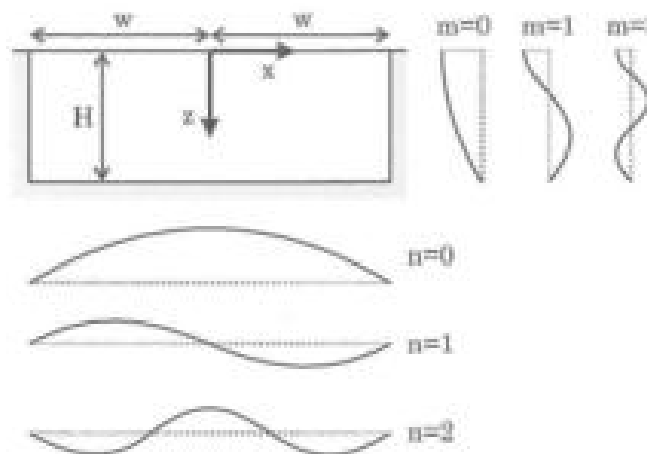


Fig. 5.32: Eigenmodes of a rectangular basin as proposed by Bard and Bouchon (1985).

$$f_0^{SV} = f_R^{SV} \sqrt{1 + \left(\frac{2.9H}{L}\right)^2} \quad (5.29)$$

where f_R^P and f_R^{SV} are the 1D fundamental frequencies.

From these relations, it can be noticed that the ratio between the 2D and the 1D fundamental frequencies is larger for SV -waves. The influence of the vertical aspect ratio $\kappa_v = H/L$ is then larger for horizontally polarized waves (i.e. vertically incident SV -waves). As depicted in Fig. 5.33, the influence of the basin width is much larger in the case of shear waves. From their work, Bard and Bouchon (1985) defined two different ranges for the aspect ratio: for small aspect ratios (between 0 and 0.3), where 1D propagation and lateral propagation are combined, whereas for larger aspect ratios, 2D resonance dominates.

Exact solution. For plane oblique SH -waves in rectangular basins, Rodriguez-Zamora et al. (1995) derived the exact solution in terms of harmonic displacement $u(x, z, \omega)$:

$$\frac{u}{u_0} = \frac{4}{\pi} \sum_{n=0}^{\infty} \left\{ \frac{(-1)^n}{2n+1} \frac{1}{\omega_n^2 - \omega^2} \times \left[\omega_n^2 e^{-ik_n z} - \omega^2 \left(\cos k_n a \frac{\cos k_n x}{\cos k_n a} - i \sin k_n a \frac{\sin k_n x}{\sin k_n a} \right) \right] \frac{\cos \omega x}{V_{S_1}} \right\} \quad (5.30)$$

where u_0 is the displacement at the base of the rectangular deposit, h the basin depth, a its half-width, V_{S_1} and V_{S_2} are the shear wave velocities in the bedrock and the basin,

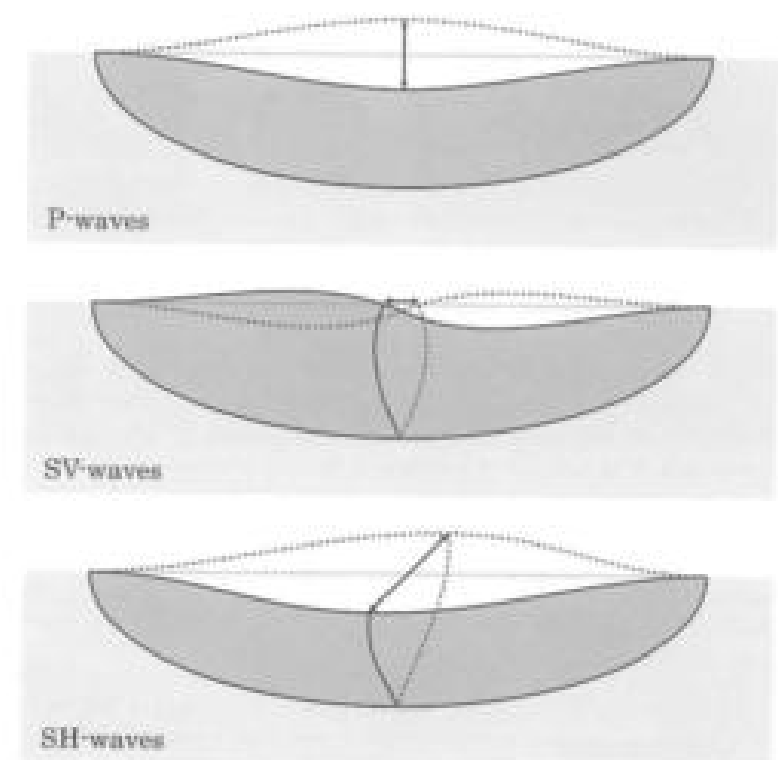


Fig. 5.33: Basin modes for various wave types as proposed by Bard and Bouchon (1985).

respectively, θ the wave incidence, and denoting:

$$\left\{ \begin{array}{l} \omega_0 = \frac{2\pi V_{S_1}}{4h} \\ \omega_n = (2n+1)\omega_0 \\ \bar{\omega} = \omega \sqrt{1 - \frac{V_{S_1}^2}{V_{S_2}^2} \sin^2 \theta} \\ k' = \frac{\omega}{V_{S_1} \sin \theta} \\ k_n = \frac{\sqrt{\omega^2 - \omega_n^2}}{V_{S_1}} \end{array} \right. \quad (5.31)$$

From these expressions, the basin response may be computed. Rodriguez-Zamora et al. (1995) also analysed the case of a cylindrical 3D basin having its vertical cross-section identical to the previous 2D rectangular model (i.e. axisymmetrical around the vertical

axis). They found that the difference between the 2D and the 3D models is large at the centre of the basin. Near the basin edge, the difference is much less.

Sine-shaped basins

Bard and Bouchon (1985) studied 2D sine-shaped basins and derived a simple relation to discriminate between 2D resonances and 1D resonances of geological profiles:

$$\left(\frac{H}{L}\right)_c = \frac{0.65}{\sqrt{C_v - 1}} \quad (5.32)$$

Considering the velocity contrast between the basin and the bedrock, denoted C_v , as well as the shape ratio H/L (H : depth; L : width), their empirical relation defines the values $(C_v, H/L)$ leading to 2D resonances and those leading to 1D resonance combined to lateral propagation (Fig. 5.34). For a shape ratio of 1, the velocity contrast should be larger than 2 to reach 2D resonance.

To derive this relation, Bard and Bouchon (1985) compared the motion phase for various cases and defined as 2D resonances the situations where the phase is constant along a sufficient part of the basin surface. In such cases, the 2D geometry has a significant effect on the modal features of the basin.

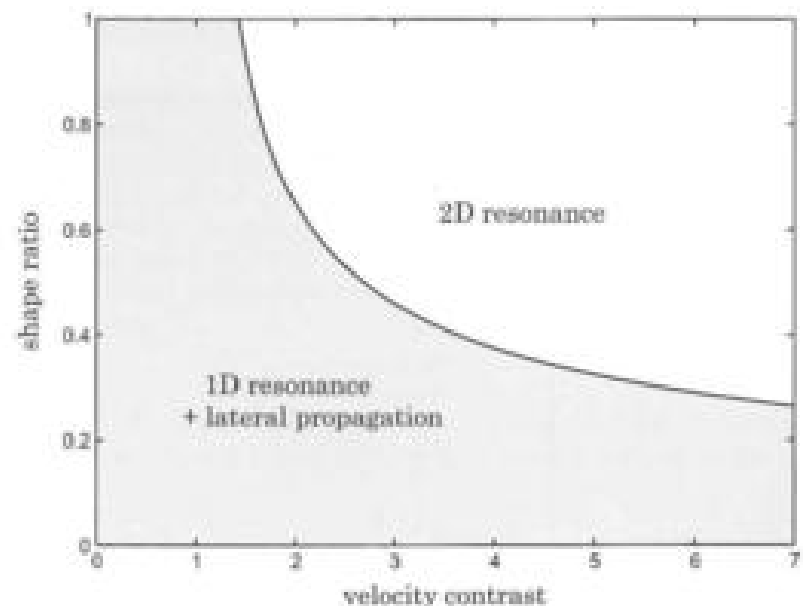


Fig. 5.34: Limit between 1D and 2D resonances as proposed by Bard and Bouchon (1985).

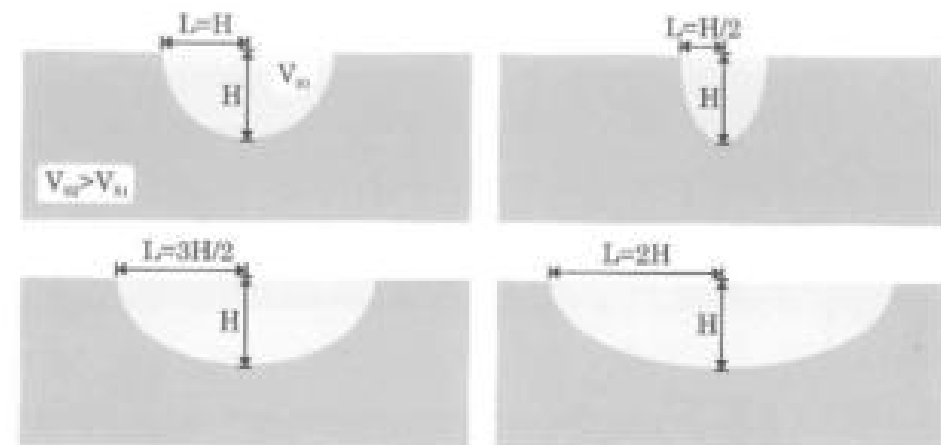


Fig. 5.35: Cylindrical basins with variable horizontal shape ratios $\kappa_h = L/H$.

Otherwise, 1D resonance dominates and lateral propagation due to the finite geometrical extent of the basin is observed. In this case, the fundamental frequency of the basin is not significantly influenced by its 2D geometry. Nevertheless, as it will be discussed in the following for actual shallow basins, the influence of lateral propagation on the amplification level may be large.

5.5.3 Cylindrical basins

In addition to the case of rectangular and sine-shaped basins, the influence of the basin geometry will now be investigated in the case of 2D circular basins (i.e. cylindrical with a circular cross-section). The case of 3D theoretical basins will be discussed in the next section.

As depicted in Fig. 5.35 (top left), we consider in this paragraph a homogeneous elastic circular basin (half-width L equivalent to the depth H) having a shear wave velocity V_{S_2} laying over a homogeneous elastic half-space with $V_{S_1} > V_{S_2}$. The propagation of plane vertical SH -waves is analyzed using the Boundary Element Method in the frequency domain (Bonnet, 1999; Dangla, 1988). Similarly to previous studies, the analysis is performed considering dimensionless variables such as the amplification factor A , the velocity contrast ($V_{S_2} > \sqrt{2}V_{S_1}$ herein) and finally the depth/wavelength ratio (i.e. H/Λ) which is, for a constant depth, proportional to the frequency.

The amplification factor at the free-surface is depicted in Fig. 5.36 as a function of the normalized distance x/L for different values of the depth/wavelength ratio H/Λ . The maximum amplification factor is about 1.7 for normalized frequency values $H/\Lambda=0.34$ and 0.87. For these frequencies, the maximum amplification is found at the centre of the basin. Conversely, for the normalized frequency $H/\Lambda=0.62$, the maximum amplification

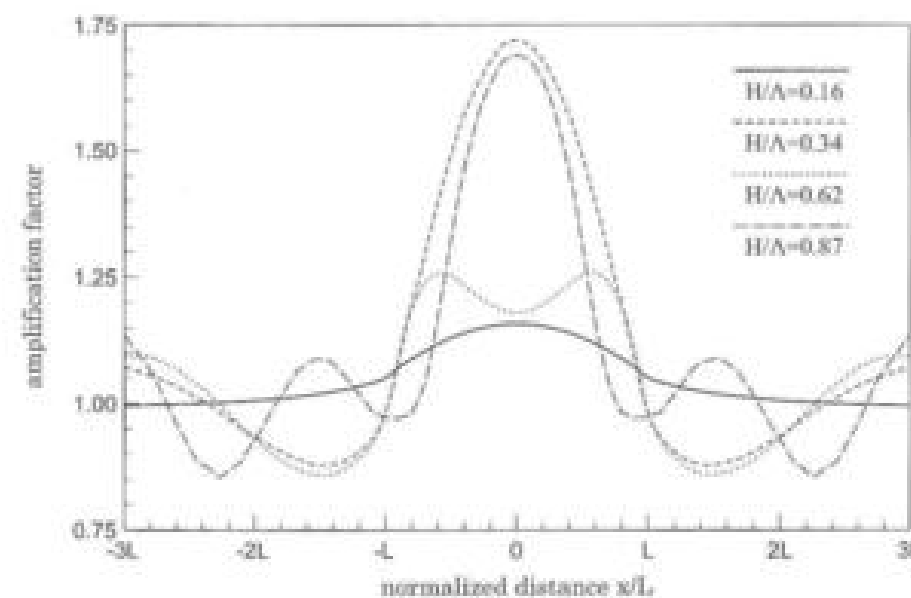


Fig. 5.36: Amplification A at the surface of a circular basin for various depth/wavelength ratios: $H/\lambda=0.16$; $A=1.15$ - $H/\lambda=0.34$; $A=1.72$ - $H/\lambda=0.62$; $A=1.56$ - $H/\lambda=0.87$; $A=1.83$.

appears at the basin edges. These results may also be analyzed at depth. As shown in Fig.5.37, the maximum amplification values are reached at the free-surface except for the normalized frequency $H/\lambda=0.87$. In this case, the amplification at the surface reaches 1.7 (Fig.5.36) whereas the maximum is above 1.8 at depth (Fig.5.37). For higher frequencies, depending on the basin geometry, focusing effects may occur and modify the motion amplification.

5.5.4 Cylindrical basin vs horizontally layered soil

In order to assess the 2D effects in the ground motion amplification, the numerical results for a cylindrical basin are compared to the case of a single layer soil. As already shown in Chapter 3, for a plane SH -wave, the amplification in a single layer soil can be quantified theoretically through the following transfer function:

$$|T_{12}(\omega)| = \frac{1}{\sqrt{\cos^2 k_{z_1} H + \tilde{\chi}^2 \sin^2 k_{z_1} H}} \quad (5.33)$$

$$\text{with: } k_{z_1} = \frac{\omega \cos \theta_1}{V_{S_1}} \quad \text{and} \quad \tilde{\chi} = \sqrt{\frac{\rho_1 \mu_1 \cos \theta_1}{\rho_2 \mu_2 \cos \theta_2}} \quad (5.34)$$

where ω is the circular frequency, (V_{S_1}, μ_1) and (V_{S_2}, μ_2) are the velocities and shear moduli in the basin and the bedrock respectively, θ_1 and θ_2 are the angles between the

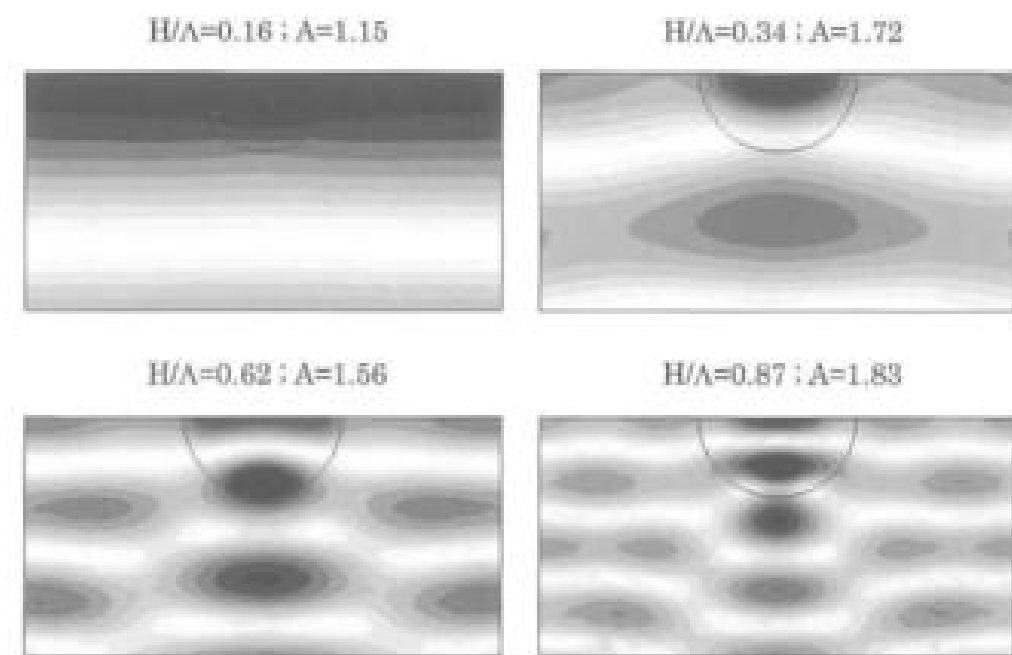


Fig. 5.37: Amplification of the seismic motion in a cylindrical basin for various depth/wavelength ratios (H/λ) with A denoting the maximum amplification factor.

direction of propagation of the wave and the vertical direction, in the layer and the bedrock respectively (θ_1 is calculated from θ_2 (Chapter 3)).

The motion amplification due to the single layer soil is determined from Eq.(5.33) using the same properties as for the cylindrical basin and considering two different thicknesses:

- the layer thickness H_1 is identical to the maximum depth of the cylindrical basin, that is $H_1 = H$,
- the layer thickness H_1 is smaller than the maximum depth of the cylindrical basin, that is $H_1 = H/\sqrt{2}$.

In Fig.5.38, the amplification obtained for the one-layered soil with two different thicknesses is compared to that reached in the cylindrical basin. The horizontal scale corresponds to the normalized frequency H/λ .

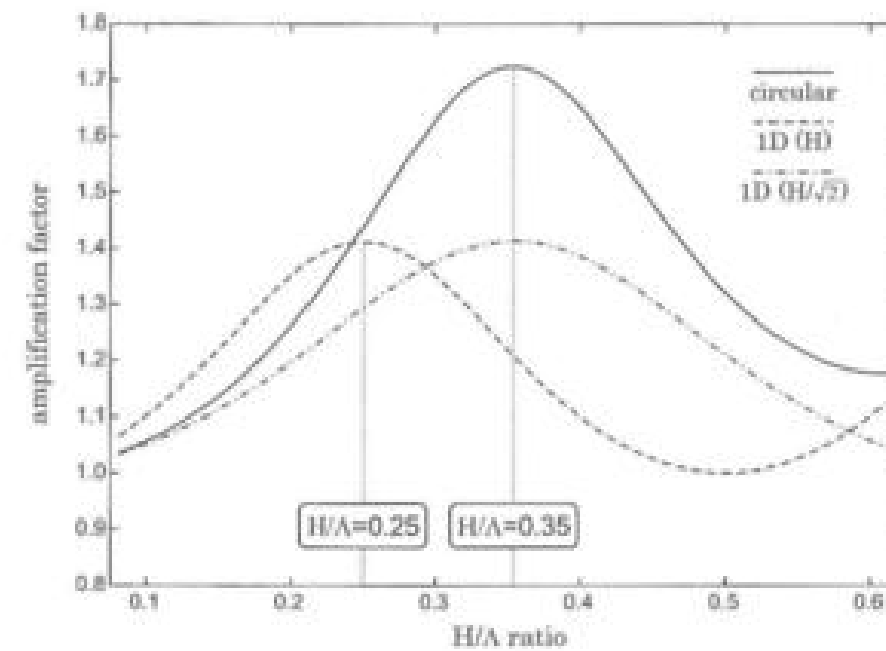


Fig. 5.38: Amplification for a single layer soil and a cylindrical basin ($H_l = H$ and $H_l = H/\sqrt{2}$) as a function of the normalized frequency H/λ .

The main differences between both types of alluvial deposits are the following:

- the two cases involving a single layer soil ($H_l = H$ and $H_l = H/\sqrt{2}$) lead to the same maximum amplification value (1.41) since it only depends on the mechanical properties of the layer (the corresponding frequency nevertheless depending on the layer thickness).
- the amplification obtained at the centre of the cylindrical basin (1.73) is significantly larger than in the single layer cases. For the cylindrical basin, a 2D effect hence strengthens the amplification of seismic waves when compared to a horizontal layer having the same depth.
- the frequency of the amplification peak is larger for the cylindrical basin ($H/\lambda=0.35$) than for the one-layered soil with thickness $H_l = H$ ($H/\lambda=0.25$ as classically admitted). Conversely, for a thickness $H_l = H/\sqrt{2}$, the one-layered case leads to the same frequency as the cylindrical basin (Fig.5.38). In terms of fundamental frequency, the cylindrical basin is then close to a one-layered soil with a thickness $H_l = H/\sqrt{2}$. It is due to the fact that the cylindrical basin is stiffer than the one-layered soil (finite geometrical extent).

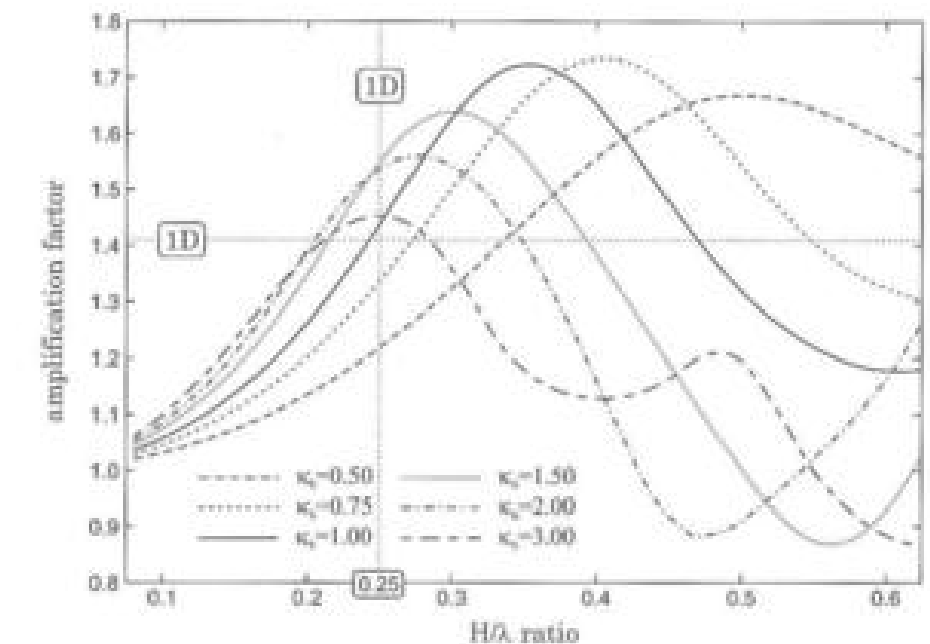


Fig. 5.39: Amplification factor at the centre of elliptical basins as a function of the normalized frequency (H/λ) for various horizontal shape ratios κ_h ($\kappa_h=0.5, 0.75, 1.0, 1.5, 2.0$ and 3.0): comparison with the 1D case.

5.5.5 Elliptical basins with variable shape ratio

Previous results show a significant amplification increase in the case of a cylindrical basin because of 2D effects influencing seismic wave propagation. In order to assess the 2D effects for ground motion amplification, various shape ratios are now considered. As depicted in Fig.5.35, the horizontal shape ratio is defined as $\kappa_h = L/H$ and is equal to 1 for a circular basin. The various cases considered herein correspond to the following shape ratio values: $\kappa_h=0.5$; $\kappa_h=0.75$; $\kappa_h=1.0$; $\kappa_h=1.5$; $\kappa_h=2.0$ and $\kappa_h=3.0$. Starting from the circular case, two narrow basin cases and three wide basin cases are investigated. The amplification-frequency curves at the centre of the basin are compared for all shape ratios in Fig.5.39.

From Fig.5.39, the influence of the shape ratio on the ground motion amplification may be characterized as follows:

- the shape ratios below 1 lead to lower amplification levels,
- the normalized frequency related to the maximum amplification decreases when the shape ratio increases (weaker 2D effects),
- for the largest shape ratio ($\kappa_h=3.0$), the maximum amplification (1.45) is close to

Table 5.1: Comparison of maximum amplifications and related normalized frequencies for elliptical alluvial basins with variable shape ratio.

Shape ratio	A_{\max}	H/λ for A_{\max}
$\kappa_h = 0.50$	1.67	0.50
$\kappa_h = 0.75$	1.73	0.40
$\kappa_h = 1.00$	1.73	0.35
$\kappa_h = 1.50$	1.64	0.31
$\kappa_h = 2.00$	1.56	0.27
$\kappa_h = 3.00$	1.45	0.26

that obtained for the one-layered soil (1.41) and the related normalized frequency (0.26) is slightly different from that of the 1D case (0.25 for $H_l = H$).

For each shape ratio, the maximum amplification and the related normalized frequencies are gathered in Table 5.1. In addition to these two parameters, the shape ratio may also influence the location of the maximum amplification areas (basin edge effects, focusing effects, etc). In the following, 3D theoretical cases will firstly be discussed and actual alluvial basins will then be considered.

5.5.6 2D/1D aggravation factor

As shown by previous results, the influence of 2D effects may be large. For actual basins, it is possible to consider codes provisions, mainly based on 1D analyses, or to record and compute the 2D wavefield in the geological profile. Since it may be costly in terms of geotechnical investigation and numerical requirements, some authors proposed simplified methods to account for 2D effects. Pitilakis et al. (1999) proposed an aggravation factor in order to increase the amplification level from 1D analysis to 2D predictions. These authors analyzed seismic wave amplification in the Volvi basin (Greece) and performed numerous 1D and 2D analyses. From these comparisons, they found that the 2D effects are significant and proposed the following 2D/1D aggravation factor, denoted \bar{A} :

$$\begin{cases} \bar{A} = 1 + 2 \left(\frac{T}{T_1} \right)^3 & \text{for } T \in [0, T_1] \\ \bar{A} = 3.0 & \text{for } T \in [T_1, T_2] \\ \bar{A} = 1 + 2 \left(\frac{T_2}{T} \right)^3 & \text{for } T \in [T_2, T_{\max}] \end{cases} \quad (5.35)$$

As depicted in Fig.5.40, in the period range $[T_1, T_2]$, the aggravated spectral amplification is hence three times the 1D spectral amplification. The aggravation factor decreases rapidly for shorter, and longer, periods. This proposal is very interesting since it accounts for 2D effects in a simple way. The aggravation level, and related period range, should probably be assessed for various basin geometries and different soil layering.

5.6 Amplification of seismic waves in 3D alluvial basins

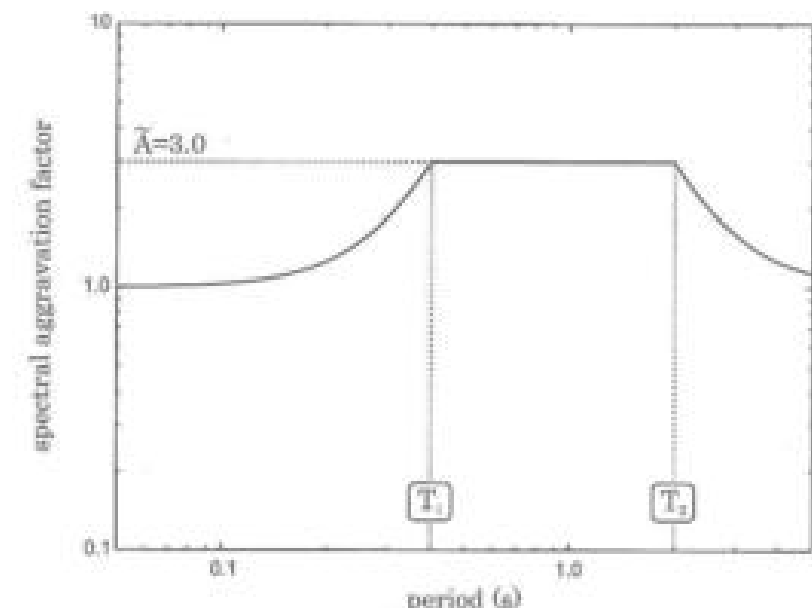


Fig. 5.40: Spectral aggravation factor as proposed by Pitilakis et al. (1999).

Since it is a well documented site studied by many authors (Chávez-García et al., 2000; Makra et al., 2002; Pitilakis et al., 1999; Riepl et al., 1998; Scambia et al., 2005), wave amplification at the Volvi Euroseistest site will be investigated in the following.

5.6 Amplification of seismic waves in 3D alluvial basins

The amplification of seismic waves is now investigated in the case of 3D alluvial basins. Various theoretical basins have been proposed by several authors: the semi-spherical basin (Sánchez-Sesma, 1983), the semi-ellipsoidal basin (Clouetan, 1990; Mossessian and Dravinski, 1990), the moon-valley model (Sánchez-Sesma and Luzón 1995), etc. Some results showing the influence of 3D effects are discussed in this section.

5.6.1 Semi-spherical basin

Description of the problem

Numerous papers have investigated the 3D wave diffraction by a semi-spherical canyon (Lee, 1978; Liao et al., 2004; Yokoi, 2003) or 3D seismic wave amplification by surface heterogeneities (Dravinski, 2003; Komatitsch and Vilotte, 1998; Moczo et al., 2002; Sánchez-Sesma, 1983; Sánchez-Sesma and Luzón, 1995). The first example considered in this section corresponds to a semi-spherical alluvial basin in an elastic half space. As depicted in Fig.5.41, the basin radius is denoted R and a plane P -wave is considered.

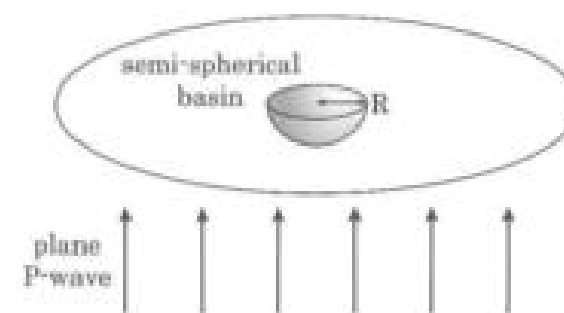


Fig. 5.41: Amplification of a plane vertical P -wave by a semi-spherical basin: model description.

Several results have been published for the case of a semi-spherical alluvial basin (Dravinski, 2003; Lec, 1984; Sánchez-Sesma, 1983). The results of Sánchez-Sesma (1983) are derived using a series expansion method. For the semi-spherical basin and the half-space, Sánchez-Sesma chose the mechanical parameters as follows:

- shear moduli: $\mu_R/\mu_E = 0.3$,
- mass densities: $\rho_R/\rho_E = 0.6$,
- Poisson's ratios: $\nu_R = 0.30$ and $\nu_E = 0.25$.

where subscript R refers to the alluvial basin and subscript E to the half-space.

Reference solution

Similarly to the previous sections, the results were computed by Sánchez-Sesma (1983) in the frequency domain at a given normalized frequency corresponding to the diameter-to-wavelength ratio $\eta_P = 2R/\Lambda_P$ where Λ_P is the P wavelength in the alluvial basin.

In Fig. 5.42, the amplification of the seismic motion computed by Sánchez-Sesma (1983) at the free-surface is displayed vs normalized distance x/R (normalized frequency $\eta_P = 0.50$). The amplification factor at the centre of the semi-spherical basin for the vertical component is 2.82 (i.e. 5.64 in amplitude to be compared to 2.00 for the half-space). This amplification value is larger than for the one-layered case or the 2D circular basin (§5.5.3) since, for the semi-spherical basin, focusing effects are very strong (Sánchez-Sesma, 1983; Dangla et al., 2005).

As shown in Fig. 5.42, a horizontal motion component due to wave conversions also appears. At this frequency, the maximum horizontal motion is reached at approximately $x/R=0.5$. It should be noticed that the normalized frequency $\eta_P = 0.50$ corresponds to the fundamental frequency of the 1D case (the wavelength being $\Lambda_P = 4R$ with R the depth of the basin). As already shown in the 2D circular case (§5.5.3), the fundamental

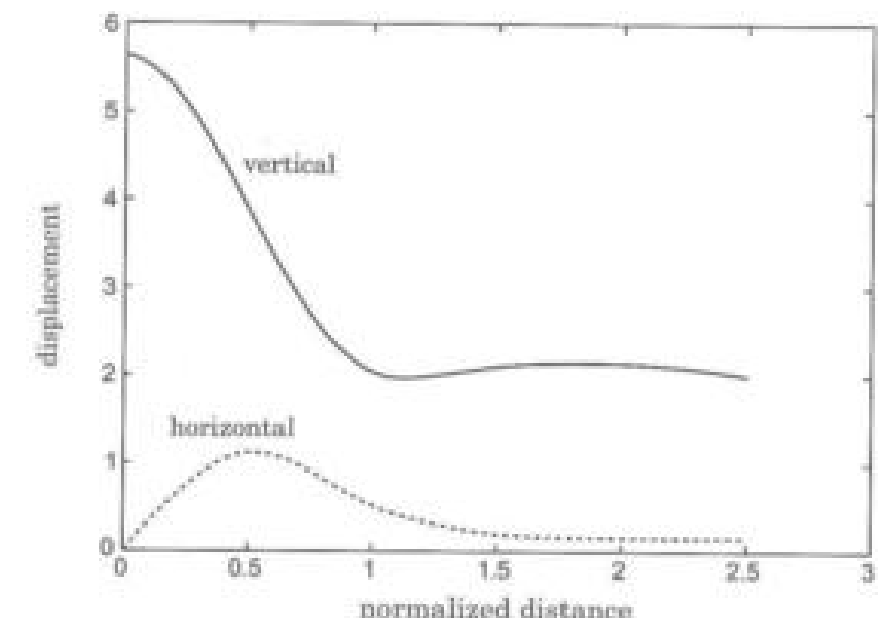


Fig. 5.42: Vertical and horizontal surface motions computed by Sánchez-Sesma (1983) for a semi-spherical basin at normalized frequency $\eta_P = 0.50$.

frequency for the 3D semi-spherical basin is surely much higher.

5.6.2 Sine-shaped basin

As also considered by Bard and Bouchon (1985) in the 2D case, Sánchez-Sesma (1983) computed the amplified wavefield in the case of 3D axisymmetrical sine-shaped basins (vertically incident P -wave). The numerical results are plotted in Fig. 5.43 (solid line) for normalized frequency $\eta_P = 0.50$. At the centre of the basin, the vertical component is amplified by a factor close to 3 (when compared to free-field), that is very close to the amplification factor obtained for the semi-spherical basin (dashed line). The amplitude of the transverse component is also equivalent to the previous case.

However, the spatial variation of the amplitude is much faster than in the semi-spherical case. This is certainly due to the fact that the effective width for the sine-shaped basin is smaller than its real width due to very small dipping angles at its edges. As suggested by Bard and Bouchon (1985), the actual width of the sine-shaped basin must be reduced by a factor of about 2. Such a scaling factor has been applied to the results of the sine-shaped basin to plot the dotted curve in Fig. 5.43. It appears that, for normalized frequency $\eta_P = 0.50$, these scaled results are very close to the results of

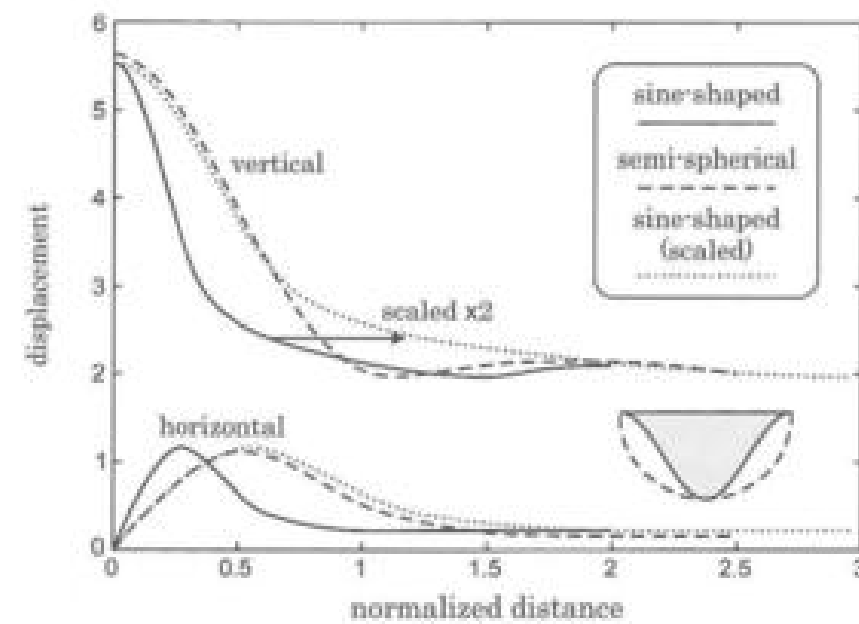


Fig. 5.43: Surface motion computed by Sánchez-Sesma (1983) for a 3D sine-shaped basin at normalized frequency $\eta_F = 0.50$: comparison with the semi-spherical case (dashed) and the scaled sine-shaped case (dotted).

the semi-spherical basin. The equivalence suggested by Bard and Bouchon (1985) for 2D sine-shaped basins hence appears to be valid in the 3D case.

5.6.3 Semi-spherical basin and oblique incidences

Using the FM-accelerated BEM, Chaillat et al. (2009) computed the seismic wavefield for an oblique incident *SV*-wave. Such results were also proposed by Mossessian and Dravinski (1990) and comparisons between both numerical methods were performed by Chaillat et al. (2009).

In the case of an oblique incident *P*-wave ($\theta = 30^\circ$), the numerical results from Chaillat (2008) are plotted in Fig. 5.44 for two different normalized frequencies $k_p a/\pi = 1.0$ (left) and $k_p a/\pi = 2.0$ (right). The three motion components are displayed: $|U_x|$ (top), $|U_y|$ (middle) and $|U_z|$ (bottom). The spectral amplification is found to be large in the basin but, due to the oblique incidence, the propagation phenomena are very different along the *x* and *y* axes.

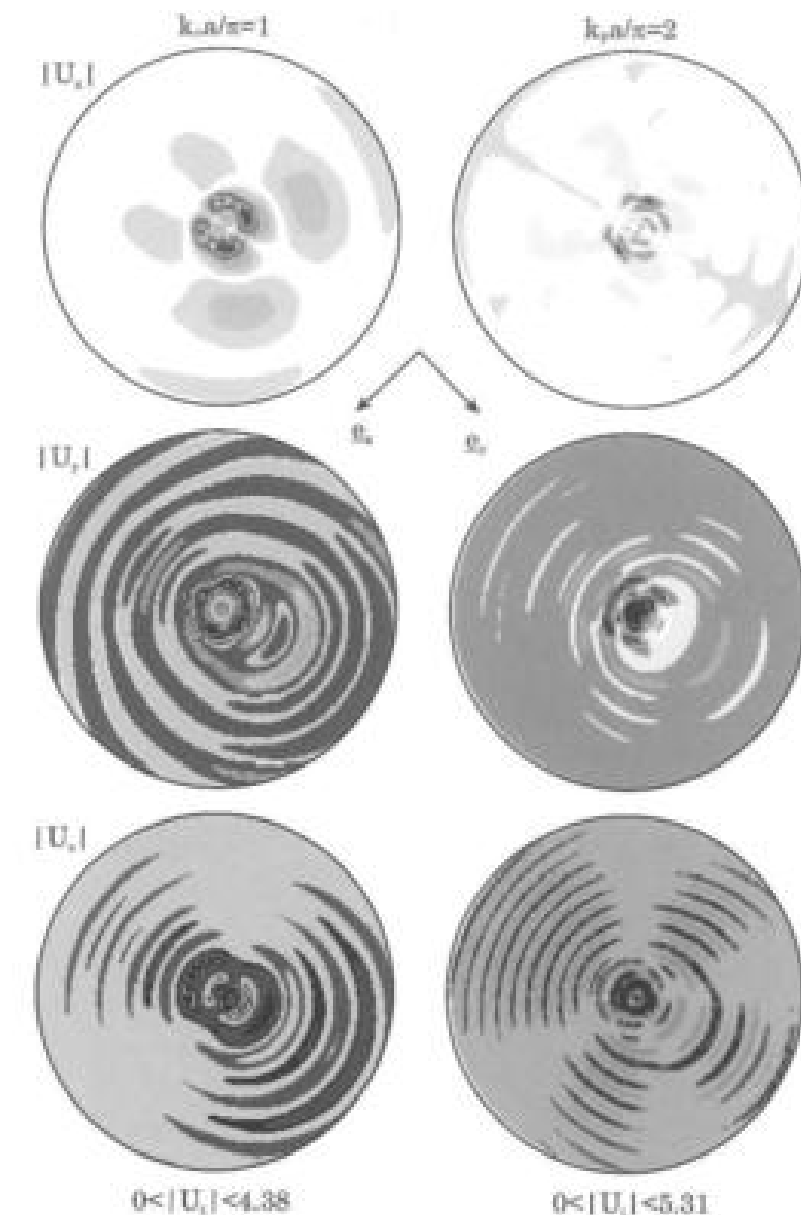


Fig. 5.44: Amplification of a plane oblique *P*-wave ($\theta = 30^\circ$) in a semi-spherical basin at normalized frequencies 1.0 (left) and 2.0 (right): $|U_x|$ top, $|U_y|$ middle and $|U_z|$ bottom, from (Chaillat, 2008). See <http://qsha.obs.ujf-grenoble.fr> for data and additional results.

5.6.4 Semi-ellipsoidal basin

The case of semi-ellipsoidal basins, which are non-axisymmetric, has mainly been investigated by Mossessian and Dravinski (1990) and Clousteau (1990). They computed the seismic wavefield in the time domain as well as in the frequency domain. Their results are very different when considering the major or the minor axis due to the asymmetry of the basin (and possibly the incidence if it is oblique). Chaillat et al. (2009) recently modelled this problem using the Fast Multipole Method and comparing with Mossessian and Dravinski (1990). For a plane oblique *SV*-wave ($\theta = 30^\circ$) at normalized frequencies 0.25 and 1.0, the seismic wavefield computed by Chaillat et al. (2009) is displayed in Fig.5.45.

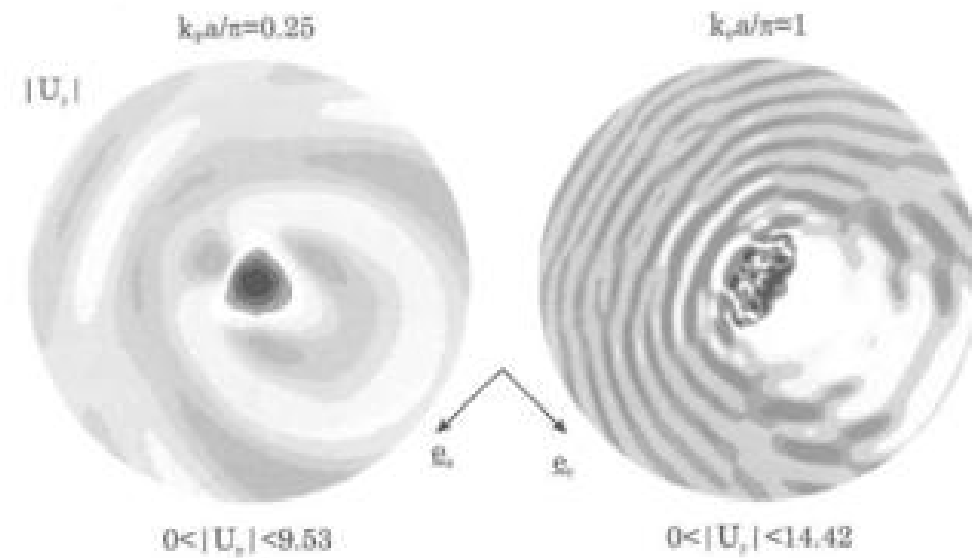


Fig. 5.45: Amplification of a plane oblique *SV*-wave ($\theta = 30^\circ$) in a semi-ellipsoidal basin at normalized frequencies 0.25 (left) and 1.0 (right), from (Chaillat et al., 2009).

5.6.5 Moon-valley model

The moon-valley model is also a typical 3D non-axisymmetric model: a large semi-sphere is truncated by a smaller semi-sphere to generate a moon-shaped surface (Fig.5.46). This model was for instance studied by Sánchez-Sesma and Luzon (1995). For such a basin, Stupazzini (2004) computed the 3D seismic wavefield in time-domain by the Spectral Element Method. His results are displayed in Fig.5.46 (bottom) for an oblique ($\theta = 30^\circ$) plane *SH*-wave. The seismograms show that interesting propagation and amplification phenomena occur in such a non axisymmetrical basin. Stupazzini (2004) also compared his results with those computed by Sánchez-Sesma and Luzon (1995).

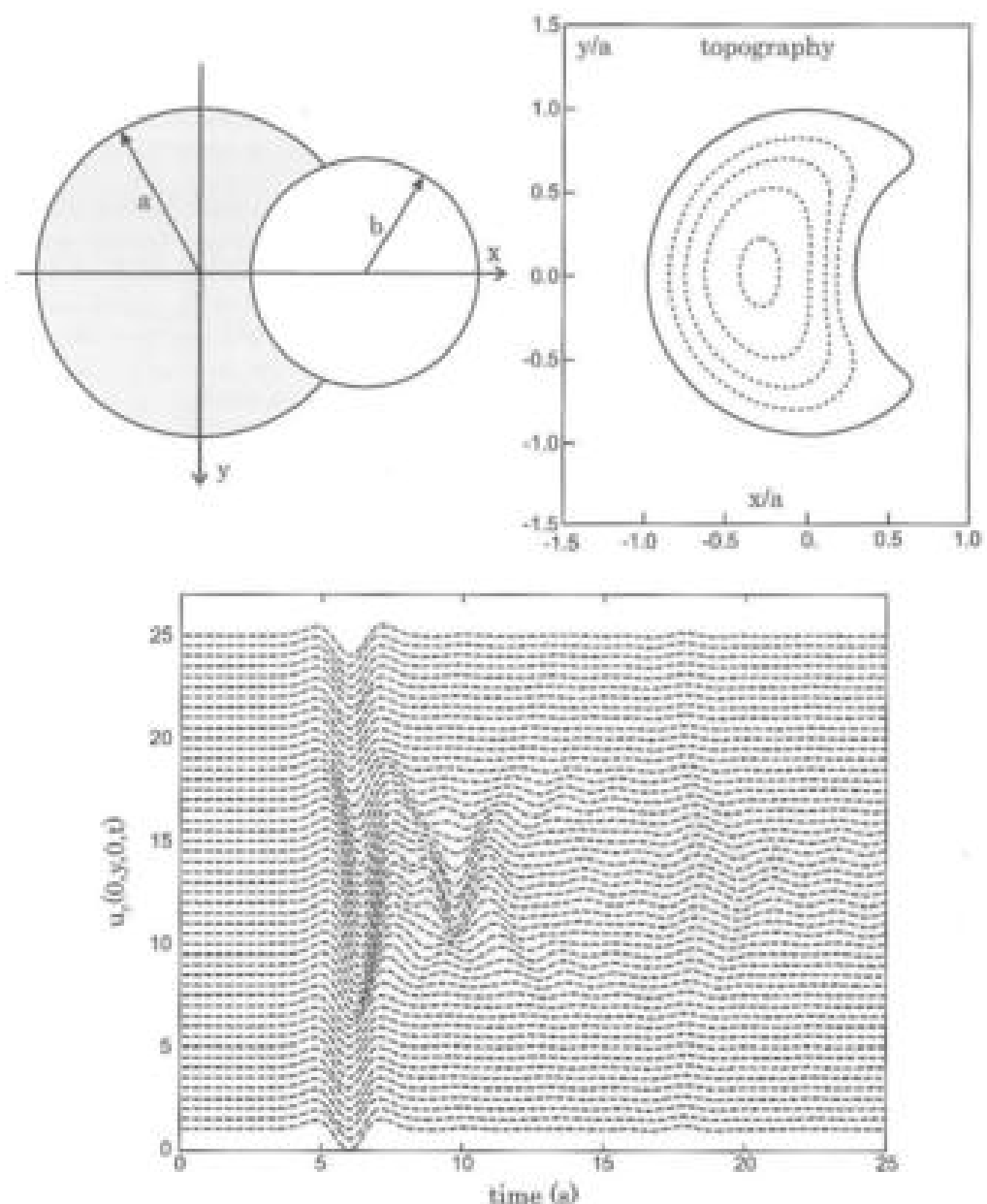


Fig. 5.46: 3D moon-valley geometry (top) studied by various authors (e.g. Sánchez-Sesma and Luzon, 1995). Numerical results (bottom) computed in time domain by the Spectral Element Method (Stupazzini, 2004).

5.7 Modal approaches to analyze site effects

5.7.1 Amplification of the seismic motion and resonance

The amplification of the seismic motion in alluvial basins is mainly due to the resonance of surficial layers at peculiar frequencies. Site effects may thus be analyzed in terms of vibratory resonance of a surface geological structure (Bard and Bouchon, 1985; Dobry et al., 1976; Paolucci, 1999). Dobry et al. (1976) proposed several closed-form solutions to estimate the fundamental frequency of simple geological structures (two-layered, multi-layered soils, etc). In this section, the fundamental frequency of a geological structure is determined through a simplified modal approach based on Rayleigh's approximation (Paolucci, 1999). A full modal characterization of an actual site will also be proposed.

5.7.2 Various types of modal approaches

The use of modal approaches to characterize geological structures is widely spread (Paolucci, 1999; Zhao, 1996). These approaches generally yield the fundamental frequency of geological structures accounting for their geometry (Bard and Bouchon, 1985; Paolucci, 1999; Semblat et al., 2003a,b) or the heterogeneities in the deposit (Dobry et al., 1976; Hadjim, 2002; Pecker, 2005; Zhao, 1996). Starting from several simple assumptions, it is hence possible to estimate the fundamental frequency of various alluvial deposits. It is nevertheless difficult to directly compare the various frequencies in terms of amplification. The main assumptions considered in these modal methods will be compared in the following.

Methods adapted to 1D fillings

Dobry et al. (1976) were the first ones to propose a full modal characterization of geological structures. For a homogeneous or inhomogeneous horizontal layer (linear variation of the shear modulus) or a multilayered soil, they proposed closed-form solutions for the fundamental period of geological structures. For a horizontal layer with thickness H and shear modulus μ varying linearly with the depth z , they assumed the following expression for $\mu(z)$:

$$\frac{\mu(z)}{\mu_H} = K^2 + \frac{1 - K^2}{H} z \quad (5.36)$$

where $K = \sqrt{\frac{\mu_0}{\mu_H}}$, μ_0 and μ_H denoting the modulus at the top and at the base of the layer.

To estimate the period of the layer, denoted by T , Dobry et al. derived the properties of the homogeneous equivalent layer writing $T = \frac{4H}{V_{eq}}$, where $V_{eq} = \sqrt{\frac{G_{eq}}{\rho}}$ at the equivalent depth z_{eq} defined by:

$$\frac{z_{eq}}{H} = \left(\frac{a_1}{H}\right)^2 (1 - K^2) - \frac{K^2}{1 - K^2} \quad (5.37)$$

where a_1 is the first root of equation:

$$J_0(a_1)Y_1(Ka_1) - J_1(Ka_1)Y_0(a_1) = 0 \quad (5.38)$$

5.7 Modal approaches to analyze site effects

J_i and Y_i denote the order i Bessel and Weber Bessel functions (resp.). Dobry et al. (1976) also proposed a generalization of these results for two-layered and multi-layered soils. Using this method, more recent results (Hadjim, 2002) proposed an iterative approach to estimate the fundamental period of multi-layered deposits.

In the case of arbitrary variations of the shear modulus μ with depth z , closed-form solutions proposed by Pecker (2005) are presented in Chapter 2 (§2.12).

Methods for 2D or 3D deposits

To characterize the resonance of alluvial basins, Paolucci (1999) proposed a simplified method involving the Rayleigh approximation. This method may be used for any type of 2D or 3D deposit. It consists in minimizing the ratio between the strain energy and the kinetic energy in order to estimate the fundamental frequency. This method is described in details in §5.7.3 and is used to estimate the modal features of an actual alluvial deposit.

5.7.3 Simplified modal method

The modal method considered herein aims at estimating the fundamental frequency of a geological structure. Wave propagation is a complex phenomenon leading to a strong amplification at various frequencies (Semblat et al., 2000) but, as a practical goal, it is interesting to determine the fundamental frequency through simplified approaches. As shown by Paolucci (1999), the Rayleigh method allows a fast and reliable estimation of the fundamental frequency of a geological structure.

This method considers that the displacement of an elastic system in one of its eigenmodes may be approximated by that of a one degree of freedom system. We shall investigate herein the first eigenmode characterized by the frequency $\omega_0 = 2\pi f_0$. Denoting W the elastic energy of the system and K its kinetic energy, the conservation of the total energy of an elastic system implies that $W_{max} = K_{max}$. The displacement $u_k(x, t)$ corresponding to the time-harmonic vibrations at frequency ω_0 may be written as:

$$u_k(x, t) = \psi_k(x)e^{i\omega_0 t} \quad (5.39)$$

where x denotes the space coordinate, $i = \sqrt{-1}$, t the time and $\psi_k(x)$ the modal shape along direction k . The kinetic energy may hence be calculated:

$$K(t) = \int_{\Omega} \frac{1}{2} \rho(x) \left(\frac{\partial u_k}{\partial t} \right)^2 d\Omega = -\omega_0^2 e^{2i\omega_0 t} \int_{\Omega} \frac{1}{2} \rho(x) \psi_k^2(x) d\Omega \quad (5.40)$$

$$\text{thus: } K_{max} = \max_t K(t) = -\omega_0^2 \int_{\Omega} \frac{1}{2} \rho(x) \psi_k^2(x) d\Omega \quad (5.41)$$

The elastic energy W hence reads as follows:

$$W(t) = \int_{\Omega} \sigma_{jk}(x) e_{jk}(x) d\Omega \quad (5.42)$$

where $\epsilon_{ij} = \frac{1}{2}(u_{i,j} + u_{j,i})$ is the strain tensor and $\sigma_{ij} = \lambda c_{ij}\delta_{ij} + 2\mu c_{ij}$ the stress tensor obtained through Hooke's law with δ_{ij} the Kronecker symbol, λ and μ the Lame coefficients.

As for K_{max} , W reaches its maximum value when $|e^{2\omega_0 t}| = 1$. We thus obtain:

$$\omega_0^2 = \frac{\int_{\Omega} \sigma_{ji}(x) e_{ji}(x) d\Omega}{\int_{\Omega} \rho(x) \psi_k^2(x) d\Omega} \quad (5.43)$$

The fundamental frequency of the model, Eq.(5.43), leads to the exact fundamental frequency of the system when the actual mode shape is known. However, since the exact solution is generally unknown, the value of ω_0 may be estimated through an adequate approximation, $\tilde{\psi}_k$, of ψ_k . This approximation must fulfill the geometrical compatibilities and the boundary conditions. Nevertheless, Paolucci (1999) demonstrated that the second condition may not be fully satisfied and that the modal shape may be chosen in a wide variety of functions only satisfying the geometrical compatibilities. One may then estimate the fundamental frequency using the following expression:

$$\omega_0^2 \leq \frac{\int_{\Omega} \delta_{ji}(x) e_{ji}(x) d\Omega}{\int_{\Omega} \rho(x) \tilde{\psi}_k^2(x) d\Omega} \quad (5.44)$$

Various modal shapes may be chosen in order to minimize the approximate fundamental frequency.

5.7.4 Features of the various modal methods

The main features of the various modal methods are gathered in Table 5.2. For each modal method, Table 5.2 details the types of deposits possibly investigated by the method. The simplified modal approach proposed by Dobry *et al.* (1976) and Hadjian (2002) may be considered for one-dimensional homogeneous and heterogeneous geological structures. As presented in Chapter 2 (§2.12), it is even possible to find closed-form solutions for arbitrarily inhomogeneous 1D profiles (Pecker, 2005). Two-dimensional alluvial deposits may be investigated by the method proposed by Bard and Bouchon (1985). The method proposed by Paolucci (1999) may be used for homogeneous and heterogeneous 2D or 3D alluvial basins. The method proposed by Semblat *et al.* (2003b) is adapted to any type of homogeneous or heterogeneous deposit (1D, 2D or 3D) and, furthermore, the seismic excitation may be accounted for through a simplified modal superposition approach.

5.7.5 Fundamental frequency of a geological structure

To use the simplified modal method, we consider a shallow geological profile located in the centre of Nice, France. This alluvial site has been extensively studied through various

Table 5.2: Various modal methods and types of deposits possibly investigated.

Authors	homog.	heterog.	1D	2D	3D	excitation
Dobry <i>et al.</i> (1976)	yes	yes	yes	no	no	no
Hadjian (2002)	yes	yes	yes	no	no	no
Bard & Bouchon (1985)	yes	no	yes	yes	no	no
Paolucci (1999)	yes	yes	no	yes	yes	no
Pecker (2005)	yes	yes	yes	no	no	no
Semblat <i>et al.</i> (2003b)	yes	yes	(yes)	yes	(yes)	(yes)

experimental surveys as well as numerical analyses (Semblat *et al.*, 2000). This shallow basin will be also considered in the next section to investigate seismic wave propagation and amplification. The basin is assumed homogeneous and its vibratory resonance is analyzed for anti-plane motion (*SH*-waves). The mechanical properties of both media (basin and bedrock) are the following:

- basin: $\rho=2000 \text{ kg/m}^3$, $\mu=180 \text{ MPa}$, $\nu=0.2$, that is $V_S=300 \text{ m/s}$;
- bedrock: $\rho=2300 \text{ kg/m}^3$, $\mu=4500 \text{ MPa}$, $\nu=0.2$, that is $V_S=1400 \text{ m/s}$.

where ρ is the mass density, μ is the shear modulus, ν the Poisson's ratio and V_S the shear wave velocity.

As depicted in Fig.5.47, the basin/bedrock interface may be described by two sinusoidal functions as follows:

- western deepest part of the basin: $f(x, z) = (h_1 + 1) \cdot \cos(2.7 \cdot 10^{-3}x + 1.55)$
- eastern shallowest part of the basin: $g(x, z) = (h_2 + 2) \cdot \cos(2.8 \cdot 10^{-3}x - 1.3)$

Amongst the admissible modal shapes, the following ones are chosen (Paolucci, 1999):

$$\tilde{\psi}_2(x, z) = \cos^r \frac{\pi}{2} (1 - f(x, z)) \sin^{2s+1} \frac{(n+1)\pi}{2} \left(1 + \frac{x}{a}\right) \cos^t \frac{(2m+1)\pi}{2} \frac{z}{b} \quad (5.45)$$

where $f(x, z)$ is the function given previously; $r \geq 1$ and $t \geq 1$ are real parameters, $s=0, 1, \dots$ is an integer, m and n denotes the orders of the modes along the vertical and horizontal directions (respectively).

In this case, the inequality giving the fundamental frequency is the following:

$$\omega_0^2 \leq \min_{r,s,t} \frac{\int_{\Omega} \mu \left[\left(\frac{\partial \tilde{\psi}_2}{\partial x} \right)^2 + \left(\frac{\partial \tilde{\psi}_2}{\partial z} \right)^2 \right] dx dz}{\int_{\Omega} \mu \tilde{\psi}_2^2(x, z) dx dz} \quad (5.46)$$

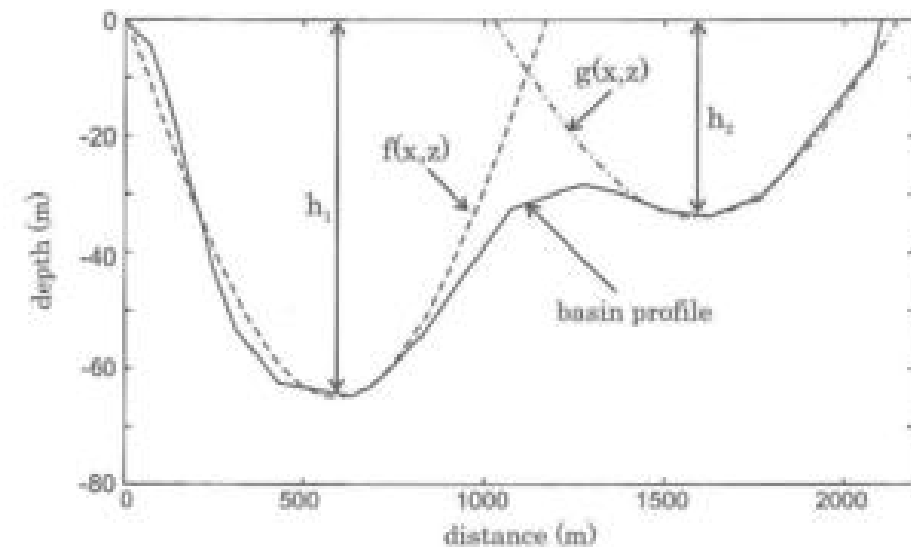


Fig. 5.47: Description of the homogeneous geological profile for the simplified modal approach (Sembat et al., 2003a).

Table 5.3: Fundamental frequencies of a shallow basin (Nice, France) obtained by the simplified modal approach (Sembat et al., 2003a).

Shear modulus	Fundamental freq. western part	Fundamental freq. eastern part
μ_1	1.50 Hz	2.86 Hz
μ_2	1.23 Hz	2.34 Hz
μ_3	1.07 Hz	2.02 Hz

5.7.6 Modal estimation of the fundamental frequency

For the Nice basin, the results are computed by the Rayleigh approximation for the first mode considering different values of the shear modulus: $\mu_1=180$ MPa (i.e. $V_{S_1}=300$ m/s), $\mu_2=120$ MPa (i.e. $V_{S_2}=245$ m/s) and $\mu_3=90$ MPa (i.e. $V_{S_3}=212$ m/s). The values of the fundamental frequency are given in Table 5.3 for the deepest part (West) and the shallowest part (East) of the basin. These values range between 1.07 and 1.50 Hz in the deepest part and 2.02 and 2.86 Hz in the shallowest part. They will be compared to the peaks of the site/reference spectral ratios in the next paragraph.

5.7.7 Simplified modal method vs experimental spectral ratios

The fundamental frequencies of the Nice basin estimated by the simplified modal method are now compared to the frequencies obtained from the peaks in the experimental spectral ratios (Sembat et al., 2000). The vertical lines displayed in Fig.5.48 represent the fundamental frequencies for the deepest and shallowest parts of the basin and for various shear moduli (μ_1 ; μ_2 ; μ_3).

For the deepest part of the basin, the fundamental frequency f_1 estimated for μ_3 (solid line) is in very good agreement with the experimental amplification peaks. For the shallowest part of the basin, the frequency value obtained for shear modulus μ_1 (dotted-dashed line) is close to the second amplification peak in the experimental spectral ratio.

These comparisons show the interest of the simplified modal method to estimate the modal features of 2D (as well as 3D) alluvial deposits. Through this homogeneous model, the influence of the wave velocity in the basin, in terms of fundamental frequency, may be easily assessed. In the following, the numerical results obtained by the Rayleigh approximation will also be compared to the frequencies corresponding to the maximum amplification computed by the Boundary Element Method through the analysis of seismic wave propagation in the profile (Sembat et al., 2000).

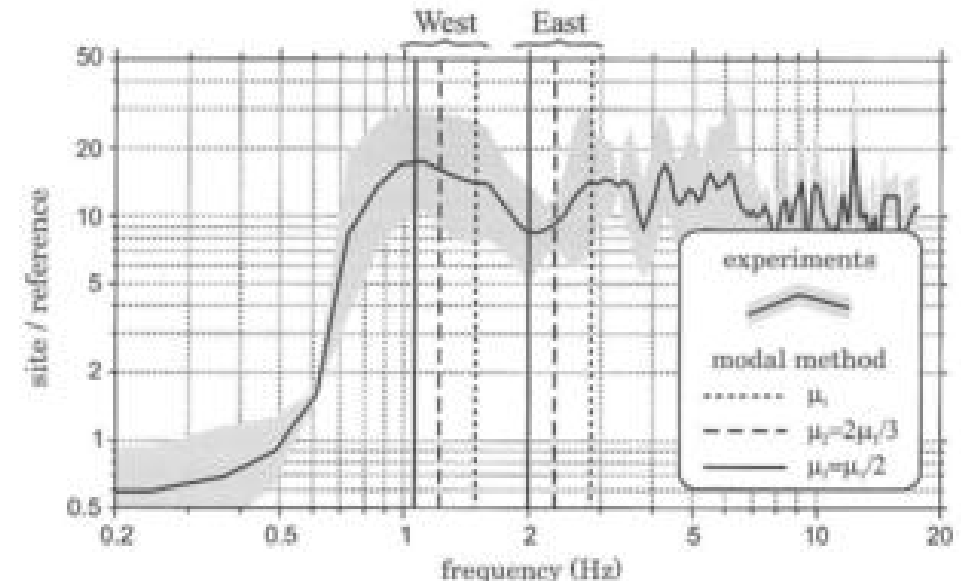


Fig. 5.48: Fundamental frequencies of a shallow basin (Nice, France) estimated by the simplified modal approach and comparison with experimental spectral ratios (Sembat et al., 2003a).

5.8 Amplification in shallow basins (e.g. Nice)

5.8.1 Analysis of site effects in Nice (France)

Measurements at the alluvial site

The French Riviera is located in a moderate seismicity area and an important seismic event is mainly expected in the Genoa gulf (magnitude 6 at 30 km from the coast). In the city of Nice, the geological structure was studied in great details by the seismic risks team of the CETE Méditerranée (Duval, 1996). As in many other cities, the highest density of population is found in the areas located on alluvial deposits.

A first experimental survey (1984) allowed the determination of the regional seismic risk and the characterization of various geological areas having very different seismic responses. The seismicity was recorded during one year (1992) at four sites where the seismic amplification may be important (Duval, 1996). Experimental measurements were performed to characterize site effects in the southern part of the area of Nice central station. As depicted in Fig.5.49, this area corresponds to a shallow alluvial deposit located in an ancient North-South valley. Eastward, the Cimiez hill is due to a bedrock outcropping.



Fig. 5.49: Shallow alluvial deposit in the centre of Nice (French Riviera).

Spectral ratios

From the experimental survey, the site/reference spectral ratios may be computed. Comparing the measurements performed at different sites, the spectral ratios show the influence of the layer depth on the peak frequency (Duval, 1996). An interesting method using ambient noise (microtremors) has also been performed (see Chapter 3). The stability of ambient noise has been studied in the time and frequency domains through spectral ratios between the horizontal and the vertical motion components (denoted H/V). It has been established from comparisons between standard spectral ratios (i.e. site/reference ratios) that the H/V spectral ratio allows the determination of the fundamental frequency of the soil.

The real earthquake, as well as microtremor, recordings clearly show a ground motion amplification at the centre of the basin between 1 Hz and 2 Hz (Duval, 1996).

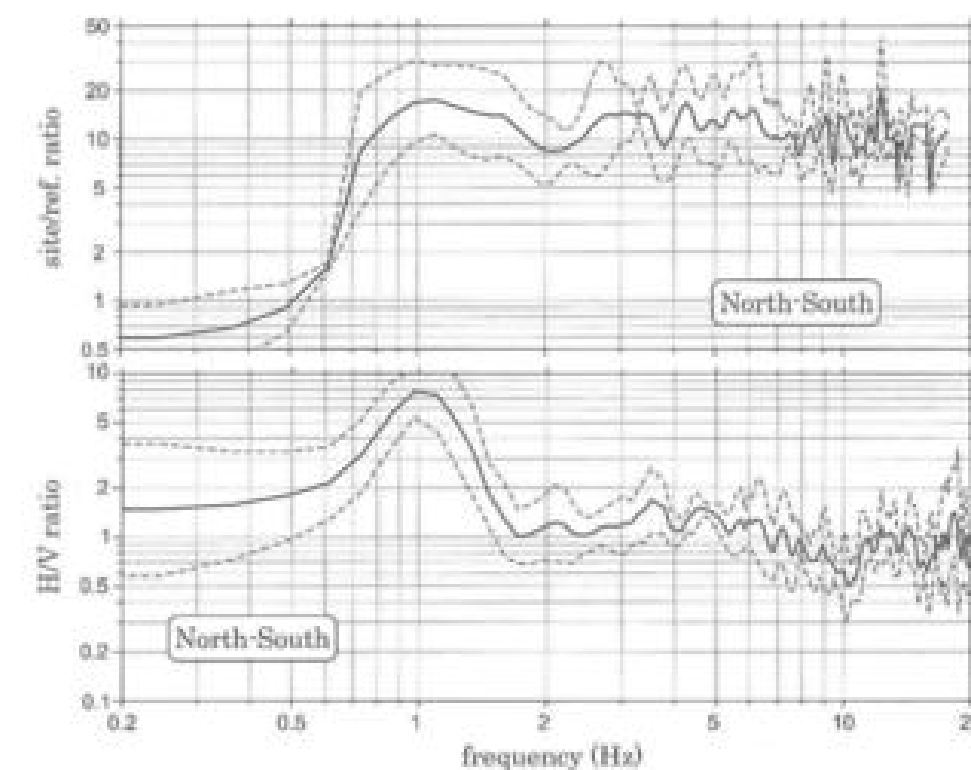


Fig. 5.50: Experimental measurements at the shallow alluvial site (Nice): standard spectral ratios from weak seismic motion (top) and H/V spectral ratios from microtremor recordings (bottom) (Semblat et al., 2000).

These results are displayed in Fig.5.50 through the spectral ratios computed from weak seismic motion measurements (top) and H/V spectral ratios from microtremor recordings (bottom). The measurements are performed at the alluvial site (*ALS* site) and at the reference bedrock station (*REF* site). The fundamental frequency estimated from microtremor recordings is very close to that determined by standard spectral ratios (Fig.5.50). However, the H/V spectral ratio is much less than the site/reference ratio and decreases at higher frequencies. Above the deepest part of the basin, the amplification factor obtained from site/reference spectral ratios (Fig.5.50 top) reaches a maximum value of 20 around 1.5 Hz.

To investigate time-domain amplification, several accelerograms recorded in the centre of Nice are displayed in Fig.5.51. For a seismic event of similar magnitude (feb. 2001, M4.6 earthquake), the discrepancy in amplitude is very large. The 'Alsace-Lorraine' (*ALS*) alluvial site leads to the largest amplitudes and time durations.

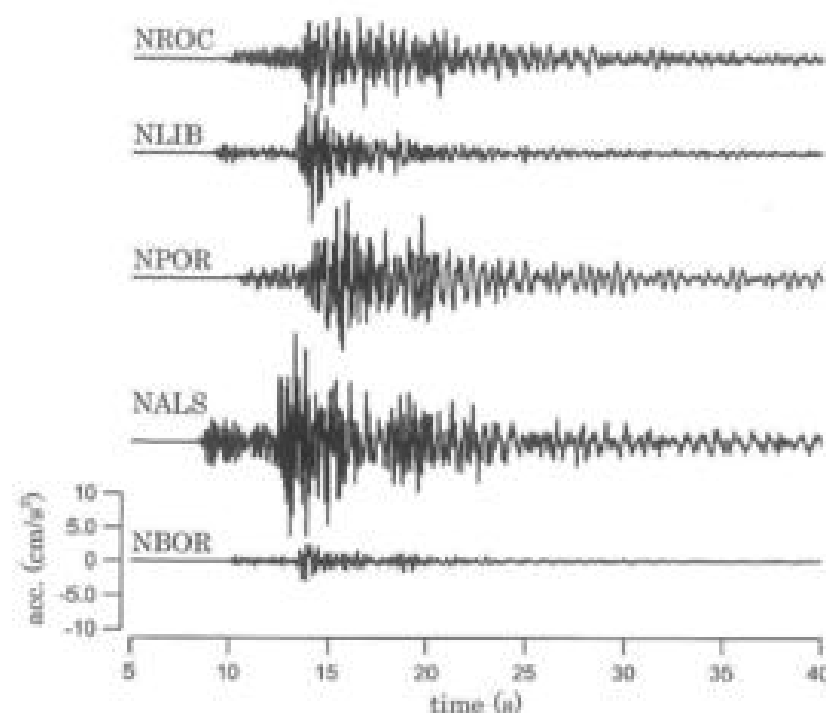


Fig. 5.51: Accelerograms recorded at various locations in the city of Nice during the feb.2001, M4.6 earthquake (from CETE Méditerranée, Nice, France).

5.8.2 Amplification from 1D transfer functions

To analyse seismic wave amplification in this shallow basin, a simple estimation may be performed assuming a single layer soil over an elastic half-space. For the analytical and numerical analyses, a 2D East-West profile is now considered. The average mechanical properties of the materials are chosen as follows:

- alluvial deposit: $\rho_1=2000 \text{ kg/m}^3$, $\mu_1=180 \text{ MPa}$, thus $V_{S_1}=300 \text{ m/s}$,
- bedrock: $\rho_2=2300 \text{ kg/m}^3$, $\mu_2=4500 \text{ MPa}$, thus $V_{S_2}=1400 \text{ m/s}$.

Considering a plane vertical SH -wave, the closed-form of the transfer function, derived in Chapter 3, is recalled through Eq.(5.1). In its deepest part, the alluvial deposit is assumed as a constant depth layer with $H=64 \text{ m}$, whereas the shallowest part is modelled by a $H'=32 \text{ m}$ deep layer. These values correspond to the maximum depth in each part of the basin (Fig.5.49).

Computing the transfer function from Eq.(5.1), the curves corresponding to depths H and H' are displayed in Fig.5.52. The maximum amplification factor is below 6 for both depth values and the related frequencies are respectively:

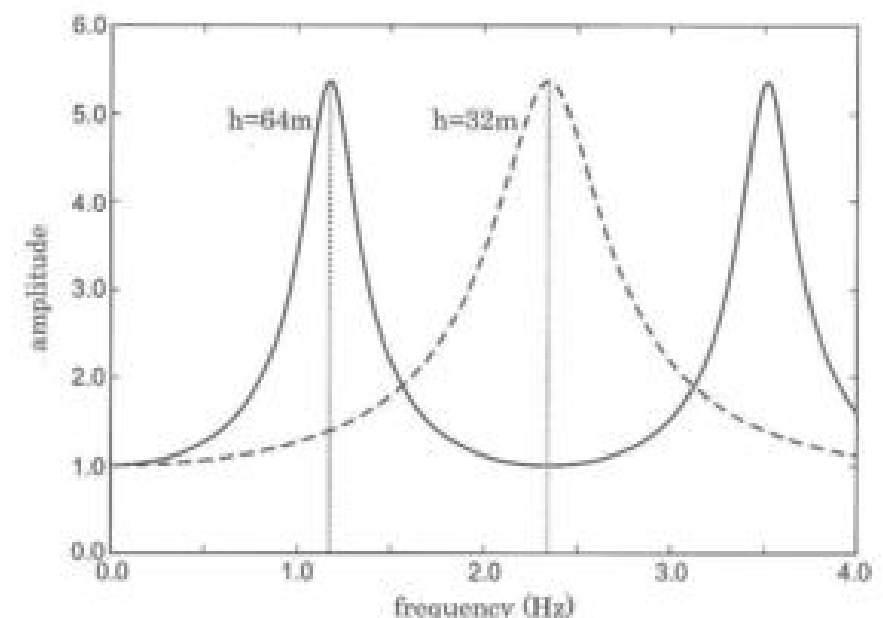


Fig. 5.52: 1D transfer function for the deepest (solid) and the shallowest (dashed) part of the Nice basin.

- for the deepest part ($H=64 \text{ m}$): $f_0=1.2 \text{ Hz}$,
- for the shallowest part ($H'=32 \text{ m}$): $f'_0=2.3 \text{ Hz}$.

From these 1D results, the fundamental frequencies are in good agreement with the frequencies estimated from the maximum values of the spectral ratios (Fig.5.50). Conversely, the 1D spectral amplification of the ground motion is much smaller than the experimental one (nearly 20). It is hence necessary to consider a more realistic model to quantify site effects in the basin. A 2D model involving the Boundary Element Method (see Chapter 4) will be studied in the following.

5.8.3 2D model of the geological profile

The East-West geological profile depicted in Fig.5.49 is considered but the exact 2D geometry of the basin is now modelled through a Boundary Element Model. The alluvial deposit is still assumed homogeneous and the mechanical properties are the same as previously. The incident wavefield is a plane vertical SH -wave. In Fig.5.53, the Boundary Element mesh is depicted (top) for the solution of the integral equation and additional interior points are chosen (bottom) for the a posteriori computation of the seismic wavefield within the basin and bedrock (integral representation formula, see Chapter 4).

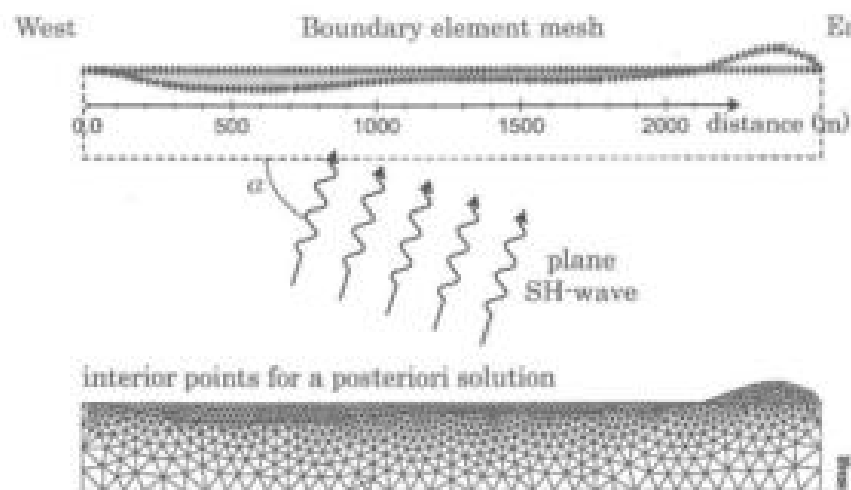


Fig. 5.53: Boundary Element mesh of the alluvial deposit in the centre of Nice for a plane *SH*-wave (top) and additional interior points (bottom) (Semblat *et al.*, 2000).

The model involves the fundamental solution (Green's function) of the free-space for the deposit and the hill (bounded media). It involves the fundamental solution of the half-space to accurately model the bedrock as a sub-domain of a half-space. The computation is performed using the FEM/BEM code CESAR-LCPC (Humbert *et al.*, 2005).

5.8.4 Amplification of a plane *SH*-wave

Considering the model depicted in Fig. 5.53, the Boundary Element Method allows to compute the wavefield along the boundary and interfaces. The amplification factor is derived afterwards removing the free-surface effect. The isovales of the amplification factor are given in Fig. 5.54 for different frequencies. The amplification is large at the surface of the deposit since it reaches a maximum value of 15.0 at frequency 1.6 Hz. The largest amplification is found in the deepest part of the deposit. However, for the highest frequency (Fig. 5.54, bottom), the amplification factor in the shallowest part of the basin significantly increases. The results displayed in Fig. 5.54 clearly show that, for the two highest frequencies (1.6 and 2.0 Hz), the maximum amplification occurs across several small areas. It corresponds to the fact that, at these frequencies, the wavelengths are much shorter than at lower frequencies.

The 3D curve displayed in Fig. 5.55 shows the variations of the amplification factor at the surface of the deposit as a function of distance and frequency. It is then possible to assess the amplification level at each frequency as well as the location and extent of the

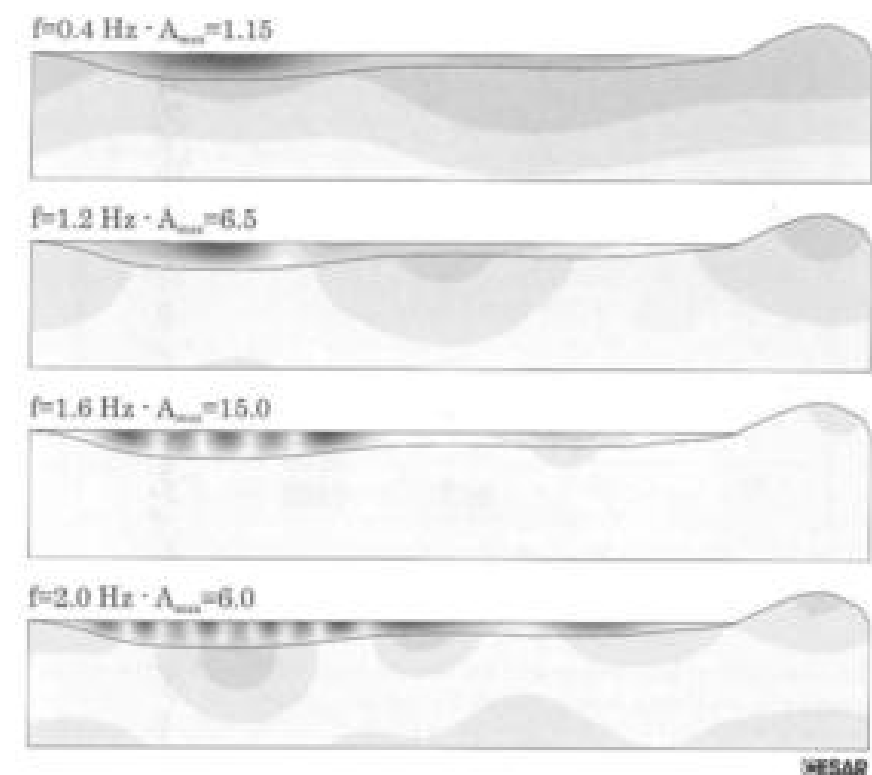


Fig. 5.54: BEM simulations of the amplification process for a plane vertical *SH*-wave in a shallow geological profile located in the centre of Nice (Semblat *et al.*, 2000).

related maximum amplification area. In Fig. 5.55, the amplification factor remains low for frequencies below 0.8 Hz. Above this frequency, a significant amplification appears in the deepest part of the basin (West). For higher frequencies, several high amplification areas are assessed in the western part of the deposit. Above 1.5 Hz, the amplification factor in the shallowest part of the deposit (East) increases progressively. Between 2.0 and 2.5 Hz, the amplification decreases in the deepest part and becomes even larger in the shallowest part.

The results from Figs 5.54 and 5.55 show that the ground motion amplification reaches a maximum value of 15.0 at approximately 1.6 Hz. These results are in good agreement with the frequency values previously estimated from the 1D approach. In the 2D numerical simulations, the fundamental frequency is nevertheless slightly larger than that given by the transfer function. It can be easily explained since the 1D approach considers a horizontal layer having a constant depth equivalent to the deepest local part of the basin,

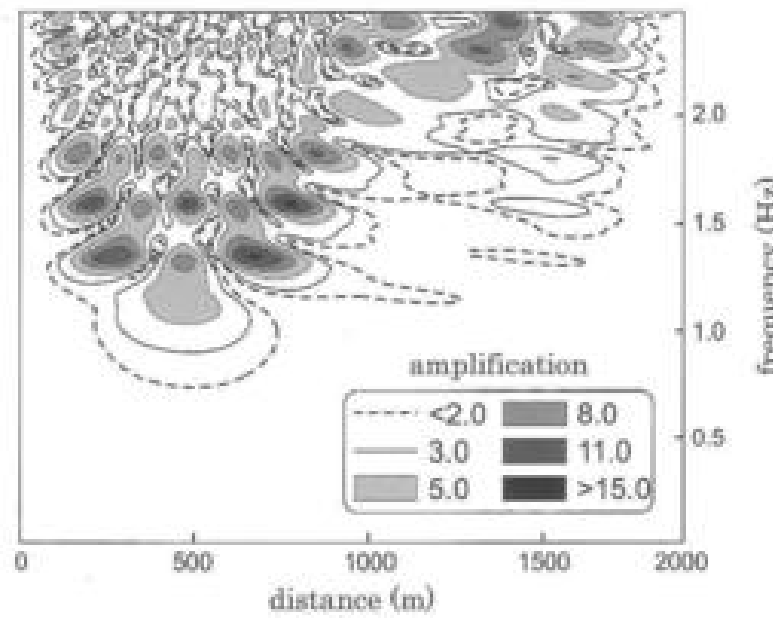


Fig. 5.55: Amplification computed at the surface of the Nice basin as a function of distance and frequency (Sembat et al., 2000).

thus leading to an underestimated fundamental frequency. The 2D amplification level estimated numerically by the Boundary Element Method is nearly three times larger than obtained in the 1D analysis. Even for a shallow basin, the numerical model allows the detailed description of the geometry of the deposit leading to trapped surface waves and, consequently, to stronger site effects. These values appear to be in good agreement with the experimental ones displayed in Fig.5.50.

5.8.5 Influence of attenuation

In the BEM formulation, a Zener viscoelastic model is introduced to analyze the influence of attenuation on the amplification process (Sembat et al., 2000). The undamped amplification is compared to several damped cases in Fig.5.56 ($Q^{-1}=0.02$; $Q^{-1}=0.04$ and $Q^{-1}=0.06$). The influence of attenuation is found to be significant since the reduction ranges from 20% to 50% depending on the attenuation Q^{-1} . This result is consistent with previous remarks on the effect of trapped surface waves propagating from one edge of the basin to the other. When trapped (due to the velocity contrast between the basin and the bedrock), these waves propagate through an attenuating medium and are simultaneously amplified and attenuated. This phenomenon may even be more complex for strong seismic motion, i.e. larger attenuation in the soil (Gélis et al., 2008; Delépine et al., 2007).

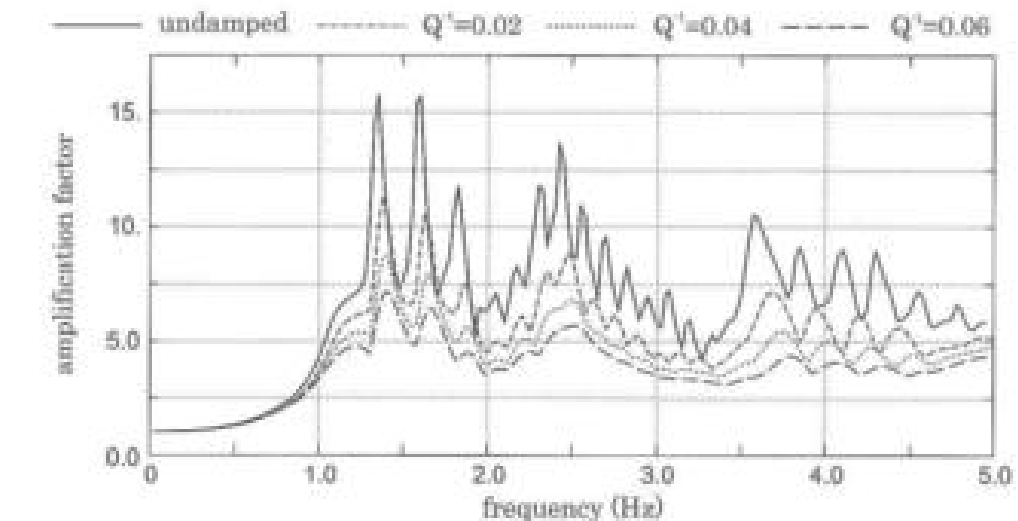


Fig. 5.56: Overall amplification factor in the centre of Nice for various attenuations (Sembat et al., 2000).

5.8.6 1D and 2D amplification vs experimental results

The numerical results are now compared to the experimental spectral ratios computed from real earthquake measurements (weak motions). Since computations were also performed for P and SV waves, Sembat et al. (2000) considered the site/reference spectral ratios along the three directions of space: vertical, North-South, East-West. The geological profile being oriented along the East-West direction (Fig.5.49), the vertically incident P -wave corresponds to vertical motion, SH -wave to antiplane motion along the North-South direction and the SV -wave to an East-West polarized motion.

The numerical and experimental results for the North-South component are displayed in Fig.5.57. The numerical results correspond to the maximum overall amplification, defined in (Sembat et al., 2000), and for the experimental results both the mean value (dotted line) and the standard deviation (shaded area) are depicted. The comparisons for the three motion components are given in (Sembat et al., 2000).

For the North-South component (Fig.5.57), the 2D results are computed for the shear modulus value $\mu_2 = \mu_1/2=90$ MPa, that is $V_{S_2}=212$ m/s. The agreement with the experimental results is very good in terms of amplification level. The two main amplifications obtained experimentally, in the deepest part of the deposit (above 1.0 Hz) and in the shallowest part (above 2.5 Hz), are retrieved with the 2D BEM model. However, the experimental spectral ratios are lower than the numerical amplification factor at low frequencies (below 0.6 Hz).

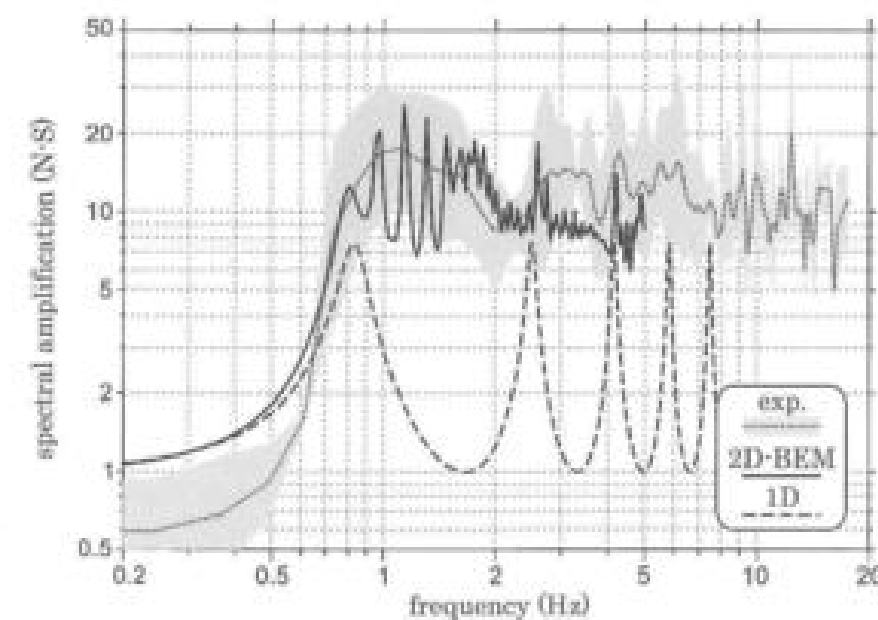


Fig. 5.57: Comparison between the weak motion measurements (dotted/shaded), the 1D transfer function (dashed) and the 2D BEM results (solid) for the North-South component in the centre of Nice.

Conversely, the discrepancy between the 1D transfer function and the experimental results is large. The frequency of maximum amplification is not exactly found by the 1D analysis and the amplification level is even strongly underestimated in some frequency ranges. In this shallow basin, the 1D estimation of seismic wave amplification is not reliable when compared to experimental spectral ratios. A 2D aggravation factor will be discussed in the next section.

5.8.7 2D/1D aggravation factor

Gélis et al. (2008) also studied the amplification of seismic waves in the centre of Nice. They computed the seismic wavefield using the Finite Difference Method (Sucuget et al., 2000). As shown in Fig. 5.58, the 2D/1D aggravation factor is estimated for a vertically incident wave (top) and for various incidences (middle). The maximum aggravation factor is found around 3, that is close to the maximum value proposed by Pitilakis et al. (1999). The results involving various incidences (middle) lead to larger aggravation factors in a certain frequency range (4 to 6 Hz) which is similar to that suggested by Pitilakis et al. (1999). In the softer part of the basin (1200–1400 m), the aggravation factor may even reach an approximate value of 4 (Fig. 5.58). In their paper, Gélis et al. (2008) also proposed several 2D simulations for strong motions using a nonlinear

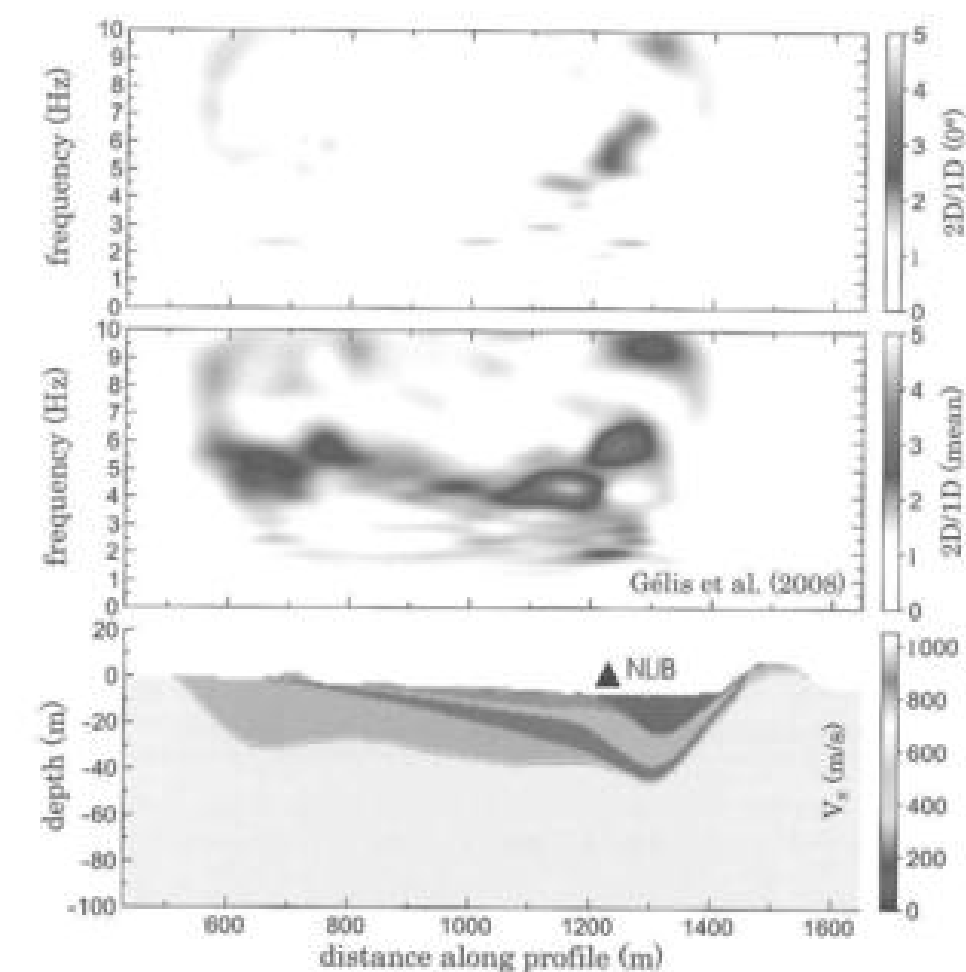


Fig. 5.58: 2D/1D aggravation factor vs distance and frequency for the Nice profile: numerical estimation for a vertically incident wave (top) and mean value for several computations at various incidence angles (middle) (Gélis et al., 2008).

constitutive model. From these computations, they observed deamplification above 2 Hz and a shift of the resonant frequency to lower frequencies. Such results show the influence of combined geometrical effects (2D/3D) and constitutive effects (nonlinearities).

5.8.8 Comparison with the simplified modal method

The 2D fundamental frequencies of the alluvial basin were previously computed by the simplified modal approach (§5.7.3). Several values of the shear modulus of the deposit

were considered: $\mu_1=180$ MPa (i.e. $V_S=300$ m/s), $\mu_2=120$ MPa (i.e. $V_S=245$ m/s) and $\mu_3=60$ MPa (i.e. $V_S=212$ m/s). The numerical results obtained by the Rayleigh method are compared to the frequencies leading to the maximum amplification in the 2D BEM simulations. The comparison is shown in Table 5.4 for the deepest part (left) and the shallowest part (right) of the basin.

Table 5.4: Comparison between the peak frequencies from the 2D BEM simulations and the fundamental frequencies estimated by the simplified modal method.

Shear modulus	Freq. western part		Freq. eastern part	
	BEM	modal	BEM	modal
μ_1	1.35 Hz	1.50 Hz	2.42 Hz	2.86 Hz
μ_2	1.30 Hz	1.23 Hz	2.13 Hz	2.34 Hz
μ_3	1.13 Hz	1.07 Hz	1.75 Hz	2.02 Hz

From these results, it may be concluded that the fundamental frequencies obtained from the Rayleigh approximation are in good agreement with that observed in the 2D BEM computations. As it can be seen in Fig.5.57, the 1D analysis leads to significantly lower frequencies. For a homogeneous basin model, the Rayleigh approximation is hence a reliable mean to estimate the fundamental frequency of 2D/3D alluvial basins.

5.8.9 Time-domain simulations

From the frequency domain results computed by the Boundary Element Method (Semblat et al., 2000), the time domain response of the basin may be easily derived considering the Fourier transforms at each point. The Feb. 2001 earthquake is chosen as the seismic input and the results are computed for a duration of 60 s. As shown in Fig.5.59, the largest amplification is found in the deepest part of the basin (Kham, 2004). The influence of trapped surface waves may thus be considered as very large. The duration increase is also very important in this part of the basin. The time histories also show that the shallowest part of the basin mainly amplifies higher frequency components.

5.8.10 Comparisons with a deep alluvial basin

To compare the amplification in the shallow deposit in Nice to deep and irregular alluvial deposits, the case of Caracas (Venezuela) is now considered (Duval et al., 1998). As shown previously, topographic site effects may be significant at this site while the stratification may even lead to larger amplifications. The irregular Caracas basin leads to a very different amplification/frequency dependence than the shallow Nice deposit with many large amplification peaks (Semblat et al., 2002a). Furthermore, the maximum amplification is found at the surface in the case of Nice whereas large amplification

5.8 Amplification in shallow basins (e.g. Nice)

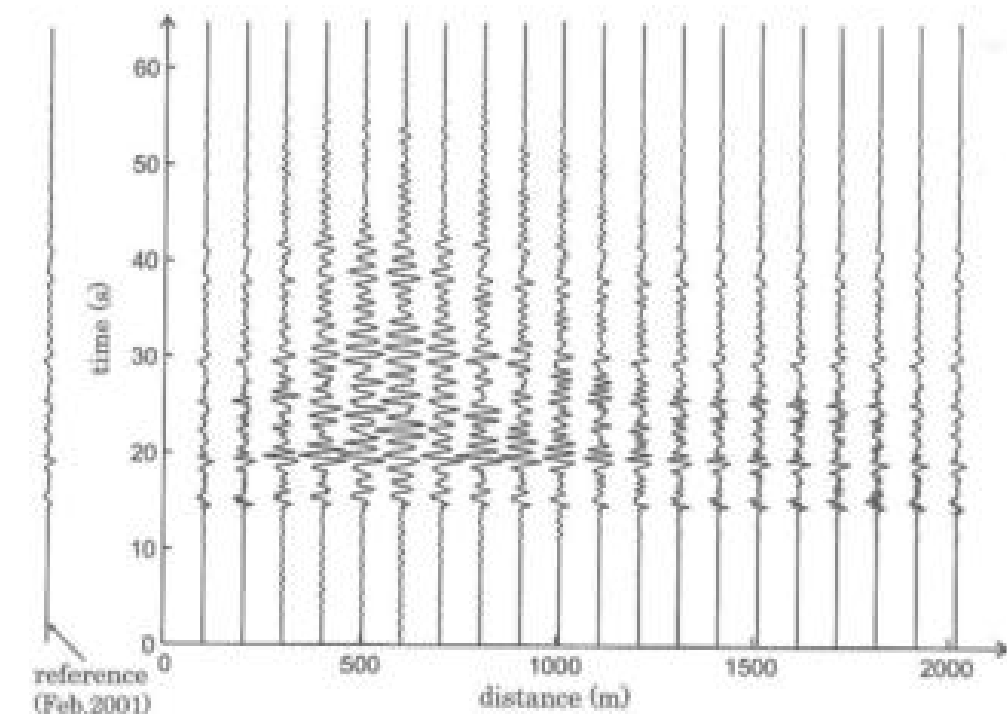


Fig. 5.59: Simulated wavefield in the alluvial basin for the Feb. 2001 earthquake in the centre of Nice (Kham, 2004).

areas also appear at depth in the Caracas basin. As shown in Fig.5.60, focusing effects strongly govern the variations of the seismic motion with depth:

- in the case of Nice (top), the ground motion is maximum at the free-surface and regularly decreases with depth,
- in the case of Caracas (bottom), the ground motion may be large at the free-surface as well as in some deep areas where focusing of seismic waves may lead to significant amplifications.

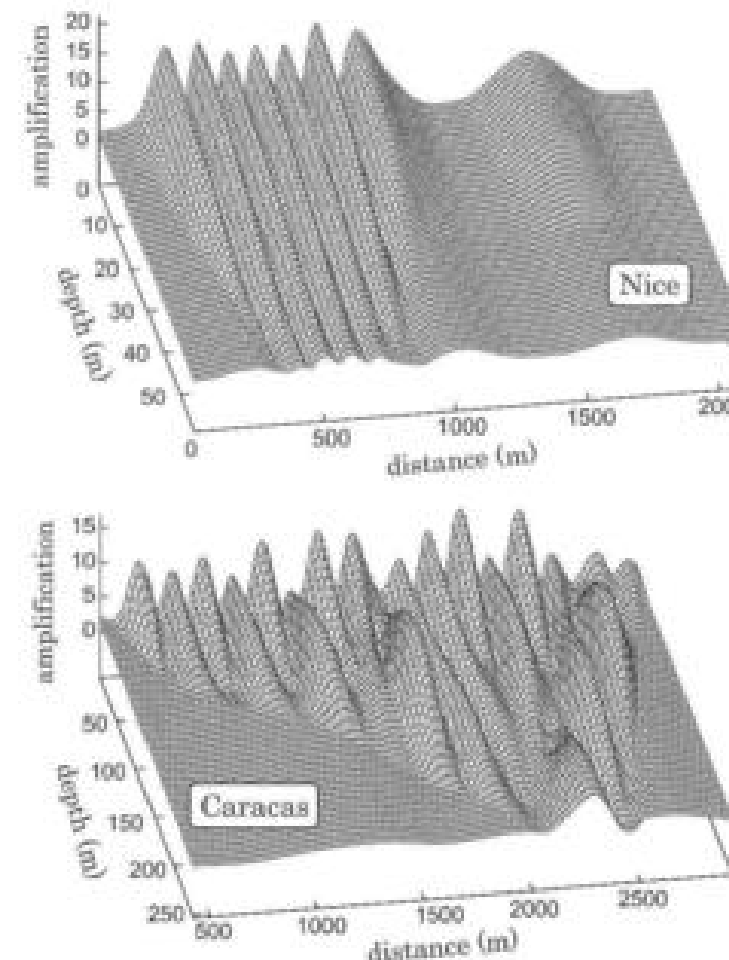


Fig. 5.60: Surface and in-depth amplification for a shallow (Nice, top) and a deep (Caracas, bottom) deposit (Semblat et al., 2002a).

5.9 Amplification in a deep basin (Volvi)

5.9.1 The Volvi EuroSeisTest

Location and main features

In this section, we shall consider a deep irregular basin located in Volvi, Greece. The Volvi EuroSeisTest is a European test site created through grants of the European Commission in the framework of the research programme "Global Change and Natural Disasters" (Jongmans et al., 1998; Makra et al., 2005; Riepl et al., 1998). Several european research programmes (e.g. EuroSeisRisk) investigated site effects and soil-structure interaction through this test site (<http://euroseis.civil.auth.gr/>).

The EuroSeisTest is located in an alluvial valley at 30km north-east of the city of Thessaloniki in Greece (Fig.5.61). It is an active seismotectonic area where the large 1978 Thessaloniki earthquake occurred. The basin is 6km long and more than 200m deep. Permanent and temporary sensors arrays are used on the test site to measure actual (earthquakes) as well as artificial dynamic loadings.

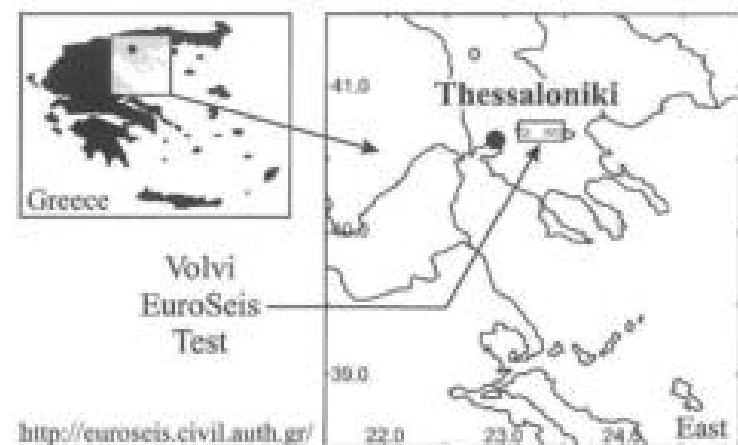


Fig. 5.61: Map of the Volvi area showing the EuroSeisTest (Semblat et al., 2005).

Geotechnical and geophysical analyses of the site conditions are numerous and it is known in details. These analyses were performed at the test site or in the lab. Consequently, the soil properties are well-known and fully reliable. The geological structure is depicted in Fig.5.62.

Experimental results in the Volvi basin

Several recorded accelerograms are displayed in Fig.5.62 for the Arnea M5.8, 1997 earthquake. The amplification is found to be large in the deepest part of the basin (e.g. *TST* station). The *PRO* station being the reference station, there is nearly no amplification at that location (see (Chávez-García et al., 2002) for a discussion on this critical point). At the *STC* and *STE* stations, the amplification is also significant and is mainly due to basin edge effects. As it will be discussed hereafter, the influence of large faults in the Volvi graben may also influence the propagation process.

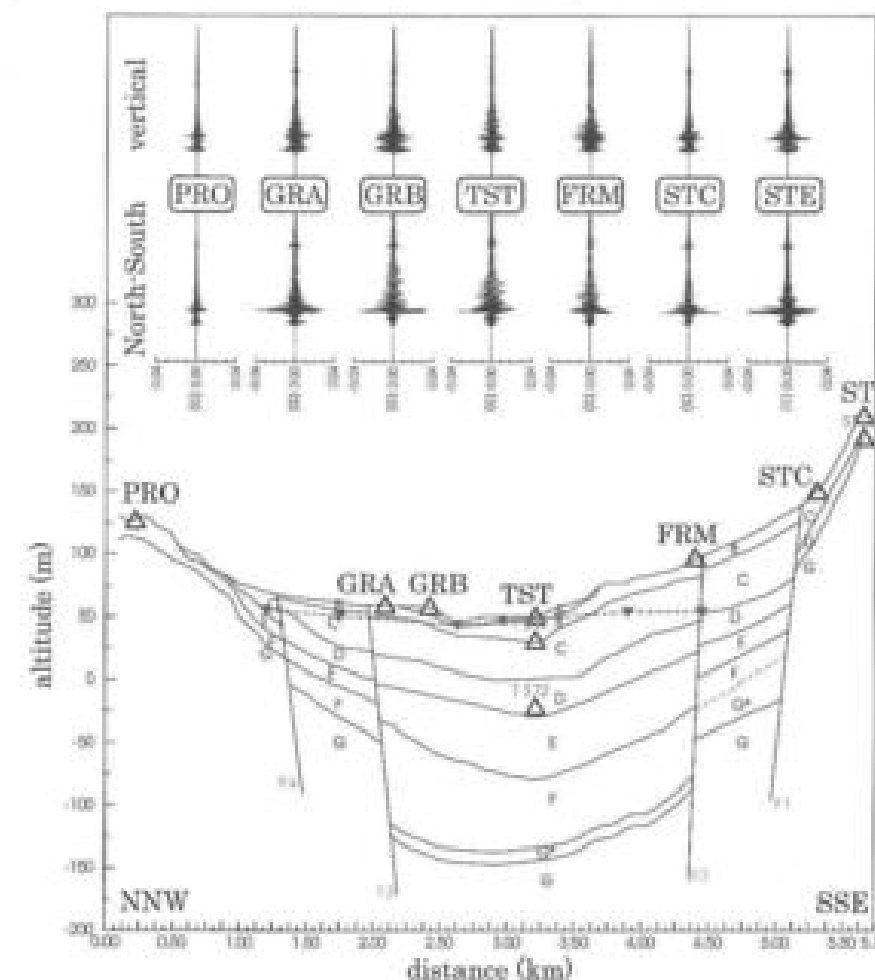


Fig. 5.62: Measurements from the Volvi test site (Arnea M5.8, 1997 event) showing the amplification process in the basin (Pitilakis et al., 1999).

The seismogram recorded at the *TST* station during the Arnea M5.8, 1997 earthquake is displayed in Fig.5.63 (top). Chávez-García et al. (2000) computed the time-frequency transform of this record, Fig.5.63 (bottom). When compared to the same plot for the *PRO* reference station (Chávez-García et al., 2000), the influence of site amplification at the *TST* station is obvious:

- the largest peaks in the low frequency range (i.e. close to the fundamental frequency of the basin) appear between 20 and 25 s leading to a longer motion duration than at the *PRO* site (where the energy is mainly localized between 15 and 17 s),
- between 15 and 17 s, only the higher frequency components (≈ 3 Hz) are large at the *TST* site,
- comparing the Peak Ground Acceleration between the *TST* and *PRO* reference station leads to an amplification level of nearly 3.

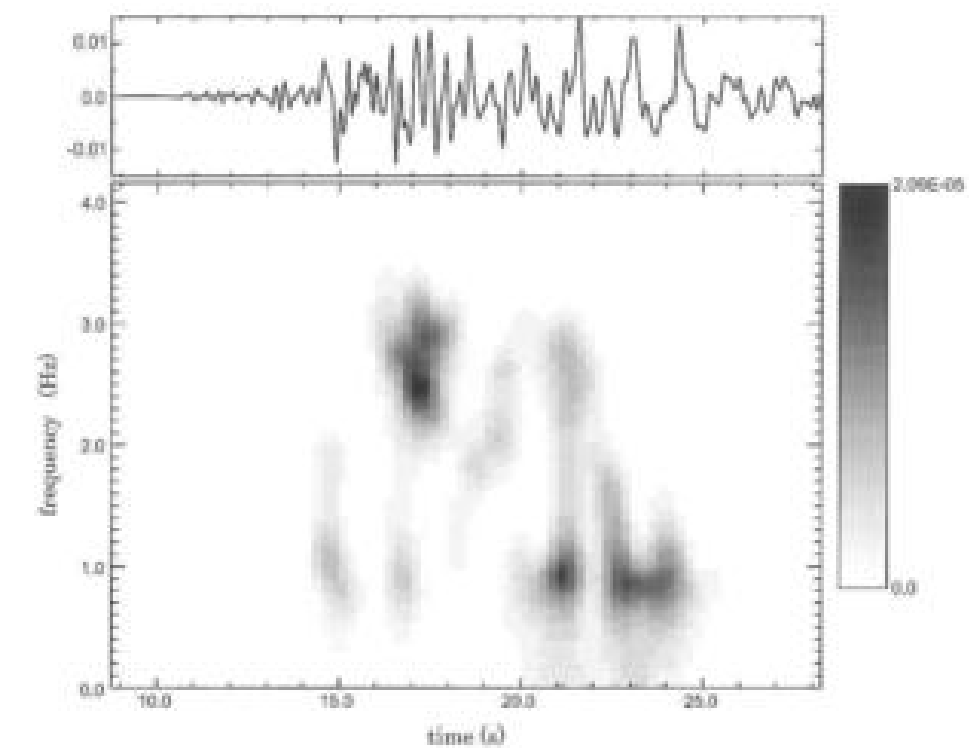


Fig. 5.63: Accelerogram (top) measured in g at the *TST* station (Volvi basin) during the Arnea M5.8, 1997 event and its time-frequency transform (bottom), (Chávez-García et al., 2000).

5.9.2 Simplified and complete models of the Volvi basin

Various models for the Volvi basin

For the Volvi test site, several geotechnical models have been proposed. In this section, we shall choose one of them and derive two numerical models: a simplified one with only two soil layers and a complete one involving six soil layers. The main goal is to investigate the influence of the knowledge of the local geology on site effects computations.

The basin model considered hereafter was proposed by LGIH (Eng. Geology Laboratory, Hydrogeology and Geophysical Prospecting) from the University of Liège (Belgium), (Jongmans et al., 1998). This geotechnical model is depicted in Fig.5.64 (top) with a correction giving an horizontal free surface but respecting layers depths as proposed by P.Y. Bard (LCPC/LGII, University of Grenoble). Other geological models were also proposed by Raptakis et al. (2000) and Chávez-García et al. (2000) and were used for 2D analyses of site effects.

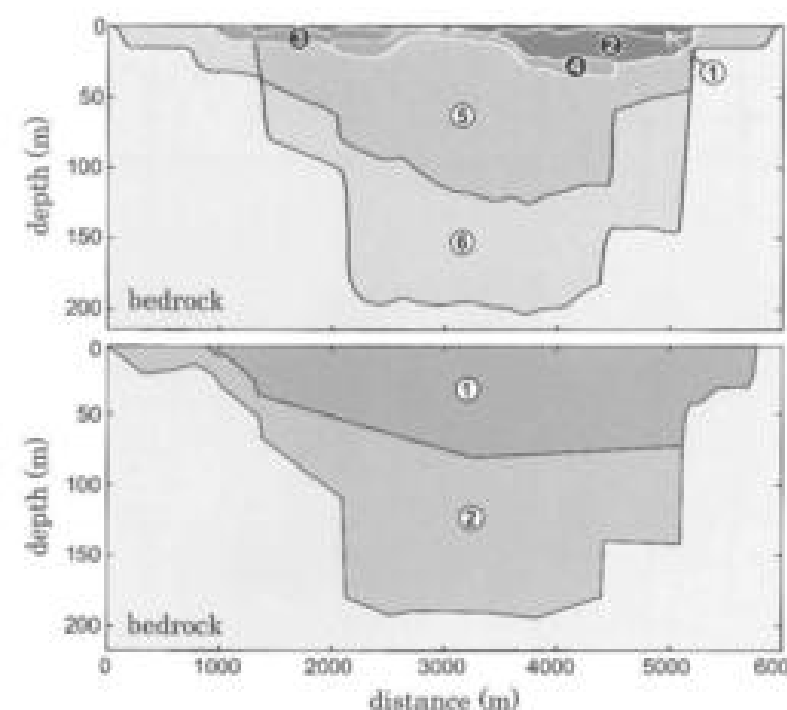


Fig. 5.64: Geotechnical models of the Volvi basin: complete model (top) and simplified model (bottom) as proposed by Semblat et al. (2005).

As suggested in the work of Makra et al. (2002), we firstly considered a simplified model with only two layers on an elastic bedrock. As depicted in Fig.5.64 (bottom), the various layers of the geotechnical model are combined to derive a simplified two-layer model. The mechanical properties of the simplified model are given in Table 5.5 and are estimated as mean velocity values of the velocities of the detailed profile (Semblat et al., 2005). The complete model (actual layering) directly corresponds to Fig.5.64 (top) with six different layers on an elastic bedrock. The mechanical properties of the complete basin model are detailed in Table 5.6. The purpose is now to analyse seismic wave amplification for the Volvi basin by the Boundary Element Method and compare both models for site effects and especially basin effects.

5.9.3 SH wave amplification in the Volvi basin

Amplification in the basin

In this section, the seismic excitation is a plane *SH*-wave with vertical incidence. For the simplified model, amplification values estimated through BEM simulations are given in Fig.5.65 for various frequencies. The main features of the amplification patterns are as follows:

- For 0.6 Hz: the largest amplification occurs in the deepest part of the basin and this case seems to correspond to the fundamental mode of vibration of the basin. Nevertheless, the maximum amplification factor is not very high (i.e. below 3).
- For 0.8 Hz: two areas of large amplification appear along the free surface in the central part of the basin with a rather high maximum value (9.5).
- For 1.0 Hz: maximum amplification is reached at the free surface but the main amplification area (9.5) is shifted to the right in the intermediate part of the basin.
- For 1.2 Hz: amplification areas also concern the left medium depth part of the basin and the maximum value is slightly lower (7.5).
- For 1.8 Hz: both free surface and deeper areas reach large amplifications (8.3). The largest amplification corresponds to the extreme left of the medium depth part of the basin.
- For 2.4 Hz: with such wavelengths, the shallow right part of the basin shows large amplifications with both surface and deep processes. There is nearly no amplification in the deepest central part of the basin.

Basin effects for the simplified and complete models

Six points are chosen along the Volvi profile and are marked in Fig.5.66. They are located at 1000m from one another and these areas correspond to various basin depths. In Fig.5.66, the amplification/frequency curves are displayed for each of these locations.

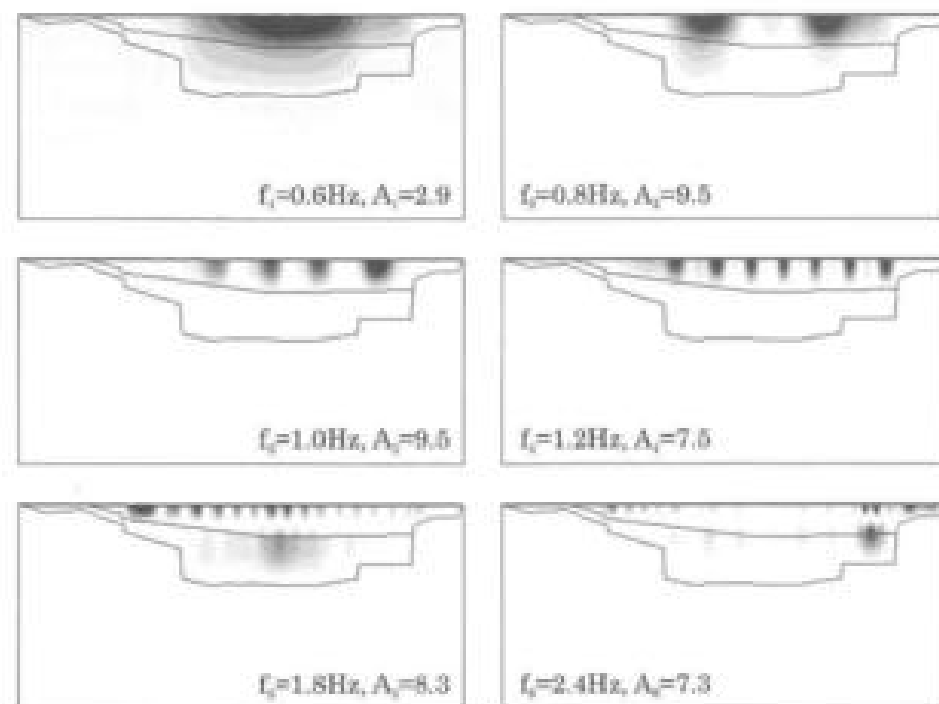


Fig. 5.65: Amplification values in the Volvi basin estimated numerically (simplified basin model) at various frequency: frequency values f_r and related maximum amplifications A_r (Semblat *et al.*, 2005).

Table 5.5: Properties of the soil layers for the simplified model of the Volvi basin (Fig.5.64, bottom).

Soil layers	mass density	Young's modulus	Poisson's ratio
layer 1	2100 kg/m ³	677 MPa	0.280
layer 2	2200 kg/m ³	3595 MPa	0.453
bedrock	2600 kg/m ³	4390 MPa	0.249

Solutions for the simplified model are compared to those of the complete model. From these curves, we can make the following comments:

- Point 1 ($d=380m$): for this location, there is almost no amplification (at the scale of the maximum amplification curves). The basin depth is small and there is no very soft soil layer at this point.

Table 5.6: Properties of the soil layers for the complete model of the Volvi basin (Fig.5.64, top).

Soil layers	mass density	Young's modulus	Poisson's ratio
layer 1	1700 kg/m ³	180 MPa	0.33
layer 2	1800 kg/m ³	300 MPa	0.33
layer 3	1800 kg/m ³	300 MPa	0.33
layer 4	2000 kg/m ³	530 MPa	0.48
layer 5	2200 kg/m ³	1200 MPa	0.47
layer 6	2300 kg/m ³	3300 MPa	0.49
bedrock	2600 kg/m ³	4200 MPa	0.19

- Point 2 ($d=1380m$): as shown in Fig.5.66, the maximum amplification is around 9 and is reached for frequency 1.9Hz. This rather high frequency value can be explained by the moderate depth in this part of the basin.
- Point 3 ($d=2380m$): there is a large amplification at 0.8Hz reaching the maximum value of 11. This point is in the deepest part of the basin but amplification remains nevertheless significant in the medium frequency range ($f=1.9\text{Hz}$) due to the influence of the shallowest left part of the basin which is accurately modelled with the complete model (larger amplification).
- Point 4 ($d=3380m$): this point is in the central part of the basin and the amplification factor reaches its maximum in a lower frequency range. The maximum amplification level is close to the previous ones and the corresponding frequency is identical. For this point, there is also large amplifications around 2.0Hz and above 4Hz: differences between simplified and complete models are enhanced in the medium frequency ranges, due to the influence of the subsurface layers.
- Point 5 ($d=4380m$): the maximum amplification (11) corresponds to frequency 0.8Hz. For this location, amplification for the simplified model is quite low (less than 6) for other frequencies whereas amplification for the complete model is clearly stronger (around 8) for the medium frequency range. This difference may be due to lateral heterogeneities, particularly strong for the complete model. The amplification pattern at 0.8Hz shown in Fig.5.65 leads to maximum amplification in this particular area.
- Point 6 ($d=5380m$): for this point, the basin depth is slightly smaller than in point 2 but the soil layers are softer. We get significant amplification values for the simplified model and the maximum (9.0) is reached at frequency 2.8Hz whereas for the complete model, there is no significant amplification.

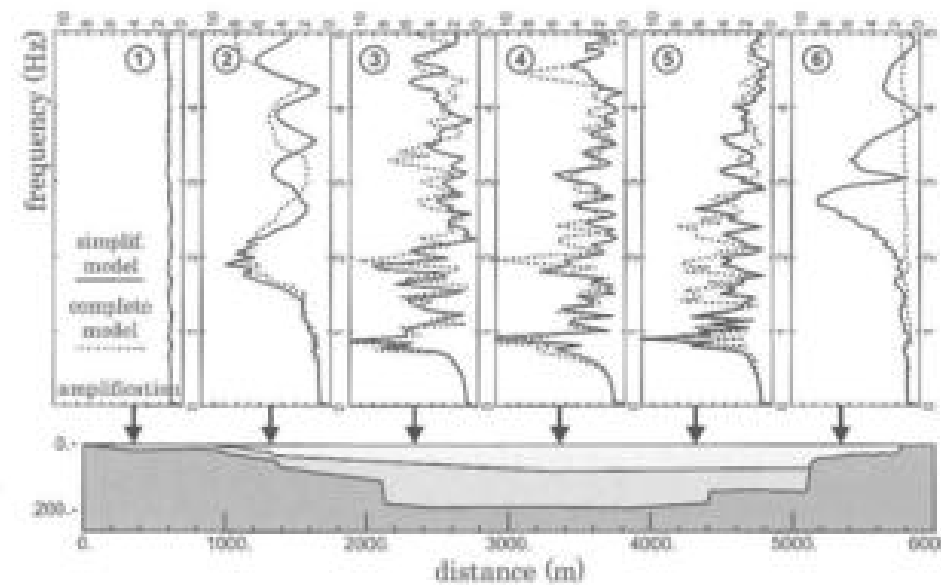


Fig. 5.66: Amplification/frequency curves for various locations along the Volvi basin surface: simplified (solid) and complete (dashed) models (Sembat et al., 2005).

The amplification values estimated numerically by the Boundary Element Method are close to experimental ones (Pitilakis et al., 1999). When compared to 1D analysis of amplification (Makra et al., 2002), 2D estimations lead to larger values since the actual amplification process is strongly influenced by lateral heterogeneities (see following sections). These effects are clear in the previous numerical results (Fig.5.66) and we will investigate later their influence on time domain response and seismic signal duration.

5.9.4 Comparisons between simplified and complete models

As described in Tables 5.5 and 5.6, the simplified model is a two-layered basin over an elastic bedrock whereas the complete model includes 6 different soil layers over the bedrock. The purpose of the comparison is to assess the influence of the soil layering description on seismic wave amplification analysis including basin effects. To compare the simplified basin model to the complete one, we will analyze both frequency and time domain results.

Comparison of amplification vs frequency and distance for both models (SH wave)

As shown in Fig.5.67, the complete model (6 layers) leads to a larger number of amplification peaks on both edges of the basin near faults F1 (South) and F4 (North). These peaks of large amplification are especially located in three different areas:

- $f \in [2-3\text{Hz}]$ and $x=4000\text{m}$,
- $f \in [3-4\text{Hz}]$ and $x=2500\text{m}$,
- $f \in [4-5\text{Hz}]$ and $x=1500\text{m}$.

The transfer functions for each basin model are displayed in Fig.5.67 as isolines vs distance and frequency. The largest amplification corresponds to the same frequency $f_0 \approx 0.8\text{Hz}$ for both models. It is located in two different areas of the basin. This phenomenon is not due to the near surface layering since the simplified model also shows a 'double fundamental mode' (Makra et al., 2002). This observation is also made by Chávez-García et al. (2000) who suggests that it corresponds to the contribution of surface waves.

Comparison for a Ricker wavelet (SH-wave)

To fully understand the influence of the basin model description of both vertical and horizontal heterogeneities, the results computed in the frequency domain are transformed as time domain responses at the free surface. For both models (simplified and complete), we consider an upward propagating SH-wave described by a Ricker wavelet whose spectrum is centered at 1 Hz. From the frequency domain BEM results presented in previous sections, the time domain seismic waves are computed along the free surface. The time histories are displayed in Fig.5.68 along the basin for both types of models.

From the time domain solutions derived from the simplified model (Fig.5.68, top), the unamplification process appears clearly. The effect of lateral heterogeneities (basin effects) is obvious since wave reflections on basin edges occur. The amplification of the first arrivals also shows the influence of the velocity contrast in the central (deepest) part of the basin. Seismic wave amplification in the simplified Volvi basin is then influenced by both vertical (soil layering) and lateral (basin effects) heterogeneities.

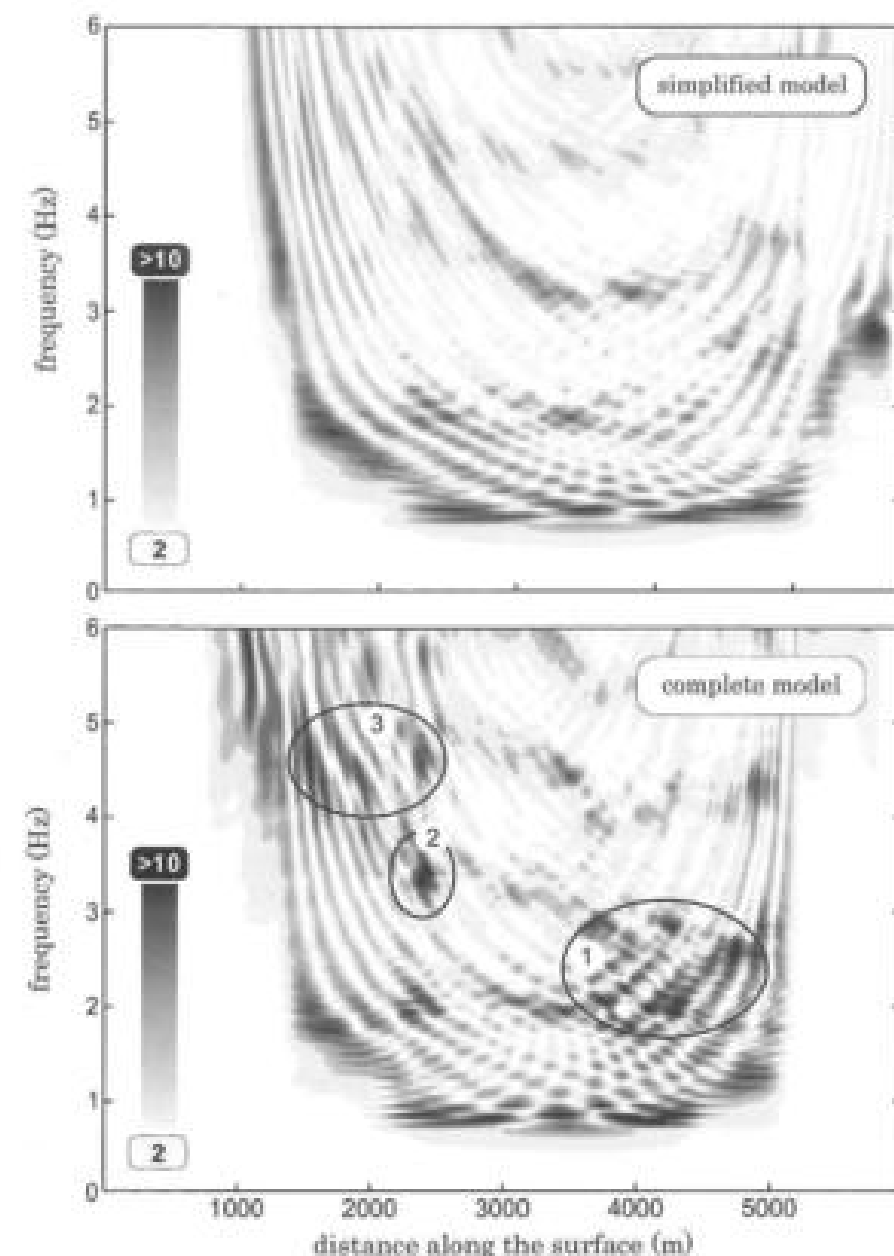


Fig. 5.67: SH wave amplification vs frequency and distance for the simplified (top) and complete (bottom) models of the Volvi basin (Semblat et al., 2005).

When compared to solutions derived from the complete Volvi model (Fig.5.68, bottom), the amplification of the first arrivals is larger than for the simplified basin model (since the magnitude scale between two following traces is twice that of the latter model). The soil layering being described more precisely, the amplification due to velocity contrast is thus larger. Furthermore, the direct Ricker wavelet is combined with reflected and refracted waves to give a more complex wavefield (Fig.5.68). It is especially the case on both left and right sides of the deepest part of the basin. It is possibly due to the combination of vertical and lateral heterogeneities influences. Since the velocity contrasts are described more precisely in the complete model, the lateral wave propagation in each layer is made easier and the global amplification process enhanced. Concerning the signal duration, it is significantly increased showing once more the combined influence of basin effect and soil layering.

The influence of the soil layering of the basin on the amplification process as well as on the signals duration raises the need for a very detailed knowledge of the soil properties and layers geometry. This is a key point to have reliable predictions of surface seismic motion in alluvial deposits.

Comparison for a real time accelerogram (SH-wave)

A real earthquake is now considered and the surface motion is computed in time domain for both basin models. The June 1994 earthquake ($M=3$) is presented but other computations for the May 1995 Arnaia earthquake were also performed and are discussed by Kham (2004). The incident seismic motion is chosen as the reponse at the *PRO* station (North). As shown in Fig.5.69, the signals are then computed at all other station locations along the free surface for both the simplified and complete models. As previously discussed by Chávez-García et al. (2002), the quality of the reference station is very important and *PRO* is the best one in the area but is still located on a very thin alluvial layer approximately at point 1 of Fig.5.66. In Fig.5.69, the measurements made at the different stations are given (top) for the sake of comparison. June 1994 signals are filtered above 6Hz. The scale of the signals is identical for all cases. Slight differences are observed between measured *PRO* signals and computed ones because *PRO* is not a perfect bedrock station (Chávez-García et al., 2002).

As shown in Fig.5.69, both models lead to a large amplification of the signals as well as an increase of their duration in the central part of the basin. This trend is in good agreement with the measurements which show a large amplification at the centre of the basin. The complete model generally gives larger amplification (closer to the measurements) since it describes more precisely the soil layering near the free surface. It is especially the case for the *GRE* station for which the influence of near surface geology appears significant.

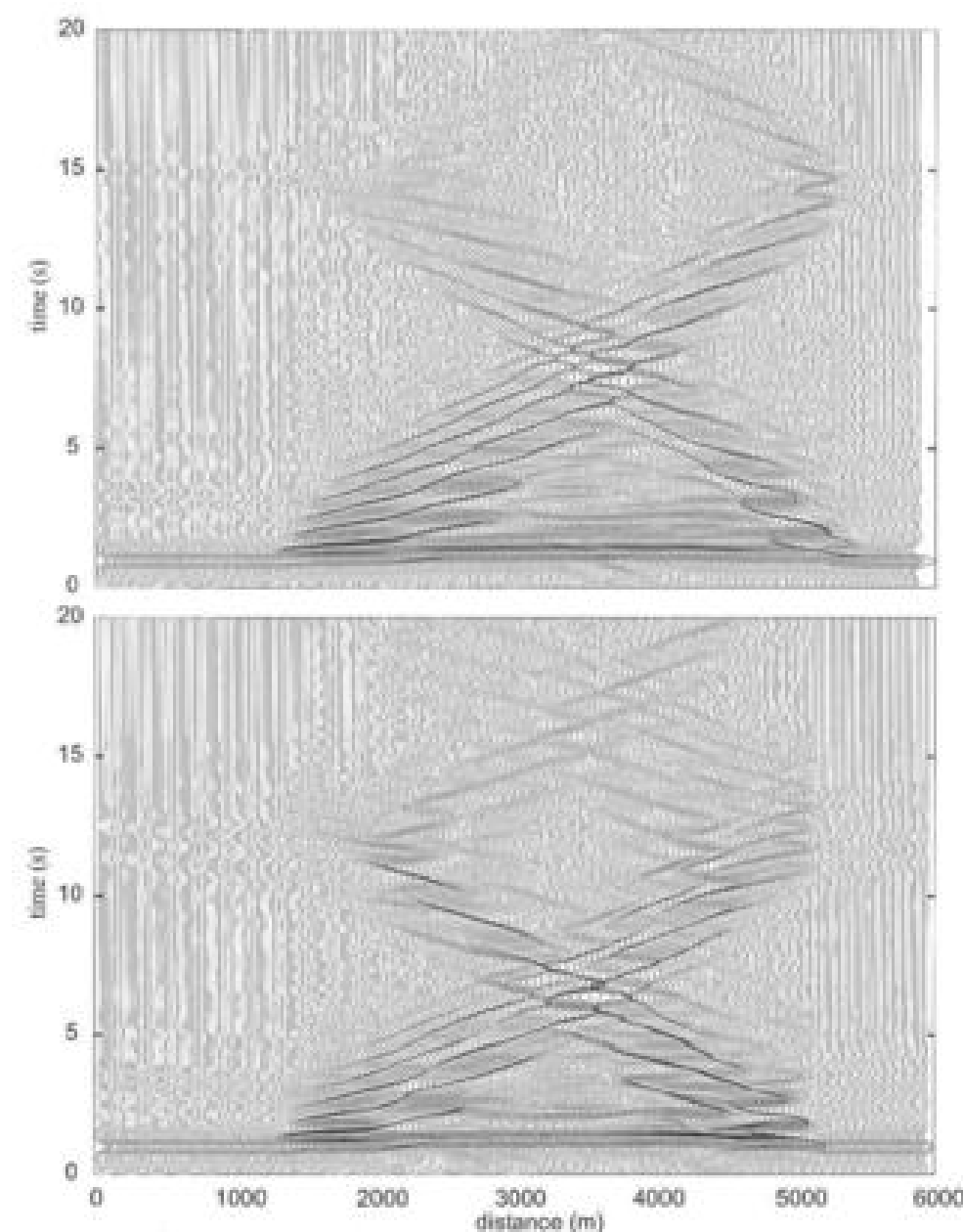


Fig. 5.68: Time domain responses for the simplified (top) and the complete (bottom) Volvi basin models under a 1Hz Ricker excitation (Semblat et al., 2005).

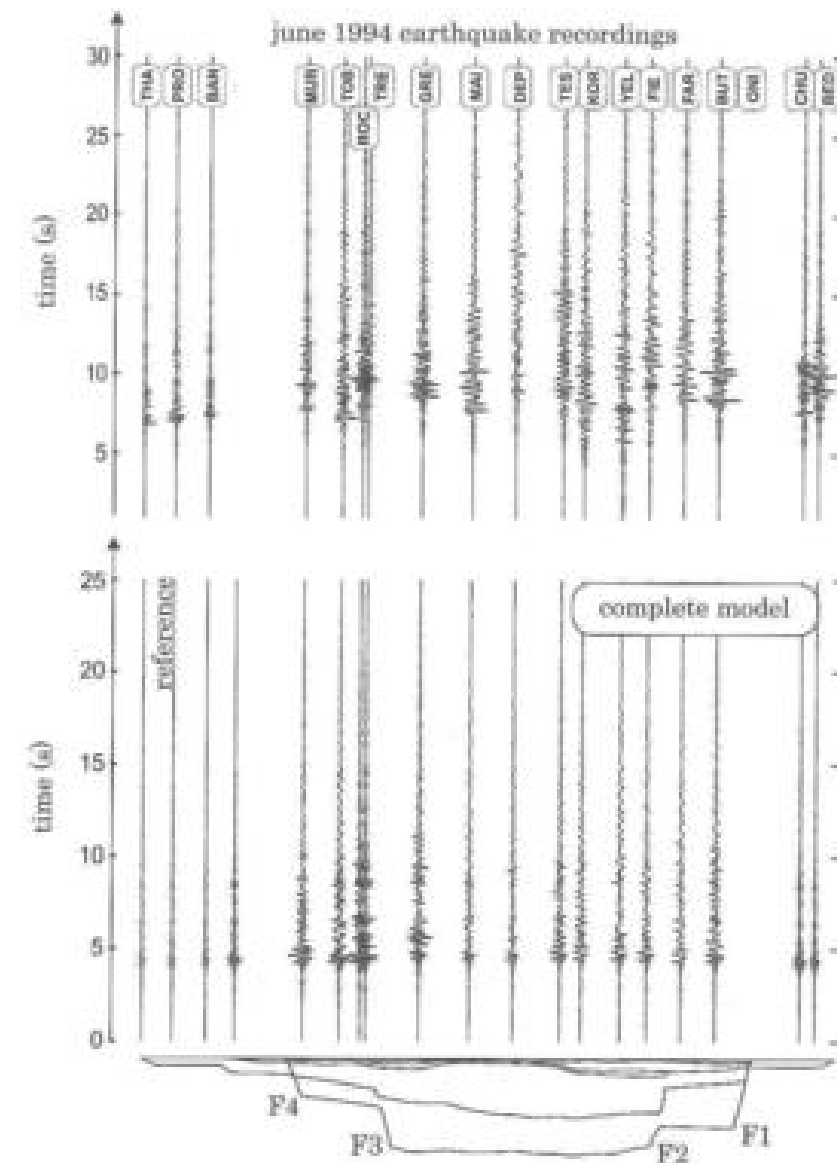


Fig. 5.69: Accelerograms along the Volvi basin for the june 1994 earthquake. Comparison with the simplified (top) and the complete (bottom) basin models solutions for the bedrock station (*PRO*) signal (input) (Semblat et al., 2005).

5.9.5 SV-wave amplification in the Volvi basin

The amplification of *SV*-waves in the Volvi basin is now considered. Figure 5.70 first shows the transfer function of the complete model for a vertical plane *SV* wave. The amplification of both horizontal and vertical motions is displayed as isolines vs distance (along the free surface) and frequency.

The main amplification areas of the horizontal motion of the basin under *SH* wave excitation (Fig.5.67) are recovered in the case of *SV*-wave (Fig.5.70). Their locations are identical in both distance and frequency: the fundamental resonance mode is located at the centre of the basin ($x=3500$ m and $f_0=0.8$ Hz); a large number of amplification peaks also appears on both sides of the model between faults F4 and F3 ($x \in [1000-2000]$ m) and faults F2 and F1 ($x \in [4000-5000]$ m). The corresponding frequency ranges are $f \in [1-3]$ Hz and $f \geq 4$ Hz respectively.

In Fig.5.70 (top), three main amplification areas appear at frequencies 1Hz, 2Hz and 3Hz (resp.) all along the basin width. They correspond to the contribution of the main surface geological structures at lower depths for larger frequencies. Thus, the third amplification area at 3Hz is linked to the resonance of superficial layers well described by the complete model. This superficial resonance was not so strong in the case of *SH*-waves (Fig.5.67).

The transfer function of the vertical motion (Fig.5.70, bottom) gives even more interesting results, since it shows 2D effects due to wave conversion at the layers interfaces as well as surface waves generation. Two particular areas can be noticed:

- The first amplification area, ranging from frequencies 1 and 2Hz and distances 2500m and 4500m, confirms 2D effects involving the deepest part of the basin.
- The second area, located at large frequencies ($f \geq 3$ Hz) and at the basin edges, is associated to the generation of surface waves.

These areas also correspond to the cases where the discrepancy between the simplified and the complete model is the largest (*SH* wave excitation). This is a good reason to consider the complete model rather than the simplified one to investigate such detailed amplification processes.

5.9.6 2D/1D aggravation factor

Makra et al. (2005) also studied the amplification of seismic waves in Volvi. They computed the seismic wavefield at various station locations using the Finite Difference Method (Moczo , 2002). As shown in Fig.5.71, the 2D/1D aggravation factor is found to be nearly 3 for stations *FRM*, *TST*, *GRB* and *GRA*. This value is close to the maximum value proposed by Pitilakis et al. (1999) and that estimated in the case of Nice by Gélin et al. (2008), Fig.5.58.

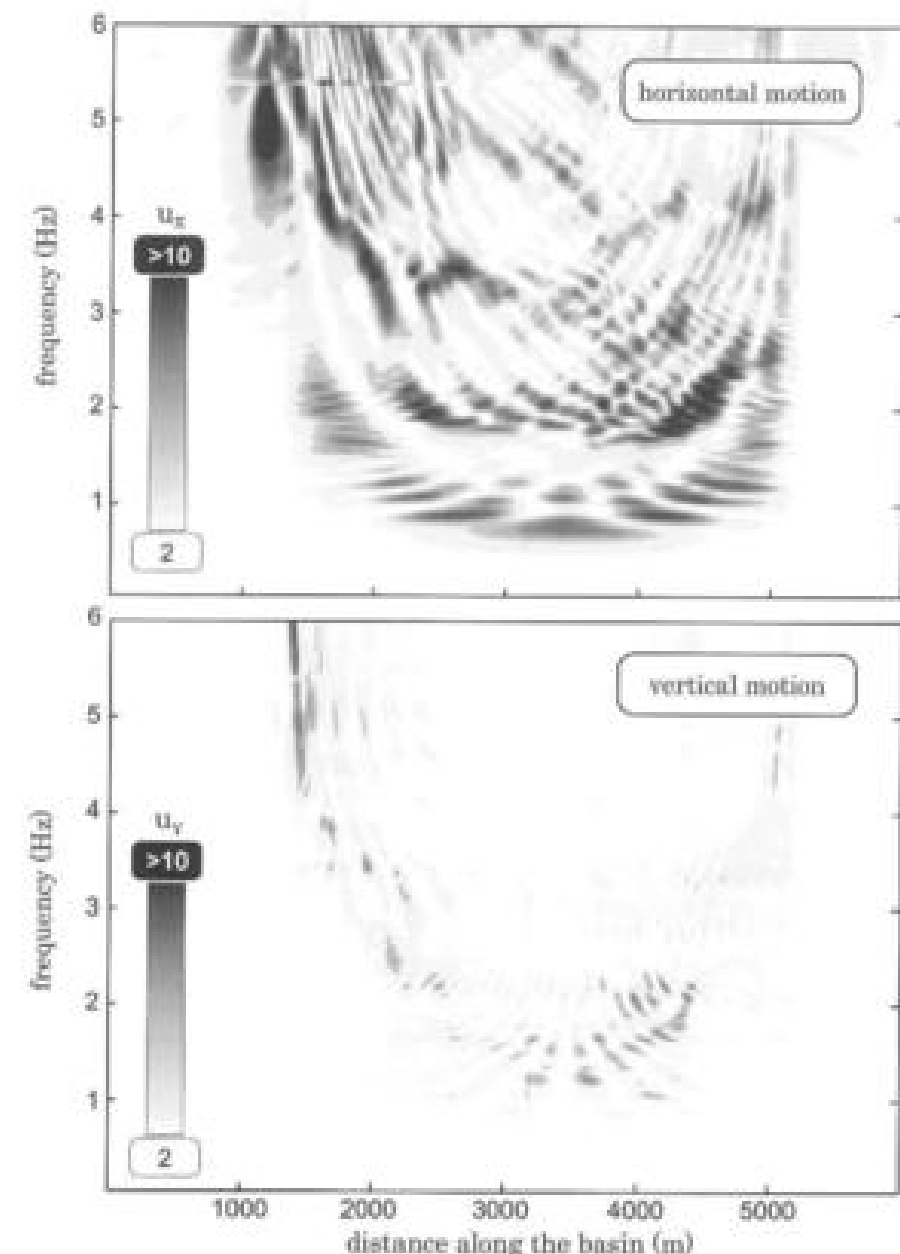


Fig. 5.70: Transfer function for the complete Volvi basin model under *SV*-wave: amplification of horizontal (top) and vertical (bottom) motions (Sembrot et al., 2005).

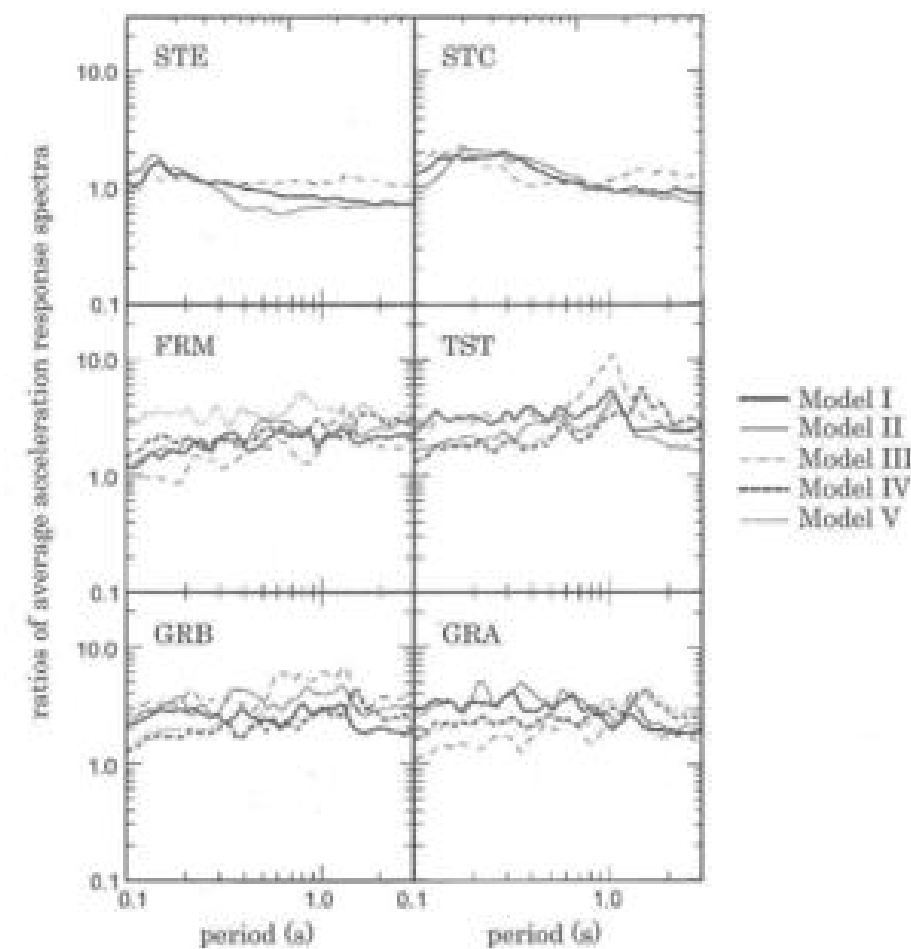


Fig. 5.71: 2D/1D aggravation factor for the Volvi EuroSeisTest at different station locations (Makra et al., 2005).

Conversely, for the *STE* and *STC* stations (Fig. 5.71, top), Makra et al. (2005) found no 2D/1D aggravation. Since these stations are located on very shallow deposits, 1D amplification is mainly involved at these sites. Despite their location, the influence of basin edge effects is also surprisingly small, it is probably due to the fact that the *STE* and *STC* stations are 'beyond' the F_1 fault (i.e. outside the Volvi graben).

5.9.7 Conclusions on site effects in Volvi

The complexity of the geotechnical models depends on the available field data as well as the required accuracy and reliability for the target parameters to characterise seismic wave amplification. The seismic response of the Volvi basin has been studied using two

different numerical models: a very simplified one not taking into account the topmost alluvial layers and a more complete model including a detailed description of the surface soil layering. The main purpose of this comparison is to discuss the influence of the knowledge of the geological structure of the site on the quality of site effects computations. The main conclusions of the analysis are as follows:

- Both models give reliable representation of 2D basin effects and the related seismological processes: an increase of the amplification of the seismic motion (when compared to a 1D analysis) and a duration lengthening in the central part of the basin. Both models give a correct estimation of the main resonance of the basin, in both amplitude and frequency.
- The influence of superficial soil layers shown by the complete model (LGIH) is sometimes significant but mainly influences the high frequency content of the signals as well as (trapped) surface waves propagation.
- The comparison between *SV*-wave amplification and *SH*-wave analysis also shows significant differences between both approaches: the *SH* model is rather simple but does not represent the influence of the basin complex geometry (especially around the graben edges) which is quite important on the local amplification of the seismic motion. These aspects, due to the scattering of *SV*-waves, are taken into account in the *SV*-model, but lead to larger computational costs.
- The amplification spectra, commonly used, do not fully describe 2D site effects and give only a partial view of the amplification processes (for instance, complex scattering phenomena or spatial variability of the seismic motion due to surface waves). An accurate description of the subsurface lithology through complete geological models is necessary to make such detailed analyses.
- As discussed by Riepl et al. (1998), the influence of the azimuth of the source on the local amplification of the seismic motion seems to be significant. This issue was not discussed in the previous simulations since we wanted to avoid additional focusing effects in both numerical models (due to source location) for the sake of easier comparisons. Further analyses (Pedersen et al., 1995) involving local sources rather than plane waves (considered herein) will be needed probably for both 2D and 3D models.
- Such parameters as the frequency content of the seismic event is also important to make the choice of the most suitable (simplified vs detailed) model.
- The 2D/1D aggravation factor was shown to be significant in the deepest part of the basin (Fig. 5.71). The level of aggravation found by Makra et al. (2005) for Volvi is close to that found for the Nice basin by Gélis et al. (2008).
- Finally, the amplification level is found to be large in all cases since we only considered weak motions (small earthquakes). In the case of strong earthquakes, the soil nonlinearity may lead to some deamplification in the surficial soil layers (Bonilla, 2000; Delipine et al., 2007; Gélis et al., 2008; Heuze et al., 2004; Kwok et al., 2008).

5.10 Wave-structure interaction

5.10.1 From soil-structure to wave-structure interaction

Wave propagation in soils may be analyzed in the case where civil engineering structures are located above the soil. As already discussed in Chapter 4, it is then necessary to account for the coupling between the structure and the soil (Fig.5.72). Indeed, when the structure moves under a seismic excitation, it may radiate waves that induce perturbations in the ground motion when compared to the free-field case. Consequently, it is not always possible to prescribe, at the base of the structure, the free-field seismic motion in order to simulate its effect on the structure. In the frequency range of earthquakes, this perturbation may be neglected for small or light structures but not for large or massive ones.

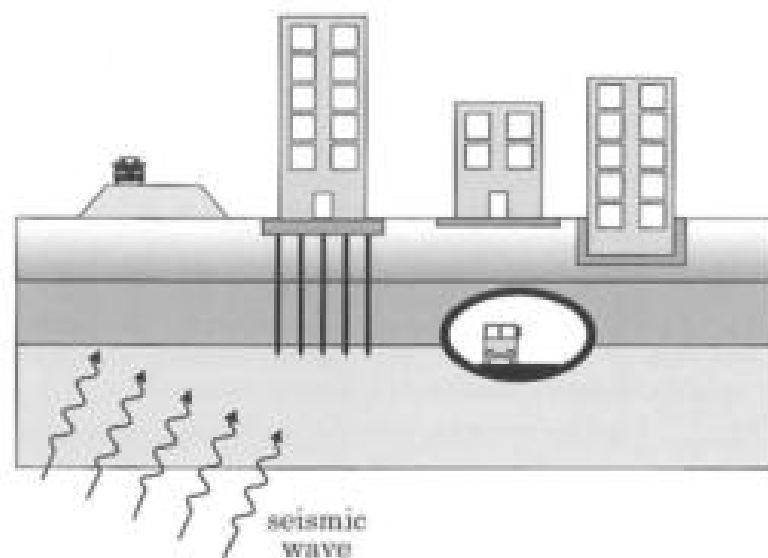


Fig. 5.72: Various types of problems involving wave-structure interaction.

5.10.2 Seismic analysis for buildings

The analysis of dynamic soil-structure interaction may be performed through numerical methods. The first example proposed herein to illustrate the problem of soil-structure interaction is depicted in Fig.5.73. A 50 m high and 30 m wide building is founded on the soil. The soil and the building are hit by a harmonic plane *SH*-wave. The building and the soil are assumed as homogeneous isotropic elastic bodies and are modelled by the Boundary Element Method (Semblat and Dangla, 2005).

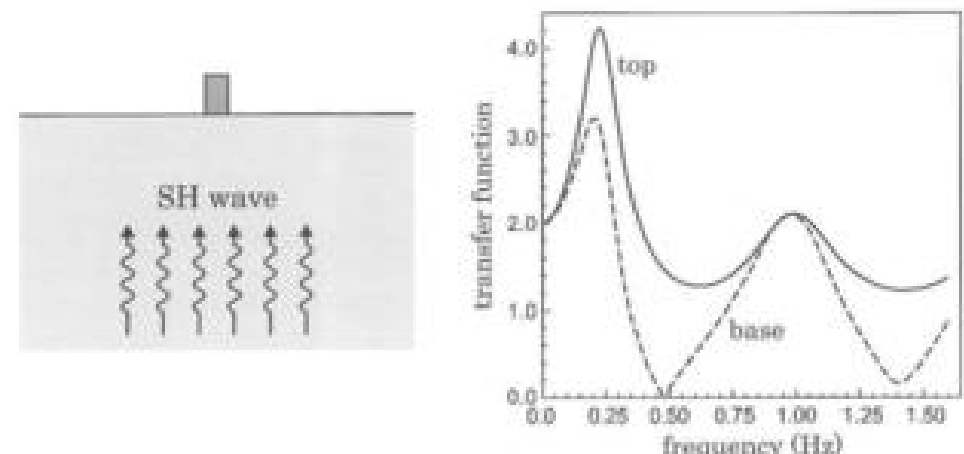


Fig. 5.73: Soil-structure model and numerical results in terms of displacement transfer function at the top and base of the building (Semblat and Dangla, 2005).

The displacement transfer functions at the base and at the top of the building are plotted in Fig.5.73 with respect to frequency for a vertically incident wave. For very low frequencies (long wavelengths), the seismic waves are not sensitive to the influence of the building and the amplitude of the free-field is retrieved (superposition of the incident and reflected waves, that is 2).

In Fig.5.73, specific frequencies for which the base displacement is zero can be noticed. They correspond to the resonant frequencies of the building for the fixed base condition. Nevertheless, as shown in Fig.5.73, the top displacement at these frequencies does not reach its maximum. This result characterizes dynamic soil-structure interaction: the maximum top displacement is reached at frequencies also depending on the soil properties. It is thus mandatory to account for this phenomenon to analyze the dynamic response of the building. It is even possible to derive the frequencies leading to the maximum top displacement from the analysis of soil-structure interaction.

The BEM solution has been previously computed at the free surface and the interface between the soil and the building. The wavefield in the soil is now estimated using the integral representation formula (see Chapter 4). The displacement isovalue are displayed in Fig.5.74 in the case of one building (top) or three identical buildings (bottom). The soil-structure interaction at low frequencies (left) is found to be small when compared to higher frequencies (right). In the case of three buildings, the interaction between the buildings (and through the soil) may be significant since there are some important differences in the buildings motions (esp. at $f=0.2\text{Hz}$ and 0.4Hz).

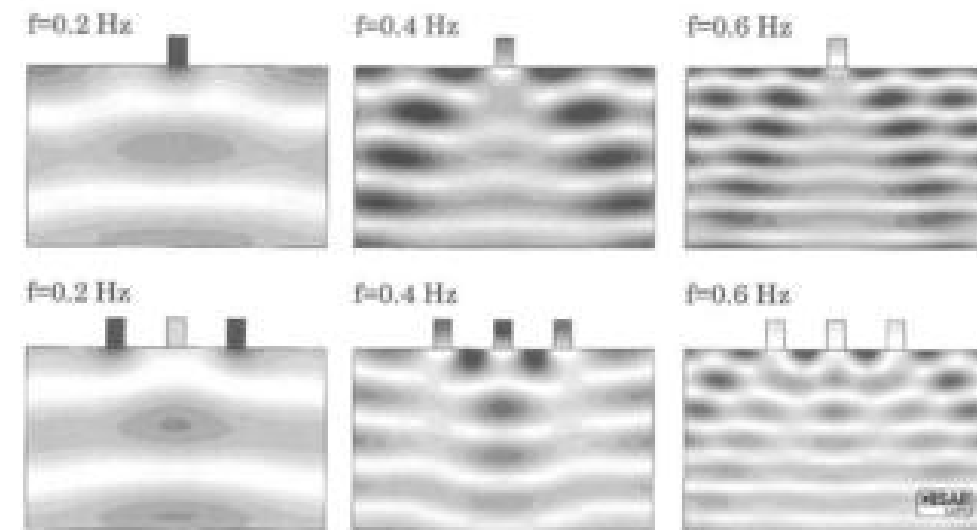


Fig. 5.74: Displacement isovalue in the case of one (top) or three buildings (bottom) (Semblat and Dangla, 2005).

5.10.3 Seismic interaction with underground structures

At the local scale, one may also consider the interaction between an underground cavity (tunnel, mines, etc) and a seismic wave propagating through the soil. The damages observed on underground structures after strong earthquakes assess the vulnerability of such structures especially in their cross-section (Kurose, 2000). For underground structures, the current seismic codes are mainly based on equivalent static approaches in which the complex wave propagation phenomena are not taken into account.

The interaction between a plane *SH*-wave and a tunnel will now be simulated by the Boundary Element Method (see Chapter 4). Considering a homogeneous half-space, the interference patterns (displacement field) displayed in Fig.5.75 illustrate the interaction between the seismic wavefield and the tunnel for two different incidence angles. The wave/tunnel interaction may be strong at certain frequencies influencing both the displacement and tractions along the tunnel wall, but also the seismic wavefield at the free surface (Fig.5.75). The wave/tunnel interaction may indeed increase the displacement field in some areas but also, as depicted in Fig.5.75, lead to some *shadow* areas with a very low displacement amplitude (above the tunnel for $\theta = 90^\circ$ or on the right for $\theta = 60^\circ$). As shown by Kurose (2000) or Khan et al. (2002b), the interaction is governed by the ratio between the dimensions and depth of the tunnel on one hand, and the wavelength of the seismic wavefield on the other. The numerical solutions computed by the Boundary Element Method and displayed in Fig.5.75 are compared to closed-form solutions in (Khan et al., 2002b).

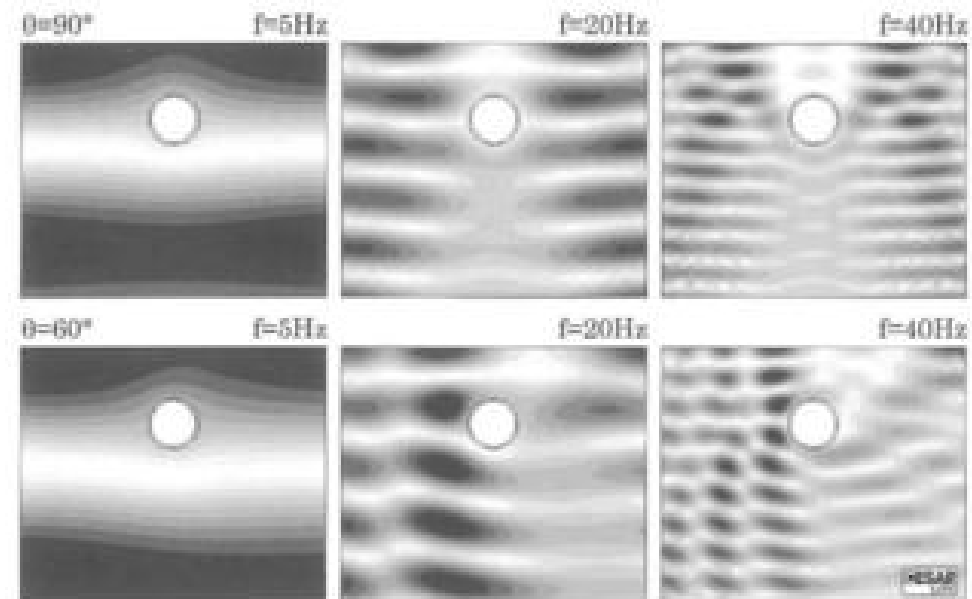


Fig. 5.75: BEM simulations of wave/tunnel interaction: seismic wavefield for two incidences ($\theta = 90^\circ$, top, and $\theta = 60^\circ$, bottom) and different frequencies (Semblat and Dangla, 2005).

5.10.4 Seismic interactions at the local and global scales

From soil-structure to site-city interaction

The analysis of wave/structure interaction may be performed at a local or global (i.e. large) scale (Bard et al., 2005; Boutin and Roussillon, 2004). Indeed, for alluvial basins located in densely urbanized areas, the buildings may influence the propagation of seismic wave near the free surface. Furthermore, as previously evidenced by several authors (Guéguen et al., 2000; Khan et al., 2006; Virgin and Bard, 1996), the vibration of a structure at the free surface generates a radiated wavefield into the soil. The dynamic soil/structure interaction will be firstly analyzed at the local scale of a single building. At the global scale, the influence of surface structures, such as buildings, on the propagation of seismic waves will then be analyzed in the case of an entire alluvial basin. Dynamic soil/structure interaction may thus be investigated at various scales:

- the local scale (e.g. single building) corresponds to classical dynamic soil-structure interaction (*SST*) and involves the building foundation and a part of the neighbouring soil;

- the intermediate scale concerns one or several buildings as well as the soil at the geotechnical scale (layered soil). Waves generated by the vibration of the structure may have a significant influence on the motion of the neighbouring structures (see Fig.5.74);
- the global scale represents an entire city and the geological profile (e.g. alluvial basin) and the interaction is thus considered as site-city interaction (*SCI*) for instance (Semblat et al., 2008). It may lead to significant modifications of the seismic wavefield due to the dynamic response of the numerous buildings involved in the city.

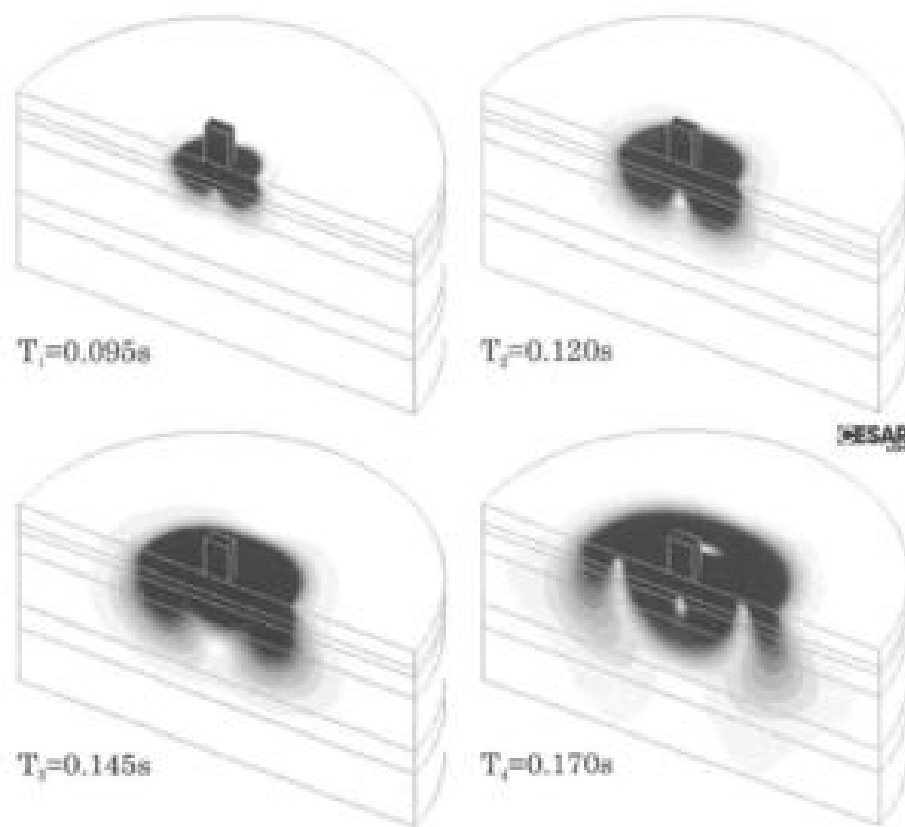


Fig. 5.76: FEM simulations of dynamics experiments performed at Volvi EuroSeisTest: displacement wavefield generated by the vibration of a building mock-up at different times $T_1=0.095\text{s}$, $T_2=0.120\text{s}$, $T_3=0.145\text{s}$ and $T_4=0.170\text{s}$ (Bard et al., 2005).

Local seismic interaction

At the local scale, beyond the classical soil-structure interaction, soil-structure-soil interaction (*SStSI*) may appear as a link between the dynamic response of the structures and the seismic waves radiated into the soil. This case is illustrated in Fig.5.76 where, considering dynamic experiments performed at Volvi EuroSeisTest (Greece), the three-dimensional seismic wavefield radiated by a vibrating building is computed by the Finite Element Method (see Chapter 4). As in the case of seismic wave amplification, the velocity contrast between the soil layers governs the propagation of the radiated surface waves. From the experimental and numerical results obtained by Guéguen et al. (2000), the wavefield radiated by the structure may be trapped in the surficial soil layers and hence be propagated along large distances. As illustrated in Fig.5.76, the directivity of the three-dimensional wavefield also characterizes the way the energy is transmitted from the structure to the soil.

Global seismic interaction

Seismic interaction between structures at large scales. At an intermediate scale, the structure-to-structure through the soil interaction may also be significant. It may be assessed at the scale of several structures: the wavefield radiated into the soil by some of these structures may influence the motion of neighbouring structures (Fig.5.74). The level of such interactions depends on the dynamic features of the structures, as well as the fundamental frequencies of the soil layers (Bard et al., 2005; Clouet and Aubry, 2001; Lombert et al., 2004; Tsogka and Virgin, 2003). For this type of interaction, detailed results are proposed in (Bard et al., 2005), (Guéguen et al., 2000) and (Kham et al., 2006).

Seismic interaction at the scale of an alluvial basin. At a global scale, the seismic interaction between an alluvial basin and a large number of buildings may be considered (Bielak et al., 1999; Chávez-García and Cárdenas-Soto, 2002). As depicted in Fig.5.77, the shallow alluvial basin, located in Nice and studied earlier in this chapter, is combined with a building network of variable density. The site-city interaction was studied for various urban configurations and soil layering by Kham et al. (2006) and Semblat et al. (2008).



Fig. 5.77: Model for the analysis of site-city interaction in a shallow alluvial basin (Semblat et al., 2008).

Modifications of the seismic ground motion. The influence of the buildings on the seismic ground motion is analyzed by the Boundary Element Method in the frequency domain (see Chapter 4). The urban seismic wavefield is compared to the free-field ground motion studied earlier in this chapter, as well as in (Semblat *et al.*, 2000). The perturbations, u_p , are then defined as the difference between the total wavefield, u_t , and the free-field motion u_{ff} : $u_p = u_t - u_{ff}$. The numerical results are displayed in Fig. 5.78 in terms of perturbations for a given city configuration. The influence of the building network is found to be significant. As shown in (Kham *et al.*, 2006), the radiated wavefield is larger when the eigenfrequencies of the buildings are close to the fundamental frequencies of the alluvial deposit. Furthermore, complex directivity effects may be observed in Fig. 5.78. They are due to simple or multiple interactions between the structures and the alluvial basin (Semblat *et al.*, 2008). At the global scale, the dynamic interaction between the soil/site and the surface constructions may then be significant especially in dense urban areas. As shown by (Semblat *et al.*, 2008), it may lead to detrimental as well as beneficial effects on the ground motion along the basin surface.

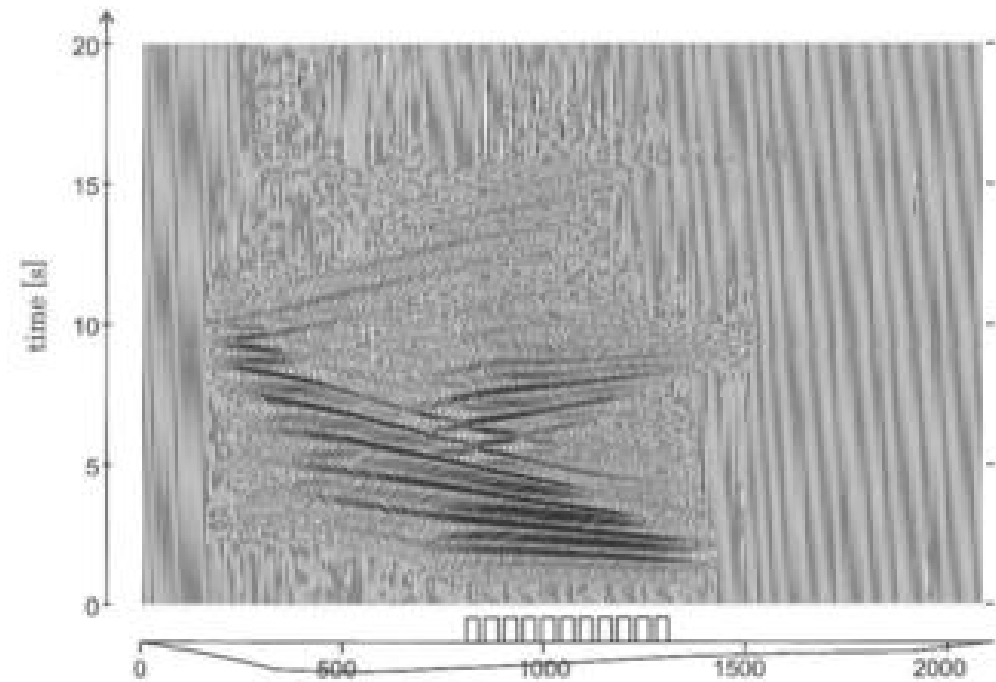


Fig. 5.78: Influence of site-city interaction on the amplification of the seismic ground motion in a shallow alluvial basin (Nice, France): perturbations u_p for a given city configuration (Semblat *et al.*, 2008).

Appendices

Appendix A

Several operators in mechanics

A.1 Vectors and product of vectors

In this book, vectors are denoted as underlined characters as follows:

$$\underline{u} \quad \text{or} \quad u_i \quad (i = x, y, z) \quad \text{in components} \quad (\text{A.1})$$

The product of two vectors \underline{u} and \underline{v} is written:

$$\underline{u} \cdot \underline{v} \quad \text{or} \quad u_i v_i \quad (i = x, y, z) \quad \text{in components} \quad (\text{A.2})$$

where the summation on repeated indices is considered.

It yields a scalar and corresponds to the classical inner-product.

A.2 Tensors and product

2nd order tensors are denoted as double-underlined characters as follows:

$$\underline{\underline{\sigma}} \quad \text{or} \quad \sigma_{ij} \quad (i, j = x, y, z) \quad \text{in components} \quad (\text{A.3})$$

The product of a 2nd order tensor $\underline{\underline{\sigma}}$ and a vector \underline{n} is defined as:

$$\underline{\underline{\sigma}} \cdot \underline{n} = \underline{t} \quad \text{with:} \quad t_i = \sigma_{ij} n_j \quad (i, j = x, y, z) \quad (\text{A.4})$$

A.3 Gradient and Laplacian

A.3.1 Definitions

The gradient is denoted $\underline{\nabla}$ and is such as:

$$\underline{\nabla} = \frac{\partial}{\partial x} \underline{e}_x + \frac{\partial}{\partial y} \underline{e}_y + \frac{\partial}{\partial z} \underline{e}_z \quad (\text{A.5})$$

The Laplacian is denoted Δ and is defined by:

$$\Delta = \nabla^2 = \frac{\partial^2}{\partial x^2} + \frac{\partial^2}{\partial y^2} + \frac{\partial^2}{\partial z^2} \quad (\text{A.6})$$

A.3.2 Examples

The gradient of a scalar variable u is a vector defined as follows:

$$\nabla(u) = \frac{\partial u}{\partial x} e_x + \frac{\partial u}{\partial y} e_y + \frac{\partial u}{\partial z} e_z \quad (\text{A.7})$$

The Laplacian of a scalar variable u is a scalar expressed as:

$$\Delta(u) = \nabla^2(u) = \frac{\partial^2 u}{\partial x^2} + \frac{\partial^2 u}{\partial y^2} + \frac{\partial^2 u}{\partial z^2} \quad (\text{A.8})$$

The product of the gradient by a second order tensor $\underline{\underline{\sigma}}$ yields a vector:

$$\nabla \cdot \underline{\underline{\sigma}} = \sum_j \frac{\partial \sigma_{xj}}{\partial j} e_x + \sum_j \frac{\partial \sigma_{yj}}{\partial j} e_y + \sum_j \frac{\partial \sigma_{zj}}{\partial j} e_z \quad j = x, y, z \quad (\text{A.9})$$

This expression is used in the equilibrium equation (Chapter 3).

The gradient of a vector \underline{u} yields a second order tensor, written under matrix form as follows:

$$\nabla(\underline{u}) = \nabla \underline{u} = \begin{pmatrix} \frac{\partial u_x}{\partial x} & \frac{\partial u_x}{\partial y} & \frac{\partial u_x}{\partial z} \\ \frac{\partial u_y}{\partial x} & \frac{\partial u_y}{\partial y} & \frac{\partial u_y}{\partial z} \\ \frac{\partial u_z}{\partial x} & \frac{\partial u_z}{\partial y} & \frac{\partial u_z}{\partial z} \end{pmatrix} \quad (\text{A.10})$$

Similar expressions in cylindrical or spherical coordinates may be found in (Salençon, 2001) or (Fung and Tong, 2001).

Appendix B

Synthetic wavelets

B.1 Ricker wavelet

The Ricker wavelets are defined by considering the derivatives of a Gaussian at various orders (Mavroeidis and Papageorgiou, 2003; Ryan, 1994).

- The Ricker wavelet at order 0 (i.e. gaussian) is thus:

$$R_0(t) = \frac{A}{2} \exp \left[-\pi^2 \frac{(t - t_s)^2}{t_p^2} \right] \quad (\text{B.1})$$

- At order 1 (first derivative of $R_0(t)$), the Ricker wavelet is:

$$R_1(t) = -A \pi \frac{t - t_s}{t_p} \exp \left[-\pi^2 \frac{(t - t_s)^2}{t_p^2} \right] \quad (\text{B.2})$$

- As already detailed in Chapter 4, the 2nd order Ricker wavelet (second derivative of $R_0(t)$) is defined as:

$$R_2(t) = A \left(2\pi^2 \frac{(t - t_s)^2}{t_p^2} - 1 \right) \exp \left[-\pi^2 \frac{(t - t_s)^2}{t_p^2} \right] \quad (\text{B.3})$$

where t_s gives the time corresponding to the maximum amplitude for the 0th order and 2nd order Ricker wavelets and t_p the fundamental period of the 2nd order wavelet.

The time variations of these Ricker wavelets are displayed in Fig.B.1 and the related spectra in Fig.B.2. As shown in Fig.B.1 for the 2nd order Ricker wavelet (bottom), it is also possible to define the wavelet breadth t_b as (Ryan, 1994):

$$t_b = \frac{\sqrt{6}t_p}{\pi} \simeq 0.78t_p \quad (\text{B.4})$$

t_b corresponds to the time delay between both secondary peaks of the 2nd order Ricker wavelet.

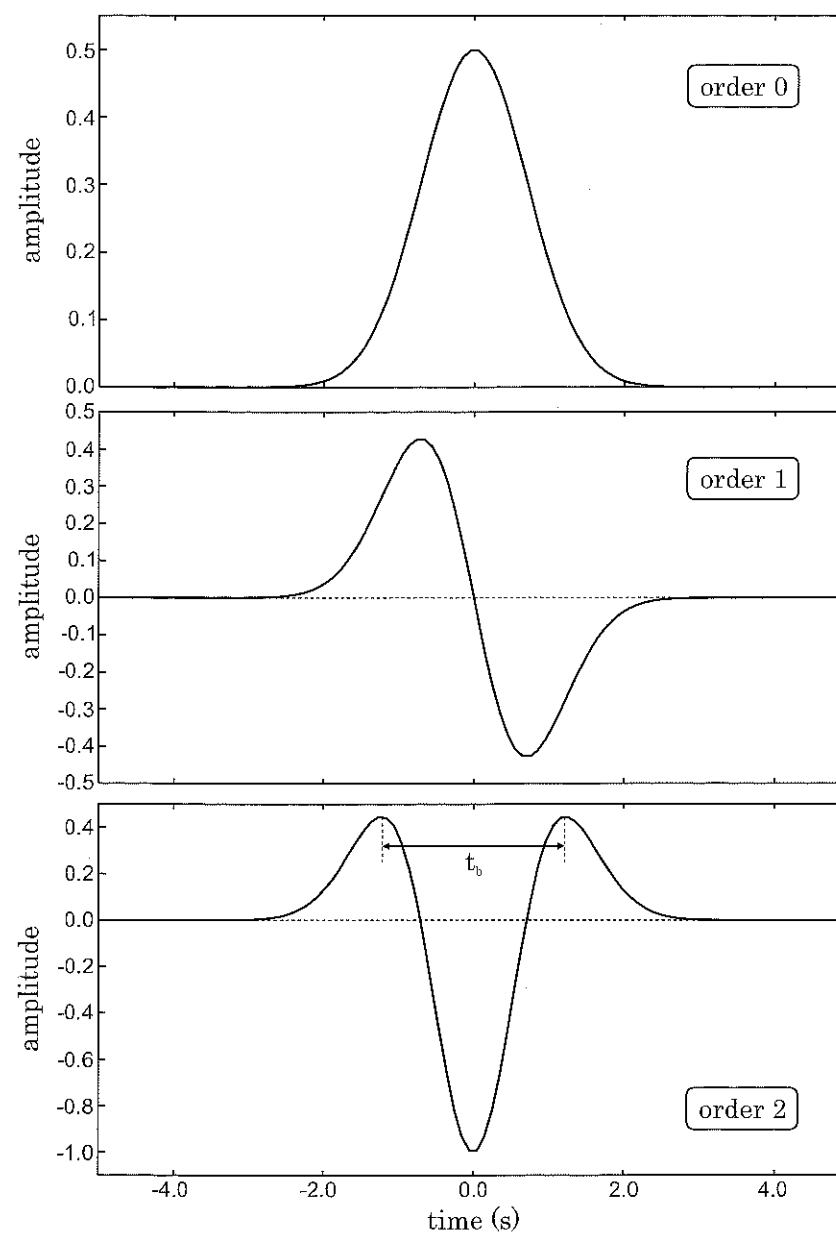


Fig. B.1: Ricker wavelets at various orders: 0th order (top), 1st order (middle) and 2nd order (bottom), also see Chapter 4.

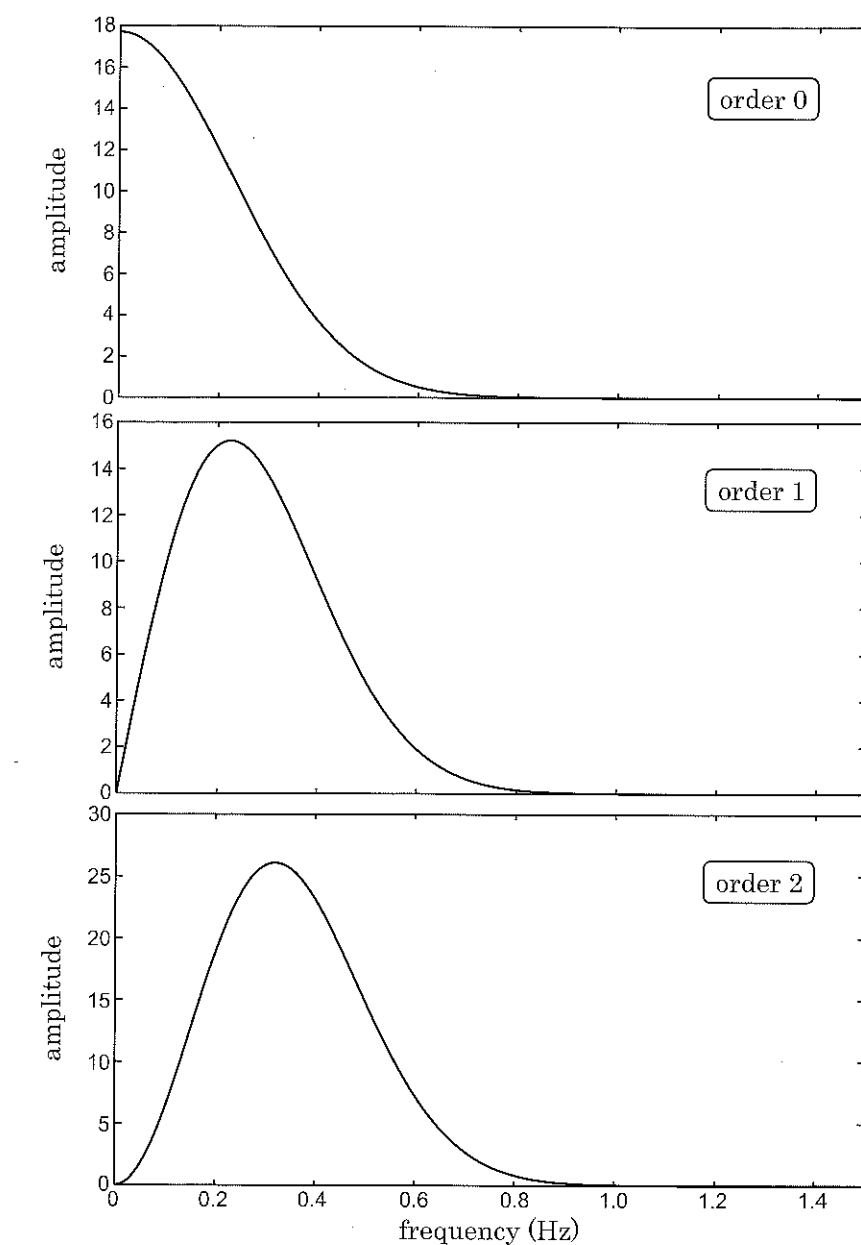


Fig. B.2: Fourier spectra of Ricker wavelets at various orders: 0th order (top), 1st order (middle) and 2nd order (bottom).

B.2 Gabor wavelet

The Gabor wavelet is defined as follows (Mavroeidis and Papageorgiou, 2003):

$$f(t) = A \exp\left(-\frac{4\pi^2 f_p^2}{\gamma^2} t^2\right) \cos(2\pi f_p t + \nu) \quad (\text{B.5})$$

where: A is the amplitude,
 f_p is the fundamental frequency,
 ν is the phase angle,
 γ characterizes the oscillatory character.

The Gabor wavelet and its Fourier spectrum are displayed in Fig.B.3 for various γ values (with $f_p = 1\text{Hz}$ and $\nu = 0$).

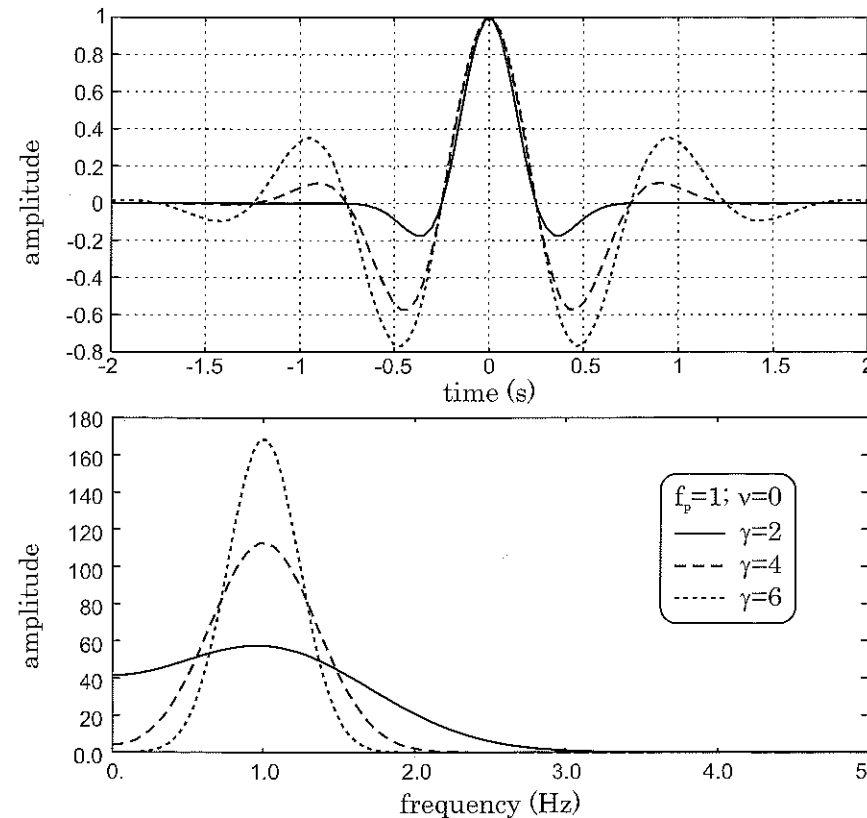


Fig. B.3: Gabor wavelet (top) and its Fourier spectrum (bottom) for $f_p = 1\text{Hz}$ and $\nu = 0$.

B.3 Mavroeidis & Papageorgiou wavelet

The wavelet recently proposed by Mavroeidis and Papageorgiou (2003) is such as:

$$f(t) = \frac{A}{2} \left[1 + \cos\left(\frac{2\pi f_p}{\gamma} t\right) \right] \cos(2\pi f_p t + \nu) \quad (\text{B.6})$$

where: A is the amplitude,
 f_p is the fundamental frequency,
 ν is the phase angle,
 γ characterizes the oscillatory character.

The Mavroeidis & Papageorgiou wavelet and its Fourier spectrum are displayed in Fig.B.4 for $f_p = 0.2\text{Hz}$, $\gamma=4$ and $\nu = 0$. Mavroeidis & Papageorgiou (2003) performed many seismic waveform identifications using their wavelet and comparing with the Gabor wavelet.

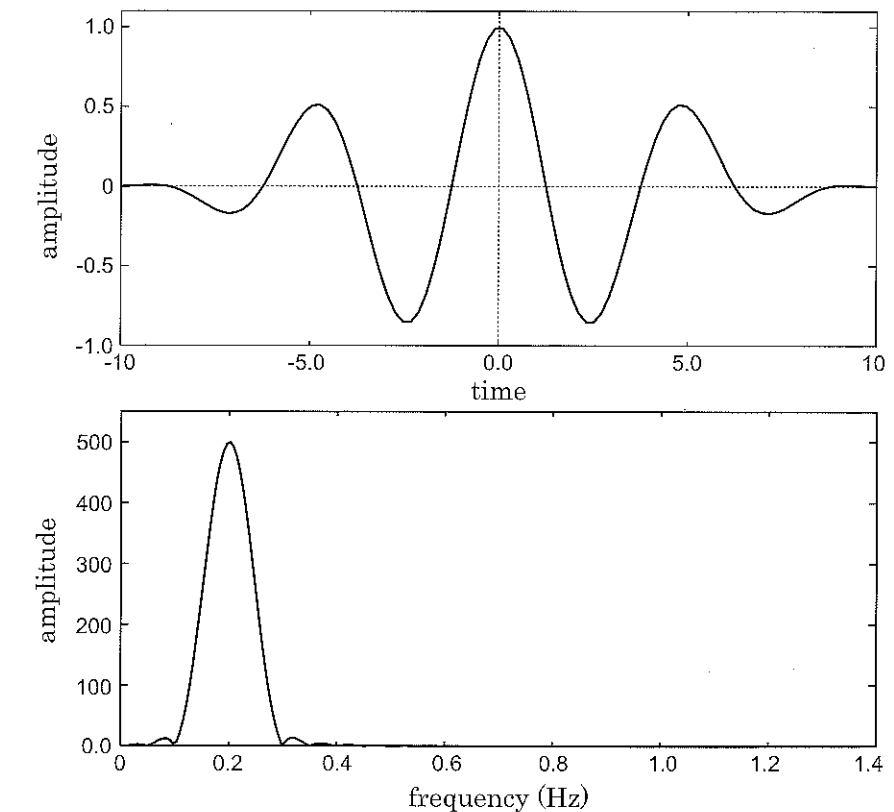


Fig. B.4: Mavroeidis & Papageorgiou wavelet (top) and its Fourier spectrum (bottom) for $f_p = 0.2\text{Hz}$, $\gamma=4$ and $\nu = 0$.

B.4 Generalized Rayleigh wavelet

The generalized Rayleigh wavelet is defined as follows (Mavrocidis and Papageorgiou, 2003):

$$f(t) = A(-1)^k \frac{\exp[i(\nu + \frac{\pi}{2})]}{(i + \frac{2\pi f_p t}{k})^{k+1}} \quad (\text{B.7})$$

where: A is the amplitude,
 f_p is the fundamental frequency,
 ν is the phase angle,
 k controls the number of "lobes".

The generalized Rayleigh wavelet and its Fourier spectrum are displayed in Fig.B.5 for various k values (with $f_p = 1\text{Hz}$ and $\nu = 0$).

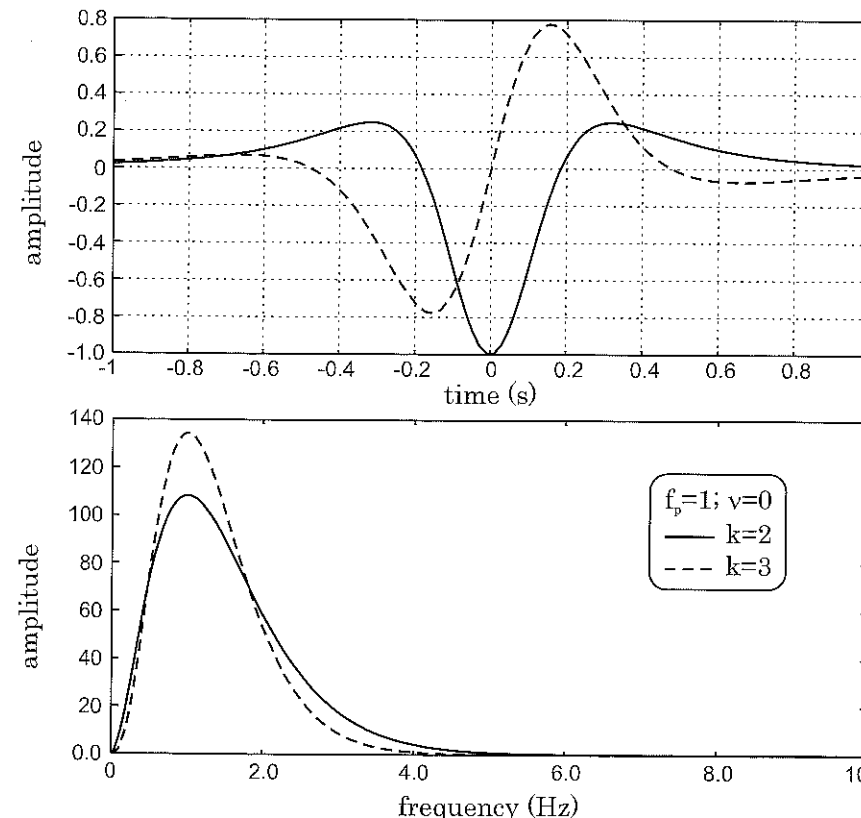


Fig. B.5: Generalized Rayleigh wavelet (top) and its Fourier spectrum (bottom) for $f_p = 1\text{Hz}$ and $\nu = 0$.

B.5 Küpper wavelet

The Küpper wavelet is defined as follows (Mavroeidis and Papageorgiou, 2003):

$$f(t) = A \left[\sin\left(m \frac{\pi t}{T}\right) - \frac{m}{m+2} \sin\left((m+2) \frac{\pi t}{T}\right) \right] \quad (\text{B.8})$$

where: A is the amplitude,
 T is the duration,
 m controls the number of half-cycles.

The Küpper wavelet and its Fourier spectrum are displayed in Fig.B.6 for various m values (with $T = 5\text{s}$).

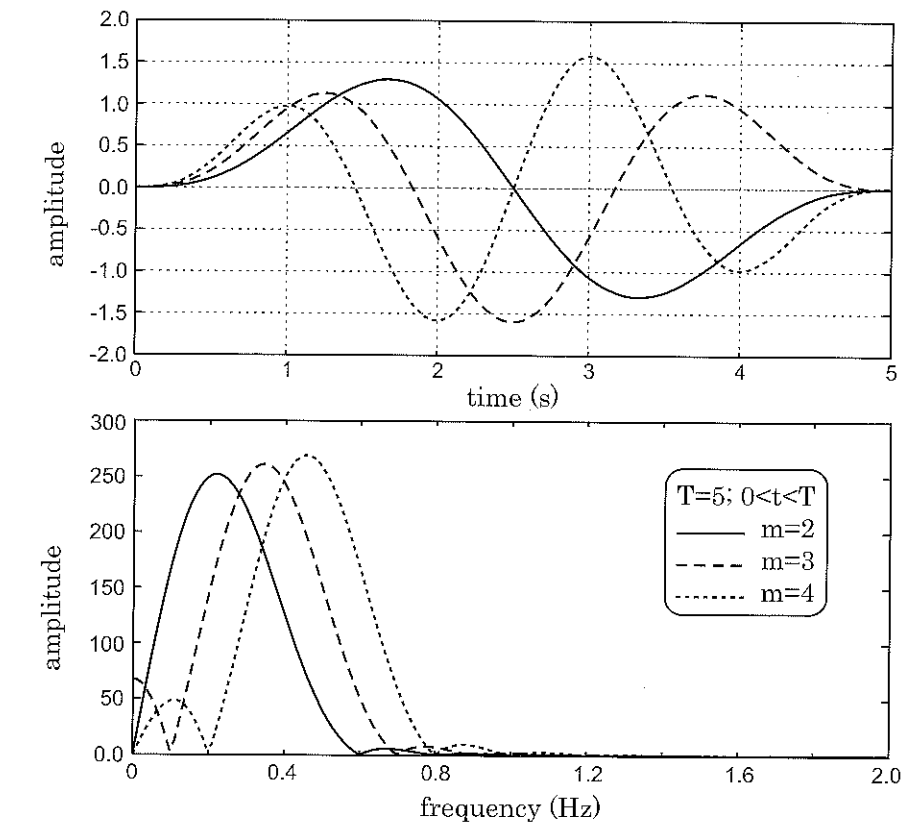


Fig. B.6: Küpper wavelet (top) and its Fourier spectrum (bottom) for $T = 5$.

B.6 Ormsby wavelet

The Ormsby wavelet is defined as follows (Ryan, 1994):

$$f(t) = A \left\{ \left[\frac{\pi f_4^2}{f_4 - f_3} \operatorname{sinc}^2(\pi f_4 t) - \frac{\pi f_3^2}{f_4 - f_3} \operatorname{sinc}^2(\pi f_3 t) \right] - \left[\frac{\pi f_2^2}{f_2 - f_1} \operatorname{sinc}^2(\pi f_2 t) - \frac{\pi f_1^2}{f_2 - f_1} \operatorname{sinc}^2(\pi f_1 t) \right] \right\} \quad (\text{B.9})$$

where: f_1 and f_2 define the lower range frequency band,
 f_3 and f_4 define the higher range frequency band.

The normalized Ormsby wavelet and its Fourier spectrum are displayed in Fig.B.7 for various higher frequency values f_3 and f_4 (with $f_1=5\text{Hz}$ and $f_2=10\text{Hz}$). For the Ormsby wavelet, the spectrum is very flat in the frequency band of interest.

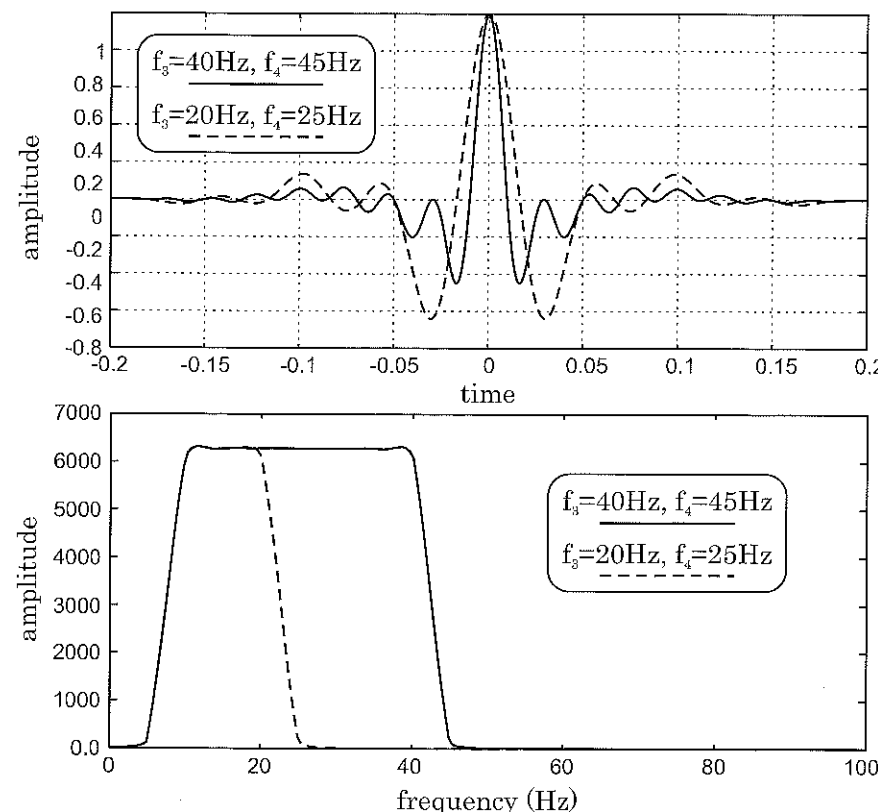


Fig. B.7: Ormsby wavelet (top) and its Fourier spectrum (bottom) for $f_1=5\text{Hz}$ and $f_2=10\text{Hz}$.

The following wavelet types were mainly proposed as analyzing wavelets for time-frequency signal processing (Daubechies, 1992; Jaffard *et al.*, 2001).

B.7 Morlet wavelet

The analyzing wavelet proposed by Morlet *et al.* (1984) may be defined as follows:

$$f(t) = \exp\left(-\frac{t^2}{2}\right) \cos 5t \quad (\text{B.10})$$

Various scalings may be applied to this wavelet. The Morlet wavelet and its Fourier spectrum are displayed in Fig.B.8.

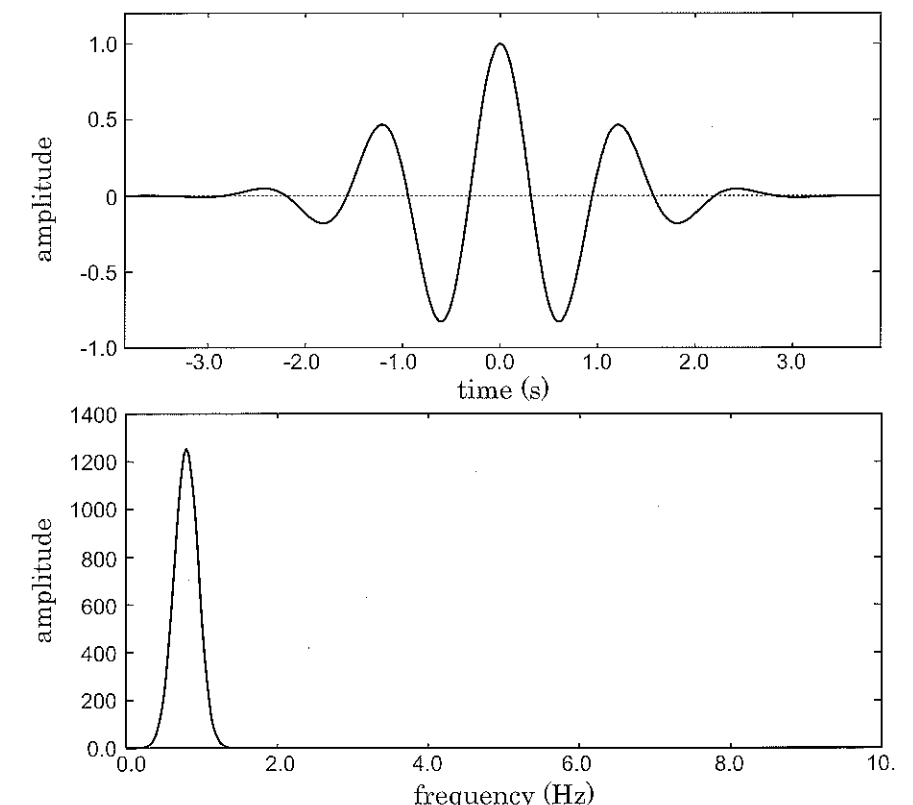


Fig. B.8: Morlet wavelet (top) and its Fourier spectrum (bottom).

B.8 Meyer wavelet

Other types of analyzing wavelets have been proposed from the theoretical work of Meyer (Jaffard *et al.*, 2001). The decomposition of a signal on a set of wavelets raises the need for the definition of *orthogonal wavelet bases*. The set of Meyer wavelets ψ_{jk} is defined in the frequency domain as follows:

$$\psi_{jk}(f) = 2^{\frac{j}{2}} \psi(2^j f - k) \quad (\text{B.11})$$

$$\text{where: } \psi(f) = \exp\left(-i\frac{f}{2}\right) \sqrt{\gamma(f)} \quad (\text{B.12})$$

$$\begin{aligned} \text{with: if } f \in \left[0, \frac{2\pi}{3}\right] & \quad \gamma(f) = 0 \\ \text{if } f \in \left[\frac{2\pi}{3}, \frac{4\pi}{3}\right] & \quad \gamma(f) = \theta\left(\frac{3f}{2\pi} - 1\right) \\ \text{if } f \in \left[\frac{4\pi}{3}, \frac{8\pi}{3}\right] & \quad \gamma(f) = \theta\left(2 - \frac{3f}{4\pi}\right) \\ \text{if } f \in \left[\frac{8\pi}{3}, +\infty\right[& \quad \gamma(f) = 0 \end{aligned} \quad (\text{B.13})$$

One of the best set of θ functions was found to be as follows (Jaffard *et al.*, 2001):

$$\theta_n(f) = \frac{\int_0^f x^n (1-x)^n dx}{\int_0^1 x^n (1-x)^n dx} \quad (\text{B.14})$$

Considering Eq.(B.12) for $n = 1$ (i.e. $\theta(f) = 3f^2 - 2f^3$), the $\gamma(f)$ function and the Fourier spectrum of the Meyer wavelet are displayed in Fig.B.9 (top and middle resp.). The Meyer wavelet in time domain, computed using the inverse Fourier transform, is also plotted in Fig.B.9 (bottom).

When compared to the Morlet wavelet, the shape of the Meyer wavelet leads to lower amplitude secondary peaks. One of the main interest of Meyer wavelets is that it leads to an orthogonal base of wavelets which is very interesting for decomposition and synthesis purposes (Jaffard *et al.*, 2001). Daubechies (1992) also proposed various types of wavelets.

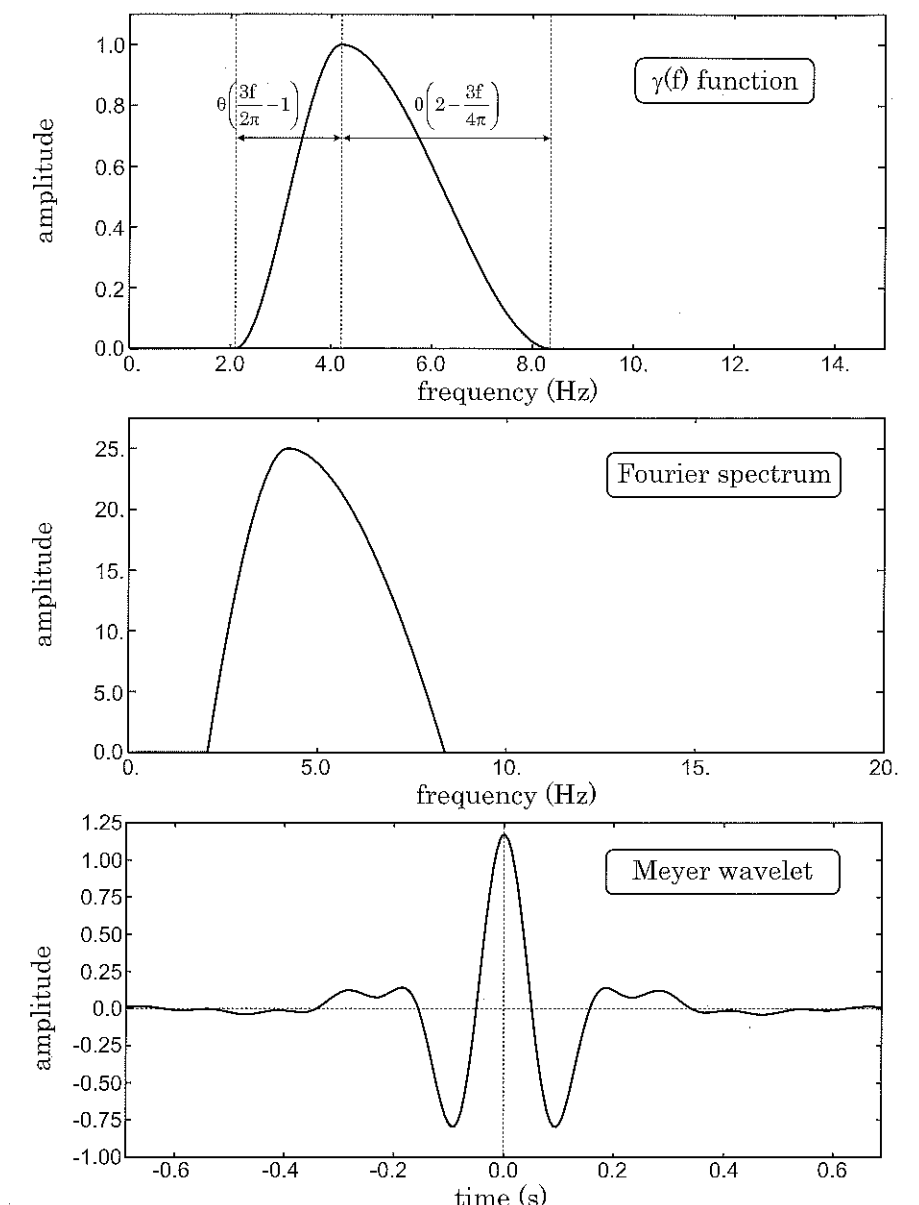


Fig. B.9: Meyer wavelet: $\gamma(f)$ function (top), Fourier spectrum (middle) and time-domain signal (bottom) for $n=1$.

B.9 Double-*M* wavelet

In the field of train induced vibrations, the double-*M* wavelet characterizes the excitation induced by the bogie on the track. It is defined by two gaussians (Ricker signals at order zero). Al Shaer *et al.* (2008) proposed the following combination:

$$F(t, Q, v) = \frac{QY}{2} \left[X \frac{(vt-a)^2}{d^2} + X \frac{(vt-a-L)^2}{d^2} \right] \quad (\text{B.15})$$

where Q is the load supported by the axle, v is the train speed, t is the time, d the distance between two sleepers, a a critical distance, L the distance between two axles of a bogie, X and Y are dimensionless variables depending on the elasticity modulus of the soil.

The double-*M* wavelet proposed by Al Shaer *et al.* (2008) is depicted in Fig.B.10.

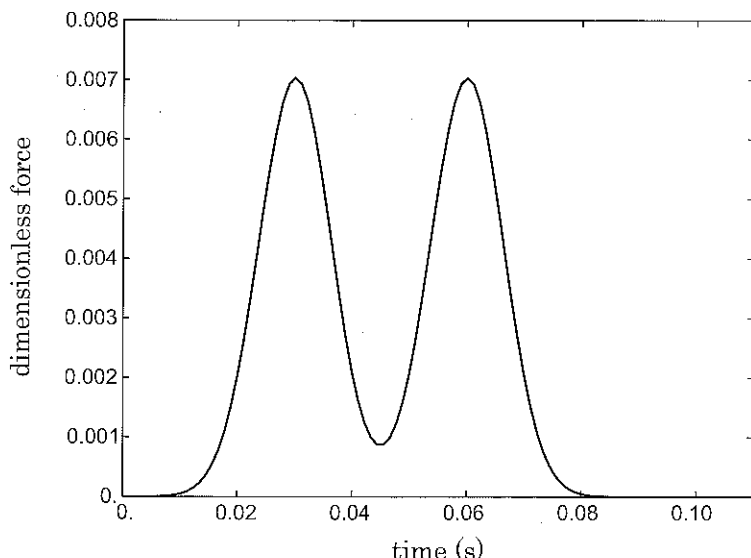


Fig. B.10: Double-*M* wavelet (dimensionless load F/Q) considered to model dynamic loadings by trains (Al-Shaer *et al.*, 2008).

Appendix C

Spectral analysis and filtering

C.1 Fourier transform

The mathematical properties of the Fourier transform have not been discussed yet. The analysis of signals in the frequency domain is very often made using Fourier transforms: amplitude spectra, transfer functions, coherency, filtering, etc (Scherbaum, 2006).

C.1.1 Definitions

For an integrable function $x(t)$, the Fourier transform $x^*(\omega)$ exists and may be written under the following form:

- direct transform:

$$x^*(\omega) = \int_{-\infty}^{+\infty} x(t) \exp(-i\omega t) dt \quad (\text{C.1})$$

- inverse transform:

$$x(t) = \frac{1}{2\pi} \int_{-\infty}^{+\infty} x^*(\omega) \exp(i\omega t) d\omega \quad (\text{C.2})$$

The Fourier transform $x^*(\omega)$ is generally called the *complex spectrum* of the signal $x(t)$. The function $x^*(\omega)$ being complex, it is often studied in terms of amplitude and phase (i.e modulus and argument) through the *amplitude spectrum* $|x^*(\omega)|$ and the *phase spectrum* $\arg(x^*(\omega))$.

As discussed in Chapters 2 and 3, choosing a $e^{+i\omega t}$ time harmonic dependence is compatible with such definitions. Conversely, if a $e^{-i\omega t}$ harmonic dependence is chosen, one must use a direct transform to calculate $x(t)$ from $x^*(\omega)$ and an inverse transform to compute $x^*(\omega)$ from $x(t)$.

These definitions may be used in the case where the signal has a continuous amplitude and a continuous time base. The experimental signals are digitized when recorded: they

are at the same time *sampled* (*discrete time*) and *quantified* (*discrete amplitude*). The analysis of experimental signals in the frequency domain is thus performed thanks to the *discrete Fourier transform* (Mari *et al.*, 1999; Scherbaum, 2006).

C.1.2 Main properties

Denoting \mathcal{F} the Fourier transform, its main properties are the following (Scherbaum, 2006):

- Involution: $x^*(t) \xrightarrow{\mathcal{F}} x(-f)$
- symmetry: $x(-t) \xrightarrow{\mathcal{F}} x^*(-f)$
- advance/delay: $x(t \pm t_0) \xrightarrow{\mathcal{F}} x^*(f)e^{\pm i\omega t_0}$
- derivation: $\frac{d^n x(t)}{dt^n} \xrightarrow{\mathcal{F}} (i\omega f)^n x^*(f)$
- $(-2i\pi t)^n x(t) \xrightarrow{\mathcal{F}} \frac{d^n x^*(f)}{df^n}$
- convolution: $x(t) * y(t) \xrightarrow{\mathcal{F}} x^*(f)y^*(f)$
- $x(t).y(t) \xrightarrow{\mathcal{F}} x^*(f) * y^*(f)$

C.1.3 Usual transforms

The Fourier transforms of the following usual functions are (Scherbaum, 2006):

$$\begin{aligned} \delta(t) &\xrightarrow{\mathcal{F}} 1 \\ 1 &\xrightarrow{\mathcal{F}} \delta(f) \\ e^{\pm i\omega t} &\xrightarrow{\mathcal{F}} \delta(f \mp f_0) \\ \text{sign}(t) &\xrightarrow{\mathcal{F}} \frac{1}{i\omega} \\ \Pi_T(t) &\xrightarrow{\mathcal{F}} T \frac{\sin \pi f T}{\pi f T} \\ \frac{\sin \pi f_0 t}{\pi f_0 t} &\xrightarrow{\mathcal{F}} \frac{1}{f_0} \Pi_{f_0}(f) \\ \Lambda_T(t) &\xrightarrow{\mathcal{F}} T \left(\frac{\sin \pi f T}{\pi f T} \right)^2 \\ e^{-\pi t^2} &\xrightarrow{\mathcal{F}} e^{-\pi f^2} \end{aligned}$$

where Π_T denotes the step function and Λ_T the triangular function of duration T .

C.1.4 Fourier transforms of synthetic wavelets

For synthetic wavelets, the theoretical Fourier transforms (direct or inverse) may be determined using Eqs (C.1) and (C.2). As shown in Fig.C.1, the theoretical amplitude spectrum is determined against positive as well as negative frequencies.

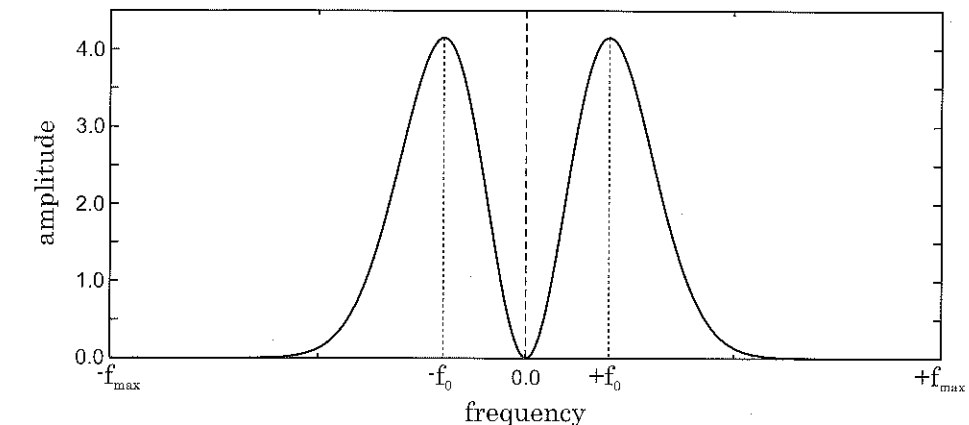


Fig. C.1: Theoretical Fourier (amplitude) spectrum of a Ricker wavelet.

When computing numerically the Fourier transform of a discrete signal (e.g. Fast Fourier Transform (FFT)), the values corresponding to the negative frequencies are translated to the right part of the spectrum (fictitious higher frequencies). As depicted in Fig.C.2 for a 2nd order Ricker wavelet ($t_p = 0.5s$), the amplitude spectrum (top) is obtained under a different form when compared to the theoretical Fourier spectrum displayed in Fig.C.1. The first half of the numerical transform corresponds to the spectral components of the signal between 0 and $+f_{max}$ whereas the second half is related to the spectral components between $-f_{max}$ and 0 (periodic signals). In Fig.C.2, the real part (middle) and the imaginary part (bottom) of the Fourier spectrum are also plotted.

Translating the second part of the spectrum to the left of the first part, the real and imaginary parts of the Fourier spectrum are as depicted in Fig.C.3 (Ricker wavelet with $t_p = 2.0s$). As shown in this figure, the real part of the spectrum is even whereas the imaginary part is odd.

C.1.5 Wave propagation in viscoelastic media

In order to simulate wave propagation in viscoelastic media, it is convenient to work in the frequency domain and to use the exact expressions of the complex modulus and wavenumber (see Chapter 2). The analysis may be only performed for the first half of the Fourier spectrum (from 0 to f_{max}).

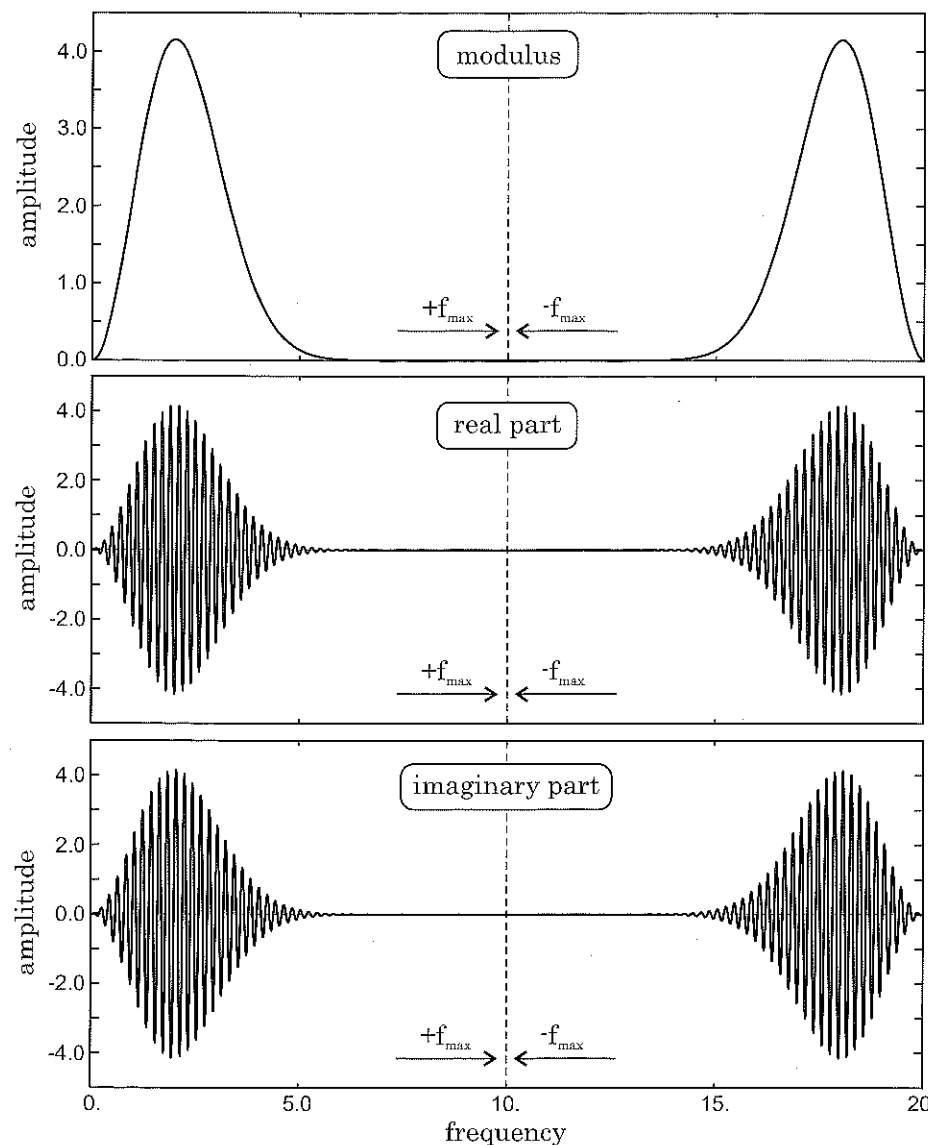


Fig. C.2: FFT of a Ricker wavelet with $t_p = 0.5\text{s}$: modulus (top), real part (middle) and imaginary part (bottom).

C.1 Fourier transform

As shown in Fig.C.3, the real part of the spectrum is even whereas the imaginary part is odd. The Fourier spectrum of the propagated signal may thus be computed using the first part of the spectrum of the original signal. The second part of the spectrum of the propagated signal may then be computed by taking the conjugate of the values of the first part. The inverse Fourier transform finally yields the propagated signal in time domain.

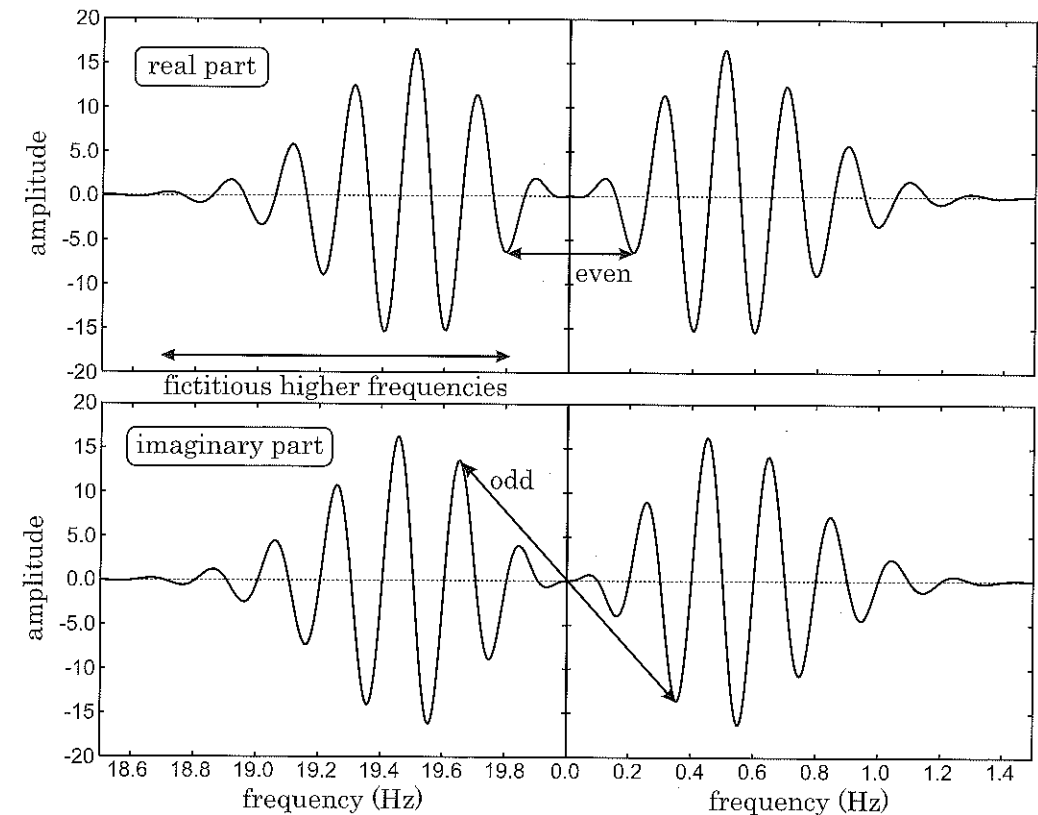


Fig. C.3: FFT of a Ricker wavelet with $t_p = 2.0\text{s}$ at lower frequencies and translated "negative" frequencies showing the even real part (top) and the odd imaginary part (bottom).

C.1.6 Fourier transforms of actual signals

We have chosen a record from the Nice Feb.2001 earthquake to compute the Fourier spectrum and briefly illustrate filtering techniques. The accelerogram recorded at the *ALS* alluvial site (see Chapter 5) is displayed in Fig.C.4 (top) and its amplitude spectrum (i.e. modulus of the Fourier transform) is plotted at the bottom. Most of the large spectral components are found between 1 and 8 Hz.

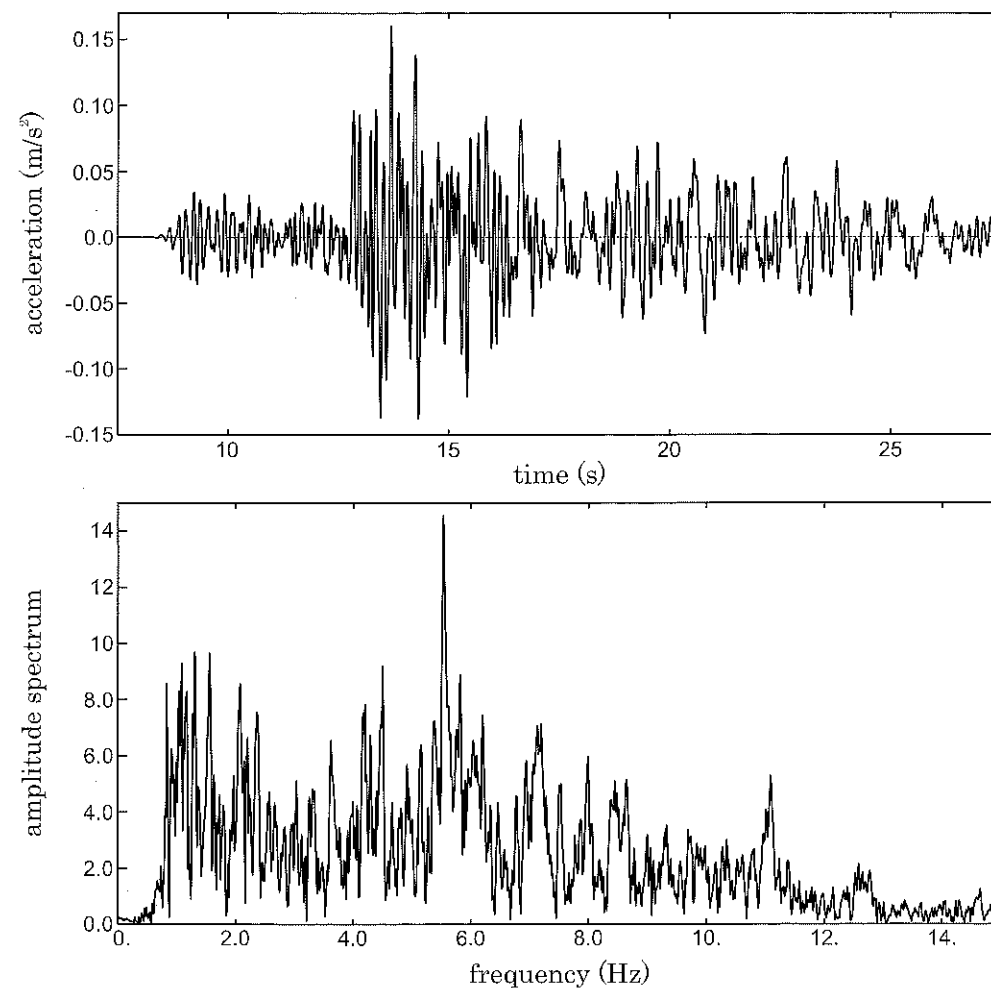


Fig. C.4: Accelerogram (top) and its amplitude Fourier spectrum (bottom) recorded at the *ALS* site in Nice, France (Feb.2001 earthquake).

C.2 Filtering

C.2.1 Classical filters

Various filtering techniques are available: Butterworth, Chebychev, Bessel, etc (Boore, 2005; Mari *et al.*, 1999; Scherbaum, 2006). For instance, the Butterworth filter is designed to have a frequency response as flat as possible in the bandpass of interest. The n th order Butterworth filter is defined by the following gain:

$$G^2(\omega) = \frac{G_0^2}{1 + \left(\frac{\omega}{\omega_c}\right)^{2n}} \quad (\text{C.3})$$

The gain of Butterworth filters at various orders is displayed in Fig.C.5 as a function of frequency.

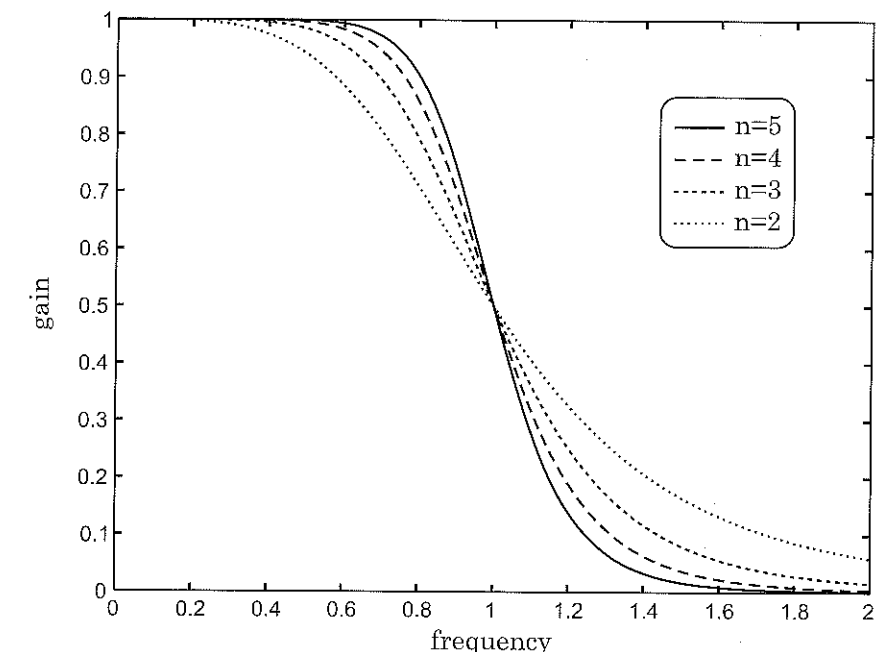


Fig. C.5: Gain vs frequency for low-pass Butterworth filters at orders 2, 3, 4 and 5.

C.2.2 Filtered signals: examples

As depicted in Fig.C.6, the accelerogram recorded at the *ALS* station during the Feb.2001 earthquake (Fig.C.4, top) is filtered using various Butterworth filters with $f_c = 8.0$ Hz.

The influence of the type of filter on the final waveform of the filtered signal appears to be significant (Boore, 2005; Scherbaum, 2006).

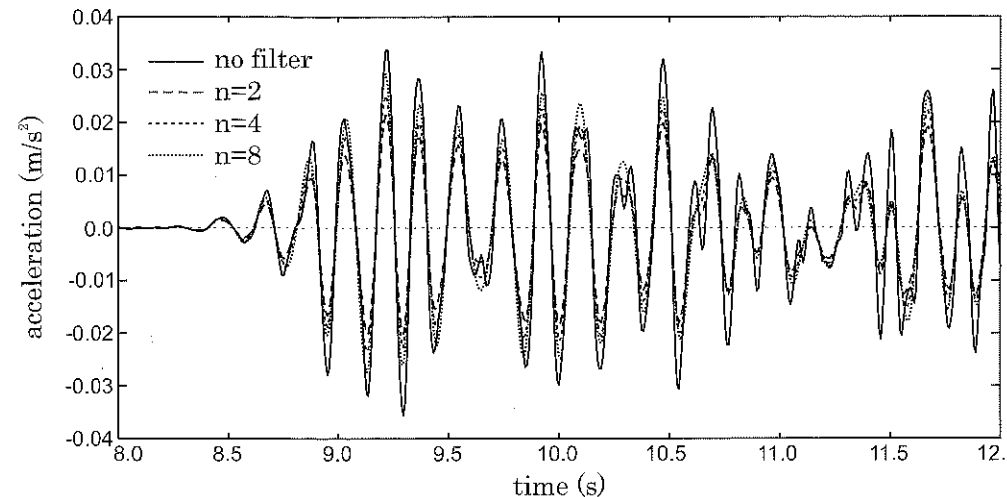


Fig. C.6: Accelerogram recorded in Nice (France) and filtered using various Butterworth filters.

C.3 Hilbert transform and envelope curve

C.3.1 Definition

The Hilbert transform \mathcal{H} of a signal $s(t)$ is defined as follows (Aki and Richards, 1980; Scherbaum, 2006):

$$\mathcal{H}(s(t)) = \frac{1}{\pi} \int_{-\infty}^{+\infty} \frac{s(\tau)}{\tau - t} d\tau \quad (\text{C.4})$$

The practical computation of the Hilbert transform is made directly considering the complex spectrum of the signal, $s^*(\omega)$, and its spectral Hilbert transform, $\mathcal{H}(s^*(\omega))$:

$$\mathcal{H}(s^*(\omega)) = -i \operatorname{sign}(\omega) s^*(\omega) \quad (\text{C.5})$$

where $\operatorname{sign}(\omega)$ is the sign of ω .

To compute the Hilbert transform, one firstly considers the time signal $s(t)$. Its Fourier transform $s^*(\omega)$ is then multiplied by a step function ($\operatorname{sign}(\omega)$) to get the frequency domain Hilbert transform. Using an inverse Fourier transform, the Hilbert transform $\mathcal{H}(s(t))$ is finally computed.

The Hilbert transform $\mathcal{H}(s(t))$ of $s(t)$ allows to separate the information related to phase and amplitude. The complex function $S(t)$, defined as $S(t) = s(t) + i\mathcal{H}(s(t))$, represents the *complex envelope* of the signal (this function is often called the *analytical signal*).

C.3.2 Envelope curves

From the Hilbert transform and the complex envelope of the signal $S(t)$, its envelope may be easily determined (Farnbach, 1975). The information related to amplitude are given by the modulus of this function $|S(t)|$ which defines the *envelope curve*. The information related to the phase are taken from the argument of $S(t)$. The envelope curve characterizes the propagation from the energetic point of view and allows the estimation of the group velocity.

A typical envelope curve is proposed in Fig.C.7 for a filtered signal recorded during centrifuge dynamic experiments (see Chapter 3). The peaks in the envelope curve indicate the various wave packets characterizing the way the energy of the signal is propagated.

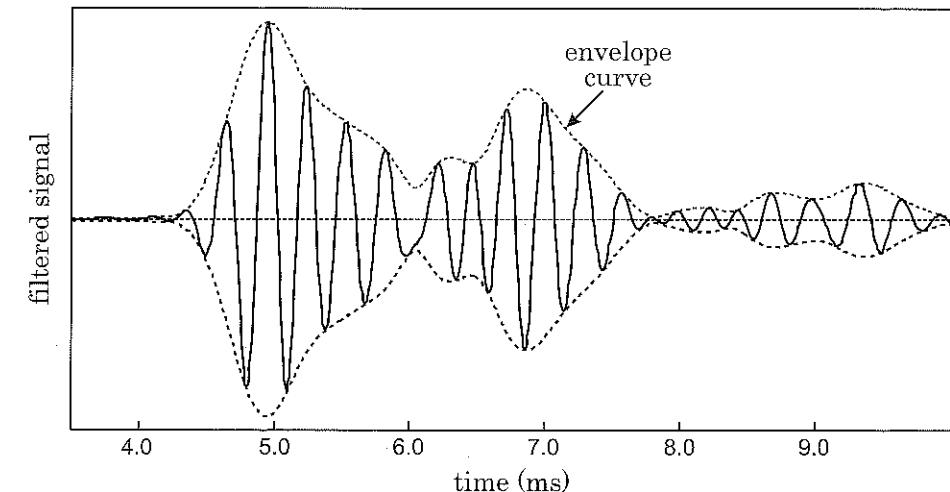


Fig. C.7: Typical envelope curve computed by the Hilbert transform from accelerograms recorded during centrifuge tests (Semblat and Luong, 1998).

Appendix D

Propagating waves: duration, velocity, echoes

D.1 From acceleration to displacement

D.1.1 Integration of accelerograms

It is often necessary to integrate accelerograms to obtain velocities or displacements. When computing such integrals, it is mandatory to carefully account for the integration constants (Boore and Bommer, 2005). This problem is crucial since the direct integration of acceleration signals leads to spurious ramps in resulting velocities or displacements (see Fig. D.1, top).

D.1.2 Baseline correction

One way to correctly compute the integrated signals consists in performing baseline corrections: the trend observed in an integrated signal is corrected by choosing an adequate baseline corrections. As shown in Fig. D.1, various baseline corrections methods are available to correctly integrate acceleration signals: multi-segment baseline corrections may for instance be performed in some cases (Boore and Bommer, 2005).

D.1.3 Spectral methods

As discussed by Boore and Bommer (2005), filtering techniques (e.g. low-cut filters to reduce low-frequency noise) are also an interesting mean to perform accurate integrations of accelerograms.

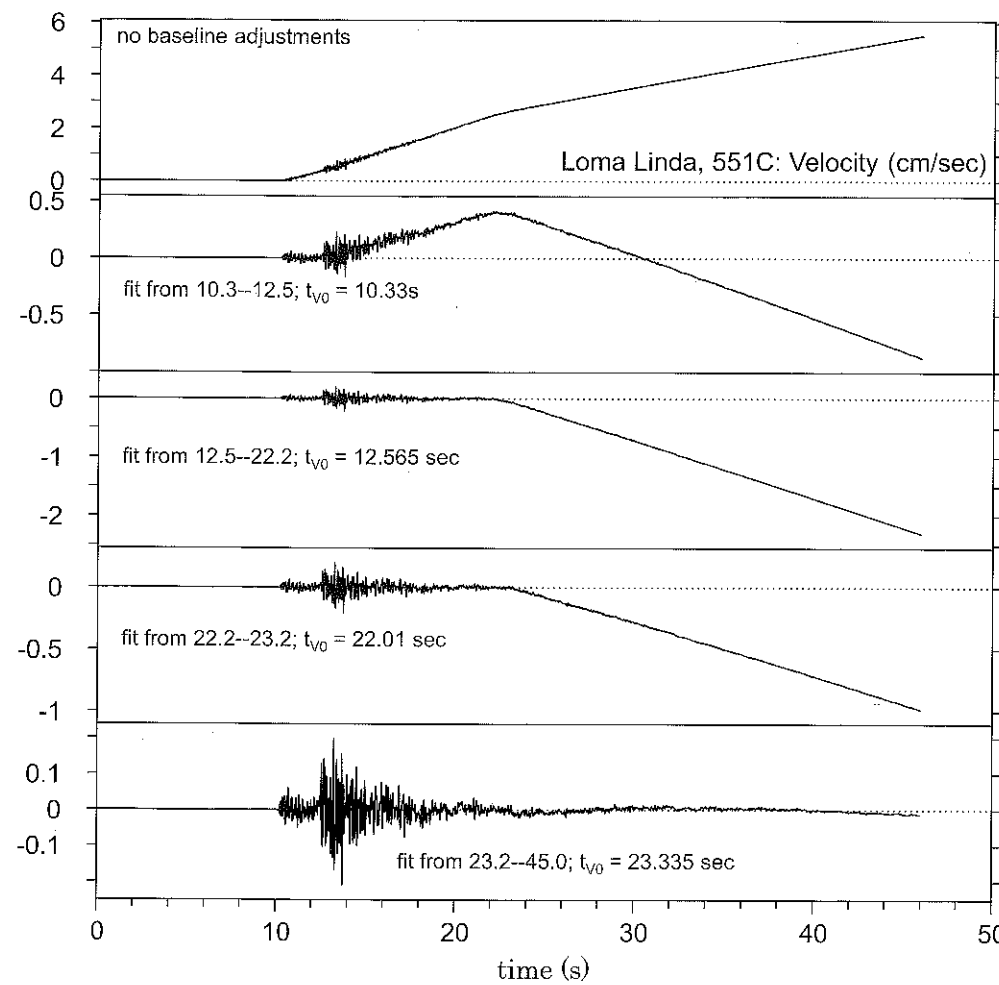


Fig. D.1: Various baseline corrections to integrate accelerograms and avoid unrealistic ramps (Boore and Bommer, 2005).

D.2 PGA, PGV, PGD

Peak ground motion values are often used in various fields of application in terms of acceleration (*PGA*), velocity (*PGV*) or displacement (*PGD*). As shown in Fig. D.2 for the Feb.2001 Nice earthquake, the *PGA* (top) and the *PGD* (bottom) are very easily estimated from the maximum values in the curves. It is an important feature of the ground motion since it may be used for the comparison of ground motions due to various earthquakes as well as for the determination of the response spectra widely used in the

field of earthquake engineering. However, several other important features of the recorded signals are crucial for the detailed characterization of the ground motion (number of cycles, duration, etc).

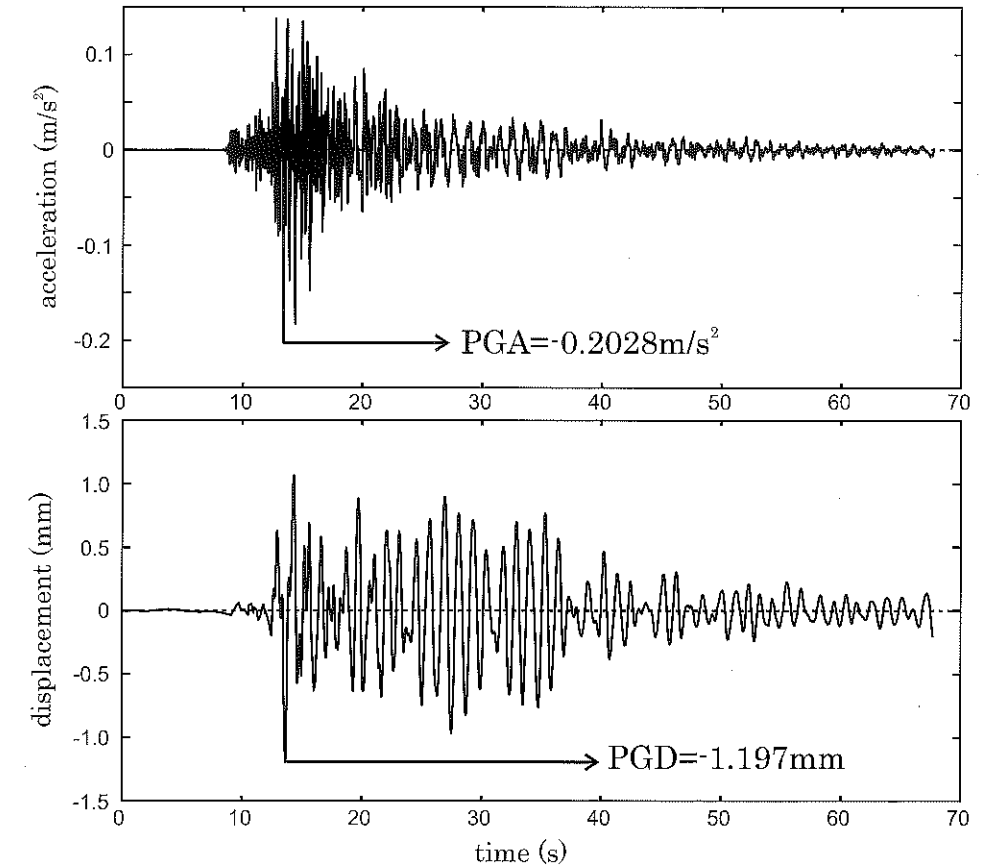


Fig. D.2: Peak Ground Acceleration (top) and Peak Ground Displacement (bottom) of a seismogram recorded during the Feb.2001 Nice earthquake (RAP, CETE-Med).

D.3 Signal duration

The peak ground motion (*PGA*, *PGV* or *PGD*) is not sufficient to fully characterize the features of a seismic wave or vibration induced in the soil. We may have a large peak but very few secondary peaks or, conversely, numerous intermediate amplitude peaks but no very large ones. It is thus interesting to estimate the signal duration, to investigate the way the energy of the signal is distributed in time.

The duration d of a signal $s(t)$ is defined from its energy $\mathcal{E}_s(t)$:

$$\mathcal{E}_s(t) = \int_0^t s^2(t) dt \quad (\text{D.1})$$

Various definitions of duration may be considered (Bommer and Martinez-Pereira, 1999). As suggested by Trifunac and Brady (1975), the signal duration may be chosen as the time interval $[t_{5\%}; t_{95\%}]$, $t_{5\%}$ and $t_{95\%}$ being the times such as: $\mathcal{E}_s(t_{5\%}) = 5\%\mathcal{E}_{max}$ and $\mathcal{E}_s(t_{95\%}) = 95\%\mathcal{E}_{max}$. This signal duration is often called the Trifunac duration or the 5%-95% duration (Bommer and Martinez-Pereira, 1999).

In Fig. D.3, a seismogram recorded during the Feb.2001 Nice earthquake is considered to compute the signal energy. Estimating the 5% \mathcal{E}_{max} and 95% \mathcal{E}_{max} threshold, the duration may be easily determined: $d = 22.5\text{s}$.

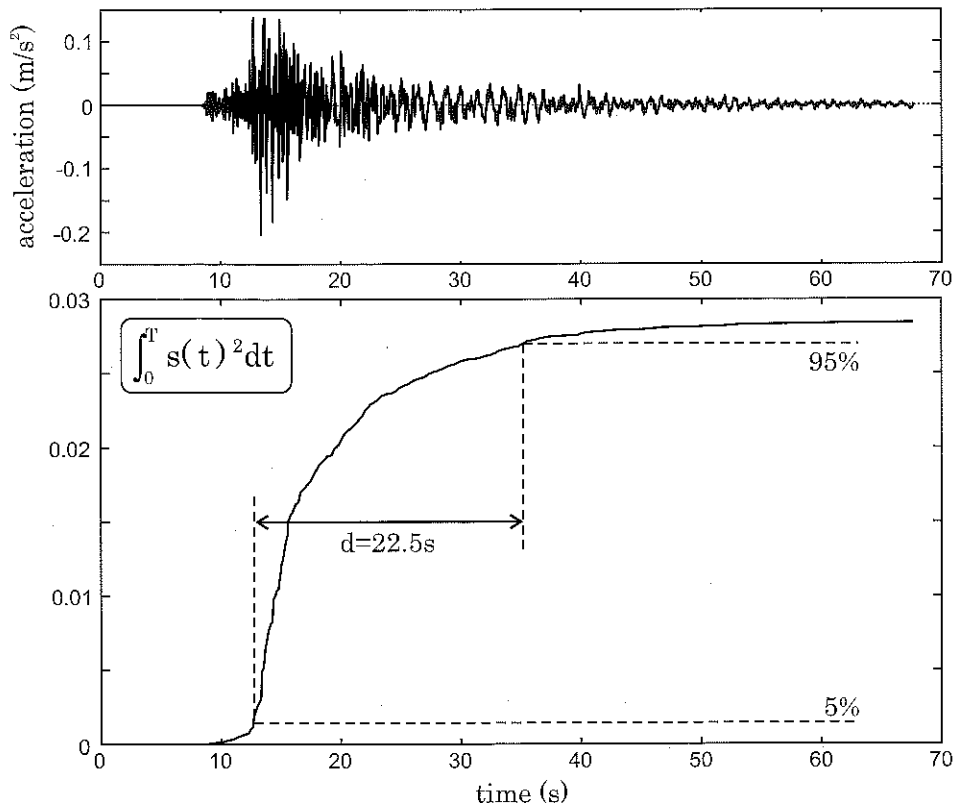


Fig. D.3: Definition of the 5-95% duration for a seismogram recorded during the Feb.2001 Nice earthquake (RAP, CETE-Med).

D.4 Estimation of wave velocity

Wave velocity is the key parameter to investigate wave propagation in solids. However, as already discussed in Chapters 2 and 3, various types of velocities may be considered and the estimation on actual recordings is often difficult due to such phenomena as reflections, attenuation, dispersion, scattering, etc.

D.4.1 Peak to peak estimation

A simple method consists in directly estimating the velocity on the signals recorded in the experiments. The *peak to peak estimation* is the simplest method to estimate the wave velocity, but it is necessary to have a good similarity of the peak shapes in each signal. When dispersion is significant, such a simple procedure is generally difficult to apply because the peaks shape may be distorted during the propagation process.

Figure D.4 displays several accelerograms recorded during centrifuge experiments (Chapter 3). The peak to peak estimation may be easily performed, but the peak shape nevertheless changes during the propagation process.

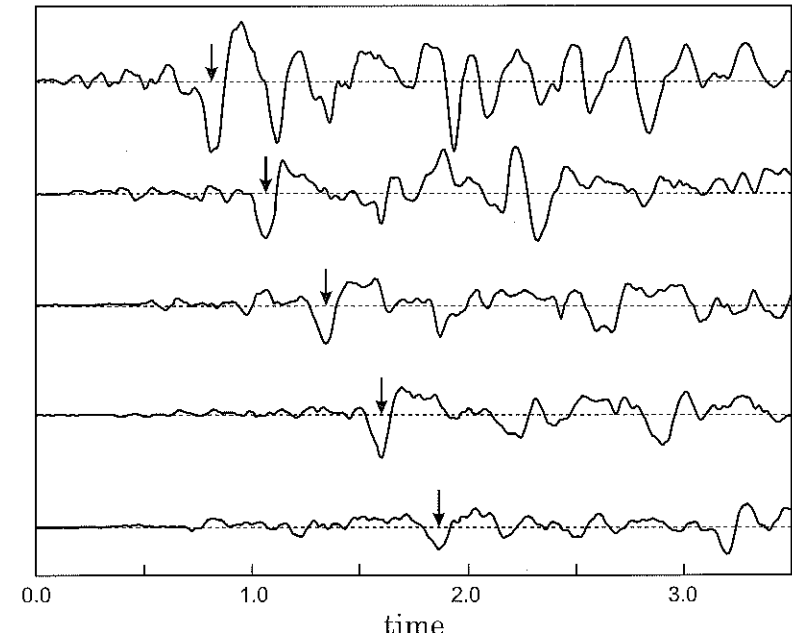


Fig. D.4: Direct determination (peak to peak) of the propagation delays on time signals recorded in centrifuge experiments (Chapter 3).

D.4.2 Cross-correlation function

The *cross-correlation function* allows a more global analysis of the transmission of a wave through various paths or processes. Denoting $x(t)$ and $y(t)$ the input and output signals respectively, the cross-correlation function $R_{xy}(\tau)$ is defined under the following form (Mari *et al.*, 1999; Scherbaum, 2006):

$$R_{xy}(\tau) = \lim_{T \rightarrow \infty} \frac{1}{T} \int_0^T x(t)y(t + \tau)dt \quad (\text{D.2})$$

The cross-correlation function leads to the propagation delays of a wave through various paths. It also allows to characterize the similarities between two signals. Figure D.5 displays a cross-correlation function computed from signals recorded during cross-hole tests (Chapter 3). The delay between two signals is directly estimated from the abscissa of the largest peak.

The peak to peak estimation gives very poor information about the propagation process. The cross-correlation function is a much powerful tool but it may be influenced by the wave reflections on the medium boundaries or some heterogeneities in the medium. In such cases, it is mandatory to analyze this specific problem.

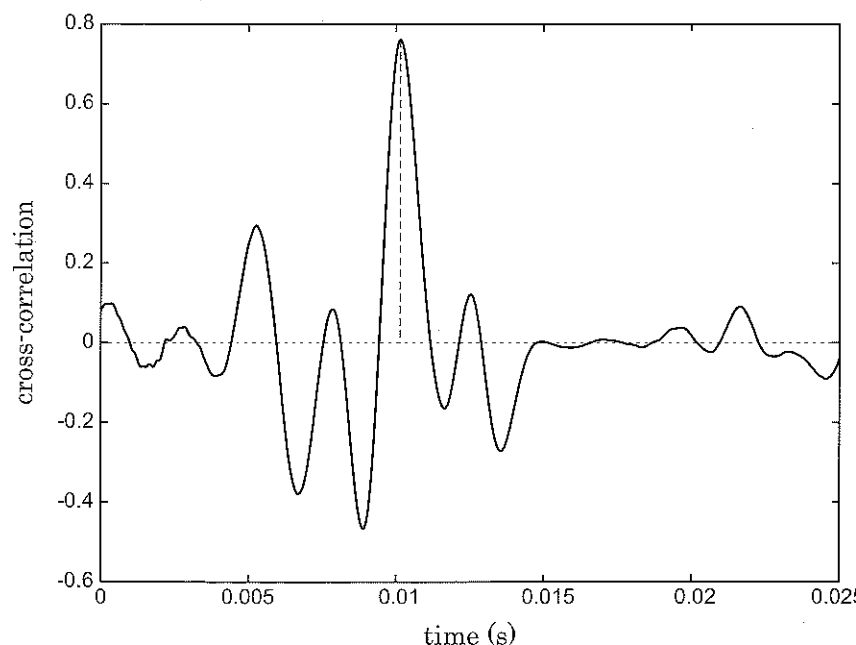


Fig. D.5: Cross-correlation function for two signals measured during cross-hole tests (see Chapter 3).

D.5 Detection of reflected waves and echoes

D.5.1 Autocorrelation function

The *autocorrelation function* $R_{xx}(\tau)$ is defined under a form similar to that of the cross-correlation function, that is:

$$R_{xx}(\tau) = \lim_{T \rightarrow \infty} \frac{1}{T} \int_0^T x(t)x(t + \tau)dt \quad (\text{D.3})$$

This function is equivalent to a cross-correlation function between the signal and itself. It allows to study the similarities between different parts of the signal. It is thus possible to evidence some periodicities or the influence of reflected waves or echoes due to propagation along multiple paths (Scherbaum, 2006; Semblat, 1995).

Since the cross-correlation and the auto-correlation are defined as convolution products, they may be easily computed in the frequency domain using the Fourier transform.

D.5.2 Real cepstrum

The *cepstrum* is a powerful tool often used in the fields of acoustics, image processing, speech synthesis or mechanical engineering (Kunt, 1986; Sessarego, 1990; Tubach, 1989; Ulrych, 1971). The real cepstrum of a signal is defined as a double (direct and inverse) Fourier transform under the following form:

$$\mathcal{C}_r(t) = \mathcal{F}^{-1} [\log |\mathcal{F}(s(t))|] \quad (\text{D.4})$$

As the autocorrelation function, it allows the detection of echoes or periodic excitations in complex signals (Semblat and Luong, 1998). As it will be shown later, it is possible with such techniques to combine the complex cepstrum with *cepstral windowing* techniques to remove echoes from a signal. In certain cases (delay of the reflected wave close to the pseudo-periods of the signal), the direct and reflected waves may be combined. The cepstral method is powerful to analyze such complex situations.

D.5.3 Time phase

The *time phase* is computed by using the Hilbert transform, $h(t)$, of the signal $s(t)$. This function allows to separate, in the signal, information related to the amplitude and information related to the phase. If the reflected wave arrivals cannot be pointed out in the time signal, it may be detected in the time phase diagram (Semblat, 1995). The derivative of the time phase also allows an efficient detection of echoes or reflections.

Appendix E

Echo removal by homomorphic filtering

E.1 Basic principles

The homomorphic filtering of signals results from a generalization of the theory of linear systems. The main goal is to change the vectorial space in order to *transform convolution operators in addition operators*. It is thus necessary to find a *homomorphism associating the convolution to the addition operator*. The convolution in time becoming a multiplication in the frequency domain (see appendix C), we can use the logarithm to relate both operators. The homomorphism thus results from the composition of two transformations as follows:

$$\begin{array}{c} \text{Fourier} \\ \text{transform} \\ \boxed{* \text{ operator}} \end{array} \Rightarrow \begin{array}{c} \text{complex} \\ \text{logarithm} \\ \boxed{\times \text{ operator}} \end{array} \Rightarrow \begin{array}{c} + \text{ operator} \end{array}$$

This transformation replaces the convolution relation by a simple addition. the homomorphic treatment is widely used in speech processing (Tubach, 1989) since it allows the characterization of the noise source.

In seismology, Ulrych (1971) used the homomorphic deconvolution to analyze the attenuation and dispersion of elastic waves separating the sources terms and those due to the propagation. Its main advantage is that no preliminary assumptions on the propagation process are needed.

E.2 Computation of the complex cepstrum

The definition of the real cepstrum \mathcal{C}_r is given in §D.5 through Eq.(D.4). In this expression, the logarithm is real valued since it is computed from the modulus of the Fourier transform, namely the amplitude spectrum. To compute the *complex cepstrum* \mathcal{C} , the

complex logarithm is considered. The complete procedure is described in Fig.E.1.

Denoting \mathcal{F} the Fourier transform and Log the complex logarithm, the expression of the complex cepstrum $\mathcal{C}(\tau)$ of a time signal $s(t)$ is the following:

$$\mathcal{C}(\tau) = \mathcal{F}^{-1} [\text{Log} (\mathcal{F}(s(t)))] \quad (\text{E.1})$$

If $s^*(f)$ is the Fourier transform of $s(t)$, the complex logarithm is directly expressed as a function of its real and imaginary parts:

$$\text{Log}[s^*(f)] = \text{Log} |s^*(f)| + i\text{Arg}[s^*(f)] \quad (\text{E.2})$$

This relation raises the problem of the computation of the phase spectrum $\text{Arg}[s^*(f)]$ since it is generally defined in the range $[-\pi, \pi]$. Furthermore, considering the properties of the logarithm, the phase spectrum must fulfil the following relation:

$$\text{if } s^*(f) = s_R^*(f)s_I^*(f), \quad \text{Arg}[s^*(f)] = \text{Arg}[s_R^*(f)] + \text{Arg}[s_I^*(f)] \quad (\text{E.3})$$

To solve these problems, it is necessary to have a continuous phase spectrum. The phase is then called the *unwrapped phase*. This procedure is strongly sensitive to the accuracy of the data. Tribolet (1977) proposed a phase unwrapping algorithm considering the expression of its derivative. Denoting s_R^* and s_I^* the real and imaginary parts of the complex spectrum $s^*(f)$, the derivative of the complex spectrum is the following:

$$\frac{d(\text{Arg}[s^*(f)])}{df} = \frac{s_R^*(f) \frac{ds_I^*(f)}{df} - s_I^*(f) \frac{ds_R^*(f)}{df}}{|s^*(f)|^2} \quad (\text{E.4})$$

Using this expression and considering several other steps (see synthesis below), it is possible to compute the complex cepstrum $\mathcal{C}(\tau)$.

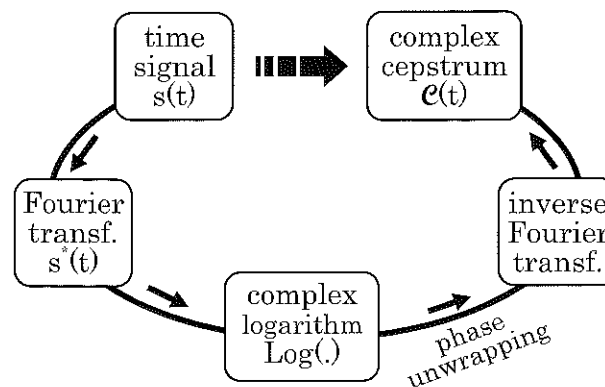


Fig. E.1: Procedure to compute the complex cepstrum of a signal.

E.3 Removing echoes thanks to cepstral filtering

E.3.1 Principle of the method

Removing echoes or reflections can be performed thanks to the complex cepstrum defined previously. As depicted in Fig.E.2, the complex cepstrum displays several peaks due to the different arrival times characterizing the various propagation paths (reflected or scattered waves). To remove such waves, it is possible to remove the corresponding peaks in the complex cepstrum thanks to a weighting window (*cepstral window*). The *inverse cepstral transform* then allows to retrieve the time signal free of reflected waves (Semblat and Luong, 1998; Ulrych, 1971).

E.3.2 Homomorphic filtering: summary

The different steps of the analysis are the following:

- time signal $s(t)$,
- truncate the initial part of $s(t)$ for $t < 0$,
- multiply by a decreasing exponential to smooth the phase,
- compute the Fourier transform $s^*(f) = s_R^*(f) + i s_I^*(f)$
- compute the derivative of the phase:

$$\frac{d(\text{Arg}(s^*(f)))}{df} = \frac{s_R^* \frac{ds_I^*}{df} - s_I^* \frac{ds_R^*}{df}}{|s^*(f)|^2} \quad (\text{E.5})$$

- low-pass filtering of the derivative (with mean value correction)
- estimation of the continuous phase, or *unwrapped phase*, $\widetilde{\text{Arg}}(s^*(f))$ by integration,
- computation of $\mathcal{C}^*(f) = \log(|s^*(f)|) + i\widetilde{\text{Arg}}(s^*(f))$ Fourier transform of the complex cepstrum,
- computation of the complex cepstrum $\mathcal{C}(\tau)$ by inverse Fourier transform,
- cepstral windowing (also called "*liftering*") of the complex cepstrum $\mathcal{C}_{lift}(\tau) = W(\tau)\mathcal{C}(\tau)$
- liftered time signal: $s_{lift}(t) = \mathcal{F}^{-1}[\exp[\mathcal{F}(\mathcal{C}_{lift}(\tau))]]$

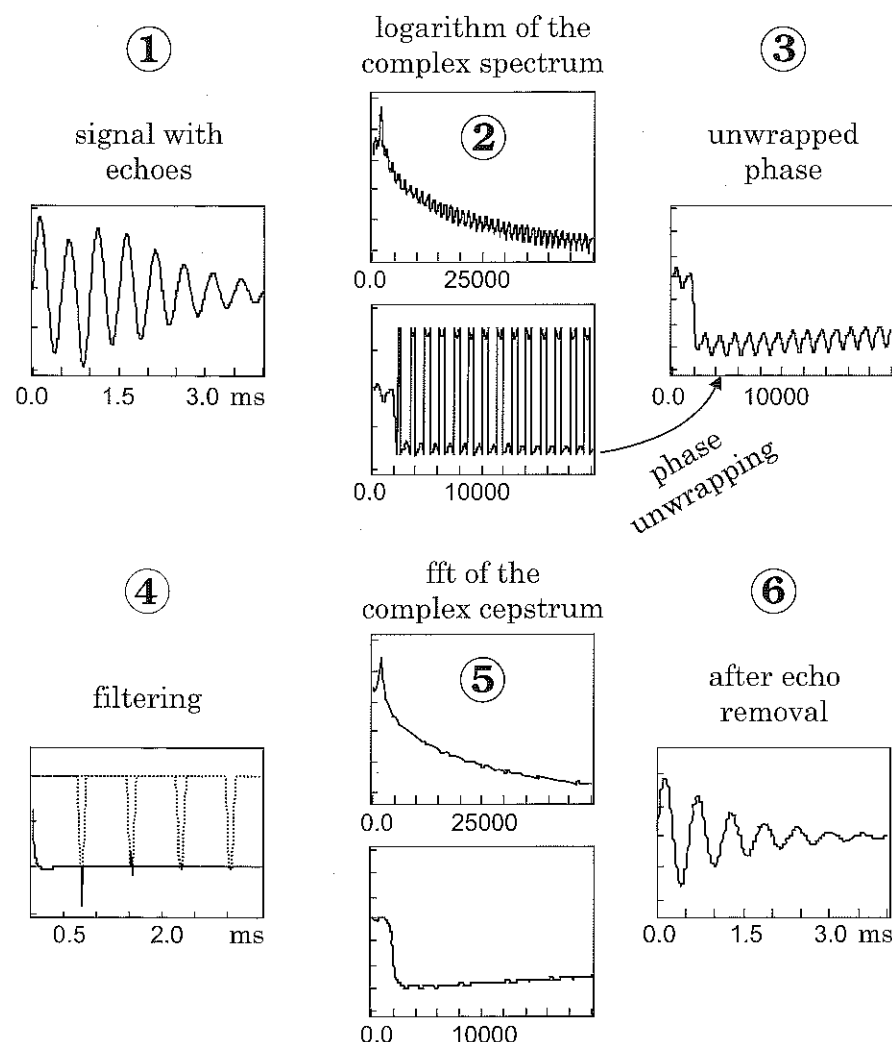


Fig. E.2: Procedure to remove echoes by cepstral filtering for a synthetic signal (Semblat and Luong, 1998).

E.3.3 Application to actual measurements

As already shown in §D.5, the (real or complex) cepstrum allows the detection of reflected wave arrivals. If the peaks corresponding to the reflections are removed by multiplying the complex cepstrum by a weighting window, the reflections will be removed from the signal itself after inverse cepstral transformation.

Figure E.3 displays an acceleration signal (dashed) recorded during centrifuge experiments (Chapter 3). As shown in Fig.E.2 (step 4) for a synthetic signal, the reflected wave arrivals can be detected and removed (step 6). The same signal after homomorphic filtering (Fig.E.3, solid) is nearly free of any reflected wave.

This technique seems to be very efficient for the signals measured in centrifuge tests (Fig.E.3). This method is very interesting since it can be applied to longer signals, even if the reflected waves are combined with the direct waves (e.g. Fig.E.2).

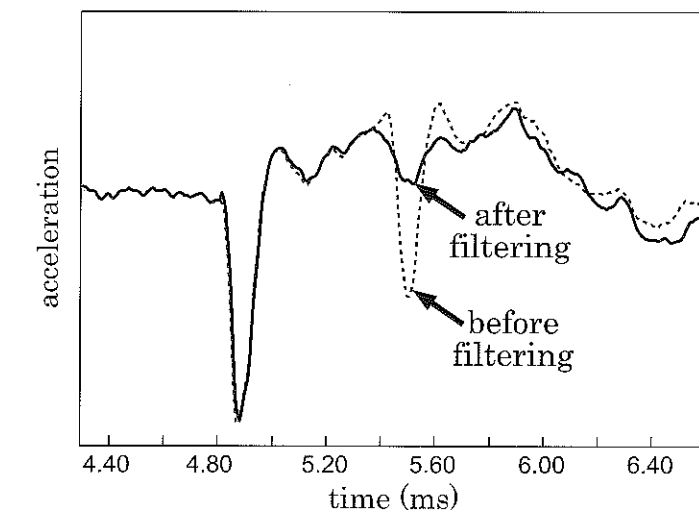


Fig. E.3: Removing reflected waves by homomorphic filtering for an actual signal recorded during centrifuge experiments (Semblat and Luong, 1998).

References

References

- [1] Abe S., Kobayashi Y., Ikawa T. (1990). Seismic characteristics of the weight-dropping source, *Journal Phys. Earth*, 38, pp.189-212.
- [2] Abraham O., Channas R., Cote P., Pedersen H., Semblat J.F. (2004). Mechanical characterization of heterogeneous soils with surface waves: experimental validation on reduced scale physical models, *Near Surface Geophysics*, 2, pp.249-258.
- [3] Abramowitz M., Stegun I.A. (1970). *Handbook of mathematical functions*, 9th edition, Dover Publications Inc., New York.
- [4] Achenbach J.D., *Wave propagation in elastic solids*, North-Holland, 1973.
- [5] Adalier K., Elgamal A.W. (2002). Seismic response of adjacent dense and loose saturated sand columns, *Soil Dynamics and Earthquake Engineering*, 22(2), pp.115-127.
- [6] Agarwal T.K., Ishibashi I., Anisotropic elastic constants of granular assembly from wave velocity measurements, *Advances in Micromechanics of Granular Materials* (H.H.Shen), 1992.
- [7] Aki K., Richards P.G. (1980). *Quantitative Seismology*, Freeman and Co., New-York.
- [8] Aki K., Larner K.L. (1970). Surface Motion of a Layered Medium Having an Irregular Interface due to Incident Plane SH Waves, *Journal of Geophysical Research*, 75, pp.1921-1941.
- [9] Al Shaer A., Duhamel D., Sab K., Foret G., Schmitt L. (2008). Experimental settlement and dynamic behavior of a portion of ballasted railway track under high speed trains, *Journal of Sound and Vibration*, 316(1-5), pp.211-233.
- [10] Andersen L., Clausen J. (2008). Impedance of surface footings on layered ground, *Computers and Structures*, 86, pp.72-87.
- [11] Andersen L., Nielsen S.R.K. (2005). Reduction of ground vibration by means of barriers or soil improvement along a railway track, *Soil Dynamics and Earthquake Engineering*, 25, pp.701-716.

- [12] Anderson D.G. (1974). *Dynamic modulus of cohesive soils*, Ph.D. Dissertation, University of Michigan.
- [13] Arulanandan K., Canclini J., Anandarajah A. (1982). Simulation of earthquake motions in the centrifuge, *Journal of Geotechnical Engineering (A.S.C.E)*, 108(GT5), pp.730-742.
- [14] Assimaki D., Kausel E., Whittle A. (2000). Model for dynamic shear modulus and damping in granular soils, *Jal of Geotechnical and Geoenvironmental Eng.*, 126(10), pp.859-869.
- [15] Aubry D., Clouteau D. (1991). A regularized boundary element method for stratified media, *1st Int. Conf. on Mathematical and Numerical Aspects of Wave Propagation (SIAM)*.
- [16] Autenzio O. (1997), *Frontières absorbantes et éléments infinis en dynamique*, Master thesis, LCPC/University Paris 6.
- [17] Aviles J., Sánchez-Sesma F.J. (1983). Piles as barriers for elastic waves, *Journal of Geotechnical Engineering (A.S.C.E)*, 109(9), pp.1133-1146.
- [18] Backus G.E., Gilbert J.F. (1967). Numerical applications of a formalism for geophysical inverse problems, *Geophys. J. Roy. Astr. Soc.*, 13, pp.247-276.
- [19] Badri M., Mooney H.M. (1987). Q measurements from compressional seismic waves in unconsolidated sediments, *Geophysics*, 52(6), pp.772-784.
- [20] Baise L.G., Dreger D.S., Glaser S.D. (2003). The effect of shallow San Francisco bay sediments on waveforms recorded during the Mw 4.6 Bolinas California Earthquake, *Bulletin of the Seismological Society of America*, 93, pp.465-479.
- [21] Balaban M.M., Green A.E., Naghdi P.M. (1970). Acceleration waves in elastic-plastic materials, *International Journal of Engineering Sciences*, 8, pp.315-335.
- [22] Bamberger A., Chavent G., Lailly P. (1980). *Etude de schémas numériques pour les équations de l'élastodynamique linéaire*, Research report No.41, INRIA, France.
- [23] Banerjee P.K., Ahmad S., Chen K. (1988). Advanced application of BEM to wave barriers in multi-layered three-dimensional soil media, *Earthquake Engineering and Structural Dynamics*, 16, pp.1041-1060.
- [24] Bard P.Y., Chazelas J.L., Guéguen P., Kham M., Semblat J.F. (2005). *Assessing and managing earthquake risk - Chap.5 : Site-city interaction*, Eds: C.S. Oliveira, A. Roca and X. Goula, Springer, 375 pages.
- [25] Bard P.Y., Riepl-Thomas J. (2000). Wave propagation in complex geological structures and their effects on strong ground motion, *Wave motion in earthquake eng.*, Kausel & Manolis eds, WIT Press, Southampton, Boston, pp.37-95.

- [26] Bard P.Y., Bouchon M. (1985). The two dimensional resonance of sediment filled valleys, *Bulletin of the Seismological Society of America*, 75, pp.519-541.
- [27] Bard P.Y., Bouchon M. (1980a). The seismic response of sediment-filled valleys. Part 1. The case of incident SH waves, *Bulletin of the Seismological Society of America*, 70, pp. 1263-1286.
- [28] Bard P.Y., Bouchon M. (1980b). The seismic response of sediment-filled valleys. Part 2. The case of incident P and SV waves, *Bulletin of the Seismological Society of America*, 70, pp. 1921-1941.
- [29] Basu U., Chopra A.K. (2003). Perfectly matched layers for time-harmonic elastodynamics of unbounded domains: theory and finite-element implementation, *Computer Methods in Applied Mechanics and Engineering*, 192, pp.1337-1375.
- [30] Bathe K.J. (1995). *Finite Element Procedures*, Prentice-Hall, Englewood Cliffs.
- [31] Beatty K.S., Schmitt D.R., Sacchi M. (2002). Simulated annealing inversion of multi-mode Rayleigh wave dispersion curves for geological structure, *Geophysical Journal International*, 151, pp.622-631.
- [32] Beauval C., Bard P.Y., Moczo P., Kristek J. (2003). Quantification of frequency-dependent lengthening of seismic ground-motion duration due to local geology: applications to the Volvi area (Greece), *Bulletin of the Seismological Society of America*, 93, pp.371-385.
- [33] Bécache E., Fauqueux S., Joly P. (2003). Stability of perfectly matched layers, group velocities and anisotropic waves, *Jal Computational Physics*, 188(2), pp.399-433.
- [34] Beresnev I.A., Nikolaev A.V. (1988). Experimental investigations of nonlinear seismic effects, *Physics of the Earth and Planetary Interiors*, 50, pp.83-87.
- [35] Beskos D.E. (1997). Boundary elements methods in dynamic analysis: Part II (1986-1996), *Applied Mechanics Reviews (ASME)*, 50(3), 149-197.
- [36] Beskos D.E., Dasgupta B., Vardoulakis I.G. (1986). Vibration isolation using open or filled trenches, *Computational Mechanics*, 1, pp.43-63.
- [37] Bettes P. (1992). *Infinite elements*, Penshaw Press, Sunderland, U.K.
- [38] Bielak J., Loukakis K., Hisada Y., Yoshimura C. (2003). Domain Reduction Method for Three-Dimensional Earthquake Modeling in Localized Regions, Part I: Theory, *Bulletin of the Seismological Society of America*, 93(2), pp.817-824.
- [39] Bicak, J., J. Xu, and O. Ghattas (1999). Earthquake ground motion and structural response in alluvial valleys, *Jal of Geotechnical and Geoenvironmental Eng.*, 125, pp.413-423.

- [40] Bisch P., Langeoire A., Prat M., Semblat J.F. (1999). *Ouvrages en interaction (Emploi des Éléments Finis en Génie Civil), Chap. 7 : Modélisation des ouvrages en zone sismique - propagation d'ondes*, pp.467-562, Hermès, Paris, France.
- [41] Blangy J.P., Strandenes S., Moos D., Nur A. (1993). Ultrasonic velocities in sands-revisited, *Geophysics*, 58(3), pp.344-356.
- [42] Bodet L., van Wijk K., Bitri A., Abraham O., Côte Ph., Grandjean G., Leparoux D. (2005). Surface-wave dispersion inversion limitations from laser-Doppler experiments, *Journal of Environmental and Engineering Geophysics*, 10(2), pp.151-162.
- [43] Bohlen T. (2002). Parallel 3D viscoelastic finite difference seismic modelling, *Computers and Geosciences*, 28, pp.887-899.
- [44] Bommer J.J., Martinez-Pereira A. (1999). The effective duration of earthquake strong motion, *Journal of Earthquake Engineering*, 3, pp.127-172.
- [45] Bonilla L.F., Archuleta R.J., Lavallée D. (2005). Hysteretic and Dilatant Behavior of Cohesionless Soils and Their Effects on Nonlinear Site Response: Field Data Observations and Modeling, *Bulletin of the Seismological Society of America*, 95(6) pp.2373-2395.
- [46] Bonilla F. (2000). *Computation of Linear and Nonlinear Site Response for Near Field Ground Motion*, Ph.D., University of California at Santa Barbara.
- [47] Bonnefoy-Claudet S., Cornou C., Orhnberger M., Wathelet M., Bard P.Y., Cotton F., Fäh D. (2004). H/V ratio and seismic noise wavefield, *Geophysical Research Abstracts*, 6.
- [48] Bonnet M., Frangi A. (2007). *Analyse des solides déformables par la méthodes des éléments finis*, Ecole Polytechnique Editions.
- [49] Bonnet M. (1999). *Boundary integral equation methods for solids and fluids*, Willey, Chichester.
- [50] Bonnet M., Bui H.D. (1993). Regularization of the displacement and traction BIE for 3D elastodynamics using indirect methods, in *Advances in Boundary Element Techniques*, Kane JH, Maier G., Tosaka N. and Atluri SN (eds), Springer-Verlag, Berlin, pp.1-29.
- [51] Bonnet M., Maier G., Polizzotto C. (1998). Symmetric Galerkin boundary element methods, *ASME Applied Mechanics Reviews*, 51(11), pp.669-704.
- [52] Bonnet G., Heitz J.F. (1989). Effets non linéaires en dynamique des sols : essais in situ, *Revue Française de Géotechnique*, 46, pp.19-30.
- [53] Boore D.M. (2005). On pads and filters: processing strong-motion data, *Bulletin of the Seismological Society of America*, 95(2), pp.745-750.

- [54] Boore D.M., Bommer J.J. (2005). Processing of strong-motion accelerograms: needs, options and consequences, *Soil Dynamics and Earthquake Engineering*, 25, pp.93-115.
- [55] Boore D.M. (2004). Can site response be predicted?, *Journal of Earthquake Engineering*, 8(1), pp.1-41.
- [56] Boore D.M. (1972). A note on the effect of simple topography on seismic SH waves, *Bulletin of the Seismological Society of America*, 62, pp.275-284.
- [57] Bouchon M., Campillo M., Gaffet S. (1989). A Boundary Integral Equation-Discrete Wavenumber Representation Method to Study Wave Propagation in Multilayered Media Having Irregular Interfaces, *Geophysics*, 54, pp.1134-1140.
- [58] Bouchon M. (1985). A simple complete numerical solution to the problem of diffraction of SH waves by an irregular surface, *Journal of the Acoustical Society of America*, 77, pp.1-5.
- [59] Bouchon M., Aki K. (1977). Near-field of a seismic source in a layered medium with irregular interfaces, *Geophys. J. R. Astr. Soc.*, 50, pp.669-684.
- [60] Bouchon M. (1973). Effects of topography on surface motion, *Bulletin of the Seismological Society of America*, 63, pp.615-622.
- [61] Bouckovalas G.D., Papadimitriou A.G. (2005). Numerical evaluation of slope topography effects on seismic ground motion, *Soil Dynamics and Earthquake Engineering*, 25(7-10), pp.547-558.
- [62] Bourbié T., Coussy O., Zinszner B. (1987). *Acoustics of porous media*, Technip-Institut Français du Pétrole, Paris, France.
- [63] Bourdeau C., Havenith H.B. (2008). Site effects modelling applied to the slope affected by the Suusamyr earthquake (Kyrgyzstan, 1992), *Engineering Geology*, 97, pp.126-145.
- [64] Bourdeau C. (2005). *Effets de site et mouvements de versant en zones sismiques: apport de la modélisation numérique*, PhD thesis, Ecole Nationale Supérieure des Mines de Paris, France.
- [65] Bourdin B., Luong M.P., Morlier P. (1989). Caractérisation des non linéarités apparues lors des essais de vibrations forcées en centrifugeuse, *Revue Française de Géotechnique*, 47, pp.39-59.
- [66] Boutin C., Roussillon P. (2004). Assessment of the urbanization effect on seismic response, *Bulletin of the Seismological Society of America*, 94(1), pp.251-268.
- [67] Bozzano F., Caserta A., Govoni A., Marra F., Martino S. (2008). Static and dynamic characterization of alluvial deposits in the Tiber River Valley: New data for assessing potential ground motion in the City of Rome, *Journal of Geophysical Research*, 113, B01303.

- [68] Bragov A.M., Lomunov A.K. (1994). Mechanical properties of some polymers and composites at strain rates of 1000/s, *Journal de physique*, 4(8), pp. 337-342.
- [69] Bravo M.A., Sánchez-Sesma F.J., Chávez-García F.J. (1988). Ground motion on stratified alluvial deposits for incident SH waves, *Bulletin of the Seismological Society of America*, 78, pp.436-450.
- [70] Brebbia C.A., Telcs J.C.F., Wrobel L.C. (1984). *Boundary element techniques*, Springer.
- [71] Brennan A.J., Madabhushi S.P.G. (2002). Effectiveness of vertical drains in mitigation of liquefaction, *Soil Dynamics and Earthquake Engineering*, 22(9-12), pp.1059-1065.
- [72] Brennan B.J. (1980). Pulse propagation in media with frequency-dependent Q, *Geophysical Research Letters*, 7, pp.211-213.
- [73] Brothers P.W., Sinclair G.B., Segedin C.M. (1977). Uniform indentation of the elastic half-space by a rigid rectangular punch, *International Journal of Solids and Structures*, 13, pp.1059-1072.
- [74] Bui H.D., Loret B., Bonnet M. (1985). Régularisation des équations intégrales de l'élastostatique et de l'élastodynamique, *Comptes-Rendus Académie des Sciences Paris (II)*, 300, pp.633-636.
- [75] Bui H.D., *Introduction aux problèmes inverses en mécanique des matériaux*, Eyrolles, Paris, 1993.
- [76] Campanella R. G., Stewart W. P. (1992). Seismic cone analysis using digital signal processing for dynamic site characterization, *Canadian Geotechnical Journal*, 29(3), pp.477-486.
- [77] Campillo M. (2006). Phase and correlation in 'random' seismic fields and the reconstruction of the Green function, *Pure appl. geophys.*, 163, pp.475-502.
- [78] Carcione J.M., Kosloff D., Kosloff R. (1988). Wave propagation simulation in a linear viscoelastic medium, *Geophysical Journal International*, 95, pp.597-611.
- [79] Cascante G., Vanderkooy J., Chung W. (2005). A new mathematical model for resonant-column measurements including eddy-current effects, *Canadian Geotechnical Journal*, 42, pp.121-135.
- [80] Chadwick E., Bettess P., Laghrouche O. (1999). Diffraction of short waves modelled using new mapped wave envelope finite and infinite elements, *International Journal for Numerical Methods in Eng.*, 45, pp.335-354.
- [81] Chaillat S., Bonnet M., Semblat J.F. (2009). A new fast multi-domain BEM to model seismic wave propagation and amplification in 3D geological structures, *Geophysical Journal International* (to appear).

- [82] Chaillat S., Bonnet M., Semblat J.F. (2008). A multi-level fast multipole BEM for 3-D elastodynamics in the frequency domain, *Computer Methods in Applied Mechanics and Engineering*, 197, pp.4233-4249.
- [83] Chaillat S. (2008). *Fast multipole method for 3-D elastodynamic boundary integral equations. Application to seismic wave propagation*, PhD thesis, Ecole Nationale des Ponts et Chaussées.
- [84] Chaljub E. (2006). Spectral element modeling of 3D wave propagation in the alpine valley of Grenoble, France, *3rd International Symposium on the Effects of Surface Geology on Seismic Motion*, Grenoble, France.
- [85] Chaljub E., Capdeville Y., Villette J.P. (2003). Solving Elastodynamics in a Fluid-Solid Heterogeneous Sphere: a Parallel Spectral Element Approximation on Non-Conforming Grids, *Jal of Computational Physics*, 187(2), pp.457-491.
- [86] Chammas R., Abraham O., Cote P., Pedersen H.A., Semblat J.F. (2003). Characterization of heterogeneous soils using surface waves: homogenization and numerical modeling, *International Journal of Geomechanics (ASCE)*, 3(1), pp.55-63.
- [87] Chantawarangul K. (1993). *Numerical simulations of three-dimensional granular assemblies*, PhD Thesis, University of Waterloo, Canada.
- [88] Chávez-García F., Raptakis D., Makra K., Pitilakis K. (2002). The importance of the reference station in modelling site effects up to larger frequencies. The case of Euroseistest, *12th European Conference on Earthquake Engineering*, London, United Kingdom.
- [89] Chávez-García F.J., Cardenas-Soto M. (2002). The contribution of the built environment to the "free-field" ground motion in Mexico city, *Soil Dynamics and Earthquake Eng.*, 22, pp.773-780.
- [90] Chávez-García F.J., Raptakis D.G., Makra K., Pitilakis K.D. (2000). Site effects at Euroseistest-II. Results from 2D numerical modelling and comparison with observations, *Soil Dynamics and Earthquake Eng.*, 19(1), pp.23-39.
- [91] Chávez-García F.J., Stephenson W.R., Rodríguez M. (1999). Lateral propagation effects observed at Parkway, New Zealand. A case history to compare 1D vs 2D effects, *Bulletin of the Seismological Society of America*, 89, pp.718-732.
- [92] Chazelas J.L., Abraham O., Semblat J.F. (2001). Identification of Different Seismic Waves Generated by Foundation Vibration in the Centrifuge: Travel Time, Spectral and Numerical Investigations, *Fourth International Conference on Recent Advances in Geotechnical Earthquake Engineering and Soil Dynamics*, San Diego, California, USA.
- [93] Chhab A.G., el Naggar M.H. (2003). Design of efficient base isolation for hammers and presses, *Soil Dynamics and Earthquake Engineering*, 23, pp.127-141.

- [94] Chen J.T., Hong H.K. (1999). Review of dual boundary element methods with emphasis on hypersingular integrals and divergent series, *Applied Mechanics Reviews*, 52(1), pp.17-33.
- [95] Cheney J.A., Brown R.K., Dhat N.R., Hor O.Y.Z. (1990). Modeling free-field conditions in centrifuge models, *Journal of Geotechnical Engineering*, 116(9), pp.1347-1367.
- [96] Chou P.C., Hashemi J., Chou A., Rogers H.C. (1991). Experimentation and finite element simulation of adiabatic shear bands in controlled penetration impact, *International Journal of Impact Engineering*, 11(3), pp.305-321.
- [97] Chow Y.K., Yong D.M., Yong K.Y., Lee S.L. (1990). Monitoring of dynamic compaction by deceleration measurements, *Computers and Geotechnics*, 10, pp.189-209.
- [98] Chow Y.K., Yong D.M., Yong K.Y., Lee S.L. (1992). Dynamic compaction of loose sand deposits, *Soils and Foundations*, 32(4), pp.93-106.
- [99] Chow Y.K., Yong D.M., Yong K.Y., Lee S.L. (1992). Dynamic compaction analysis, *Journal of Geotechnical Engineering (A.S.C.E)*, 118(8), pp.1141-1156.
- [100] Chung R.M., Yokel F.Y., Drnevich V.P. (1984). Evaluation of dynamic properties of sands by resonant column testing, *Geotechnical Testing Journal*, 7(2), pp.60-69.
- [101] Clough R.W., Penzien J. (1993). *Dynamics of structures*, Mc-Graw Hill, New-York, USA.
- [102] Clouteau D., Al-Hussaini T., Degrande G., Hunt H. (2001). Stochastic modelling of traffic induced vibrations, *1st Albert Caquot International Conference*, Paris, France.
- [103] Clouteau D., Aubry D. (2001). Modifications of the ground motion in dense urban areas, *Journal of Computational Acoustics*, 9, pp.1659-1675.
- [104] Clouteau D. (1990). *Propagation d'ondes dans des milieux hétérogènes. Application à la tenue des ouvrages sous séismes*, PhD thesis, Ecole Centrale de Paris, France.
- [105] Coe C.J., Prevost J.H., Scanlan R.H. (1985). Dynamic stress wave reflections/attenuation: earthquake simulation in centrifuge soil models, *Earthquake Engineering and Structural Dynamics*, 13, pp.109-128.
- [106] Cohen G., Joly P., Roberts J.E., Tordjman N. (2001). Higher order triangular finite elements with mass lumping for the wave equation, *SIAM Journal on Numerical Analysis*, 38(6), pp.2047-2078.
- [107] Cohen G., Joly P., Tordjman N. (1994). Higher-order finite elements with mass-lumping for the 1D wave equation, *Finite Elements in Analysis and Design*, 16(3-4), pp.329-336.

- [108] Collino F., Joly P., Millot F. (1997). Fictitious domain method for unsteady problems: application to electromagnetic scattering, *Journal of Computational Physics*, 138(2), pp.907-938.
- [109] Cornou C., Bard P.Y., Dietrich M. (2003). Contribution of dense array analysis to the identification and quantification of basin-edge-induced waves, *Bulletin of the Seismological Society of America*, 93(6), pp.2604-2623.
- [110] Critescu N. (1974). *Dynamic plasticity*, North-Holland.
- [111] Curnier A. (1993). *Méthodes numériques en mécanique des solides*, Presses Polytechniques et Universitaires Romandes, Lausanne, Switzerland.
- [112] Dangla P., Semblat J.F., Xiao H.H., Delépine N. (2005). A Simple and Efficient Regularization Method for 3D BEM: Application to Frequency-Domain Elastodynamics, *Bulletin of the Seismological Society of America*, 95(5), pp. 1916-1927.
- [113] Dangla P. (1988). A plane strain soil-structure interaction model, *Earthquake Engineering and Structural Dynamics*, 16, pp.1115-1128.
- [114] Dangla P. (1989). *Couplage éléments finis équations intégrales en élastodynamique et interaction sol-structure*, PhD Thesis, Ecole Nationale des Ponts et Chaussées, Paris, France.
- [115] Dangla P., Vanhoove J.P. (1988). Transmission des vibrations par les tunnels ferroviaires: validation expérimentale d'un modèle de calcul, *International Conference on Measurements and Testing in Civil Engineering*, Lyon, France.
- [116] Darve E. (2000). The Fast Multipole Method: Numerical Implementation, *Journal of Computational Physics*, 160(1), pp.195-240.
- [117] Das B.M. (1983). *Fundamentals of soil dynamics*, Elsevier, New-York, USA.
- [118] Daubechies I.D. (1992). *Ten lectures on Wavelets*, SIAM.
- [119] Dauksher W., Emery A.F. (1999). An evaluation of the cost effectiveness of Chebyshev spectral and p -finite element solutions to the scalar wave equation, *International Journal for Numerical Methods in Engineering*, 45, pp.1099-1113.
- [120] Dauksher W., Emery A.F. (1999). An evaluation of the cost effectiveness of Chebyshev spectral and p -finite element solutions to the scalar wave equation, *International Journal for Numerical Methods in Engineering*, 45, pp.1099-1113.
- [121] Davies E.D.H., Hunter S.C. (1963). The dynamic compression testing of solids by the method of the split Hopkinson pressure bar, *Journal of Mechanics and Physics of Solid*, 11, pp.155-179.
- [122] Day S.M. (1998). Efficient simulation of constant-Q using coarse-grained memory variables, *Bulletin of the Seismological Society of America*, 88(4), pp.1051-1062, 1998.

- [123] Day S.M., Minster J.B. (1984). Numerical simulation of attenuated wavefields using a Padé approximant method, *Geophysical Journal of the Royal Astron. Society*, 78, pp.105-118.
- [124] Delavaud E. (2007). *Numerical modelling of wave propagation in complex geological media*, PhD Thesis (in French), University Paris VII/Institute of the Physics of the Earth, Paris.
- [125] Delépine N., Bonnet G., Semblat J.F., Lenti L. (2007). A simplified non linear model to analyze site effects in alluvial deposits, *4th International Conference on Earthquake Geotechnical Eng.*, Thessaloniki, Greece.
- [126] Delépine N., Semblat J.F. (2006). Site effects in a deep alpine valley for various seismic sources, *3rd International Symposium on the Effects of Surface Geology on Seismic Motion*, Grenoble, France.
- [127] Deraemaeker A., Babuška I., Bouillard P. (1999). Dispersion and pollution of the FEM solution for the Helmholtz equation in one, two and three dimensions, *International Journal for Numerical Methods in Engineering*, 46, pp.471-499.
- [128] Dobrin M.B., Lawrence P.L., Sengbush R.L. (1954). Surface and near-surface waves in the Delaware basin, *Geophysics*, 19(4), pp.695-715.
- [129] Dobry R., Owczis I., Urzua A. (1976). Simplified procedures for estimating the fundamental period of a soil profile, *Bulletin of the Seismological Society of America*, 66, pp.1293-1321.
- [130] Dormieux L. (1989). Détermination de caractéristiques dynamiques d'un sol à l'aide d'un essai pressiométrique cyclique, *Revue Française de Géotechnique*, 46, pp.31-41.
- [131] Dowding C.H. (1985). *Blast vibration monitoring and control*, Prentice-Hall, 297 p.
- [132] Dravinski M. (2003). Scattering of elastic waves by a general anisotropic basin. Part 2: a 3D model, *Earthquake Engineering and Structural Dynamics* 32, pp.653-670.
- [133] Dravinski M., Mossessian T.K. (1987). Scattering of Plane Harmonic P , SV and Rayleigh Waves by Dipping Layers of Arbitrary Shape, *Bulletin of the Seismological Society of America*, 77, pp.212-235.
- [134] Driad-Lebeau L., Lokmane N., Semblat J.F., Bonnet G. (2009). Local amplification of deep mining induced vibrations, Part 1: Experimental evidence for site effects in a coal basin, *Soil Dynamics and Earthquake Engineering*, 29(1), pp.39-50.
- [135] Drnevich V.P. (1977). Resonant column testing. Problems and solutions, *Symposium on Dynamic Soil and Rock Testing in the Field and Laboratory for Seismic Studies*, ASTM, Denver, USA.
- [136] Drnevich V.P., Richart F.E. (1970). Dynamic prestraining of dry sand, *Journal of the Soil Mechanics and Foundations Division (A.S.C.E.)*, 96, pp.453-469.

- [137] Duval A.M., Méneroud J.P., Vidal S., Bard P.Y. (1998). Relation between curves obtained from microtremor and site effects observed after Caracas 1967 earthquake, *11th European Conference on Earthquake Engineering*, Paris, France.
- [138] Duval A.M. (1996). *Détermination de la réponse d'un site aux séismes à l'aide du bruit de fond. Evaluation expérimentale*, PhD thesis University Paris VI, Etudes et Recherches des LPC, GT62, LCPC, Paris, France.
- [139] Edlinger M.L., P.Gratacos, P.Montmitonnet, E.Felder (1993). Finite element analysis of elastoplastic indentation with a deformable indenter, *European Journal of Mechanics (A/Solids)*, 12(5), pp.679-698.
- [140] Edouard S., Legras B., Lefevre F., Eymard R. (1996). The effect of small-scale inhomogeneities on ozone depletion in the Arctic, *Nature*, 384, pp.444-447.
- [141] Ekqvist T., Wiberg N.E. (2002). Wave propagation related to high-speed train: A scaled boundary FE-approach for unbounded domains, *Computer Methods in Applied Mechanics and Engineering*, 191(36), pp.3947-3964.
- [142] Emmerich H., Korn M. (1987). Incorporation of attenuation into time-domain computations of seismicwave fields, *Geophysics*, 52(9), pp.1252-1264.
- [143] Eringen A.C., Suhubi E.S. (1975). *Elastodynamics (vol. II-linear theory)*, Academic Press.
- [144] Eshraghi H., Dravinski M. (1989). Scattering of plane harmonic SH , SV , P and Rayleigh waves by non-axisymmetric three-dimensional canyons: a wave function expansion approach, *Earthquake Engineering and Structural Dynamics*, 18, pp.983-998.
- [145] Faccioli E., Maggio F., Paolucci R., Quarteroni A. (1997). 2D and 3D elastic wave propagation by a pseudo-spectral domain decomposition method, *Journal of Seismology*, 1, pp.237-251.
- [146] Faccioli E., Maggio F., Quarteroni A., Taghan A. (1996). Spectral-Domain Decomposition Methods for the Solution of Acoustic and Elastic Wave Equations, *Geophysics*, 61, pp.1160-1174.
- [147] Fäh D., Suhadolc P., Mueller St., Panza G.F. (1994). A hybrid method for the estimation of ground motion in sedimentary basins: quantitative modeling for Mexico city, *Bulletin of the Seismological Society of America*, 84(2), pp.383-399.
- [148] Farnbach J.S. (1975). The complex envelope in seismic signal analysis, *Bulletin of the Seismological Society of America*, 65(4), pp.951-962.
- [149] Felice C.W. (1985). *The response of soil to impulse loads using the S.H.P.B technique*, PhD Thesis, University of Utah, Salt Lake City, USA.
- [150] Felice C.W., Gaffney E.S., Brown J.A. (1987). Dynamic high stress experiments on soil, *Geotechnical Testing Journal*, 10(4), pp.192-202.

- [151] Felice C.W., Gaffney E.S., Brown J.A. (1991). Extended split Hopkinson bar analysis for attenuating materials, *Journal of Engineering Mechanics (ASCE)*, 117(5), pp.1119-1135.
- [152] Festa G., Villette J.P., Delavaud E. (2005). Interaction between surface waves and absorbing boundaries for wave propagation in geological basins : 2D numerical simulations, *Geophysical research letters*, 32(20), pp.L20306.1-L20306.4.
- [153] Festa G., Nielsen S. (2003). PML absorbing boundaries, *Bulletin of the Seismological Society of America*, 93(2), pp.891-903.
- [154] Fiala P., Degrande G., Augusztinovicz F. (2007). Numerical modelling of ground-borne noise and vibration in buildings due to surface rail traffic, *Journal of Sound and Vibration*, 301(3-5), pp.718-738.
- [155] Finn L. (2007). Earthquake Engineering in Canada: A Selective Overview, *9th Canadian Conference on Earthquake Engineering*, Ottawa, Canada.
- [156] Flanagan D.P., Belytschko T. (1981). A uniform strain hexahedron and quadrilateral with orthogonal hourglass control, *International Journal for Numerical Methods in Engineering*, 17, pp.679-706.
- [157] Foti S. (2003). Small-strain stiffness and damping ratio of Pisa clay from surface wave tests, *Géotechnique*, 53(5), pp.455-461.
- [158] Foti S. (2000). *Multistation Methods for Geotechnical Characterization using Surface Waves*, PhD thesis, Politecnico di Torino, Italy.
- [159] François S., Pyl L., Masoumi H.R., Degrande G. (2007). The influence of dynamic soil-structure interaction on traffic induced vibrations in buildings, *Soil Dynamics and Earthquake Engineering*, 27(7), pp.655-674.
- [160] Frankel A., Vidale J. (1992). A Three-Dimensional Simulation of Seismic Waves in the Santa Clara Valley, California, from a Loma Prieta Aftershock, *Bulletin of the Seismological Society of America*, 82, pp.2045-2074.
- [161] Fujiwara H. (1998). The fast multipole method for the integral equations of seismic scattering problems, *Geophysical Journal International*, 133, pp.773-782.
- [162] Fujiwara H. (2000). The fast multipole method for solving integral equations of three-dimensional topography and basin problems, *Geophysical Journal International*, 140, pp.198-210.
- [163] Fung Y.C., Tong P. (2001). *Classical and Computational Solid Mechanics*, World Scientific Publishing.
- [164] Fung T.C. (1997). Unconditionally stable higher-order Newmark methods by sub-stepping procedure, *Computer Methods in Applied Mechanics and Engineering*, 147, pp.61-84.

- [165] Futterman W.I. (1962). Dispersive body waves, *Journal of Geophysical Research*, 67(13), pp.5279-5291.
- [166] Gaffet S., Bouchon M. (1989). Effects of two-dimensional topographies using the discrete wavenumber-boundary integral equation method in P-SV cases, *Journal of the Acoustical Society of America*, 85(6), pp.2277-2283.
- [167] Gambin M. (1985). Dix ans de consolidation dynamique, *Annales de l'Institut Technique du Bâtiment et des Travaux Publics (I.T.B.T.P.)*, 433.
- [168] Gao G.Y., Li Z.Y., Qiu Ch., Yue Z.Q. (2006). Three-dimensional analysis of rows of piles as passive barriers for ground vibration isolation, *Soil Dynamics and Earthquake Engineering*, 26, pp.1015-1027.
- [169] Gaul L., Schanz M. (1999). A comparative study of three boundary element approaches to calculate the transient response of viscoelastic solids with unbounded domains, *Computer Methods in Applied Mechanics and Engineering*, 179(1-2), pp.111-123.
- [170] Géli L., Bard P.Y., Jullien B. (1988). The effect of topography on earthquake ground motion: a review and new results, *Bulletin of the Seismological Society of America*, 7, pp.42-63.
- [171] Gélis C., Bonilla L.F., Régnier J., Bertrand E., Duval A.M. (2008). On the use of a Saenger's finite difference stencil to model 2D P-SV nonlinear basin response: application to Nice, France, *Seismic Risk 2008: Earthquake in North-West Europe*, Liege, Belgium.
- [172] Gélis C., Leparoux D., Virieux J., Bitri A., Operto S., Grandjean G. (2005). Detection of underground cavities: dispersion diagram analysis for synthetic finite difference data, *Journal of Environmental and Engineering Geophysics*, 10(2), pp.111-122.
- [173] Gerdes K. (1998). A summary of infinite element formulations for exterior Helmholtz problems. *Computer Methods in Applied Mechanics and Engineering*, 164(1), pp.95-105.
- [174] Gilbert F., Backus G. (1966). Propagator matrices in elastic wave and vibration problems, *Geophysics*, 31, pp.326-332.
- [175] Gil-Zepeda S.A., Montalvo-Arrieta J.C., Vai R., Sánchez-Sesma F.J. (2003). A hybrid indirect boundary element-discrete wave number method applied to simulate the seismic response of stratified alluvial valleys, *Soil Dynamics and Earthquake Engineering*, 23(1), pp.77-86.
- [176] Givoli D. (1992). *Numerical Methods for Problems in infinite domains*, Elsevier.
- [177] Gladwin M.T., Stacey F.D. (1974). Anelastic degradation of acoustic pulses in rock, *Physics of the Earth and Planetary Interiors*, 8, pp.332-336.

- [178] Graves R.W. (1996). Simulating seismic wave propagation in 3D elastic media using staggered-grid finite differences, *Bulletin of the Seismological Society of America*, 86, pp.1091-1106.
- [179] Greengard L., Huang J., Rokhlin V., Wandzura S. (1998). Accelerating fast multipole methods for the Helmholtz equation at low frequencies. *IEEE Comp. Sci. Eng.*, 5(3), pp.32-38.
- [180] Groby J.P., Tsogka C., Virgin A. (2005). Simulation of seismic response in a city-like environment, *Soil Dynamics and Earthquake Engineering*, 25(7-10), pp.487-504.
- [181] Guéguen P., Cornou C., Garambois S., Banton J. (2007). On the limitation of the H/V spectral ratio using seismic noise as an exploration tool: Application to the Grenoble valley (France), a small apex ratio basin, *Pure and Applied Geophysics*, 164(1), pp.115-134.
- [182] Guéguen P., Bard P.Y., Oliveira C.S. (2000). Experimental and Numerical Analysis of Soil Motions Caused by Free Vibrations of a Building Model, *Bulletin of the Seismological Society of America*, 90(6), pp.1464-1479.
- [183] Guelin P., Nowacki W.K. (1984). Remarques sur les ondes d'accélération dans un continu élastoplastique avec hystérésis, *Archiv Mech.*, 36(1), pp.49-66.
- [184] Guiggiani M. (1994). Hypersingular formulation for boundary stress evaluation. *Eng. Analysis Boundary Elements*, 13, pp.169-179.
- [185] Guiggiani M., Krishnasamy G., Rudolphi T.J., Rizzo F.J. (1992). A general algorithm for the numerical solution of hypersingular boundary integral equations, *ASME Journal of Applied Mechanics*, 59, pp.604-614.
- [186] Habib P. (1967). Sur un mode de glissement des massifs rocheux, *Comptes Rendus de l'Académie des Sciences*, t.264, Série A, pp.151-153.
- [187] Hadjian A.H. (2002). Fundamental period and mode shape of layered soil profiles, *Soil Dynamics and Earthquake Engineering*, 22(9-12), pp.885-891.
- [188] Haskell N.A. (1953). The dispersion of surface waves in multi-layered media, *Bulletin of the Seismological Society of America*, 43(1).
- [189] Hansson P.A., Sandberg G. (1997). Mass matrices by minimization of modal errors, *International Journal for Numerical Methods in Engineering*, 40, pp.4259-4271.
- [190] Hardin B.O. (1965). The nature of damping in sands, *Jal of the Soil Mechanics and Foundation Division (ASCE)*, 91(SM1), pp.63-97.
- [191] Hardin B.O., Drnevich V.P. (1972a). Shear modulus and damping in soils : measurement and parameter effects, *Journal of the Soil Mechanics and Foundations Division (A.S.C.E)*, 98, pp.603-624.

- [192] Hardin B.O., Drnevich V.P. (1972b). Shear modulus and damping in soils : design equations and curves, *Journal of the Soil Mechanics and Foundations Division (A.S.C.E)*, 98, pp.667-691.
- [193] Hardy C., Baronet C.N., Tordion G.V. (1971). The elasto-plastic indentation of a half-space by a rigid sphere, *International Journal for Numerical Methods in Engineering*, 3, pp.451-462.
- [194] Hashash Y.M.A., Park D. (2001). Non-linear one-dimensional seismic ground motion propagation in the Mississippi embayment, *Engineering Geology*, 62(1-3), pp.185-206.
- [195] Haskell N.A. (1953). The dispersion of surface waves on multilayered media, *Bulletin of the Seismological Society of America*, 43, pp.17-34.
- [196] Hata S., K.Tateyama (1991). Theoretical approach to impact soil compaction through plastic wave propagation, *Journal of Terramechanics*, 28(4), pp.349-358.
- [197] Haupt W.A. (1977). Surface-waves in non-homogeneous half-space, *Proceedings of DMSR 77*, 1, Karlsruhe, Germany.
- [198] Heierli W. (1962). Inelastic wave propagation in soil columns, *Journal of the Soils Mechanics and Foundations Division (A.S.C.E)*, 88(6), pp.33-63.
- [199] Heitz J.F. (1992). *Propagation d'ondes en milieu non linéaire. Applications au génie parasismique et à la reconnaissance des sols*, PhD Thesis, University Joseph Fourier, Grenoble, France.
- [200] Heuze F., Archuleta R., Bonilla F., Day S., Doroudian M., Elgamal A., Gonzales S., Hoehler M., Lai T., Lavallee D., Lawrence B., Liu P.C. (2004). Estimating site-specific strong earthquake motion, *Soil Dynamics and Earthquake Eng.*, 24, pp.199-223.
- [201] Hisada Y. (1995). An efficient method for computing Green's functions for a layered halfspace with sources and receivers at close depths (Part 2), *Bulletin of the Seismological Society of America*, 85(4), 1080-1093.
- [202] Huang A.B., Ma M.Y., Lee J.S. (1992). A micromechanical study of penetration tests in granular material, *Advances in Micromechanics of Granular Materials* (H.H.Shen), Elsevier.
- [203] Hu N., Guo Z., Katz I.N. (1998). Bounds for eigenvalues and condition numbers in the p -version of the finite element method, *Mathematics of Computation*, 224(67), pp.1423-1450.
- [204] Hughes T.J.R., Reali A., Sangalli G. (2008). Duality and Unified Analysis of Discrete Approximations in Structural Dynamics and Wave Propagation: Comparison of p -method Finite Elements with k -method NURBS, *Computer Methods in Applied Mechanics and Engineering*, 197(49-50), pp.4104-4124.

- [205] Hughes T.J.R. (1987). *Linear static and dynamic finite element analysis*, Prentice-Hall, Englewood Cliffs, New Jersey.
- [206] Humbert P., Fezans G., Dubouchet A., Remaud D. (2005). CESAR-LCPC : A computation software package dedicated to civil engineering uses, *Bulletin des Laboratoires des Ponts et Chaussées*, 256-257, pp.7-37.
- [207] Hunaidi O. (1998). Evolution-based genetic algorithms for analysis of non-destructive surface wave tests on pavements, *NDT & E International*, 31(4), pp.273-280.
- [208] Iai S., Morita T., Kameoka T., Matsumaga Y., Abiko K. (1995). Response of a dense sand deposit during 1993 Kushiro-Oki earthquake, *Soils and Foundations*, 35(1), pp.115-131.
- [209] Idriss I.M., Seed H.B., Serff N. (1974). Seismic response by variable damping finite elements, *Journal of the Geotechnical Engineering Division (ASCE)*, pp.1-13.
- [210] Idriss I.M., Seed H.B. (1967). Response of earth banks during earthquakes, *Journal of the Soil Mechanics and Foundations Division, ASCE*, 93(SM3), pp.61-82.
- [211] Ihlenburg F., Babuška I. (1995). Dispersion analysis and error estimation of Galerkin finite element methods for the Helmholtz equation, *International Journal for Numerical Methods in Engineering*, 38, pp.3745-3774.
- [212] Ishihara K., Towhata I. (1983). Sand response to cyclic rotation of principal stress directions as induced by wave loads, *Soils and Foundations*, 23(4), pp.11-26.
- [213] Jaffard S., Meyer Y., Ryan R.D. (2001). *Wavelets, tools for Science and Technology*, SIAM, 256 p.
- [214] Jennings P.C. (1970). Distant motions from a building vibration test, *Bulletin of the Seismological Society of America*, 60, pp.2037-2043.
- [215] Joly P. (1982). *Les ondes de Rayleigh numériques*, Research Report No.107, INRIA, Rocquencourt, France.
- [216] Jongmans D., Pitilakis K., Demanet D., Raptakis D., Riepl J., Horrent C. (1998). EuroSeistest: determination of the geological structure of the Volvi basin and validation of the basin response, *Bulletin of the Seismological Society of America*, 88, pp.473-87.
- [217] Jongmans D. (1991). Near-source pulse propagation: application to *Q*-determination, *Geophysical prospecting*, 39, pp.943-952.
- [218] Ju S.H., Lin H.T. (2004). Analysis of train-induced vibrations and vibration reduction schemes above and below critical Rayleigh speeds by finite element method, *Soil Dynamics and Earthquake Engineering*, 24, pp.993-1002.

- [219] Jumin P. (1992). Contribution de la pénétration dynamique des pieux à la reconnaissance des sols, application au battage des ancrages et au piézocône, PhD Thesis, University Bordeaux I.
- [220] Karlström A., Boström A. (2007). Efficiency of trenches along railways for trains moving at sub- or supersonic speeds, *Soil Dynamics and Earthquake Engineering*, 27, pp.625-641.
- [221] Kattis S.E., Polyzos D., Beskos D.E. (1999). Modelling of pile wave barriers by effective trenches and their screening effectiveness, *Soil Dynamics and Earthquake Engineering*, 18(1), pp.1-10.
- [222] Kausel E., Assimaki D. (2002). Seismic simulation of inelastic soils via frequency-dependent moduli and damping, *Journal of Engineering Mechanics (ASCE)*, 128(1), 34-47.
- [223] Kausel E. (2006). *Fundamental Solutions in Elastodynamics, A Compendium*, Cambridge University Press, 260 p.
- [224] Kausel E. (2000). The thin-layer method in seismology and earthquake engineering, in *Wave Motion in Earthquake Engineering*, E. Kausel and G. Manolis (Editors), WIT Press, Southampton, UK, pp.193-213.
- [225] Kausel E., Roessel J.M. (1981). Stiffness matrices for layered soils, *Bulletin of the Seismological Society of America*, 71(6), pp.1743-1761.
- [226] Kawase H. (2003). Site effects on strong ground motions, in *International Handbook of Earthquake and Engineering Seismology*, Part B, W.H.K. Lee and H. Kanamori (eds.), Academic Press, London, pp.1013-1030.
- [227] Kawase H., Matsushima S., Graves R.W., Somerville P.G. (2000). Strong motion simulation of Hyogo-ken Nanbu (Kobe) earthquake considering both the heterogeneous rupture process and the 3-D basin structure, *12th World Conference on Earthquake Engineering*, Auckland, New Zealand.
- [228] Kawase H., Sato T. (1992). Simulation analysis of strong motions in the Ashigara valley considering one- and two-dimensional geological structures, *Journal of the Physics of the Earth*, 40, pp.27-56.
- [229] Kawase H., Aki K. (1989). A study on the response of a soft basin for incident S, P and Rayleigh waves with special reference to the long duration observed in Mexico City, *Bulletin of the Seismological Society of America*, 79, pp.1361-1382.
- [230] Kawase H. (1988). Time-domain response of a semicircular canyon for incident SV, P, and Rayleigh waves calculated by the discrete wavenumber boundary element method, *Bulletin of the Seismological Society of America*, 78, pp.1415-1437.
- [231] Kennett B.L.N. (1974). Reflections, rays, and reverberations, *Bulletin of the Seismological Society of America*, 64, pp.1685-1696.

- [232] Kham M., Semblat J.F., Bard P.Y., Dangla P. (2006). Seismic Site-City Interaction: Main Governing Phenomena through Simplified Numerical Models, *Bulletin of the Seismological Society of America*, 96(5), pp.1934-1951.
- [233] Kham M. (2004). *Propagation d'ondes sismiques dans les bassins sédimentaires: des effets de site à l'interaction site-ville*, PhD thesis, Ecole Nationale des Ponts et Chaussées, France.
- [234] Kham M., Semblat J.F., Xiao H.H., Boudin-Romdhane N., Dangla P. (2002a). Numerical modelling of site amplification vs experimental data from Tunisia, *12th European Conference on Earthquake Engineering*, London, UK.
- [235] Kham M., Semblat J.F., Kurose A., Xiao H.H., Dangla P. (2002b). Wave/cavity interaction : analytical and BEM approaches, *12th European Conference on Earthquake Engineering*, London, UK.
- [236] Kim S.M., Liao S.T., Roesset J.M. (1999). Simulation of the cross-hole method in isotropic and anisotropic media, *International Journal for Numerical and Analytical Methods in Geomechanics*, 23, pp.1101-1119.
- [237] Klepaczko J.R., Gary G., Barberis P. (1991). Behaviour of rock salt in uniaxial compression at medium and high strain rates, *Arch. Mechanics*, 43(4), pp.499-517.
- [238] Kjartansson E. (1979). Constant Q wave propagation and attenuation, *Journal of Geophysical Research*, 84, pp.4737-4748.
- [239] Koerner R.M., Lord A.E. Jr, McCabe W.M., Curran J.W. (1976). Acoustic emission behaviour of granular soils, *Journal of the Geotechnical Engineering Division (A.S.C.E)*, 102(7), pp.761-773.
- [240] Kolsky H. (1949). An investigation of the mechanical properties of material at a very high rate of loading, *Proceedings of the Physical Society B*, 60, pp.676-701.
- [241] Kokusho T. (1980). Cyclic triaxial test of dynamic soil properties for wide strain range, *Soils and Foundations*, 20, pp.45-60.
- [242] Komatitsch D., Martin R. (2007). An unsplit convolutional Perfectly Matched Layer improved at grazing incidence for the seismic wave equation, *Geophysics*, 72(5), pp.155-167.
- [243] Komatitsch D., Liu Q., Tromp J., Süss P., Stidham C., Shaw J.H. (2004). Simulations of Ground Motion in the Los Angeles Basin based upon the Spectral-Element Method, *Bulletin of the Seismological Society of America*, 94(1), pp.187-206.
- [244] Komatitsch D., Vilotte J.P., Vai R., Castillo-Covarrubias J.M., Sanchez-Sesma F.J. (1999). The spectral element method for elastic wave equations - Application to 2D and 3D seismic problems, *International Journal for Numerical Methods in Engineering*, 45, pp.1139-1164.

- [245] Komatitsch, D., Vilotte J.P. (1998). The Spectral Element Method: An Efficient Tool to Simulate the Seismic Response of 2D and 3D Geological Structures, *Bulletin of the Seismological Society of America*, 88(2), pp.368-392.
- [246] Komatitsch D., Vilotte J.P. (1996). Simulation of Elastic Wave Propagation in Complex Media Using an Explicit Parallel Spectral Element Method, *American Geophysical Union (AGU) Fall Meeting*, Abstract #S41D-15, San Francisco, USA.
- [247] Kouoh-Bille L., Sánchez-Sesma F.J., Wirgin A. (1991). Réponse résonante d'une montagne cylindrique à une onde sismique SH, *Comptes-Rendus Académie des Sciences Paris*, 312(II), pp.849-854.
- [248] Kramer S.L. (1996). *Geotechnical earthquake engineering*, Prentice-Hall, Englewood Cliff, N.J.
- [249] Kunt M. (1986). *Traitemenr numérique des signaux*, Traité d'électricité, Presses Polytechniques Romandes, pp.293-324.
- [250] Kurose A. (2000). Effets des séismes sur les ouvrages souterrains, PhD thesis, Ecole Polytechnique, Palaiseau, France.
- [251] Kwok A.O., Stewart J.P., Hashash Y.M.A. (2008). Nonlinear ground response analysis of Turkey Flat shallow stiff soil site to strong ground motion, *Bulletin of the Seismological Society of America*, 98(1), pp.331-343.
- [252] Lachat, J.G., and J.O. Watson (1976). Effective numerical treatment of boundary integral equations: a formulation for three-dimensional elastostatics, *International Journal for Numerical Methods in Engineering*, 10, pp.991-1005.
- [253] Lade P.V. (1977). Elasto-plastic stress-strain theory for cohesionless soil with curved yield surfaces, *International Journal of Solids and Structures*, 13, pp.1019-1035.
- [254] Laghrouche (1996). *Simulation numérique de propagations d'ondes dans les sols - Application à l'isolation vibratoire*, PhD thesis, University of Nantes, France.
- [255] Lai C.G., Rix G.J., Foti S., Roma V. (2002). Simultaneous Measurement and Inversion of Surface Wave Dispersion and Attenuation Curves, *Soil Dynamics and Earthquake Engineering*, 22(9-12), pp.923-930.
- [256] Lai C.G. (1998). *Simultaneous inversion of Rayleigh phase velocity and attenuation for near-surface site characterization*, PhD Thesis, Georgia Institute of Technology.
- [257] Lebrun B., Hatzfeld D., Bard P.Y. (2001). Site effects study in urban area: experimental results in Grenoble, *Pure and Applied Geophysics*, 158, pp.2543-2557.
- [258] Lee V.W. (1978). *Displacements near a three-dimensional hemispherical canyon subjected to incident plane waves*, Report No. CE 78-16, University of Southern California, 126 p.

- [259] Lee V.W. (1984). Three-dimensional diffraction of plane P, SV & SH waves by a hemispherical alluvial valley, *Soil Dynamics and Earthquake Engineering*, 3, pp.133-144.
- [260] Lefeuvre-Mesgouez G., Peplow A.T., Le Houédec D., Jones D.V. (1998). Ground vibrations due to high speed moving harmonic load, *12th Engineering Mechanics Conference*, San Diego, 17-20 May.
- [261] Lefeuvre-Mesgouez G., Peplow A.T., Le Houédec D. (2002). Surface vibration due to a sequence of high speed moving harmonic rectangular loads, *Soil Dynamics and Earthquake Engineering*, 22, pp.459-473.
- [262] Le Tallec P. (2007). *Mécanique des milieux continus*, Ecole Polytechnique, Palaiseau, France.
- [263] Liao W.I., Teng T.J., Yeh C.S. (2004). A series solution and numerical technique for wave diffraction by a three-dimensional canyon, *Wave Motion*, 39, pp.129-142.
- [264] Liao S., Sangrey D.A. (1978). Use of piles as isolation barriers, *Journal of the Geotechnical Division (A.S.C.E)*, 104(9), pp.1139-1152.
- [265] Lighthill M.J. (1965). Group velocity, *Journal of the Institute of Mathematics and its Applications*, 1, pp.1-28.
- [266] Liu H.P., Anderson D.L., Kanamori H. (1976). Velocity dispersion due to anelasticity: Implications for seismology and mantle composition, *Geophys. J. R. Astron. Soc.*, 47, pp.41-58.
- [267] Lockner D.A., Walsh J.B., Byerlee J.D. (1977). Changes in seismic velocity and attenuation during deformation of granite, *Journal of Geophysical Research*, 82(33), pp.5374-5378.
- [268] Lokmane N., Bonnet G., Semblat J.F., Driad L. (2003). Seismic loading due to mining : wave amplification and vibration of structures, *Geophysical Research Abstracts (EGS)*, 5, p.14204.
- [269] Lombaert G., Clouteau D., Ishizawa O., Mezher N. (2004). The city-site effect: a fuzzy substructure approach and numerical simulations, *11th International Conference on Soil Dynamics and Earthquake Engineering*, University of California at Berkeley, USA.
- [270] Lombaert G., Degrande G. (2003). The experimental validation of a numerical model for the prediction of the vibrations in the free field produced by road traffic, *Journal of Sound and Vibration*, 262, pp.309-331.
- [271] Lomnitz C. (1957). Linear dissipation in solids, *Journal of Applied Physics*, 28, pp.201-205.

- [272] Loret B., Simões F.M.F., Martins J.A.C. (1997). Growth and decay of acceleration waves in non-associative elastic-plastic fluid-saturated porous media, *International Journal of Solids and Structures*, 34(13), pp.1583-1608.
- [273] Loret B., Luong M.P. (1982). A double deformation mechanism model for sand, *Fourth International Conference on Numerical Methods in Geomechanics*, Edmonton, Canada.
- [274] Lucet N. (1989). *Vitesse et atténuation des ondes élastiques soniques et ultrasoniques dans les roches sous pression de confinement*, PhD Thesis, University Paris VI, 264 p.
- [275] Luong M.P. (1993). Centrifuge tests - A dynamic approach, *Soil Dynamics and Geotechnical Earthquake Engineering*, pp.19-48, Balkema, Rotterdam.
- [276] Luong M.P. (1986). Mesure des propriétés dynamiques des sols, *Revue Française de Géotechnique*, 37, pp.17-28.
- [277] Luong M.P. (1986). Characteristic threshold and infrared vibrothermography of sand, *A.S.T.M Geotechnical Testing Journal*, 9(2).
- [278] Luong M.P. (1980). Stress-strain aspects of cohesionless soils under cyclic and transient loading, *International Symposium on Soils under Cyclic and Transient Loading: Soils under cyclic and transient loading*, Balkema, pp.315-324, Swansea.
- [279] Lysmer J., Waas G. (1972). Shear waves in plane infinite structures, *Journal of Engineering Mechanics Division (ASCE)*, 98(EM1).
- [280] Lysmer J. (1970). Lumped mass method for Rayleigh waves, *Bulletin of the Seismological Society of America*, 60(1), pp.89-104.
- [281] Ma S., Archuleta R.J., Page M.T. (2007). Effects of large-scale surface topography on ground motions, as demonstrated by a study of the San Gabriel mountains, Los Angeles, California, *Bulletin of the Seismological Society of America*, 97(6), pp.2066-2079.
- [282] MacCartor G.D., Wortman W.R. (1990). Analysis of nuclear Salmon free-field ground motion data for non linear attenuation, *Journal of Geophysical Research*, 95(B13), pp.21805-21821.
- [283] Makra K., Chávez-García F.J., Raptakis D., Pitilakis K. (2005). Parametric analysis of the seismic response of a 2D sedimentary valley: implications for code implementations of complex site effects, *Soil Dynamics and Earthquake Engineering*, 25(4), pp.303-315.
- [284] Makra K., Raptakis D., Chávez-García F.J., Pitilakis K. (2002). How important is the detailed knowledge of a 2D soil structure for site response evaluation ?, *12th European Conference on Earthquake Engineering*, London, UK.

- [285] Manolis G.D., Beskos D.E. (1988). *Boundary Element Methods in Elastodynamics*. Unwin-Hyman (Chapman & Hall), London, UK.
- [286] Mari J.L., Glangeaud F., Coppens F. (1999). *Signal processing for geologists and geophysicists*, Technip Ed., Paris, France, 480 p.
- [287] Masoumi H.R., Degrande G., Lombaert G. (2007). Prediction of free field vibrations due to pile driving using a dynamic soil-structure interaction formulation, *Soil Dynamics and Earthquake Engineering*, 27(2), pp.126-143.
- [288] Matasovic N., Vucetic M. (1995). Generalized cyclic-degradation-pore-pressure generation model for clays, *Journal of Geotechnical Engineering (ASCE)*, 121(1), pp.33-42.
- [289] Matsushima S., Kawase H. (2006). Re-Evaluation of Near Source Strong Ground Motion During the 1995 Kobe Earthquake Considering The Heterogeneity of Source and 3-D Basin, *Third International Symposium on the Effects of Surface Geology on Seismic Motion*, Grenoble, France, paper No.141, pp.617-625.
- [290] Mavko G.M. (1979). Frictional attenuation: an inherent amplitude dependence, *Journal of Geophysical Research*, 84(B9), pp.4769-4775.
- [291] Mavroeidis G.P., Papageorgiou A.S. (2003). A mathematical representation of near-fault ground motions, *Bulletin of the Seismological Society of America*, 93(3), pp.1099-1131.
- [292] May T.W., Bolt B.A. (1982). The effectiveness of trenches in reducing seismic motion, *Earthquake Engineering and Structural Dynamics*, 10, pp.195-210.
- [293] Mayne P.W., Jones J.S. Jr (1983). Impact stresses during dynamic compaction, *Journal of Geotechnical Engineering (A.S.C.E)*, 109(10), pp.1342-1346.
- [294] Medina F., Taylor R.L. (1983). Finite element techniques for problems of unbounded domains, *International Journal of Numerical Methods in Engineering*, 19, pp.1209-1226.
- [295] Meek J.W., Wolf J.P. (1992). Cone models for homogeneous soil, *Journal of Geotechnical Engineering (ASCE)*, 118(5), pp.667-685.
- [296] Mellal A., Modaressi H. (1998). A simplified numerical approach for nonlinear dynamic analysis of multilayered media, *11th European Conference on Earthquake Engineering*, Balkema ed., Paris, France.
- [297] Ménard-Soltraitement (2002). *Mesure de vibration lors de travaux de compactage dynamique*, Report by Ménard-Soltraitement and measurements by SEGG on a dynamic compaction site in Huelva (Spain), Nozay, France.
- [298] Ménard L. (1974). La consolidation dynamique des sols de fondation, *Annales de l'ITBTP*, 320, pp.194-222.

- [299] Mestat P. (1993). *Lois de comportement des géomatériaux et modélisation par la méthode des éléments finis*, Etudes et recherches des laboratoires des ponts et chaussées, Série Géotechnique GT.52, Laboratoire Central des Ponts et Chaussées, Paris, France.
- [300] Meunier J. (1974). *Contribution à l'étude des ondes et des ondes de choc dans les sols*, PhD Thesis, University of Grenoble, France.
- [301] Meza-Fajardo K.C., Papageorgiou A.S. (2008). A Nonconvolutional, Split-Field, Perfectly Matched Layer for Wave Propagation in Isotropic and Anisotropic Elastic Media: Stability Analysis, *Bulletin of the Seismological Society of America*, 98(4), pp.1811-1836.
- [302] Mikhailenko B.G. (1999). Spectral Laguerre method for the approximate solution of time dependent problems, *Applied Math. Letters*, 12, pp.105-110.
- [303] Mizutami H., Geller R.J., Takeuchi N. (2000). Comparison of accuracy and efficiency of time-domain schemes for calculating synthetic seismograms, *Physics of the Earth and Planetary Interiors*, 119, pp.75-97.
- [304] Moczo P., Kristek J., Halada L. (2004). *The Finite Difference Method for seismologists: an introduction* (SPICE project), 150 p., Comenius University, Bratislava, Slovakia.
- [305] Moczo P., Kristek J., Vavrycuk V., Archuleta R.J., Halada L. (2002). 3D Heterogeneous Staggered-Grid Finite-Difference Modeling of Seismic Motion with Volume Harmonic and Arithmetic Averaging of Elastic Moduli and Densities, *Bulletin of the Seismological Society of America*, 92(8), pp.3042-3066.
- [306] Moczo P., Bard P.Y. (1993). Wave diffraction, amplification and differential motion near strong lateral discontinuities, *Bulletin of the Seismological Society of America*, 83, pp.85-106.
- [307] Modaressi M., Benzenati I. (1992). An absorbing boundary element for dynamic analysis of two-phase media, *10th World Conference on Earthquake Engineering*, Madrid, pp.1157-1163.
- [308] Moeen-Vaziri N., Trifunac M.D. (1988). Scattering and diffraction of plane SH-waves by two-dimensional inhomogeneities, *Soil Dynamics and Earthquake Engineering*, 7(4), pp.179-200.
- [309] Moeen-Vaziri N., Trifunac M.D. (1985). Scattering of plane SH-waves by cylindrical canals of arbitrary shape, *Soil Dynamics and Earthquake Engineering*, 4(1), pp.18-23.
- [310] Molenkamp F., Kay S. (1997). Comparison of convergence of 8-node and 15-node elements, *Int. Symposium on Numerical Models in Geomechanics (NUMOG)*, 415-419, Montréal, Canada.

- [311] Morlet J., Grossmann A. (1984). Decomposition of Hardy functions into square integrable wavelets of constant shape, *S.I.A.M Journal Math. Anal.*, 15, pp.723-736.
- [312] Mossessian T.K., Dravinski M. (1990). Amplification of elastic waves by a three dimensional valley, *Earthquake Engineering and Structural Dynamics*, 19, pp.681-691.
- [313] Müller G. (1983). Rheological properties and velocity dispersion of a medium with power-law dependence of Q on frequency, *Journal of Geophysics*, 54(1), pp.20-29.
- [314] el Naggar M.H., Novak M. (1994). Non-linear model for dynamic axial pile response, *Journal of Geotechnical Engineering (A.S.C.E)*, 120(2), pp.308-329.
- [315] Nagy G., Murakami H., Hegemier G.A., Florence A.L., Experimental and analytical study of the dynamic response of low-porosity brittle rocks, *Journal of Geophysical Research*, 98(B12), pp.22081-22094, 1993.
- [316] Ng C.W.W., Li X.S., Van Laak P.A., Hou D.Y.J. (2004). Centrifuge modeling of loose fill embankment subjected to uni-axial and bi-axial earthquakes, *Soil Dynamics and Earthquake Engineering*, 24(4), pp.305-318.
- [317] Nguyen T.L., Semblat J.F., Reiffsteck P., Lenti L. (2008). Anisotropic Velocity and Attenuation for Shear Waves in a Layered Soil by Resonant Column Tests, *Seismological Research Letters*, 79(2).
- [318] Nigbor R.L., Imai T. (1994). The suspension P-S velocity logging method, in *Geophysical Characterization of Sites*, ISSMFE, R.D. Woods ed., Balkema.
- [319] Nishimura N. (2002). Fast multipole accelerated boundary integral equation methods, *Applied Mechanics Reviews*, 55, pp.299-324.
- [320] Niu Z.R., Zhou H.L. (2004). The natural boundary integral equation in potential problems and regularization of the hypersingular integral, *Computers and Structures*, 82, pp.315-323.
- [321] Nowacki W.K. (1978). *Stress waves in non elastic solids*, Pergamon Press.
- [322] Nowacki W.K., Raniecki B. (1987). Theoretical analysis of dynamic compacting of soil around a spherical source of explosion, *Archiv. Mechanics*, 39(4), pp.359-384.
- [323] Pao, Y.H., Mow C.C. (1973). *Diffraction of elastic waves and dynamic stress concentrations*, Crane, Russak & Company Inc.
- [324] Paolucci R., Mostabilini L. (2006). Non-dimensional site amplification functions for basin edge effects on seismic ground motion, *Third International Symposium on the Effects of Surface Geology on Seismic Motion (ESG)*, Grenoble, France.
- [325] Paolucci R., Spinelli D. (2006). Ground motion induced by train passage, *Journal of Engineering Mechanics*, 132(2), pp.201-210.

- [326] Paolucci R., Maffei A., Scandella L., Stupazzini M., Vanini M. (2003). Numerical prediction of low-frequency ground vibrations induced by high-speed trains at Ledsgaard, Sweden, *Soil Dynamics and Earthquake Engineering*, 23, pp.425-433.
- [327] Paolucci R. (2002). Amplification of earthquake ground motion by steep topographic irregularities, *Earthquake Engineering and Structural Dynamics*, 31, pp.1831-1853.
- [328] Paolucci R. (1999). Shear resonance frequencies of alluvial valleys by Rayleigh's method, *Earthquake Spectra*, 15, pp.503-521.
- [329] Papageorgiou A.S., Kim J. (1991). Study of the propagation and amplification of seismic waves in Caracas Valley with reference to the 29 July 1967 earthquake: SH waves, *Bulletin of the Seismological Society of America*, 81, pp.2214-2233.
- [330] Patera A.T. (1984). A spectral element method for fluid dynamics: laminar flow in a channel expansion, *Journal of Computational Physics*, 54, pp.468-488.
- [331] Pecker A. (2008). *Dynamique des structures et des ouvrages*, Ecole Nationale des Ponts et Chaussées, 220 p. (<http://www.enpc.fr/>).
- [332] Pecker A. (2005). Maximum ground surface motion in probabilistic seismic hazard analyses, *Journal of Earthquake Engineering*, 9(1), pp.187-211.
- [333] Pecker A. (1984). *Soil dynamics* (in French), Presses de l'Ecole Nationale des Ponts et Chaussées, Paris, France, 259 pp.
- [334] Pecker A., Dupas J.M. (1981). Etude expérimentale du comportement d'une vase sous chargement cyclique, *Revue Française de Géotechnique*, 5.
- [335] Pedersen H.A., Campillo M., Sánchez-Sesma F.J. (1995). Azimuth dependent wave amplification in alluvial valleys, *Soil Dynamics and Earthquake Engineering*, 14(4), pp.289-300.
- [336] Phillips E. (1869). De l'équilibre des solides élastiques, *Comptes Rendus de l'Académie des Sciences*, tome 68, Paris, France.
- [337] Piau M. (1975). Ondes d'accélération dans les milieux élastoplastiques viscoplastiques, *Journal de Mécanique*, 14(1).
- [338] Pietzsch D., Poppy W. (1992). Simulation of soil compaction with vibratory rollers, *Journal of Terramechanics*, 29(6), pp.585-597.
- [339] Pitarka A.S., Takenaka H., Suetsugu D. (1994). Modeling strong motion in the Ashigara Valley for the 1990 Odawara, Japan, earthquake, *Bulletin of the Seismological Society of America*, 84(5), pp.1327-1335.
- [340] Pitilakis K.D., Raptakis D., Lontzetidis K., Tika-Vassilikou Th., Jongmans D. (1999a). Geotechnical and geophysical description of EURO-SEISTEST using field, laboratory tests and moderate strong-motion recordings, *Journal of Earthquake Engineering*, 3, pp.381-409.

- [341] Pitilakis K.D., Raptakis D.G., Makra K.A. (1999b). Site effects : recent considerations and design provisions, *2nd International Conference on Earthquake Geotechnical Engineering*, Lisbon, Balkema ed, pp.901-912.
- [342] Poran C.J., Heh K.S., Rodriguez J.A. (1992). Impact behavior of sand, *Soils and Foundations*, 32(4), pp.81-92.
- [343] Pousset G., Bonilla L.F., Cotton F., Margerin L. (2006). Nonstationary Stochastic Simulation of Strong Ground Motion Time Histories Including Natural Variability: Application to the K-Net Japanese Database, *Bulletin of the Seismological Society of America*, 96(6), pp.2103-2117.
- [344] Prevost J.H. (1985). A simple plasticity theory for frictional cohesionless soils, *Soil Dynamics and Earthquake Engineering*, 4(1), pp.9-17.
- [345] Pyke R. (1979). Nonlinear soil models for irregular cyclic loadings, *Journal of the Geotechnical Engineering Division (A.S.C.E)*, 105(6), pp.715-726.
- [346] Raptakis D.G., Chávez-García F.J., Makra K., Pitilakis K.D. (2000). Site effects at Euroseistest-I. Determination of the valley structure and confrontation of observations with 1D analysis, *Soil Dynamics and Earthquake Engineering*, 19(1), pp.1-22.
- [347] Reddy J.N. (2004). *An Introduction to Nonlinear Finite Element Analysis*, Oxford University Press, Oxford, UK, 488 p.
- [348] Reinoso E., Wrobel L.C., Power H. (1997). Three-dimensional scattering of seismic waves from topographical structures, *Soil Dynamics and Earthquake Engineering*, 16, pp.41-61.
- [349] Richart F.E., Woods R.D., Hall J.R. (1970). *Vibrations of soils and foundations*, Prentice-Hall.
- [350] Ricker N. (1943). Further developments in the wavelet theory of seismogram structure, *Bulletin of the Seismological Society of America*, 33(3), pp.197-228.
- [351] Ricker N. (1953). The form and laws of propagation of seismic wavelets, *Geophysics*, 18, pp.10-40.
- [352] Riepl J., Bard P.Y., Hatzfeld D., Papaioannou, Nechstein S. (1998). Detailed evaluation of site response estimation methods across and along the sedimentary valley of Volvi (EuroSeistest), *Bulletin of the Seismological Society of America*, 88, pp.488-502.
- [353] Rivière J. (1983). *Interaction sol-structure lors d'un séisme ; simulation en centrifugeuse*, PhD Thesis, University Bordeaux I, France.
- [354] Rocher-Lacoste F., Lenti L., Lasseret M., Saule R. (2007). Comparative vibration behaviour of vibratory and impact driven prefabricated concrete piles, *8th Int. Conference on the Application of Stress-Wave Theory to Piles*, Lisbon, Portugal.

- [355] Rodríguez-Zúñiga J.L., Sánchez-Sesma F.J., Pérez-Rocha L.E. (1995). Seismic response of shallow alluvial valleys: the use of simplified models, *Bulletin of the Seismological Society of America*, 85(3), pp.890-899.
- [356] Rovelli A., Scognamiglio L., Marra F., Caserta A. (2001). Edge-Diffracted 1-Sec Surface Waves Observed in a Small-Size Intramountain Basin (Colfiorito, Central Italy), *Bulletin of the Seismological Society of America*, 91(6), pp.1851-1866.
- [357] Ryan H. (1994). Ricker, Ormsby, Klauder, Butterworth - A choice of wavelets, *Canadian Society of Exploration Geophysicists Recorder*, 19(7), pp.8-9.
- [358] Sabetta F., Pugliese A. (1996). Estimation of response spectra and simulation of nonstationary earthquake ground motions, *Bulletin of the Seismological Society of America*, 86(2), pp.337-352.
- [359] Sadd M.H., Qiu Lun, Boardman W.G., Shukla A. (1992). Modelling wave propagation in granular media using elastic networks, *International Journal of Rock Mechanics and Mining Science*, 29(2), pp.161-170.
- [360] Saenger E.H., Gold N., Shapiro S.A. (2000). Modeling the propagation of elastic waves using a modified finite-difference grid, *Wave Motion*, 31, 77-92.
- [361] Salençon J., *Handbook of continuum mechanics: general concepts, thermoelasticity*, Springer, 2001.
- [362] Sánchez-Sesma F.J., Vai R., Dretta E., Palencia V.J. (2000). Fundamentals of elastic wave propagation for site amplification studies, *Wave Motion in Earthquake Engineering*, E. Kausel and G. Manolis (Editors), WIT Press, Southampton, UK, pp.1-36.
- [363] Sánchez-Sesma F.J., Luzón F. (1995). Seismic Response of Three-Dimensional Alluvial Valleys for Incident P, S and Rayleigh Waves, *Bulletin of the Seismological Society of America*, 85, pp.269-284.
- [364] Sánchez-Sesma F.J., Ramos-Martínez J., Campillo M. (1993). An indirect boundary element method applied to simulate the seismic response of alluvial valleys for incident P, S and Rayleigh waves, *Earthquake Engineering and Structural Dynamics*, 22, pp.279-295.
- [365] Sánchez-Sesma F.J., Campillo M. (1991). Diffraction of P, SV Rayleigh waves by topographic features: a boundary integral formulation, *Bulletin of the Seismological Society of America*, 81, pp.2234-2253.
- [366] Sánchez-Sesma F.J., Velazquez S.A. (1987). On the seismic response of a dipping layer, *Wave Motion*, 9(5), pp.387-391.
- [367] Sánchez-Sesma F.J. (1985). Diffraction of elastic SH waves by wedges, *Bulletin of the Seismological Society of America*, 75(5), pp.1435-1446.

- [368] Sánchez-Sesma F.J. (1983). Diffraction of elastic waves by three-dimensional surface irregularities, *Bulletin of the Seismological Society of America*, 73(6), pp.1621-1636.
- [369] Sánchez-Sesma F.J., Rosenblueth E. (1979). Ground motion at canyons of arbitrary shape under incident SH waves, *Earthquake Engineering and Structural Dynamics*, 7, pp.441-450.
- [370] Saxena S.K., Reddy K.R. (1989). Dynamic moduli and damping ratios for Monterey n°0 sand by resonant column tests, *Soils and Foundations*, 29, pp.37-51.
- [371] Schanz M., Antes H. (1997). A new visco- and elastodynamic time domain boundary element formulation, *Computational Mechanics*, 20(5), pp.452-459.
- [372] Scherbaum F. (2006). *Of Poles and Zeros: Fundamentals of Digital Seismology*, Springer, 280 p.
- [373] Scherbaum F., Palme C., Langer H. (1994). Model parameter optimization for site-dependent simulation of ground motion by simulated annealing: re-evaluation of the Ashigara valley prediction experiment, *Natural Hazards*, 10(3), pp.275-296.
- [374] Schnabel P.B., Lysmer J., Seed H.B. (1972). *SHAKE: A computer program for earthquake response analysis of horizontally-layered sites*, Report No. EERC-72/12, Earthquake Engineering Research Center, University of California at Berkeley, Berkeley, CA, USA.
- [375] Schofield R. (2004). Seismic measurements at the Stateline Wind Project and a prediction of the seismic signal that the proposed Maiden Wind Project would produce at LIGO. LIGO-T020104-00-Z LIGO Project, <http://www.ligo.caltech.edu/docs/T/T020104-00.pdf>.
- [376] Schwab F., Knopoff L. (1970). Surface-wave dispersion computations, *Bulletin of the Seismological Society of America*, 60, pp.321-344.
- [377] Scott R.A., Pearce R.W. (1975). Soil compaction by impact, *Géotechnique*, 25(1), pp.19-30.
- [378] Seed H.B., Wong R.T., Idriss I.M., Tokimatsu K. (1986). Moduli and damping factors for dynamic analyses of cohesionless soils, *Journal of Geotechnical Engineering*, 112(11), pp.1016-1032.
- [379] Seed H.B. (1974). *Landslides during earthquakes due to soil liquefaction*, Terzaghi Lectures, American Society of Civil Engineers, pp.193-261, New-York.
- [380] Segol G., Lee P.C.Y., Abel J.F. (1978). Amplitude reduction of surface waves by trenches, *Journal of the Engineering Mechanics Division (A.S.C.E)*, 104(3), pp.621-641.

- [381] Semblat J.F., Kham M., Bard P.Y. (2008). Seismic wave propagation in alluvial basins and influence of site-city interaction, *Bulletin of the Seismological Society of America*, 98(6), pp. 2665-2678.
- [382] Semblat J.F., Leroy Y. (2007). *Sismologie et Tectonique*, Ecole Polytechnique, Palaiseau, France (<http://www.polytechnique.fr/>).
- [383] Semblat J.F., Dangla P. (2005). Modeling wave propagation and soil-structure interaction: Finite element and boundary element approaches, *Bulletin des Laboratoires des Ponts et Chaussées*, 256-257, pp.163-178.
- [384] Semblat J.F., Kham M., Parara E., Bard P.Y., Pitilakis K., Makra K., Raptakis D. (2005). Site effects: basin geometry vs soil layering, *Soil Dynamics and Earthquake Engineering*, 25(7-10), pp.529-538.
- [385] Semblat J.F., Paolucci R., Duval A.M. (2003a). Simplified vibratory characterization of alluvial basins, *Comptes-Rendus Geoscience*, 335(4), pp.365-370.
- [386] Semblat J.F., Duval A.M., Dangla P. (2003b). Modal superposition method for the analysis of seismic wave amplification, *Bulletin of the Seismological Society of America*, 93(3), pp.1144-1153.
- [387] Semblat J.F., Dangla P., Kham M., Duval A.M. (2002a). Seismic site effects for shallow and deep alluvial basins: in-depth motion and focusing effect, *Soil Dynamics and Earthquake Engineering*, 22(9-12), pp.849-854.
- [388] Semblat J.F., Duval A.M., Dangla P. (2002b). Seismic Site Effects in a Deep Alluvial Basin: Numerical Analysis by the boundary element method, *Computers and Geotechnics*, 29(7), pp. 573-585.
- [389] Semblat J.F., Brioist J.J. (2001). Higher order finite elements for 1D and 2D analysis of numerical wave dispersion, *10th International Conference on Computer Methods and Advances in Geomechanics (IACMAG)*, Tucson, USA.
- [390] Semblat J.F., Duval A.M., Dangla P. (2000). Numerical analysis of seismic wave amplification in Nice (France) and comparisons with experiments, *Soil Dynamics and Earthquake Engineering*, 19(5), pp.347-362.
- [391] Semblat J.F., Brioist J.J. (2000). Efficiency of higher order finite elements for the analysis of seismic wave propagation, *Journal of Sound and Vibration*, 231(2), pp.460-467.
- [392] Semblat J.F., Luong M.P., Gary G. (1999). 3D-Hopkinson bar : new experiments for dynamic testing on soils, *Soils and Foundations*, 39(1), pp.1-10.
- [393] Semblat J.F., Luong M.P. (1998). Wave propagation through soils in centrifuge experiments, *Journal of Earthquake Engineering*, 2(1), pp.147-171.
- [394] Semblat J.F. (1998). Amortissement et dispersion des ondes : points de vue physique et numérique, *Revue Française de Génie Civil*, 2(1), pp.91-111.

- [395] Semblat J.F., Brioist J.J. (1998). Wave propagation in non-homogeneousuly damped medium: numerical vs expcrmental approach, *11th European Conference on Earthquake Engineering*, Paris, France.
- [396] Semblat J.F. (1997). Rheological interpretation of Rayleigh damping, *Journal of Sound and Vibration*, 206(5), pp.741-744.
- [397] Semblat J.F. (1995). *Sols sous sollicitations dynamiques et transitoires : réponse dynamique aux barres de Hopkinson, propagation d'ondes en milieu centrifugé*, Rapport Etudes et Recherches des Laboratoires des Ponts et Chaussées, GT60, 206 p., LCPC, Paris, France.
- [398] Semblat J.F. (1989). *Précontrainte des sols et sollicitations dynamiques*, Master thesis, ENTPE, Vaulx-en-Velin, France.
- [399] Sessarego J.P., Sageloli J., Degoul P., Flandrin P., Zakharia M. (1990). Analyse temps-fréquence de signaux en milieux dispersifs. Application à l'étude des ondes de Lamb, *Journal d'Acoustique*, 3, pp.273-280.
- [400] Sextos A.G., Pitilakis K.D., Kappos A.J. (2003). Inelastic dynamic analysis of RC bridges accounting for spatial variability of ground motion, site effects and soil-structure interaction phenomena. Part 1: Methodology and analytical tools, *Earthquake Engineering & Structural Dynamics*, 32(4), pp.607-627.
- [401] Shen H.H., Satake M., Mehrabadi M., Chang C.S., Campbell C.S. (1992). Advances in micromechanics of granular materials, *Proceedings of the second US/Japan seminar on micromechanics of granular materials*, Elsevier, 461 p.
- [402] Sheng X., Jones C.J.C., Thompson D.J. (2006). Prediction of ground vibration from trains using the wavenumber finite and boundary element methods, *Journal of Sound and Vibration*, 293, pp.575-586.
- [403] Shibusawa S., Oida A. (1992a). Transient load test system for evaluating dynamic soil behavior hierarchies by differences in the period of motion, *Journal of Teramechanics*, 29(2), pp.161-171.
- [404] Shibusawa S., Oida A. (1992b). Dependency of observation parameters on soil dynamic parameters in unconfined impact compression tests, *Journal of Teramechanics*, 29(3), pp.289-306.
- [405] Shukla A., Damania C. (1987). Experimental investigation of wave velocity and dynamic contact stresses in an assembly of disks, *Journal of Experimental Mechanics*, 27(3), pp.268-281.
- [406] Shukla A., Zhu C.Y., Xu Y. (1992). Dynamic stresses in granular assemblies with microstructural defects, *Journal of Engineering Mechanics (ASCE)*, 118(1), pp.190-201.
- [407] Sieffert J.G., Tison L., Thiel G. (1990). Recherche d'un critère d'efficacité en cours de pilonnage intensif, *Revue Française de Géotechnique*, 51, pp.61-67.

- [408] Sinclair G.B., Follansbec P.S., Johnson K.L. (1985). Quasi-static normal indentation of an elasto-plastic half-space by a rigid sphere (II. Results), *International Journal of Solids and Structures*, 21(8), pp.865-888.
- [409] Singh S.K., Mena E., Castro R. (1988). Some aspects of source characteristics of the 19 September 1985 Michoacan earthquake and ground motion amplification in and near Mexico City from strong motion data, *Bulletin of the Seismological Society of America*, 78(2), pp. 451-477.
- [410] Skipp B.O. (1997). Ground vibration-codes and standards, *Proceedings of the Conference on Ground Dynamics and Man-made processes*, Institution of Civil Engineers, London, UK.
- [411] Skipp B.O. ed. (1966). *Vibration in civil engineering*, Symposium of the International Association for Earthquake Engincering (London 1965), Butterworths, London, UK.
- [412] Skoglund G.R., Marcuson W.F., Cunny R.W. (1976). Evaluation of resonant column test devices, *Journal of Geotechnical Engineering Division (ASCE)*, 102(GT11).
- [413] Sladek V., Sladek J., Tanaka M. (2001). Numerical integration of logarithmic and nearly logarithmic singularity in BEMs, *Applied Mathematical Modelling*, 25, pp.901-922.
- [414] Sladek V., Sladek J. (1998). Singular integrals and boundary elements, *Computer Methods in Applied Mechanics and Engineering*, 157, pp.251-266.
- [415] Sladek V., Sladek J., Tanaka M. (1997). Evaluation of $1/r$ integrals in BEM formulations for 3-D problems using coordinate multitransformations, *Engineering Analysis with Boundary Elements*, 20, pp.229-244.
- [416] Sloan S.W., Randolph F.M. (1982). Numerical prediction of collapse loads using Finite element methods, *International Journal for Numerical and Analytical Methods in Geomechanics*, 6, pp.47-76.
- [417] Sommerville P.G. (1998). Emerging art: earthquake ground motion, *ASCE Geotechnical Special Publications*, Dakoulas et al eds, 1, pp.1-38.
- [418] Sorrentino S., Fasana A. (2007). Finite element analysis of vibrating linear systems with fractional derivative viscoelastic models, *Journal of Sound and Vibration*, 299, pp.839-853.
- [419] Stephenson R.W. (1978). Ultrasonic testing for determining dynamic soil moduli, *Dynamic Geotechnical Testing*, American Society for Testing and Materials (ASTM STP 654), pp.179-195.
- [420] Stewart J.R., Hughes T.J.R. (1998). A tutorial in elementary finite element error analysis: a systematic presentation of a priori and a posteriori error es-timates, *Computer Methods in Applied Mechanics and Engineering*, 158, pp.1-22.

- [421] Stewart R.R., Toksöz M.N., Timur A. (1983). Strain dependent attenuation: observations and a proposed mechanism, *Journal of Geophysical Research*, 88(B1), pp.546-554.
- [422] Stokoe K.H., Nazarian S. (1985). Use of Rayleigh waves in liquefaction studies, in *Measurement and use of Shear Wave Velocity for Evaluating Dynamic Soil Properties (ASCE)*, R.D. Woods ed., New York, USA, pp.1-17.
- [423] Stokoe K.H., Hoar R.J. (1978). Variable affecting in situ seismic measurements, *Proceedings of the Conference on Earthquake Engineering and Soil Dynamics*, ASCE, Pasadena, USA.
- [424] Stoll R.D. (1979). Experimental studies of attenuation in sediments, *Journal of the Acoustical Society of America*, 66(4), pp.1152-1160.
- [425] Studman C.J., Moore M.A., Jones S.E. (1977). On the correlation of indentation experiments, *Journal of Physics (D: Applied Physics)*, 10, pp.949-956.
- [426] Stupazzini M., *A Spectral element approach for 3D dynamic soil-structure interaction problems*, PhD Thesis, Politecnico di Milano, 2004.
- [427] Takahashi A., Takemura J. (2005). Liquefaction-induced large displacement of pile-supported wharf, *Soil Dynamics and Earthquake Engineering*, 25, 11, pp.811-825.
- [428] Takahashi T., Nishimura N., Kobayashi S. (2003). A fast BIEM for three-dimensional elastodynamics in time domain, *Engineering Analysis with Boundary Elements*, 27, pp.491-506.
- [429] Tanaka M., Sladek V., Sladek J. (1994). Regularization Techniques Applied to Boundary Element Methods. *Applied Mechanics Reviews*, 47, pp.457-499.
- [430] Tarantola A. (1987). *Inverse Problem Theory*, Elsevier, Amsterdam.
- [431] Taylor P.W., Larkin T.J. (1978). Seismic site response of nonlinear soil media, *Journal of the Geotechnical Engineering Division (A.S.C.E.)*, 104(3), pp.369-393.
- [432] Taylor T., Fragaszy R.J., Ho C.L. (1991). Projectile penetration in granular soils, *Journal of Geotechnical Engineering (A.S.C.E.)*, 117(4), pp.658-672.
- [433] Theodoulidis N.P., Bard P.Y. (1995). Horizontal to vertical spectral ratio and geological conditions: an analysis of strong motion data from Greece and Taiwan (SMART-1), *Soil Dynamics and Earthquake Engineering*, 14(3), pp.177-197.
- [434] Thomson W.T. (1950). Transmission of elastic waves through a stratified solid medium, *Journal of Applied Physics*, 21, pp.89-93.
- [435] Transvib, (2006). *International Symposium on Vibratory pile driving and deep soil vibratory compaction*, H. Gonin, A. Holeyman, F. Rocher-Lacoste eds, LCPC, Paris, France.

- [436] Trbolet J.M. (1977). A new phase unwrapping algorithm, *IEEE Transactions on Acoustics, Speech and Signal Processing*, 25(2), pp.170-177.
- [437] Trifunac M.D., Brady A.G. (1975). On the correlation of seismic intensity scales with the peaks of recorded strong ground motion, *Bulletin of the Seismological Society of America*, 65(1).
- [438] Trifunac M.D. (1973). Scattering of plane SH waves by a semi-cylindrical canyon, *Int. Journal of Earthquake Engineering and Structural Dynamics*, 1, pp.267-281.
- [439] Tsogka C., Virgin A. (2003). Seismic response of a set of blocks partially embedded in soft soil, *Comptes-Rendus Mecanique*, 331(3), 217-224.
- [440] Towhata I. (2008). *Geotechnical Earthquake Engineering*, Springer, 684 p.
- [441] Tubach J.P. (1989). Analyse spectrale de la parole, in *La parole et son traitement automatique*, Masson Ed., Paris, France, pp.265-301.
- [442] Uetake T., Kudo K. (2005). Assessment of Site Effects on Seismic Motion in Ashigara Valley, Japan, *Bulletin of the Seismological Society of America*, 95(6), pp.2297-2317.
- [443] Ulrych T.J. (1971). Application of homomorphic deconvolution to seismology, *Geophysics*, 36(4), pp.650-660.
- [444] Veyera G.E., Ross C.A. (1995). High strain rate testing of unsaturated sands using a S.H.P.B., *Third International Conference on Recent Advances in Geotechnical Earthquake Engineering and Soil Dynamics*, St-Louis, USA.
- [445] Virieux J. (1986). P-SV Wave Propagation in Heterogeneous Media: Velocity-Stress Finite-Difference Method, *Geophysics*, 51, pp.889-901.
- [446] Wathelet M., Jongmans D., Ohrnberger M. (2004). Surface wave inversion using a direct search algorithm and its application to ambient vibration measurements, *Near Surface Geophysics*, 2, pp.211-221.
- [447] Whitman R.V. (1957). The behaviour of soils under transient loadings, *Proceedings of the 4th International Conference on Soil Mechanics and Foundation Engineering*, vol.I, p.207, London, UK.
- [448] Virgin A., Bard P-Y. (1996). Effects of buildings on the duration and amplitude of ground motion in Mexico city, *Bulletin of the Seismological Society of America*, 86, pp.914-920.
- [449] Wolf J.P. (2003). *The scaled boundary finite element method*, Wiley, Chichester, UK.
- [450] Wood W.L., Bossak M., Zienkiewicz O.C. (1981). An Alpha modification of Newmark's method, *International Journal for Numerical Methods in Engineering*, 15, pp.1562-1566.

- [451] Woods R.D. (1978). Measurement of dynamic soils properties, *Proceedings of the Conference on Earthquake Engineering and Soil Dynamics*, ASCE, Pasadena, USA.
- [452] Woods R.D., Barnett N.E., Sagesser R. (1974). Holography-A new tool for soil dynamics, *Journal of the Geotechnical Engineering Division (A.S.C.E)*, 100(11), pp.1231-1247.
- [453] Woods R.D. (1968). *Screening of surface waves in soils*, Technical report IP-804, University of Michigan, USA, 57 p.
- [454] Yerli H.R., Temel B., Kiral E. (1999). Multi-wave transient and harmonic infinite elements for two-dimensional unbounded domain problems, *Computers and Geotechnics*, 24(3), pp.185-206.
- [455] Yokoi T. (2003). The higher order Born approximation applied to improve the solution of seismic response of a three-dimensional canyon by the Indirect Boundary Method, *Physics of the Earth and Planetary Interior*, 137, pp.97-106.
- [456] Yoo T.S., Selig E.T. (1979). Dynamics of vibratory-roller compaction, *Journal of the Geotechnical Engineering Division (A.S.C.E)*, 105(10), pp.1211-1231.
- [457] Yoshimura C., Bielak J., Hisada Y., Fernández A. (2003). Domain Reduction Method for Three-Dimensional Earthquake Modeling in Localized Regions, Part II: Verification and Applications, *Bulletin of the Seismological Society of America*, 93(2), pp.825-840.
- [458] Zahradník J., Moczo P., Hron F. (1994). Blind prediction of the site effects at Ashigara valley, Japan, and its comparison with reality, *Natural Hazards*, 10(1-2), pp.149-170.
- [459] Zhao H., Gary G., Klepaczko J.R. (1997). On the use of a viscoelastic split Hopkinson pressure bar, *International Journal of Impact Engineering*, 19(4), pp.319-330.
- [460] Zhao J.X. (1996). Estimating modal parameters for a simple soft-soil site having a linear distribution of shear wave velocity with depth, *Earthquake Engineering and Structural Dynamics*, 25(2), pp.163-178.
- [461] Zienkiewicz O.C., Taylor R.L. (2005). *The Finite Element Method for Solid and Structural Mechanics*, Elsevier Butterworth-Heinemann, 631 p.
- [462] Zienkiewicz O.C., Bando K., Bettess P., Emson C., Chiam T.C. (1985). Mapped infinite elements for exterior wave problems, *International Journal for Numerical Methods in Engineering*, 21(7), pp.1229-1251.

Index

Index

- Absorbing boundaries
 - absorbing layers (PML), 289, 291, 292
 - Domain Reduction Methods, 297
 - filtering PML, 292, 293
 - infinite elements, 286–289
 - local absorbing condition (1D), 70, 283
 - local absorbing condition (2D), 284, 285
 - multidirectional PML, 293–295
- Anisotropy, 137
- Attenuation, 79, 83, 91, 92, 125, 277, 293, 386
 - Attenuation factor, 86, 125, 197, 204, 258
- Beam vibrations
 - cone models, 120
 - eigenmodes (axial), 62
 - eigenmodes (torsion), 73
 - normal force, 68
 - Principle of Virtual Work, 53
- Blast
 - Hopkinson bar tests, 103
 - mines (in), 33
 - quarries (in), 34
- Boundary Element Method
 - examples, 344, 348, 383, 397
 - Fast Multipole Method, 306
 - FEM/BEM coupling, 296
 - formulation, 298
 - frequency domain, 298
 - fundamental solutions, 299
 - integral equation, 299
 - integral representation, 299
 - introduction, 240
 - radiation conditions, 303
 - regularization, 301
 - time domain, 308
- unbounded media, 302
- validation, 304
- Causality, 77
- Centrifuge experiments
 - dynamic loading, 192
 - general, 190
 - geometrical damping, 197
 - numerical model, 204
 - scaling factors, 188, 189
 - simplified attenuation, 197
 - viscoelastic models, 197
 - viscoelastic simulations, 199
- Cepstrum, 449, 451
- Compaction
 - dynamic, 24
 - vibratory, 28
- Complex modulus, 257
- Cone models, 119
- Constitutive equation, 59, 72, 75, 112, 133, 137, 247
- Creep function, 77, 82
- Cross hole, 230, 234, 235
- Cross-correlation, 233, 448
- Cyclic tests, 122
- Damping
 - Caughey, 275
 - damping profiles, 279
 - damping ratio, 94, 95, 101, 126, 275, 276
 - fractional derivatives, 278
 - frequency band-width, 101, 126
 - geometrical, 76, 175, 197, 199
 - logarithmic decrement, 101, 125, 126
 - material, 76, 197, 199, 277

- Rayleigh, 275, 276, 278
 Discrete Wavenumber Method, 240
 Dispersion (wave)
 centrifuge experiments (in), 207
 dispersion curve, 213, 220, 222, 223
 group velocity, 87
 Love waves, 208, 209, 214
 NCQ model, 93
 phase velocity, 87
 Rayleigh waves, 216, 217
 rheology (due to), 87, 258
 Down hole, 227
 Duration, 445, 446
 Eigenfrequencies
 1D heterogeneous soil, 117, 209, 213
 2D basins, 378, 379
 alluvial basins, 357
 resonant bar, 122
 resonant column, 99
 Eigenmodes
 1D axial (bars), 63
 1D heterogeneous soil, 116, 117, 214, 374
 1D torsion (bars), 74
 alluvial basins, 359
 resonant column, 99, 100
 Equilibrium
 1D medium, 57
 3D (displacements), 134
 3D medium, 133
 Filtering
 examples, 207, 440
 filters, 433, 439
 homomorphic, 206, 451–455
 Finite Difference Method, 240
 Finite Element Method
 α -HHT method, 254
 average acceleration method, 254
 Caughey damping, 275
 central difference method, 253, 254, 264
 critical frequency, 254
 Domain Reduction Methods, 297
 equation of motion, 252
 FEM/BEM coupling, 296
 higher order elements, 256, 260, 269, 272, 273
 infinite elements, 286
 introduction, 240
 isoparametric element, 251
 linear acceleration method, 254
 mass matrix, 264, 268, 269
 multistep methods, 254
 Newmark method, 253
 numerical anisotropy, 275
 numerical damping, 255, 258, 275, 281
 numerical dispersion, 257–260, 262, 264, 265, 270, 273, 275
 quadrilateral element, 249, 252, 262
 Rayleigh damping, 275, 276, 278
 reference element, 251
 shape functions, 248–250
 spatial discretization, 248, 253
 stability conditions, 254
 time discretization, 253
 time steps, 264
 time-integration schemes, 253
 triangular element, 252, 262
 weak formulation, 247
 Fourier transform, 78, 84, 140, 183, 200, 219, 235, 433, 435–438
 Galerkin method, 248
 Gradient, 419
 Group velocity, 87
 Heterogeneous soil profile, 112, 214, 374
 Hilbert transform, 440, 441, 449
 Hopkinson bars
 3D device, 108
 axial strain, 107
 axial stress, 107
 experimental device, 104
 radial stress, 110
 strain in specimen, 107
 stress in specimen, 108
 wave reflection, 69, 104
 Isolation (vibration)

- efficiency, 45, 314, 317
 holes (by), 314–317
 identical two-layers case, 171
 interface wave, 168
 multilayered case, 168
 numerical simulations, 44
 optimal layer thickness, 157
 piles (by), 314, 318, 319
 single layer (*P*), 160
 single layer (*SH*), 154, 159
 single layer (*SV*), 165
 trains (for), 46
 transmission (multilayered), 169, 172
 transmission coefficient (*P*), 163
 transmission coefficient (*SH*), 156, 158, 160
 transmission coefficient (*SV*), 167
 trenches (by), 42, 313, 318, 320
 Kolsky test, 123
 Lamé constants, 133
 Laplacian, 419
 Loading history, 77
 Maxwell-Betti theorem, 298
 Modulus
 complex, 78, 81
 relaxed, 79
 resonant column (from), 99
 unrelaxed, 79
 Nuisances (vibrations), 20, 32, 33, 37, 39
 Oedometric test, 103, 108, 110
 Particle velocity, 23, 27, 28, 35, 37, 62, 107
 Peak Ground motion, 444
 Phase velocity, 86, 87, 207
 Pile driving
 dynamic pile driving, 21
 longitudinal waves, 64
 vibratory pile driving, 22
 wave reflection, 21, 23, 65
 Plane waves in a surface layer
 SH-waves, 180
 eigenfrequencies, 184
 transfer function, 183, 184, 186
 Plane waves in half-space
 P – *SV* case, 177
 SH case, 176
 Plastic waves, 123
 Polarization, 139–143
 Principle of Virtual Work
 general, 54, 131, 247, 298
 rate of work (external forces), 56, 132
 rate of work (internal forces), 54–56, 132
 rate of work (quantities of acceleration), 57, 132
 Quality factor
 constant Q model, 91
 definitions, 125
 example, 354
 Hardin's law, 279
 nearly constant Q model, 92
 rheology (from), 79, 81, 83
 rise time, 124
 Saxena's law, 279
 spectral ratio, 124
 Stewart's law, 280
 Reflection-refraction at an interface
 P-wave, 147, 150
 SH-wave, 144, 145
 SV-wave, 152
 amplification, 323
 critical incidence, 147, 150, 152, 225
 equation of continuity, 144, 149
 heterogeneous bar, 68
 Hopkinson bars, 104
 interface wave, 147, 150, 152
 plane waves, 142
 Relaxation function, 77, 82
 Resonant column
 actual test, 99
 damping, 101
 equivalent linear model, 94
 experimental results, 102
 principles, 97

specimen motion, 98
 wave equation, 98
Ricker wavelet
 original, 241
 simplified, 243
Scattering
 cylindrical cavity, 308
 spherical cavity, 309–311
Seismic cone, 229
Seismic refraction, 224
Shocks
 dynamic compaction, 24–26
 Hopkinson bar tests, 103
Site effects
 2D aggravation factor, 366, 388, 406
 2D resonance, 358, 360
 Ashigara valley, 324
 Caracas basin, 325
 Caracas topography, 348
 circular canyons, 342
 Civita di Bagnoregio, 350–352
 cylindrical basin, 361, 363, 364
 dipping layer, 352–355
 elliptical basin, 365
 experimental characterization, 327
 Grenoble basin, 324
 Kobe basin, 50
 Las Colinas (landslide), 353
 Los Angeles basin, 324
 Mexico basin, 324
 moon-valley model, 372, 373
 Nice basin, 376, 380, 382, 384, 387
 rectangular basin, 356–358
 reference station, 381, 394, 403
 semi-ellipsoidal basin, 372
 semi-spherical basin, 367–371
 semi-spherical canyon, 344
 shape ratio, 358, 360, 361, 365
 sine-shaped (3D), 369, 370
 spectral amplification, 330
 time-domain amplification, 330
 topography (2D), 334
 topography (crest), 336
 topography (hill), 338

topography aggravation factor, 336, 339, 356
 transfer function, 328
 triangular canyons, 340–342
 Volvi basin, 366, 393, 394, 396–398, 400, 406
 wall-layer model, 355
Site-city interaction, 413, 414, 416
Snell-Descartes law, 144, 149, 152, 159, 162, 225
Soil-structure interaction, 119
Spectral Analysis of Surface Waves, 208, 218
Spectral Element Method, 240, 255, 349
Spectrum
 amplitude, 433
 complex, 433
 Fourier, 433
 phase, 433
 Standard spectral ratio, 328, 380, 381
Steady State Rayleigh Method, 218
Strain level, 19, 102, 103, 126, 128
Strain rate, 21, 26, 103, 108, 110, 112
Strong formulation, 246
Super-seismic, 41
Surface waves
 dispersion, 208, 214, 216, 218
 Love, 208, 210, 214
 Love waves, 179
 Rayleigh, 43, 177, 178, 216
Suspension logging, 227
Tensors, 419
Time discretization, 248
Traffic
 double-M loading, 243
 moving loads, 40
 railways, 39
 road, 36, 38
Transfer function, 183–187, 328, 329, 333, 382
Transmittivity
 multilayered case, 168
 single layer (P), 160
 single layer (SH), 154, 159

single layer (SV), 165
Wave vector, 140
Wave velocity
 V_P/V_S ratio, 135
 1D longitudinal waves, 60, 138
 anisotropic medium, 137
 estimation, 447
 heterogeneous soil, 113
 pressure waves, 104, 107, 135
Rayleigh, 178
 shear waves, 72, 76, 98, 135, 154, 185
 typical values, 60, 72, 136
Wave-structure interaction, 410
Wavefield
 P -waves, 135, 139, 195, 245
 S -waves, 135, 245
 SH -waves, 139
 SV -waves, 139
 body waves, 135
 displacements, 143
 monochromatic waves, 140
 plane waves, 138
 polarization, 139–143
Rayleigh, 179
 spherical, 138, 174, 193, 197, 198
 surface waves, 140
 uncoupled, 134, 142
Wavelength, 43, 99, 126, 157, 158, 218, 220, 261, 264
Wavelets
 double-M, 243, 432
 Gabor, 424
 Generalized Rayleigh wavelet, 426
 Küpper, 427
 Mavroeidis & Papageorgiou, 425
 Meyer, 430, 431
 Morlet, 429, 430
 Ormsby, 428
 Ricker (damped pulse), 241, 242
 Ricker (simplified), 243, 421–423, 436
 triangular, 88
Wavenumber
 complex, 85
 dispersion, 87
Weak formulation, 247
Wind turbines, 31

specimen motion, 98
 wave equation, 98
Ricker wavelet
 original, 241
 simplified, 243
Scattering
 cylindrical cavity, 308
 spherical cavity, 309–311
Seismic cone, 229
Seismic refraction, 224
Shocks
 dynamic compaction, 24–26
 Hopkinson bar tests, 103
Site effects
 2D aggravation factor, 366, 388, 406
 2D resonance, 358, 360
 Ashigara valley, 324
 Caracas basin, 325
 Caracas topography, 348
 circular canyons, 342
 Civita di Bagnoregio, 350–352
 cylindrical basin, 361, 363, 364
 dipping layer, 352–355
 elliptical basin, 365
 experimental characterization, 327
 Grenoble basin, 324
 Kobe basin, 50
 Las Colinas (landslide), 353
 Los Angeles basin, 324
 Mexico basin, 324
 moon-valley model, 372, 373
 Nice basin, 376, 380, 382–384, 387
 rectangular basin, 356–358
 reference station, 381, 394, 403
 semi-ellipsoidal basin, 372
 semi-spherical basin, 367–371
 semi-spherical canyon, 344
 shape ratio, 358, 360, 361, 365
 sine-shaped (3D), 369, 370
 spectral amplification, 330
 time-domain amplification, 330
 topography (2D), 334
 topography (crest), 336
 topography (hill), 338

topography aggravation factor, 336, 339, 356
 transfer function, 328
 triangular canyons, 340–342
 Volvi basin, 366, 393, 394, 396–398, 400, 406
 wall-layer model, 355
Site-city interaction, 413, 414, 416
Snell-Descartes law, 144, 149, 152, 159, 162, 225
Soil-structure interaction, 119
Spectral Analysis of Surface Waves, 208, 218
Spectral Element Method, 240, 255, 349
Spectrum
 amplitude, 433
 complex, 433
 Fourier, 433
 phase, 433
 Standard spectral ratio, 328, 380, 381
Steady State Rayleigh Method, 218
Strain level, 19, 102, 103, 126, 128
Strain rate, 21, 26, 103, 108, 110, 112
Strong formulation, 246
Super-seismic, 41
Surface waves
 dispersion, 208, 214, 216, 218
 Love, 208, 210, 214
 Love waves, 179
 Rayleigh, 43, 177, 178, 216
Suspension logging, 227
Tensors, 419
Time discretization, 248
Traffic
 double-M loading, 243
 moving loads, 40
 railways, 39
 road, 36, 38
Transfer function, 183–187, 328, 329, 333, 382
Transmittivity
 multilayered case, 168
 single layer (P), 160
 single layer (SH), 154, 159

single layer (SV), 165
Wave vector, 140
Wave velocity
 V_P/V_S ratio, 135
 1D longitudinal waves, 60, 138
 anisotropic medium, 137
 estimation, 447
 heterogeneous soil, 113
 pressure waves, 104, 107, 135
 Rayleigh, 178
 shear waves, 72, 76, 98, 135, 154, 185
 typical values, 60, 72, 136
Wave-structure interaction, 410
Wavfield
 P -waves, 135, 139, 195, 245
 S -waves, 135, 245
 SH -waves, 139
 SV -waves, 139
 body waves, 135
 displacements, 143
 monochromatic waves, 140
 plane waves, 138
 polarization, 139–143
 Rayleigh, 179
 spherical, 138, 174, 193, 197, 198
 surface waves, 140
 uncoupled, 134, 142
Wavelength, 43, 99, 126, 157, 158, 218, 220, 261, 264
Wavelets
 double-M, 243, 432
 Gabor, 424
 Generalized Rayleigh wavelet, 426
 Küpper, 427
 Mavroeidis & Papageorgiou, 425
 Meyer, 430, 431
 Morlet, 429, 430
 Ormsby, 428
 Ricker (damped pulse), 241, 242
 Ricker (simplified), 243, 421–423, 436
 triangular, 88
Wavenumber
 complex, 85
 dispersion, 87
Weak formulation, 247
Wind turbines, 31